2013

QCD
and
High Energy Interactions

Sponsored by

. CNRS (Centre National de la Recherche Scientifique)
. IN2P3 (Institut National de Physique Nucléaire et de Physique des Particules)
. NSF (National Science Foundation)
. FNRS (Fond National de la Recherche Scientifique)
. BSP (Belgian Science Policy)

XLVIIIth Rencontres de Moriond
La Thuile, Aosta Valley, Italy – March 9-16, 2013

2013 QCD and High Energy Interactions

© Published by ARISF, 2013

ISBN : 978-2-9546400-1-3

web

All rights reserved. This book, or parts thereof, may not be reproduced in any form or by any means, electronic or mechanical, including photocopying, recording or any information storage and retrieval system now known or to be invented, without written permission from the publisher.

Proceedings of the XLVIIIth RENCONTRES DE MORIOND

QCD and High Energy Interactions

La Thuile, Aosta Valley Italy *March 9-16, 2013*

2013

QCD and High Energy Interactions

edited by

Etienne Augé,

Jacques Dumarchez

and

Jean Trân Thanh Vân

The XLVIIIth Rencontres de Moriond

2013 QCD and High Energy Interactions

was organized by :

Etienne Augé (IN2P3, Paris)
Jacques Dumarchez (LPNHE, Paris)

with the active collaboration of :

E. Berger (A.N.L. Argonne)
S. Bethke (M.P.I. Munich)
A. Capella (L.P.T. Orsay)
A. Czarnecki (U. Alberta)
D. Denegri (C.E.A. Saclay)
N. Glover (Durham)
B. Klima (Fermilab)
M. Krawczyk (University of Warsaw)
L. McLerran (Brookhaven Nat. Lab.)
B. Pietrzyk (L.A.P.P. Annecy)
L. Schoeffel (CEA - IRFU/SPP - Saclay)
Chung-I Tan (Brown University)
J. Trân Thanh Vân (L.P.T. Orsay)
U. Wiedemann (CERN)

2013 RENCONTRES DE MORIOND

The XLVIIIth Rencontres de Moriond were held in La Thuile, Valle d'Aosta, Italy.

The first meeting took place at Moriond in the French Alps in 1966. There, experimental as well as theoretical physicists not only shared their scientific preoccupations, but also the household chores. The participants in the first meeting were mainly french physicists interested in electromagnetic interactions. In subsequent years, a session on high energy strong interactions was added.

The main purpose of these meetings is to discuss recent developments in contemporary physics and also to promote effective collaboration between experimentalists and theorists in the field of elementary particle physics. By bringing together a relatively small number of participants, the meeting helps develop better human relations as well as more thorough and detailed discussion of the contributions.

Our wish to develop and to experiment with new channels of communication and dialogue, which was the driving force behind the original Moriond meetings, led us to organize a parallel meeting of biologists on Cell Differentiation (1980) and to create the Moriond Astrophysics Meeting (1981). In the same spirit, we started a new series on Condensed Matter physics in January 1994. Meetings between biologists, astrophysicists, condensed matter physicists and high energy physicists are organized to study how the progress in one field can lead to new developments in the others. We trust that these conferences and lively discussions will lead to new analytical methods and new mathematical languages.

The XLVIIIth Rencontres de Moriond in 2013 comprised three physics sessions:

- March 2 - 9: "Electroweak Interactions and Unified Theories"
- March 9 - 16: "QCD and High Energy Hadronic Interactions"
- March 9 - 16: "Very High Energy Phenomena in the Universe"

We thank the organizers of the XLVIIIth Rencontres de Moriond:

- A. Abada, E. Armengaud, J. Conrad, S. Davidson, P. Fayet, J.-M. Frère, P. Hernandez, L. Iconomidou-Fayard, P. Janot, M. Knecht, J. P. Lees, S. Loucatos, F. Montanet, L. Okun, J. Orloff, A. Pich, S. Pokorski, D. Wood for the "Electroweak Interactions and Unified Theories" session,

- E. Augé, E. Berger, S. Bethke, A. Capella, A. Czarnecki, D. Denegri, N. Glover, B. Klima, M. Krawczyk, L. McLerran, B. Pietrzyk, L. Schoeffel, Chung-I Tan, J. Trân Thanh Vân, U. Wiedemann for the "QCD and High Energy Hadronic Interactions" session,

- Jean-Luc Atteia, Fabien Cavalier, Alessandro de Angelis, Jacques Dumarchez, Fabrice Feinstein, Yannick Giraud-Héraud, Christophe Magneville, Günther Sigl, for the "Very High Energy Phenomena in the Universe" session

and the conference secretariat and technical staff:

V. de Sá-Varanda and C. Bareille, I. Cossin, G. Dreneau, D. Fligiel, N. Ribet, S. Vydelingum.

We are also grateful to Francesco Cante, Ida Liseno, Elisabetta Cicchi, Roberta Musio and the Planibel Hotel staff who contributed through their hospitality and cooperation to the well-being of the participants, enabling them to work in a relaxed atmosphere.

The Rencontres were sponsored by the Centre National de la Recherche Scientifique, the Institut National de Physique Nucléaire et de Physique des Particules (IN2P3-CNRS), the Fonds de la Recherche Scientifique (FRS-FNRS), the Belgium Science Policy and the National Science Foundation. We would like to express our thanks for their encouraging support.

It is our sincere hope that a fruitful exchange and an efficient collaboration between the physicists and the astrophysicists will arise from these Rencontres as from previous ones.

E. Augé, J. Dumarchez and J. Trân Thanh Vân

Contents

1. Higgs

Study of Higgs production in the bosonic decay channels at ATLAS	E. Mountricha	3
Study of the Higgs Production in bosonic decays channels with the CMS detector	C. Ochando	7
Search for Standard Model Scalar Boson Decaying to Fermions at the LHC	D. Puigh	11
Measurements of Higgs boson properties in ATLAS	T. Adye	15
Higgs Candidate Property Measurements with the Compact Muon Solenoid	A. Whitbeck	21
Composite or elementary? Probing the nature of the Higgs	A. Kamińska	27
Determination of Higgs Spin and Parity at the LHC	M. Mühlleitner	31
Efficient, Automatic and Accurate QCD predictions for Higgs (and alike) production at the LHC	M. Zaro	35
Higgs couplings after Moriond	B. Dumont	41
The global electroweak Standard Model fit after the Higgs discovery	M. Baak	45
LHC Beam Operations: Past, Present and Future	M. Kuhn	55

2. New Phenomena

Searches for BSM Higgs Bosons at the LHC	M. Boehler	63
2HDM confronting LHC data	R. Santos	67
Invariants and flavour in the general two-Higgs doublet model	M. Rebelo	71
Third generation SUSY searches at the LHC	A. Favareto	75
SUSY Searches for Inclusive Squark and Gluino Production at the LHC	A. Mann	81
NLO calculations with GOSAM	G. Luisoni	85
SUSY Searches for Electroweak Production of Gauginos and Sleptons at the LHC	P. Everaerts	91
Searches for Heavy Resonances at the LHC	S. Harper	97
Do current LHC data really pose a problem for constrained SUSY?	L. Roszkowski	103

3. Heavy Flavour

Heavy flavour production at ATLAS and CMS	E. Bouhova-Thacker	109
Measurement of heavy-flavor properties at CMS and ATLAS	R. Covarelli	113
Measurement of γ Angle Using $B \to DK$ at LHCb	W. Qian	119
Indirect CP violation in the B_s^0 system at LHCb	W. Hulsbergen	123
Searches for New Physics in Bottom Hadron Decays at the Tevatron	S. Leo	127
Measurements of direct CP violation in charm decays at LHCb	S. Stahl	131
Constraints on new physics from rare (semi-)leptonic B decays	D. Straub	135
B and C spectroscopy at LHCb	G. Manca	139
Lattice computation of $B \to D^*$, $D^{**}\ell\nu$ form factors at finite heavy masses	M. Atoui	143
Charmonium study at BESIII	C. Ji	149
Recent results on bottomonium(-like) states at Belle	P. Krokovny	155
Baryon production in B decays and e^+e^- collisions	U. Tamponi	159
Time reversal violation for entangled neutral mesons	J. Bernabéu	165

4. Top

Top quark mass measurements at the TeVatron	G. Petrillo	173
Top quark production at the LHC	M. Aoki	179
Measurements of Top Quark Properties at the TeVatron	D. Orbaker	183
Measurements of Top Quark properties at the LHC	E. Yazgan	187
Measuring top-quark polarization in top-pair + missing energy events	H. Zhang	191
Single Top Quark Physics at the TeVatron	C. Schwanenberger	195

5. Heavy Ion

Heavy-ion session: a (quick) introduction	B. Hippolyte	201
Azimuthal Anisotropy from STAR Experiment	Y. Pandit	207
Search for chiral magnetic effects in au+au collisions at STAR	H. Ke	211
Propagation of nonlinear gauge theory and corresponding phenomenology in deconfined strong interaction matter	S.-Y. Li	215
Flow phenomena in CMS	Q. Wang	219
Flow phenomena in ATLAS	A. Andreazza	223
The Double Ridge Phenomenon in p–Pb Collisions Measured with ALICE	J. F. Grosse-Oetringhaus	229
Long-range angular correlations by strong color fields in hadronic collisions	K. Dusling	231
Jet Results in pp and Pb-Pb Collisions at ALICE	O. Busch	235
Hard probes with ATLAS	I. Grabowska-Bold	239
Hard Probes in CMS	Y. Mao	243
Jet tomography of AA-collisions at RHIC and LHC energies	B. Zakharov	247
From jet quenching to wave turbulence	E. Iancu	251
PHENIX Results on J/ψ and ψ' from d+Au collisions and implications for cold nuclear matter	X. He	257
Heavy flavor and dilepton production in STAR experiment	J. Bielcik	261
Open heavy–flavour and quarkonium measurements with ALICE at the LHC	F. Fionda	265
Diffraction and ultraperipheral collisions at ALICE	E. Kryshen	269

6. Low Energy

Recent results on hadron physics at KLOE	P. Moskal	275
Study of the rare decay $K^{\pm} \to \pi^{\pm}\gamma\gamma$ in the NA48/2 and NA62 experiments at CERN	M. Piccini	279
$\tau^- \to \pi^-\eta^{(\prime)}\nu_\tau$ decays	P. Roig	283
Hadronic Cross Section Measurements with ISR and the Implications on $g_\mu - 2$	K. Griessinger	287

7. QCD

Latest jets results from the LHC	K. Rabbertz	293
Theoretical developments in jet physics at hadron colliders	J. Pires	297
Pileup Subtraction for Jet Shapes	J. Kim	301
Nonperturbative corrections and showering in NLO-matched event generators	F. Hautmann	305
QCD resummation in the framework of supersymmetry	B. Fuks	309
Combining higher-order resummation with multiple nlo calculations and parton showers in the Geneva Monte Carlo framework	S. Alioli	313
Photon production at the LHC	R. Lafaye	317
QCD in 2D Flux Tube	A. Koshelkin	323
Asymptotic high-energy behavior of hadronic total cross sections from Lattice QCD	E. Meggiolaro	327
W/Z+Jets and W/Z+HF Production at the Tevatron	S. Camarda	331
Vector boson production in association with jets and heavy flavor quarks at the LHC	K. Theofilatos	335
Diboson production cross section at LHC	V. Lombardo	339
WZ and W+jets production at large transverse momenta beyond NLO	S. Sapeta	343

8. Structure, Function, Diffraction

Structure Functions and PDF determination at HERA	R. Plačakytė	349
Progress in the NNPDF global analysis	C. Deans	353
Towards an unbiased determination of parton distributions with QED corrections	S. Carrazza	357
Vector Meson Production From Gauge/Gravity Duality	M. Djuric	361
Diffraction at HERA	R. Polifka	365
New Model for Hadroproduction tested with DIS at HERA	A. Bylinkin	369
One-loop multi-leg calculations in gauge theories: the Golem library	M. S. Zidi	373

9. Summary Talks

Experimental Summary	D. Denisov	379
Theoretical Summary	M. Mangano	407

List of participants 419

1.
Higgs

STUDY OF HIGGS PRODUCTION IN THE BOSONIC DECAY CHANNELS AT ATLAS

E. MOUNTRICHA
On behalf of the ATLAS Collaboration
Brookhaven National Laboratory, Department of Physics, Upton, NY, United States

The latest results on the studies of the Higgs production in the bosonic decay channels at ATLAS are reported, involving the $H \to \gamma\gamma$, $H \to ZZ^{(*)}$, $H \to WW^{(*)}$ and $H \to Z\gamma$ decay channels. The full 2011 and 2012 LHC data samples have been used corresponding to 4.6-4.8fb^{-1} at $\sqrt{s} = 7$TeV and 20.7 fb^{-1} at $\sqrt{s} = 8$TeV, respectively.

1 Introduction

In summer 2012 the ATLAS and CMS collaborations announced the discovery of a Higgs-like boson [1,2]. Since then, the LHC Run I has been completed and the full data samples have been analyzed. The new particle's properties (mass, spin/parity, couplings) have been studied. In the following, the updated results on the signal strength and mass are presented, complemented with the studies on the properties of the new particle.

2 Updated results in the $H \to \gamma\gamma$ channel and properties measurement

$H \to \gamma\gamma$ is a high mass resolution channel with the simple topology of two high E_{T} isolated photons. The signal-background discriminating variable is the di-photon invariant mass, $m_{\gamma\gamma}$, (Figure 1 (left)) with an expected resolution of 1.77 GeV [3]. The signal-over-background (S/B) ratio is ~3% in the mass region around $m_H = 125$ GeV containing 90% of the expected signal. The background processes are the irreducible di-photon continuum and events with jets misidentified as photons. To increase the sensitivity due to the different mass resolution and S/B ratio, and to separate the different production modes (gluon fusion (ggF), vector boson fusion (VBF) and associated production (VH)), 14 categories are used [3]. The excess observed at ~126.5 GeV is quantified by the p_0 probability (Figure 1 (center)). The observed significance is 7.4σ, while the expected one is $4.1\,\sigma$.

In Figure 1 (right) the best fit value of m_H and signal strength (μ), defined as the ratio of the observed number of signal events to the expected one from the Standard Model (SM), are

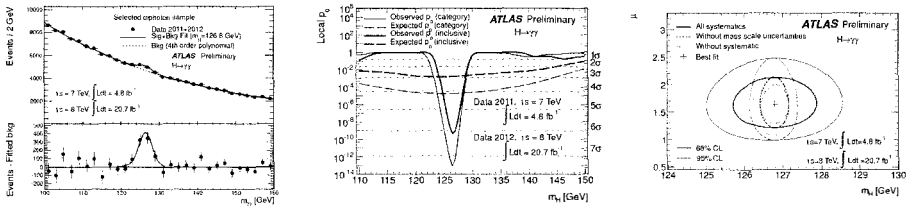

Figure 1: Left: Invariant mass distribution of di-photon candidates along with the signal-plus-background fit to the data. Center: The observed and expected local p_0 as a function of m_H. Right: The best-fit values of m_H and μ, and their 68% (blue) and 95% (red) CL contours. Ref. [3]

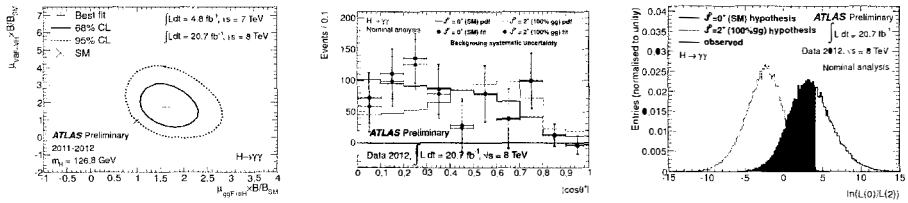

Figure 2: Left: The best-fit values of $\mu_{\mathrm{ggF+t\bar{t}H}}$ x $\mathrm{B/B_{SM}}$ and $\mu_{\mathrm{VBF+VH}}$ x $\mathrm{B/B_{SM}}$ and their 68% (solid) and 95% (dashed) CL contours. Center: Distribution of the background-subtracted data in the signal region as a function of $|\cos\theta^*|$. Right: Expected distributions of the test statistics q for the spin-0 and spin-2 hypotheses. Ref. [3,4]

shown. The mass is measured to be 126.8 ± 0.2 (stat) ± 0.7 (syst) GeV, where the systematic uncertainty is dominated by the photon energy scale uncertainties. The measured μ is 1.65 ± 0.24 (stat) $^{+0.25}_{-0.18}$ (syst). In the VBF enriched category a $2.0\,\sigma$ excess is observed at $m_H = 126.5$ GeV. The best fit signal strength grouped into the "bosonic" (VBF, VH) and "fermionic" (ggF, $\mathrm{t\bar{t}H}$) production modes is in agreement with the SM expectation within $2\,\sigma$ (Figure 2 (left)).

The new particle's spin has been studied comparing the SM spin-0^+ hypothesis to spin-2^+_m "graviton-like" with minimal couplings [4]. The discriminants used are the $m_{\gamma\gamma}$ and the angular distribution of the photons in the resonance rest frame, $|\cos\theta^*|$, (Figure 2 (center)). The observation is compatible with the spin-0^+ hypothesis and spin-2^+_m is excluded at 99.3% $\mathrm{CL_s}$ assuming the spin-2^+_m resonance is produced purely via gluon fusion (Figure 2 (right)).

3 Updated results in the $H \to ZZ^{(*)} \to 4\ell$ channel and properties measurement

$H \to ZZ^{(*)} \to 4\ell$, with $\ell = e, \mu$, is a high mass resolution channel with the very clean signature of two pairs of same-flavor, opposite-charge leptons. The four-lepton invariant mass ($m_{4\ell}$)

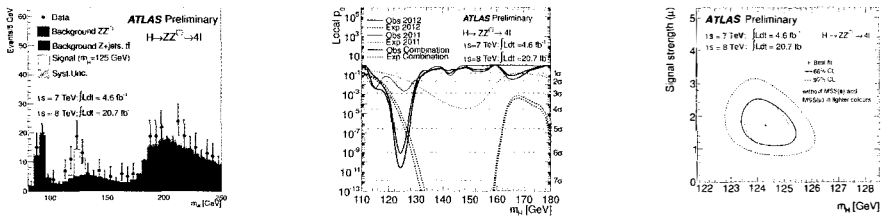

Figure 3: Left: The distribution of the four-lepton invariant mass, $m_{4\ell}$, for the selected candidates. Center: The observed and expected local p_0-value for the 2011 and 2012 data sets, and their combination. Right: Likelihood ratio contours in the μ-m_H plane that, in the asymptotic limit, correspond to 68% and 95% level contours. Ref. [5]

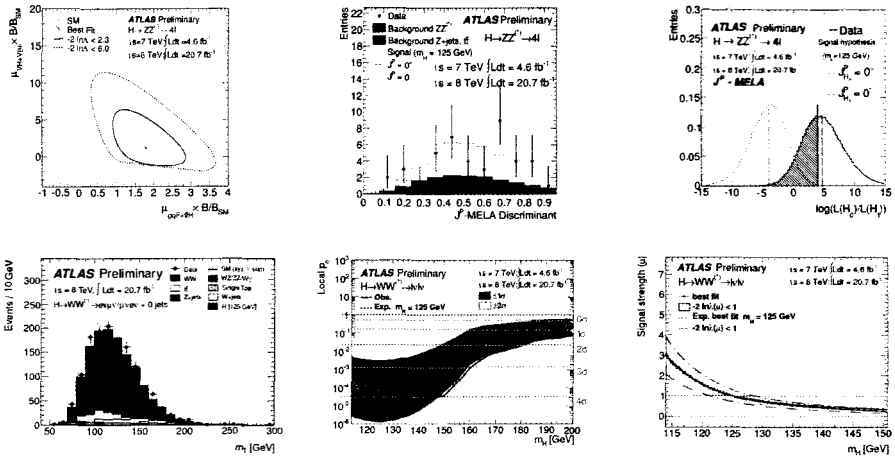

Figure 4: Left: Distribution of the transverse mass, m_{T}, for 8 TeV data for the $e\mu + \mu e$ channel in $\mathrm{N_{jet}} = 0$. Center: The observed and expected local p_0-value. Right: Signal strength as a function of m_H. Ref. [6]

discriminant (Figure 3 (left)) provides an expected resolution of 1.9 GeV with a S/B ratio of 1.6 at $m_H = 125\,\mathrm{GeV}$ [5]. The background processes consist of the irreducible $ZZ^{(*)}$ production and the reducible $t\bar{t}$ and Z+jets production estimated from control regions in data. To increase the sensitivity, categories are used according to the lepton flavor. The excess observed at 124.3 GeV (Figure 3 (center)) has a significance of 6.6 σ, while 4.4 σ is expected.

The best fit value of m_H is $124.3^{+0.6}_{-0.5}$ (stat) $^{+0.5}_{-0.3}$ (syst) GeV, where the systematic uncertainty is dominated by the energy and momentum scale uncertainties while μ is $1.7^{+0.5}_{-0.4}$ (Figure 3 (right)). VBF and VH enriched categories have been added. The rates of various production modes are in agreement with the SM expectation within 2 σ (Figure 3 (left)).

The spin of the new particle has been studied comparing the SM spin-0^+ to other spin/parity hypotheses. The discriminant ($\mathrm{J^P}$-MELA) for this study is based on five production and decay angles [5], and the dilepton invariant masses (m_{12}, m_{34}) (Figure 3 (center)). The observation is compatible with the SM spin-0^+ hypothesis while spin-0^- and spin-1^+ states are excluded at 97.8% $\mathrm{CL_s}$ or higher in favour of spin-0^+ (Figure 3 (right)).

4 Updated results in the $H \to WW^{(*)} \to \ell\nu\ell\nu$ channel and properties measurement

$H \to WW^{(*)} \to \ell\nu\ell\nu$ is a high rate but low mass resolution channel with the signature of two opposite charged isolated leptons and missing transverse energy ($E_{\mathrm{T}}^{\mathrm{miss}}$). Due to the presence of two neutrinos in the final state, a transverse mass is used as discriminant (m_{T}) (Figure 4 (left)). The S/B ratio ranges from 0.15-0.26 [6]. The background processes are $WW^{(*)}$, top, W+jets, Drell-Yan and diboson production, estimated from control regions in data. Categories are used based on the number of jets in the event and on the lepton flavor.

The significance of the observed excess at $m_H = 125\,\mathrm{GeV}$ is 3.8 σ, while 3.7 σ is expected (Figure 4 (center)). At 125 GeV μ is 1.01 ± 0.21 (stat) ± 0.19 (theory) ± 0.12 (syst) ± 0.04 (lumi) (Figure 4 (right)), where the experimental systematic uncertainty is dominated by b-tagging efficiency and jet energy scale/resolution. The inclusive cross section has been calculated for $\sqrt{s} = 8\,\mathrm{TeV}$ and $m_H = 125\,\mathrm{GeV}$ to be $\sigma \cdot \mathrm{BR} = 6.0 \pm 1.1$ (stat) ± 0.8 (theory) ± 0.7 (syst) ± 0.3 (lumi) pb. An excess over background of 2.5 σ is observed in the VBF enriched category assuming $m_H = 125\,\mathrm{GeV}$. The rates of the different production modes are in agreement with the SM expectation within 1 σ (Figure 5 (left)).

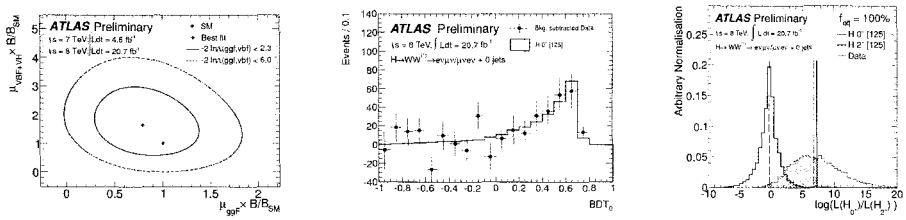

Figure 5: Left: Likelihood contours for separate ggF and VBF signal strength parameters. Center: The distribution for the spin analysis discriminant for spin-0^+ hypothesis. Right: Test statistics distributions when assuming the spin-0^+ hypothesis and testing the spin-2^+_m hypothesis. Ref. [6,8]

The new particle's spin has been studied using the 8 TeV data sample by comparing the SM spin-0^+ hypothesis to the spin-2^+_m. The discriminants (BDT [7]) for this study are based on $m_{\ell\ell}$, $m^{\mathrm{T}}_{\ell\ell}$, $\Delta\phi_{\ell\ell}$ and m_{T} (Figure 5 (center)) [8]. The observation is compatible with the SM spin-0^+ hypothesis while spin-2^+_m is excluded at more than 95% $\mathrm{CL_s}$ (Figure 5 (right)).

5 First results on the $H \to Z\gamma$ channel

$H \to Z\gamma$ is a high resolution but low rate channel with two opposite charged, isolated leptons and an isolated photon in the final state. The discriminant used in this channel is the $\Delta m = m_{\ell\ell\gamma} - m_{\ell\ell}$ and the mass resolution is $\sim$1.6 GeV. The background processes considered are the irreducible $Z\gamma$ production and events with Z and a jet misidentified as a photon. No excess has been observed in data. The observed upper limit on the SM Higgs production cross section for $m_H = 125\,\mathrm{GeV}$ is $18.2\,\sigma_{\mathrm{SM}}$, while $13.5\,\sigma_{\mathrm{SM}}$ is the expected.

6 Summary

The first and preliminary results on the $H \to \gamma\gamma$, $H \to ZZ^{(*)} \to 4\ell$, $H \to WW^{(*)} \to \ell\nu\ell\nu$ and $H \to Z\gamma$ channels have been presented using the full LHC Run I ATLAS data. The signal significance in the individual $H \to \gamma\gamma$ and $H \to 4\ell$ channels is $\sim 7\,\sigma$. The signal strength and rates of the different production modes are found to be consistent with the SM expectation within 2σ, while observation is compatible with the spin-0^+ hypothesis.

References

1. ATLAS collaboration, *Phys. Lett.* B **716**, 1 (2012).
2. CMS collaboration, *Phys. Lett.* B **716**, 30 (2012).
3. ATLAS collaboration, ATLAS-CONF-2013-012, http://cdsweb.cern.ch/record/1523698.
4. ATLAS collaboration, ATLAS-CONF-2013-029, http://cdsweb.cern.ch/record/1527124.
5. ATLAS collaboration, ATLAS-CONF-2013-013, http://cdsweb.cern.ch/record/1523699.
6. ATLAS collaboration, ATLAS-CONF-2013-030, http://cdsweb.cern.ch/record/1527126.
7. B. P Roe *et al*, *Nucl. Instrum. Methods* A **543**, 577 (2005).
8. ATLAS collaboration, ATLAS-CONF-2013-031, http://cdsweb.cern.ch/record/1527127.
9. ATLAS collaboration, ATLAS-CONF-2013-009, http://cdsweb.cern.ch/record/1523683.

Study of the Higgs Production in bosonic decays channels with the CMS detector

C. Ochando
Laboratoire Leprince-Ringuet, UMR 7638, Ecole Polytechnique,
91128 Palaiseau Cedex, France

The latest results on the standard model Higgs boson studies in bosonic decays from the CMS experiment are reported. The analysis use pp collisions data recorded by the CMS detector at the LHC, corresponding to integrated luminosities up to 5.1 fb^{-1} (19.6 fb^{-1}) at $\sqrt{s}$ = 7 (8) TeV. The observation of a new boson at a mass near 126 GeV is confirmed and some of its properties are shown.

1 Introduction

The standard model (SM) [1,2,3] relies on the existence of the Higgs boson (H, with mass m_H), a scalar particle associated with the field responsible for the spontaneous electroweak symmetry breaking [4,5,6,7,8,9]. In 2012, the ATLAS and CMS experiments reported the discovery a new boson at a mass around 125 GeV [10,11], compatible with the SM Higgs boson.

This letter reports the latest results from CMS with the full available statistics of the RunI of the LHC in the $H \to VV$ modes (where V stands for W, Z or γ). They have the largest sensitivity among all Higgs decays, a very good precision on the mass and can provide informations on the spin-parity state. The latter, as well as the combination of all measurements is provided elsewhere [12,13]. These proceedings focus on low mass studies (m_H <180 GeV) and only $W \to \ell\nu$ and $Z \to \ell\ell$ (where ℓ is for electron or muon) are considered.

2 H→WW→ $2\ell 2\nu$ analysis

In the H→WW→ $2\ell 2\nu$ channel [14], we search for an excess of events with two high transverse momenta (p_T) leptons of opposite charge and large missing transverse momentum (E_T^{miss}) due to undetected neutrinos. As no mass peak can be fully reconstructed, a precise control of the backgrounds is mandatory. The main one originates from non-resonant WW production. Additional contributions arise from Drell-Yan, top quark as well as W+jets or diboson processes (WZ, $W\gamma^{(*)}$, ZZ).

The event sample is split into categories of different background composition and signal-to- background ratios: same-flavor (SF) and different-flavor (DF) leptons, events with zero or one jet [a]. The reconstructed transverse mass (m_T) distribution is shown on Fig. 1 (left) for the DF category and in the 0-jet bin. A broad excess of events, compatible with the production of Higgs boson with m_H =125 GeV, can be appreciated.

The final result is extracted using a two-dimensional ($m_{\ell\ell}$, m_T)[b] shape analysis for events belonging to the DF category, and by a cut-based approach for the events falling into the SF category. The observed (expected) significance is 4.0 (5.1) standard deviations (σ) for m_H =125 GeV, as shown in Fig. 1 (right). The signal strength μ_{SM}, relative to the expectation for the SM Higgs boson, is measured to be $\mu_{SM} = 0.76 \pm 0.21$ at 125 GeV.

[a] The category with at least two jets, dedicated to the Vector Boson Fusion (VBF) production mode, was not updated in time for this conference.

[b] $m_{\ell\ell}$ is the invariant mass of the dilepton pair, m_T is the transverse mass reconstructed from the transverse momentum

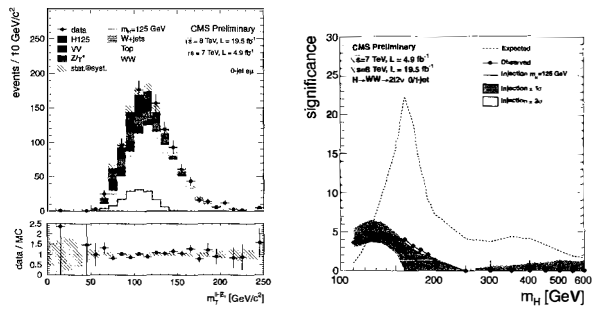

Figure 1: Distribution of the transverse mass m_T for the DF category and 0-jet bin (left). Observed (blue) and expected (dashed) statistical significance as a function of m_H (right). The expected significance (black) under the presence of a m_H=125 GeV Higgs is also shown.

3 $H \to ZZ \to 4\ell$ analysis

The $H \to ZZ \to 4\ell$ analysis [15] exhibits a clean experimental signature consisting of a narrow resonance over a small continuum background. The mass peak is built from four primary isolated and identified leptons. As low signal yields are expected, this channel critically relies on the performances of the leptons reconstruction and selection algorithms. The dominant irreducible background is from non-resonant ZZ (or $Z\gamma^*$) production. It is estimated from simulation. Additional reducible background sources arise from $Zb\bar{b}$, $t\bar{t}$, Z+ jets or WZ+ jets events where at least one jet is misidentified as lepton. It is estimated from real data.

The reconstructed four-lepton invariant-mass (m_{4l}) distribution is shown on Fig. 2 (left). A clear peak around $m_{4\ell} = 126$ GeV is seen. A matrix element likelihood approach [16,17,18] is used to build a kinematic discriminant (K_D) so as to further improve the separation between signal and background. To enhance the sensitivity to the production mechanisms, the event sample is split into two categories based on the jet multiplicity: events with fewer than two jets (C1) and events with at least two jets (C2).

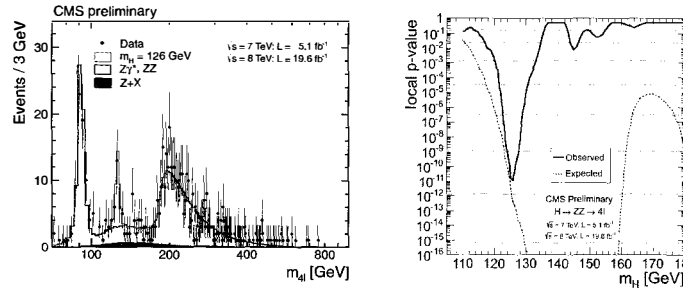

Figure 2: Distribution of the four-lepton reconstructed mass (left).Points represent the data, shaded histograms represent the background and the unshaded histogram the signal expectation. Expected (dashed) and observed (solid) local p-values (right) as a function of the Higgs boson mass.

The final result is extracted using a three dimensional model ($m_{4\ell}$, K_D, X) where X is $p_T/m_{4\ell}$ in C1 and a linear discriminant formed combining VBF sensitive variables in C2. The local p-values, representing the significance of local excesses relative to the background expectation are shown on Fig. 2 (right). The minimum is reached around $m_{4\ell} = 125.8$ GeV and corresponds to an observed (expected) local significance of 6.7 (7.1) σ. The signal strength μ_{SM} is measured to be $\mu_{SM} = 0.91^{+0.30}_{-0.24}$ at 125.8 GeV.

of the dilepton pair and the E_T^{miss} vector.

4 H→ $\gamma\gamma$ analysis

The H→ $\gamma\gamma$ analysis[19] searches for a narrow peak built from two high p_T photons over a smoothly falling background due to QCD prompt diphoton production and to events with at least on jet misidentified as photon.

To increase the sensitivity, events are separated into mutually exclusive classes: diphoton events without any tagging object (untagged), diphoton events with jets consistent with the VBF topology, and diphoton events with leptons or large E_T^{miss}, consistent with W/Z associated production (VH).

Two analyses are presented: one uses Multi-Variate-Analysis (MVA) techniques for both the photon identification and the event classification for untagged or VBF-like classes while the other is using cut-based approaches. The MVA classifier for the untagged category uses as input an event-by-event estimate of the diphoton mass resolution, a photon identification score for each photon, and kinematic informations about the photons and the diphoton system. Being the most sensitive, the MVA analysis results are taken as baseline. The background in the signal region is estimated from fits to each of the observed diphoton mass distributions in data.

The weighted diphoton invariant-mass distribution is shown on Fig. 3 for both analysis. A clear peak around $m_H = 125$ GeV is seen. The local p-values are shown on Fig. 4 for both analysis. The minimum is reached around $m_H = 125$ GeV and corresponds to a local significance of 3.2 (3.9) σ for an expectation of 4.2 (3.5) σ for the MVA (cut-based) analysis. The signal strength μ_{SM} is measured to be $\mu_{SM} = 0.78^{+0.28}_{-0.26}$ ($1.11^{+0.30}_{-0.32}$) at 125 (124.5) GeV for the MVA (cut-based) analysis.

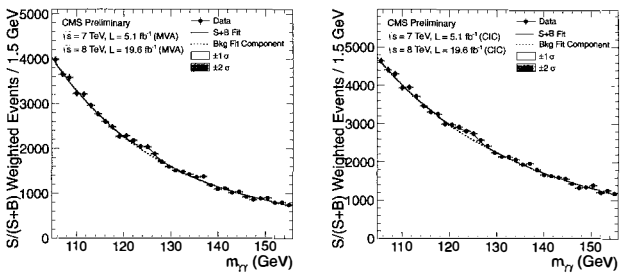

Figure 3: The diphoton mass spectrum weighted by the ratio of signal-to-background in each event class for the MVA (left) and cut-based (right) analysis.

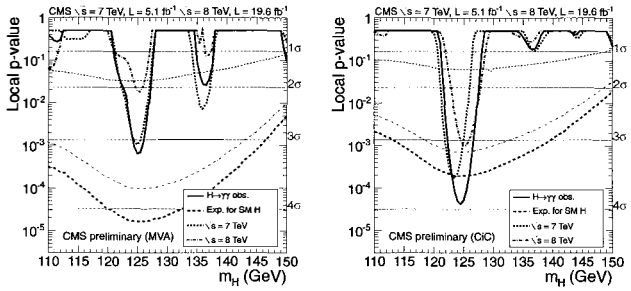

Figure 4: Expected (dashed) and observed (solid) local p-values as a function of the Higgs boson mass for the MVA (left) and cut-based (right) analysis.

5 Properties: mass and production mechanisms

The mass m_X of the observed state is measured with the high resolution channels: $ZZ \to 4\ell$ and $\gamma\gamma$. The mass and its uncertainty are extracted from one-dimensional scan of the test statistic $q(m_X)$. It is

shown on Fig. 5 (left) for the two channels separately. The resulting fit gives $m_X = 125.8 \pm 0.5$ (stat) ± 0.2 (syst) ($m_X = 125.4 \pm 0.5$ (stat) ± 0.6 (syst)) for the $ZZ \to 4\ell$ ($\gamma\gamma$) analysis.

The production mechanisms can be slit into two categories depending on whether the production is induced by vector bosons (VBF, VH) or fermions (ggH, ttH). Two signal strength modifiers (μ_V, μ_F) are introduced as scale factors to the SM expected cross section. A two-dimensional (μ_V, μ_F) fit is performed assuming the measured mass hypothesis in each channel. Fig. 5 shows the resulting fits for the $ZZ \to 4\ell$ and $\gamma\gamma$ channels. The measured values are consistent with the expectations from the production of a SM Higgs boson.

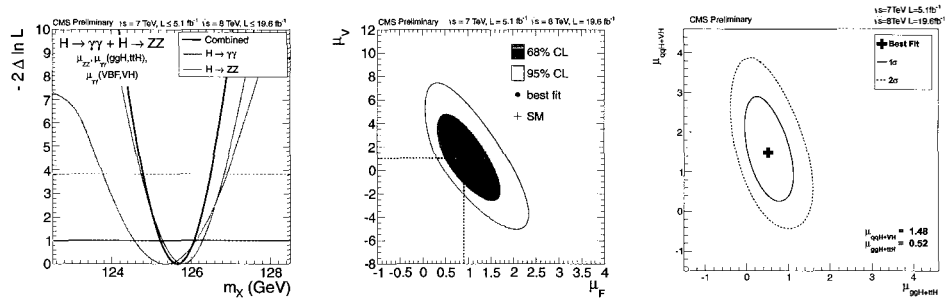

Figure 5: 1D test statistics $q(m_X) = -2\Delta lnL$ scan vs tested m_X (left) for the ZZ (red) and $\gamma\gamma$ (green) channel. Likelihood contours on the signal strength modifiers associated with fermions (μ_F) and vector bosons (μ_V) for the ZZ (middle) and $\gamma\gamma$ (right) channels.

6 Conclusion

The latest results on the standard model Higgs boson studies in bosonic decays from the CMS experiment has been presented, using data samples corresponding to integrated luminosities up to 5.1 fb^{-1} (19.6 fb^{-1}) at $\sqrt{s} = 7$ (8) TeV in pp collisions at LHC. The observation of a new boson at a mass near 126 GeV is confirmed and its properties are consistent so far with the production of a SM Higgs boson.

References

1. S. L. Glashow, Nucl. Phys. **22** (1961) 579.
2. S. Weinberg, "A Model of Leptons," Phys. Rev. Lett. **19** (1967) 1264.
3. A. Salam, in Elementary particle physics: relativistic groups and analyticity, N. Svartholm, ed., p. 367. Almqvist &Wiskell, 1968. Proceedings of the eighth Nobel symposium.
4. F. Englert and R. Brout, Phys. Rev. Lett. **13** (1964) 321.
5. P. W. Higgs, Phys. Lett. **12** (1964) 132.
6. P. W. Higgs, Phys. Rev. Lett. **13** (1964) 508.
7. G. S. Guralnik, C. R. Hagen and T. W. B. Kibble, Phys. Rev. Lett. **13** (1964) 585.
8. P. W. Higgs, Phys. Rev. **145** (1966) 1156.
9. T. W. B. Kibble, Phys. Rev. **155** (1967) 1554.
10. S. Chatrchyan *et al.* [CMS Collaboration], Phys. Lett. B **716** (2012) 30.
11. G. Aad *et al.* [ATLAS Collaboration], Phys. Lett. B **716** (2012) 1.
12. CMS Collaboration, CMS-PAS-HIG-13-005 (2013).
13. A. Whitbeck, these proceedings.
14. CMS Collaboration, CMS-PAS-HIG-13-003 (2013).
15. CMS Collaboration, CMS-PAS-HIG-13-002 (2013).
16. Y. Gao et al., Phys. Rev. D **81** (2010) 075022
17. S. Bolognesi et al., Phys. Rev. D **86** (2012) 095031
18. P. Avery et al., arXiv:1210.0896 [hep-ph].
19. CMS Collaboration, CMS-PAS-HIG-13-001 (2013).

Search for Standard Model Scalar Boson Decaying to Fermions at the LHC

Darren Puigh
Department of Physics, The Ohio State University,
Columbus, OH, U.S.A.

The results from searches for a Standard Model Higgs boson decaying to fermions at the LHC are presented. Using a combination of data collected in proton-proton collisions at center-of-mass energies of 7 TeV and 8 TeV by the ATLAS and CMS detectors, new limits are set on the cross section times branching fractions of the Higgs boson decaying to bottom quarks, muons, and tau leptons for several production mechanisms.

1 Introduction

With the recent observation [1,2] of a new boson with a mass near 125 GeV/c^2 at the Large Hadron Collider (LHC), the focus of searches for the Standard Model (SM) Higgs boson has shifted to evaluating the consistency of this new particle with SM expectations. Both the ATLAS [3] and the CMS [4] collaborations presented preliminary results that the new particle is a Higgs boson [5,6,7,8,9]. These collaborations performed a number of measurements and found that the results prefer that the new particle have no spin and positive parity, consistent with the SM Higgs boson. In addition, the measurements of the branching ratios of the new particles to bosons ($H \to WW,\ ZZ,\ \gamma\gamma$) are consistent with SM expectation. In order to determine if this new particle is the Higgs boson of the SM, we need to precisely measure its branching ratio into all final states, including those with fermions.

2 Higgs decays to bottom quarks

At a mass of 125 GeV/c^2, the SM Higgs boson decays predominantly into a bottom-anti bottom quark pair ($b\bar{b}$). Therefore, the observation of $H \to b\bar{b}$ is essential to characterize the nature of the new boson. However, the rate of $b\bar{b}$ production at the LHC from the QCD multi-jet background is many orders of magnitude larger than the rate of Higgs production. To reduce the backgrounds and investigate different

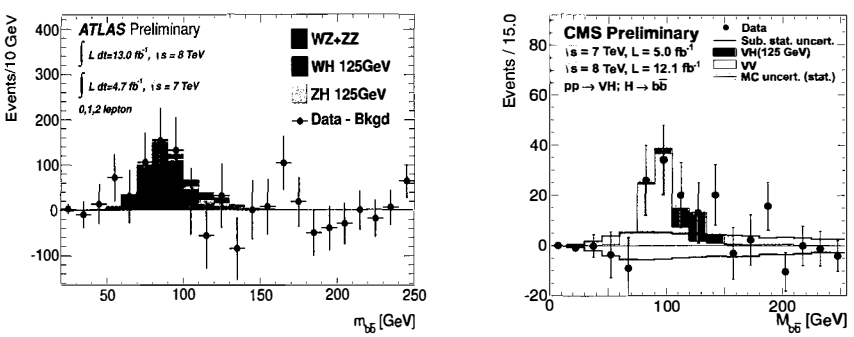

Figure 1: The distribution of $m_{b\bar{b}}$ in data after subtraction of all backgrounds except diboson backgrounds for ATLAS (left) and CMS (right). In both cases, the diboson background is visible and described well.

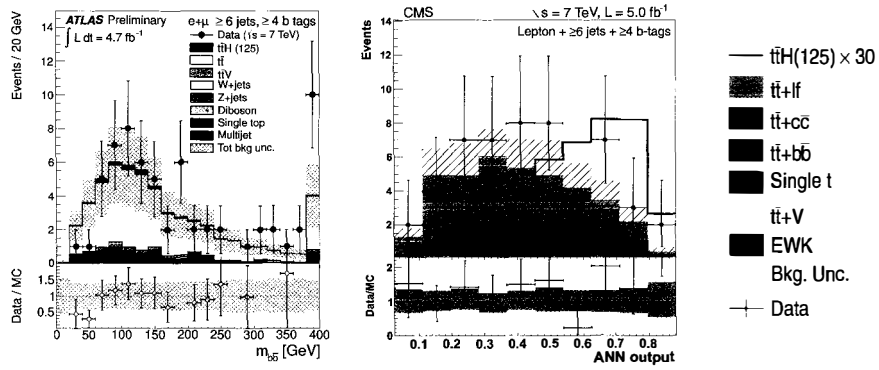

Figure 2: Signal discriminant distributions of the $t\bar{t}H$ analysis for ATLAS (left) and CMS (right) after requiring one well-identified lepton (electron or muon), $\geq$6 jets, and $\geq$4 b-tagged jets.

Higgs production mechanisms, the ATLAS and CMS experiments performed searches for the Higgs boson produced in association with a vector boson (WH or ZH) or a top quark pair ($t\bar{t}H$).

2.1 Higgs produced in association with vector bosons

The search for Higgs produced in association with a vector boson, W or Z, was performed in the decay channels $ZH \to \ell^+\ell^- b\bar{b}$, $WH \to \ell\nu b\bar{b}$, and $ZH \to \nu\nu b\bar{b}$, where ℓ refers to either an electron or a muon. Events must also possess two jets that are identified as originating from a b quark (b-tagged). After separating events based on the number of charged leptons, events are further sub-divided based on the transverse momentum of the vector boson and either the number of additional jets (ATLAS) or the tightness of the b-tag requirement (CMS). ATLAS used the $m_{b\bar{b}}$ distribution as its signal discriminator, while CMS used the output discriminant of a boosted-decision-tree (BDT) algorithm [10].

To show the validity of the Higgs search procedure, both experiments performed a fit of the $m_{b\bar{b}}$ distribution treating the diboson background as the signal of interest. Diboson production with a Z boson decaying to $b\bar{b}$ has a very similar signature to $H \to b\bar{b}$. Figure 1 shows the $m_{b\bar{b}}$ distribution in data after subtraction of all backgrounds except diboson backgrounds for ATLAS and CMS, and the data are consistent with the presence of a diboson signal with a rate approximately as expected from the SM [11,12].

The experiments both used 5 fb^{-1} of 7 TeV data and about half of the available 8 TeV data (12-13 fb^{-1}) in their search for VH production in the $b\bar{b}$ channel. For $m_H = 125$ GeV/c^2, ATLAS obtained an observed (expected) upper limit on the production cross section times branching ratio of 1.8 (1.9) times the SM prediction [11]. Similarly, CMS found an observed (expected) limit of 2.5 (1.2) times the SM prediction, corresponding to a local significance of 2.2σ [12].

2.2 Higgs produced in association with top quark pairs

The $t\bar{t}H$ mechanism is the only production mode directly sensitive to the top-Higgs Yukawa coupling. Furthermore, searching for $t\bar{t}H$ can also be used to probe new physics models that predict increased rates of $t\bar{t}H$ production without changing Higgs branching ratios [13,14].

Events were split based on the decay of the $t\bar{t}$ system: where one of the W bosons from the top quark decays to a charged lepton and a neutrino and the other W boson decays to a quark-antiquark pair (lepton+jets), or where both of the W bosons decay to charged leptons and neutrinos (dilepton). After requiring an intitial event selection involving kinematics, object identification and quality cuts, events were categorized based on the number of jets and the number of b-tagged jets they contain. A signal discriminator is used to further improve signal sensitivity: ATLAS used either the scalar sum of the jet transverse momentum or the reconstructed $m_{b\bar{b}}$, depending on the category, and CMS used the output discriminant of an artificial neural network (ANN) algorithm [15]. Figure 2 shows the signal discriminators for the most sensitive categories of ATLAS and CMS.

Using 5 fb^{-1} of data at 7 TeV and focusing on the lepton+jets channel, ATLAS set an observed (expected) upper limit on $t\bar{t}H$ production in the $b\bar{b}$ channel of 13.1 (10.5) times the SM expectation [16] for

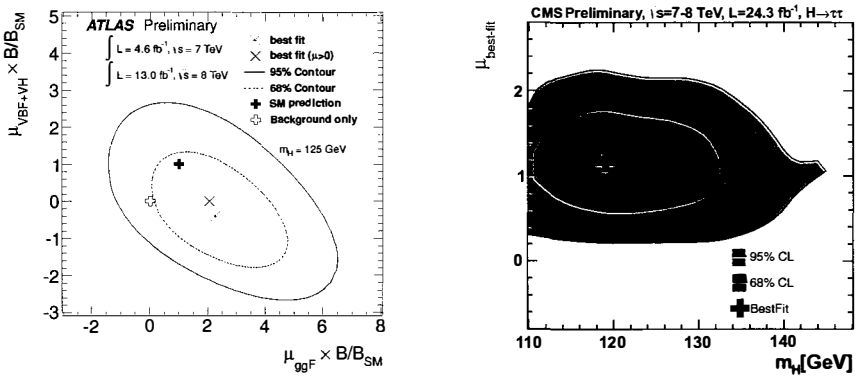

Figure 3: Left: ATLAS result showing the best fit of the signal strength for vector boson fusion and associated production of $H \to \tau\tau$ versus gluon fusion. Right: CMS result on the best fit of signal strength for total $H \to \tau\tau$ production compared to the SM expectation as a function of the Higgs mass.

$m_H = 125$ GeV/c^2. CMS combined 5 fb^{-1} of 8 TeV data with 5 fb^{-1} of 7 TeV data to set an observed (expected) limit of 5.8 (5.2) times SM expectation [17] for the same mass.

3 Higgs decays to leptons

In addition to Higgs decaying to $b\bar{b}$, the other experimentally accessible channels at the LHC for investigating Higgs decaying to fermions are $H \to \mu\mu$ and $H \to \tau\tau$.

3.1 Higgs decays to muons

The $H \to \mu\mu$ decay provides an experimentally clean final-state signature with a good resolution on the mass of the Higgs boson. It is also the best channel to investigate the Higgs coupling to second generation fermions at the LHC. One of the difficulties of this channel is that there is a large background from $Z/\gamma^* \to \mu\mu$. ATLAS performed a search in this channel by selecting events with two muons, where the di-muon system was boosted, and then performed a fit on the invariant mass of the di-muon system to extract a signal. Seeing no excess in 20 fb^{-1} of data at 8 TeV, the observed (expected) limit for $m_H = 125$ GeV/c^2 was 9.8 (8.2) times the SM prediction [18].

3.2 Higgs decays to tau leptons

The branching ratios for Higgs decaying to fermions are proportional to the square of the fermion mass. Due to the large m_τ, the $H \to \tau\tau$ decay is important for testing Yukawa couplings in the case of leptons.

The search strategies for $H \to \tau\tau$ were similar for ATLAS [19] and CMS [20,21]. Events were categorized based on the number of jets, the boost of the system, the transverse momentum of the leptons (e, μ, τ_h), and the final-state signature ($e\mu$, $\mu\mu$, $e\tau_h$, $\mu\tau_h$, $\tau_h\tau_h$). Selections on the event topology were made to suppress background. The dominant background in this search was $Z \to \tau\tau$, which was estimated by taking $Z \to \mu\mu$ events from data and replacing the muons by simulated τ decays.

Due to the neutrinos resulting from the tau decays, the invariant mass of the di-tau system ($m_{\tau\tau}$) is not fully constrained. In order to get the best estimate for $m_{\tau\tau}$, ATLAS used the Missing Mass Calculator method [22], and CMS used a maximum likelihood method (SVFit algorithm) [20]. A simultaneous fit of $m_{\tau\tau}$ across the different categories and channels was used to extract the signal.

The ATLAS experiment used 5 fb^{-1} of data at 7 TeV and 13 fb^{-1} of data at 8 TeV, and the observed (expected) limit on SM $H \to \tau\tau$ was found to be 1.9 (1.2) times the SM prediction [19]. Using 5 fb^{-1} of data recorded at 7 TeV and 19 fb^{-1} of data at 8 TeV, an excess of events was observed by the CMS experiment, with a maximum local significance of 2.9σ [20] at $m_H = 120$ GeV/c^2. Figure 3 shows the best fit of the signal strength for different $H \to \tau\tau$ production modes and as a function of m_H.

4 Summary

ATLAS and CMS have performed searches for a Standard Model Higgs boson decaying to fermions. Limits were set on the cross section times branching fraction of Higgs decaying to bottom quarks, muons, and tau leptons. Excesses in the $b\bar{b}$ and $\tau\tau$ channels are consistent with SM Higgs expectations with local significances 2.2σ and 2.9σ, respectively.

References

[1] ATLAS Collaboration, "A Particle Consistent with the Higgs Boson Observed with the ATLAS Detector at the Large Hadron Collider," *Science* **338** no. 6114, (2012) 1576–1582.

[2] CMS Collaboration, "A New Boson with a Mass of 125 GeV Observed with the CMS Experiment at the Large Hadron Collider," *Science* **338** no. 6114, (2012) 1569–1575.

[3] ATLAS Collaboration, "The ATLAS Experiment at the CERN Large Hadron Collider," *Journal of Instrumentation* **3** no. 08, (2008) S08003. `http://stacks.iop.org/1748-0221/3/i=08/a=S08003`.

[4] CMS Collaboration, "The CMS experiment at the CERN LHC," *Journal of Instrumentation* **3** no. 08, (2008) S08004. `http://stacks.iop.org/1748-0221/3/i=08/a=S08004`.

[5] ATLAS Collaboration, "Study of the spin of the Higgs-like boson in the two photon decay channel using 20.7 fb-1 of pp collisions collected at $\sqrt{s} = 8$ TeV with the ATLAS detector," Tech. Rep. ATLAS-CONF-2013-029, CERN, 2013. `http://cds.cern.ch/record/1527124`.

[6] ATLAS Collaboration, "Study of the spin properties of the Higgs-like particle in the $H \to WW \to e\nu\mu\nu$ channel with 21 fb^{-1} of $\sqrt{s} = 8$ TeV data collected with the ATLAS detector.," Tech. Rep. ATLAS-CONF-2013-031, CERN, 2013. `http://cds.cern.ch/record/1527127`.

[7] ATLAS Collaboration, "Combined coupling measurements of the Higgs-like boson with the ATLAS detector using up to 25 fb^{-1} of proton-proton collision data," Tech. Rep. ATLAS-CONF-2013-034, CERN, 2013. `http://cds.cern.ch/record/1528170`.

[8] CMS Collaboration, "Updated measurements of the Higgs boson at 125 GeV in the two photon decay channel," Tech. Rep. CMS-PAS-HIG-13-001, CERN, 2013. `http://cds.cern.ch/record/1530524`.

[9] CMS Collaboration, "Properties of the Higgs-like boson in the decay H to ZZ to 4l in pp collisions at sqrt s =7 and 8 TeV," Tech. Rep. CMS-PAS-HIG-13-002, CERN, 2013. `http://cds.cern.ch/record/1523767`.

[10] B. P. Roe, H.-J. Yang, J. Zhu, Y. Liu, I. Stancu, and G. McGregor, "Boosted decision trees as an alternative to artificial neural networks for particle identification," *Nuclear Instruments and Methods in Physics Research Section A: Accelerators, Spectrometers, Detectors and Associated Equipment* **543** no. 23, (2005) 577 – 584.

[11] ATLAS Collaboration, "Search for the Standard Model Higgs boson in produced in association with a vector boson and decaying to bottom quarks with the ATLAS detector," Tech. Rep. ATLAS-CONF-2012-161, CERN, 2012. `http://cds.cern.ch/record/1493625`.

[12] CMS Collaboration, "Search for the standard model Higgs boson produced in association with W or Z bosons, and decaying to bottom quarks for HCP 2012," Tech. Rep. CMS-PAS-HIG-12-044, CERN, 2012. `http://cds.cern.ch/record/1493618`.

[13] C. Degrande, J. Gerard, C. Grojean, F. Maltoni, and G. Servant, "Probing Top-Higgs Non-Standard Interactions at the LHC," *JHEP* **1207** (2012) 036, `arXiv:1205.1065 [hep-ph]`.

[14] A. Carmona, M. Chala, and J. Santiago, "New Higgs Production Mechanism in Composite Higgs Models," *JHEP* **1207** (2012) 049, `arXiv:1205.2378 [hep-ph]`.

[15] B. D. Ripley, *Pattern Recognition and Neural Networks*. Cambridge University Press, Jan., 1996.

[16] ATLAS Collaboration, "Search for the Standard Model Higgs boson produced in association with top quarks in proton-proton collisions at $\sqrt{s}$= 7 TeV using the ATLAS detector," Tech. Rep. ATLAS-CONF-2012-135, CERN, 2012. `http://cds.cern.ch/record/1478423`.

[17] CMS Collaboration, "Search for the standard model Higgs boson produced in association with a top-quark pair in pp collisions at the LHC," `arXiv:1303.0763 [hep-ex]`.

[18] ATLAS Collaboration, "Search for a Standard Model Higgs boson in $H \to \mu\mu$ decays with the ATLAS detector," Tech. Rep. ATLAS-CONF-2013-010, CERN, 2013. `http://cds.cern.ch/record/1523695`.

[19] ATLAS Collaboration, "Search for the Standard Model Higgs boson in H to tau tau decays in proton-proton collisions with the ATLAS detector," Tech. Rep. ATLAS-CONF-2012-160, CERN, 2012. `http://cds.cern.ch/record/1493624`.

[20] CMS Collaboration, "Search for the Standard-Model Higgs boson decaying to tau pairs in proton-proton collisions at sqrt(s) = 7 and 8 TeV," Tech. Rep. CMS-PAS-HIG-13-004, CERN, 2013. `http://cds.cern.ch/record/1528271`.

[21] CMS Collaboration, "Search for the standard model Higgs boson decaying to tau pairs produced in association with a W or Z boson," Tech. Rep. CMS-PAS-HIG-12-053, CERN, 2013. `http://cds.cern.ch/record/1528147`.

[22] A. Elagin, P. Murat, A. Pranko, and A. Safonov, "A new mass reconstruction technique for resonances decaying to," *Nuclear Instruments and Methods in Physics Research Section A: Accelerators, Spectrometers, Detectors and Associated Equipment* **654** no. 1, (2011) 481 – 489.

Measurements of Higgs boson properties in ATLAS

Tim Adye, on behalf of the ATLAS Collaboration.
Particle Physics Department, Rutherford Appleton Laboratory, Didcot, United Kingdom

Combined measurements of the properties of the Higgs boson using the full pp collision data sample recorded in 2011–2012 by the ATLAS experiment at the LHC are presented. The combined mass measurement derived from the $H\to\gamma\gamma$ and $H\to ZZ^{(*)}\to 4\ell$ channels is $m_H = 125.5 \pm 0.2\,(\text{stat})\,^{+0.5}_{-0.6}\,(\text{sys})$ GeV. The signal strength, from the combination of the $H\to\gamma\gamma$, $H\to ZZ^{(*)}\to 4\ell$, and $H\to WW^{(*)}\to \ell\nu\ell\nu$ channels, as well as the $H\to\tau\tau$ and $H\to b\bar{b}$ channels using a partial dataset, is determined to be $\mu = 1.30\pm0.13\,(\text{stat})\pm0.14\,(\text{sys})$. The cross section ratio between vector boson mediated and gluon initiated Higgs boson production processes is found to be $\mu_{\text{VBF}+VH}/\mu_{\text{ggF}+t\bar{t}H} = 1.2^{+0.7}_{-0.5}$, with more than 3σ evidence for Higgs production through vector-boson fusion. Measurements of relative branching fraction ratios, as well as combined fits testing the fermion and vector boson couplings, ratio of couplings to W and Z, and the possible contribution of new particles show no significant deviation from the Standard Model expectation.

1 Introduction

The observation of a new particle in the search for the Standard Model (SM) Higgs boson at the LHC,[1] reported by the ATLAS[2,3] and CMS[4] Collaborations, is a milestone in the quest to understand electroweak symmetry breaking.[5–7] The ATLAS Collaboration has since reported first measurements of the particle's coupling properties,[8] and updated measurements of its signal strength[9] and mass.[10] Presented here[11,12] are new measurements of the mass, signal strengths, and coupling properties from a combination of decay modes using $4.8\,\text{fb}^{-1}$ of pp collision data at $\sqrt{s} = 7$ TeV and $20.7\,\text{fb}^{-1}$ at $\sqrt{s} = 8$ TeV for the three most sensitive channels $H\to\gamma\gamma$,[13,14] $H\to ZZ^{(*)}\to 4\ell$,[13,15] and $H\to WW^{(*)}\to \ell\nu\ell\nu$;[13,16] and using $4.8\,\text{fb}^{-1}$ at $\sqrt{s} = 7$ TeV and $13\,\text{fb}^{-1}$ at $\sqrt{s} = 8$ TeV for the $H\to\tau\tau$[17,18] and $H\to b\bar{b}$[17,19] channels.

2 Mass measurements

The mass of the new particle can be measured precisely from fits to the data for the $H\to\gamma\gamma$ and $H\to ZZ^{(*)}\to 4\ell$ channels: $m_H = 126.8 \pm 0.2\,(\text{stat}) \pm 0.7\,(\text{sys})$ GeV and $124.3^{+0.6}_{-0.5}\,(\text{stat})\,^{+0.5}_{-0.3}\,(\text{sys})$ GeV are found in the two cases, respectively.

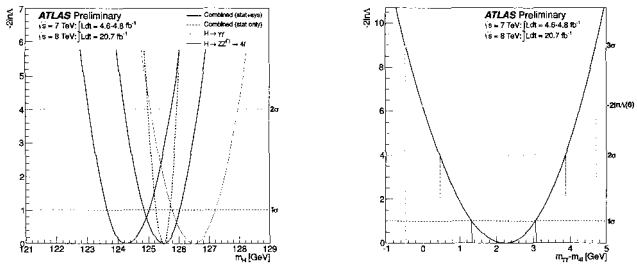

(a) (b)

Figure 1: The profile likelihood ratio $-2\ln\Lambda(m_H)$ as a function of (a) m_H and (b) the mass difference, $\Delta m_H = m_H^{\gamma\gamma} - m_H^{4\ell}$, for the $H\to\gamma\gamma$ and $H\to ZZ^{(*)}\to 4\ell$ channels and their combination. In both cases the signal strength parameters, $\mu_{\gamma\gamma}$ and $\mu_{4\ell}$, are allowed to vary independently.[11]

A combined measurement based on these two channels is obtained from the profile likelihood ratio $\Lambda(m_H)$,[20] as shown in Figure 1(a). The signal strength is allowed to vary between the two channels by treating $\mu_{\gamma\gamma}$ and $\mu_{4\ell}$ as independent nuisance parameters. The combined mass is measured to be $m_H = 125.5 \pm 0.2\,(\text{stat})\,^{+0.5}_{-0.6}\,(\text{sys})$ GeV.

To quantify the consistency between the fitted $m_H^{\gamma\gamma}$ and $m_H^{4\ell}$ values, the data are fitted with the profile likelihood ratio $\Lambda(\Delta m_H)$, where the parameter of interest is the mass difference $\Delta m_H = m_H^{\gamma\gamma} - m_H^{4\ell}$. The average mass m_H and the signal strengths $\mu_{\gamma\gamma}$ and $\mu_{4\ell}$ are treated as independent nuisance parameters. As shown in Figure 1(b), the resulting estimated mass difference is $\Delta\hat{m}_H = 2.3^{+0.6}_{-0.7}\,(\text{stat}) \pm 0.6\,(\text{sys})$ GeV. The probability of a single Higgs boson producing a value of $\Lambda(\Delta m_H)$ disfavoring the $\Delta m_H = 0$ hypothesis by more than that observed in the data is found to be 1.5% (2.4σ), using Monte Carlo ensemble tests.

The significance of the mass difference is also tested using rectangular pdfs for the systematic mass scale uncertainties coming from the $Z \to ee$ calibration procedure, the material upstream of the electromagnetic calorimeter, and the energy scale of the presampler detector. Rectangular pdfs give a flat *a priori* likelihood in the range of the quoted $\pm 1\sigma$ uncertainty intervals for these three sources and a zero probability outside this range. With this treatment, the consistency between the two mass measurements increases to 8% (1.7σ).

3 Signal strength

The Higgs boson production rate is measured in terms of the signal strength parameter μ, a scale factor with respect to the SM predicted rate. The observed overall signal strength μ is determined from a fit to the data where all channels are combined, using the profile likelihood ratio $\Lambda(\mu)$. The mass is fixed to the measured value $m_H = 125.5$ GeV. Figure 2(a) shows the measured signal strengths for the individual channels as well as their combination, $\hat{\mu} = 1.30 \pm 0.13\,(\text{stat}) \pm 0.14\,(\text{sys})$.

The compatibility between this measurement and the SM Higgs boson expectation ($\mu = 1$) is about 9%. It increases to about 40% if rectangular pdfs are used for the dominant theoretical systematic uncertainties from the $gg \to H$ QCD scale and PDF variations. The overall compatibility between the signal strengths measured in the five individual channels and their SM predictions is about 8%. The compatibility between the measured individual $\hat{\mu}$ values and their combination is 13%. The dependence of the combined value of $\hat{\mu}$ on the assumed m_H is relatively weak: changing the mass hypothesis by ± 1 GeV changes $\hat{\mu}$ by about ± 4%.

In order to test which values of signal strength and Higgs mass are simultaneously consistent with the data for the $H\to\gamma\gamma$ and $H\to ZZ^{(*)}\to 4\ell$ channels, the profile likelihood ratio $\Lambda(\mu, m_H)$

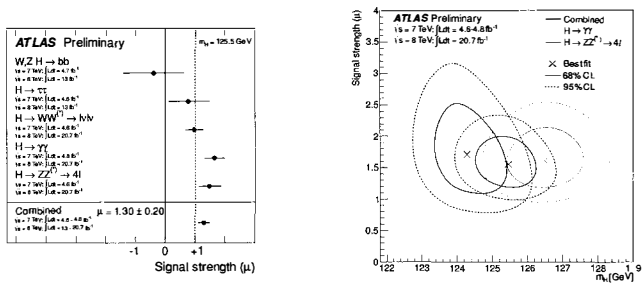

(a) (b)

Figure 2: (a) Measurements of the signal strength parameter μ at $m_H = 125.5$ GeV for the individual channels and their combination.[12] (b) Confidence level intervals in the (μ, m_H) plane for the $H \to ZZ^{(*)} \to 4\ell$ and $H \to \gamma\gamma$ channels and their combination, including all systematic uncertainties. The markers indicate the maximum likelihood estimates $(\hat{\mu}, \hat{m}_H)$ in the corresponding channels.[11]

is used. The resulting 68% and 95% CL contours are shown in Figure 2(b).

4 Production and decay modes

The signal strengths of different production processes contributing to the same final state are determined, exploiting the sensitivity offered by the use of event categories in the analyses of each channel.

The data are fitted separating vector-boson-mediated processes (VBF and VH) from gluon-initiated processes (ggF and ttH) involving fermions (mainly top-quark loops). The signal strength parameters, $\mu_{\mathrm{ggF}+t\bar{t}H} = \mu_{\mathrm{ggF}} = \mu_{t\bar{t}H}$ and $\mu_{\mathrm{VBF}+VH} = \mu_{\mathrm{VBF}} = \mu_{VH}$, are measured for each of the final states, $H \to \gamma\gamma$, $H \to ZZ^{(*)}$ $H \to WW^{(*)} \to \ell\nu\ell\nu$, and $H \to \tau\tau$, as shown in Figure 3(a).

The combination of these results can be made in a model-independent way (i.e. without assumptions on the Higgs decay branching ratios) by measuring the ratio, $\mu_{\mathrm{VBF}+VH}/\mu_{\mathrm{ggF}+t\bar{t}H} = 1.2^{+0.7}_{-0.5}$. The results of the fit to the data for the individual channels and their combination are shown in Figure 3(b). Good agreement with the SM expectations is observed.

To test the sensitivity to VBF production alone, the data are also fitted with the ratio $\mu_{\mathrm{VBF}}/\mu_{\mathrm{ggF}+t\bar{t}H}$, profiling μ_{VH}. From the combination of the four channels, the same value of $\mu_{\mathrm{VBF}}/\mu_{\mathrm{ggF}+t\bar{t}H} = 1.2^{+0.7}_{-0.5}$ is obtained. This result provides 3.1σ evidence for VBF production, with the p-value for vanishing VBF being 0.09%.

Conversely, to study the decay modes independently of the production modes, the ratio of branching ratios, relative to their SM expectations are studied. The best-fit values for each decay mode ratio is $\rho_{\gamma\gamma/ZZ} = 1.1^{+0.4}_{-0.3}$, $\rho_{\gamma\gamma/WW} = 1.7^{+0.7}_{-0.5}$, and $\rho_{ZZ/WW} = 1.6^{+0.8}_{-0.5}$, all in agreement with the SM expectation of 1.

5 Higgs couplings

A relative coupling, κ_i, is defined as the ratio of the measured coupling to the SM one. For each observed final state of the SM Higgs boson, the production and decay rates involve several couplings. For example in the $gg \to H \to \gamma\gamma$ mode, the production rate from gluon fusion is proportional to the square of the effective Higgs-gluon coupling, κ_g^2, where κ_g is itself a function of the Higgs couplings to the particles running in the loops, principally the top, κ_t. The diphoton decay rate is proportional to the square of the effective photon coupling, κ_γ^2, itself a function of κ_W and κ_t, describing the interference between the W and top loops. The data do not

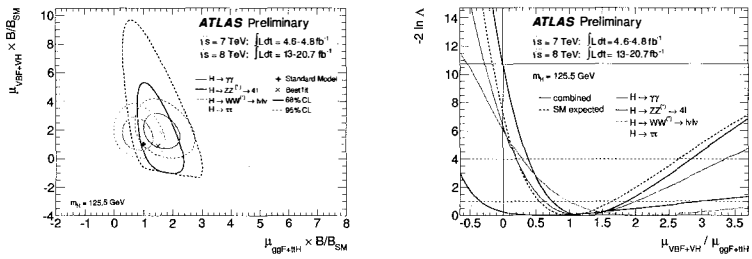

(a) (b)

Figure 3: (a) Likelihood contours for the $H\to\gamma\gamma$, $H\to ZZ^{(*)}\to 4\ell$, $H\to WW^{(*)}\to \ell\nu\ell\nu$, and $H\to\tau\tau$ channels in the $(\mu_{\mathrm{ggF}+t\bar{t}H}, \mu_{\mathrm{VBF}+VH})$ plane. Both $\mu_{\mathrm{ggF}+t\bar{t}H}$ and $\mu_{\mathrm{VBF}+VH}$ are modified by the decay mode-specific branching ratio factors $\mathrm{B/Bs_M}$. (b) Likelihood curves for the ratio $\mu_{\mathrm{VBF}+VH}/\mu_{\mathrm{ggF}+t\bar{t}H}$ for these channels and their combination (observed and SM expectation).[12]

allow a complete determination of all the elementary couplings, so a few benchmark models are considered.[21]

5.1 Fermion versus vector couplings

In this model, all fermion (relative) couplings are taken equal ($\kappa_F = \kappa_t = \kappa_b = \kappa_\tau$), as are the vector boson couplings ($\kappa_V = \kappa_W = \kappa_Z$). The model assumes that $gg \to H$ production and $H\to\gamma\gamma$ decays occur only through loops of SM particles and that there are no non-SM decays contributing to the total width (additional models, measuring $\lambda_{FV} = \kappa_F/\kappa_V$, allow these assumptions to be relaxed[12]). Figure 4(a) shows the corresponding likelihood contours in the κ_V,κ_F plane. The relative sign between κ_F and κ_V corresponds to the interference of the top and W loops in $H\to\gamma\gamma$ decays, where $\kappa_V > 0$ by convention and $\kappa_F < 0$ would indicate a non-SM interference. The 68% CL intervals, profiling over the other parameter, are $\kappa_V \in [0.91, 0.97]\cup[1.05, 1.21]$ and $\kappa_F \in [-0.88, -0.75]\cup[0.73, 1.07]$, with the SM-like minimum, $\kappa_F > 0$, slightly favoured. The (2D) compatibility with the SM hypothesis 8%.

5.2 W and Z couplings (custodial symmetry)

Identical coupling scale factors for the W and Z are an important ingredient of the SM, often referred to as custodial symmetry. From the previous model with the total width free, κ_W and κ_Z are now separated, and their ratio, λ_{WZ}, is probed. Figure 4(b) shows the likelihood curve for λ_{WZ}, while profiling $\lambda_{FZ} = \kappa_F/\kappa_Z$ and $\kappa_{ZZ} = \kappa_Z \cdot \kappa_Z/\kappa_H$ in the fit. The 68% CL interval is $\lambda_{WZ} \in [0.64, 0.87]$, with a (3D) compatibility with the SM hypothesis of 5%.

5.3 Contribution from non-SM particles

This model assumes that all couplings take their SM values ($\kappa_i = 1$), but the effective couplings to gluons and photons, κ_g and κ_γ, are taken as independent, allowing for additional contributions from new particles in the loops. As a first step, the model assumes that these particles do not contribute to the total width through invisible or undetected decay modes. Figure 4(c) shows the likelihood contours in the κ_g,κ_γ plane. The best fit values, profiling over the other parameter, are $\kappa_g = 1.08 \pm 0.14$ and $\kappa_\gamma = 1.23^{+0.16}_{-0.13}$. The (2D) compatibility with the SM hypothesis is 5%.

In a second step, the assumption on the total width is released. The free parameters are κ_g, κ_γ, and $\mathrm{BR_{inv.,undet.}}$, where the latter represents the branching ratio to possible invisible and undetected decay modes. Figure 4(d) shows the likelihood as a function of $\mathrm{BR_{inv.,undet.}}$, profiling

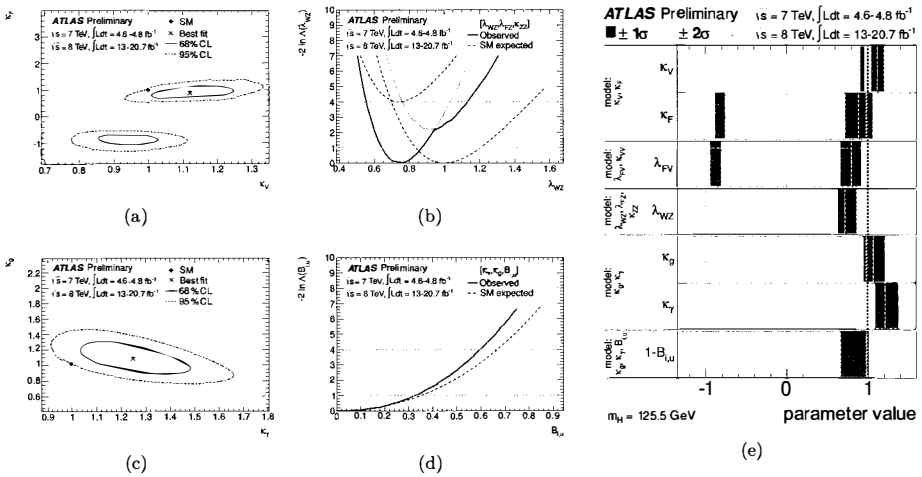

Figure 4: Fits to four benchmark coupling models: likelihood contours for (a) κ_F and κ_V (fermion and vector couplings) and (c) κ_g and κ_γ (effective $gg \to H$ and $H \to \gamma\gamma$ couplings); and likelihood curves for (b) $\lambda_{WZ} = \kappa_W/\kappa_Z$ (couplings to W and Z) and (d) $BR_{inv.,undet.}$ (branching fraction to invisible or undetectable decay modes). The dashed curves in (b) and (d) show the SM expectation. The thin dotted lines in (b) indicate the continuation of the likelihood curve when restricting the parameters to either the positive or negative sector of λ_{FZ}. (e) Summary of the coupling scale factor measurements. The best-fit values are represented by the solid vertical lines. The measurements in the different coupling benchmark models are strongly correlated, as they are obtained from fits to the same experimental data. They should not be considered as independent measurements.[12]

over κ_g and κ_γ. The 95% CL upper limit is $BR_{inv.,undet.} < 0.6$, with a (3D) compatibility with the SM hypothesis of 10%.

6 Conclusion

An update of the properties of the newly discovered Higgs-like boson using the full 2011–2012 data set for the three most sensitive channels $H \to \gamma\gamma$, $H \to ZZ^{(*)} \to 4\ell$ and $H \to WW^{(*)} \to \ell\nu\ell\nu$ is presented.

The measured mass, based on fits to the spectra of the $H \to \gamma\gamma$ and $H \to ZZ^{(*)} \to 4\ell$ channels, is $m_H = 125.5 \pm 0.2\,(\text{stat})\,^{+0.5}_{-0.6}\,(\text{sys})$ GeV. The difference of the mass measurements between the two channels is $2.3^{+0.6}_{-0.7}\,(\text{stat}) \pm 0.6\,(\text{sys})$ GeV, corresponding to a probability of a common mass of 1.5% (2.4σ) or 8% (1.7σ), depending on the treatment of mass scale systematic uncertainties.

A combined strength of $\hat{\mu} = 1.30 \pm 0.13\,(\text{stat}) \pm 0.14\,(\text{sys})$ is obtained. The cross section ratio between vector-boson mediated and gluon initiated Higgs boson production processes is determined to be $\mu_{\text{VBF}+VH}/\mu_{\text{ggF}+t\bar{t}H} = 1.2^{+0.7}_{-0.5}$, with 3.1σ evidence for VBF production.

The compatibility of the measurements with the SM Higgs boson predictions is tested using various coupling models. A summary of all coupling scale factor measurements is shown in Figure 4(e), all being compatible with the SM Higgs expectation at the 5–10% level. No significant deviation from the SM prediction is observed in any of the fits performed.

References

1. L. Evans and P. Bryant, JINST **3** no. 08, (2008) S08001.
2. ATLAS Collaboration, JINST **3** (2008) S08003.
3. ATLAS Collaboration, Phys. Lett. **B 716** (2012) 1, `arXiv:1207.7214 [hep-ex]`.

4. CMS Collaboration, Phys. Lett. **B 716** (2012) 30, arXiv:1207.7235 [hep-ex].
5. F. Englert and R. Brout, Phys. Rev. Lett. **13** (1964) 321–323.
6. P. W. Higgs, Phys. Rev. Lett. **13** (1964) 508–509.
7. G. S. Guralnik, C. R. Hagen, and T. W. B. Kibble, Phys. Rev. Lett. **13** (1964) 585–587.
8. ATLAS Collaboration, ATLAS-CONF-2012-127 (2012).
9. ATLAS Collaboration, ATLAS-CONF-2012-162 (2012).
10. ATLAS Collaboration, ATLAS-CONF-2012-170 (2012).
11. ATLAS Collaboration, ATLAS-CONF-2013-014 (2013).
12. ATLAS Collaboration, ATLAS-CONF-2013-034 (2013).
13. E. Mountricha, *these proceedings*.
14. ATLAS Collaboration, ATLAS-CONF-2013-012 (2013).
15. ATLAS Collaboration, ATLAS-CONF-2013-013 (2013).
16. ATLAS Collaboration, ATLAS-CONF-2013-030 (2013).
17. D. Puigh, *these proceedings*.
18. ATLAS Collaboration, ATLAS-CONF-2012-160 (2012).
19. ATLAS Collaboration, ATLAS-CONF-2012-161 (2012).
20. G. Cowan, K. Cranmer, E. Gross, and O. Vitells, Eur. Phys. J. **C71** (2011) 1554.
21. LHC Higgs Cross Section Working Group, A. David *et al.*, LHCHXSWG-2012-001 (2012), arXiv:1209.0040 [hep-ph].

Higgs Candidate Property Measurements with the Compact Muon Solenoid

Andrew Whitbeck, on behalf of the CMS Collaboration
Department of Physics and Astronomy, Johns Hopkins University, Baltimore 21218, USA

Property measurements of the Higgs boson candidate are presented using proton-proton collision data collected with the Compact Muon Solenoid (CMS) detector corresponding to integrated luminosities of 5.1 fb^{-1} at $\sqrt{s}$=7 TeV and up to 19.6 fb^{-1} at $\sqrt{s}$=8 TeV. Combined mass measurements using the ZZ and $\gamma\gamma$ decay channels and consistency of couplings of the observed boson with respect to those predicted from the SM Higgs boson is tested using data corresponding to 5.1 fb^{-1} at $\sqrt{s}$=7 TeV and up to 12.2 fb^{-1} at $\sqrt{s}$=8 TeV. The spin-parity of the boson is studied using the ZZ and WW decay channels.

1 Introduction

The Standard Model (SM) of electroweak interaction[1,2,3] utilizes a complex doublet scalar field to spontaneously break electroweak symmetry in order for the weak gauge bosons to acquire mass and predicts a massive neutral scalar, the Higgs boson[4,5,6,7]. In July 2012, the CMS and ATLAS collaborations announced[8,9] the discovery of a new Higgs-like boson at a mass around 125 GeV. These proceedings present property measurements of this Higgs-like resonance using the CMS detector[10]. Combining different channels we present the mass measurement as well as the consistency of production and decay rates and couplings with respect to expectation from SM Higgs using 5.1 (12.2) fb^{-1} of data at $\sqrt{s}$ =7 (8) TeV. Finally, the consistency of data with respect several different spin-parity hypotheses is tested.

2 Combined properties

The combination of signal strength measurements in different channels can provide information about the properties of the observed resonance. In this section, results combining a number of channels to measure or constrain resonance properties are presented. These results were obtained using up to 5.1 (12.2) fb^{-1} of the 7 (8) TeV datasets[a]. The details of each individual channel can be found elsewhere[11,12,13,14,15,16,17].

2.1 Mass measurement

The measurement of the resonance mass is done by simultaneously fitting for the mass, m_X, and the signal strength, μ, in both the ZZ and $\gamma\gamma$ channels, the two high resolution decay channels. The 68% CL contours are shown as a function of μ and m_X in the left plot of figure 1. The red and green contours correspond to the individual scan in the ZZ and $\gamma\gamma$ channel respectively while the black is the combination of the two. The relative signal strength in the two channels is fixed to SM expectation.

[a]Results obtained from the $\gamma\gamma$ channel correspond to 5.3 fb^{-1} of the 8 TeV dataset.

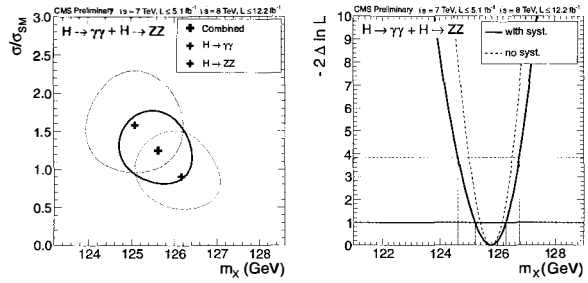

Figure 1: Distribution of -2ln$\mathscr{L}$ vs μ and m_X (left) for the $\gamma\gamma$ channel (green), the ZZ channel (red), and the combination of the two (black). The right plot shows the combination of the $\gamma\gamma$ and ZZ channels profiling the signal strength of each of channel.

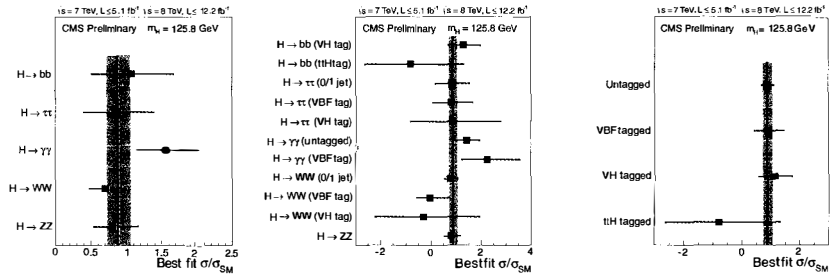

Figure 2: left: Values of μ for the combination (solid vertical line) and for sub-combinations grouped by decay mode (points). middle: Values of μ for the combination (solid vertical line) and for contributing channels (points). right: Values of μ for the combination (solid vertical line) and for sub-combinations grouped by a signature enhancing specific production mechanisms (points). The 68% CL interval is represented by the green band for the combination and the red bars for the sub-combinations.

To be more model independent, the 1D -2ln$\mathscr{L}$ scan of m_X is done by profiling μ separately in the ZZ channel as well as in the untagged and di-jet categories of the $\gamma\gamma$ channel. The 1D -2ln$\mathscr{L}$ scan for this measurement is shown in the right plot of figure 1 and the 68% CL interval is found to be $m_X = 125.8 \pm 0.4$ (stat) ± 0.4 (syst) GeV.

2.2 Signal strengths

The compatibility of the observed excess with the SM Higgs prediction can be first assessed by measuring the combined signal strength and the signal strength channel by channel. Figure 2 shows the 68% CL interval of the combined signal strength, green band, and the 68% CL interval of the signal strength measured by individual channels. All channels individually as well as the combination of all channels are consistent with SM expectation. The 68% CL interval for the combined signal strength is found to be 0.88 ± 0.21 when $m_X = 125.8$ GeV.

2.3 Compatibility of data with SM Higgs couplings

The total event yield in any channel can be related to the partial and total width of the Higgs as follows

$$N(xx \to H \to yy) \sim \sigma(xx \to H) \times \mathscr{B}(H \to yy) \sim \frac{\Gamma_{xx}\Gamma_{yy}}{\Gamma_{tot}}.$$

Thus, there are eight parameters, $\Gamma_{WW}, \Gamma_{ZZ}, \Gamma_{tt}, \Gamma_{bb}, \Gamma_{\tau\tau}, \Gamma_{gg}, \Gamma_{\gamma\gamma}, \Gamma_{tot}$, which describe the rates of the current searches. Testing for possible deviations from SM Higgs expectations can be

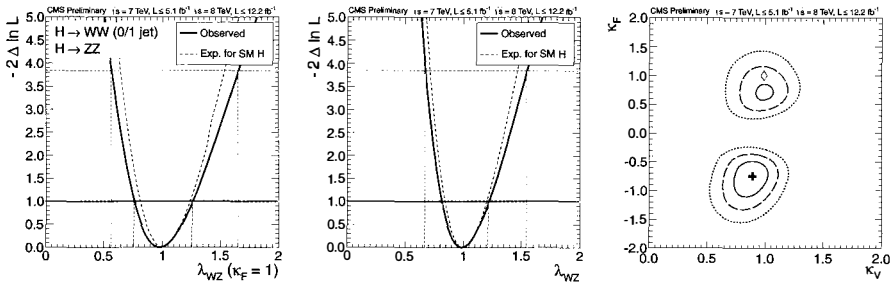

Figure 3: left: 1D test statistics q(λ_{WZ}) scan vs the coupling modifier ratio λ_{WZ}, profiling the coupling modifier κ_Z and all other nuisances. The coupling to fermions is taken to be the SM one ($\kappa_f = 1$). middle: 1D test statistics q(λ_{WZ}) scan vs the coupling modifier ratio λ_{WZ}, profiling the coupling modifiers κ_Z and κ_f and all other nuisances. right: 2D test statistics q(κ_V, κ_f) scan. Solid, dashed, and dotted contour represent the 68%, 95%, and 99.7% CL areas.

formulated in terms of scale factors, κ_i, which represent deviations with respect to the SM Higgs partial widths, e.g. $\kappa_W^2 = \Gamma_{WW}/\Gamma_{WW}^{SM}$. Any deviations from $\kappa_i = 1$ would imply physics beyond the SM. The measurements presented in this section are following the prescription of the LHC Higgs Cross Section Working Group[21].

By requiring an approximate custodial symmetry, tree-level relations between the W and Z masses as well as the W and Z couplings to the Higgs boson can be protected against large radiative corrections. Thus, large discrepancies of the ratio of the W and Z couplings to Higgs are an indication of physics beyond the standard model. To test this, we fit for the ratio $\lambda_{WZ} = \kappa_W/\kappa_Z$. In order to properly account for small differences in the VBF fraction between the $H \to ZZ$ and $H \to WW$ channels, κ_Z is profiled. The fits are then done in two different ways, using only the $H \to ZZ$ and $H \to WW$ channels, left plot of figure 3, and using all channels profiling κ_f[b] in addition to κ_Z, middle plot of figure 3. We find that in both cases λ_{WZ} is consistent with SM expectation and fix it to unity for all subsequent measurements. The 95% CL interval for λ_{WZ} using the ZZ and WW channels is [0.57,1.65], and [0.67,1.55] using the combination of all channels.

We also test the compatibility of data with respect to the SM Higgs using two parameters, κ_v and κ_f, which are scaling factors for all W/Z couplings and fermionic couplings respectively. Since $\Gamma_{\gamma\gamma}$ is induced via a W and top loop, it scales as $|\alpha\kappa_V + \beta\kappa_f|^2$. As such, the $\gamma\gamma$ channel is the only channel sensitive to the relative sign between κ_V and κ_f. The right plot of figure 3 shows the -2ln$\mathscr{L}$ scan vs κ_V, κ_f. The global minimum lies in the (+,-) quadrant because of the excess in the $\gamma\gamma$ channel. However, the data is still consistent with the standard model within 2σ. Fixing κ_V (κ_f) to unity, the 95% CL interval for κ_f (κ_V) is found to be [0.40,1.12] ([0.78,1.19]).

Since $H \to \gamma\gamma$ and $g\,g \to H$ are induced through loops, κ_γ and κ_g are sensitive to the presence of new particles. The left plot of figure 4 shows the -2ln$\mathscr{L}$ scan for κ_γ and κ_g and is consistent with the SM to within 2σ. Profiling either κ_γ (κ_g), we find that the 95% CL interval for κ_g (κ_γ) is [0.55,1.07] ([0.98,1.92]). BSM decay channels can be probed by fitting for $BR_{BSM} = \Gamma_{BSM}/\Gamma_{tot}$. When profiling κ_γ and κ_g the 95% CL interval for BR_{BSM} is found to be [0.00,0.62].

We can also test for asymmetries between either quark and lepton or up-type and down-type fermions. These deviation can occur in different flavors of two Higgs doublet models. Two ratios are constructed to test these hypotheses, $\lambda_{du} = \kappa_d/\kappa_u$ and $\lambda_{\ell q} = \kappa_\ell/\kappa_q$. The middle plot of figure 4 shows the -2ln$\mathscr{L}$ scan vs λ_{du} with κ_V and κ_u profiled. The 95% CL interval for λ_{du} is [0.45,1.66]. The right plot of figure 4 shows the -2ln$\mathscr{L}$ scan vs $\lambda_{\ell q}$ with κ_V and κ_q profiled. The

[b] κ_f is a single modifier for all couplings to fermions

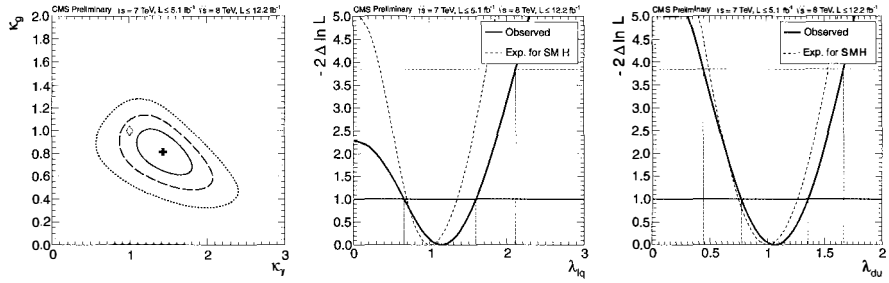

Figure 4: left: 2D test statistics q(κ_g, κ_γ) scan assuming that $\Gamma_{BSM} = 0$. Solid, dashed, and dotted contours show the 68%, 95%, and 99.7% CL ranges. middle: 1D test statistics q(λ_{du}) scan vs the coupling modifier ratio λ_{du}, profiling the coupling modifiers κ_u and κ_V and all other nuisances. κ_u, and κ_V are always taken to be positive. right: 1D test statistics q($\lambda_{\ell q}$) scan vs the coupling modifier ratio $\lambda_{\ell q}$, profiling the coupling modifiers κ_u and κ_V and all other nuisances. κ_q, and κ_V are always taken to be positive.

J^P	production	comment	expect ($\mu = 1$)	obs. 0^+	obs. J^P	CL_s
0^-	$gg \to X$	pseudoscalar	$2.6\sigma(2.8\sigma)$	0.5σ	3.3σ	0.16%
0_h^+	$gg \to X$	higher dim operator	$1.7\sigma(1.8\sigma)$	0.0σ	1.7σ	8.1%
2^+_{mgg}	$gg \to X$	minimal couplings	$1.8\sigma(1.9\sigma)$	0.8σ	2.7σ	1.5%
2^+_{mqq}	$q\bar{q} \to X$	minimal couplings	$1.7\sigma(1.9\sigma)$	1.8σ	4.0σ	$< 0.1\%$
1^-	$q\bar{q} \to X$	exotic vector	$2.8\sigma(3.1\sigma)$	1.4σ	$> 4.0\sigma$	$< 0.1\%$
1^+	$q\bar{q} \to X$	exotic pseudovector	$2.3\sigma(2.6\sigma)$	1.7σ	$> 4.0\sigma$	$< 0.1\%$

Table 1: List of models used in analysis of spin-parity hypothesis corresponding to the pure states of the type noted. The expected separation is quoted for two scenarios, when the signal strength for each hypothesis is pre-determined from the fit to data and when events are generated with SM expectation for the signal yield ($\mu = 1$). The observed separation quotes consistency of the observation with the 0^+ model or J^P model, and corresponds to the scenario when the signal is pre-determined from the fit to data. The last column quotes the CL_s criterion for the J^P models.

95% CL interval for $\lambda_{\ell q}$ is [0.00,2.11]. Both measurements are consistent with SM expectation.

3 Spin-Parity

Understanding the spin and quantum numbers of the new boson is an important check of the SM. Different J^P quantum numbers and different couplings manifest themselves in the angular and mass correlations of di-boson decays allowing ZZ and WW events to be used to constrain the spin and parity of the boson. Using hypothesis testing, we evaluated the consistency of data with respect to either the SM Higgs hypothesis or six alternative J^P hypotheses. The alternative models tested are outline in Table 1 and discussed in detail elsewhere[20]. Results presented in this section are using up to 5.1 (19.6) fb^{-1} for the 7 (8) TeV dataset.

3.1 ZZ

The ZZ spin-parity analysis is done using a 2D unbinned likelihood to describe data. Analogous to how the signal strength measurement is performed[18], events are described using two variables. The first variable is a kinematic discriminant (KD) to separate signal from background, D_{bkg}, built from the combination of $m_{4\ell}$ and the KD used in the signal strength measurements[18]. The second is a KD which separates SM Higgs from some alternative J^P signal and is built from the seven dimensional probability for either SM Higgs, P_{SM}, or an alternative model, P_{J^P},

$$D_{J^P} = \frac{P_{SM}}{P_{SM}+P_{J^P}} = [1 + \frac{P_{SM}(m_{Z_1},m_{Z_2},\vec{\Omega};m_{4\ell})}{P_{J^P}(m_{Z_1},m_{Z_2},\vec{\Omega};m_{4\ell})}]^{-1},$$

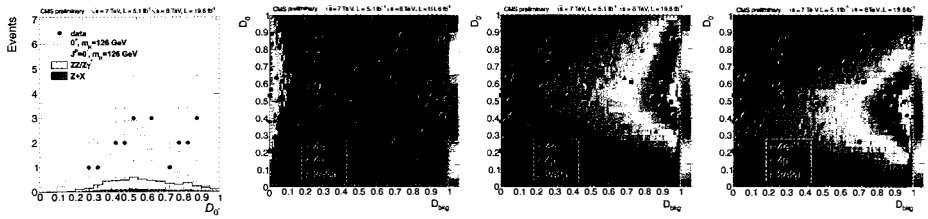

Figure 5: Distributions of D_{JP} with the requirement $D_{bkg} > 0.5$. Distributions in data (points with error bars) and expectations for background and signal are shown.Distributions of D_{0-} vs D_{bkg} for background (left), SM Higgs (middle), and pseudoscalar (right). MC expectation is represented by the color map while data is represented by black points.

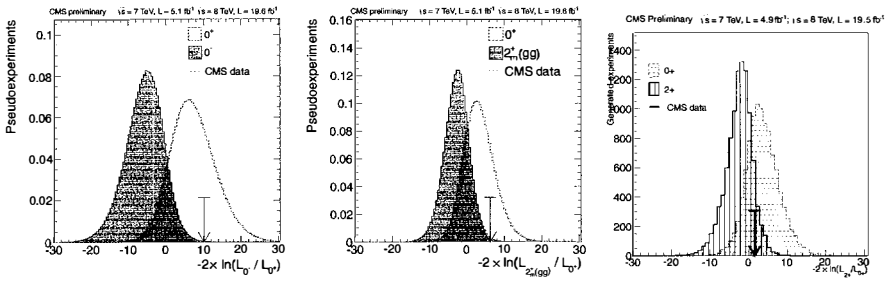

Figure 6: left,middle: Distribution test statistic for two signal types (0^+, yellow histogram, and J^P, blue histogram) for m_H = 126 GeV. Separation between 0^+ and 0^- (2^+_{mgg}) is shown on the left (middle). The arrow indicates the observed q-value. right: Distribution of test statistic, q, for SM Higgs hypothesis (purple histogram) and minimal coupling graviton hypothesis (blue histogram). Green arrow shows the q-value for data.

where Ω represents the five decay angles. The D_{0-} distributions after selecting events where $D_{bkg} > 0.5$ are shown in figure 5 along with the 2D distributions D_{bkg} vs. D_{0-} for background, SM Higgs, and pseudoscalar MC. All distributions are shown in the mass range 106< $m_{4\ell}$ <141 GeV.

Hypothesis tests were performed testing the SM Higgs hypothesis against each of the six alternative hypotheses, J^P=$0^-, 0^+_h, 1^+, 1^-, 2^+_{mgg}, 2^+_{mq\bar{q}}$. Toys were generated according to each hypothesis assuming either the SM Higgs cross section ($\mu = 1$) or using the best-fit signal strength from data for each hypothesis. The test statistic (q = -2ln($\mathscr{L}_{JP}/\mathscr{L}_{SM}$)) distributions for each measurement are shown in figure 6. A CL_s criterion is defined as

$$CL_s = \mathscr{P}(q \geq q_{obs}|J^P)/\mathscr{P}(q \geq q_{obs}|SM).$$

Table 1 shows the expected separation, the observed separation assuming either the J^Por the 0^+ hypothesis, and the CL_s value for each of the six alternative hypotheses. The expected separations range from 1.7-2.8σ while the CL_s values range from 0.1%-10% when generating toys from the best-fit μ.

A fit for the continuous parameter, f_{a3}, was also performed. This parameter represents the amount of CP-violation present in data and can be defined as

$$f_{a3} = |A_3|^2/(|A_1|^2 + |A_3|^2).$$

A_1, A_2, and A_3 are defined in terms of the most general amplitude for a scalar decaying to two vector bosons,

$$A = v^{-1}\epsilon_1^{*\mu}\epsilon_2^{*\nu}(a_1 g_{\mu\nu}m_H^2 + a_2 q_\mu q_\nu + a_3\epsilon_{\mu\nu\alpha\beta}q_1^\alpha q_2^\beta) = A_1 + A_2 + A_3,$$

where ϵ_i are the Z boson polarization vectors, q_i the Z boson momenta, a_i couplings, m_H the mass of the resonance, and $\epsilon_{\mu\nu\alpha\beta}$ the Levi-Civita tensor. In this measurement, we fix $A_2 = 0$.

Non-zero contributions from the A_3 term imply f_{a3} will be non-zero while if the resonance is either a pure SM Higgs (pseudoscalar), f_{a3} would be 0 (1). It should be stressed that f_{a3} is not a parameter which defines the mixture of parity-even and parity-odd states. The latter would require a model-dependent interpretation of the f_{a3} measurement. The best-fit value is found to be f_{a3}=$0.00^{+0.23}_{-0.00}$ and the 95% CL interval is [0.0,0.58].

3.2 WW

The WW spin-parity analysis is done using a 2D binned likelihood, $m_{\ell\ell}$ vs m_T[19], to describe data. The SM Higgs hypothesis is tested only against the minimal coupling graviton model produced through gluon-gluon fusion, $J^P = 2^+_{mgg}$. Distributions of the test statistic q = -2ln($\mathscr{L}_{2^+_{mgg}}/\mathscr{L}_{SM}$) are shown for SM Higgs hypothesis (purple) and the alternative hypothesis (blue) in the right plot of figure 6. The expected separation is 1.9 σ while the observed significance is 1.3 (0.9) σ with respect to the 2^+_{mgg} (0^+) hypothesis, slightly disfavoring the 2^+_{mgg} hypothesis, which corresponds to a CL_s value of 12% when generating toys from the best-fit μ.

4 Conclusions

Property measurements have been presented for the Higgs-like resonance. The best-fit mass is found to be 125.8 $\pm$0.4(stat) $\pm$0.4 (syst) GeV. The best-fit signal strength combining all channels is found to be 0.88 $\pm$0.21 measured at the best-fit mass. The consistency of the couplings of the observed boson with respect to SM Higgs expectation is tested in various ways and no significant deviation is found.

Consistency of kinematic distributions with respect to either the SM Higgs hypothesis and several alternative signal hypotheses of various spin and parity has been tested. In all cases, data is found to disfavor the alternative hypotheses. We find that data disfavors the 0^-, 2^+_{mgg}, 2^+_{mqq}, 1^+, and 1^- hypotheses at more than 2σ.

References

1. S. L. Glashow, Nucl. Phys. **22**, 579 (1961).
2. S. Weinberg, Phys. Rev. Lett. **19**, 1264 (1967).
3. A. Salam, Conf. Proc. C **680519**, 367 (1968).
4. F. Englert and R. Brout, Phys. Rev. Lett. **13**, 321 (1964).
5. P. W. Higgs, Phys. Lett. **12**, 132 (1964).
6. P. W. Higgs, Phys. Rev. Lett. **13**, 508 (1964).
7. G. S. Guralnik, C. R. Hagen and T. W. B. Kibble, Phys. Rev. Lett. **13**, 585 (1964).
8. S. Chatrchyan *et al.* [CMS], Phys. Lett. B **716**, 30 (2012) [arXiv:1207.7235 [hep-ex]].
9. G. Aad *et al.* [ATLAS], Phys. Lett. B **716**, 1 (2012) [arXiv:1207.7214 [hep-ex]].
10. S. Chatrchyan *et al.* [CMS], JINST **3**, S08004 (2008).
11. CMS Collaboration, CMS-PAS-HIG-12-015 (2012).
12. CMS Collaboration, CMS-PAS-HIG-12-044 (2012).
13. CMS Collaboration, CMS-PAS-HIG-12-043 (2012).
14. CMS Collaboration, CMS-PAS-HIG-12-051 (2012).
15. CMS Collaboration, CMS-PAS-HIG-11-024 (2011).
16. CMS Collaboration, CMS-PAS-HIG-12-003 (2012).
17. CMS Collaboration, CMS-PAS-HIG-12-041 (2012).
18. CMS Collaboration, CMS-PAS-HIG-13-002 (2013).
19. CMS Collaboration, CMS-PAS-HIG-13-003 (2013).
20. S. Bolognesi et al. Phys. Rev. D **86**, 095031 (2012) [arXiv:1208.4018 [hep-ph]].
21. LHC Higgs Cross Section Working Group et al., arxiv::1209.0040

COMPOSITE OR ELEMENTARY? PROBING THE NATURE OF THE HIGGS

ANNA KAMIŃSKA
Rudolf Peierls Centre for Theoretical Physics, University of Oxford, 1 Keble Road, OX1 3NP, Oxford, UK

I discuss consequences of electroweak symmetry breaking by strong dynamics, assuming the existence of a light composite scalar appearing as a pseudo-Goldstone boson of some global symmetry of the new strongly interacting sector. In such a scenario, the composite scalar has properties very similar to the Standard Model Higgs, but the existence of additional resonances with different spins is also expected. Properties and phenomenology of lightest spin-1 resonances are considered in a simple general effective Lagrangian description. The question whether the effects of spin-1 resonances can be observed at the LHC, shedding light on the nature of the Higgs boson, is addressed.

1 Introduction

A composite Higgs boson originating from electroweak symmetry breaking induced by some new strongly interacting sector is a viable alterative to an elementary, Standard Model (SM) - like Higgs scenario. It does not suffer under the hierarchy problem and its properties at energies low with respect to the scale of strong dynamics can be very similar to the properties of the SM scalar. Moreover, the composite Higgs boson can be made naturally light with respect to the compositeness scale when it appears as a pseudo-Goldstone boson (PGB) of the global symmetry breaking of the strong sector. The minimal model of this kind is based on the $SO(5) \to SO(4)$ global symmetry breaking pattern [1], which produces a full pseudo-Goldstone composite Higgs doublet.

In order to gain a better understanding of the electroweak symmetry breaking mechanism it is crucial to look for signatures distinguishing a composite Higgs boson from an elementary Higgs boson. First of all, the couplings of a PGB composite Higgs to W and Z gauge bosons and to fermions are modified with respect to the couplings of an elementary Higgs boson. The modification is scaled by the parameter $\xi = (v/f_\pi)^2$, which describes the squared ratio of the electroweak scale to the scale of strong dynamics. In the minimal composite Higgs model the couplings of the composite scalar to W and Z gauge bosons is given by

$$\mathcal{L}^{(2)} = \frac{1}{2}\partial_\mu h \partial^\mu h + \frac{v^2}{4}\left(1 + 2a\frac{h}{v} + b\frac{h^2}{v^2} + ...\right) \mathrm{Tr}\left\{D^\mu U\, D_\mu U^\dagger\right\} \qquad (1)$$

where $U = e^{i\pi^a(x)\sigma^a/v}$ parameterizes Goldstone bosons corresponding to longitudinal W and Z and transforms as $g_L U g_R^\dagger$ under the global $SU(2)_L \times SU(2)_R$ group gauged by the electroweak group. Couplings $a = \sqrt{1-\xi}$, $b = 1-2\xi$ reproduce the Standard Model values $a_{SM} = b_{SM} = 1$ in the limit $\xi \to 0$ with $v = const.$ Hence, we expect ξ to be small, $\xi \lesssim 0.3$. In fact, the departure from SM-like Higgs couplings might not be detectable at the LHC. Hence it is worth to look simultaneously for other signatures of strong electroweak breaking related to resonances of different spins. Both spin-1/2 and spin-1 resonances should contribute to indirect (electroweak precision tests, flavor observables) and direct signals of physics beyond the Standard Model. Here I focus on effects of spin-1 resonances, constructing a simple, general and self-consistent effective framework to study their properties and LHC phenomenology.

2 Building the effective Lagrangian

In order to introduce spin-1 resonances into the effective description I use the formalism of hidden local symmetry [2], which works very well for the description of vector resonances in low energy QCD. Generalizing this formalism to arbitrary global symmetry breaking patterns $\mathcal{G} \to \mathcal{H}$ means that in order to write down the effective Lagrangian for the analogue of vector resonances one has to add a new 'hidden' gauge group $\mathcal{H}_{local}$, which gauge bosons provide the degrees of freedom needed for the description of spin-1 resonances. Then the new building block for the effective Lagrangian is a sigma-model field S related to $\mathcal{G} \times \mathcal{H}_{local} \to \mathcal{H}$ symmetry breaking and transforming as

$$S \;\to\; g\, S\, h^\dagger, \qquad g \in \mathcal{G},\; h \in \mathcal{H}_{local}, \quad \langle S \rangle = \mathbf{1}. \tag{2}$$

The leading order effective Lagrangian term

$$\mathcal{L} \ni v_1^2 \mathrm{Tr}\left\{ D_\mu S D^\mu S^\dagger \right\} \tag{3}$$

introduces through covariant derivatives of S mixing terms and interactions between gauge fields of the Standard Model electroweak group sitting in $\mathcal{G}$ and the new 'hidden' local group. The symmetry breaking pattern can be further modified to take into account more and more spin-1 states. Eigenstates in the spin-1 sector are now combinations of W_μ^a, B_μ and hidden gauge ρ_μ fields. However, if we assume a hierarchy of couplings $g, g' \ll g_\rho$, the lightest eigenstates correspond at the leading order in g/g_ρ to Standard Model W, Z and photon fields, while the heavy eigenstates correspond at the leading order to ρ fields. Moreover, for small values of ξ, there exists a 'pairing up' between gauge bosons corresponding to $SU(2)_L$ ($SU(2)_R$) and $SU(2)_{L\,hidden}$ ($SU(2)_{R\,hidden}$) groups respectively, which leads to the conclusion that ρ_L and ρ_R resonances have the strongest interactions with Standard Model particles and are most important from the point of view of LHC phenomenology.

3 LHC phenomenology

In this section we will focus on the minimal $SO(5) \to SO(4)$ composite Higgs model with lightest vector resonances ρ_L and ρ_R corresponding to $SO(4)_{hidden}$. This setup should be representative for the LHC phenomenology of spin-1 resonances in general composite Higgs models. The most general leading order effective Lagrangian related to $SO(5) \times SO(4)_{hidden} \to SO(4)$ has 3 free parameters, which can be chosen as ξ, g_ρ and $g_{\rho\pi\pi}$, where g_ρ is the 'hidden' gauge coupling and $g_{\rho\pi\pi}$ describes the mean interaction of a single ρ resonance with two pions corresponding to W_L and Z_L. The mass of spin-1 resonances is given by $m_\rho^2 \approx 2 g_\rho g_{\rho\pi\pi} v^2/\xi$. Interactions of heavy spin-1 eigenstates with SM matter fields are introduced by the admixture of heavy $\tilde{\rho}_L$ and $\tilde{\rho}_R$

eigenstates in Standard Model fields

$$
\begin{aligned}
W_\mu^\pm &\approx \tilde{W}_\mu^\pm - \frac{\sqrt{2}}{2}\sqrt{2-\xi}\,\frac{g}{g_\rho}\tilde{\rho}_{L\,\mu}^\pm \\
Z_\mu &\approx \tilde{Z}_\mu - \frac{\sqrt{2-\xi}}{\sqrt{2}}\frac{g^2-g'^2}{g_\rho\sqrt{g^2+g'^2}}\tilde{\rho}_{L\,\mu}^0 - \frac{2\sqrt{2-2\xi}}{(2-\xi)^{3/2}}\frac{g'^2}{g_\rho\sqrt{g^2+g'^2}}\tilde{\rho}_{R\,\mu}^0 \\
A_\mu &\approx \tilde{A}_\mu - \sqrt{\frac{2}{2-\xi}}\frac{e}{g_\rho}\tilde{\rho}_{L\,\mu} + \sqrt{\frac{2-2\xi}{2-\xi}}\frac{e}{g_\rho}\tilde{\rho}_{R\,\mu}.
\end{aligned}
\tag{4}
$$

The couplings of ρ resonances with the third generation of fermions can be enhanced by partial compositeness, but we neglect this effect here. One can notice that the coupling of a ρ resonance to two fermions is enhanced for small values of ξ, while for a given value of m_ρ and g_ρ the coupling of a ρ resonance to two SM gauge bosons scales down with ξ. Numerical analysis shows that spin-1 resonances are mainly produced in the Drell-Yan process. The production cross section of neutral (smooth line) and charged (dashed line) ρ_L resonances at the LHC at 8 TeV and 14 TeV is given in Fig. 1 for $\xi = 0.2$ and $g_\rho = 4$. Branching ratios of a neutral resonance with these parameters are given in Fig. 2. One can notice that while the width is dominated by the production of SM gauge boson pairs or a Higgs boson accompanied by a gauge boson, branching ratios into quark pairs and lepton pairs are non-negligible. As it turns out, due to low backgrounds, LHC searches for dilepton resonances [3] give at present the most stringent exclusion limits for spin-1 resonances. The impact of LHC searches on the parameter space of spin-1 resonances spanned by g_ρ and $g_{\rho\pi\pi}$ can be seen in Fig. 3 for $\xi = 0.2$ and in Fig. 4 for $\xi = 0.07$. The various colors in these figures describe the approximate cutoff of the effective description derived by the analysis of perturbative unitarity of longitudinal gauge boson scattering (numbers on yellow background give the energy of the cutoff in TeV). Black curves and numbers on white background correspond to the ρ resonance mass, also in TeV. White regions are excluded because the cutoff drops below the resonance mass. Black regions are excluded by direct LHC searches. One can notice that the exclusion limits go up to 1.5 TeV for $\xi = 0.2$ and 2 TeV for $\xi = 0.07$. They go down with growing values of g_ρ, as the interaction with SM matter fields become suppressed.

It is interesting to compare exclusion limits from direct searches with the ones originating form electroweak precision tests. Figures 5 and 6 show the $\hat{S} = \frac{g^2}{16\pi}S$ parameter for $\xi = 0.2$ and $\xi = 0.07$ (black curves with labels on white background). It can be seen that the LHC direct searches are already exploring the parameter space consistent with electroweak precision data.

4 Conclusions

Properties and LHC phenomenology of spin-1 resonances were studied using a simple, general effective description built using the hidden local symmetry formalism. It shows that for small values of ξ the spin-1 resonance coupling to two fermions is enhanced. The resonances are mainly Drell-Yan produced and they decay mostly to SM gauge boson pairs or a Higgs boson accompanied by a gauge boson, but branching ratios into fermion pairs are non-negligible. The most stringent exclusion limits are obtained from searches for resonant dilepton production at the LHC. Direct searches are already probing the parameter space of spin-1 resonances allowed by electroweak precision data.

Acknowledgments

This work has been supported by a Marie Curie Initial Training Network Fellowship PITN-GA-2009-237920-UNILHC.

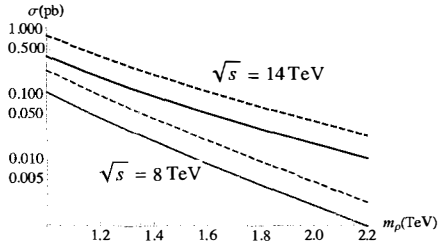

Figure 1: Drell-Yan production cross section of ρ_L.

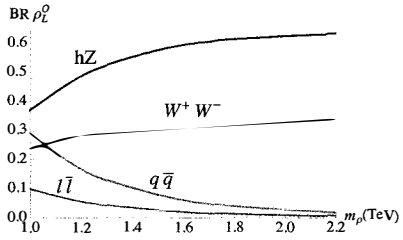

Figure 2: Branching ratios of a neutral ρ_L.

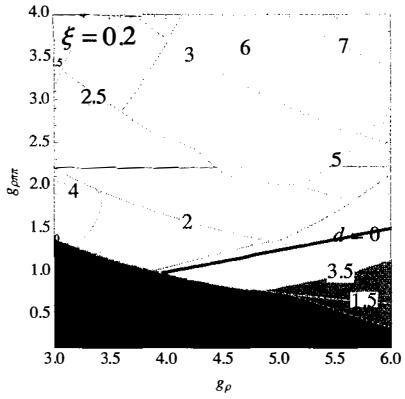

Figure 3: LHC exclusion limits for $\xi = 0.2$.

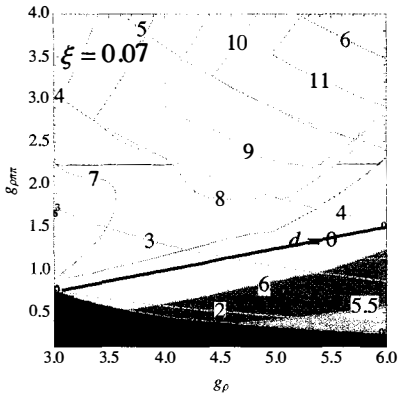

Figure 4: LHC exclusion limits for $\xi = 0.07$.

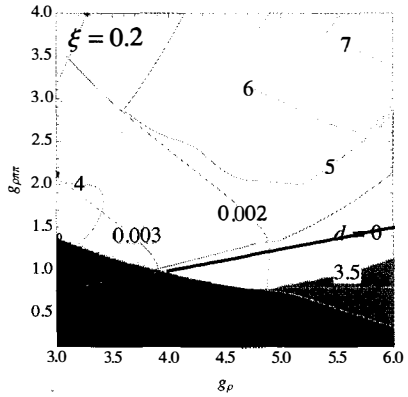

Figure 5: Values of $\hat{S}$ for $\xi = 0.2$.

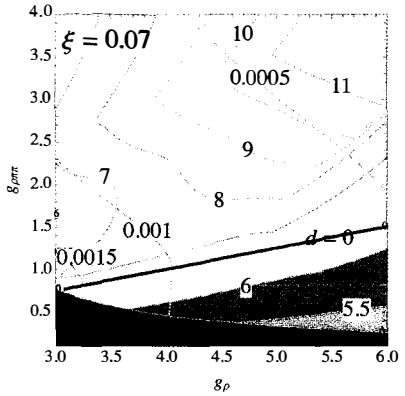

Figure 6: Values of $\hat{S}$ for $\xi = 0.07$.

References

1. K. Agashe, R. Contino, A. Pomarol, Nucl. Phys. **B719** (2005) 165-187. [hep-ph/0412089].
2. M. Bando, T. Kugo and K. Yamawaki, Phys. Rept. **164** (1988) 217.
3. S. Chatrchyan *et al.* [CMS Collaboration], arXiv:1212.6175 [hep-ex].

Determination of Higgs Spin and Parity at the LHC

M. M. Mühlleitner
Institut für Theoretische Physik, KIT, D-76049 Karlsruhe, Germany

After the discovery of a new scalar particle by the Large Hadron Collider (LHC) experiments ATLAS and CMS, its properties have to be determined, in order to clarify if it is really the Higgs boson, *i.e.* the particle related to the Higgs mechanism. This requires the measurement of its couplings to the Standard Model (SM) particles, the determination of its spin and parity quantum numbers and finally the extraction of the Higgs boson trilinear and quartic self-couplings. In this contribution it will be shown how spin and parity quantum numbers of the SM Higgs boson can unambiguously be determined at the LHC.

1 Introduction

The discovery of a 125 GeV Higgs boson [1,2] has triggered a large number of investigations on the Higgs boson properties, among which the determination of the spin (J), parity (P) and charge conjugation (C) quantum numbers [3], which are for the SM Higgs boson $J^{PC} = 0^{++}$. The Higgs sector of extensions beyond the SM, like *i.e.* supersymmetry, may additionally contain CP-odd scalar (pseudoscalar) particles or Higgs states which are CP-violating mixtures between CP-even and CP-odd components.

The charge conjugation quantum number $C = +$ follows from the observation of decays into $\gamma\gamma$ for pure states in a C-invariant theory.

The spin/parity quantum numbers can be investigated in a systematic way by analyzing the helicity amplitudes of production and decay processes. They do not only provide necessary and sufficient conditions to assign the J^{PC} quantum numbers of real states but also test possible CP-violating Higgs bosons. On the production side gluon and vector boson fusion and Higgs-strahlung give access to the spin/parity quantum numbers. For the decays systematic analyses have been performed in Z^*Z decays with subsequent leptonic Z^* and Z decays, in $\gamma\gamma$ decays and in CP-violating decays into fermions or massive gauge bosons. In the following the decays into virtual and real Z bosons and into photon final states will be analyzed with respect to the determination of the CP quantum numbers. It will be shown that the spin and parity of the SM Higgs boson can be unambiguously determined and that negative parity assignment and higher spin states can be ruled out by combining angular correlations with threshold distributions.

2 Higgs Boson Decay into ZZ^*

The decay of a general pure spin/parity unpolarized boson state H^J into a pair of a virtual Z^* and a real Z boson which subsequently decay into leptons $l_i^\pm$ ($i = 1, 2$),

$$H^J \to Z^*Z \to (l_1^+ l_1^-)(l_2^+ l_2^-)\,, \tag{1}$$

gives access to the spin/parity quantum numbers of H^J. Denoting the polar angles of the leptons $l^-_{1,2}$ in the rest frame of the virtual and real Z bosons by $\theta_{1,2}$, see Fig. 1(a), the differential decay distribution of the polar angles can be expressed in terms of four independent helicity

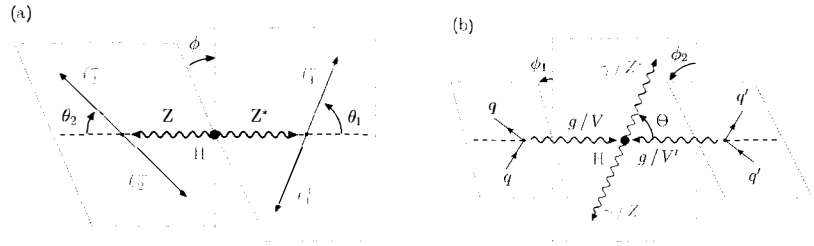

Figure 1: (a) Definition of the polar angles θ_i $(i = 1, 2)$ of the leptons $\ell^-_{1,2}$ in the rest frame of the virtual Z^* and real Z bosons and of the azimuthal angle ϕ for the decay $H^J \to Z^*Z \to (\ell^-_1\ell^+_1)(\ell^-_2\ell^+_2)$. (b) Higgs production through gluon fusion/vector boson fusion ($V = W^\pm, Z$) with subsequent decay into $\gamma\gamma$ and Z^*Z in the Higgs rest frame.

amplitudes [4]

$$\frac{1}{\Gamma}\frac{d\Gamma}{d\cos\theta_1 d\cos\theta_2} = \mathcal{N}^{-1}\Big[\sin^2\theta_1\sin^2\theta_2\,|\mathcal{T}_{00}|^2 + \frac{1}{2}(1+\cos^2\theta_1)(1+\cos^2\theta_2)[|\mathcal{T}_{11}|^2 + |\mathcal{T}_{1,-1}|^2] + (1+\cos^2\theta_1)\sin^2\theta_2\,|\mathcal{T}_{10}|^2 + \sin^2\theta_1(1+\cos^2\theta_2)\,|\mathcal{T}_{01}|^2\Big], \quad (2)$$

fixing the mass squared M_*^2 of the virtual Z^* boson and suppressing the quartic term involving the P-violating parameters which are small for leptonic Z decays. By $\mathcal{N}$ we denote the normalisation factor. Bose symmetry implies for the helicity amplitudes the relations $\mathcal{T}_{\lambda\lambda'} = n_H\mathcal{T}_{-\lambda,-\lambda'}$ and $\mathcal{T}_{\lambda\lambda'}[Z, Z^*] = (-1)^J\mathcal{T}_{\lambda'\lambda}[Z^*, Z]$, with the normality given by $n_H = P(-1)^J$. The azimuthal distribution of the Z-decay planes is given by

$$\frac{1}{\Gamma}\frac{d\Gamma}{d\phi} = \frac{1}{2\pi}\Big[1 + n_H\,|\zeta_1|\cos 2\phi\Big] \quad \text{with} \quad |\zeta_1| = |\mathcal{T}_{11}|^2/\Big[2\sum|\mathcal{T}_{\lambda\lambda'}|^2\Big], \quad (3)$$

again suppressing the terms proportional to the small P-violating parameters. The normality of the Higgs state uniquely determines the sign of the ϕ modulation. Figure 2(a) shows the characteristic behaviour of the azimuthal angle between the Z decay planes. The distributions of the positive (SM) and negative parity decay are mutually anti-cyclic. Such behaviour is also given in jet-jet correlations of electroweak gauge bosons and gluon fusion [3].

In the SM, by angular momentum conservation only two decay helicity amplitudes are non-vanishing, $\mathcal{T}_{00} = (M_H^2 - M_*^2 - M_Z^2)/(2M_*M_Z)$ and $\mathcal{T}_{11} = -1$, so that the angular distributions read [4]

$$\frac{1}{\Gamma_H}\frac{d\Gamma_H}{d\cos\theta_1\cos\theta_2} = \frac{9}{16}\frac{1}{\gamma^4+2}\Big[\gamma^4\sin^2\theta_1\sin^2\theta_2 + \frac{1}{2}(1+\cos^2\theta_1)(1+\cos^2\theta_2)\Big] \quad (4)$$

$$\frac{1}{\Gamma_H}\frac{d\Gamma_H}{d\phi} = \frac{1}{2\pi}\Big[1 + \frac{1}{2}\frac{1}{\gamma^4+2}\cos 2\phi\Big], \quad (5)$$

with $\gamma^2 = (M_H^2 - M_*^2 - M_Z^2)/(2M_*M_Z)$. At the Z^*Z threshold the rise of the distribution in the Z^* invariant mass becomes

$$\frac{d\Gamma[H \to Z^*Z]}{dM_*^2} \Rightarrow \beta \sim \sqrt{(M_H - M_Z)^2 - M_*^2}/M_H \quad \text{for} \quad M_* \Rightarrow M_H - M_Z\,. \quad (6)$$

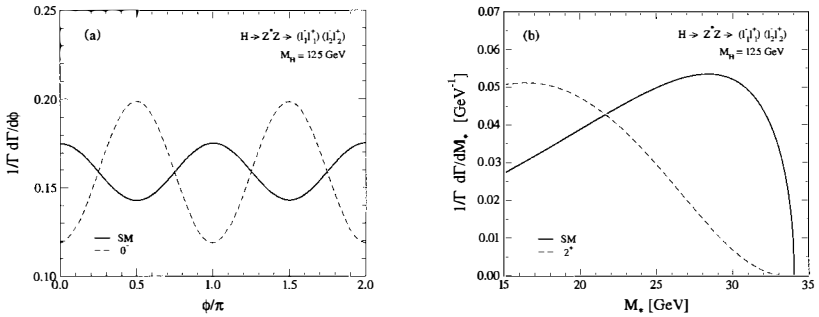

Figure 2: (a) Azimuthal angular distribution between the two Z decay planes for spin = 0 with positive parity in the SM compared with negative parity; (b) Threshold distribution of the decay width $H^J \to Z^*Z$ for the SM and spin-2 even normality bosons, with a Higgs boson mass of 125 GeV.

The necessary conditions for the spin-zero character of the SM Higgs boson are hence given by the observation of the angular distributions associated with the helicity amplitudes $\mathcal{T}_{00}$, $\mathcal{T}_{11}$ and of the steep threshold rise $\sim \beta$. They are also sufficient, as any other spin/parity combination necessarily generates different combinations of threshold power and angular correlations for any pure state, see also [4]. Ambiguities in the angular correlations for higher spin states can be resolved if supplemented by suppression at the threshold. If $(1 + \cos\theta_1^2)\sin^2\theta_2$ and $\sin^2\theta_1(1 + \cos^2\theta_2)$ polar-angle correlations are absent, there is a pronounced difference in the threshold behaviour of the spin-0 SM and spin-2 even normality bosons with identical 4ℓ angular correlations, *cf.* Fig. 2(b).

3 Higgs Boson Decay into $\gamma\gamma$

Furthermore, information on any spin of the Higgs boson can be obtained from the combination of Higgs boson production in gluon fusion with the decay into photons [3],

$$gg \to H^J \to \gamma\gamma\,. \tag{7}$$

The information on the spin is given by the distribution in the polar angle Θ of the final state photons with respect to the incoming partons in the Higgs boson rest frame. Both initial state helicities $\mu - \mu'$ and final state helicities $\lambda - \lambda'$ take the values 0 and ± 2 and add up incoherently in the differential distribution

$$\frac{1}{\sigma}\frac{d\sigma[gg \to H^J \to \gamma\gamma]}{d\cos\Theta} = (2J+1)\left[\mathcal{X}_0\mathcal{Y}_0\mathcal{D}^J_{00} + \mathcal{X}_0\mathcal{Y}_2\mathcal{D}^J_{02} + \mathcal{X}_2\mathcal{Y}_0\mathcal{D}^J_{20} + \mathcal{X}_2\mathcal{Y}_2\mathcal{D}^J_{22}\right]\,, \tag{8}$$

with the probabilities for production $\mathcal{X}_{0,2}$ and decay $\mathcal{Y}_{0,2}$ derived from the $gg \to H^J$ production and $H^J \to \gamma\gamma$ decay helicity amplitudes. The squared Wigner functions $\mathcal{D}^J_{m\lambda} = \frac{1}{2}\{[d^J_{m\lambda}(\Theta)]^2 + [d^J_{m,-\lambda}(\Theta)]^2\}$ generally take the non-trivial maximum power of

$$\mathcal{D}^J \sim \cos^{2J}\Theta\,, \tag{9}$$

independently of the helicity indices 0 or 2. The angular distribution of the photon axis hence provides a characteristic signal of the involved Higgs spin. The spin zero of the Higgs boson manifests itself in an isotropic distribution. Any other spin assignment leads to non-trivial polar angular distributions. Figure 3 for the polar angular distributions shows, that while spin-zero Higgs production is isotropic, any other spin assignment entails non-trivial polar angular

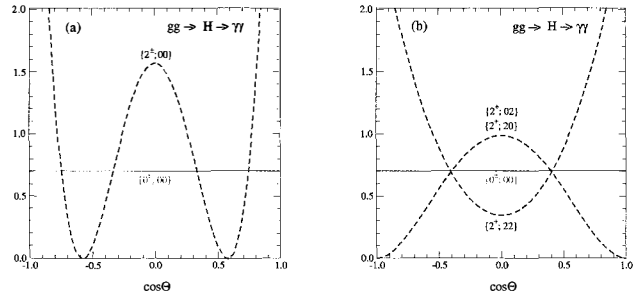

Figure 3: Polar angular distributions of the $\gamma\gamma$ axes in the rest frame of the Higgs boson: the flat SM Higgs signal compared with potential spin-2 distributions; (a) the 'scalar assignment' $\{2;00\}$ and (b) the 'tensor assignment' $\{2;22\}$ and the 'mixed assignments', $\{2;02\}$ and $\{2;20\}$ (all distributions normalized over the interval $|\cos\Theta| \leq 1/\sqrt{2}$). The upper indices denote the allowed parity associated with the distributions in $\gamma\gamma$ decays.

distributions. The figure compares the angular distribution of a SM Higgs boson with $\mathcal{D}^0_{00} = 1$ ($\mathcal{X}_0 = \mathcal{Y}_0 = 1$) with those of spin-2 particles for the 'scalar assignment' $\{2;00\}$ and the 'tensor assignment' $\{2;22\}$. The polar angular distribution can therefore be exploited, whenever a diphoton final state is observed as demanded for a Higgs boson, to determine the spin of the decaying particle and eventually rule out any non-zero spin assignment. Analogously, the decay into ZZ^* can be analyzed if the angular distribution of the ZZ^* axis is measured.

4 Conclusions

It has been shown that spin and parity of the SM Higgs boson can be unambiguously determined at the LHC: The coefficients of the angular distributions of the Higgs boson decay into ZZ^* have to be measured and compared with the unique SM predictions. Additionally the threshold behaviour has to be shown to be linear in the gauge boson helicity as predicted in the SM case. All other states $0^-, 1^\pm, 2^\pm, ...$ are excluded by proving the absence of specific angular correlations (supplemented by high-power threshold factors for even normality states). The observation of isotropic angular correlations between the Z^*Z or $\gamma\gamma$ final state axes and the initial-state parton axis strengthens the conclusion of observing a Higgs boson with spin zero and positive parity.

Acknowledgments

I would like to thank the organizers of "Rencontres de Moriond QCD 2013" for the nice and inspiring atmosphere during the workshop.

References

1. G. Aad *et al.* [ATLAS Collaboration], Phys. Lett. B **716** (2012) 1 [arXiv:1207.7214 [hep-ex]]; G. Aad *et al.* [ATLAS Collaboration], ATLAS-CONF-2012-162.
2. S. Chatrchyan *et al.* [CMS Collaboration], Phys. Lett. B **716** (2012) 30 [arXiv:1207.7235 [hep-ex]]; S. Chatrchyan *et al.* [CMS Collaboration], CMS-PAS-HIG-12-045.
3. *See with references therein:* S. Y. Choi, M. M. Muhlleitner and P. M. Zerwas, Phys. Lett. B **718** (2013) 1031 [arXiv:1209.5268 [hep-ph]].
4. S. Y. Choi, D. J. Miller, 2, M. M. Muhlleitner and P. M. Zerwas, Phys. Lett. B **553** (2003) 61 [hep-ph/0210077].

Efficient, Automatic and Accurate QCD predictions for Higgs (and alike) production at the LHC

Marco Zaro

Centre for Cosmology, Particle Physics and Phenomenology (CP3),
Université Catholique de Louvain
Chemin du Cyclotron 2, B-1348 Louvain-la-Neuve, Belgium

We present a new approach for the determination of the newly discovered resonance at the LHC. This approach is completely generic and model-independent, and it is based on an effective field theory approach. In this approach one can test the different spin and parity hypotheses for the new resonance, with the possibility of including in a consistent manner QCD corrections. We present results at NLO matched with parton shower obtained within the automatic aMC@NLO framework and we compare them with MLM merged samples, showing general good agreement in production and decay related observables.

1 Introduction

After the enthusiasm for the discovery of the new boson at the LHC[1,2], the attention is rapidly shifting towards the measurement of its properties, to assess whether it is or not the Higgs boson as predicted by the Standard Model (SM). These studies consist in systematically testing the various hypotheses and validating them against the data. Any of such hypotheses (e.g. spin and/or parity of this new resonance) needs to be translated into a prediction for the relevant observables. To this aim, two different approaches can be followed: the first approach, implemented e.g. in the JHU code[3,4] consists in introducing all possible couplings, the only constraint being Lorentz symmetry, without any assumption on new physical states. This approach has the limitations of having a large number of free parameters, and, most important, of not allowing the inclusion of higher order corrections in the computation. An alternative approach is the one of building an effective theory, based on the symmetries of the SM, assuming its validity up to a cutoff scale Λ. The number of extra parameters can be therefore reduced by imposing symmetries and by keeping only the lowest dimension operators. This approach has the advantage of providing a theory which is renormalizable order by order in $1/\Lambda$, therefore allowing the inclusion of higher order QCD corrections.

Using the effective theory approach, we will present results for the various spin/parity hypotheses, both at NLO matched to parton shower, employing aMC@NLO, and following the MLM merging prescription[5], as automatically implemented in MadGraph 5[6], to include matrix-element description up to two extra jets. The two approaches are found to reasonably agree for all the studied observables.

2 The Lagrangian

The effective field theory Lagrangian[7] can be written in terms of spin 0, 1 and 2 sectors, corresponding to the possible hypotheses on the nature of the new resonance X, (Higgs boson from now on). Again, we stress that any other new state in the theory is supposed to be heavier than the cutoff Λ.

2.1 Spin 0

The construction of the effective Lagrangian for the spin-0 states is obtained by requiring that the parameterization should i) allow to easily recover the SM case, ii) include 0^- state couplings typical of SUSY or generic 2HDM, iii) allow CP-mixing between 0^+ and 0^- states (parameterized by an angle α, iv) cover the minimal higher dimensional operator beyond the SM for the 0^+ state.
The interaction Lagrangian with fermions and vector-bosons for the spin-0 case is given by

$$\mathcal{L}_0^f = -[c_\alpha \kappa_{Hff} g_{Hff}\, \bar{\psi}_f \psi_f + s_\alpha \kappa_{Aff} g_{Aff}\, \bar{\psi}_f i\gamma_5 \psi_f] X_0, \tag{1}$$

and

$$\begin{aligned}
\mathcal{L}_0^V &= \Big[c_\alpha \kappa_{\rm SM} \big[\tfrac{1}{2} g_{HZZ}\, Z_\mu Z^\mu + g_{HWW}\, W_\mu^+ W^{-\mu}\big] - \frac{1}{4}\big[c_\alpha \kappa_{H\gamma\gamma} g_{H\gamma\gamma}\, A_{\mu\nu} A^{\mu\nu} + s_\alpha \kappa_{A\gamma\gamma} g_{A\gamma\gamma}\, A_{\mu\nu} \widetilde{A}^{\mu\nu}\big] \\
&- \frac{1}{2}\big[c_\alpha \kappa_{HZ\gamma} g_{HZ\gamma}\, Z_{\mu\nu} A^{\mu\nu} + s_\alpha \kappa_{AZ\gamma} g_{AZ\gamma}\, Z_{\mu\nu} \widetilde{A}^{\mu\nu}\big] - \frac{1}{4}\big[c_\alpha \kappa_{Hgg} g_{Hgg}\, G^a_{\mu\nu} G^{a,\mu\nu} + s_\alpha \kappa_{Agg} g_{Agg}\, G^a_{\mu\nu} \widetilde{G}^{a,\mu\nu}\big] \\
&- \frac{1}{4}\frac{1}{\Lambda}\big[c_\alpha \kappa_{HZZ}\, Z_{\mu\nu} Z^{\mu\nu} + s_\alpha \kappa_{AZZ}\, Z_{\mu\nu} \widetilde{Z}^{\mu\nu}\big] - \frac{1}{2}\frac{1}{\Lambda}\big[c_\alpha \kappa_{HWW}\, W^+_{\mu\nu} W^{-\mu\nu} + s_\alpha \kappa_{AWW}\, W^+_{\mu\nu} \widetilde{W}^{-\mu\nu}\big]\Big] X_0,
\end{aligned} \tag{2}$$

where the (reduced) field strength tensors are

$$V_{\mu\nu} = \partial_\mu V_\nu - \partial_\nu V_\mu \quad (V = A, Z, W^\pm), \qquad G^a_{\mu\nu} = \partial_\mu G^a_\nu - \partial_\nu G^a_\mu + g_s f^{abc} G^b_\mu G^c_\nu, \tag{3}$$

and the dual tensor is

$$\widetilde{V}_{\mu\nu} = \frac{1}{2}\epsilon_{\mu\nu\rho\sigma} V^{\rho\sigma}. \tag{4}$$

This parametrization allows to describe the mixing between CP-even and CP-odd states via the c_α parameter and correspondingly to give an effective description of a reasonably ample range of CP-violating scenarios, such as those arising in SUSY or in a generic 2HDM.

2.2 Spin 1

The spin-1 X interaction Lagrangian with fermions is

$$\mathcal{L}_1^f = \sum_{f=u,d} \bar{\psi}_f \gamma_\mu (\kappa_{f_a} a_f - \kappa_{f_b} b_f \gamma_5) \psi_f X_1^\mu, \tag{5}$$

where u and d denote the up-type and down-type quarks, respectively. The a_f and b_f are by default set to their SM-like value, i.e.

$$a_u = \frac{g}{2c_W}\Big(\frac{1}{2} - \frac{4}{3}s_W^2\Big), \quad b_u = \frac{g}{2c_W}\frac{1}{2}, \qquad a_d = \frac{g}{2c_W}\Big(-\frac{1}{2} + \frac{2}{3}s_W^2\Big), \quad b_d = -\frac{g}{2c_W}\frac{1}{2}. \tag{6}$$

The XWW interaction at the lowest dimension is in general[8]

$$\begin{aligned}
\mathcal{L}_1^W &= +i\kappa_{V_1} g_{WWZ}(W^+_{\mu\nu} W^{-\mu} - W^-_{\mu\nu} W^{+\mu}) X_1^\nu + i\kappa_{V_2} g_{WWZ} W^+_\mu W^-_\nu X_1^{\mu\nu} \\
&- \kappa_{V_3} W^+_\mu W^-_\nu (\partial^\mu X_1^\nu + \partial^\nu X_1^\mu) + i\kappa_{V_4} W^+_\mu W^-_\nu \widetilde{X}_1^{\mu\nu} \\
&- \kappa_{V_5} \epsilon_{\mu\nu\rho\sigma} [W^{+\mu}(\partial^\rho W^{-\nu}) - (\partial^\rho W^{+\mu}) W^{-\nu}] X_1^\sigma,
\end{aligned} \tag{7}$$

where $g_{WWZ} = e \cot\theta_W$. Similarly, the XZZ interaction is given by [9]

$$\mathcal{L}_1^Z = -\kappa_{V_3} X_1^\mu (\partial^\nu Z_\mu) Z_\nu - \kappa_{V_5} \epsilon_{\mu\nu\rho\sigma} X_1^\mu Z^\nu (\partial^\rho Z^\sigma). \quad (8)$$

For the $X_1 = 1^-$ case (in parity-conserving scenarios) the non vanishing κ parameters are:

$$\kappa_{f_a, V_1, V_2, V_3} \neq 0. \quad (9)$$

Conversely, for the $X_1 = 1^+$ case one has:

$$\kappa_{f_b, V_4, V_5} \neq 0. \quad (10)$$

2.3 Spin 2

The spin-2 X interaction Lagrangian starts from the dimension-five terms [10,11,12,13]:

$$\mathcal{L}_2^f = -\frac{1}{\Lambda} \sum_{f=q,\ell} \kappa_f T_{\mu\nu}^f X_2^{\mu\nu}, \quad (11)$$

and

$$\mathcal{L}_2^V = -\frac{1}{\Lambda} \kappa_V T_{\mu\nu}^V X_2^{\mu\nu} - \frac{1}{\Lambda} \kappa_\gamma T_{\mu\nu}^\gamma X_2^{\mu\nu} - \frac{1}{\Lambda} \kappa_g T_{\mu\nu}^g X_2^{\mu\nu}, \quad (12)$$

where $V = Z, W^\pm$ and $T_{\mu\nu}^i$ is the energy-momentum tensor of the SM fields; see e.g. [14] for the explicit forms. The even higher dimensional terms [4], dimension-seven, are also implemented.
In these proceedings we will only consider the lowest dimension $X_2 = 2^+$ case. The common Randall-Sundrum (RS) case corresponds to the graviton coupling universally to the different energy-momentum tensors, i.e.

$$\kappa_f = \kappa_g = \kappa_\gamma = \kappa_V \neq 0\,. \quad (13)$$

In general, there is no real constraint (such as gauge invariance, for example) that enforces this condition, and one may be interested in probing different coupling strengths to the different parts of the energy momentum tensor. We will show and comment these results in Sec. 3.2.

3 Results

We now turn to the presentation of some illustrative result. As said, our approach allows to consistently include effects of extra QCD radiation, both by merging different matrix-element multiplicities with the MLM scheme, or by matching NLO computations with parton showers in the aMC@NLO framework.

3.1 aMC@NLO vs. MLM merging

Fig. 1 shows prediction for the transverse momentum of the Higgs boson, in different spin/parity hypotheses: the main frames show curves obtained with the MLM merging procedure, while the lower frames show the ratio of each curve over the corresponding NLO matched to parton shower prediction. The employed parton shower is Pythia 6 (p_T-ordered), and distributions are all normalised to 1. Differences in the main frame can be traced to the different initial state which are probed. At the LO, $0^\pm$ are only gg-initiated, 2^+ receives most of its contribution from gg initial state ($\sim 95\%$), while $1^\pm$ are only $q\bar{q}$-initiated. This turns into harder (more central) transverse momentum (pseudorapidity) distributions for $0^\pm$ and 2^+ with respect to $1^\pm$. The comparison between MLM and aMCatNLO samples shows nice agreement between the two, their ratios always being close to unity, with the exception of the p_T distribution at large values of the transverse momentum, where MLM samples are slightly harder, as a consequence of the inclusion of matrix-elements up to 2 extra jets, multiplicity not covered by the NLO computation.

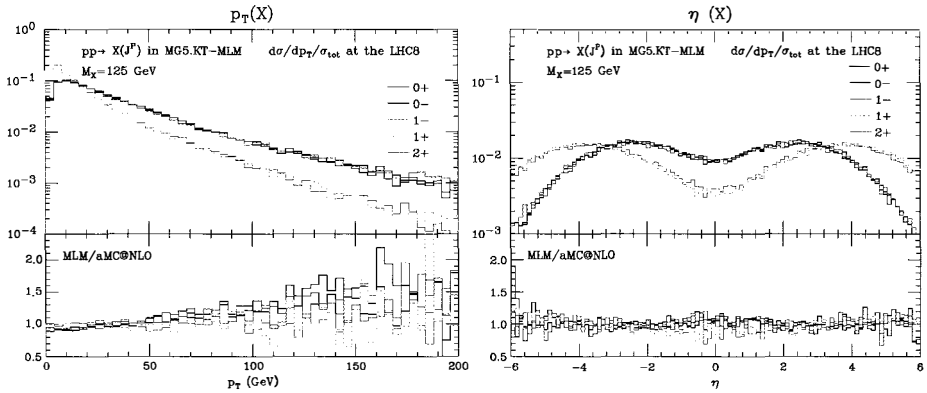

Figure 1: Higgs boson transverse momentum (left) and pseudorapidity(right) distributions for different spin/parity hypotheses. The upper frame shows the MLM-merged curves (including up to two extra jets), whereas the lower plot shows, for each prediction, the ratio of the curve in the upper plot over the corresponding one obtained with aMC@NLO. Events are showered with Pythia 6 (p_T-ordered).

This general good agreement between the two methods is also confirmed when one studies the decay products (decay to $\gamma\gamma$, $4l$, $2l2\nu$ final states can be included keeping all spin-correlation effects). For the sake of brevity, we will not show plots relative to decay products here.

3.2 Different coupling strength for the spin-2 case

After the presentation of the results for the different spin/parity cases, we turn to discuss the possibility of changing, in the spin-2 case, the strength of the coupling to the different parts of the energy-momentum tensor. Since, as said in Sec. 3.1, the spin-2 case is almost entirely gluon-initiated, one would expect, at least at the LO, almost no change when the coupling to quarks, κ_q, is suppressed. In the other extreme case, when instead the coupling to gluons (κ_g) is suppressed, one would expect a behaviour similar to that of the quark-initiated spin-1 cases. Even if this is correct at LO, NLO corrections completely change the picture, as shown by Fig. 2 (where the aMC@NLO predictions, matched with Herwig 6[15,16], are shown): as soon as one moves away from the equal-coupling case, the transverse momentum distribution shows a very hard tail. This tail is the consequence of a unitarity-violating behaviour of the real-emission matrix-elements (to which terms proportional to both κ_q and κ_g contribute, arising when $\kappa_q \neq \kappa_g$. In this case, the LO (+PS) prediction does not catch this feature.

4 Conclusion

We have outlined a new approach to study the properties of the Higgs boson, within an effective theory approach. Our approach is generic and model independent, the only assumption being the possible new states of the theory to be heavier than our theory cutoff Λ. We have shown predictions for the different spin/parity cases, finding good agreement between MLM merging and aMC@NLO matching procedures.Due to the lack of space, we have not presented in these proceedings any plot relative to observables related with the decay products. Nevertheless the decay of the Higgs boson can be included in the computation keeping full spin-correlations. MLM matched samples can be generated automatically by MadGraph 5 and special aMC@NLO codes have been prepared and made available, for the different spin/parity cases and with different decays of the Higgs boson, on the aMC@NLO website[17].

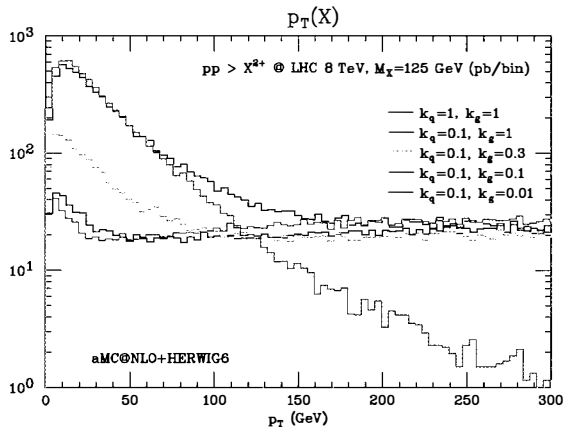

Figure 2: Transverse momentum distribution for a spin-2 Higgs boson, with various values of the coupling strength to quarks and gluons. Distributions are obtained with aMC@NLO and showered with Herwig 6.

Acknowledgments

The results presented here would have not been possible without the contribution of many people in this collaborations: P. Artoisenet, P. de Aquino, F. Demartin, R. Frederix, S. Frixione, F. Maltoni, M. K. Mandal, P. Mathews, K. Mawatari, V. Ravindran, S. Seth, P. Torrielli. We would like to thank the organizers of the Moriond conference for the nice atmosphere, and all the participants for the excellent presentations. We are specially indebted with M. Mangano for very instructive discussions. MZ acknowledges the support from the Belgian IAP network and IISN for the participation to the conference. This work is partially supported by the ERC grant 291377 "LHCtheory: Theoretical predictions and analyses of LHC physics: advancing the precision frontier", by the IISN "MadGraph" convention 4.4511.10, by the IISN "Fundamental interactions" convention 4.4517.08 and by the Belgian IAP Program BELSPO P7/37.

References

1. Georges Aad et al. Observation of a new particle in the search for the Standard Model Higgs boson with the ATLAS detector at the LHC. *Phys.Lett.*, B716:1–29, 2012.
2. Serguei Chatrchyan et al. Observation of a new boson at a mass of 125 GeV with the CMS experiment at the LHC. *Phys.Lett.*, B716:30–61, 2012.
3. Yanyan Gao, Andrei V. Gritsan, Zijin Guo, Kirill Melnikov, Markus Schulze, et al. Spin determination of single-produced resonances at hadron colliders. *Phys.Rev.*, D81:075022, 2010.
4. Sara Bolognesi, Yanyan Gao, Andrei V. Gritsan, Kirill Melnikov, Markus Schulze, et al. On the spin and parity of a single-produced resonance at the LHC. *Phys.Rev.*, D86:095031, 2012.
5. Johan Alwall, Stefan Hoche, F. Krauss, N. Lavesson, L. Lonnblad, et al. Comparative study of various algorithms for the merging of parton showers and matrix elements in hadronic collisions. *Eur.Phys.J.*, C53:473–500, 2008.
6. Johan Alwall, Michel Herquet, Fabio Maltoni, Olivier Mattelaer, and Tim Stelzer. MadGraph 5 : Going Beyond. *JHEP*, 1106:128, 2011.
7. *http://feynrules.irmp.ucl.ac.be/wiki/HiggsCharacterization* .
8. Kaoru Hagiwara, R.D. Peccei, D. Zeppenfeld, and K. Hikasa. Probing the Weak Boson

Sector in e+ e- to W+ W-. *Nucl.Phys.*, B282:253, 1987.
9. Wai-Yee Keung, Ian Low, and Jing Shu. Landau-Yang Theorem and Decays of a Z' Boson into Two Z Bosons. *Phys.Rev.Lett.*, 101:091802, 2008.
10. Gian F. Giudice, Riccardo Rattazzi, and James D. Wells. Quantum gravity and extra dimensions at high-energy colliders. *Nucl.Phys.*, B544:3–38, 1999.
11. Tao Han, Joseph D. Lykken, and Ren-Jie Zhang. On Kaluza-Klein states from large extra dimensions. *Phys.Rev.*, D59:105006, 1999.
12. John Ellis, Ricky Fok, Dae Sung Hwang, Veronica Sanz, and Tevong You. Distinguishing 'Higgs' Spin Hypotheses using gamma gamma and WW* Decays. 2012.
13. Christoph Englert, Dorival Goncalves-Netto, Kentarou Mawatari, and Tilman Plehn. Higgs Quantum Numbers in Weak Boson Fusion. *JHEP*, 1301:148, 2013.
14. Kaoru Hagiwara, Junichi Kanzaki, Qiang Li, and Kentarou Mawatari. HELAS and MadGraph/MadEvent with spin-2 particles. *Eur.Phys.J.*, C56:435–447, 2008.
15. G. Corcella, I.G. Knowles, G. Marchesini, S. Moretti, K. Odagiri, et al. HERWIG 6: An Event generator for hadron emission reactions with interfering gluons (including supersymmetric processes). *JHEP*, 0101:010, 2001.
16. G. Corcella, I.G. Knowles, G. Marchesini, S. Moretti, K. Odagiri, et al. HERWIG 6.5 release note. 2002.
17. *http://amcatnlo.web.cern.ch/amcatnlo/* .

HIGGS COUPLINGS AFTER MORIOND

BÉRANGER DUMONT
Laboratoire de Physique Subatomique et de Cosmologie, UJF Grenoble 1, CNRS/IN2P3, INPG, 53 Avenue des Martyrs, F-38026 Grenoble, France

Performing fits to all publicly available data, we analyze the extent to which the latest results from the LHC and Tevatron (including new results presented at the Rencontres de Moriond) constrain the couplings of the Higgs boson-like state at ~ 125 GeV, as well as possible decays into invisible particles.

1 Setup of the analysis

The recent discovery [1,2] of a new particle with mass around 125 GeV and properties consistent with a Standard Model (SM) Higgs boson is clearly the most significant news from the Large Hadron Collider (LHC). This discovery was supported by consistent measurements by the CDF and D0 collaborations at the Tevatron [3] and completes our picture of the SM. However, the SM leaves many fundamental questions open—perhaps the most pressing issue being that the SM does not explain the value of the electroweak scale, *i.e.* the Higgs mass, itself. Clearly, a prime goal after the discovery is to thoroughly test the SM nature for this Higgs-like signal.

The experimental collaborations have presented detailed results for several different channels, including $\gamma\gamma$, $ZZ^{(*)}$, $WW^{(*)}$, $b\bar{b}$, $\tau\tau$ final states and invisible decays. With these measurements, a comprehensive study of the properties of the Higgs-like state becomes possible and has the potential for revealing whether or not the Higgs sector is as simple as envisioned in the SM, see *e.g.* [4] and references therein. Here, we provide an update of the Higgs couplings fits of [4], based on the most recent results from the LHC and Tevatron presented at this conference. (A long paper [5] is in preparation.)

Following [4], we parametrize deviations from the SM couplings by the Lagrangian

$$\mathcal{L} = g\left[C_V\left(m_W W_\mu W^\mu + \frac{m_Z}{\cos\theta_W} Z_\mu Z^\mu\right) - C_U \frac{m_t}{2m_W}\bar{t}t - C_D\frac{m_b}{2m_W}\bar{b}b - C_D\frac{m_\tau}{2m_W}\bar{\tau}\tau\right] H\,. \quad (1)$$

where we introduce scaling factors C_I. We assume a single $C_W = C_Z \equiv C_V$ and that the reduced couplings to up-type and down-type fermions, C_U and C_D, are independent parameters. In general, the C_I can take on negative as well as positive values; there is one overall sign ambiguity which we fix by taking $C_V > 0$.

In addition to the tree-level couplings given above, the H has couplings to $\gamma\gamma$ and gg that are first induced at one loop and are completely computable in terms of C_U, C_D and C_V if only loops containing SM particles are present. We define $\overline{C}_\gamma$ and $\overline{C}_g$ to be the ratio of these couplings so computed to the SM (*i.e.* $C_U = C_V = C_V = 1$) values. However, in some of our fits we will also allow for additional loop contributions ΔC_γ and ΔC_g from new particles; in this case $C_\gamma = \overline{C}_\gamma + \Delta C_\gamma$ and $C_g = \overline{C}_g + \Delta C_g$. The largest set of independent parameters in our fits is thus $C_U,\ C_D,\ C_V,\ \Delta C_\gamma,\ \Delta C_g$.

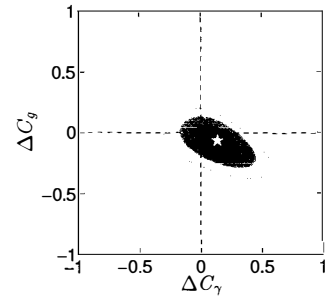

Figure 1: Two parameter fit of ΔC_γ and ΔC_g, assuming $C_U = C_D = C_V = 1$ (Fit I). The red, orange and yellow ellipses show the 68%, 95% and 99.7% CL regions, respectively. The white star marks the best-fit point.

The experimental results are given in terms of signal strengths $\mu(X, Y)$, the ratio of the observed rate for some process $X \to H \to Y$ relative to the prediction for the SM Higgs. As in [4], we adopt the simple technique of computing the χ^2 associated with a given choice of the input parameters following the standard definition:

$$\chi^2 = \sum_k \frac{(\overline{\mu}_k - \mu_k)^2}{\Delta\mu_k^2}, \tag{2}$$

where k runs over all the experimentally defined production/decay channels employed, μ_k is the observed signal strength for a channel k, $\overline{\mu}_k$ is the value predicted for that channel for a given choice of parameters and $\Delta\mu_k$ is the experimental error for that channel. The $\overline{\mu}_k$ associated with each experimentally defined channel is further decomposed as $\overline{\mu}_k = \sum T_k^i \, \widehat{\mu}_i$, where the T_k^i give the amount of contribution to the experimental channel k coming from the theoretically defined channel i and $\widehat{\mu}_i$ is the prediction for that channel for a given choice of C_U, C_D, C_V and (for fits where treated as independent) C_γ and C_g. For the computation of the $\widehat{\mu}_i$ including NLO corrections we follow the procedure recommended by the LHC Higgs Cross Section Working Group [6].

2 Results

In order to probe the SM nature of the observed Higgs boson, we perform the following fits:

I) fit of ΔC_γ and ΔC_g, assuming $C_U = C_D = C_V = 1$;

II) fit of C_U, C_D and C_V, assuming $\Delta C_\gamma = \Delta C_g = 0$;

III) fit of C_U, C_D, C_V, ΔC_γ and ΔC_g, restricted to $C_U > 0$ and $C_D > 0$.

2.1 Fit I: ΔC_γ and ΔC_g

In this first case, we allow for additional new physics contributions to the $\gamma\gamma$ and gg couplings, parameterized by ΔC_γ and ΔC_g, coming from loops involving non-SM particles. This fit, which we refer to as Fit I, is designed to determine if the case where all tree-level Higgs couplings are equal to their SM values can be consistent with the data. For example, such a fit is relevant in the context of UED models where the tree-level couplings of the Higgs are SM-like [7,8].

Figure 1 displays the results of this fit in the ΔC_g versus ΔC_γ plane. The best fit is obtained for $\Delta C_\gamma = 0.14$, $\Delta C_g = -0.06$, and has $\chi^2_{\rm min} = 17.6$ for 20 degrees of freedom (d.o.f.), giving a p-value of 0.61. We note that the SM (*i.e.* $C_U = C_D = C_V = 1$, $\Delta C_\gamma = \Delta C_g = 0$) has $\chi^2 = 19.0$ for 22 d.o.f., implying a p-value of 0.65.

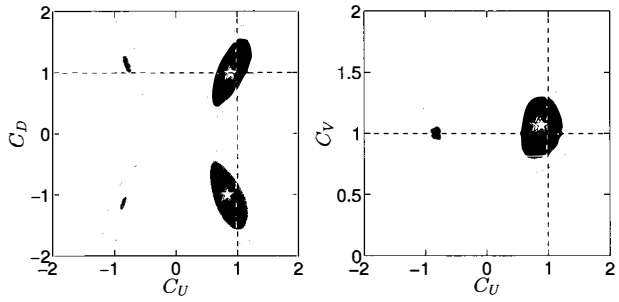

Figure 2: Two-dimensional χ^2 distributions for the three parameter fit of C_U, C_D, C_V with C_γ and C_g as computed in terms of C_U, C_D, C_V (Fit II). Color code as in the previous figure.

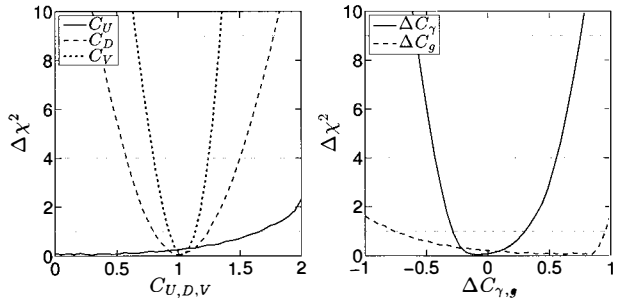

Figure 3: One-dimensional χ^2 distributions for the five parameter fit of C_U, C_D, C_V, ΔC_γ and ΔC_g (Fit III).

2.2 Fit II: C_U, C_D and C_V

Next, we let C_U, C_D and C_V vary, assuming there are no new particles contributing to the effective Higgs couplings to gluons and photons, *i.e.* we take $\Delta C_\gamma = \Delta C_g = 0$, implying C_γ and C_g as computed from the SM particle loops. Such parametrization is relevant in the context of 2HDM with a heavy charged Higgs, that does not contribute to the loop-induced $H \to \gamma\gamma$ process.

Our results are shown in Fig. 2. We consider two best fits points, having positive and negative C_D. The one with $C_D > 0$ is located at $C_U = 0.89$, $C_D = 0.99$, $C_V = 1.07$, and $C_U = 0.84$, and has $\chi^2_{\rm min} = 17.7$ for 19 d.o.f., giving a p-value of 0.54. (The one with $C_D < 0$ is almost equivalent—the sign of C_D only affects mildly the loop-induced processes—and has $\chi^2_{\rm min} = 17.6$.) Contrary to the situation at the end of 2012 [4] we note that the regions having $C_U < 0$, in which the $H \to \gamma\gamma$ rate is significantly enhanced, are disfavored at the level of 2.4σ. This mainly comes from the update of the CMS $H \to \gamma\gamma$ results presented at this conference [9].

2.3 Fit III: C_U, C_D, C_V, ΔC_γ and ΔC_g

Finally, in Fit III, we allow for new particles entering the loop, parametrized by ΔC_γ and ΔC_g, in addition to the tree-level parameters C_U, C_D and C_V, leading therefore to five free parameters. This encompasses a very broad class of models. The associated 1d plots are given in Fig. 3.

The main differences as compared to Fit **II** is that C_U is only weakly constrained by the data. Allowing for additional contributions to $H \to \gamma\gamma$ and gluon fusion, parametrized by ΔC_γ and ΔC_g, account for the observed rates of these processes. C_U is then only determined from

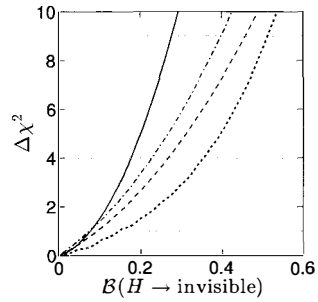

Figure 4: $\Delta\chi^2$ distributions for the branching ratio of invisible Higgs decays. The full, dashed, and dotted lines correspond, respectively, to the cases of 1) SM couplings, 2) arbitrary ΔC_γ and ΔC_g (Fit I), and 3) deviations of C_U, C_D, C_V from 1 (Fit II). We also show as dash-dotted line the variant of case 3) with $C_U, C_D > 0$ and $C_V \leq 1$.

the results on associated top pair production. The best fit is at $C_U = 0$, $C_D = 1.02$, $C_V = 1.04$, $\Delta C_\gamma = -0.16$, $\Delta C_g = 0.82$ and has $\chi^2_{\text{min}} = 17.2$ for 17 d.o.f., giving a p-value of 0.44.

2.4 Limits on invisible decays of the Higgs

The current measurements can also be used to derive limits on the invisible decays of the Higgs, as was done in [10]. We also include in our fit the ATLAS limit on $ZH \to \ell\ell + \text{invisible}$ [11]. Our results are shown in Fig. 4. The 95% CL limits on $\mathcal{B}(H \to \text{invisible})$ range from 18% to 35%, depending on our assumption on the couplings of the Higgs boson.

Acknowledgments

I would like to sincerely thank Geneviève Bélanger, Ulrich Ellwanger, John F. Gunion and Sabine Kraml for the rewarding collaboration on [4,5,10] and the opportunity to present these studies on behalf of the group at the Rencontres de Moriond. Partial financial support by IN2P3 under contract PICS FRUSA No. 5872 and by US DOE grant DE-FG03-91ER40674 is gratefully acknowledged.

References

1. G. Aad *et al.* [ATLAS Collaboration], Phys. Lett. B **716** (2012) 1 [arXiv:1207.7214].
2. S. Chatrchyan *et al.* [CMS Collaboration], Phys. Lett. B **716** (2012) 30 [arXiv:1207.7235].
3. T. Aaltonen *et al.* [CDF and D0 Collaborations], arXiv:1303.6346.
4. G. Belanger, B. Dumont, U. Ellwanger, J. F. Gunion and S. Kraml, JHEP **1302** (2013) 053 [arXiv:1212.5244].
5. G. Belanger, B. Dumont, U. Ellwanger, J. F. Gunion and S. Kraml, in preparation.
6. LHC Higgs Cross Section Working Group, A. David, A. Denner, M. Duehrssen, M. Grazzini, C. Grojean, *et al.*, arXiv:1209.0040.
7. F. J. Petriello, JHEP **0205** (2002) 003 [hep-ph/0204067].
8. G. Belanger, A. Belyaev, M. Brown, M. Kakizaki and A. Pukhov, arXiv:1207.0798.
9. CMS Collaboration, CMS-PAS-HIG-13-001 (Mar 2013).
10. G. Belanger, B. Dumont, U. Ellwanger, J. F. Gunion and S. Kraml, arXiv:1302.5694.
11. ATLAS Collaboration, ATLAS-CONF-2013-011 (Mar 2013).

The global electroweak Standard Model fit after the Higgs discovery

M. Baak[a], R. Kogler[b] (for the Gfitter group)
[a] *CERN, Geneva, Switzerland*
[b] *Institut für Experimentalphysik, Universität Hamburg, Germany*

We present an update of the global Standard Model (SM) fit to electroweak precision data under the assumption that the new particle discovered at the LHC is the SM Higgs boson. In this scenario all parameters entering the calculations of electroweak precision observalbes are known, allowing, for the first time, to over-constrain the SM at the electroweak scale and assert its validity. Within the SM the W boson mass and the effective weak mixing angle can be accurately predicted from the global fit. The results are compatible with, and exceed in precision, the direct measurements. An updated determination of the S, T and U parameters, which parametrize the oblique vacuum corrections, is given. The obtained values show good consistency with the SM expectation and no direct signs of new physics are seen. We conclude with an outlook to the global electroweak fit for a future e^+e^- collider.

1 Introduction

The electroweak fit of the Standard Model (SM) has a long tradition in particle physics. It relies on the predictability of the SM, where all electroweak observables can be expressed as functions of five parameters. A tremendous amount of pioneering work from the theoretical community in the calculation of radiative corrections, as well as from the experimental community in the measurement of electroweak precision observables, led to a correct prediction [1] of the top-quark mass m_t before its actual discovery in 1995 [2, 3][a]. This success has given confidence in the calculations of radiative corrections, including loop-contributions from the Higgs boson.

The discovery of the top quark left the Higgs boson mass M_H as the last free parameter of the SM without experimental constraints. The focus of the electroweak fits shifted to precisely predicting M_H from electroweak precision observables (EWPO). However, while the loop corrections to the W- and Z-propagators involving the top quark lead to an approximate quadratic dependence, M_H enters only logarithmically in the calculation of electroweak observables, leading to weaker constraints on M_H than on m_t. Nevertheless, improvements in theoretical and experimental precision, especially on m_t, M_W and the hadronic contribution to the running of the electromagnetic coupling for the five light quarks $\Delta\alpha^{(5)}_{\text{had}}(s)$, led to a rather precise SM prediction of $M_H = 96^{+31}_{-24}$ GeV [5].

This was the status of the electroweak fit at the discovery of the new Higgs-like boson reported by the ATLAS and CMS collaborations [6, 7] The predicted value is in very good agreement with its measured mass of ~ 126 GeV. Most recent measurements and analyses of the properties of this newly discovered boson, as presented at this conference, show good consistency with the assumption that the new particle is indeed the SM Higgs boson [8].

[a] The observed top quark mass was $176 \pm 8(\text{stat}) \pm 10(\text{sys.})$ GeV and $199^{+19}_{-21}(\text{stat.}) \pm 22(\text{sys.})$ GeV as measured by the CDF and D0 collaborations. This is in very good agreement with the SM prediction of $m_t = 178^{+19}_{-22}$ GeV [4], as obtained from electroweak precision data.

Supposing that the new particle is the SM Higgs boson, all parameters entering electroweak precision observables are known, allowing a full assessment of the consistency of the SM at the electroweak scale [9]. We interpret the new particle as the SM Higgs boson and present an update of the SM electroweak fit using the Gfitter framework [10]. The Gfitter results shown here have been recently published elsewhere [11].

A detailed study of the implications of the value of M_H as input to the electroweak fit shows an improvement in precision on the predictions of M_W and the effective weak mixing angle $\sin^2\theta^\ell_{\text{eff}}$. We also report updated constraints on the oblique parameters S, T, U, which parametrize possible contributions to oblique vacuum corrections from physics beyond the SM (BSM) and hence allow to constrain new models through EWPO. We also use the projected experimental uncertainties from a future e^+e^- facility to derive the expected precision of SM predictions for electroweak observables.

2 The global electroweak fit with Gfitter

A detailed description of the calculations and experimental input used in the electroweak fit is given elsewhere [11] and only the most important features are given here. The mass of the W boson and the effective weak mixing angle are calculated at two-loop order, including leading terms beyond the two loop calculation [12–14]. We use the full $\mathcal{O}(\alpha_S^4)$ calculation [15, 16] of the QCD Adler function, which stabilizes the perturbative QCD expansion in the calculation of the Z-boson width. An improved prediction of R_b^0, the hadronic partial decay width of $Z \to b\bar{b}$, is used, which includes the complete calculation of fermionic two-loop corrections [17]. The calculation of the vector and axial-vector couplings, g_A^f and g_V^f, used in the calculation of the partial and total widths of the Z and W bosons, relies on accurate parametrizations [18–21]. Theoretical uncertainties are implemented using the *R*fit scheme, which corresponds to a linear addition of theoretical and experimental uncertainties. The two uncertainties considered are due to missing higher orders in the calculations of M_W and $\sin^2\theta^\ell_{\text{eff}}$ and have been estimated to be $\delta_{\text{th}} M_W = 4\,\text{MeV}$ [12] and $\delta_{\text{th}} \sin^2\theta^\ell_{\text{eff}} = 4.7 \cdot 10^{-5}$ [13].

The experimental input used in the fit include the electroweak precision data measured at the Z-pole together with their correlations [22]. For the mass and width of the W boson the latest world average is used, $M_W = 80.385 \pm 0.015\,\text{GeV}$ and $\Gamma_W = 2.085 \pm 0.042\,\text{GeV}$, obtained from measurements by the LEP and Tevatron experiments [23]. While the leptonic contribution to the running of the electromagnetic coupling strength can be calculated with very high precision, the value of the hadronic contribution is obtained from a fit to experimental data supplemented by perturbative calculations, $\Delta\alpha^{(5)}_{\text{had}}(M_Z^2) = (2757 \pm 10) \cdot 10^{-5}$ [24].

For the mass of the top quark we use the average from the direct measurements by the Tevatron experiments $m_t = 173.18 \pm 0.94\,\text{GeV}$ [25]. Biases in the measurement of m_t due to a mis-modeling of non-perturbative color-reconnection effects in the fragmentation process, initial and final state radiation and kinematics of the b-quark, have been studied by the CMS collaboration [26]. With the current precision no significant deviation is observed between the measured values and the predictions using different models. An additional ambiguity in the interpretation of m_t originates from the top's finite decay width, with additional uncertainty which is difficult to estimate quantitatively. The effect of an additional theoretical uncertainty of 0.5 GeV on m_t has been studied, and the fit shows only a slight deterioration in precision. This uncertainty is not included in the standard fit setup.

A naïve combination of the measured values of M_H from the ATLAS and CMS experiments as reported in [6, 7], gives $M_H = 125.7 \pm 0.4\,\text{GeV}$, where the systematic uncertainties are treated as fully uncorrelated. Treating them as fully correlated only changes the uncertainty to 0.5 GeV, with a negligible effect on the fit result due to the weak dependence on M_H.

3 The SM fit

The SM electroweak fit is performed in three scenarios [11]. In the first scenario all input parameters are used, allowing to test the validity of the SM. The results are compared to the second scenario, where the fit is performed without the inclusion of M_H to assess the effect of knowing M_H in the electroweak fit. In the third scenario individual observables are removed one by one from the fit which allows for an indirect determination of these with an accurate uncertainty calculation.

The SM fit including all input data converges with a minimum value of the test statistics of $\chi^2_{\rm min} = 21.8$, obtained for 14 degrees of freedom. Calculating the naïve p-value gives Prob$(21.8, 14) = 0.08$. The smallness of the p-value with respect to previous results [5] is not due to the inclusion of M_H, but rather due to the new calculation of R_b^0 which has a very small dependence on M_H, as described below.

Performing the fit without M_H as input parameter, the fit converges at a minimum of $\chi^2_{\rm min} = 20.3$ for 13 degrees of freedom, corresponding to a p-value of 0.09. In this case the fit converges for a value of $M_H = 94^{+25}_{-22}$ GeV, in good agreement with the direct measurement.

The result of the fit is shown in Fig. 1 in terms of the pull value, which is defined as deviation between the SM prediction and the measured parameter in units of the measurement uncertainty. The fit results are shown for both scenarios, including the M_H measurement (colored bars) and without M_H (grey bars), where in general the result of the fit does not change significantly between the two scenarios. Very small pull values, as for example observed for the light quark masses but also for M_H, indicate that the input accuracy exceeds the fit requirements. No single pull value exceeds 3σ, showing an overall satisfying consistency of the SM.

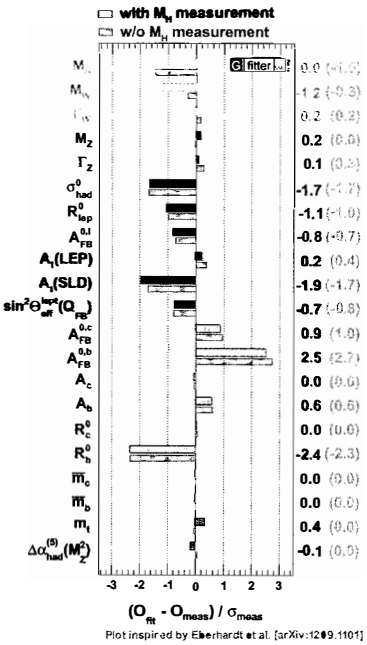

Figure 1: Differences between the SM prediction and the measured parameter, in units of the uncertainty for the fit including M_H (color) and without M_H (grey).

The largest deviations between the SM prediction and the measurements are observed in the b-sector. Both observables directly sensitive to $Z \to b\bar{b}$, the forward-backward asymmetry $A^{0,b}_{\rm FB}$ and the partial width R^0_b, show large deviations of 2.5σ and -2.4σ, respectively. While the effect in $A^{0,b}_{\rm FB}$ has been known for a long time, the large deviation in R^0_b is new, owing to the improved two-loop calculation which exhibits an unexpected large negative correction [17]. Using the one-loop result for R^0_b only, the pull value is -0.8σ. Both parameters show only very little dependence on the inclusion of M_H, with deviations of 2.7σ and -2.3σ in the fit scenario without including M_H.[b]

In order to assess the validity of the fit we use Monte Carlo simulation to generate pseudo experiments. For each simulation we generate SM parameters according to Gaussian distributed values around their expected values with standard deviations equal to the full experimental uncertainty. The obtained $\chi^2_{\rm min}$ distribution for all toy datasets is shown in Fig. 2(a). Good agreement between the MC simulation and the idealized distribution for 14 degrees of freedom

[b] It is intriguing to observe that an increase of the right-handed coupling of the $Z \to b\bar{b}$ vertex of 25%, while leaving the left-handed coupling unchanged, can resolve both deviations.

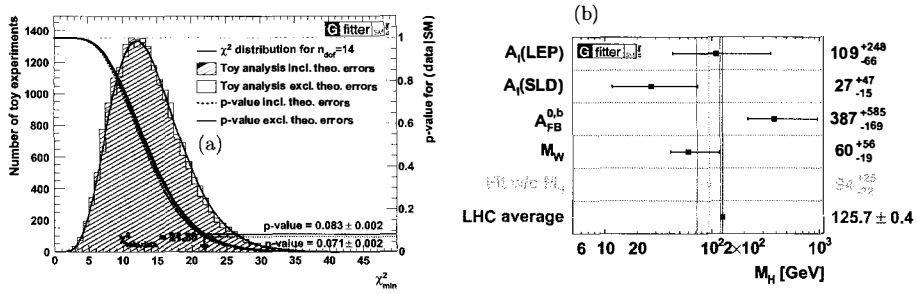

Figure 2: Distribution of the $\chi^2_{\rm min}$ value obtained from pseudo Monte Carlo simulations (a). Shown are distributions obtained by including (hatched) and excluding (green) the theory uncertainties $\delta_{\rm th}$, compared with the idealized χ^2 distribution assuming Gaussian distributed errors with 14 degrees of freedom. The arrows indicate the $\chi^2_{\rm min}$ value obtained from the fit to data. The result from a determination of M_H using only the given observable is shown in (b).

is found. The result from the fit to data is indicated as red arrow and the obtained p-value is consistent between the MC simulation and the idealized χ^2 distribution. The influence of the theoretical uncertainties on the p-value of the full SM fit amounts to about 0.01.

Except for the value of M_H itself, the largest change in the result due to the inclusion of M_H is the prediction of M_W. For this observable the pull value changes from -0.3 to -1.2, due to the small value of M_H preferred by the M_W measurement. This effect is shown in Fig. 2(b), where indirect determinations of M_H are displayed, obtained by removing all sensitive observables from the fit except the given one. For comparison, also the indirect fit result using all input parameters except for M_H (grey band) and the direct measurement (green line) are shown. The values obtained from the fit including the measurements of the leptonic asymmetries A_ℓ, as measured by the LEP and SLD collaborations, and M_W show good agreement. The value of M_H obtained from the hadronic forward-backward asymmetry $A^{0,b}_{\rm FB}$ shows a tendency towards large values of M_H, with a discrepancy of 2.5σ.

4 Predictions for key observables

The inclusion of M_H in the fit results in a large improvement in precision for the indirect determination of several SM parameters. Without the inclusion of M_H, the indirect determination of the top mass gives $m_t = 171.5^{+8.9}_{-5.3}$ GeV. Including the knowledge about M_H, the fit value obtained is

$$m_t = 175.8\,^{+2.7}_{-2.4}\ \text{GeV}, \tag{1}$$

where the uncertainty is reduced by a factor of 2–3. The value of m_t agrees well with the direct determination [25] and the cross-section based determination under the assumption that there is no new physics contributing to the cross section measurement [27].

The $\Delta\chi^2$ profiles versus M_W and $\sin^2\theta^\ell_{\rm eff}$ without using the corresponding measurements are shown in Fig. 3. For the indirect determination of $\sin^2\theta^\ell_{\rm eff}$ all observables directly sensitive to $\sin^2\theta^\ell_{\rm eff}$, like asymmetry parameters and the full and partial decay widths, are excluded from the fit. Solid blue lines show the result of the fit including M_H, where the effect of the theory uncertainty is shown as blue band. The same fit, without information on M_H is shown in grey. An improvement in precision of more than a factor of two can be observed for the indirect determination of M_W and $\sin^2\theta^\ell_{\rm eff}$. Also shown are the direct measurements of the aforementioned W mass and the LEP/SLD average of the effective weak mixing angle $\sin^2\theta^\ell_{\rm eff} = 0.23153 \pm 0.00016$ [22], which show good agreement with the obtained values.

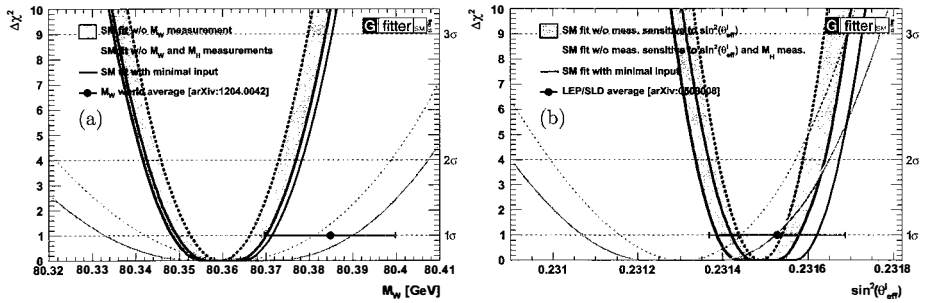

Figure 3: $\Delta\chi^2$ profiles for the indirect determination of M_W (a) and $\sin^2\theta^\ell_{\rm eff}$ (b). The result from a fit including M_H as input parameter is shown in blue and the fit without M_H is shown in grey. The dotted lines indicate the fit result by setting the theoretical uncertainties $\delta_{\rm th}$ to zero and the band corresponds to the full result. Also shown are the direct measurements and the SM prediction using a minimal set of parameters (black solid lines).

The fit value obtained for M_W is

$$\begin{aligned} M_W &= (80.3593 \pm 0.0056_{m_t} \pm 0.0026_{M_Z} \pm 0.0018_{\Delta\alpha_{\rm had}} \\ &\qquad \pm 0.0017_{\alpha_S} \pm 0.0002_{M_H} \pm 0.0040_{\rm theo})\ {\rm GeV}\,, \\ &= (80.359 \pm 0.011_{\rm tot})\ {\rm GeV}\,, \end{aligned} \tag{2}$$

which exceeds the experimental world average in precision. The different uncertainty contributions originate from the uncertainties in the input values of the fit. The dominant uncertainty is due to the top quark mass, followed by the theory uncertainty of 4 MeV. Due to the weak, logarithmic dependence on M_H the contribution from the uncertainty on the Higgs mass is very small compared to the other sources of uncertainty. The deviation between the value of M_W obtained from the fit and the direct measurement is not significant with the current precision (1.2σ). However, improvements in the determination of m_t as well as reduced theoretical uncertainties from higher-order calculations and a more precise direct determination of M_W – as expected from the analyses of the full dataset recorded by the Tevatron experiments – will reduce the uncertainties significantly.

The indirect determination of $\sin^2\theta^\ell_{\rm eff}$ gives

$$\begin{aligned} \sin^2\theta^\ell_{\rm eff} &= 0.231496 \pm 0.000030_{m_t} \pm 0.000015_{M_Z} \pm 0.000035_{\Delta\alpha_{\rm had}} \\ &\qquad \pm 0.000010_{\alpha_S} \pm 0.000002_{M_H} \pm 0.000047_{\rm theo}\,, \\ &= 0.23150 \pm 0.00010_{\rm tot}\,, \end{aligned} \tag{3}$$

which is compatible and more precise than the average of the LEP/SLD measurements. The total uncertainty is dominated by that from the measurements of $\Delta\alpha_{\rm had}$ and m_t. The contribution from the uncertainty in M_H is again very small.

The measurement of M_H allows for a first time to predict SM observables with a minimal set of parameters. A fit using only this minimal set of input measurements (here chosen to be M_H, $\alpha_S(M_Z^2)$, the fermion masses and M_Z, G_F and $\Delta\alpha^{(5)}_{\rm had}(M_Z^2)$ for the electroweak sector) is shown by the solid black lines in Fig. 3. The agreement in central value and precision of these results with those from Eq. (2) and (3) illustrates the marginal additional information provided by the other observables once M_H is known.

An important consistency test of the SM is the simultaneous, indirect determination of m_t and M_W. This is particularly interesting since contributions from new physics may lead to

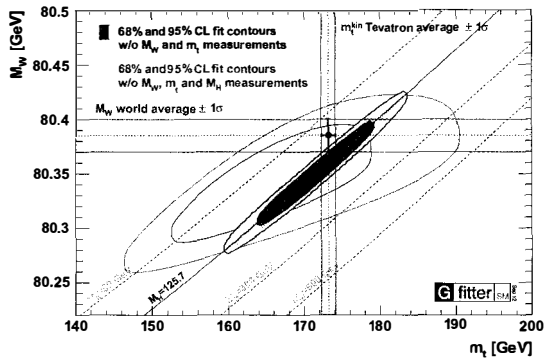

Figure 4: 68% and 95% confidence level (CL) contours in the m_t–M_W plane for the fit including M_H (blue) and excluding M_H (grey). In both cases the direct measurements of M_W and m_t were excluded from the fit. The values of the direct measurements are shown as green bands with their one standard deviations. The dashed diagonal lines show the SM prediction for M_W as function of m_t for different assumptions of M_H.

discrepancies between the measured values and the predictions in the m_t–M_W plane. A scan of the $\Delta\chi^2$ profile is shown in Fig. 4 for the scenario including M_H in the fit (blue) and without M_H (grey). The knowledge of M_H improves the precision of the indirect determination of M_W and m_t significantly. Very good agreement between the indirect determinations of M_W and m_t and the direct measurements is observed, showing impressively the consistency of the SM and leaving little room for signs of new physics.

5 Oblique Parameters

If the scale of new physics (NP) is much higher than the mass of the W and Z bosons, beyond the SM physics appears dominantly through vacuum polarization corrections, also known as oblique corrections, in the calculation of EWPO. Their effects on the electroweak precision observables can be parametrized by three gauge self-energy parameters (S, T, U) introduced by Peskin and Takeuchi [28, 29]. The parameter S describes new physics contributions to neutral current processes at different energy scales. T is sensitive to isospin violation and U ($S+U$) is sensitive to new physics (NP) contributions to charged currents. U is only sensitive to the W mass and width, and is usually very small in NP models (often: $U = 0$).

Constraints on the S, T, U parameters are derived from the global fit to the electroweak precision data, namely from the difference between the oblique vacuum corrections determined from the experimental data and the corrections expected in a reference SM (defined by fixing m_t and M_H). The reference SM for the S, T, U calculation is now updated to $M_{H,\mathrm{ref}} = 126\,\mathrm{GeV}$ and $m_{t,\mathrm{ref}} = 173\,\mathrm{GeV}$. With this one finds for S, T, U:

$$S = 0.03 \pm 0.10\,, \quad T = 0.05 \pm 0.12\,, \quad U = 0.03 \pm 0.10\,, \tag{4}$$

with correlation coefficients of $+0.89$ between S and T, and -0.54 (-0.83) between S and U (T and U). Fixing $U = 0$ one obtains $S|_{U=0} = 0.05 \pm 0.09$ and $T|_{U=0} = 0.08 \pm 0.07$, with a correlation coefficient of $+0.91$.

Fig. 5 shows the 68%, 95% and 99% CL allowed regions in the (S,T) plane for freely varying U (a) and the constraints found when fixing $U = 0$ (b). For illustration purposes, also the SM prediction is shown. The M_H measurement reduces the allowed SM area from the grey sickle, defined by letting M_H float within the range of [100, 1000] GeV, to the narrow black strip. The

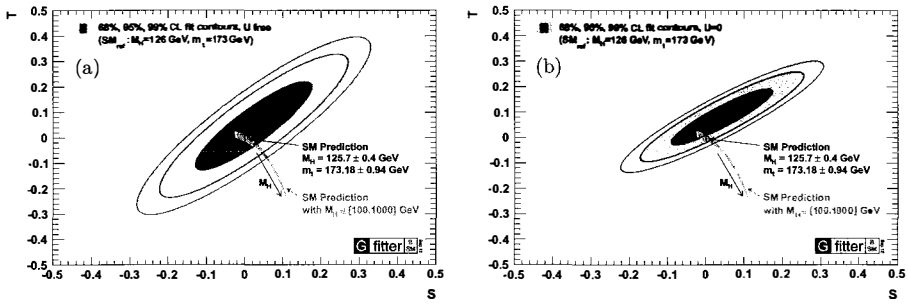

Figure 5: Experimental constraints on the S and T parameters with respect to the SM reference ($M_{H,\mathrm{ref}} = 126$ GeV and $m_{t,\mathrm{ref}} = 173$ GeV). Shown are the 68%, 95% and 99% CL allowed regions, where the third parameter U is left unconstrained (a) or fixed to 0 (b). The prediction in the SM is given by the black (grey) area when including (excluding) the M_H measurements.

experimental constraints on S, T, U can be compared now to specific NP model predictions. Since the oblique parameters are found to be small and consistent with zero, possible NP models may only affect the electroweak observables weakly.

6 Prospects of the SM fit for a future e^+e^- collider

The SM leaves many questions open which can only be addressed by BSM physics, which is expected to play a role at the electroweak scale of $\mathcal{O}(1)$ TeV. So far no direct signs of new physics have been observed at the LHC and also the SM shows good self-consistency at the loop-level up to very high precision. A future e^+e^- facility would help tremendously to precisely measure the production mechanisms and branching ratios of the Higgs boson. Furthermore, it would allow for precise measurements of the EWPO, such as m_t, $\sin^2\theta^\ell_{\mathrm{eff}}$, R^0_ℓ and M_W, to further assert the validity of the SM through the electroweak fit.

In the following we study the impact of expected EWPO measurements on the SM electroweak fit assuming the design parameters and predicted precisions obtained for the International Linear Collider (ILC) with the GigaZ option [30–32]. This study aims at a comparison of the accuracies of the measured and predicted electroweak observables. Two scenarios are considered. In the first scenario the central values of the input observables are chosen to agree with the SM prediction for a Higgs mass of 125.8 GeV according to the present measurement. In the second scenario it is assumed that the central value of the SM prediction for M_H does not change and all SM parameters are chosen to agree with $M_H = 94$ GeV.

Total experimental uncertainties of 6 MeV for M_W, $13 \cdot 10^{-5}$ for $\sin^2\theta^\ell_{\mathrm{eff}}$, $4 \cdot 10^{-3}$ for R^0_ℓ, and 100 MeV for m_t (interpreted as pole mass) are assumed [31]. The exact achieved precision on the Higgs mass is irrelevant for this study. For the hadronic contribution to the running of the QED fine structure constant at the Z pole, $\Delta\alpha^{(5)}_{\mathrm{had}}(M_Z^2)$, an uncertainty of $4.7 \cdot 10^{-5}$ is assumed,[c] compared to the currently used uncertainty of $10 \cdot 10^{-5}$ [24]. The other input observables to the electroweak fit are taken to be unchanged from the current settings.

The most important theoretical uncertainties in the fit are those affecting the M_W and $\sin^2\theta^\ell_{\mathrm{eff}}$ predictions arising from unknown higher-order corrections. We assume in the following that theoretical developments have led to improved uncertainties of only half the present values,

[c] The uncertainty on $\Delta\alpha^{(5)}_{\mathrm{had}}(M_Z^2)$ will benefit below the charm threshold from the completion of BABAR analyses and the ongoing program at VEPP-2000. At higher energies improvements are expected from charmonium resonance data from BES-3, and a better knowledge of α_S from the R^0_ℓ measurement and reliable lattice QCD predictions [33].

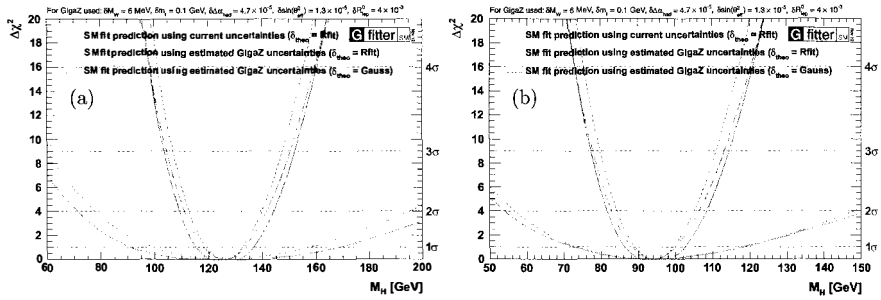

Figure 6: ILC projection of the $\Delta\chi^2$ profiles as a function of the Higgs mass for electroweak fits compatible with an SM Higgs boson of mass 125.8 GeV (a) and 94 GeV (b). The measured Higgs boson mass is not used as input in the fit. The grey bands show the results obtained using present uncertainties [11], and the yellow bands indicate the results for the hypothetical future scenario (a) and corresponding input data shifted to accommodate a 94 GeV Higgs boson but unchanged uncertainties (b). The thickness of the bands indicates the effect from the theoretical uncertainties treated according to the *R*fit prescription. The long-dashed line in each plot shows the curves when treating the adding the theoretical uncertainties in according to Gaussian distributed values.

$\delta_{\rm th} M_W = 2\,\text{MeV}$ and $\delta_{\rm th} \sin^2\theta^\ell_{\rm eff} = 1.5 \cdot 10^{-5}$.

The indirect prediction of the Higgs mass at 126 GeV achieves an uncertainty of $^{+12}_{-10}$ GeV. Keeping the present theoretical uncertainties in the prediction of M_W and $\sin^2\theta^\ell_{\rm eff}$ would worsen the accuracy of the M_H prediction to $^{+20}_{-17}$ GeV, whereas neglecting theoretical uncertainties altogether would improve it to ± 7 GeV. This emphasizes the importance of theoretical updates.

For M_W the prediction with an estimated uncertainty of 5 MeV is similarly accurate as the assumed measurement, while the prediction of $\sin^2\theta^\ell_{\rm eff}$ with an uncertainty of $4 \cdot 10^{-5}$ is three times less accurate than the expected experimental precision. The fit would therefore particularly benefit from additional experimental improvement in M_W. The accuracy of the indirect determination of the top mass is 1.2 GeV, which is similar to that of the present experimental determination. The fit would therefore benefit significantly from a reduction of the uncertainty on m_t to a value of about 100 MeV. The measurement of R^0_ℓ would result in a precision measurement of the strong coupling constant with an experimental uncertainty of 0.4% and a theoretical uncertainty of only 0.1%, which has been achieved already today owing to the full $\mathcal{O}(\alpha_s^4)$ calculation of the QCD Adler function [15, 16].

Profiles of $\Delta\chi^2$ as a function of the Higgs mass for present and future electroweak fits compatible with a SM Higgs boson of mass 125.8 GeV and 94 GeV are shown in Fig. 6(a) and (b), respectively. The measured Higgs boson mass is not used as input in these fits. If the experimental input data, currently predicting $M_H = 94^{+25}_{-22}$ GeV, were left unchanged with respect to the present values, but had uncertainties according to the ILC expectations, a deviation of the measured M_H exceeding 4σ could be established with the fit, see Fig. 6(b). Such a conclusion does not strongly depend on the treatment of the theoretical uncertainties (*R*fit versus Gaussian, i.e. quadratic addition) as can be seen by comparison of the solid yellow and the long-dashed yellow $\Delta\chi^2$ profiles.

Additionally to establishing a precise statement about the compatibility of the directly measured value of M_H and the SM prediction, the high precision measurements of EWPO at the ILC would significantly improve the indirect determination of SM parameters which has a high sensitivity to additional contributions of new physics on the loop-level and complements direct searches for new physics. Prospects for the precision of the simultaneous indirect determination of m_t and M_W are shown in Fig. 7(a) together with the present and expected precision of the m_t and M_W measurements. The gain in precision of the indirect measurements is about a factor

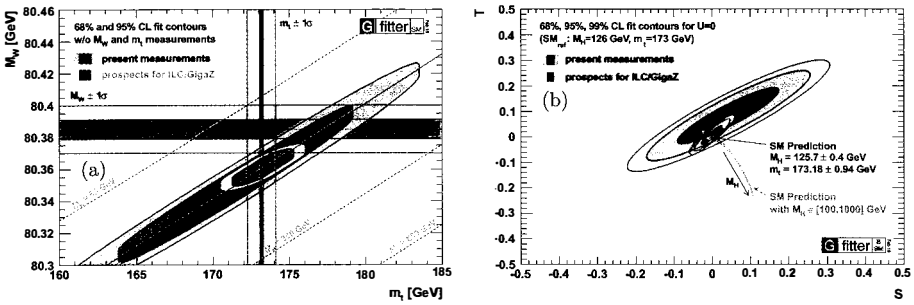

Figure 7: ILC projection of the contour lines of 68%, 95% CL allowed regions in the m_t–M_H plane. Shown are the current indirect determinations (blue) and the expected precision using prospects for ILC measurements of EWPO (orange). The present direct measurements together with the experimental uncertainties are shown as light green bands, the prospects for the uncertainties on m_t and M_H are shown as dark green bands. Contour lines of 68%, 95% and 99% CL allowed regions on the S and T parameters for $U = 0$ with respect to the SM reference ($M_{H,\mathrm{ref}} = 126\,\mathrm{GeV}$ and $m_{t,\mathrm{ref}} = 173\,\mathrm{GeV}$) (b). The prediction in the SM is given by the black (grey) area when including (excluding) the M_H measurements.

of three with respect to the current determinations. Assuming that the central values of m_t and M_W do not change from their present values, a deviation between the SM prediction and the direct measurements would be prominently visible.

The precisely measured EWPO would also help to constrain new physics through oblique corrections. The expected constraints on the S and T parameters are shown in Fig. 7(b), where an improvement of more than a factor of 3 seems to be possible.

7 Conclusion

Assuming the newly discovered particle at ∼126 GeV to be the Standard Model (SM) Higgs boson, all SM parameters entering electroweak precision observables are known. For the first time, the fit can over-constrain the SM at the electroweak scale and evaluate its validity. We reported here on the most recent results from the electroweak fit [11].

The measured value of the Higgs mass agrees at 1.3σ with the indirect prediction from the electroweak fit. The global fit to all the electroweak precision data and the measured Higgs mass results in a goodness-of-fit p-value of 7%. Only a fraction of the contribution to the "incompatibility" stems from the Higgs mass. The largest deviation between the best fit result and the data is introduced by $A_{\mathrm{FB}}^{0,b}$ – a known tension – and by R_b^0. A revisit of these two quantities would be very interesting, both theoretically and experimentally.

The knowledge of the Higgs mass dramatically improves the SM predictions of several key observables, in particular of the top mass, the W-mass, and $\sin^2\theta_{\mathrm{eff}}^{\ell}$. The predicted uncertainties decrease by a factor of ~ 2.5, from 6.2 to 2.5 GeV, 28 to 11 MeV, and $2.3 \cdot 10^{-5}$ to $1.0 \cdot 10^{-5}$ respectively. Theoretical uncertainties due to unknown higher-order electroweak and QCD corrections contribute approximately half of the uncertainties in the M_W and $\sin^2\theta_{\mathrm{eff}}^{\ell}$ predictions.

The observed agreement of these quantities between the indirect determinations and measurements demonstrates the impressive consistency of the SM. The improved accuracy of the indirect determination of M_W sets a benchmark for new direct measurements.

Updated values for the oblique parameters S, T, U have been presented, using the measured value of the Higgs mass as a reference, and indicate that possible new physics models may affect the electroweak observables only weakly.

Finally, the perspectives of the electroweak fit considering a future e^+e^- collider running

also at energies at the Z-pole have been analyzed. Assuming a good control over systematic effects results in improved accuracy of the predictions for the top mass, the W-mass, $\sin^2\theta^\ell_{\rm eff}$ and $\alpha_S(M_Z^2)$ with a factor of three or greater. We point out that, in order to fully exploit the experimental potential, theoretical developments are mandatory, in particular in the accuracy of M_W and $\sin^2\theta^\ell_{\rm eff}$, requiring the calculation of higher order electroweak and QCD corrections.

References

[1] The ALEPH, DELPHI, L3, OPAL Collaborations, the LEP Electroweak Working Group, (1995), CERN-PPE-95-172.

[2] CDF Collaboration, F. Abe *et al.*, Phys. Rev. Lett. **74**, 2626 (1995), [hep-ex/9503002].

[3] D0 Collaboration, S. Abachi *et al.*, Phys. Rev. Lett. **74**, 2632 (1995), [hep-ex/9503003].

[4] C. Campagnari and M. Franklin, Rev. Mod. Phys. **69**, 137 (1997), [hep-ex/9608003].

[5] M. Baak *et al.*, Eur. Phys. J. **C72**, 2003 (2012), [1107.0975].

[6] ATLAS Collaboration, G. Aad *et al.*, Phys. Lett. B (2012), [1207.7214].

[7] CMS Collaboration, S. Chatrchyan *et al.*, Phys. Lett. B (2012), [1207.7235].

[8] B. Dumont, these proceedings (2013), [1305.4635].

[9] O. Eberhardt *et al.*, Phys. Rev. Lett. **109**, 241802 (2012), [1209.1101].

[10] H. Flacher *et al.*, Eur. Phys. J. **C60**, 543 (2009), [0811.0009], Err.-ibid. C71 (2011) 1718.

[11] M. Baak *et al.*, Eur. Phys. J. **C72**, 2205 (2012), [1209.2716], regular updates at http://cern.ch/gfitter.

[12] M. Awramik, M. Czakon, A. Freitas and G. Weiglein, Phys. Rev. **D69**, 053006 (2004), [hep-ph/0311148].

[13] M. Awramik, M. Czakon and A. Freitas, JHEP **0611**, 048 (2006), [hep-ph/0608099].

[14] M. Awramik, M. Czakon, A. Freitas and G. Weiglein, Phys. Rev. Lett. **93**, 201805 (2004), [hep-ph/0407317].

[15] P. Baikov, K. Chetyrkin and J. H. Kuhn, Phys. Rev. Lett. **101**, 012002 (2008), [0801.1821].

[16] P. Baikov, K. Chetyrkin, J. Kuhn and J. Rittinger, Phys. Rev. Lett. **108**, 222003 (2012), [1201.5804].

[17] A. Freitas and Y.-C. Huang, JHEP **1208**, 050 (2012), [1205.0299].

[18] K. Hagiwara, S. Matsumoto, D. Haidt and C. Kim, Z. Phys. **C64**, 559 (1994), [hep-ph/9409380], Order of authors changed in journal.

[19] K. Hagiwara, Ann. Rev. Nucl. Part. Sci. **48**, 463 (1998).

[20] G.-C. Cho and K. Hagiwara, Nucl. Phys. **B574**, 623 (2000), [hep-ph/9912260].

[21] G.-C. Cho, K. Hagiwara, Y. Matsumoto and D. Nomura, JHEP **1111**, 068 (2011), [1104.1769].

[22] The ALEPH, DELPHI, L3, OPAL, SLD Collaborations, the LEP Electroweak Working Group, the SLD Electroweak and Heavy Flavour Working Groups, Phys. Rept. **427**, 257 (2006), [hep-ex/0509008].

[23] CDF Collaboration, D0 Collaboration, Tevatron Electroweak Working Group, [1204.0042].

[24] M. Davier, A. Hoecker, B. Malaescu and Z. Zhang, Eur. Phys. J. **C71**, 1515 (2011), [1010.4180].

[25] CDF Collaboration, D0 Collaboration, T. Aaltonen *et al.*, [1207.1069].

[26] CMS Collaboration, S. Chatrchyan *et al.*, CMS-PAS-TOP-12-029 (2012).

[27] S. Alekhin, A. Djouadi and S. Moch, Phys. Lett. **B716**, 214 (2012), [1207.0980].

[28] M. E. Peskin and T. Takeuchi, Phys. Rev. Lett. **65**, 964 (1990).

[29] M. E. Peskin and T. Takeuchi, Phys. Rev. **D46**, 381 (1992).

[30] ECFA/DESY LC Physics Working Group, J. Aguilar-Saavedra *et al.*, hep-ph/0106315.

[31] ILC Collaboration, G. Aarons *et al.*, 0709.1893.

[32] ILD Concept Group - Linear Collider Collaboration, T. Abe *et al.*, 1006.3396.

[33] M. Davier, *private communication*, Nov 2012.

LHC Beam Operations: Past, Present and Future

Maria Kuhn
CERN, Geneva, Switzerland

Abstract

A brief overview of LHC operations over the last 3 years is provided. Luminosity performance has been satisfactory and the factors that have been exploited are outlined. Availability and operational efficiency are discussed. Finally a brief overview of the planned long shutdown is given and estimates of the potential post shutdown performance are briefly enumerated.

1 Introduction

The LHC re-started initial commissioning with beam at the end of 2009. Since then the LHC has had three years of operations as summarized in Table 1. Essentially, 2010 was devoted to commissioning and establishing confidence in the critical machine protection system. 2011 saw the start of exploitation and the exploration of performance limits. Pushing these limits, outlined below, allowed the instantaneous luminosity performance to be increased throughout 2011. 2012 was a production year at an increased center of mass (COM) energy of 8 TeV. Again limits were pushed revealing some challenging issues at high bunch and total beam intensity.

The integrated luminosity performance over the 3 years can be regarded as good, with the LHC delivering enough integrated luminosity to enable ATLAS and CMS to announce the discovery of a Higgs-like boson on July 4^{th} 2012.

Table 1: LHC operations 2010 - 2012

Year	Overview	COM energy	ATLAS/CMS integrated luminosity [fb^{-1}]
2010	Commissioning	7 TeV	0.04
2011	Exploring limits	7 TeV	6.1
2012	Production	8 TeV	23.1

One of the main features of operations in 2011 and 2012 was the use of high bunch intensity with 50 ns bunch spacing. As discussed below, this gave good instantaneous luminosity performance but at the cost of high pile-up to the high luminosity experiments. In 2011 the mean number of collision per crossing (mu) was around 12 with Poisson tails up to approximately 20. In 2012 mu had increased to around 30 collisions/crossing at the beginning of a fill with tails up to approximately 40.

Besides the delivery of high instantaneous and integrated luminosity to ATLAS and CMS, the LHC team was also able to deliver physics to a number of other users.

- 2010 and 2011 saw lead-lead ion runs which delivered 9.7 and 166 μb^{-1} respectively at an energy of 3.5Z TeV. Here the clients were ALICE, ATLAS and CMS.

- Luminosity levelling at around 4×10^{32} $cm^{-2}s^{-1}$ via transverse separation, with a tilted crossing angle, enabled LHCb to collect 1.2 and 2.2 fb^{-1} in 2011 and 2012 respectively.
- ALICE enjoyed some sustained proton-proton running in 2012 at around 5×10^{30} $cm^{-2}s^{-1}$ with collisions between enhanced satellite bunches and the main bunches.
- There was a successful $\beta^* = 1$ km run for TOTEM and ALFA. With t_{min} of approximately 0.0004 GeV^2 this was the first LHC measurement in Coulomb-Nuclear Interference region.
- The three years operational period culminated in successful proton-lead run at the start of 2013. Here the clients were ALICE, ATLAS, CMS and LHCb.

2 Performance

Basic variations on the equation for the luminosity of a collider are shown in Eq. 1, assuming round beams and equal values of the beta function for both beams in both planes in the latter equation.

$$\mathcal{L} = \frac{N^2 k_b f}{4\pi\sigma_x^*\sigma_y^*}F = \frac{N^2 k_b f\gamma}{4\pi\epsilon_n\beta^*}F \quad (1)$$

Here N is the number of particles per bunch, k_b is the number of bunches, f is the revolution frequency, γ is the usual relativistic factor, σ_x^* and σ_y^* are the horizontal and vertical beam sizes at the interaction point, ϵ_n is the normalized transverse emittance, β^* is the value of the beta function at the interaction point and F is the geometrical reduction factor arising from the crossing angle.

The corresponding values for these parameters at the peak performance of the LHC (so far) are shown in Table 2. The design report values are displayed for comparison. Remembering that the beam size is naturally larger at lower energy, it can be seen that the LHC has achieved 77% of design luminosity at 4 sevenths of the design energy with a β^* of 0.6 m (cf. design value of 0.55 m) with half nominal number of bunches.

Table 2: Performance related parameter overview

Parameter	Value in 2012	Design value
Beam energy [TeV]	4	7
β^* in IP 1,2,5,8 [m]	0.6,3.0,0.6,3.0	0.55
Bunch spacing [ns]	50	25
Number of bunches	1374	2808
Average bunch intensity [protons per bunch]	1.6 - 1.7×10^{11}	1.15×10^{11}
Normalized emittance at start of collision [μm]	2.5	3.75
Peak luminosity [$cm^{-2}s^{-1}$]	7.7×10^{33}	1×10^{34}
Max. mean number of collisions per bunch crossing	$\approx$40	19
Stored beam energy [MJ]	$\approx$140	362

One of the main reasons for the impressive luminosity has been the excellent beam quality delivered by the injectors. As shown in Table 3 the injector complex has succeeded in delivering beam with significantly more protons per bunch (ppb) than nominal with lower emittances than nominal. This is particularly significant for the 50 ns beam.

The LHC has proven capable of absorbing these brighter beams, notably from a beam-beam perspective. The clear cost has been increased pile-up for the high luminosity experiments which they have successfully learnt to deal with.

In brief the LHC has achieved good luminosity performance via the following.

- Exploiting the important advantage that high bunch intensities bring (with luminosity proportional to N_b^2). Here the bunch intensity has been up to 150% of nominal with the 50 ns bunch spacing.

Table 3: 2012 values of beam parameters at exit of SPS

Bunch spacing [ns]	Bunch intensity [ppb]	Emittance [μm]
50	1.7×10^{11}	1.8
25	1.2×10^{11}	2.7

- The normalized emittance going into collisions has been around 2.5 μm, thanks to very good injector performance and ability to conserve the emittance through the Booster, PS, and SPS. Some systematic blow-up at injection and in the ramp is seen in the LHC.
- It has proved possible to squeeze to a β^* of 60 cm thanks to measurement of a very good aperture in the interaction regions (credit to alignment, respect of mechanical tolerances, optics measurement and correction, and orbit correction).
- The total intensity has reached $2.2{\times}10^{14}$ i.e. 70% of nominal. Here a fully trustworthy machine protection has been instrumental in providing the confidence to routinely deal with 140 MJ beams.

3 Overview of Machine Characteristics

The performance described above is on the back of some excellent system performance and some fundamental characteristics of the LHC [1].

- There is excellent single beam lifetime and on the whole the LHC enjoys excellent vacuum conditions.
- There is excellent field quality, coupled with good correction of non-linearities.
- Head-on beam-beam is not a limitation although long range has to be taken reasonably seriously with enough separation at the long range encounters guaranteed by sufficiently large crossing angles.
- Collective effects have been seen with the high bunch intensities. Single and coupled bunch instabilities have been surpressed using a range of tools (high chromaticity, Landau damping octupoles and transverse feedback).

Very good understanding of the beam physics and a good level of operational control has been established.

- There is better than expected aperture due excellent alignment and respect of mechanical tolerances.
- The β^* reach has been established and exploited. Reduction has been pursued aggressively, exploiting: the better than specified available aperture; tight collimator settings; and very good stability and reproducibility.

The complex operational cycle is now well established and is robust.

- The pre-cycle, injection process, 450 GeV machine, ramp, squeeze, collide are largely sequencer driven. There is generally good beam lifetime throughout the whole process.
- A strict pre-cycling regime means the magnetic machine is remarkably reproducible. This is reflected in the optics, orbit, collimator set-up, tune and chromaticity.
- Operations is unpinned by superb performance of machine protection and associated systems (beam interlock system, beam dump system, beam loss monitors, and collimation system). There is rigorous machine protection follow-up, qualification, and monitoring; all non-conformities are examined rigorously. The importance of this to the success of the LHC so far cannot be over stressed - there has been a move from commissioning to real confidence in less than two years.

Availability has, in general, been very good considering the size, complexity and operating principles of the LHC. An outline of 2012's availability is shown in Table 4. The percent of scheduled physics time spent in "Stable beams" in 2012 was around 36% of a total scheduled time for proton-proton physics of around 200 days. This is encouraging for a machine only 3 years into its operational lifetime. The machine is performing well and a huge amount of experience and understanding has

been gained. There is good system performance, excellent tools, and reasonable availability following targeted consolidation. This is the legacy for post long shutdown 1 operation.

Table 4: LHC availability 2012

Mode	% of scheduled time
Access	13.8%
Setup	27.6%
Beam in	15.0%
Ramp and squeeze	7.1%
Stable beams	36.5%

4 Long Shutdown 1 (LS1)

The primary aim of LS1 is the consolidation of the superconducting splices in the magnet interconnects following the incident of 2008. This will allow the current in the main dipole and quadrupole circuits to be increased to the 6.5 and then 7 TeV level. Besides this a huge amount of maintenance and other consolidation work is to be performed. Some key LS1 work packages are outlined below [1].

- Measure all splices and repair the defective ones. Repeat for the 6 splices per interconnect (2 splices for the main dipoles and 4 for the 2 main quadrupole circuits). There are approximately 1700 interconnects in the machine.
- Consolidate interconnects with a new design (clamp, shunt)
- Finish installation of pressure release mechanisms on cryostats not yet so equipped
- Magnet consolidation: the exchange of weak cryo-magnets
- Consolidation of the current lead feed-boxes (DFBAs)
- Install collimators with integrated button BPMs (tertiary collimators and a few secondary collimators)
- Extensive experiments consolidation and upgrades
- Plus a lot of other maintenance work covering cryogenics, quench protection, electrical infrastructure, cooling and ventilation, Radio Frequency, beam dump absorber and magnet, change of dump switches (radiation), electron cloud mitigations

5 Possible Limitations for Post LS1

The most important issue to be discussed here is that of electron cloud. Although this has not been a serious issue with the 50 ns beam, there are potential problems with the 25 ns foreseen for post LS1 operation.

There were 3.5 days of scrubbing with 25 ns beams at 450 GeV between 6 and 9 December 2012. The tests saw regular filling of the ring with up to 2748 bunches with a total intensity per beam of up to 2.7×10^{14}. Scrubbing effects in the arcs saw quite rapid conditioning observed in the first stages. The secondary electron yield (SEY) evolution significantly slows down during the last scrubbing fills (more than expected by estimates from laboratory measurements and simulations) and preliminary conclusions [4] are that an electron cloud free environment with 25 ns beam after scrubbing at 450 GeV seem not be reachable in acceptable time. Operation with high heat load and electron cloud density (with blow-up) seems to be unavoidable with a corresponding slow intensity ramp-up. (In 2015 following the warm-up and opening of the entire ring to atmosphere, the SEY and vacuum conditions will be reset and initial re-conditioning will be required.)

UFOs (Unidentified Falling Objects) have now been exquisitely well studied and simulated [3]. There were occasional dumps in 2012 following adjustment of BLM thresholds at the appropriate time-scales (the beam loss spike caused by a UFO is typically of order 1 ms). With the increase

in energy to 6.5 TeV and the proposed move to 25 ns there is potentially serious problem with the UFOs become harder (energy) and potentially more frequent (25 ns). Investigations have continued and potentially encouraging results from the 2013 quench test program are noted [3].

6 Post LS1 Operational Scenarios

6.1 Beam from the Injectors LS1 to LS2

The bunch spacings and associated performance on offer from the injectors post LS1 are shown in Table 5. 50 ns proved a good choice in 2011 and 2012 opening the way to an increased number of bunches and the excellent performance in terms of emittance and bunch intensity. The best that was taken into collisions in 2012 was around 1.7 $\times 10^{11}$ ppb with an emittance of around 2.5 μm going into collision. Further imaginative developments on the PS side have led to the creation of the so-called BCMS (Batch Compression and (bunch) Merging and (bunch) Splittings) scheme [5] which offer remarkably low emittance coupled with healthy bunch intensity as shown in Table 5.

Table 5: Post LS1 beam parameters at the exit of SPS

Scheme	Bunch intensity [10^{11} ppb]	Emittance exit SPS [μm]	Emittance into collisions [μm]
25 ns	1.15	2.8	3.75
25 ns BCMS	1.15	1.4	1.9
50 ns	1.65	1.7	2.3
50 ns BCMS	1.6	1.2	1.6

6.2 50 versus 25 ns

50 ns offers:

- lower total beam current;
- higher bunch intensity (at the cost of having to wrestle with beam instabilities);
- lower emittance.

However the perhaps crippling cost at 6.5 TeV is the very high pile-up which will certainly require levelling to be operationally useful. On the other hand 25 ns has a number of negative points which include:

- more long range collisions: requiring a larger crossing angle and thus higher β^*;
- higher emittance;
- seriously more electron cloud with the need for scrubbing;
- higher UFO rate;
- higher injected bunch train intensity;
- higher total beam current.

However, the push will be to go for 25 ns to avoid the inefficiencies and cost of high pile-up.

6.3 Potential Performance

The potential performance for four scenarios enumerated in Table 5 are shown in Table 6. The estimates assume:

- a beam energy of 6.5 TeV;
- a 1.1 ns bunch length (nominal);
- a scheduled 150 days of proton physics with a reasonable optimistic availability (Hübner factor ≈ 0.2);
- 85 mb visible cross-section.

It should be noted that the 50 ns options necessitates the use of a levelling scheme of some sort, as yet unproven operationally.

From Table 6 one notes the following.

Table 6: Post LS1 performance estimates - usual caveats apply

Scheme	Number of bunches	Bunch intensity [10^{11} ppb]	β^*_x[cm]/β^*_y[cm]/ half crossing angle [μrad]	Emittance [μm]	Peak luminosity	Pile-up	Int. lumi. fb^{-1}
25 ns	2760	1.15	55/43/189	3.75	9.3×10^{33}	25	24
25 ns BCMS	2520	1.15	45/43/149	1.9	1.7×10^{34}	52	45
50 ns	1380	1.6	42/43/136	2.3	1.6×10^{34} level to 0.8×10^{34}	87 level to 44	40
50 ns BCMS	1260	1.6	38/43/115	1.6	2.3×10^{34} level to 0.8×10^{34}	138 level to 44	40

- The nominal 25 ns parameters gives more-or-less nominal luminosity at 6.5 TeV as might be expected.
- The BCMS 25 ns scheme gives peak luminosities of 1.7×10^{34}cm^{-2}s^{-1} with peak <mu> of around 50 with 83% of the nominal intensity.
- The now operational 50 ns scheme gives a virtual luminosity of 1.6×10^{34} cm^{-2}s^{-1} but with a pile-up of over 70 making levelling mandatory.
- The BCMS 50 ns scheme gives a virtual luminosity of 2.3×10^{34} cm^{-2}s^{-1} with a pile-up of over 100 making levelling even more mandatory.

7 Conclusions

The LHC has shown the results of excellent design, construction, and installation. Operation is now well bedded in and both instantaneous and integrated luminosity performance is healthy. The injector complex has performed very well and delivered 50 ns beam with high bunch intensities and low emittance. Machine availability has been reasonable for a machine the size and complexity of the LHC.

The LHC carries forward a wealth of experience from operation at 3.5 and 4 TeV, and is anticipating operation at 6.5 TeV in 2015 following a two year shutdown. There are potential issues. Measures to address and mitigate these are under examination.

Acknowledgments

The success of the LHC represents a huge international effort at all phases: design, construction, installation, commissioning and operations.

References

1. M. Lamont, Status of the LHC, Proceedings of the International Workshop on Discovery Physics at the LHC - Kruger 2012.
2. R. Tomas Garcia, Optics and dynamic aperture at 4 and 6.5 TeV, Proceedings of the LHC Beam Operation workshop - Evian 2012 (to be published).
3. T. Baer, UFOs, Proceedings of the LHC Beam Operation workshop - Evian 2012 (to be published).
4. G. Iadarola, Electron Cloud and Scrubbing, Proceedings of the LHC Beam Operation workshop - Evian 2012 (to be published).
5. R. Steerenberg, Post LS1 25 ns and 50 ns options from the injectors, Proceedings of the LHC Beam Operation workshop - Evian 2012 (to be published).

2.
New Phenomena

Searches for BSM Higgs Bosons at the LHC

M. Boehler on behalf of the ATLAS and CMS collaborations
Albert-Ludwigs-Universität Freiburg, Physikalisches Institut, Hermann-Herder-Str.3 , D-79104 Freiburg, Germany

Searches for Higgs bosons in different extensions of the Standard Model which predict additional neutral and charged Higgs bosons are presented. These include the Minimal Supersymmetric extension of the Standard Model (MSSM), the next-to Minimal Supersymmetric extension of the Standard Model (nMSSM), two Higgs doublet models, four-generation and fermiophobic models. Results are based on data collected by the ATLAS and CMS experiments in proton-proton collisions at centre-of-mass energies of 7 TeV and 8 TeV. No excess is found in either charged nor neutral Higgs Boson searches. Model-independent and model-dependent exclusion limits are presented for these searches.

1 Introduction

The ATLAS and CMS experiments have performed many searches for beyond the standard model (BSM) Higgs bosons at the LHC. An overview of the most recent results focusing on analyses with an integrated lumiosity above 1 fb^{-1} is presented, classified as charged or neutral Higgs boson searches.

2 Charged Higgs Boson Searches

2.1 Charged Higgs Boson Searches for $H^+ \to \tau\nu$

Both ATLAS and CMS perform searches for light charged Higgs bosons that assume $m_{H^+} < m_{\text{top}}$, where the charged Higgs bosons are produced in top-quark decays. Since H^+ decays predominantly into $\tau + \nu$, top-quark pair events with tau lepton final states are investigated.

The ATLAS analysis[1] is based on 4.6 fb^{-1} of pp collisions at $\sqrt{s} = 7$ TeV. The final states jets+τ_{lep}, τ_{lep}+τ_{had} and $\tau_{had} + jets$ are considered. The results agree with SM expectations and 95% CL upper limits on $\mathcal{BR}(t \to bH^+)$ between 5% and 1% are set for 90 GeV $< m_H^+ <$ 150 GeV, assuming $\mathcal{BR}(H^+ \to \tau\nu) = 100\%$. An update of this analysis[2] exploits the fact that top-quark pair decays with charged Higgs bosons would violate the lepton universality due to the enhanced coupling to the tau leptons. The ratio of event yields with and without tau leptons are compared with SM expectations, reducing systematic uncertainties while improving the upper limit on the $\mathcal{BR}(t \to H^+b)$ to 0.8%-3.4% after combining with the τ_{had}+jets final state from Ref[1]. Limits in the Minimal Supersymmetric extension of the Standard Model (MSSM) are set for the m_h^{max} scenario[4], shown in Figure 1 (left).

The analogous CMS search[3] uses 2 fb^{-1} of data in four final states: $e\tau_{had}$, $\mu\tau_{had}$, $e\mu$, and τ_{had}+jets. Upper limits on $\mathcal{BR}(t \to H^+b)$ in the range of 2-4% are achieved. In the m_h^{max} scenario, tan(β) values above 16 can be excluded (Fig 1(right)). An update in the $\mu\tau_{had}$ channel[5] with a luminosity of 4.9 fb^{-1} improves the upper limits on $\mathcal{BR}(t \to H^+b)$ to 2-3% for 90 $< m_H^+ <$ 160 GeV.

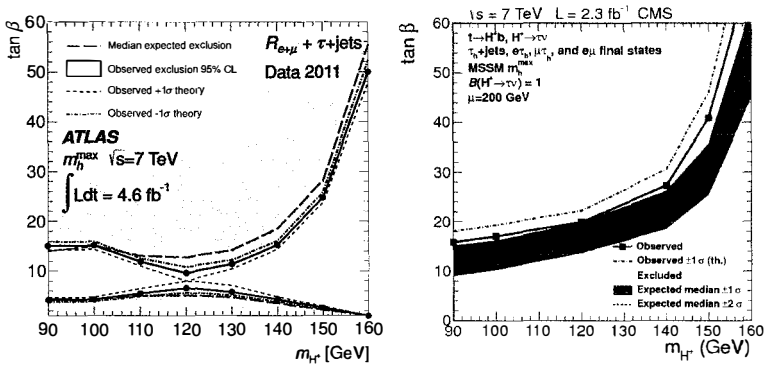

Figure 1: Limits for charged Higgs boson production from top-quark decays in the m_{H^+}-$\tan\beta$ plane. ATLAS results[2] (left) are derived using τ_{had}+jets events and the ratio $R_{e+\mu}$, while CMS results[3] (right) are shown in the context of the m_h^{max} scenario of the MSSM.

2.2 Doubly-charged Higgs Boson Searches

ATLAS and CMS searches for doubly-charged Higgs bosons use 4.9 fb^{-1} of data at $\sqrt{s} = 7$ TeV. The CMS analysis[6] uses three and more charged leptons of any flavour and is sensitive to pair-produced ϕ^{++},ϕ^{--} and $\phi^{\pm\pm}$,$\phi^{\mp}$ associated production with degenerate masses. No excess is observed and both upper limits at 95 % CL on the ϕ^{++} production cross section and lower bounds on the $\phi^{\pm\pm}$ masses are reported. For $\mathcal{BR}(\phi^{\pm\pm} \to \ell^{\pm}\ell^{\pm}) = 100\%$ in the different lepton final states, doubly-charged Higgs boson masses between 204 and 459 GeV can be excluded. Four benchmark scenarios with different BR are studied and doubly-charged Higgs boson masses between 383 and 408 GeV are excluded.

The ATLAS analysis[7] searches for a narrow resonance in the mass spectrum of prompt, high-p_T leptons pairs with the same electric charge. Lower bounds on doubly-charged Higgs bosons masses of 409, 409, and 398 GeV are obtained, assuming pair production, coupling to left-handed fermions, and a branching ratio of 100% for final states ee, eμ, and $\mu\mu$, respectively.

3 Neutral Higgs Boson Searches

3.1 Neutral Higgs Boson Searches for $\phi \to \tau\tau$

The ATLAS analysis[8] uses up to 4.9 fb^{-1} of 7 TeV data to search for Higgs Boson decays into muon or tau lepton pairs. No significant excess is observed and exclusion limits for the production cross-section at 95% CL are derived separately for a generic Higgs boson ϕ as a function of the mass for both gluon-gluon fusion and b-quark associated production (see Fig. 2(left)). Exclusion limits in the m_h^{max} scenario as a function m_A and $\tan\beta$ are also set.

The CMS analysis[9] focuses on di-tau final states, based on the data corresponding to the integrated luminosities of 4.9 fb^{-1} at 7 TeV and 12.1 fb^{-1} at 8 TeV. Final states with and without additional b-quarks are considered. No excess is observed in the di-tau mass-spectra and exclusion limits are interpreted in the m_h^{max} scenario. The combined limit is shown in Fig. 2(right), where $\tan\beta$ values down to 5 are excluded for $m_A < 220$ GeV.

3.2 Searches for invisible Higgs boson decays

The ATLAS search for invisible Higgs decays[13] considers events with Higgs bosons produced in association with a Z boson. Leptonic Z boson decays are used to tag the events. The

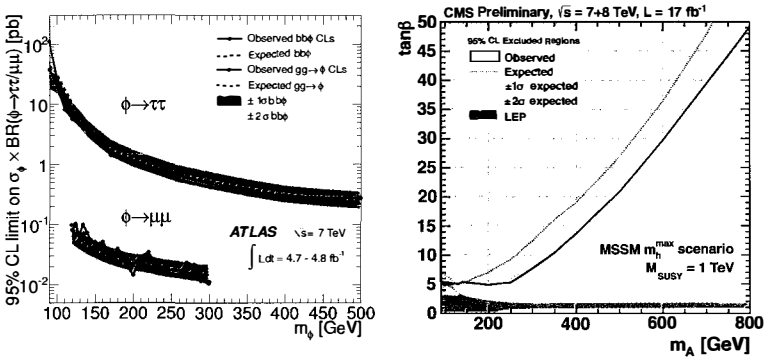

Figure 2: Expected (dashed line) and observed (solid line) ATLAS 95% CL limits on the cross-section for gluon-fusion and b-associated Higgs boson production times the branching ratio into τ and μ pairs, respectively[8] (left). CMS exclusion at 95% CL in the $\tan\beta$-m_A parameter space for the MSSM m_h^{max} scenario[9] (right).

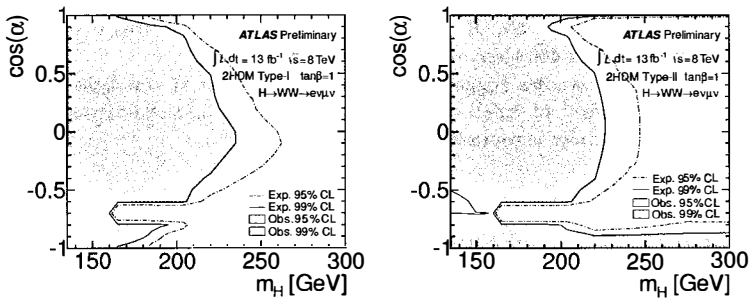

Figure 3: Exclusion contours at the 95% and 99% CL are determined in the $\cos\alpha$-m_H-plane for different values of $\tan\beta$ ranging from 1 to 50 (here the plots for $\tan\beta = 1$ are shown) for type-I (a) and type-II (b) 2HDMs[10].

$E_{\mathrm{T}}^{\mathrm{miss}}$ variable is used to search for an excess in 4.7 fb^{-1} and 13.0 fb^{-1} of 7 TeV and 8 TeV data. Assuming a ZH production rate for a SM Higgs boson with $m_h = 125$ GeV, branching fractions for invisible Higgs decays greater than 65% are excluded at 95% CL. Limits are also set on the cross section times invisible branching fraction of a possible additional Higgs-like boson exclude masses from 170–300 GeV at 95% CL.

3.3 Searches for Higgs bosons in Two Higgs Doublet Models

Given the observation a Higgs boson with $m_{\mathrm{H}} = 125$ GeV, searches for additional neutral Higgs bosons in extensions such as two-Higgs-doublet models (2HDM) are important. The ATLAS analysis[10] searches for a heavier CP-even scalar boson in $H \to WW \to e\nu\mu\nu$ decay modes in 13.0 fb^{-1} of data at 8 TeV. To maximise the sensitivity of the analysis, an artificial neural network technique is used. No evidence for a second scalar boson is observed in the mass range 135 to 300 GeV. Exclusion limits are set for 2HDM of type-I and type-II[11,12] as a function of the two mixing angles α and β and the Higgs mass m_H. Figure 3 shows the exclusion limits in the m_H-$\cos\alpha$ plane for $\tan\beta = 1$ for a 2HDM of type-I (a) and type-II (b).

3.4 *Four-generation and Fermiophobic Higgs Searches*

CMS searches for Higgs bosons in the context of the SM extension including a fourth generation of fermions with masses up to 600 GeV (SM4) and in fermiophobic models[14]. The searches include up to 5.1 fb^{-1} of 7 TeV and up to 5.1 fb^{-1} of 8 TeV data. Three decay modes ($\tau\tau$, WW and ZZ) are investigated and combined to exclude a SM4 Higgs boson in the mass range 110-600 GeV at 99% CL. The fermiophobic analysis exploits diphoton decays, excluding a fermiophobic Higgs boson in the mass range 110-147 GeV at 95% CL.

The ATLAS SM4 Higgs search[15] analyses up to 2.3 fb^{-1} of data at 7 TeV, and Higgs boson masses are excluded at 95% CL between 119-593 GeV. The fermiophobic search[16] uses 4.7 fb^{-1} at 7 TeV and excludes Higgs masses between 110-118.0 GeV and 119.5-121.0 GeV.

3.5 *Searches for Higgs Boson Decays to light CP-odd Scalars*

In some extensions of the SM, such as Minimal Composite Higgs Model or Next-to-Minimal Supersymmetric Standard Model, the Higgs boson can couple to light CP-odd scalar particles. The ATLAS experiment presents a study[17] of Higgs decays with di-photon final states based on 4.9 fb^{-1} of 7 TeV data. The Higgs decays via $H \dashrightarrow aa$, where a is a light CP-odd scalar that decays in two collimated photons, mimicking di-photon final states. Using a modified photon identification for this topology, exclusion limits of 0.1, 0.1 and 0.2 pb are set on the Higgs production cross-section times $\mathcal{BR}(H \to aa \to 4\gamma)$ in the range of 110 GeV $< m_H <$ 150 GeV for the $m_a = 100$, 200, and 400 MeV, respectively.

The CMS analysis[18] studies Higgs bosons decays into a pair of new light bosons decaying into di-muons with 5.3 fb^{-1} of 7 TeV data. An upper limit of 0.78±0.05 fb on the production cross section times BR times acceptance is obtained.

References

1. ATLAS Collaboration, *JHEP* **039**, 1206 (2012).
2. ATLAS Collaboration, arXiv:1212.3572, submitted to JHEP.
3. CMS Collaboration, *JHEP* **07**, 143 (2012).
4. M. Carena *et al*, arXiv:hep-ph/9912223.
5. CMS Collaboration, CMS-PAS-HIG-12-005, https://cds.cern.ch/record/1502246.
6. CMS Collaboration, *Eur. Phys. J.* C **72**, 2189 (2012).
7. ATLAS Collaboration, arXiv:1210.5070, submitted to the Eur. Phys. J. C.
8. ATLAS Collaboration, *JHEP* **02**, 095 (2013).
9. CMS Collaboration, CMS-PAS-HIG-12-050, https://cds.cern.ch/record/1493521.
10. ATLAS Collaboration, ATLAS-CONF-2013-027, https://cds.cern.ch/record/1525887.
11. Chen, Chien-Yi and Dawson, S., *Phys. Rev.* D **87**, 055016 (2013).
12. A. Djouadi, *Phys. Rept.* **459**, 1-241 (2008).
13. ATLAS Collaboration, ATLAS-CONF-2013-011, https://cds.cern.ch/record/1523696.
14. CMS Collaboration, arXiv:1302.1764, submitted to Phys. Lett. B.
15. ATLAS Collaboration, ATLAS-CONF-2011-135, https://cds.cern.ch/record/1383838
16. ATLAS Collaboration, *Eur. Phys. J.* C **72**, 2157 (2012).
17. ATLAS Collaboration, ATLAS-CONF-2012-079, https://cds.cern.ch/record/1460391
18. CMS Collaboration, arXiv:1210.7619, submitted to Phys. Lett. B

2HDM CONFRONTING LHC DATA

P.M. FERREIRA

Instituto Superior de Engenharia de Lisboa - ISEL, 1959-007 Lisboa, Portugal

Centro de Física Teórica e Computacional, Faculdade de Ciências, Universidade de Lisboa, Av. Prof. Gama Pinto 2, 1649-003 Lisboa, Portugal

RUI SANTOS

Instituto Superior de Engenharia de Lisboa - ISEL, 1959-007 Lisboa, Portugal

Centro de Física Teórica e Computacional, Faculdade de Ciências, Universidade de Lisboa, Av. Prof. Gama Pinto 2, 1649-003 Lisboa, Portugal

MARC SHER

High Energy Theory Group, College of William and Mary, Williamsburg, Virginia 23187, U.S.A.

JOÃO P. SILVA

Instituto Superior de Engenharia de Lisboa, 1959-007 Lisboa, Portugal

Centro de Física Teórica de Partículas (CFTP), Instituto Superior Técnico, Universidade Técnica de Lisboa, 1049-001 Lisboa, Portugal

Almost all data collected at the LHC during the 7 and 8 TeV runs has now been analysed by the ATLAS and CMS collaborations. Its consistency with the Standard Model (SM) predictions has cornered the CP-conserving two-Higgs doublet model (2HDM) into the SM limit, $\sin(\beta - \alpha) = 1$. However, there are still allowed regions of the 2HDM parameter space away from this limit. In this work we discuss how the 2HDM is performing in view of the LHC data together with the remaining available experimental and theoretical constraints.

1 Introduction

The discovery of a neutral Higgs boson [1] at CERN's Large Hadron Collider (LHC) has now been confirmed. Hence, all extensions of the Standard Model (SM) have to abide to the existence of a Higgs boson with SM like properties and with a mass of around 125 GeV. The two-Higgs doublet model (2HDM) is one of the simplest extension of the SM. It is built with the addition of a second complex scalar doublet to the SM field content. Consequently, one obtains a richer particle spectrum with one charged and three neutral scalars. All neutral scalars could in principle be the scalar discovered at the LHC [2]. However, a pure pseudo-scalar state with a 125 GeV mass has now been experimentally ruled out [3]. In the next section we present the 2HDM model and in the following sections we discuss how well the most common CP-conserving 2HDM can accommodate the LHC data.

2 The Model

The addition of a second complex scalar doublet to the SM's Yukawa Lagrangian gives rise to the appearance of scalar exchange flavour changing neutral currents (FCNCs) which are known to be strongly constrained by experiment. Avoiding those dangerous FCNCs can be accomplished by simply imposing a Z_2 symmetry on the scalar doublets, $\Phi_1 \to \Phi_1$, $\Phi_2 \to -\Phi_2$, and a corresponding symmetry to the fermion fields. This leads to the well known four Yukawa model types I, II, Y (III, Flipped) and X (IV, Lepton Specific)[4]. The scalar potential in a softly broken Z_2 symmetric 2HDM can be written as

$$\begin{aligned} V(\Phi_1,\Phi_2) &= m_1^2\Phi_1^\dagger\Phi_1 + m_2^2\Phi_2^\dagger\Phi_2 + (m_{12}^2\Phi_1^\dagger\Phi_2 + \text{h.c.}) + \frac{1}{2}\lambda_1(\Phi_1^\dagger\Phi_1)^2 + \frac{1}{2}\lambda_2(\Phi_2^\dagger\Phi_2)^2 \\ &\quad +\lambda_3(\Phi_1^\dagger\Phi_1)(\Phi_2^\dagger\Phi_2) + \lambda_4(\Phi_1^\dagger\Phi_2)(\Phi_2^\dagger\Phi_1) + \frac{1}{2}\lambda_5[(\Phi_1^\dagger\Phi_2)^2 + \text{h.c.}]\,, \end{aligned} \tag{1}$$

where Φ_i, $i = 1, 2$ are complex SU(2) doublets. All parameters except for m_{12}^2 and λ_5 are real as a consequence of the hermiticity of the potential. We will focus on the CP-conserving potential where m_{12}^2, λ_5 and the VEVs are all real. In this model the three CP-eigenstates are usually denoted by h and H (CP-even) and A (CP-odd). As shown in[5], once a CP-conserving vacuum configuration is chosen, all charge breaking stationary points are saddle points with higher energy. Hence, the 2HDM is stable at tree-level against charge breaking and once a non-charge breaking vacuum is chosen the model has two charged Higgs bosons that complete the 2HDM particle spectrum. We choose as free parameters of the model, the four masses, the rotation angle in the CP-even sector, α, the ratio of the vacuum expectation values, $\tan\beta = v_2/v_1$, and the soft breaking parameter redefined as $M^2 = m_{12}^2/(\sin\beta\cos\beta)$ (see[6] for a review of the model). The remaining theoretical and experimental constraints used in this work were recently discussed in[7].

3 Results and discussion

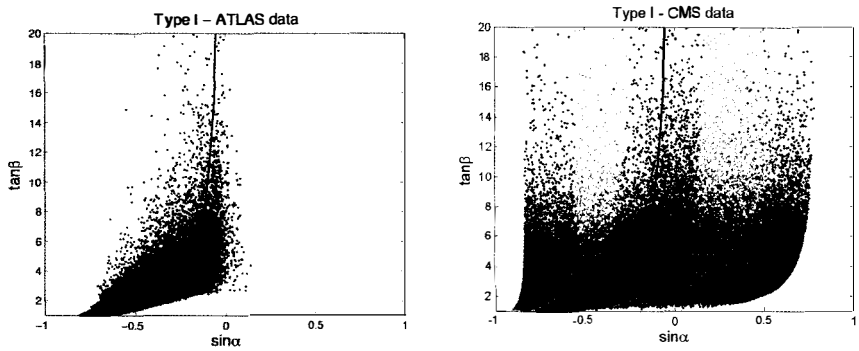

Figure 1: Points in the ($\sin\alpha$, $\tan\beta$) plane that passed all the constraints in model type I using the ATLAS data analysis (left) and using the CMS data analysis (right) at 1σ in green (light grey) and 2σ in blue (dark grey). Also shown is the line for the SM limit $\sin(\beta - \alpha) = 1$.

We randomly generate points in the model's parameter space such that $m_h = 125$ GeV, 90 GeV $\leq m_A \leq 900$ GeV, $m_h < m_H \leq 900$ GeV, $1 \leq \tan\beta \leq 40$, $-(900)^2$ GeV$^2 \leq m_{12}^2 \leq 900^2$ GeV^2 and $-\pi/2 \leq \alpha \leq \pi/2$. In order to respect the flavour constraints we take 90 GeV $\leq m_{H^\pm} \leq 900$ GeV for type I while for type II the allowed range is 360 GeV $\leq m_{H^\pm} \leq 900$ GeV. We define the quantities R_f as the ratio of the number of events predicted in the 2HDM

to that obtained in the SM for a given final state f.

$$R_f = \frac{\sigma(pp \to h)_{\rm 2HDM}}{\sigma(pp \to h_{\rm SM})} \frac{\rm BR(h \to f)_{2HDM}}{\rm BR(h_{SM} \to f)}, \tag{2}$$

where h is the lightest CP-even Higgs (125 GeV), σ is the Higgs production cross section, BR the branching ratio, and $h_{\rm SM}$ is the SM Higgs boson. In our analysis, we include all Higgs production mechanisms, namely, gluon-gluon fusion using HIGLU at NLO [8], vector boson fusion (VBF) [9], Higgs production in association with either W, Z or $t\bar{t}$ [9], and $b\bar{b}$ fusion [10]. A number of similar studies where LHC data was used to constrain the 2HDM were presented in [11].

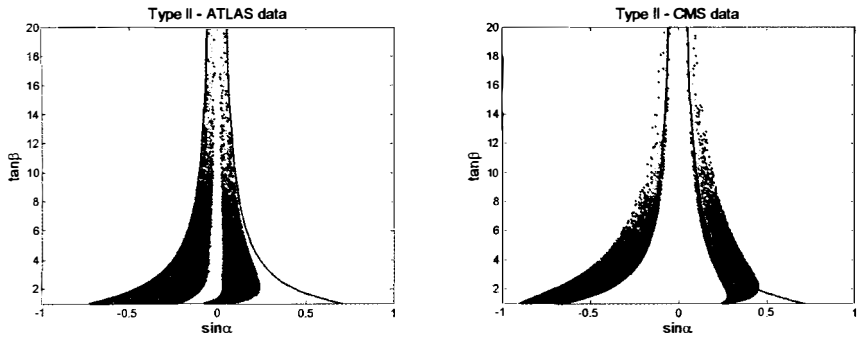

Figure 2: Points in the ($\sin\alpha$, $\tan\beta$) plane that passed all the constraints in model type II using the ATLAS data analysis (left) and using the CMS data analysis (right) at 1σ in green (light grey) and 2σ in blue (dark grey). Also shown are the lines for the SM limit $\sin(\beta-\alpha)=1$ (negative $\sin\alpha$) and for the limit $\sin(\beta+\alpha)=1$.

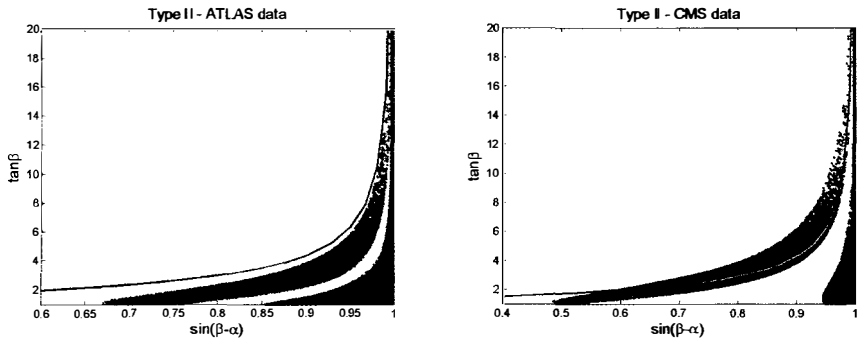

Figure 3: Points in the ($\sin(\beta-\alpha)$, $\tan\beta$) plane that passed all the constraints in model type II using the ATLAS data analysis (left) and using the CMS data analysis (right) at 1σ in green (light grey) and 2σ in blue (dark grey). Also shown are the lines for the SM limit $\sin(\beta-\alpha)=1$ and for the limit $\sin(\beta+\alpha)=1$.

In figure 1 we present the results for the type I model in the ($\sin\alpha$, $\tan\beta$) plane using the ATLAS data [12] (left) and the CMS data [13] (right). The differences between the two plots are easy to understand. The ATLAS data analysis forces R_{ZZ} to be large but as we have previously shown [7] R_{ZZ} can never be above one in type I. Consequently, no points survive at 1σ. With the CMS data analysis plenty of 1σ points survive because all R_{VV} are below one. The 1σ region is slightly away from the SM limit because the central values of R_{VV} are below one. Further, we see in both plots a large dispersion of values around the SM limit. The reason is that $R_{VV} \approx \sin^2(\beta-\alpha)$ in the limit where $BR(h \to b\bar{b}) \approx 1$ and this function is very sensitive from deviations from 1.

In figure 2 we now show similar plots for the type II model. In type II, R_{VV} is not a sensitive quantity[7]. Therefore both the 1σ and the 2σ points are very close to the two limiting lines. The difference between the two plots is that the points tend to concentrate below the limiting lines for ATLAS and above the same lines for CMS. This is of course a consequence of the central values of the ATLAS R_{VV} being above the SM while the CMS ones are below the SM expectation. Finally we present in figure 3 plots similar to the ones in figure 2 but now in the ($\sin(\beta-\alpha)$, $\tan\beta$) plane. Again we see the same trend with the allowed points on opposite sides of the limiting lines, $\sin(\beta-\alpha)=1$ and $\sin(\beta+\alpha)=1$. We should point out that remarkably (even being very conservative), we can already say that values of $\sin(\beta-\alpha)$ below 0.5 are excluded at 2σ. Even more interesting is that for values of $\sin(\beta-\alpha)$ below say 0.8 $\tan\beta$ has to be below 4. Hence, in type II large values of $\tan\beta$ are only allowed close to the SM limit.

Acknowledgments

The works of P.M.F. and R.S. are supported in part by the Portuguese *Fundação para a Ciência e a Tecnologia* (FCT) under contract PTDC/FIS/117951/2010, by FP7 Reintegration Grant, number PERG08-GA-2010-277025, and by PEst-OE/FIS/UI0618/2011. The work of J.P.S. is funded by FCT through the projects CERN/FP/109305/2009 and U777-Plurianual, and by the EU RTN project Marie Curie: PITN-GA-2009-237920. The work of MS is supported by the NSF under Grant No. PHY-1068008.

References

1. G. Aad *et al.* [ATLAS Collaboration], Phys. Lett. B **716**, 1 (2012); S. Chatrchyan *et al.* [CMS Collaboration], Phys. Lett. B **716**, 30 (2012).
2. P. M. Ferreira, R. Santos, M. Sher, J. P. Silva, Phys. Rev. D **85**, 077703 (2012); P. M. Ferreira, R. Santos, M. Sher, J. P. Silva, Phys. Rev. D **85**, 035020 (2012); G. Burdman, C. E. F. Haluch, R. D. Matheus, Phys. Rev. D **85**, 095016 (2012).
3. The ATLAS collaboration, ATLAS-CONF-2013-013; CMS-PAS-HIG-13-002.
4. V. D. Barger, J. L. Hewett and R. J. N. Phillips, Phys. Rev. D **41** (1990) 3421; M. Aoki, S. Kanemura, K. Tsumura and K. Yagyu, Phys. Rev. D **80** (2009) 015017.
5. P. M. Ferreira, R. Santos and A. Barroso, Phys. Lett. B **603** (2004) 219 [Erratum-ibid. B **629** (2005) 114]; A. Barroso, P. M. Ferreira, R. Santos, Phys. Lett. B **632**, 684 (2006); M. Maniatis, A. von Manteuffel, O. Nachtmann, F. Nagel, Eur. Phys. J. C **48**, 805 (2006); I. P. Ivanov, Phys. Rev. D **75**, 035001 (2007) [Erratum-ibid. D **76**, 039902 (2007)]; I. P. Ivanov, Phys. Rev. D **77**, 015017 (2008).
6. G. C. Branco, P. M. Ferreira, L. Lavoura, M. N. Rebelo, M. Sher and J. P. Silva, Phys. Rept. **516**, 1 (2012).
7. A. Barroso, P. M. Ferreira, R. Santos, M. Sher and J. P. Silva, arXiv:1304.5225 [hep-ph].
8. M. Spira, arXiv:hep-ph/9510347.
9. https://twiki.cern.ch/twiki/bin/view/LHCPhysics/CrossSectionsFigures #Higgs_production_cross_sections
10. R.V. Harlander and W.B. Kilgore, Phys. Rev. D **68**, 013001 (2003).
11. C. -Y. Chen and S. Dawson, Phys. Rev. D **87**, 055016 (2013) B. Coleppa, F. Kling and S. Su, arXiv:1305.0002 [hep-ph]; C. -W. Chiang and K. Yagyu, arXiv:1303.0168 [hep-ph]; M. Krawczyk, D. Sokolowska and B. Swiezewska, arXiv:1303.7102 [hep-ph]; A. Celis, V. Ilisie and A. Pich, arXiv:1302.4022 [hep-ph]; B. Grinstein and P. Uttayarat, arXiv:1304.0028 [hep-ph]; A. Arhrib, C. -W. Chiang, D. K. Ghosh and R. Santos, Phys. Rev. D **85**, 115003 (2012); [ATLAS Collaboration], ATLAS-CONF-2013-027.
12. The ATLAS collaboration, ATLAS-CONF-2013-012, ATLAS-CONF-2013-030, ATLAS-CONF-2013-034.
13. The CMS collaboration, CMS notes CMS-PAS-HIG-13-001, CMS-PAS-HIG-13-003 and CMS-PAS-HIG-13-003.

INVARIANTS AND FLAVOUR IN THE GENERAL TWO-HIGGS DOUBLET MODEL

M. N. REBELO

Universidade Técnica de Lisboa, Centro de Física Teórica de Partículas (CFTP), Instituto Superior Técnico, Av. Rovisco Pais, P-1049-001 Lisboa, Portugal.

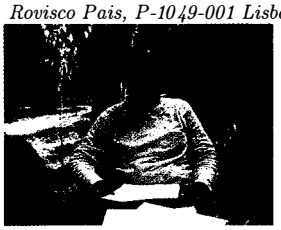

We construct weak basis invariants which can give insight into the physical implications of any flavour model, written in an arbitrary weak basis (WB) in the context of 2HDM.

1 Introduction

The LHC has started the "Higgs Era" with the discovery of a scalar boson with a mass of approximately 126 GeV [1], [2], which seems to behave like the Standard Model (SM) Higgs boson. There are very good motivations to consider models with two Higgs doublets [3], [4] despite the fact that the SM is a very successful theory. Most observations in the hadronic sector are in agreement with the SM predictions apart from a few anomalies and tensions. However, in the leptonic sector the SM has to be extended in order to accommodate neutrino masses and leptonic mixing. Furthermore, accounting for the baryon asymmetry of the Universe requires new sources of CP violation thus providing a possible motivation to consider two Higgs doublet models. Supersymmetry, if discovered, will also require the existence of two Higgs doublets. The discovery of a charged Higgs at the LHC in the future would be an important step towards the experimental confirmation of the need to extend the Higgs sector of the SM.

Models with two Higgs doublets have potentially large Higgs mediated flavour changing neutral currents (FCNC). Experimentally FCNC are strongly constrained. There are several possible ways of suppressing these currents. Natural flavour conservation [5] or the imposition of alignment [6] eliminate tree level Higgs FCNC. In alternative, one may have FCNC at tree level suppressed by small entries of the Cabibbo– Kobayashi – Maskawa matrix, V_{CKM}. The first models of this type based on a symmetry were built by Branco, Grimus and Lavoura [7] and later on extended in Refs [8], [9]. This talk is based on work done in collaboration with Botella and Branco [10].

2 General Framework

The flavour structure of two Higgs doublet models is given by the Yukawa interactions:

$$L_Y = -\overline{Q_L^0}\ \Gamma_1 \Phi_1 d_R^0 - \overline{Q_L^0}\ \Gamma_2 \Phi_2 d_R^0 - \overline{Q_L^0}\ \Delta_1 \tilde{\Phi}_1 u_R^0 - \overline{Q_L^0}\ \Delta_2 \tilde{\Phi}_2 u_R^0\ + \text{h. c.} \tag{1}$$

where Γ_i and Δ_i denote the Yukawa couplings of the lefthanded quark doublets Q_L^0 to the righthanded quarks d_R^0, u_R^0 and the Higgs doublets Φ_j. The quark mass matrices generated after spontaneous gauge symmetry breaking are given by:

$$M_d = \frac{1}{\sqrt{2}}(v_1\Gamma_1 + v_2 e^{i\alpha}\Gamma_2), \quad M_u = \frac{1}{\sqrt{2}}(v_1\Delta_1 + v_2 e^{i\alpha}\Delta_2), \tag{2}$$

where $v_i \equiv |<0|\phi_i^0|0>|$ and α denotes the relative phase of the vacuum expectation values (vevs) of the neutral components of Φ_i. The matrices M_d, M_u are diagonalized by the usual bi-unitary transformations:

$$U_{dL}^\dagger M_d U_{dR} = D_d \equiv diag\ (m_d, m_s, m_b) \tag{3}$$

$$U_{uL}^\dagger M_u U_{uR} = D_u \equiv diag\ (m_u, m_c, m_t) \tag{4}$$

The neutral and the charged Higgs interactions obtained from Eq. (1) are of the form

$$\begin{aligned} \mathcal{L}_Y(\text{quark, Higgs}) \ &= \ -\overline{d_L^0}\frac{1}{v}\left[M_d H^0 + N_d^0 R + iN_d^0 I\right] d_R^0 - \\ &- \ \overline{u_L^0}\frac{1}{v}\left[M_u H^0 + N_u^0 R + iN_u^0 I\right] u_R^0 - \\ &- \ \frac{\sqrt{2}H^+}{v}(\overline{u_L^0} N_d^0\, d_R^0 - \overline{u_R^0} N_u^{0\dagger}\, d_L^0) + \text{h.c.} \end{aligned} \tag{5}$$

where $v \equiv \sqrt{v_1^2 + v_2^2} \approx 246$ GeV, and H^0, R are orthogonal combinations of the fields ρ_j, arising when one expands [11] the neutral scalar fields around their vacuum expectation values, $\phi_j^0 = \frac{e^{i\alpha_j}}{\sqrt{2}}(v_j + \rho_j + i\eta_j)$, choosing H^0 in such a way that it has couplings to the quarks which are proportional to the mass matrices, as can be seen from Eq. (5). Similarly, I denotes the linear combination of η_j orthogonal to the neutral Goldstone boson. The matrices N_d^0, N_u^0 are given by:

$$N_d^0 = \frac{1}{\sqrt{2}}(v_2\Gamma_1 - v_1 e^{i\alpha}\Gamma_2), \quad N_u^0 = \frac{1}{\sqrt{2}}(v_2\Delta_1 - v_1 e^{-i\alpha}\Delta_2) \tag{6}$$

The flavour structure of the quark sector of two Higgs doublet models is thus fully specified in terms of the four matrices M_d, M_u, N_d^0, N_u^0. The physical neutral Higgs fields are combinations of H^0, R and I. Flavour changing neutral currents are controlled by N_d^0 and N_u^0.

3 Weak Basis Invariants

The four flavour matrices M_d, M_u, N_d^0, N_u^0 contain a large redundancy of parameters which results from the fact that under a weak basis (WB) transformation they change transforming as

$$\begin{aligned} M_d \to M_d' = W_L^\dagger M_d W_R^d, \qquad M_u \to M_u' = W_L^\dagger M_u W_R^u, \\ N_d^0 \to N_d^{0\prime} = W_L^\dagger N_d^0 W_R^d, \qquad N_u^0 \to N_u^{0\prime} = W_L^\dagger N_u^0 W_R^u \end{aligned} \tag{7}$$

without altering their physical content. Different Lagrangians related to each other by WB transformations describe the same physics. In view of the above redundancy, it is of great interest to construct WB invariants which can be very useful in the analysis of the physical

content of the flavour sector of two Higgs doublet models[10] by following the technique that was introduced in[12] to the study of CP violation in the SM. This technique was later generalized to many different scenarios, in particular to the study of explicit CP violation in the scalar sector of multi-Higgs doublet models prior to gauge symmetry breaking[13] as well as CP violation in the scalar sector after this breaking[14] and also taking into account both the scalar and the fermionic sector[15].

In this framework, it is clear that one can build new WB basis invariants which do not arise in the SM by evaluating traces of blocks of matrices involving the up and down quark sector, like for example $M_\gamma N_\gamma^{0\dagger}$ or $N_\gamma^0 N_\gamma^{0\dagger}$. For definiteness let us consider the WB invariant $\mathrm{tr}(M_d N_d^{0\dagger})$ and note that its physical significance becomes transparent in the WB where M_d is diagonal, real, since in this basis the matrix N_d^0 already coincides with the couplings to the physical quarks. In this basis one has:

$$I_1 \equiv \mathrm{tr}(M_d N_d^{0\dagger}) = m_d (N_d^*)_{11} + m_s (N_d^*)_{22} + m_b (N_b^*)_{33} \tag{8}$$

We denote N_d, the matrix N_d^0 in the basis where it couples to the physical quarks. This invariant is not sensitive to Higgs-mediated FCNC, but $\mathrm{Im}(I_1)$ is specially important, since it probes the phases of $(N_d)_{jj}$ which contribute to the electric dipole moment of down-type quarks. Obviously, one can construct an analogous invariant for the up-quark sector, namely $\mathrm{tr}(M_u N_u^{0\dagger})$. Let us now consider a WB invariant which is sensitive to the off-diagonal elements of N_d, namely:

$$I_2 \equiv \mathrm{tr}\left[M_d N_d^{0\dagger}, M_d M_d^\dagger\right]^2 = -2 m_d m_s (m_s^2 - m_d^2)^2 (N_d^*)_{12} (N_d^*)_{21} -$$
$$-2 m_d m_b (m_b^2 - m_d^2)^2 (N_d^*)_{13} (N_d^*)_{31} - 2 m_s m_b (m_b^2 - m_s^2)^2 (N_d^*)_{23} (N_d^*)_{32}, \tag{9}$$

where we have kept the notation used in Eq. (8), having evaluated I_2 in the WB where M_d is real and diagonal. WB invariants are also important to study CP violation. In the SM a necessary and sufficient condition for CP invariance is the vanishing of the WB invariant[12] :

$$I_1^{CP} \equiv \mathrm{tr}\,[H_u, H_d]^3 = 6i (m_t^2 - m_c^2)(m_t^2 - m_u^2)(m_c^2 - m_u^2) \times$$
$$\times (m_b^2 - m_s^2)(m_b^2 - m_d^2)(m_s^2 - m_d^2) \mathrm{Im} Q_{uscb} \tag{10}$$

where $H_{d,u} \equiv (M_{d,u} M_{d,u}^\dagger)$, Q stands for a rephasing invariant quartet of V_{CKM}, defined by $Q_{\alpha i \beta j} \equiv V_{\alpha i} V_{\beta j} V_{\alpha j}^* V_{\beta i}^*$ ($\alpha \neq \beta$, $i \neq j$) with $V_{CKM} \equiv U_{uL}^\dagger U_{dL}$. The fact that V_{CKM} is not the identity reflects the fact that $U_{dL} \neq U_{uL}$, i.e. that there is misalignment of the matrices H_d, H_u in flavour space. For three generations I_1^{CP} is proportional to $\det[H_u, H_d]$, introduced in Ref. [16]. In the present framework there are four matrices relevant for flavour rather than the two mass matrices of the SM, therefore we can generalise the definition of I_1^{CP} to diferent WB invariants sensitive to the misalignment of different pairs of Hermitian matrices, such as, for example $I_2^{CP} \equiv \mathrm{tr}\left[H_u, H_{N_d^0}\right]^3$ or $I_3^{CP} \equiv \mathrm{tr}\left[H_d, H_{N_d^0}\right]^3$, with $H_{N_d^0} \equiv N_d^0 N_d^{0\dagger}$.

In the SM the lowest order WB invariant sensitive to CP violation is given by Eq. (10) and has dimension twelve in powers of mass. The richer flavour structure of models with two Higgs doublets allows for lower order invariants sensitive to CP violation, namely, for instance:

$$I_9^{CP} \equiv \mathrm{Im}\ \mathrm{tr}\left[M_d N_d^{0\dagger} M_d M_d^\dagger M_u M_u^\dagger M_d M_d^\dagger\right] \tag{11}$$

In generic two Higgs doublet models one may even have lower order invariants sensitive to CP violation. However, with the imposition of a symmetry in order to suppress Higgs mediated FCNC such lower other invariants may become trivial.

Flavour symmetries and/or texture zeros reduce the number of free parameters and have physical implications. However symmetries and textures are introduced in a specific WB. Under a change of WB these will in principle cease to be apparent. In this respect the computation of weak basis invariants is a very useful tool to recognize properties related to special symmetries

or textures that may not be apparent. In Ref. [10] the summary presented here is extended and applied to two special cases: models of the type proposed by Branco, Grimus and Lavoura [7] and a special implementation of nearest – neighbour – interaction (NNI) textures [17] in the context of two Higgs doublet models based on an Abelian symmetry[18].

Acknowledgments

The author thanks the organizers of Rencontres de Moriond for the invitation to present this work anf for the very stimulating atmosphere. The work presented in this Conference was partially supported by Fundação para a Ciência e a Tecnologia (FCT, Portugal) through the projects PTDC/FIS/098188/2008 and CFTP-FCT Unit 777 (PEst-OE/FIS/UI0777/2011) which are partially funded through POCTI (FEDER), by Marie Curie ITN "UNILHC" PITN-GA-2009-237920, by Accion Complementaria Luso-Espanhola PORT2008–03, by European FEDER and FPA-2008-04002-E/PORTU by Spanish MICINN under grant FPA2008–02878 and GVPROMETEO 2010-056. More recently we would like to aknowledge the support of CERN/FP/123580/2011.

References

1. G. Aad *et al.* [ATLAS Collaboration], Phys. Lett. B **716** (2012) 1 [arXiv:1207.7214 [hep-ex]].
2. S. Chatrchyan *et al.* [CMS Collaboration], Phys. Lett. B **716** (2012) 30 [arXiv:1207.7235 [hep-ex]].
3. G. C. Branco, P. M. Ferreira, L. Lavoura, M. N. Rebelo, M. Sher and J. P. Silva, Phys. Rept. **516** (2012) 1 [arXiv:1106.0034 [hep-ph]].
4. J. F. Gunion, H. E. Haber, G. L. Kane and S. Dawson, Front. Phys. **80** (2000) 1.
5. S. L. Glashow and S. Weinberg, Phys. Rev. D **15** (1977) 1958.
6. A. Pich and P. Tuzon, Phys. Rev. D **80** (2009) 091702 [arXiv:0908.1554 [hep-ph]].
7. G. C. Branco, W. Grimus and L. Lavoura, Phys. Lett. B **380** (1996) 119 [hep-ph/9601383].
8. F. J. Botella, G. C. Branco and M. N. Rebelo, Phys. Lett. B **687** (2010) 194 [arXiv:0911.1753 [hep-ph]].
9. F. J. Botella, G. C. Branco, M. Nebot and M. N. Rebelo, JHEP **1110** (2011) 037 [arXiv:1102.0520 [hep-ph]].
10. F. J. Botella, G. C. Branco and M. N. Rebelo, Phys. Lett. B **722** (2013) 76 [arXiv:1210.8163 [hep-ph]].
11. T. D. Lee, Phys. Rev. D **8** (1973) 1226.
12. J. Bernabeu, G. C. Branco and M. Gronau, Phys. Lett. B **169** (1986) 243.
13. G. C. Branco, M. N. Rebelo and J. I. Silva-Marcos, Phys. Lett. B **614** (2005) 187 [hep-ph/0502118].
14. L. Lavoura and J. P. Silva, Phys. Rev. D **50** (1994) 4619 [hep-ph/9404276].
15. F. J. Botella and J. P. Silva, Phys. Rev. D **51** (1995) 3870 [hep-ph/9411288].
16. C. Jarlskog, Phys. Rev. Lett. **55** (1985) 1039.
17. H. Fritzsch, Phys. Lett. B **73** (1978) 317.
18. G. C. Branco, D. Emmanuel-Costa and C. Simoes, Phys. Lett. B **690** (2010) 62 [arXiv:1001.5065 [hep-ph]].

THIRD GENERATION SUSY SEARCHES AT THE LHC

ANDREA FAVARETO
On behalf of the ATLAS and CMS Collaborations
Università degli Studi di Milano & INFN Milano

The ATLAS and CMS experiments have recently searched for evidence of third generation squark production in a variety of final states, using proton-proton collision data from the Large Hadron Collider (LHC) operating at $\sqrt{s}$ = 8 TeV. A summary of the most recent results obtained in these searches is presented.

1 Introduction

Supersymmetry (SUSY [1]) is an extension of the Standard Model (SM) which naturally resolves the hierarchy problem by introducing supersymmetric partners to the known fermions and bosons. In the framework of a generic R-parity conserving minimal supersymmetric extension of the SM (MSSM), SUSY particles are produced in pairs and the lightest supersymmetric particle (LSP) is stable. In a large variety of models the LSP is the lightest neutralino, $\tilde{\chi}_1^0$, which only interacts weakly. The scalar partners of right-handed and left-handed quarks (squarks) can mix to form two mass eigenstates ($\tilde{q}_1$, $\tilde{q}_2$).

Naturalness arguments for weak-scale supersymmetry favour supersymmetric partners of the third generation quarks with masses not too far from those of their Standard Model counterparts. Production of third generation squarks (stop and sbottom, $\tilde{t}$, $\tilde{b}$) via decay of a gluino can be significant at the LHC if the mass of the gluino does not exceed the TeV scale. Stop and sbottoms with masses of a few hundred GeV can also give rise to direct pair production rates that can be observed in the data sample recorded by the ATLAS [2] and the CMS [3] detectors.

ATLAS and CMS have an extensive search program for third generation SUSY particles. These proceedings focus on new results that are interpreted in two simplified SUSY scenarios stemming from assumptions made regarding the mass spectrum: gluino-mediated and direct production of stops and sbottoms.

Production via gluino decay dominates if gluinos are not too heavy, i.e. less than about 1 TeV, and if the gluino decay branching fractions into stops or sbottoms are large. Assuming that the stop and sbottom squarks are heavier than the gluino ($\tilde{g}$), and additionally that the gluino is also heavier than the neutralino, indirect production is possible. The processes $\tilde{g}\tilde{g} \to t\bar{t}\tilde{\chi}_1^0 t\bar{t}\tilde{\chi}_1^0$ via an off-shell stop (Gtt scenario) and $\tilde{g}\tilde{g} \to b\bar{b}\tilde{\chi}_1^0 b\bar{b}\tilde{\chi}_1^0$ via an off-shell sbottom (Gbb scenario) are studied. Results are interpreted in this case in the $\tilde{g} - \tilde{\chi}_1^0$ mass plane.

In the direct production of third generation quarks scenario, four models of squark decay modes are considered. The sbottom can decay either via $\tilde{b} \to b\tilde{\chi}_1^0$ or $\tilde{b} \to t\tilde{\chi}_1^{\pm}$. For top squarks, the decays $\tilde{t} \to t\tilde{\chi}_1^0$ or $\tilde{t} \to b\tilde{\chi}_1^{\pm}$ are studied.

The final states of third generation squark production are typically extremely rich, they might include leptons (electrons or muons), multiple jets (some of which may be b-tagged), and

missing transverse energy ($E_T^{\rm miss}$). The signal is seeked in complementary search channels.

The dominant backgrounds are estimated by normalising the event yields in background dominated control regions to reduce their systematic uncertainties. Sub-dominant backgrounds (such as diboson or $t\bar{t}+W/Z$ production) are estimated using the MC simulation.

Where no significant signal is observed, limits can be set on SUSY models. The numbers of predicted and measured events in each signal region are translated into 95% confidence-level (CL) upper limits on contributions from new physics using the CLs prescription [4] with a profile log-likelihood ratio as a test statistic. The correlation of the systematic uncertainties between the signal and background is taken into account where appropriate.

All the analyses described below are performed using proton-proton collision data at $\sqrt{s} = 8$ TeV, unless stated otherwise.

2 Gluino-mediated stop and sbottom searches

One of the most sensitive analyses to the indirect production of sbottom and stop quarks specifically selects events with b-tagged jets, because the final state is rich in b-jets and top quarks. Both the ATLAS and CMS experiments have recently published some new results for gluino-mediated stop and sbottom production. In particular CMS published two new analyses selecting respectively all-hadronic [5] and single lepton [6] events. While ATLAS published a new analysis based on a same-sign dilepton selection [7].

The all-hadronic CMS analysis is based on events with large missing transverse energy, no isolated electron or muon, and at least three jets, at least one of which must be identified as a b-jet. A simultaneous examination of the number of events in exclusive bins of H_T, missing transverse energy, and b-jet multiplicity is performed, where H_T is the scalar sum of jet transverse momenta. The sample consists of an integrated luminosity of 19.4 fb^{-1} of proton-proton collision data recorded at a center-of-mass energy of 8 TeV. The results are interpreted in the context of the *Gtt* and *Gbb* models.

The analysis of final states with a single lepton (electron or muon) is also sensitive to the *Gtt* model. The same data sample of the all-hadronic analysis has been considered. Events with large missing transverse energy and multiple jets, at least two of which are tagged as originating from b-quarks, are used. The distributions of several kinematic variables are examined to discriminate signal from background using two complementary methods: the *Lepton Spectrum method* (LS) and the *Delta Phi method* (DP). In the LS method, the $E_T^{\rm miss}$ distribution is examined in events with a high H_T, while in the DP method, the angle between the lepton and W momentum vectors, $\Delta\phi(W,l)$, and the leptonic mass scale of the event, $S_T^{\rm lep} = \sqrt{p_T(W)^2 + M_T(W)^2}$, are used to suppress the $t\bar{t}$ background.

In both these analyses, based on 19.4 fb^{-1}, the event yields observed across several kinematic regions are consistent with SM backgrounds predicted using a mix of simulated event samples and control samples in the data.

The new ATLAS analysis presents the search for the production of supersymmetric particles decaying into final states with jets, b-jets, $E_T^{\rm miss}$ and two isolated leptons, e or μ, with the same electric charge (same-sign leptons). Three event classes are distinguished depending on the number of jets identified as originating from b-quark decays; zero (b-jet veto), at least 1 or 3 b-jets. The sample consists of an integrated luminosity of 20.7 fb^{-1}. No deviation from the Standard Model expectation is observed. In particular, focusing on processes that involve third generation susy particles, limits for the *Gtt* scenario are set.

Previous results from other additional channels are used to set limits in both the *Gbb* and *Gtt* scenarios. CMS presented an analysis using events with isolated same-sign leptons and at least two b-jets in the final state [8], which uses 10.5 fb^{-1}. The summary of observed and expected limits of the CMS dedicated searches for gluino pair production with gluino decaying via the

3-body decay top anti-top neutralino is shown in Fig. 1(a).

ATLAS published two all-hadronic analyses [9,10], which use respectively 12.8 fb^{-1} and 5.8 fb^{-1}. The former requires events with large $E_T^{\rm miss}$, at least 4 or 6 jets and at least three jets originating from b-quarks, and the latter requires $E_T^{\rm miss}$ and from at least 6 to at least 9 jets. ATLAS also presented an analysis [11] based on 13.0 fb^{-1} that uses events with three leptons, at least 4 jets, and $E_T^{\rm miss}$.

3 Direct stop and sbottom searches

The new ATLAS two same-sign lepton analysis described in Sec. 2 is also used to set limits on direct sbottom pair production, via the decay channel $\tilde{b} \to t\tilde{\chi}_1^{\pm}$ followed by $\tilde{\chi}_1^{\pm} \to W^{\pm}\tilde{\chi}_1^0$. Two scenarios are considered which make different assumptions about the mass relationship between the chargino and neutralino. In the first case, the assumption $m_{\tilde{\chi}_1^{\pm}} = 2 \times m_{\tilde{\chi}_1^0}$ is made, and in the second scenario, the neutralino mass is fixed to $m_{\tilde{\chi}_1^0} = 60$ GeV. Final states consist of pairs of top quarks, W bosons (real or virtual) and missing transverse momentum. Same-sign dilepton combinations arise from the decays of the top quarks and the W bosons. Limits are expressed as a function of the $\tilde{b}$ and $\tilde{\chi}_1^{\pm}$ masses. Under the assumption $m_{\tilde{\chi}_1^0} = 60$ GeV, sbottom masses of 470-480 GeV are excluded with 95% CL for chargino masses below 280 GeV. Similar limits on bottom squark masses are obtained in the other model for chargino masses up to 250 GeV.

ATLAS and CMS also presented other searches for direct sbottom pair production in both the $\tilde{b} \to t\tilde{\chi}_1^{\pm}$ and $\tilde{b} \to b\tilde{\chi}_1^0$. In particular ATLAS presented a search for direct pair production of bottom squarks, each decaying into a bottom quark and a neutralino, in events with large missing transverse momentum and 2 b-jets in the final state [12] using 12.8 fb^{-1}. The CMS two same-sign lepton analysis cited in Sec. 2 includes also a search for direct sbottom pair production decaying in $\tilde{b} \to t\tilde{\chi}_1^{\pm}$. CMS also presented an analysis focusing on the $\tilde{b} \to b\tilde{\chi}_1^0$ scenario selecting final states with 2 or 3 jets, one or two of which must be identified as a b-jet, and missing transverse energy [13]. The data sample corresponds to an integrated luminosity of 11.7 fb^{-1}.

Direct stop production has been covered in ATLAS and CMS by multiple dedicated searches, targeting different stop masses and decays. New results have been recently published. CMS presented a search for direct stop pair production in susy *R-Parity Violation* models (RPV) with leptons [14], while ATLAS presented two new analyses selecting respectively all-hadronic [15] and leptons in association with Z boson [16].

The new CMS analysis presents a search for pair production of top squarks in multilepton (at least three isolated leptons) events with one or more b-jets. The data used in this analysis correspond to 19.5 fb^{-1}. The search results are interpreted in the context of supersymmetric models with diminished missing transverse energy signatures arising from light stop pair production with RPV decays of the lightest supersymmetric particle. No excesses above the Standard Model expectations are observed.

The all-hadronic ATLAS analysis is conducted in events with large missing transverse momentum and at least 6 jets, at least two of which b-jet. The data sample correspons to an integrated luminosity of 20.5 fb^{-1}. Observations are consistent with SM expectations and exclusion limits have been placed in a model of top squark pair production, followed by the decay $\tilde{t} \to t\tilde{\chi}_1^0$.

The other new ATLAS analysis uses events with a Z boson, b-jets and large missing transverse momentum in final states with two or three leptons forming a same-flavour opposite-sign lepton pair with invariant mass consistent with the Z boson mass. The analysis is performed with 20.7 fb^{-1}. Also in this case no excess beyond the Standard Model expectation is observed. Interpretations of this result are provided for two different scenarios. The first one consist in natural gauge-mediated supersymmetry breaking scenarios where the neutralino, coming from

$\tilde{t} \to b\tilde{\chi}_1^{\pm}$ with $\tilde{\chi}_1^{\pm} \to W^{\pm}\tilde{\chi}_1^0$, is the *next-to-lightest supersymmetric particle* (NLSP) producing a Z boson and a gravitino ($\tilde{G}$) in the $\tilde{\chi}_1^0 \to Z\tilde{G}$ decay. The neutralino and chargino masses are assumed to be similar. The second scenario addresses models based on the direct production of heavy stop states ($\tilde{t}_2$) that decay to stop states ($\tilde{t}_1$) via $\tilde{t}_2 \to Z\tilde{t}_1$. In this scenario the first limits of this kind are set excluding with 95% confidence level the parameter space regions with $m_{\tilde{t}_2} < 530$ GeV and $m_{\tilde{\chi}_1^0} < 245$ GeV.

Several analyses in different final states are used to set exclusion limits in direct stop pair production scenarios, targeting again different stop masses and decay. CMS presented two analyses using respectively events with E_T^{miss}, one lepton and at least 4 jets (at least 1 b-jet) [17] with 9.7 fb^{-1}, and all-hadronic multijet events with E_T^{miss} [18] with 4.98 fb^{-1} collected with proton-proton collision data at $\sqrt{s} = 7$ TeV. ATLAS published three analyses based on events with respectively two leptons and E_T^{miss} [19] with 13.0 fb^{-1}, one lepton, at least 4 jets and E_T^{miss} [20] with 13.0 fb^{-1}, and zero leptons, 2 b-jets and E_T^{miss} [21] with 12.8 fb^{-1}. The summary of observed and expected limits of the ATLAS dedicated searches for direct stop pair production is shown in Fig. 1(b).

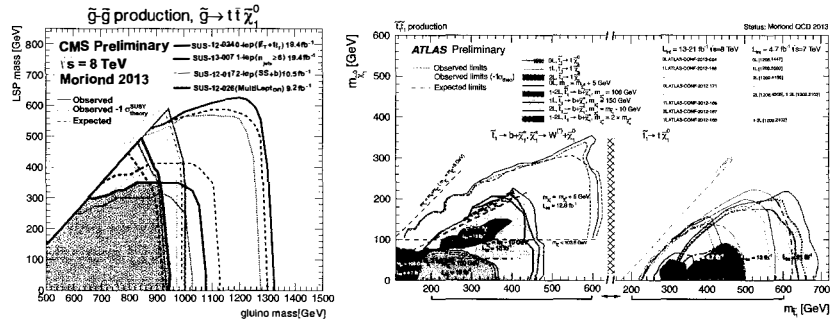

(a) (b)

Figure 1: CMS: summary of observed and expected limits of the dedicated searches for gluino pair production with gluino decaying via the 3-body decay top anti-top neutralino (a) [22]; ATLAS: summary of observed and expected limits of the dedicated searches for direct stop pair production (b) [23]

4 Conclusions

ATLAS and CMS are conducting a comprehensive set of searches sensitive to both indirect and direct production of third generation squarks. These proceedings give a summary of such searches, with emphasis on new results. The individual searches are sensitive to different complementary regions of the SUSY parameter space with sufficient overlap. Observed data are consistent with the SM background expectation, and exclusion limits are set on squark masses for the *Gbb*, *Gtt* and direct production models. The parameter space given by the naturalness argument is being filled up, but many other results using the complete 2012 data set are forthcoming.

There is so far no sign of physics beyond the SM. However, much of the parameter space remains to be probed, and the search for SUSY at the LHC will continue to be vigorously pursued.

References

1. S. P. Martin, arXiv:hep-ph/9709356
2. ATLAS Collaboration, 2008 JINST 3 S08003
3. CMS Collaboration, 2008 JINST 3 S08004
4. A.L. Read, J. Phys. G28, 2693 (2002)
5. CMS Collaboration, CMS-PAS-SUS-12-024, http://cds.cern.ch/record/1523623
6. CMS Collaboration, CMS-PAS-SUS-13-007, http://cds.cern.ch/record/1523786
7. ATLAS Collaboration, ATLAS-CONF-2013-007, https://cds.cern.ch/record/1522430
8. CMS Collaboration, JHEP03 (2013) 037
9. ATLAS Collaboration, ATLAS-CONF-2012-145, http://cds.cern.ch/record/1493484
10. ATLAS Collaboration, ATLAS-CONF-2012-103, http://cds.cern.ch/record/1472672
11. ATLAS Collaboration, ATLAS-CONF-2012-151, http://cds.cern.ch/record/1493490
12. ATLAS Collaboration, ATLAS-CONF-2012-165, http://cds.cern.ch/record/1497668
13. CMS Collaboration, arXiv:1303.2985, Submitted to EPJC1527115
14. CMS Collaboration, CMS-PAS-SUS-13-003, http://cds.cern.ch/record/1525539
15. ATLAS Collaboration, ATLAS-CONF-2013-024, https://cds.cern.ch/record/1525880
16. ATLAS Collaboration, ATLAS-CONF-2013-025, https://cds.cern.ch/record/1525881
17. CMS Collaboration, CMS-PAS-SUS-12-023, http://cds.cern.ch/record/1494074
18. CMS Collaboration, CMS-PAS-SUS-11-030, http://cds.cern.ch/record/1494575
19. ATLAS Collaboration, ATLAS-CONF-2012-167, http://cds.cern.ch/record/1497733
20. ATLAS Collaboration, ATLAS-CONF-2012-166, http://cds.cern.ch/record/1497732
21. ATLAS Collaboration, ATLAS-CONF-2013-001, http://cds.cern.ch/record/1503233
22. https://twiki.cern.ch/twiki/bin/view/CMSPublic/PhysicsResultsSUS
23. https://twiki.cern.ch/twiki/bin/view/AtlasPublic/SupersymmetryPublicResults

SUSY Searches for Inclusive Squark and Gluino Production at the LHC

A. MANN
On behalf of the ATLAS and CMS Collaborations
Ludwig-Maximilians-Universität München, Fakultät für Physik,
Am Coulombwall 1, 85748 Garching, Germany

A selection of recent searches for Supersymmetry conducted by the ATLAS and CMS collaborations is presented, summarizing the relevant results for inclusive squark and gluino production at the LHC. No indication for the existence of Supersymmetry in terms of an excess above the Standard Model background is seen by any analysis, therefore limits are reported on parameters of the various models used to interpret the findings.

1 Introduction

After a long and successful data-taking period from 2010 through 2012, the first run of the Large Hadron Collider (LHC) at CERN has come to an end. In 2012, both the ATLAS and the CMS collaboration have taken about $22\,\mathrm{fb}^{-1}$ of data at $\sqrt{s} = 8\,\mathrm{TeV}$, about four times the data available from 2010 and 2011 at a lower center-of-mass energy of $\sqrt{s} = 7\,\mathrm{TeV}$.

Already with the first proton-proton collision data from 2010 of about $35\,\mathrm{pb}^{-1}$, the searches for inclusive squark and gluino production proved to be very successful in terms of mass reach, yielding exclusion limits that rapidly surpassed those of earlier experiments. Since then, the analyses have evolved and diversified, pushing the limits on the squark, gluino and lightest gaugino masses or mass parameters to higher and higher values, aiming at more complex topologies and giving additional interpretations in other supersymmetric models.

In these proceedings, the focus will be on strong production of the scalar partners of first and second generation quarks and the fermionic partners of the gluons. For a given supersymmetric mass scale, strong production has the largest production cross sections, thus allowing to target heavy initial supersymmetric particles, signatures with small branching ratios and long decay chains. Apart from one exception all analyses presented below assume R-parity conservation, which makes the lightest supersymmetric particle (LSP) stable. Missing transverse momentum (E_T^{miss}) is therefore an important part of the searched for signature, the other being jets with high transverse momentum produced in the decay chains starting from the heavy pair-produced squarks and gluinos. Only results by the ATLAS and the CMS collaborations are considered which have been made public on or before the 11th March 2013, the date at which the corresponding talk has been given. None of the analyses has seen any significant excess of events above the expected number from the Standard Model predictions, thus all analyses interpret their findings by reporting limits on supersymmetric particle masses or model parameters.

2 Searches with the Full 2012 Dataset

The ATLAS collaboration has made public results from two searches for Supersymmetry with inclusive squark ($\tilde{q}$) and gluino ($\tilde{g}$) production which make use of the full 2012 dataset.

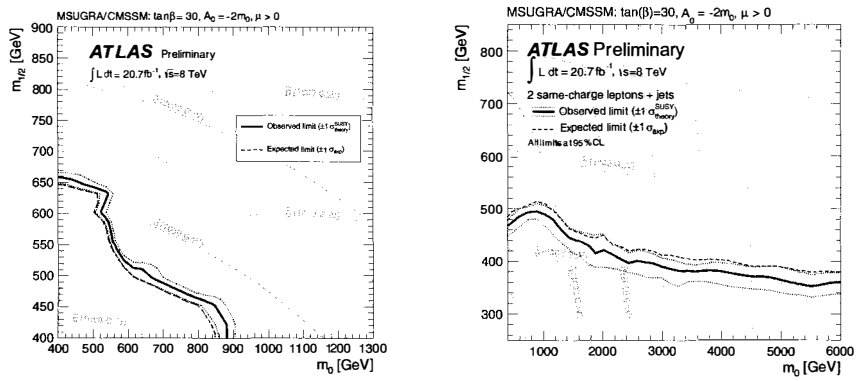

Figure 1: Expected and observed limits from the two ATLAS analyses making use of the full 2012 dataset. The plots show the interpretation of the tau + jets + E_T^{miss} results (left, [3]) and same-sign leptons + jets + E_T^{miss} results (right, [4]) in the mSUGRA/CMSSM framework. (Note the very different range on the horizontal axis.)

The first search [3] targets final states with exactly one, or two or more hadronically decaying tau leptons, together with jets and E_T^{miss}. The motivation for this search comes from models with gauge-mediated supersymmetry breaking (GMSB) where the scalar partner of the tau, the stau $\widetilde{\tau}$, is the next-to-lightest supersymmetric particle (NLSP), leading to final states with many taus. As no excess is seen, the results are interpreted in terms of limits at 95 % confidence level in three different models. The limits in the mSUGRA/CMSSM framework are shown in Figure 1, where this analysis is in particular powerful in the low m_0 region. The model parameters for the mSUGRA/CMSSM model have been chosen such that in a large part of the plane a 126 GeV Higgs can be accommodated. Not shown is the limit plot for the minimal GMSB model in the plane spanned by the parameters Λ, the SUSY breaking mass scale felt by the low-energy sector, and $\tan\beta$, the ratio of the MSSM Higgs vacuum expectation values. Here, the previous limits from 2011 data can be extended considerably, reaching now up to 70 TeV in Λ for high $\tan\beta > 50$ (corresponding to $m(\widetilde{g})$ of about 1.5 TeV), and excluding values of Λ below 54 TeV ($m(\widetilde{g}) \sim 1.2$ TeV) independent of $\tan\beta$. There is also a new interpretation in a model of natural gauge mediation, where independently of the $\widetilde{\tau}$ mass, gluino masses up to 1.14 TeV can be excluded, provided the $\widetilde{\tau}$ is the NLSP.

The second analysis [4] looks at final states with same-sign lepton pairs, together with 3 or more jets and E_T^{miss}. The motivation for this analysis is that the pair-produced gluinos have almost the same probability to give pairs of leptons with same charge or with opposite charge. Requiring a pair of leptons with same sign suppresses the background coming from Standard Model processes considerably, giving a very clean and powerful signature to look for new physics processes. The limits which are set in the same mSUGRA/CMSSM model with Higgs-compatible parameters used for the tau analysis are shown in Figure 1, excluding a large region of the mSUGRA/CMSSM parameter space. In addition, interpretations in a large number of simplified models are given, demonstrating the power and versatility of this search channel.

3 Searches with a Subset of 2012 Data

CMS has made public a study using 9.2 fb^{-1} from the 2012 dataset [5], in which models with R-parity violation (RPV) are considered. As here the LSP is no longer stable, high particle multiplicities are characteristic for supersymmetric decays rather than large E_T^{miss}. Events with 3 or more isolated leptons are selected and classified with respect to the number of opposite-sign same-flavour (OSSF) lepton pairs, the invariant mass of the OSSF lepton pairs if present, the

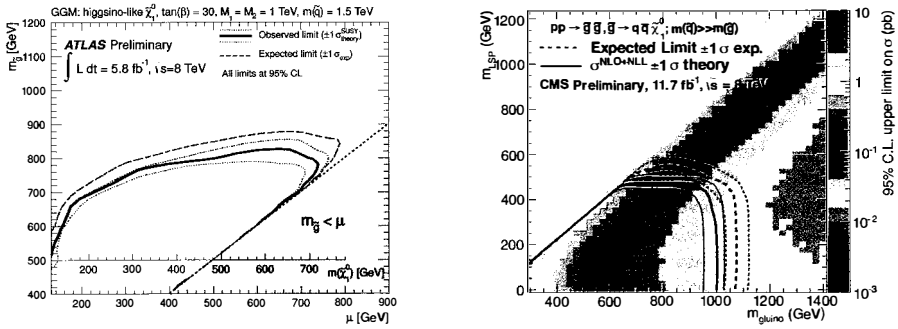

Figure 2: Left: Exclusion limits on the gluino mass and μ parameters for the GGM models with $c\tau_{\mathrm{NLSP}} < 0.1\,\mathrm{mm}$ [7]. Right: Upper limit on the cross section at 95 % confidence level as function of $m(\tilde{g})$ and $m(\tilde{\chi}_1^0)$. The solid black line indicates the observed excluded region [11].

presence of jets from bottom quarks, and the presence of a hadronically decaying tau. Together with a binning in S_T, defined as the scalar sum of E_T^{miss} and the transverse momentum (p_T) of jets and leptons, this gives in total 240 event classes, which are then combined to derive exclusion limits. Numerous models with different topologies are considered, probing all three RPV Yukawa couplings individually. In the RPV squark-gluino models, lower limits are set on $m(\tilde{g})$ and $m(\tilde{q})$ of the order of 1 to 2 TeV. In a CMSSM with RPV, $m_{1/2} < 1.15\,\mathrm{TeV}$ is excluded. An update with the full 2012 dataset, limited to interpretations with light scalar top quarks and non-zero leptonic or semileptonic RPV Yukawa couplings, has been made public recently [6].

Both ATLAS and CMS have analyses motivated from models of general gauge-mediation (GGM) with the lightest neutralino $\tilde{\chi}_1^0$ being the NLSP [7,8]. ATLAS considers a higgsino-like $\tilde{\chi}_1^0$ which decays predominantly to a Z boson and the gravitino LSP. Thus, events with jets, E_T^{miss} and same-flavour leptons with an invariant mass compatible with a Z boson are selected. Limits are set in the plane spanned by the higgsino mass parameter μ, which is roughly equal to the neutralino mass, and the gluino mass. Now using $5.8\,\mathrm{fb}^{-1}$ of data, the limits for $\tan\beta = 1.5$ improve on the 2011 results from the same analysis considerably. At a larger value of $\tan\beta = 30$, the decay $\tilde{\chi}_1^0 \to h\tilde{G}$ also becomes relevant. The excluded area for this value of $\tan\beta$, however, shown in Figure 2, is barely smaller than that at $\tan\beta = 1.5$. CMS on the other hand considers a bino- or wino-like NLSP, such that the decay to photon plus gravitino or Z plus gravitino, respectively, dominates. Two separate analyses look for events with 1 photon and 2 or more jets, or 2 photons and 1 or more jet, each with a loose selection on E_T^{miss}. With respect to their exclusion limits in the squark and gluino mass plane, the two analyses are comparable, the one-photon channel giving stronger limits in the scenario with a wino-like neutralino where less photons are expected due to the competing $\tilde{\chi}_1^0 \to Z\tilde{G}$ decays becoming more probable. From $4\,\mathrm{fb}^{-1}$ of data, $m(\tilde{g}) < 1.1\,\mathrm{TeV}$ and $m(\tilde{q}) < 1.25\,\mathrm{TeV}$ for a bino-like and $m(\tilde{g}) < 750\,\mathrm{GeV}$ and $m(\tilde{q}) < 850\,\mathrm{GeV}$ for a wino-like neutralino with $m(\tilde{\chi}_1^0) = 375\,\mathrm{GeV}$ are excluded.

The zero-lepton analyses are the latest in a series of inclusive searches for squark and gluino production. In ATLAS, this channel is split into two sub-channels with minimum jet multiplicities of 2 to 6 and 6 to 9, respectively. The most recent publications for both sub-channels use $5.8\,\mathrm{fb}^{-1}$ of 2012 data. High jet multiplicities are expected from decays of gluino pairs via off-shell stops, therefore this topology is targeted in the analysis of events with at least 6 to at least 9 jets [9]. The search with at least 2 to at least 6 jets [10] targets final states where each initial squark yields one jet plus E_T^{miss}, and each initial gluino yields two jets plus E_T^{miss}. Selection cuts on the ratio of the effective mass m_{eff}, defined as the scalar sum of E_T^{miss} and the p_T of the jets, the ratio of $E_T^{\mathrm{miss}}/m_{\mathrm{eff}}$, and the minimum angle between jets and E_T^{miss} in the transverse plane are used to suppress the dominant multi-jet background. Events with electrons or muons are rejected. The

limits on $m(\tilde{q})$ and $m(\tilde{g})$ are found to be similar for the mSUGRA/CMSSM implementation and a simplified squark-gluino-neutralino MSSM model: Equal mass light-flavor squarks and gluinos with masses below 1.5 TeV can be excluded. (Note that the values of the parameters for the mSUGRA/CMSSM grid used here differ from those used in the interpretation of the full-search datasets described above.) The corresponding zero-lepton analysis from CMS [11] has a different approach to suppress the multi-jet background. It makes use of a kinematic variable computed from the jets in each event, denoted by α_T [12], to select only events with significant genuine E_T^{miss}. In addition, selected events must have at least 2 jets, no isolated electrons, muons nor photons, and $H_T > 275\,\text{GeV}$, where H_T is the defined as the scalar sum of the transverse energies of the jets. The events are then categorised by the number of jets (2 to 3 or 4 or more) and the number of b-tagged jets and binned in H_T. Standard Model backgrounds are estimated from data control regions, which are mapped to the signal regions using transfer factors obtained from Monte Carlo. Systematic uncertainties on these transfer factors are derived from a set of closure tests. Simplified models are used to interpret the findings in terms of limits on squark or gluino and neutralino masses. With $11.7\,\text{fb}^{-1}$ of integrated luminosity, in the models with gluino or squark pair production this search is reported to be sensitive up to $m(\tilde{q},\tilde{g}) \approx 950\,\text{GeV}$, $m(\tilde{\chi}_1^0) \approx 450\,\text{GeV}$ or $m(\tilde{q},\tilde{g}) \approx 775\,\text{GeV}$, $m(\tilde{\chi}_1^0) \approx 325\,\text{GeV}$, respectively.

Finally, there is also an ATLAS result with 2012 data for the one-lepton channel with high jet multiplicity [13], using $5.8\,\text{fb}^{-1}$. The results are interpreted in the same mSUGRA/CMSSM plane as used in the ATLAS zero-lepton analysis described above. Events with exactly one isolated electron or muon, 4 or more jets and large $E_T^{\text{miss}} > 250\,\text{GeV}$ are selected. Additional selection cuts on the transverse mass of the lepton, m_{eff} and $E_T^{\text{miss}}/m_{\text{eff}}$ are applied, after which $W+$ jets and $t\bar{t}$ production remain as dominant background processes in the signal region. The background reaching the signal region is estimated using a global fit. For equal squark and gluino masses, values up to 1.24 TeV are excluded in the mSUGRA/CMSSM interpretation, for large m_0 the limit on the gluino mass is about 900 GeV. CMS also made public a 2012 update of their one-lepton analysis with interpretations in models of direct top squark pair production.

Overall, there have been many interesting updates from both experiments, demonstrating already now how much the constraints on supersymmetric models can be extended using the full 2012 dataset. None of the analyses has reported any significant excess above the Standard Model background, but on the other hand many more important results will be made public in the course of 2013. And, of course, the new data at higher center-of-mass energy anticipated for 2015 after the restart of the LHC is eagerly awaited.

References

The publications listed below are freely available from the websites of the ATLAS and CMS experiments and the CERN Document Server (`http://cds.cern.ch`).

1. ATLAS Collaboration, 2008 JINST 3 S08003
2. CMS Collaboration, 2008 JINST 3 S08004
3. ATLAS Collaboration, ATLAS-CONF-2013-026, `http://cds.cern.ch/record/1525882`
4. ATLAS Collaboration, ATLAS-CONF-2013-007, `http://cds.cern.ch/record/1522430`
5. CMS Collaboration, CMS-PAS-SUS-12-027, `http://cds.cern.ch/record/1494689`
6. CMS Collaboration, CMS-PAS-SUS-13-003, `http://cds.cern.ch/record/1525539`
7. ATLAS Collaboration, ATLAS-CONF-2012-152, `http://cds.cern.ch/record/1493491`
8. CMS Collaboration, CMS-PAS-SUS-12-018, `http://cds.cern.ch/record/1460385`
9. ATLAS Collaboration, ATLAS-CONF-2012-103, `http://cds.cern.ch/record/1472672`
10. ATLAS Collaboration, ATLAS-CONF-2012-109, `http://cds.cern.ch/record/1472710`
11. CMS Collaboration, arXiv:1303.2985 [hep-ex], submitted to EPJC
12. CMS Collaboration, CMS-PAS-SUS-08-005, `http://cds.cern.ch/record/1149915`
13. ATLAS Collaboration, ATLAS-CONF-2012-104, `http://cds.cern.ch/record/1472673`

NLO CALCULATIONS WITH GOSAM

GIONATA LUISONI [a]
Max-Planck-Institut für Physik, Föhringer Ring 6,
D-80805 München, Germany

In this talk we present the GoSam program package and summarize the latest development. GoSam has recently been used for a number of different NLO QCD computations within and beyond the Standard Model. In the first part a brief description of GoSam and of the interface with different external Monte Carlo programs is given, whereas in the second part the recent computations of processes of Higgs boson production in gluon-gluon fusion is presented.

1 Introduction

The latest experimental results in high energy physics presented in Moriond and contained in these proceedings show an increasing precision, never reached before, for many relevant physical observables. Furthermore, the new resonance recently discovered at the Large Hadron Collider (LHC) at CERN, resemble more and more a scalar Higgs boson. To pin down even more its properties and fully determine its nature, more precise data are still needed. On the other side, it is mandatory to reduce further the uncertainties in signal and background processes, which from the theoretical point of view, means to reduce the dependence on unphysical scales in the computation, like renormalization and factorization scales. To achieve this, Next-to-Leading Order (NLO) predictions are needed for a number different processes.

In the last decade much progress was made in the computation of NLO corrections to scattering processes both in Quantum Chromodynamics (QCD) and in the Electroweak (EW) sector of the Standard Model (SM), and also for theories Beyond the SM (BSM). In the last years it was possible to automatize the computation of NLO corrections, not only for the tree-level ingredients and the subtraction terms, but also for the virtual one-loop corrections. This process of automation allowed to achieve a high level of self-organization of the computation, which can now be organized in process-independent frameworks, directly interfaceable to Monte Carlo (MC) programs. These tools can perform a full simulation of an event, attaching a parton shower and the non-perturbative description to the initial parton-level NLO computation. This

[a] On behalf of the GoSam Collaboration: Hans van Deurzen, Gavin Cullen, Nicolas Greiner, Gudrun Heinrich, Pierpaolo Mastrolia, Edoardo Mirabella, Giovanni Ossola, Tiziano Peraro, Joscha Reichel, Johannes Schlenk, Johann-Felix von Soden-Fraunhofer, Francesco Tramontano.

huge progress is often referred to as the "*NLO revolution*". GoSam[1] is a program package which is part of several tools leading to this big evolution. In the following we will give a short description of its functionality and present the latest developments and phenomenological progress related to it.

2 GoSam

The GoSam program is a framework for the automatic generation and numerical computation of one-loop amplitudes. The core program consists of a python package which generates fortran95 code for the evaluation of the desired one-loop amplitudes. The amplitudes are based upon the algebraic generation of d-dimensional integrands via Feynman diagrams, which can be evaluated both using integrand-reduction techniques and tensor integrals calculation. This approach implies also the possibility to generate and compute on-the-fly the full rational term, without the need of further ad-hoc Feynman rules. For the generation of the diagrams we use QGRAF[2], whereas for the algebraic manipulation of the raw amplitudes expressions we are committed to FORM[3] and the package Spinney[4]. Finally the algebraic expressions are converted to optimized fortran95 code using Haggies[5].

At running time the diagrams can be evaluated using Samurai[7], which performs a reduction at the integrand level[6] or with Golem95 [8], which is a library for the computation of one-loop tensor integrals. The reduction method can be changed at running time. In the computations presented in the next sections Samurai is usually used as the default program and Golem95 is used as rescue program whenever an instability is detected in the integrand-reduction approach. This choice is driven by the observation that the tensor integral computation is usually slightly slower but very stable.

This approach allows one to easily compute one-loop QCD and EW corrections to processes within the SM and also beyond, by simply using an appropriate model file. While for QCD corrections the whole computation is fully automatized, for EW corrections and BSM physics the user has to provide, by hand, the correct renormalization. A number of different sample processes were generated using GoSam and successfully compared to the literature. Since the number of processes is constantly increasing, we refer to the GoSam webpage for a complete list[9].

3 Full NLO computations with GoSam

For the computation of full NLO processes GoSam is equipped with an interface using the Binoth-Les-Houches Accord (BLHA) standards[10]. This allow an automatic interface with external MC programs. So far three different MC event generators were successfully interfaced to compute NLO cross sections and distributions for a number of different processes. For details about the working principle of BLHA interface and its standards we refer to the literature[10].

An ad-hoc setup was used to interface with the MadGraph4-MadEvent-MadDipole family of programs. It was used to compute NLO QCD corrections to the production of $b\bar{b}b\bar{b}$ and later to assess the impact of the still missing one-loop contributions in the production of W^+W^-jj[12], both at hadron colliders. The latter process was first computed in[13], where parts of the loop contributions were neglected. More recently the same setup was used to compute NLO QCD corrections to neutralino pair production in association with one jet[14], and to study the impact of different isolation criteria in the production of $\gamma\gamma j$ at the LHC[15]. For this latter process a program package for the computation of the full NLO process can be downloaded from the web[9].

Using the BLHA interface GoSam was successfully interfaced with the POWHEG BOX[16]. This new interface, together with the built-in interface to MadGraph4 allows for a quick generation of new processes in the POWHEG BOX framework.

Thanks to the BLHA interface it was possible to link in a easy and automatic way also

Basic process	Number of extra jets	Highest number of extra jets
$W(\to l+\nu_l)$	$0,1,2$	3
$Z(\to l^+ + l^-)$	$0,1,2$	3
γ	-	$0,1,2,3$
$W(\to l+\nu_l)+b\bar{b}$	0	1
H in GGF	-	$0,1,2,3$
H in VBF	-	$2,3$
W^+W^+	2	-
W^+W^-	0	$1,2$ + loop induced
$W^+W^-b\bar{b}$	-	1
$t\bar{t}$	0	1
$H\,t\bar{t}$	-	$0,1$

Table 1: Processes available (center column) and to-appear (right column) as ready-to-use packages.

to the MC event generator **Sherpa** [17]. The two programs can exchange information about the process the user wishes to compute and generate all the needed ingredients. The user only needs to fill an input card for the two programs and, once the code is ready, the full calculation can be steered simply editing the **Sherpa** input card. A set of ready-to-use process packages with the full code for the loop computation is also available [9]. They only require the installation of **Sherpa** by the user, whereas the code for the virtual part is already generated and validated. The list of available processes and the one in phase of validation are summarized in Table 1.

4 Higgs plus jets production

In this section, we illustrate our recent computation of the NLO contributions to Higgs plus two jets production in Gluon-Gluon Fusion (GGF) at the LHC in the large top-mass limit [18], and also provide results for the one-loop virtual contribution to Higgs plus three jets production. The distributions for the former process are obtained by using the BLHA interface between **GoSam** and **Sherpa**.

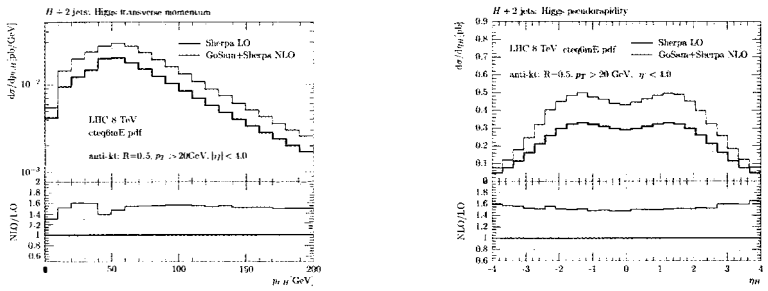

Figure 1: Transverse momentum p_T and pseudorapidity η of the Higgs boson, when produced in association with two jets.

For Hjj production, the following minimal set of processes are computed: $gg \to Hgg$, $gg \to Hq\bar{q}$, $q\bar{q} \to Hq\bar{q}$, $q\bar{q} \to Hq'\bar{q}'$. The remaining processes are obtained by performing the appropriate symmetry transformation. We work in the dimensional reduction scheme (DRED) and UV divergences have been renormalized in the $\overline{\text{MS}}$ scheme. Our results are in agreement with [19] and MCFM (v6.4) [20].

As an illustration of possible analyses that can be performed with the GoSam-Sherpa automated setup, in Fig. 1 we present the distribution of the transverse momentum p_T of the Higgs boson and its pseudorapidity η, for proton-proton collisions at the LHC at $\sqrt{s} = 8$ TeV. For details about the setup we refer to the original publication [18]. The bands show the impact of varying renormalization and factorization scale by factors of 2 around its central value, set to $\hat{H}_t = \sqrt{M_H^2 + p_{t,H}^2} + \sum_j p_{t,j}$, where $p_{t,H}$ and $p_{t,j}$ are the transverse momenta of the Higgs boson and the jets. Both distributions show a K-factor between the LO and the NLO distribution of about $1.5 - 1.6$ and a decrease of the scale uncertainty of about 50%.

All independent processes contributing to $Hjjj$ can be obtained by adding one extra gluon to the final state of the processes listed in the case of Hjj. Accordingly, we generated the codes for the virtual corrections to the processes $gg \to Hggg$, $gg \to Hq\bar{q}g$, $q\bar{q} \to Hq\bar{q}g$, $q\bar{q} \to Hq'\bar{q}'g$. Some representative one-loop diagrams are depicted right in Figure 2.

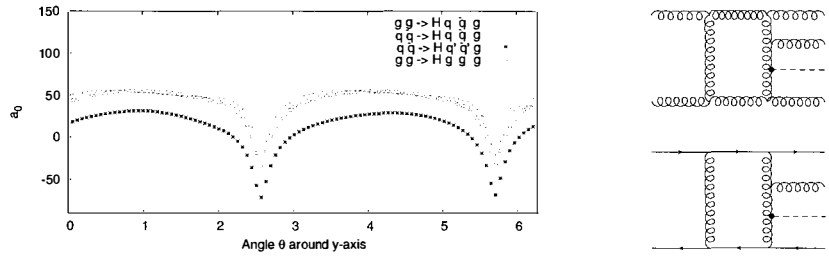

Figure 2: Left: Finite-term of the virtual matrix elements for $gg \to Hq\bar{q}g$ (red), $q\bar{q} \to Hq\bar{q}g$ (green), $q\bar{q} \to Hq'\bar{q}'g$ (red), $gg \to Hggg$ (purple). Right: sample hexagon diagrams which enter in the six-parton one-loop amplitudes for $gg \to Hggg$ and $q\bar{q} \to Hq\bar{q}g$. The dot represents the effective ggH vertex.

Choosing the momenta of the initial partons along the z-axis, we show in Figure 2 the effect on the finite parte of the virtual amplitude of rotating a phase space point through an angle θ about the y-axis.

Furthermore we verified that the values of the double and the single poles conform to the universal singular behavior of dimensionally regulated one-loop amplitudes.

5 Conclusions

GoSam is a very flexible tool for the automatic computation of one-loop amplitudes. Work is in progress to increase the generation and the running speed and to decrease the size of the generated codes. These new features will be part of new release of the code, planned for the second half of the current year.

References

1. G. Cullen, N. Greiner, G. Heinrich, G. Luisoni, P. Mastrolia, G. Ossola, T. Reiter and F. Tramontano, Eur. Phys. J. C **72** (2012) 1889 [arXiv:1111.2034].
2. P. Nogueira, J. Comput. Phys. **105** (1993) 279.
3. J. Kuipers, T. Ueda, J. A. M. Vermaseren and J. Vollinga, Comput. Phys. Commun. **184** (2013) 1453 [arXiv:1203.6543].
4. G. Cullen, M. Koch-Janusz and T. Reiter, Comput. Phys. Commun. **182** (2011) 2368 [arXiv:1008.0803].
5. T. Reiter, Comput. Phys. Commun. **181** (2010) 1301 [arXiv:0907.3714].

6. G. Ossola, C. G. Papadopoulos and R. Pittau, Nucl. Phys. B **763** (2007) 147 [hep-ph/0609007]; R. K. Ellis, W. T. Giele and Z. Kunszt, JHEP **0803** (2008) 003 [arXiv:0708.2398].
7. P. Mastrolia, G. Ossola, T. Reiter and F. Tramontano, JHEP **1008** (2010) 080 [arXiv:1006.0710].
8. G. Cullen, J.P. Guillet, G. Heinrich, T. Kleinschmidt, E. Pilon, T. Reiter and M. Rodgers, Comput. Phys. Commun. **182** (2011) 2276 [arXiv:1101.5595]; T. Binoth, J.P. Guillet, G. Heinrich, E. Pilon and T. Reiter, Comput. Phys. Commun. **180** (2009) 2317 [arXiv:0810.0992].
9. `http://gosam.hepforge.org/`
10. T. Binoth, F. Boudjema, G. Dissertori, A. Lazopoulos, A. Denner, S. Dittmaier, R. Frederix and N. Greiner *et al.*, Comput. Phys. Commun. **181** (2010) 1612 [arXiv:1001.1307].
11. N. Greiner, A. Guffanti, T. Reiter and J. Reuter, Phys. Rev. Lett. **107** (2011) 102002 [arXiv:1105.3624].
12. N. Greiner, G. Heinrich, P. Mastrolia, G. Ossola, T. Reiter and F. Tramontano, Phys. Lett. B **713** (2012) 277 [arXiv:1202.6004].
13. T. Melia, K. Melnikov, R. Rontsch and G. Zanderighi, Phys. Rev. D **83** (2011) 114043 [arXiv:1104.2327].
14. G. Cullen, N. Greiner and G. Heinrich, [arXiv:1212.5154].
15. T. Gehrmann, N. Greiner and G. Heinrich, [arXiv:1303.0824].
16. S. Alioli, P. Nason, C. Oleari and E. Re, JHEP **1006** (2010) 043 [arXiv:1002.2581].
17. T. Gleisberg, S. .Hoeche, F. Krauss, M. Schonherr, S. Schumann, F. Siegert and J. Winter, JHEP **0902** (2009) 007 [arXiv:0811.4622].
18. H. van Deurzen, *et al.*, Phys. Lett. B **721** (2013) 74 [arXiv:1301.0493].
19. R. K. Ellis, W. T. Giele and G. Zanderighi, Phys. Rev. D **72** (2005) 054018 [Erratum-ibid. D **74** (2006) 079902] [hep-ph/0506196].
20. J. M. Campbell, R. K. Ellis and C. Williams, Phys. Rev. D **81** (2010) 074023 [arXiv:1001.4495].

SUSY Searches for Electroweak Production of Gauginos and Sleptons at the LHC

Pieter Everaerts
University of California, Los Angeles, USA

The searches for direct electroweak production of supersymmetric particles in proton-proton collisions at the LHC are presented. The focus is on gaugino and slepton production, which yield final states with two or more leptons. A wide variety of complementary searches are discussed with none of them showing any indication for physics beyond the standard model.

1 Introduction

During the first years of LHC running most searches for supersymmetry (SUSY) have focused on the strong production of supersymmetric particles because of its large production cross-section. Thanks to these studies, gluinos and inclusive squarks have been probed up to masses of above 1 TeV. Electroweak production of SUSY has in general smaller cross-sections, but the production cross-sections for winos, binos or higgsinos of around 300–400 GeV are similar to those of squarks and gluinos with masses around 1–1.5 TeV. Therefore CMS[1] and ATLAS[2] have developed a set of analyses focusing on the case when squarks and gluinos would be heavy, but electroweakinos would be light.

1.1 General strategy

The focus of this note is on direct electroweak production of supersymmetric particles at a center-of-mass energy of 8 TeV. Electroweak SUSY particles such as gauginos and sleptons are pair produced and there is very little hardronic activity present in the event, other than initial-state-radiation. As a result top backgrounds can be highly suppressed by applying a veto on the amount of hadronic activity and/or the presence of b-tagged jets. The other major backgrounds of such searches are the diboson backgrounds. The easiest way to suppress these backgrounds is by requiring that there would be no Z candidate present. Of course such a cut can only be applied if no intermediate vector bosons are expected in the electroweakino decay. To further distinguish signal from background, the missing transverse energy and other kinematic variables (e.g. transverse mass) are used.

The backgrounds due to non-prompt or misidentified leptons are usually estimated using data-driven techniques that measure the probability of a non-prompt lepton to be isolated in a control sample. Simulation is used to estimate the diboson backgrounds and other rare processes, but cross-checks and corrections are applied when feasible. The normalization is usually derived from a control region; for the diboson backgrounds, corrections to the missing transverse energy and lepton resolutions are applied to make the final estimate more precise. Both CMS and ATLAS also look at cascade decays, where gluinos or squarks are pair-produced and then decay to electrokweakinos[3,4,5,6,7] but this is not discussed further in this note.

2 Chargino-Neutralino Pair production

The first model of direct electroweak SUSY production considered here is chargino-neutralino pair production. Depending on the masses of the sleptons and the sneutrinos, two different decay modes can take place. If the sleptons and sneutrinos are light, then the decay happens through intermediate sleptons and sneutrinos, and the final state contains three leptons and two lightest supersymmetric particles (LSP). This gives rise to a signature with three leptons and considerable missing transverse energy and is targeted by a three-lepton analysis, looking explicitly in events without a Z candidate.[8,9] If the intermediate slepton mass is very close to the chargino/neutralino or the LSP mass, or if the intermediate particles are predominantly staus, then the leptons are expected to be soft and then it is more likely to miss at least one of them. For this reason, targeted dilepton analyses have been developed to complement the three-lepton one.[8,10,11] If the sleptons and sneutrinos are heavy, the electroweakinos decay through vector bosons, WZ if we consider chargino-neutralino production. The W and Z boson then decay according to the standard model and have the possibility to decay into quarks or leptons. For these decays, the three-lepton analysis is still useful, but in this case, a Z candidate is explicitly required. To target the hadronic decay mode of the vector bosons, a search in the Z + dijet + E_T^{miss} final state is also performed.[8,10]

2.1 Three-lepton analysis

Both CMS and ATLAS have a three-lepton analysis to search for chargino-neutralino pair production.[8,9] Both analyses focus on three light leptons (e, μ) with an opposite-sign same flavor lepton pair present. The main backgrounds for this analysis are WZ and top pair production. To suppress the WZ production, the sample is split between a sample with and a sample without a Z candidate. The first sample can be used for cases with intermediate vector bosons, the second one for the case with intermediate sleptons and sneutrinos. A transverse mass cut, calculated with the E_T^{miss} and the third lepton, is also very efficient to suppress WZ backgrounds. To suppress the top quark backgrounds, a veto is applied on the presence of b-tagged jets in the event. The two analyses differ slightly because the ATLAS analysis focuses on 3 inclusive search regions, while the CMS analysis has 45 exclusive search regions. CMS also tries to focus on those cases where staus are prefered as intermediate particles, by looking at cases without an opposite-sign same flavor lepton pair, and at cases where one of the leptons is a hadronic tau candidate.

2.2 Same-sign dilepton analysis

In some cases one of the leptons can be too soft or fail the lepton identification. If this happens to one of the leptons from the neutralino decay, then we end up with same-sign dileptons. Same-sign dileptons are easier to use than opposite-sign dileptons since they suffer from smaller amounts of standard model backgrounds. CMS has a 8 TeV analysis for same-sign dileptons, while ATLAS provides results both for opposite-sign and same-sign dileptons but only at 7 TeV.[8,10] One of the problems in going to a dilepton analysis is that the contribution of the backgrounds due to non-prompt and misidentified leptons increases considerably. This can be countered by tightening the requirements on the lepton transverse momenta, the E_T^{miss}, or the hadronic activity. The 8 TeV analysis follows both these options with its two inclusive search regions: one of the search regions cuts very tight on the E_T^{miss} (> 200 GeV) while the other one relaxes the E_T^{miss}-requirement (> 120 GeV) but has tighter cuts on the hadronic activity.

2.3 Opposite-sign tau analysis

There is a possibility that intermediate staus are the preferred option in supersymmetry. In such cases, there is still the option of having three light leptons, but due to the branching fractions

of the tau decay, it is more likely to have one or more hadronic taus in the event. Therefore ATLAS developed a new analysis focusing on two opposite-sign hadronic taus.[11] To suppress the major backgrounds, a Z-veto and a hard cut on the the hadronic activity (a [b-tagged] jet veto) are applied. Then the stransverse mass, m_{T2}, is used for the final discrimination. The stransverse mass variable is designed for events with two undetected particles and represents a lower bound on the parent particle's mass. The major standard model backgrounds, such as WW and top pair production, have a kinematic endpoint at around 80 GeV in this variable. To estimate the non-prompt and misidentified tau backgrounds, a so-called ABCD method using the stransverse mass variable and the tau identification criteria was used.

2.4 Z+dijet analysis

If a W or a Z boson decays hadronically, the dijet signature can be used to identify this vector boson.[8] The invariant mass of the dijet pair is required to be consistent with a W or Z hypothesis, and a veto on b-tagged jets is applied to reduce the top backgrounds. The second Z boson is required to decay leptonically and to be fully reconstructed. Using the E_T^{miss} shape, a distinction can then be made between Z + jets background and the electroweakino signal. For this a template fit is performed with the Z+jets template shape derived from a γ + jets control sample and the non-prompt and misidentified leptons estimated from an eμ sample. The other backgrounds are estimated using simulated samples. The E_T^{miss} spectrum is split into different bins because the E_T^{miss} in the SUSY events depends on the chargino/neutralino and LSP masses.

2.5 Results

None of the described analyses shows any significant discrepancy between the data and the predicted yields. Limits are derived for the pair production of charginos and neutralinos. Figure 1 shows the results for the case with light intermediate sleptons and a slepton mass which is halfway between the chargino and LSP masses. The limits for the cases when intermediate staus or intermediate vector bosons are prefered can be found in Ref. [8,9,10,11].

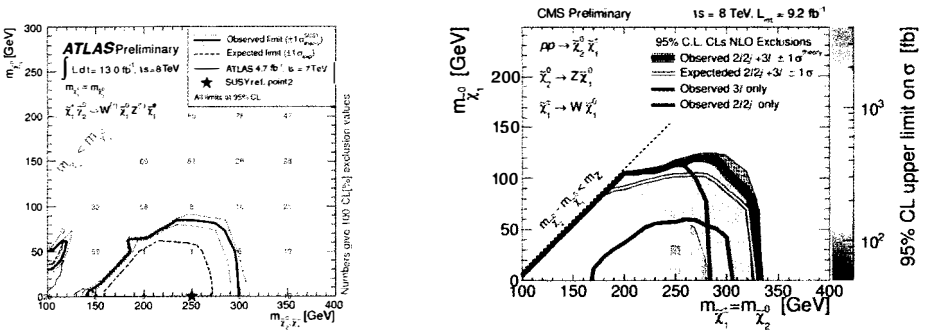

Figure 1: Limits on chargino-neutralino pair production using the three-lepton analysis. The ATLAS analysis[9] is shown on the left and the CMS one[8] on the right.

3 Slepton and chargino pair production

Slepton and chargino pair production both lead to signatures with two opposite-sign dileptons and LSPs giving large E_T^{miss}.[8,10] In the chargino case, there are extra neutrinos present in the event but the E_T^{miss} from those is expected to be considerable smaller than from the LSPs. In

the slepton case the two leptons have the same flavor because the sleptons decay to a specific lepton flavor, while the two charginos decay independently to both lepton flavors and are thus just as likely to have an opposite-flavor as a same-flavor pair. ATLAS and CMS both have an analysis which focuses on opposite-sign dileptons. To remove the large Z-related background, a mass constraint is added to the dilepton pair: the mass has to be at least 15 GeV away from the Z mass. Both analyses apply cuts on the hadronic activity (a [b-tagged] jet veto) and apply a moderate E_T^{miss} cut of around 50–60 GeV. Both analyses then perform a cut-and-count analysis using a kinematic variable that has an endpoint for W-related backgrounds. ATLAS uses the stransverse mass m_{T2} discussed in section 2.3 while CMS uses the $MC_{T,Perp}$ variable which has a similar behavior with a kinematic endpoint around 80 GeV for WW and top pair production. Chargino pair production decaying through intermediate staus has also been probed by the opposite-sign ditau analysis discussed in section 2.3.

4 R-parity violating supersymmetry

All of the SUSY searches discussed so far assume that R-parity is conserved. If R-parity is violated, the LSPs could be unstable and decay into leptons.[12] The decay of the two LSPs would lead to four leptons in the final state. ATLAS has a targeted analysis looking for four leptons with no Z candidates to search for electroweak production of gauginos and sleptons in R-parity violating models.[12] The similar CMS analysis only focuses on the production of stops[13] in R-parity violating models. If the LSP decays into a pair of leptons, the final state would have very little E_T^{miss}. All the E_T^{miss} present would come from neutrinos. That is why the analysis uses two exclusive search regions that only rely mildly on E_T^{miss}. One search region applies a moderate E_T^{miss} cut (50 GeV) to target final states with neutrinos, while the other one only cuts on the scalar sum of the transverse momenta of the leptons, jets and E_T^{miss} in the event. Again no significant excesses are observed and limits are placed on the production of winos, sleptons and sneutrinos in R-parity violating SUSY.

5 General Gauge Mediated SUSY breaking

Assuming that the gravitino is the LSP and the next-to-lightest supersymmetric particle is a neutralino, this neutralino can decay to the gravitino and a photon or a Z. In this case, neutralino pair production decaying to two Z bosons and gravitinos can be enhanced. For this final state, a four-lepton analysis is performed to complement the Z+dijet analysis (section 2.4).[8] The four lepton analysis follows the techniques of the CMS three-lepton analysis (section 2.1), but divides the data up in slightly different boxes, like number of opposite-sign same-flavor pairs, the E_T^{miss} and whether there is a Z candidate or not. ATLAS has a search focusing on the direct production of a chargino-neutralino pair where the neutralino then decays to a photon and a gravitino.[14] This search has a lepton + photon signature. Both searches did not yield any indications for physics beyond the Standard Model.

6 Conclusions

CMS and ATLAS have performed a wide variety of complementary analyses searching for direct electroweak production of SUSY. No indications for new physics are found and stringent constraints are placed on the slepton and gaugino masses. For the R-parity conserving case, chargino masses up to 600 GeV and slepton masses up to 250 GeV are probed, while for the R-parity violating case, the reach is slightly enhanced to 700 GeV for charginos and 430 GeV for sleptons.

References

1. CMS Collaboration, "The CMS Experiment at the CERN Large Hadron Collider", *JINST* 3 S08004 (2008).
2. ATLAS Collaboration, "The ATLAS Experiment at the CERN Large Hadron Collider", *JINST* 3 S08003 (2008).
3. ATLAS Collaboration, "Search for supersymmetry in final states with jets, missing transverse momentum and a Z boson at sqrt(s) = 8 TeV with the ATLAS detector", ATLAS-CONF-2012-152.
4. ATLAS Collaboration, "Search for New Phenomena in Monojet plus Missing Transverse Momentum Final States using 10 fb^{-1} of pp Collisions at sqrt(s) = 8 TeV with the ATLAS detector at the LHC", ATLAS-CONF-2012-147.
5. ATLAS Collaboration, "Search for supersymmetry in events with photons, bottom quarks, and missing transverse momentum in protonproton collisions at a centre-of-mass energy of 7 TeV with the ATLAS detector", *Phys. Lett. B* 719 (2013) 261-279.
6. CMS Collaboration, "Search for supersymmetry in events with photons and missing energy", CMS-PAS-SUS-12-018.
7. CMS Collaboration, "SUSY Search in Photon(s)+jets+MET final state with the Jet-Gamma Balance method", CMS-PAS-SUS-12-013.
8. CMS Collaboration, "Search for electroweak production of charginos, neutralinos, and sleptons using leptonic final states in pp collisions at sqrt(s) = 8 TeV", CMS-PAS-SUS-12-022.
9. ATLAS Collaboration, "Search for direct production of charginos and neutralinos in events with three leptons and missing transverse momentum in 13.0 fb^{-1} of pp collisions at sqrt(s)=8 TeV with the ATLAS detector", ATLAS-CONF-2012-154.
10. ATLAS Collaboration, "Search for direct slepton and gaugino production in final states with two leptons and missing transverse momentum with the ATLAS detector in pp collisions at sqrt(s) = 7 TeV", ATLAS-CONF-2012-076.
11. ATLAS Collaboration, "Search for electroweak production of supersymmetric particles in final states with at least two hadronically decaying taus and missing transverse momentum with the ATLAS detector in proton-proton collisions at sqrt(s) = 8 TeV", ATLAS-CONF-2013-028.
12. ATLAS Collaboration, "Search for supersymmetry in events with four or more leptons in 13.0 fb^{1} pp collisions at sqrt(s) = 8 TeV with the ATLAS detector", ATLAS-CONF-2012-153.
13. CMS Collaboration, "Search for stop in R-parity-violating supersymmetry with three or more leptons and b-tags", CMS-PAS-SUS-13-003.
14. ATLAS Collaboration, "Search for supersymmetry in events with at least one photon, one lepton, and large missing transverse momentum in protonproton collision at a center-of-mass energy of 7 TeV with the ATLAS detector", ATLAS-CONF-2012-144.

Searches for Heavy Resonances at the LHC

Sam Harper
on behalf of the ATLAS and CMS collaborations
Rutherford Appleton Laboratory, Didcot, Oxfordshire OX11 0QX, UK

These proceedings presents the results of several searches for heavy resonances using between 6 and 20 fb^{-1} of $\sqrt{s} = 8$ TeV proton-proton collision data collected by the ATLAS and CMS experiments at the LHC. No evidence of new heavy resonances is observed and limits are set at the 95% confidence level on various benchmark models.

1 Introduction

The Standard Model (SM) of particle physics has so far been a very successful theory, with experimental results being consistently in agreement with its predictions. Still it is conceivable that the SM is just an effective theory and that above some energy scale new physics emerges. Therefore there are various extensions to the SM which predict the presence of a new heavy resonances. These proceedings detail several of the most recent CMS and ATLAS searches for heavy resonances using 8 TeV proton-proton LHC data.

2 $Z' \to e^+e^-/\mu^+\mu^-$

Both CMS and ATLAS collaborations have searched for a heavy neutral spin-1 particle (Z') decaying into electron or muon pairs with approximately 20 fb^{-1} of data [3,4]. Figure 1 shows the measured mass spectra in the CMS dielectron and ATLAS dimuon channels. No significant excess is observed and limits are set at the 95% confidence level as shown in figure 2. Different conventions are used when setting cross-section limits, CMS models the signal as having zero intrinstic width while ATLAS uses the shape obtained from a Z'_{SSM} which does not interfere with the SM Z boson. Care must be taken when comparing the limits as a result. Both ATLAS and CMS exclude the benchmark Z'_{SSM} boson for masses below 2.9 TeV.

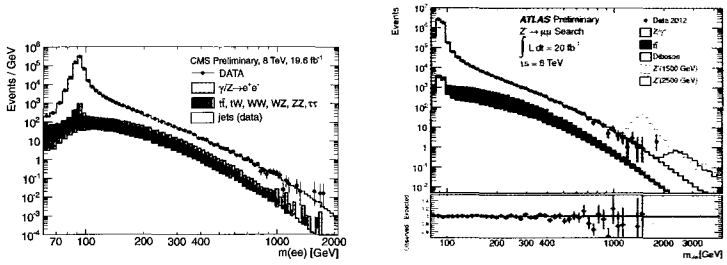

Figure 1: CMS dielectron (left) and ATLAS dimuon (right) mass spectra

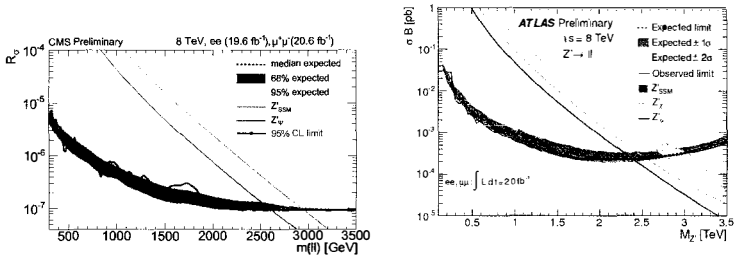

Figure 2: 95% confidence level limit on the σ.Br of a spin-1 boson vs mass using CMS (left) and ATLAS (right) dilepton mass spectra.

3 $W' \to e\nu/\mu\nu$

The CMS collaboration has searched for a charged spin-1 particle (W') decaying to $e\nu$ or $\mu\nu$ with 19.6 fb^{-1} of data [5]. The distribution of the observed transverse mass together with expected backgrounds is shown in figure 3. No significant excess is observed and as figure 4 shows, the M_T spectrum was used to set model independent limits vs M_T as well as on specific models, such as the W'_{SSM} and split UED. A W'_{SSM} boson is excluded below 3.35 TeV.

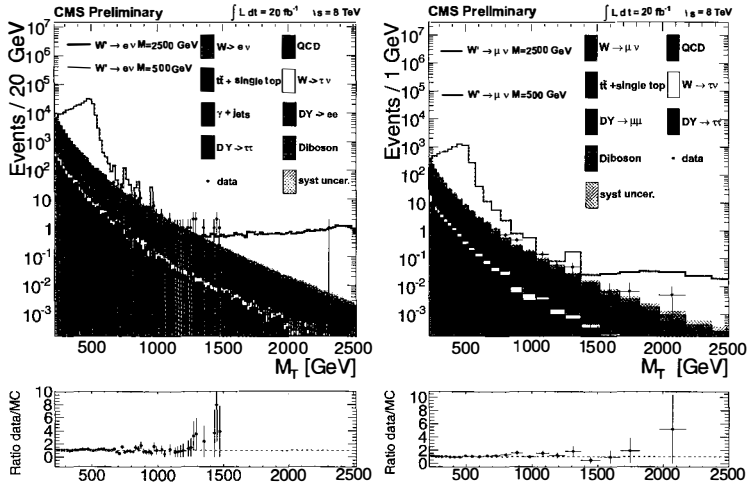

Figure 3: CMS transverse mass spectra for the electron (left) and muon (right) channels.

4 $W' \to tb$

The CMS collaboration has also searched for a W' decaying to top-bottom pairs where the top decays to either a muon or an electron using 19.6 fb^{-1} of data [6]. While not as sensitive as the lepton channel to a generic W', if the W' is right-handed and the right-handed neutrino is more massive than the W_R, the leptonic limits do not apply. Additionally, unlike the leptonic case, the W' mass can be reconstructed in this channel. Figure 5 shows the resulting mass spectrum. No significant excess is observed and limits are set on the cross-section times branching ratio.

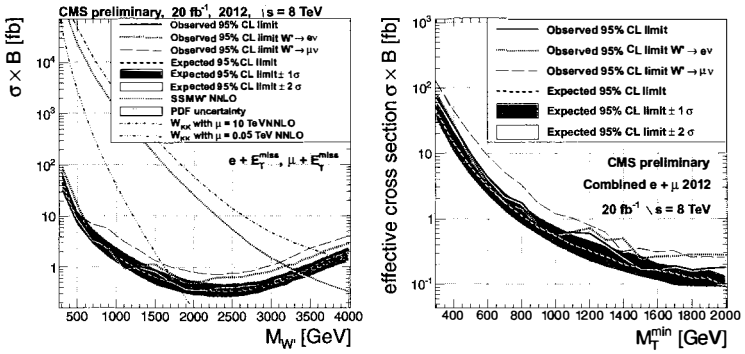

Figure 4: 95% confidence level upper limits on the $\sigma.Br$ of a W' vs transverse mass taking the signal shape into account (left) and on the effective $\sigma.Br$ above a minimum M_T threshold as a function of that threshold.

Figure 6 shows these cross-section limits vs mass and the reinterpretation of these limits into an exclusion plane of the W's coupling strength to left handed and right handed fermions.

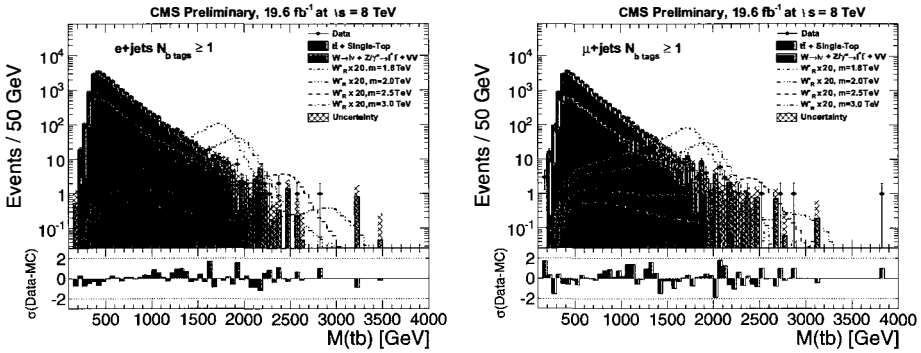

Figure 5: CMS observed top-bottom mass spectrum where the top decays to an electron (left) or a muon (right).

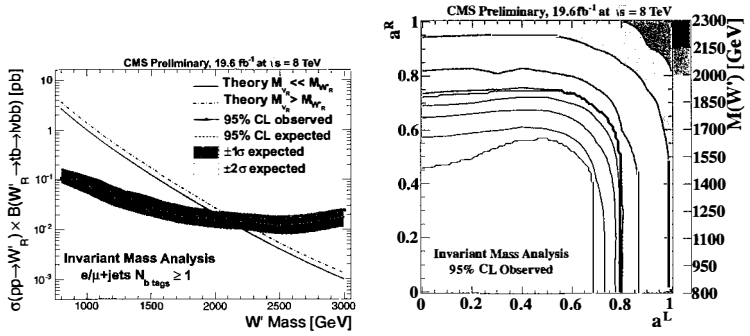

Figure 6: 95% confidence level upper limit on $\sigma(W').Br(W' \to tb)$ as a function of mass (left) and mass limits as as a function of W' coupling strength to left-handed and right-handed fermions (right).

5 Excited Leptons

The ATLAS collaboration has searched for excited electrons and excited muons using 13 fb^{-1} of data[7]. The leptons are pair produced, with one lepton in an excited state which then decays to the ground state lepton and a photon, giving a signature of two same flavor leptons and a photon. In order to generalize this search to objects other than excited leptons, the total mass of the photon and two leptons was measured rather than the mass of the excited lepton. No significant excess over the SM prediction was observed and limits were set on the excited lepton masses for various scales of compositeness. These limits are shown in figure 8.

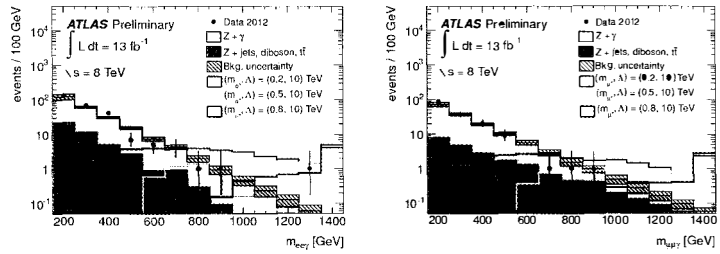

Figure 7: ATLAS observed total invariant mass of the 2 electron + 1 photon system (left) and 2 muon + 1 photon system (right).

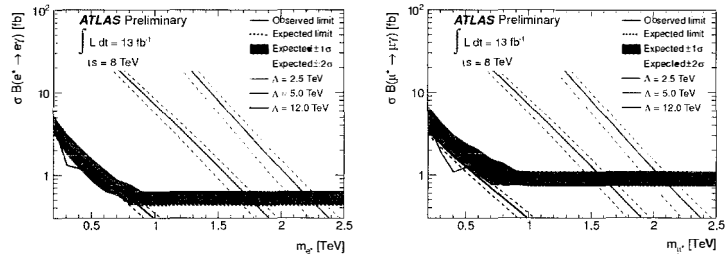

Figure 8: 95% confidence level upper limit on $\sigma.Br$ as a function of mass in for excited electrons (left) and excited muons (right).

6 Type III See-Saw

The ATLAS collaboration has searched for evidence of the lightest fermion triplet (N^+, N^-, N^0) postulated to generate neutrino masses by the type-III see-saw mechanism[8] using 5.8 fb^{-1} of data[9]. A 4 lepton final state resulting from the process $W \to N^{\pm}N^0; N^{\pm} \to l^{\pm}Z, N^0 \to l'^{\pm}W^{\mp}$, where the W and Z decay leptonically, is searched for. Only the $N^{\pm}$ mass is reconstructed, the lepton from the N^0 is solely used to tag the event to reduce background. The mass spectrum is shown in figure 9. No significant excess over the SM prediction was observed and limits were set on the cross-section times branching fraction vs fermion mass. These limits are shown in figure 10. For the $Br(N^{\pm} \to Zl^{\pm})$ and $Br(N^0 \to W^{\pm}l^{\mp})$ predicted by the type-III see-saw mechanism a lower mass bound on the N fermions is set at 245 GeV at 95% confidence level.

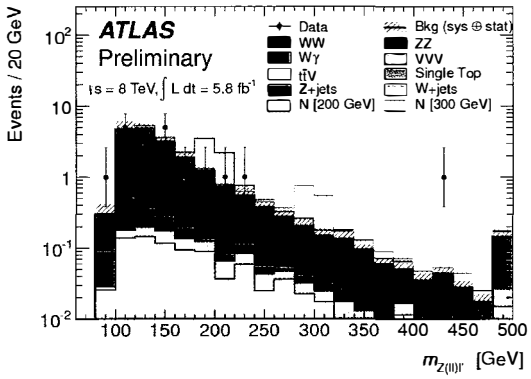

Figure 9: The ATLAS observed $Z(ll)+l$ mass spectrum where another lepton unrelated to the other three leptons is also present in the event.

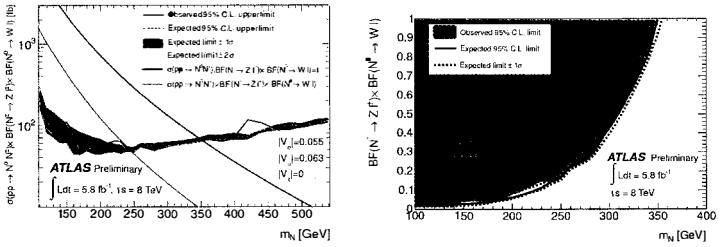

Figure 10: 95% confidence level upper limit on $\sigma.Br$ for $N^{\pm}N^{0}$ production as a function of mass (left) and $Br(N^{\pm} \to Zl^{\pm} \times Br(N^{0} \to W^{\pm}l^{\mp})$ vs mass exclusion plane (right).

7 Conclusion

The ATLAS and CMS collaborations have searched for several types of new heavy resonances using between 6 fb^{-1}and 20 fb^{-1}of proton-proton $\sqrt{s} = 8$ TeV collision data produced by the LHC. No significant excess has been observed and limits at the 95% confidence level have been set on a varity of models. Further searches for new heavy resonances are in more complicated final states are underway and will update over the coming year.

References

1. CMS Collaboration, JINST **3**, S08004 (2008).
2. ATLAS Collaboration, JINST **3**, S08003 (2008).
3. CMS Collaboration, CMS-PAS-EXO-12-061.
4. ATLAS Collaboration, ATLAS-CONF-2013-017.
5. CMS Collaboration, CMS-PAS-EXO-12-060.
6. CMS Collaboration, CMS-PAS-B2G-12-010.
7. ATLAS Collaboration, ATLAS-CONF-2012-146.
8. R. Foot, H. Lew, X.-G. He and G.C. Joshi, Z. Phys. C **44**, 441 (1989).
9. ATLAS Collaboration, ATLAS-CONF-2013-019.

Do current LHC data really pose a problem for constrained SUSY?

LESZEK ROSZKOWSKI[a]
National Centre for Nuclear Research,
Hoża 69, 00-681 Warsaw, Poland

Recent LHC results, most notably new strong limits from ATLAS and CMS on direct supersymmetry searches, reaching now the TeV scale for superpartner masses, the first measurement by LHCb of BR $\left(B_s \to \mu^+\mu^-\right)$ consistent with the Standard Model (SM), as well as the recently discovered Higgs boson with mass close to 126 GeVand with SM-like properties, have led some to people to claim that constrained supersymmetry (SUSY) has been (nearly) ruled out, one way or another. In this talk I will map out those ranges of superpartner masses that remain fully consistent with all experimental data, including the relic abundance of dark matter. I will point out that, while the LHC with increased energy will provide a rather directly way to explore those ranges, direct detection searches of dark matter (first LUX, and next one-tonne detectors) will be sensitive to almost all ranges of corresponding SUSY parameters. Improved determination of BR $\left(B_s \to \mu^+\mu^-\right)$ will potentially provide additional important information by having a capability of independently ruling out the A-funnel region in (but not beyond) the constrained MSSM.

1 Framework and main results

In this talk I will address the current status of constrained SUSY in light of some recent results[1,2], where more details and references to the literature can also be found.

There are two main avenues to investigate effective models based on softly-broken global supersymmetry (SUSY). One is to confine oneself to the framework where a given model is defined basically entirely at the electroweak (EW), or $\sim 1\,\text{TeV}$, scale, as is done in the Minimal Supersymmetric Standard Model (MSSM), or in some extensions thereof, like the Next-to-MSSM (NMSSM) with an extra Higgs singlet superfield. In this approach one faces a large number of free parameters, mostly generated by breaking SUSY softly, and strong simplifying assumptions have to be made to reduce the number to a manageable level.

Another, more motivated and over the last two decades more popular, approach has been to consider SUSY in the context of grand unification where soft SUSY breaking parameters are unified. A prime model of this class is the Constrained MSSM (CMSSM) - the most popular and economical effective SUSY model of phenomenological interest, although somewhat more relaxed scenarios, like the Constrained NMSSM (CNMSSM), or Non-Universal Higgs Model, are also often considered.

In the CMSSM, three of its four defining parameters are set at the scale of grand unification. These are the universal scalar mass m_0, the universal gaugino mass $m_{1/2}$, and the universal trilinear coupling A_0. Additionally, $\tan\beta$ (the ratio of the expectation values of the two Higgs

[a]On leave of absence from the University of Sheffield.

Figure 1: Left: Marginalized 2D posterior pdf in the $(m_0,\ m_{1/2})$ plane of the CMSSM constrained only by the Higgs mass and the LHC SUSY searches. The 68% credible regions are shown in dark blue, and the 95% credible regions in light blue. The dashed red line shows the CMS combined 95% CL exclusion bound. Right: Marginalized 2-dim. posterior pdf in the $(m_0,\ m_{1/2})$ plane of the CMSSM for $\mu > 0$, constrained by the experiments listed in Table 2 with current uncertainties for BR $\left(\mathrm{B_s} \to \mu^+\mu^-\right)$.

doublets), is defined at the electroweak scale, while the sign of the Higgs/higgsino parameter μ remains undetermined.

In the CMSSM mass limits from direct SUSY searches by ATLAS and CMS have now pushed gluino and 1st/2nd generation squark masses far beyond 1 TeV, which corresponds to $m_{1/2} \gtrsim 850$ GeV. Similar conclusions can be expected, and in some cases have been shown to hold, in less constrained models [3]. Furthermore, it has been argued that, it is hard to reproduce the mass of the discovered Higgs boson of about 126 GeV, if one restricts oneself to the SUSY breaking scale M_{SUSY} roughly below 1 TeV. This has been interpreted by some as a death kneel of the constrained SUSY approach. Such conclusions are not, however, based on experimental data but rather on theoretical expectations coming from "naturalness", or "little hierarchy problem". Instead I will adopt a pragmatic, data-driven approach, and map out ranges of SUSY parameters that are consistent with all current data. At present the most important among them are: the Higgs mass and the relic abundance of neutralino as dark matter (DM).

I will argue that generically the Higgs mass of about 126 GeV favors ranges of M_{SUSY} in the multi-TeV regime, which have so far been only very mildly constrained by direct SUSY searches. This is shown in the left panel of Fig. 1 where I show 1- and 2σ (credible) regions of Bayesian total posterior probability. In the likelihood function two constraints were included: information about SM-like Higgs with mass 125.8 GeVwas encoded via a Gaussian function assuming experimental (theory) error of 0.6 (2) GeV, while a lower limit from direct SUSY searches from CMS was included through an approximate but accurate procedure described in [2]. One can see the favored ranges of $m_{1/2}$ and m_0 lie in the multi-TeV regime, and are only very mildly constrained from below by LHC limits on SUSY.

However, as one can see in the right panel of Fig. 1, imposing the relic density of DM select some specific regions: the $\tilde{\tau}$-coannihilation (SC) region at small m_0 and large $m_{1/2}$, the A-funnel (AF) region to the right and above it, which is relatively small at 1σ but much larger at 2σ, and the focus point (FP)/hyperbolic branch (HB) region at large m_0 and $m_{1/2} \lesssim 1$ TeV. The FP/HB region is now disfavored relative to our previous analysis [1], because it produces slightly low Higgs mass and appears at only 2σ.

The region that is most prominently visible in the figure along the diagonal of the box appears as a result of extending the ranges of m_0 and $m_{1/2}$ far beyond those used in [1]; see Table 1. In the new region the lightest neutralino is higgsino-like and its mass is set by the μ-parameter and is close to 1 TeV in order to produce correct relic abundance. In some sense this region most naturally corresponds to the Higgs mass of about 126 GeV. On the other hand, it does imply very large m_0 and $m_{1/2}$ in the multi-TeV regime. While it is the dark matter density that plays the dominant role in selecting the above regions, in our Bayesian analysis and

Table 1: Priors for the parameters of the CMSSM and for the SM nuisance parameters used in our scans. Masses and A_0 are given in GeV.

CMSSM parameter	Description	Prior Range	Prior Distribution
m_0	Universal scalar mass	100, 20,000	Log
$m_{1/2}$	Universal gaugino mass	100, 10,000	Log
A_0	Universal trilinear coupling	-20,000, 20,000	Linear
$\tan\beta$	Ratio of Higgs vevs	3, 62	Linear
$\mathrm{sgn}\,\mu$	Sign of Higgs parameter	$+1$ or -1	Fixed
Nuisance	Description	Central value $\pm$ std. dev.	Prior Distribution
M_t	Top quark pole mass	173.5 ± 1.0	Gaussian
$m_b(m_b)^{\overline{MS}}_{\mathrm{SM}}$	Bottom quark mass	4.18 ± 0.03	Gaussian
$\alpha_s(M_Z)^{\overline{MS}}$	Strong coupling	0.1184 ± 0.0007	Gaussian
$1/\alpha_{\mathrm{em}}(M_Z)^{\overline{MS}}$	Inverse of electromagnetic coupling	127.916 ± 0.015	Gaussian

numerical scan we have included all relevant constraints; see Table 2 for a complete list. Suffice it to say that, in addition to dark matter density, at present three recent results from the LHC play a particularly important role in the analysis: (i) SM-like Higgs with mass 125 GeV; (ii) a lower limit on the plane $(m_0, m_{1/2})$ placed by a recent CMS analysis, for which we derived an approximate but very accurate likelihood function (see the right panel of Fig. 1 from Ref. [1]), and a comparable one obtained by ATLAS using 0-lepton search; and finally (iii) a new positive measurement of BR ($B_s \to \mu^+\mu^-$) by LHCb.

An obvious question arises whether such large ranges of SUSY mass parameters can be experimentally tested. Clearly, direct searches at the LHC will have only very limited potential in this respect, since gluino and squark masses will be probed up to about 3 and 2.7 TeV, respectively. Fortunately, there are two ways through which much larger ranges can be tested.

Firstly, future direct detection searches are expected to reach the sensitivity needed to explore basically the whole ranges of the spin-independent cross section σ_p^{SI} of dark matter scattering off nuclei. This is presented in Fig. 2. In the left panel we show 2-dim. marginalized posterior pdf in the $(m_\chi, \sigma_p^{\mathrm{SI}})$ plane for the CMSSM obtained by imposing the experiments listed in Table 2. In the left panel the current determination of BR ($B_s \to \mu^+\mu^-$), including also a substantial theory error, is used while in the right panel expected future uncertainties are assumed around the current SM value (which is slightly higher than the current central experimental value from LHCb). Note that the AF region is now absent as inconsistent with SM-like values of BR ($B_s \to \mu^+\mu^-$).

These properties of the CMSSM will allow one to basically fully explore the CMSSM for $\mu > 0$. In particular, the new generic 1 TeV higgsino region (which also appears in the NUHM?) will provide access to multi-TeV regions of M_{SUSY} via direct DM searches. This remains true for $\mu < 0$ as well, although well-known negative interference can reduce σ_p^{SI} way beyond expected experimental sensitivity for lower m_χ. Slight improvement over the current limits in σ_p^{SI} will also firmly rule out the FP/HB region which already now produces slightly too high σ_p^{SI}.

Beyond the CMSSM the role of direct detection of DM will remain very strong, including the CNMSSM [3] and even the MSSM with nine free parameters [4]. On the other hand, the discriminating role of BR ($B_s \to \mu^+\mu^-$) is less clear. While in general reducing the uncertainties in its determination (assuming it remains consistent with the SM) will rule out many otherwise allowed choices of parameters, it appears that only in the CMSSM this constraint can lead to removing the AF region from the $(m_0, m_{1/2})$, or alternatively $(m_\chi, \sigma_p^{\mathrm{SI}})$, plane. In more extended models the AF region overlaps with the other cosmologically favored regions and the impact of imposing projected BR ($B_s \to \mu^+\mu^-$) will be less clear-cut.

Table 2: The experimental measurements used to constrain the CMSSM's parameters. Masses are given in GeV.

Measurement	Mean or Range	Error: (Exp., Th.)	Distribution
Combination of:			
CMS razor 4.4/fb , $\sqrt{s} = 7\,\mathrm{TeV}$	See text	See text	Poisson
CMS α_T 11.7/fb , $\sqrt{s} = 8\,\mathrm{TeV}$	See text	See text	Poisson
m_h by CMS	$125.8\,\mathrm{GeV}$	$0.6\,\mathrm{GeV}, 3\,\mathrm{GeV}$	Gaussian
$\Omega_\chi h^2$	0.1120	0.0056, 10%	Gaussian
$\delta\,(g-2)_\mu^{\mathrm{SUSY}} \times 10^{10}$	28.7	8.0, 1.0	Gaussian
$\mathrm{BR}\left(\bar{\mathrm{B}} \to \mathrm{X_s}\gamma\right) \times 10^4$	3.43	0.22, 0.21	Gaussian
$\mathrm{BR}(\mathrm{B_u} \to \tau\nu) \times 10^4$	1.66	0.33, 0.38	Gaussian
ΔM_{B_s}	$17.719\,\mathrm{ps}^{-1}$	$0.043\,\mathrm{ps}^{-1}$, $2.400\,\mathrm{ps}^{-1}$	Gaussian
$\sin^2\theta_{\mathrm{eff}}$	0.23116	0.00012, 0.00015	Gaussian
M_W	80.385	0.015, 0.015	Gaussian
$\mathrm{BR}\left(\mathrm{B_s} \to \mu^+\mu^-\right)_{\mathrm{current}} \times 10^9$	3.2	$+1.5 - 1.2$, 10% (0.32)	Gaussian
$\mathrm{BR}\left(\mathrm{B_s} \to \mu^+\mu^-\right)_{\mathrm{proj.}} \times 10^9$	3.5 (3.2*)	0.18 (0.16*), 5% [0.18 (0.16*)]	Gaussian

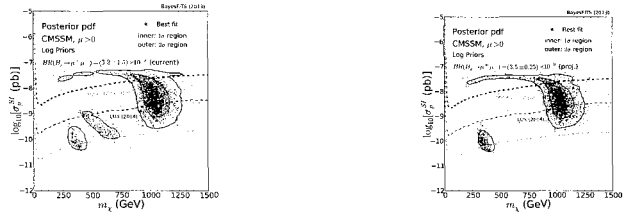

Figure 2: Left: A 2-dim. marginalized posterior pdf in the (m_χ, σ_p^{SI}) plane for the CMSSM constrained by the experiments listed in Table 2, including current uncertainties in $\mathrm{BR}\left(\mathrm{B_s} \to \mu^+\mu^-\right)$. The current XENON100 (dash-dot red) and projected LUX (dash purple) and 1-tonne (dash grey) limits are shown but not imposed. Right: The same but assuming a projected determination of $\mathrm{BR}\left(\mathrm{B_s} \to \mu^+\mu^-\right)$.

2 Procedure

In our analysis we simultaneously scan over wide ranges of the four CMSSM parameters and, in addition, over four SM nuisance parameters, as specified in Table 1. Random scans are done with our numerical code BayesFITS. The physical constraints that we impose are listed in Table 2. They are all defined and discussed in our papers [1,3,2,?].

Space limitations do not allow me to enter into a longer discussion of the procedure used and the whole range of our results. Below I will therefore only briefly summarize the main points and refer the reader to our papers for a detailed presentation of our analysis and a list of references.

The physical constraints, along with their respective experimental and theoretical errors, if available, are all incorporated in the analysis via a likelihood function. Positive measurements (e.g., the relic density $\Omega_\chi h^2$of neutralino dark matter) are all approximated by a Gaussian distribution, while experimental limits are smeared out by an error function.

References

1. A. Fowlie, et al., *Phys. Rev.* D **86**, 075010 (2012), arXiv:1206.0264.
2. K. Kowalska, L. Roszkowski, E. M. Sessolo, arXiv:1302.5956 (JHEP, to appear).
3. K. Kowalska, et al., *Phys. Rev.* D **87**, 115010 (2013), arXiv:1211.1693.
4. K. Kowalska, et al., arXiv:1306.1567.

3.
Heavy Flavour

HEAVY FLAVOUR PRODUCTION AT ATLAS AND CMS

E.V. BOUHOVA-THACKER on behalf of the ATLAS and CMS Collaborations
Department of Physics, Lancaster University,
Lancaster LA1 4YP, England

Recent measurements of open beauty and heavy quarkonium production, made by ATLAS and CMS at the Large Hadron Collider, are presented and compared to theoretical predictions.

1 Introduction

Large amounts of data have been collected by the experiments at the LHC, allowing detailed studies of heavy flavour production to be performed and setting new challenges to theory. This note presents an overview of recent results on open beauty and quarkonium production from the ATLAS and CMS collaborations, obtained using data collected at $\sqrt{s} = 7$ TeV.

2 Open Beauty Production

ATLAS have measured the B^+ production cross section [1] using 2.4 fb^{-1} of 2011 data, extending the p_T reach up to 120 GeV. Figure 1 (left) shows the B^+ cross section as a function of p_T. Superimposed are the CMS measurement for $p_T < 30$ GeV and the FONLL [2] prediction, both in good agreement with the ATLAS results.

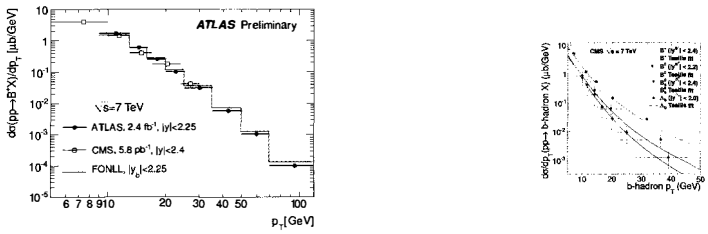

Figure 1: differential cross section of B^+ production as a function of p_T measured by the ATLAS collaboration (left), transverse momentum distribution of various B hadrons measured by the CMS collaboration (right)

An updated summary of the CMS measurements of the differential cross sections for beauty hadrons as a function of the transverse momentum of the hadrons is shown in Figure 1 (right), indicating steeper p_T distributions for heavier B hadrons.

The B hadron production cross section from partially reconstructed final states, $D^*\mu$, measured by ATLAS [3] is shown in Figure 2 (left) with a comparison to NLO predictions. The shape of the distribution is reproduced reasonably well, but the cross section is underestimated.

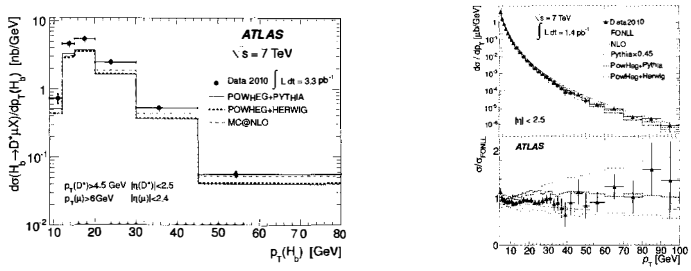

Figure 2: transverse momentum distributions of: partially reconstructed B hadrons [3] (left), and muons from heavy flavour decays [4] (right), measured by the ATLAS collaboration

Similar conclusions can be drawn from the studies of inclusive muons originating from heavy flavour decays, performed by ATLAS [4] and CMS [5]. While at lower p_T both NLO and FONLL perturbative QCD calculations show reasonable agreement with data, at high p_T, up to 100 GeV reached by ATLAS, FONLL represents the experimental data more accurately (Figure 2, right).

3 Charmonium Production

ATLAS and CMS have accumulated huge statistics of J/ψ and $\psi(2S)$ candidates decaying to two muons, allowing them to perform a multitude of measurements. Both particles can be produced either from prompt short-lived QCD sources, or from non-prompt, long-lived B hadron decays. Both cases include direct production as well as feed-down from excited states. The measured transverse decay length of the di-muon pair is used to separate prompt from non-prompt decays.

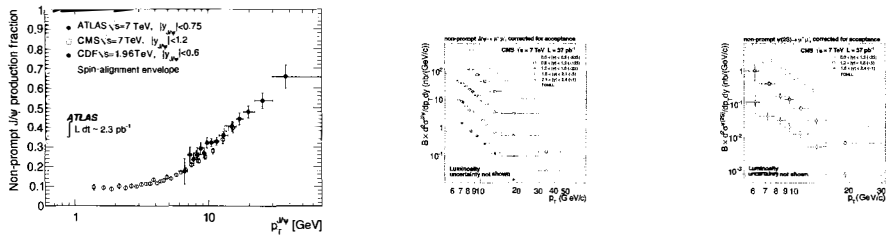

Figure 3: non-prompt J/ψ production fraction [7] at central rapidities (left) and transverse momentum distributions for non-prompt J/ψ (center) and $\psi(2S)$ (right) production [7]

The non-prompt fraction has been measured for J/ψ by ATLAS [6] and CMS [7] and for $\psi(2S)$ by CMS as a function of p_T and rapidity. The results (Figure 3, left), including CDF [8] measurements at low p_T, are in good agreement with each other. The non-prompt fraction of J/ψ starts at $\sim 10\%$ at low p_T and central rapidity and slowly increases to a plateau at high p_T, with the height of the plateau decreasing with increasing rapidity [6].

Figure 3 shows the double differential cross sections for non-prompt J/ψ (center) and $\psi(2S)$ (right), assuming unpolarised production. It is in agreement, within the uncertainties, with the FONLL calculations. There is an overall scale discrepancy observed for $\psi(2S)$.

The theoretical models seem to have more difficulty describing prompt charmonium decays. NLO calculations in Colour Singlet Models underestimate the data by a large factor as illustrated in Figure 4 (left). Inclusion of NNLO contributions [9] (without feed-down from χ_c states) improves things significantly, but the p_T dependence is still steeper than in data. The opposite is true for the Colour Evaporation Model [10]. Neither of these models has free parameters. Colour Octet

Models, such as NRQCD [11] use data to constrain a multitude of model parameters and as a consequence can describe the measured distributions reasonably well (Figure 4).

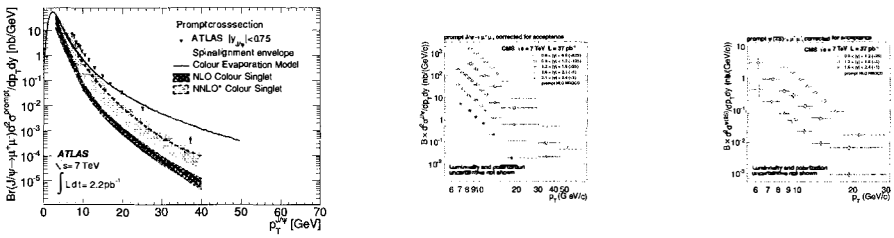

Figure 4: transverse momentum distributions for prompt J/ψ production measured by the ATLAS (left) and CMS (center) collaborations and prompt $\psi(2S)$ (right) production measured by the CMS collaboration

The production dynamics of $\psi(2S)$ are similar to J/ψ but do not include a significant feed-down from excited states. CMS [7] have measured the p_T dependence of the cross section ratio of $\psi(2S)$ to J/ψ. The non-prompt case (Figure 5, left) is described well by FONLL, while the NRQCD prediction for the prompt ratio (Figure 5, center), although consistent within the large theoretical uncertainties, seems to deviate at higher p_T.

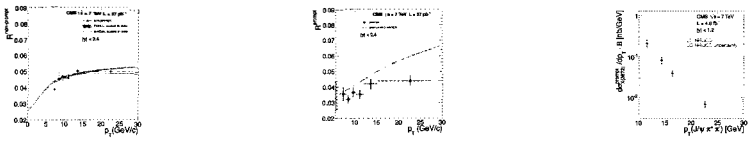

Figure 5: ratio of $\psi(2S)$ to J/ψ production cross sections as a function of p_T for non-prompt (left) and prompt (center) contributions, measured by CMS ; prompt $X(3872)$ production cross section (right), measured by CMS

CMS [12] have studied the production of X(3872) via decays to $J/\psi\pi^+\pi^-$. The ratio of the inclusive cross section to the $\psi(2S)$ one as a function of p_T and the fraction originating from B decays show no significant dependence on p_T. The prompt $X(3872)$ production cross section as a function of p_T is shown in Figure 5 (right). The NRQCD prediction significantly exceeds the measured value, while the p_T dependence is well described.

Figure 6: ratio of χ_{c2} to χ_{c1} production cross sections as a function of the J/ψ transverse momentum, measured by the CMS collaboration in $\chi_c \to J/\psi\gamma$ decays

The ratio of prompt χ_{c2} to χ_{c1} cross sections measured by CMS [13] is shown in Figure 6. The k_T factorisation prediction shape is in good agreement but a factor of 2 higher than the measurement (Figure 6, left), while NRQCD (with no specific prediction for the χ_c polarisations) is in reasonable agreement (Figure 6, right).

4 Bottomonium Production

ATLAS [14] have published results on the p_T and rapidity dependence of the production cross sections of $\Upsilon(1S)$, $\Upsilon(2S)$ and $\Upsilon(3S)$, which are in agreement with the previously published CMS results [15] but extend the p_T range up to 70 GeV (Figure 7). The measured cross section rates of $\Upsilon(2S)$ and $\Upsilon(3S)$ to $\Upsilon(1S)$ show a non-trivial p_T dependence, confirming the existence of multiple production mechanisms. The production of a new orbitally excited χ_b state, first announced by ATLAS [16], means that all three Υ states are subject to feed-down from χ_b states. The comparison with theoretical models leads to conclusions similar to the charmonium case: the Colour Singlet, Colour Evaporation [10] and Colour Octet Models [11] show reasonable agreement with data but none can reproduce the full range.

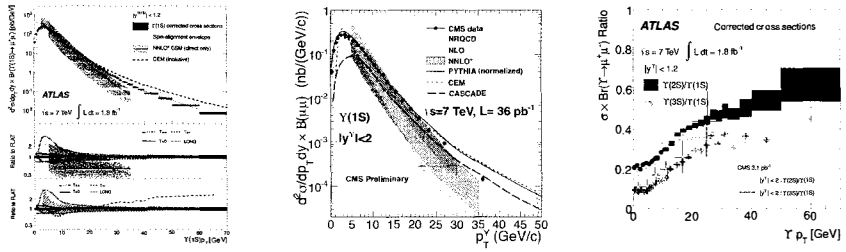

Figure 7: transverse momentum distributions for $\Upsilon(1S)$ production measured by ATLAS (left) and CMS (center); ratios of the production cross sections of $\Upsilon(2S)$ to $\Upsilon(1S)$ and $\Upsilon(3S)$ to $\Upsilon(1S)$, measured by ATLAS (right)

References

1. ATLAS collaboration, ATLAS-CONF-2013-008.
2. M. Cacciari *et al*, *JHEP* **05**, 007 (1998), *JHEP* **03**, 006 (2001).
3. ATLAS collaboration, *Nucl. Phys.* B **864**, 341 (2012).
4. ATLAS collaboration, *Phys. Lett.* B **707**, 438 (2012).
5. CMS collaboration, *JHEP* **06**, 110 (2012); CMS collaboration, *JHEP* **1103**, 090 (2011).
6. ATLAS collaboration, *Nucl. Phys.* B **850**, 387 (2012).
7. CMS collaboration, *Eur. Phys. J.* C **71**, 1575 (2011); CMS collaboration, *JHEP* **02**, 011 (2012).
8. CDF collaboration, *Phys. Rev.* D **71**, 032001 (2005); CDF collaboration, *Phys. Rev.* D **80**, 031103 (2009).
9. J.P. Lansberg, *Eur. Phys. J.* C **61**, 693 (2009); J.P. Lansberg, arXiv:1006.2750 [hep-ph].
10. V.D. Barger *et al*, *Phys. Lett.* B **91**, 253 (1980); A.D. Frawley *et al*, *Phys. Rep.* **462**, 125 (2008).
11. P. Artoisenet *et al*, *Phys. Lett.* B **653**, 60 (2007), *JHEP* **02**, 102 (2008), *Phys. Rev.* D **81**, 114018 (2010); Y.-Q. Ma *et al*, *Phys. Rev. Lett.* **106**, 042002 (2011), *Phys. Rev.* D **83**, 111503 (2011); B. Gong *et al*, *JHEP* **02**, 102 (2008); M. Butenschon *et al*, *Phys. Rev. Lett.* **106**, 022003 (2011).
12. CMS collaboration, arXiv:1210.0875 [hep-ph].
13. CMS collaboration, *Eur. Phys. J.* C **72**, 2251 (2012).
14. ATLAS collaboration, arXiv:1211.7255 [hep-ph].
15. CMS collaboration, *Phys. Rev.* D **83**, 112004 (2011).
16. ATLAS collaboration, *Phys. Rev. Lett.* **108**, 152001 (2012).

MEASUREMENT OF HEAVY-FLAVOR PROPERTIES AT CMS AND ATLAS

R. COVARELLI
Department of Physics and Astronomy, University of Rochester, 14627, Rochester, NY, United States

Thanks to the excellent performances of ATLAS and CMS in triggering on muon signals and reconstructing these particles down to low transverse momentum, large samples of heavy-flavored hadrons have been collected in the 2011 LHC run at $\sqrt{s} = 7$ TeV. The analysis of these samples has enabled both experiments to perform competitive measurements of heavy-flavor properties, such as quarkonium polarization, lifetime and CP-violation measurements, hadron spectroscopy and branching ratios of rare B decays.

ATLAS and CMS capabilities in heavy-flavor physics are almost entirely based on muon and di-muon triggers, which can collect signals down to low transverse momenta (typical values for thresholds range between 3 and 6 GeV/c), while maintaining a reasonable background rate by using high-level selection criteria. Muons are reconstructed offline using techniques which match information from the inner tracking detectors and the muon chambers, and are combined to reconstructed charged tracks to form partially and fully reconstructed final states, like for instance $B_s \to J/\psi\phi$. All analyses presented are based on the data collected by ATLAS and CMS in 2011, at a center-of-mass energy of 7 TeV, which amounts to an integrated luminosity up to 5.0 fb^{-1}.

1 Quarkonium Polarization

Theoretical predictions on quarkonium polarization at production in hadron colliders are still controversial. Calculations in Non-Relativistic QCD (NRQCD) schemes, including the color-octet mechanism, require inputs from experimental data [1] and the effect of feed-down from heavier charmonium states can be significant [2]. Recent results from the CDF experiment [3], which use advanced experimental techniques, including a simultaneous determination of all polarization parameters in difference reference frames [4], indicate that Υ mesons are not significantly polarized at high transverse momentum ($p_T \gg m_\Upsilon$). NRQCD would predict preponderance of transverse polarization.

CMS [5] performed a measurement of Υ(1S), Υ(2S) and Υ(3S) polarizations in a p_T range of 10-50 GeV/c and two rapidity bins. The method is based on the construction of posterior probability distributions which depend on the values of the polarization angles $\cos\theta$ and ϕ

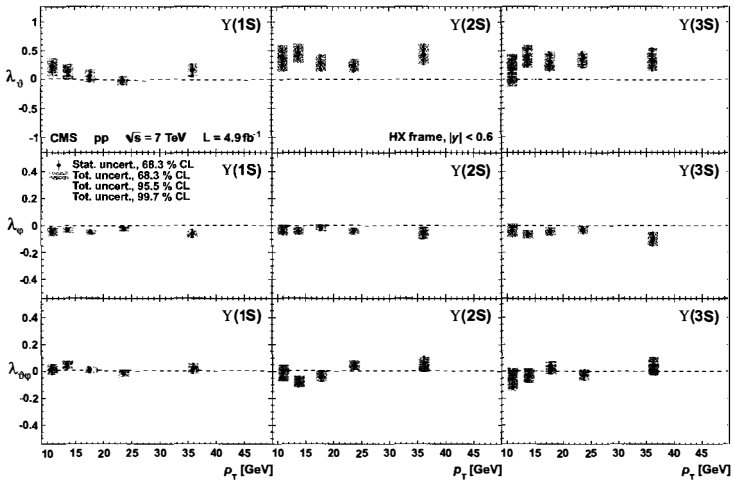

Figure 1: Fitted values of the polarization parameters λ_θ, λ_ϕ, $\lambda_{\theta\phi}$ (rows) in the helicity frame and in the rapidity bin $|y| < 0.6$ for the three states Υ(1S), Υ(2S) and Υ(3S) (columns). The notation for uncertainties is explained in the legend.

of reconstructed dimuons and on the reconstruction efficiencies, computed as a function of muon kinematic variables. Background is subtracted using fits to the dimuon invariant mass distributions. Muon efficiencies are extracted from data-driven methods[6]. The result is extracted in several reference frames and the result is cross-checked using frame-independent polarization parameters. Results for the three quarkonium states in the helicity frame are shown in Fig. 1: all of them are compatible with zero within the total uncertainties.

2 Lifetimes and CP violation

B-hadron lifetime values (and lifetime differences in case of oscillating meson systems) represent important tests of Heavy Quark Effective Theory (HQET) and lattice QCD. Experimentally the least known among B-hadron lifetimes is $\tau(\Lambda_b)$: CDF and D0 results are not in agreement[7] on its measured value and the PDG average value shows a discrepancy with HQET calculations up to order $1/m_b^2$, therefore specific corrections must be introduced to improve the consistency[8].

ATLAS and CMS [9] have measured the Λ_b lifetime, with ATLAS also reporting a mass measurement. In both experiments the decay channel $J/\psi\Lambda^0 \to \mu^+\mu^- p\pi^-$ has been used to reconstruct the Λ_b baryon, profiting from the clean dimuon signature and the displaced decay vertex of the Λ^0. The mass and lifetime values have been extracted from simultaneous fits to the $J/\psi\Lambda^0$ invariant mass (using mass constraints of the sub-products) and proper decay time distributions. Selection biases have been corrected using simulation. ATLAS obtains: $m(\Lambda_b) = 5619.7 \pm 0.7_{\text{stat.}} \pm 1.1_{\text{syst.}}$ MeV/c^2 and $\tau(\Lambda_b) = 1.449 \pm 0.036_{\text{stat.}} \pm 0.017_{\text{syst.}}$ ps, while CMS measures $\tau(\Lambda_b) = 1.503 \pm 0.052_{\text{stat.}} \pm 0.031_{\text{syst.}}$ ps. Both results are in better agreement with CDF than with D0 results, although the compatibility between the ATLAS and D0 values is within 1.6σ.

Of particular relevance for the indirect search for New Physics (NP) in processes described by "box" and "loop" diagrams is the measurement of the B_s mixing phase ($\phi_s = -2\beta_s$), whose value in the Standard Model is tightly constrained by precise measurements of quantities related to the unitarity triangle in the B_d system [10]. Its value, computed in the Standard Model (SM) hypothesis (only one CP-violating phase) is $\boldsymbol{\phi_s} = -0.0364 \pm 0.0016$ rad. Experimentally the

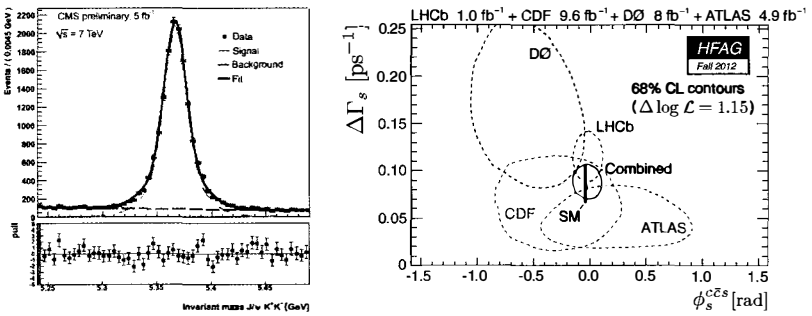

Figure 2: Left: Reconstructed $J/\psi\phi$ invariant mass in CMS with projections of the 5-dimensional fit: colored lines are explained in the legend. Right: Combination of ATLAS, Tevatron and LHCb results in the $\Delta\Gamma_s$-ϕ_s plane.

measurement can be performed using B_s decays to CP eigenstates. In the results presented here, ATLAS and CMS do not use techniques to identify the flavor of the B_s meson at production and the sensitivity to ϕ_s remains limited. CMS only measured $\Delta\Gamma_s$, fixing ϕ_s to the SM value, while ATLAS has determined both.

ATLAS and CMS [11] use the $B_s \to J/\psi\phi \to \mu^+\mu^- K^+K^-$ final state, which is relatively abundant and clean (Fig. 2 left). Because of the entangled CP-even and -odd contributions in the vector-vector meson system, the result is obtained from a five-dimensional fit to B_s mass, proper decay time, and three angular variables related to the distribution in space of the final decay products. The CMS result is $\Delta\Gamma_s = 0.048 \pm 0.024_{\text{stat.}} \pm 0.003_{\text{syst.}}$ ps^{-1}, while ATLAS measures $\Delta\Gamma_s = 0.053 \pm 0.021_{\text{stat.}} \pm 0.010_{\text{syst.}}$ ps^{-1} and $\phi_s = 0.22 \pm 0.41_{\text{stat.}} \pm 0.10_{\text{syst.}}$. While both experiments report values of $\Delta\Gamma_s$ noticeably smaller than the latest high-precision measurement by LHCb [12], this discrepancy is not statistically significant. Fig. 2 right shows the comparison of ATLAS and LHCb results using two-dimensional likelihood contours [13].

3 Hadron spectroscopy

Theories which explain the formation of hadrons often predict a very large number of states with similar quark structure and different quantum numbers. The quark model predicts baryonic combinations with one or more bottom and charm quarks, many of which have not been observed yet. Similarly, the spectroscopy of $c\bar{c}$, $b\bar{b}$ and $c\bar{b}$ states has been experimentally confirmed in many cases. Still states exist (even below the open-charm and -bottom thresholds) which have never been identified. On the other hand, the existence of a few "unconventional" states, like the $X(3872)$, which are interpreted as bound states but do not fit in the spectroscopy predicted by potential models, has been established.

ATLAS and CMS have performed searches for conventional and exotic hadron states. Using the decay chain $\Xi_b^{0*} \to \pi^+\Xi_b^- \to \pi^+ J/\psi\Xi^- \to \pi^+\mu^+\mu^-\pi^-\Lambda^0 \to \pi^+\mu^+\mu^-\pi^- p\pi^-$, CMS has observed the $J^P = 3/2^+$ partner of the Ξ_b^0. The presence of three weakly decaying particles in the chain, giving rise to detached vertices, has allowed to isolate a clean signal, as shown in Fig. 3 left. The measured mass is $5945.0 \pm 0.7_{\text{stat.}} \pm 0.3_{\text{syst.}} \pm 2.7_{m(\Xi_b^-)}$ MeV/c^2, in agreement with theoretical predictions [14]. ATLAS reported the first observation of the $\chi_b(3P)$ bottomonium state (actually the superposition of three states with different total spin) using the decay mode $\chi_b(3P) \to \Upsilon(1S,2S)\gamma \to \mu^+\mu^-\gamma$ or $\to \mu^+\mu^- e^+e^-$, where the photon conversion occurs inside the detector material [15]. The signals are shown in Fig. 3 right (for the converted-photon case), and the measured mass is $10530 \pm 5_{\text{stat.}} \pm 9_{\text{syst.}}$ MeV/c^2. Both observations exceed 6σ significance.

CMS and ATLAS have detected clear signals of $B_c^\pm \to J/\psi\pi^\pm$ (CMS also reporting evidence

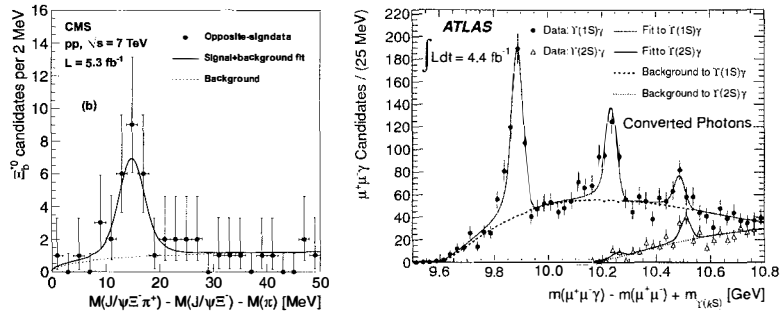

Figure 3: Left: Invariant mass difference (Δm) between the reconstructed $\pi^+\Xi_b^-$ and Ξ_b^- systems in CMS. About 20 events are peaking at $\Delta m \simeq 15$ MeV/c^2, indicating a resonant state. Right: $\Upsilon(n\mathrm{S})\gamma$ ($n = 1, 2$) reconstructed invariant mass in ATLAS, fixing the $\Upsilon(n\mathrm{S})$ masses to their PDG values. The rightmost peaks correspond to the newly-observed $\chi_b(3\mathrm{P})$ state.

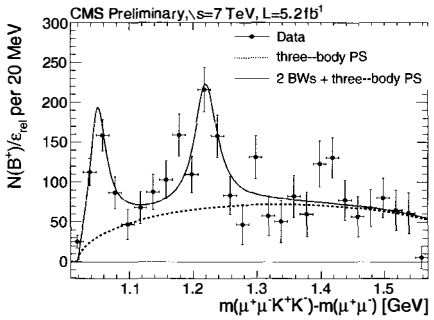

Figure 4: Invariant mass difference (Δm) between the reconstructed $J/\psi\phi$ and J/ψ systems in CMS, obtained with a bin-by-bin background subtraction technique. The distribution is fitted with a phase-space background and two Breit-Wigner shapes convoluted with resolution functions obtained from simulation.

for $B_c^\pm \to J/\psi\pi^+\pi^-\pi^\pm$) from which cross sections and ratios of branching fractions will be measured. CMS has also investigated possible resonant structures of the $J/\psi\phi$ system in the $B^\pm \to J/\psi\phi K^\pm$ decay, in order to confirm the CDF observation of a structure at $m_{J/\psi\phi} \simeq 4140$ MeV/c^2 [16]. As shown in Fig. 4, two structures are clearly seen in the bin-by-bin subtracted invariant mass spectrum of the $J/\psi\phi$ system. Further studies are ongoing in order to understand the exact nature of these structure.

4 Rare B decays

In ATLAS and CMS searches for $B_{d,s} \to \mu^+\mu^-$ decays have been performed [17]. These decays are predicted to be rare in the SM and a significant enhancement over the SM branching ratios ($\mathcal{B}_{\mathrm{SM}} \sim 10^{-10} - 10^{-9}$ [18]) is possible in most supersymmetric theories [19]. An observation of a non-SM value of the branching fraction would therefore represent an indirect evidence for NP.

In both experiments, a "normalization" sample of events with $B^+ \to J/\psi K^+$ decays is used to remove uncertainties related to the $b\bar{b}$ production cross section and the integrated luminosity, and to reduce uncertainties on efficiencies, which are determined from simulation. Selection is based on several variables, including high p_T, vertex displacement and dimuon isolation, which have been chosen to mitigate the effects of high pileup. A "blind" analysis approach is applied.

In ATLAS the selection variables are included in a Boosted Decision Tree (BDT), while CMS uses a cut-based selection, and both analyses are optimized for the best upper limit. In CMS, because of better mass resolution, the signal is separated in B_d and B_s regions.

Event-counting experiments are performed in dimuon mass regions around the B_s and B_d masses. Monte Carlo simulations are used to estimate backgrounds due to other rare B decays and combinatorial backgrounds are evaluated from the data in dimuon invariant mass sidebands. In all cases, the observed number of events is consistent with background plus SM signals. In CMS the resulting upper limits on the branching fractions are $\mathcal{B}(B_s \to \mu^+\mu^-) < 7.7 \times 10^{-9}$ and $\mathcal{B}(B_d \to \mu^+\mu^-) < 1.8 \times 10^{-9}$ at 95% CL, while ATLAS sets the limit $\mathcal{B}(B_s \to \mu^+\mu^-) < 2.2 \times 10^{-8}$ at 95% CL. It has been predicted[20] by naive luminosity scaling that CMS is expected to observe a SM $\mathcal{B}(B_s \to \mu^+\mu^-)$ with more than 3σ significance using the full data set at $\sqrt{s} = 8$ TeV.

References

1. M. Butenschön and B.A. Kniehl, *Mod. Phys. Lett.* A **28**, 1350027 (2013).
2. H.S. Shao and K.T.Chao, `arXiv:1209.4610`.
3. CDF Collaboration, *Phys. Rev. Lett.* **108**, 151802 (2012).
4. P. Faccioli *et al.*, *Phys. Rev. Lett.* **105**, 061601 (2010).
5. CMS Collaboration, *Phys. Rev. Lett.* **110**, 081802 (2012).
6. CMS Collaboration, *JINST* **7**, P10002 (2012).
7. CDF Collaboration, *Phys. Rev. Lett.* **106**, 121804 (2011); D0 Collaboration, *Phys. Rev.* D **85**, 112003 (2012).
8. F. Gabbiani *et al.*, *Phys. Rev.* D **70**, 094031 (2004).
9. CMS Collaboration, `arXiv:1304.7495`, submitted to *JHEP* (2013); ATLAS Collaboration, *Phys. Rev.* D **87**, 032002 (2012).
10. `http://ckmfitter.in2p3.fr/www/results/plots_ichep12/num/ckmEval_results.html`.
11. CMS Collaboration, CMS-PAS-BPH-11-006, ATLAS Collaboration *JHEP* **12**, 072 (2012).
12. LHCb Collaboration, `arXiv:1304.2600`, submitted to *Phys. Rev.* D (2013).
13. `http://www.slac.stanford.edu/xorg/hfag/osc/fall_2012`.
14. CMS Collaboration, *Phys. Rev. Lett.* **108**, 252002 (2012).
15. ATLAS Collaboration, *Phys. Rev. Lett.* **108**, 152001 (2012).
16. CDF Collaboration, *Phys. Rev. Lett.* **102**, 242002 (2009);
17. CMS Collaboration, *JHEP* **04**, 033 (2012); ATLAS Collaboration, *Phys. Lett.* B **713**, 180 (2012).
18. A. Buras *et al.*, *Eur. Phys. J.* C **72**, 2172 (2012).
19. G. Isidori and P. Paradisi, *Phys. Lett.* B **639**, 499 (2006).
20. D. Akeroyd *et al.*, *JHEP* **12**, 088 (2011).

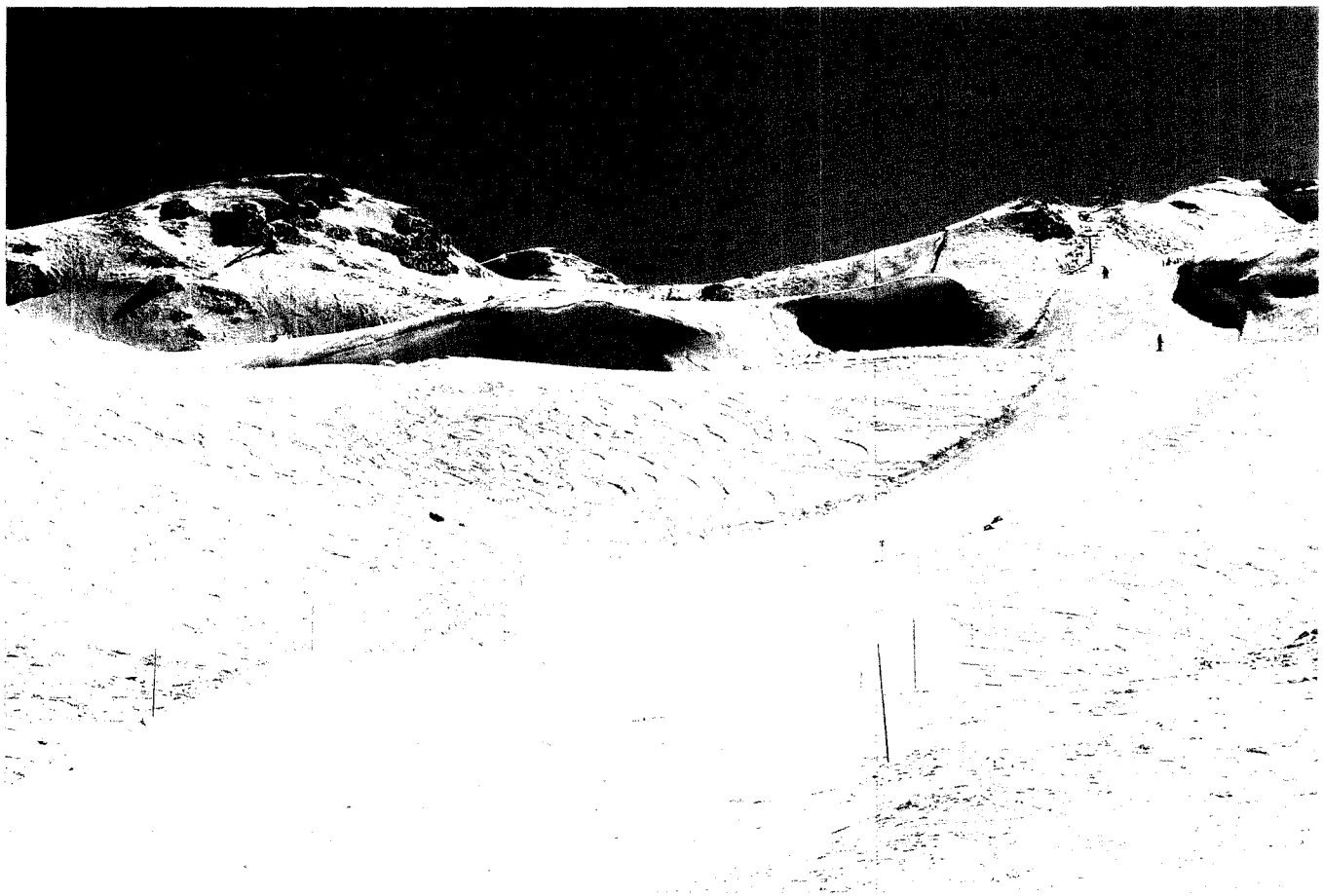

Measurement of γ Angle Using $B \to DK$ at LHCb

Wenbin Qian
on behalf of the LHCb Collaboration
Laboratoire d'Annecy-le-Vieux de Physique des Particules
Université de Savoie, CNRS/IN2P3, Annecy-le-Vieux, France

Measurements of the CKM angle γ via tree-level $b \to u$ and $b \to c$ interference are important for testing the Standard Model through the CKM unitarity constraint. In these proceedings, CP violation measurements with $B \to DK$ decays using 1 fb^{-1} of data collected in 2011 by LHCb are described, where 2-body ($\pi^+\pi^-$, K^+K^-, $K^+\pi^-$ and $K^-\pi^+$), 3-body ($K_s\pi^+\pi^-$ and $K_sK^+K^-$) and 4-body ($K^+\pi^-\pi^+\pi^-$ and $K^-\pi^+\pi^+\pi^-$) D^0 decays are considered. A combined measurement of γ using the above channels is also presented.

1 The LHCb Experiment

The LHCb apparatus [1] is an single-armed forward spectrometer covering the pseudo rapidity range $2 < \eta < 5$, designed for the study of particles containing b or c quarks. The tracking system has a momentum resolution $\Delta p/p$ that varies from 0.4% at 5 GeV/c and 0.6% at 100 GeV/c which gives a mass resolution of 10–25 MeV/c^2 depending on decay modes. One of the crucial points for the measurement of γ through B to open charm decays is hadron identification. Two ring-imaging Cherenkov detectors are used to identify charged hadrons and they offer a 95% kaon identification efficiency with a 5% pion-to-kaon misidentification rate.

The LHCb trigger consists of a hardware trigger based on information from the calorimeter and muon systems, followed by a software stage, which applies a full event reconstruction. The hardware trigger reduces the event rates from 40 MHz to 1 MHz which is further reduced to 5 kHz by the software trigger. It offers an efficiency around 20-50% for B decays with hadrons, depending on final states.

During the past two years of operation, the LHCb experiment collected 1.0 fb^{-1} of data at 7 TeV in 2011 and around 2 fb^{-1} at 8 TeV in 2012 with constant instantaneous luminosity during each bunch fill. The constant luminosity makes physics analysis less affected by pile-up effects. The results in this paper are obtained with the first 1 fb^{-1} of data.

2 The CKM Angle γ

The CKM angle γ, defined as $\gamma = \arg[-V_{ud}V_{ub}^*/(V_{cd}V_{cb}^*)]$, is one of the least well-measured parameters of the CKM unitarity triangle defined through the relation $V_{ud}V_{ub}^* + V_{cd}V_{cb}^* + V_{td}V_{tb}^* = 0$. A precise measurement of γ from tree-level interference is crucial to overconstrain the unitarity triangle while the comparison between γ at tree-level and γ at loop-level may shed light on new physics. As new physics is not expected to affect tree-level processes, γ at tree-level is theoretically clean and the relative precision $\delta\gamma/\gamma$ predicted by Standard Model is at $O(10^{-6})$. The γ angle can be accessed by different channels with interference between $b \dashrightarrow c$ and $b \to u$ transitions, it is thus important to combine measurements from different modes for better precision. It has been measured by various experiments [2,3]; the current combined precision is around $10 - 12^{\circ}$ [4,5]

Several methods to measure γ in tree decays using $B^- \to DK^-$ [a] are established, where D indicates a D^0 or $\bar{D}^0$ in this paper. There are three main methods according to different type of D decays:

1. : Gronau-London-Wyler (GLW) method [6]: γ is obtained through interference between $B^- \to D^0K^-$ and $B^- \to \bar{D}^0K^-$ where the D^0 or $\bar{D}^0$ decays to 2-body CP eigenstates, i.e. $D \to K^+K^-$, $D \to \pi^+\pi^-$ etc.

2. : Atwood-Dunietz-Soni (ADS) method [7]: γ is accessed through interference between the favoured $b \to c$ transition combined with the double-Cabbibo-suppressed $D^0 \to K^+\pi^-$ decay, and the suppressed $b \to u$ transition combined with the Cabbibo-favoured $\bar{D}^0 \to K^+\pi^-$ decay.

3. : Giri-Grossman-Soffer-Zupan (GGSZ) method [8]:γ is obtained through interference between $B^- \dashrightarrow D^0K^-$ and $B^- \to \bar{D}^0K^-$ where the D^0 or $\bar{D}^0$ meson decays to self-conjugated multi-body final states, i.e. $D \to K_s\pi^+\pi^-$, $D \to K_sK^+K^-$ etc.

The decay rate can be generally written as:

$$\Gamma(B^{\pm} \to D[\to f]K^{\pm}) = A_c^2(r_D^2 + (r_B^K)^2 + 2r_B^K r_D \mathrm{Re}(e^{i(\delta_B^K + \delta_D \pm \gamma)})), \quad (1)$$

where δ_B^K, δ_D are strong phase difference for B and D decays with different transition; r_B is the amplitude ratio between $b \to u$ and $b \to c$ transitions; r_D is the ratio of D decay amplitudes; A_c is the normalisation factor which can be cancelled out. r_B^K is around 0.1 for $B \dashrightarrow DK$ which gives better sensitivity on γ than $B \to D\pi$ decays ($r_B^{\pi} \sim 0.01$) [9]. Time-integrated CP violation using the above three methods with $B \to DK$ are measured by LHCb and discussed in the following section.

3 γ studies with $B \to DK$ at LHCb

3.1 Two-body D Decays

The following two-body D decay channels are studied: $D \to K^+K^-$, $D \to \pi^+\pi^-$, $D^0 \to K^+\pi^-$ and $D^0 \to K^-\pi^+$ with which a combined GLW and ADS analysis is performed [10]. The observables, for the GLW mode, are $R_{CP+} = 2\frac{\Gamma(B^- \to D_{CP+}K^-) + \Gamma(B^+ \to D_{CP+}K^+)}{\Gamma(B^- \to D^0K^-) + \Gamma(B^+ \to \bar{D}^0K^+)}$ and $A_{CP+} = \frac{\Gamma(B^- \to D_{CP+}K^-) - \Gamma(B^+ \to D_{CP+}K^+)}{\Gamma(B^- \to D^0K^-) + \Gamma(B^+ \to \bar{D}^0K^+)}$, which depend on γ by $R_{CP+} = 1 + (r_B^K)^2 + 2r_B^K \cos\delta_B^K \cos\gamma$ and $A_{CP+} = \frac{2r_B^K \sin\delta_B^K \sin\gamma}{R_{CP+}}$. Similar variables and their relationship with $r_B^K, \delta_B^K, \gamma$ can be defined and deduced for the ADS mode [7].

[a] Charge-conjugation is implied throughout this paper unless otherwise stated.

The above defined variables are calculated using signal yields in B^- and B^+ decays, where most of efficiency effects cancel out except those from detection asymmetry and production asymmetry which are obtained from control samples. We obtain the following results:

$$\begin{aligned} R_{CP+} &= 1.007 \pm 0.038 \pm 0.012, \\ A_{CP+} &= 0.145 \pm 0.032 \pm 0.010 \end{aligned}$$

for the GLW method, averaged over $D \to K^+K^-$ and $D \to \pi^+\pi^-$, which corresponds to a CP violation of 4.5σ significance and

$$\begin{aligned} R_{ADS}(K) &= 0.0152 \pm 0.0020 \pm 0.0004, \\ A_{ADS}(K) &= -0.52 \pm 0.15 \pm 0.02 \end{aligned}$$

for the $B \to DK$ ADS method, which corresponds to a 4.0σ significance CP violation. The first uncertainty of the result is statistical and the second one is the systematic uncertainty. Combining the two methods, we have the first observation of direct CP violation at 5.8σ significance in the 2-body D decays of $B \to DK$.

3.2 Three-body D Decays

A model independent method is applied for the GGSZ mode with $D \to K_s\pi^+\pi^-$ and $D \to K_sK^+K^-$ [11] using inputs from CLEO measurements [12]. The Dalitz plots are divided into different bins (16 for $D \to K_s\pi^+\pi^-$ and 4 for $D \to K_sK^+K^-$) according to the distributions obtained from Dalitz analysis. It should be noted that the analysis is independent from Dalitz modelling, any deviation from reality only reduces the sensitivity to γ but does not introduce bias. The number of events in each bin is given by

$$N^+_{\pm i} = h_{B^+}[K_{\mp i} + (x_+^2 + y_+^2)K_{\mp i} + 2\sqrt{K_iK_{-i}}(x_+c_{\pm i} \mp y_+s_{\pm i})], \quad (2)$$

$$N^-_{\pm i} = h_{B^-}[K_{\pm i} + (x_-^2 + y_-^2)K_{\mp i} + 2\sqrt{K_iK_{-i}}(x_-c_{\pm i} \pm y_-s_{\pm i})], \quad (3)$$

where $h_{B\pm}$ is the normalisation factor for $B^\pm$, K_i represent the Dalitz distribution in flavour-tagged D decays; c_i and s_i are inputs from CLEO measurements. $x_\pm = \mathrm{Re}[r_B^K e^{i(\delta_B^K \pm \gamma)}]$ and $y_\pm = \mathrm{Im}[r_B^K e^{i(\delta_B^K \pm \gamma)}]$ are the quantities to be measured. In total, we have around 660 signals in the $K_s\pi^+\pi^-$ mode and 100 signals in the $K_sK^+K^-$ mode. The best fitted value for $x_\pm$ and $y_\pm$ are:

$$\begin{aligned} x_- &= (0.0 \pm 4.3 \pm 1.5 \pm 0.6) \times 10^{-2}, \\ y_- &= (2.7 \pm 5.2 \pm 0.8 \pm 2.3) \times 10^{-2}, \\ x_+ &= (-10.3 \pm 4.5 \pm 1.8 \pm 1.4) \times 10^{-2}, \\ y_+ &= (-0.9 \pm 3.7 \pm 0.8 \pm 3.0) \times 10^{-2}, \end{aligned}$$

where the first error is the statistical uncertainty, the second one is the systematic uncertainty and the third one is the uncertainty from CLEO inputs. Using the above value, we can extra γ from the GGSZ mode only, which give a value of $(44^{+43}_{-38})^\circ$.

3.3 Four-body D Decays

There are also measurements using 4-body decays $D^0 \to K^-\pi^+\pi^-\pi^+$ and $D^0 \to K^+\pi^-\pi^+\pi^-$ [13]. An analysis similar to 2-body ADS analysis is performed. There are around 40 signals observed for the ADS $B \to DK$ mode which corresponds to 5.7σ observation and around 160 signals for the ADS $B \to D\pi$ mode which corresponds to more than 10σ observation. The measured value for $R^{K3\pi}_{ADS}(K)$ and $A^{K3\pi}_{ADS}(K)$ are 0.0124 ± 0.0027 and -0.42 ± 0.22 respectively. This is then used to give constraint on r_B^K which yields $r_B^K = 0.097 \pm 0.011$.

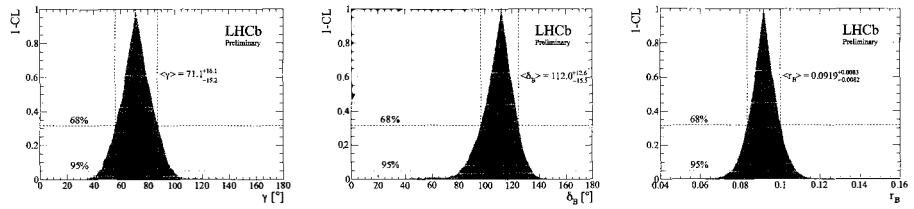

Figure 1: 1 - CL curves for γ (left), δ_B (centre) and r_B^K (right) from the combination of the measurements using $B \to DK$ decays.

3.4 γ Combination

Using the above measurements, the recent evidence for a difference in the CP asymmetries in $D \to K^+K^-$ and $D \to \pi^+\pi^-$, $\Delta a_{CP}^{dir} = (-0.656 \pm 0.154) \times 10^{-2}$ [14] and the CLEO inputs [15], a combination is made to extra γ [16]. A frequentist technique is used with D mixing effect ignored at this level. The confidence level (CL) curves of γ, δ_B and r_B^K are shown in Fig. 1. The most probable value of γ is 71.1 with 68% CL interval $[55.4, 87.7]^\circ$ and 95% CL interval $[41.4, 101.3]^\circ$. The fitted value for r_B^K and δ_B^K are 0.092 ± 0.008 and $(112.0^{+12.6}_{-15.5})^\circ$. The results are in agreement with the combined results measured by Babar [2] and Belle [3] with similar precision.

4 Conclusion

In this paper, the results of $B \to DK$ measurement at the LHCb experiment using 1 fb^{-1} of data are described. A combination is made which gives $\gamma = 71.1^\circ$ with an uncertainty around 16°; it is in agreement with the combined results published by other experiments.

References

1. A. A. Alves Jr. *et al.* (LHCb Collaboration), JINST 3 (2008) S08005
2. J. P. Lees *et al.* (BABAR Collaboration), arXiv: 1301.1029
3. K. Trabelsi (Belle Collaboration), arXiv: 1301.2033
4. J. Charles *et al.* (CKMfitter Group), Eur. Phys. J. C41, 1(2005), updated results and plots available at: http://ckmfitter.in2p3.fr
5. D. Derkach (UTfit Collaboration), arXiv: 1301.3300, updated results and plots available at: http://www.utfit.org/UTfit
6. M. Gronau and D. Wyler, Phys. Lett. B 253 (1991) 483; M. Gronau and D. London, Phys. Lett. B 265 (1991) 172
7. D. Atwood, I. Dunietz and A. Soni, Phys. Rev. Lett. 78 (1997) 3257
8. A. Giri, Y. Grossman, A. Soffer and J. Zupan, Phys. Rev. D68 (2003) 054018
9. J. Beringer *et al.* (Particle Data Group), Phys. Rev. D86, 010001 (2012)
10. R. aaij *et al.* (LHCb Collaboration), Phys. Lett. B 712 (2012) 203, arXiv: 1203.3662
11. R. aaij *et al.* (LHCb Collaboration), Phys. Lett. B 718 (2012) 43, arXiv: 1209.5869
12. J. Libby *et al.* (CLEO Collaboration), Phys. Rev. D80, 031105 (2009)
13. R. aaij *et al.* (LHCb Collaboration), arXiv: 1303.4646
14. Y. Amhis *et al.* (Heavy Flavor Averaging Group), arXiv: 1207.1158
15. N. Lowrey *et al.* (CLEO Collaboration), Phys. Rev. D80, 031105 (2009)
16. R. Aaij *et al.* (LHCb Collaboration), LHCb-CONF-2012-032

Indirect CP violation in the B_s^0 system at LHCb

Wouter Hulsbergen,
on behalf of the LHCb collaboration
Nikhef National Institute for Subatomic Physics, Amsterdam, The Netherlands

Meson-anti-meson mixing in the B_s^0 system is considered a sensitive prove of physics beyond the standard model. In this talk I summarize recent LHCb measurements of the mixing frequency, time-dependent CP violation, the B_s^0 lifetime and decay width difference and the flavour-specific asymmetry.

1 Introduction

Neutral mesons exhibit an intriguing phenomenon called flavour mixing: Because the weak interaction eigenstates are not the same as the eigenstates of the total hamiltonian, the flavour content of neutral mesons changes as a function of time. This process leads to CP violating effects that allow for stringent tests of the SM. Measurements of mixing phenomena in the B_s^0 system are particularly interesting, because, thanks to the fact that $m_B \gg \Lambda_{QCD}$, SM calculations have small uncertainty. Furthermore, new contributions to $b \to s$ transitions are so far relatively poorly constrained.

Pedagogical introductions to neutral meson mixing can be found elsewhere, e.g. in [1]. Here, we just introduce the notation. Consider the wave function $B^0(t)$ for a neutral meson that is the superposition of flavour eigenstates B^0 and $\bar{B}^0$. The time-evolution of its projections into flavour eigenstates is given by a Schrödinger equation (we adopt units such that $\hbar = c = 1$)

$$i\,\frac{\mathrm{d}}{\mathrm{d}t}\begin{pmatrix}\langle B^0|B^0(t)\rangle\\ \langle \bar{B}^0|B^0(t)\rangle\end{pmatrix} = \left[M - \frac{i}{2}\Gamma\right]\begin{pmatrix}\langle B^0|B^0(t)\rangle\\ \langle \bar{B}^0|B^0(t)\rangle\end{pmatrix}. \tag{1}$$

where M and Γ are 2x2 hermitian matrices. CPT invariance and the fact that the phases of the B^0 and $\bar{B}^0$ states can be chosen freely, make that the system can be described in terms of five physical real parameters, namely $M_{11} = M_{22}$, $\Gamma_{11} = \Gamma_{22}$, $|M_{12}|$, $|\Gamma_{12}|$ and the phase $\phi_{12} = \arg(-M_{12}/\Gamma_{12})$. Usually, these are rewritten in terms of the eigenvalues of the two mass eigenstates, labeled by L for light and H for heavy. In particular, the experimental observables are the average mass and decay width

$$m \equiv \tfrac{1}{2}(m_H + m_L) = M_{11} \qquad \Gamma \equiv \tfrac{1}{2}(\Gamma_H + \Gamma_L) = \Gamma_{11}, \tag{2}$$

the mass difference and decay width difference

$$\Delta m \equiv m_H - m_L \simeq 2|M_{12}| \qquad \Delta\Gamma \equiv \Gamma_L - \Gamma_H \simeq 2|\Gamma_{12}|\cos\phi_{12} \tag{3}$$

and the so-called flavour-specific or semi-leptonic asymmetry, which is a dimensionless quantity that signal CP violation in the mixing amplitudes and is approximately given by

$$a_{\mathrm{fs}} \simeq \frac{|\Gamma_{12}|}{|M_{12}|}\sin\phi_{12}\,. \tag{4}$$

In the SM the B_s^0 meson mixing amplitudes are dominated by the 2nd order weak interaction diagrams shown in Fig. 1 (left). Recent calculations [2] give $\Delta\Gamma_s = 0.087 \pm 0.021$ ps^{-1}, $\Delta m_s = 17.3 \pm 2.6$ ps^{-1}, $\phi_{12}^s = 0.004 \pm 0.001$ and $a_{\rm fs}^s = (1.9 \pm 0.3) \cdot 10^{-5}$. In the following I present LHCb [3] measurements of these parameters using the 2011 dataset, which comprises about 1.0 fb^{-1} of proton-proton collisions at 7 TeV.

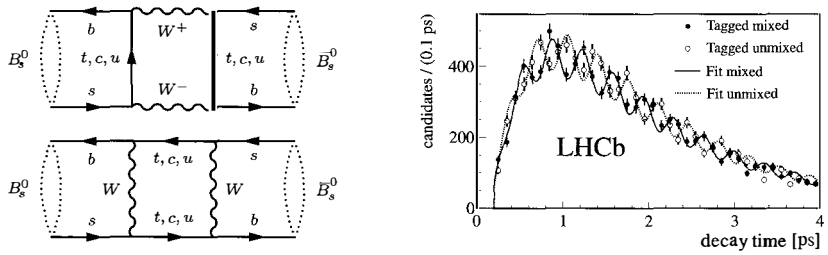

Figure 1: Left: Leading order diagrams for neutral meson mixing in the standard model. Right: decay time distribution for mixed and unmixed $B_s^0 \to D_s^+\pi^-$ candidates in 1.0 fb^{-1} of LHCb data [4].

2 Measurement of the B_s^0 oscillation frequency

The B_s^0 oscillation frequency Δm_s is measured in decays to $B_s^0 \to D_s^+\pi^-$ with the D_s^- decaying to $K^+K^-\pi^-$, $K^-\pi^+\pi^-$ or $\pi^-\pi^+\pi^-$. (Unless specifically indicated charged-conjugate modes are implied.) Flavour oscillations can be observed by comparing the flavour at the time of decay (which is determined by the charge of the $D_s^\pm$ in the final state) with the flavour at the time of production. The latter can be determined by exploiting the fact that the $\bar{b}$ and s quark in a B_s^0 meson are accompanied by respectively a b and $\bar{s}$ quark in the fragmentation. Identifying the flavour via decay products of the other b quark in the event is called opposite-side flavour tagging (OST), while relying on a reconstructed charged kaon close in phase space to the B_s^0 meson is called same-side flavour tagging (SST). Both these approaches are exploited in LHCb [5,6].

Depending on the flavour tags at production and at decay candidate events are labeled as 'mixed' (different flavour) or 'unmixed' (equal flavour). Ignoring experimental effects, the differential decay rates for mixed (plus sign) or unmixed (minus sign) events are given by

$$\frac{{\rm d}N_\pm}{{\rm d}t} \propto \frac{e^{-\Gamma_s t}}{2} \left[\cosh\left(\tfrac{1}{2}\Delta\Gamma_s\, t\right) \pm \cos\left(\Delta m_s\, t\right) \right]. \tag{5}$$

Figure 1 (right) shows the decay time distributions for mixed and unmixed $B_s^0 \to D_s^+\pi^-$ decays observed in 1.0 fb^{-1} of LHCb data. From a fit to these data the mixing frequency is found to be [4]

$$\Delta m_s = 17.768 \pm 0.023\ ({\rm stat}) \pm 0.006\ ({\rm syst})\ [{\rm ps}^{-1}] \tag{6}$$

which dominates the current world average. The systematic uncertainty is dominated by uncertainties in the length scale and momentum scale.

The distributions in Fig. 1 do not exactly follow the shape predicted by Eq. 5: The drop in efficiency at small lifetime is due to selection requirements aimed at reducing the large prompt background. The fact that the amplitude of the oscillation is not equal to unity is because of imperfections in the flavour tagging and the finite decay time resolution. Though less important for the Δm_s measurement, calibration of these effects is crucial for the measurement of time-dependent CP violation.

3 Measurements of time-dependent CP violation

Decays to CP eigenstates like $B_s^0 \to J/\psi\phi$ and $B_s^0 \to J/\psi f^0$ can be used to constrain the CP violating phase ϕ_{12}. The decay rate for decays with an initial flavour tag as B_s^0 (plus sign) or $\overline{B}_s^0$ (minus sign) is given by

$$\frac{\mathrm{d}N_\pm}{\mathrm{d}t} \propto e^{-\Gamma_s t}\left[\cosh\left(\tfrac{1}{2}\Delta\Gamma_s\, t\right) - \eta_f \cos\phi_f \sinh\left(\tfrac{1}{2}\Delta\Gamma_s\, t\right) \mp \eta_f \sin\phi_f \sin\left(\Delta m_s\, t\right)\right] \quad (7)$$

where η_f is the CP eigenvalue of the final state and the phase ϕ_f can be expressed in the phase of M_{12} and phases of elements of the CKM matrix. In the SM $\phi_f = \phi_s^{c\bar{c}s} = -0.036 \pm 0.002$ both for $B_s^0 \to J/\psi\phi$ and for $B_s^0 \to J/\psi f^0$ [2]. New contributions to the mixing diagram will alter M_{12} and thereby the phases $\phi_{12,s}$ and $\phi_s^{c\bar{c}s}$.

The $J/\psi f^0(980)$ final state is CP-odd ($\eta_f = -1$). A recent Dalitz analysis has shown that this holds to a good extend for the entire $J/\psi\pi^+\pi^-$ final state [7]. The phenomenology of the $B_s^0 \to J/\psi\phi(1020) \to \mu^+\mu^- K^+K^-$ decay is more complicated. In the K^+K^- invariant mass range near to $\phi(1020$ resonance the K^+K^- pair is predominantly in a P-wave state, but a small contribution from an S-wave exists [8]. Final states with different angular momenta lead to different values for η_f. In order to extract $\phi_s^{c\bar{c}s}$ these contributions are disentangled using the observed decay angles, requiring a so-called 'time-dependent angular analysis' of the data.

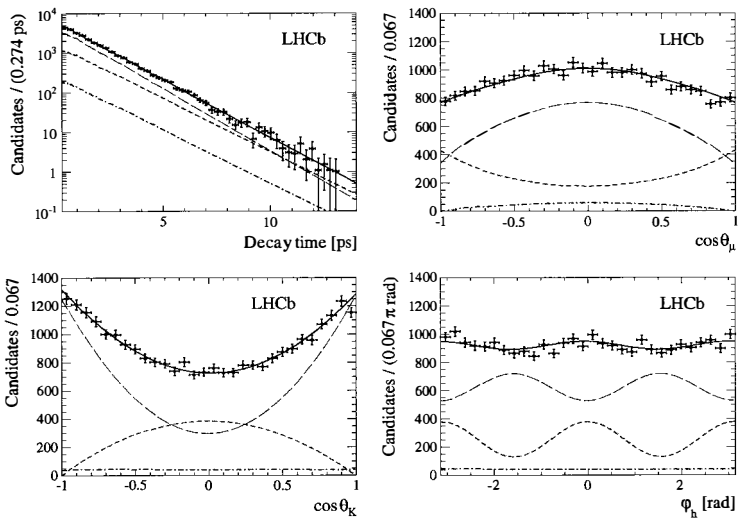

Figure 2: Background subtracted decay-time and helicity-angle distributions for $B_s^0 \to J/\psi K^+K^-$ decays in $1.0\,\mathrm{fb}^{-1}$ of LHCb data [9]. The solid blue line represents the fitted function, composed of CP-even (long-dashed red), CP-odd (short-dashed green) and S-wave (dotted-dashed purple) contributions.

Figure 2 shows distributions of the decay time and decay angles of background-subtracted $B_s^0 \to J/\psi K^+K^-$ decays, with the fitted function superimposed. From a combination with the $B_s^0 \to J/\psi f^0$ data, the following values for $\phi_s^{c\bar{c}s}$ and the lifetime parameters are extracted [9],

$$\begin{aligned}
\phi_s^{c\bar{c}s} &= 0.01 \pm 0.07\ (\mathrm{stat}) \pm 0.01\ (\mathrm{syst})\ \mathrm{rad}, \\
\Gamma_s &= 0.661 \pm 0.004\ (\mathrm{stat}) \pm 0.006\ (\mathrm{syst})\ \mathrm{ps}^{-1}, \\
\Delta\Gamma_s &= 0.106 \pm 0.011\ (\mathrm{stat}) \pm 0.007\ (\mathrm{syst})\ \mathrm{ps}^{-1},
\end{aligned} \quad (8)$$

These results are in good agreement with the SM prediction. The measurement of $\phi_s^{c\bar{c}s}$ dominates the current world average. Those for Γ_s and $\Delta\Gamma_s$ are the most precise from a single experiment. Systematic uncertainties are dominated by uncertainties of the decay angle and decay time acceptance.

The decay $B_s^0 \to \phi\phi$ also gives access to a CP violating phase, but in this case the transition proceeds predominantly through a $b \to s\bar{s}s$ penguin amplitude. In the SM, the phase $\phi_s^{s\bar{s}s}$ is expected to be close to zero, $|\phi_s^{s\bar{s}s}| < 0.02$, due to a cancellation of the phases arising from $B_s^0\overline{B}_s^0$ oscillations and decay. A first analysis of approximately 1200 candidates in $1.0\,\text{fb}^{-1}$ of LHCb data restricts the phase to the interval $\phi_s^{s\bar{s}s} \in [-2.46, -0.76]$ at 68% C.L. [10]. The p-value of the SM prediction is 16%.

4 Measurement of the flavour-specific asymmetry

CP violation in mixing is characterized by a non-zero value of ϕ_{12}, or, equivalently, the flavour-specific asymmetry a_{fs}. LHCb has measured a_{fs}^s in decays of $B_s^0 \to D_s^+\mu^-\bar{\nu}_\mu X$ [11]. The asymmetry in the yields of $D_s^-\mu^+$ and $D_s^+\mu^-$ events is related to a_{fs}^s by

$$\frac{N(D_s^-\mu^+) - N(D_s^+\mu^-)}{N(D_s^-\mu^+) + N(D_s^+\mu^-)} = \frac{a_{\text{fs}}^s}{2} + \left(\frac{a_{\text{fs}}^s}{2} - a_{\text{prod}}\right) \frac{\int_0^\infty \mathrm{d}t\, e^{-\Gamma_s t}\cos(\Delta m_s t)}{\int_0^\infty \mathrm{d}t\, e^{-\Gamma_s t}\cosh(\frac{1}{2}\Delta\Gamma_s t)} \tag{9}$$

where a_{prod} is the production asymmetry. The latter is expected to of the order of 1% at the LHC but with large uncertainty. However, thanks to the large oscillation frequency, the integral on the right-hand-side is small. From the observed asymmetry a preliminary value of

$$a_{\text{fs}}^s = (-0.24 \pm 0.54 \pm 0.33)\% \quad \textit{(prel.)} \tag{10}$$

is extracted [11], in good agreement with the SM expectation and the most precise measurement of a_{fs} in B_s^0 decays to date. The dominating systematic uncertainty stems from uncertainties in the relative efficiency of positively and negatively charged particles and is controlled by regularly reversing the direction of the magnetic field of the spectrometer.

5 Concluding remarks

I have presented recent LHCb results constraining contributions of beyond the standard model physics in $B_s^0\bar{B}_s^0$ oscillations. All measurements are in good agreement with SM expectations. The analysis of the 2012 dataset, which is approximately twice as large as the 2011 dataset presented here, is in full swing.

References

1. G. C. Branco, L. Lavoura, and J. P. Silva, Int. Ser. Monogr. Phys. **103** (1999) 1; U. Nierste, `arXiv:0904.1869`.
2. A. Lenz and U. Nierste, `arXiv:1102.4274`; A. Lenz *et al.*, Phys. Rev. **D83** (2011) 036004, `arXiv:1008.1593`.
3. LHCb Collaboration, A. A. Alves *et al.*, JINST **3** (2008) S08005.
4. LHCb collaboration, R. Aaij *et al.*, New J. Phys. **15** (2013) 053021, `arXiv:1304.4741`.
5. LHCb Collaboration, R. Aaij *et al.*, Eur. Phys. J. **C72** (2012) 2022, `arXiv:1202.4979`.
6. LHCb Collaboration, LHCb-CONF-2012-033.
7. LHCb Collaboration, R. Aaij *et al.*, Phys. Rev. **D86** (2012) 052006, `arXiv:1204.5643`.
8. LHCb Collaboration, R. Aaij *et al.*, Phys. Rev. **D87** (2013) 072004, `arXiv:1302.1213`.
9. LHCb Collaboration, R. Aaij *et al.*, `arXiv:1304.2600`, submitted to Phys. Rev. D.
10. LHCb Collaboration, R. Aaij *et al.*, `arXiv:1303.7125`, submitted to Phys. Rev. Lett.
11. LHCb Collaboration, R. Aaij *et al.*, LHCb-CONF-2012-022.

Searches for New Physics in Bottom Hadron Decays at the Tevatron

S. Leo, on behalf of CDF and D0 collaborations
University and INFN Pisa,
Polo Fibonacci Largo B. Pontecorvo 3,
Pisa 56217, Italy

Measurements of flavor changing neutral current processes play a key role in the search for new physics beyond the Standard Model. New physics could also impact the decay amplitudes of hadronic two-body charmless decays of neutral B hadrons with new particles entering in penguin diagrams. We present recent analysis results from the CDF and D0 collaborations, including observation of Λ_b and B_s^0 $b \to s\mu^+\mu^-$ transitions, an updated search for $B_s^0 \to \mu^+\mu^-$ decays, and relevant measurements of CP-violation in B_s^0 mixing and B hadron decays using the full (≈ 10 fb^{-1}) data sample available at the Tevatron.

1 Introduction

The standard model (SM) has a highly distinctive flavour structure, with no tree-level flavor changing neutral currents (FCNC), and quark mixing described by the Cabibbo-Kobayashi-Maskawa (CKM) matrix [1,2] involving only a single source of CP violation. The Tevatron $p\bar{p}$ collider, which exploited collisions at $\sqrt{s} = 1.96$ TeV, was a suitable environment to test the SM, potentially revealing new physics effects in the flavor sector. At the Tevatron, b quarks are pair-produced with large cross section[3] and generate all sorts of b hadrons. This provided access to SM-suppressed processes such as FCNC transitions and CP violation in B hadron decays. In this paper we focus on recent studies of $b \to s\mu^+\mu^-$ transitions, $B_s^0 \to \mu^+\mu^-$ decays, and CP-violation in B_s^0 mixing and B hadron decays performed by the CDF and D0 collaborations.

2 Rare Decays

In the SM framework, $b \to s\mu^+\mu^-$ transitions are dominated by FCNC processes mediated by electroweak-box and penguin-type diagrams. Many relevant new-physics processes could enhance the decay amplitude and might be observed from the interference with the SM amplitude. CDF measures various observables expected to be sensitive to possible new interactions, namely branching ratios, polarizations, forward-backward asymmetries, and the isospin asymmetry, between neutral and charged B mesons. CDF selects two oppositely-charged muon candidates with a momentum transverse to the beamline, p_T, greater than 1.5 or 2.0 GeV/c, depending on the trigger selection. The $H_b \to h\mu^+\mu^-$ events are reconstructed as signal candidates and $H_b \to J/\psi h$ events as normalization channels, where H_b represents B^0, B^+, B_s^0, or Λ_b^0 hadrons and h stands for K^+, $K^{*0(+)}$, K_S^0, ϕ or Λ hadrons. For the K^{*0}, K^{*+}, ϕ, and Λ hadrons, CDF reconstructs $K^+\pi^-$, $K_S^0\pi^+$, K^+K^- and $p^+\pi^-$ final states, respectively. The K_S^0 meson is reconstructed in the $\pi^+\pi^-$ decay mode. To enhance separation of signal from background CDF employs an artificial neural network (NN) technique. The signal yield is obtained by an unbinned maximum log-likelihood fit of the H_b invariant mass distribution. With 9.6 fb^{-1} of data [4], CDF

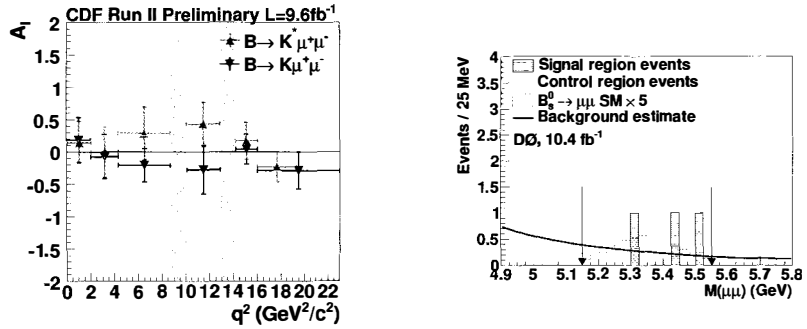

Figure 1: Left: Isospin asymetry of $B \to K\mu^+\mu^-$ and $B \to K^\star\mu^+\mu^-$. Only the statistical uncertainty is shown. Hatched regions are charmonium veto regions. Right: D0 Dimuon invariant mass distribution after un-blinding.

obtains 323 ± 24 ($B^+ \to K^+\mu^+\mu^-$), 228 ± 20 ($B^0 \to K^{\star 0}\mu^+\mu^-$), 32 ± 8 ($B^0 \to K^0_S\mu^+\mu^-$), 24 ± 6 ($B^+ \to K^{\star +}\mu^+\mu^-$), 62 ± 9 ($B^0_s \to \phi\mu^+\mu^-$) and 51 ± 8 ($\Lambda^0_b \to \Lambda\mu^+\mu^-$) signal events, with 15.6σ, 16.8σ, 4.6σ, 4.2σ, 8.9σ and 7.6σ statistical significances, respectively. This is the first observation of the $\Lambda^0_b \to \Lambda\mu^+\mu^-$ mode. Obtained yields are consistent with world average values and theoretical expectations. CDF also measures a number of observables more sensitive to NP. We report here only the results of isospin asymmetry (see Fig. 1) between neutral and charged B mesons, $A_I(B \to K\mu^+\mu^-) = [-0.11 \pm 0.13(stat) \pm 0.05(syst)] \times 10^{-6}$ and $A_I(B \to K^\star\mu^+\mu^-) = [0.16 \pm 0.14(stat) \pm 0.06(syst)] \times 10^{-6}$ which are consistent with the SM prediction, see ref. [4] for more details.

The $B^0_s \to \mu^+\mu^-$ decays are also dominated by FCNC processes, with rates further suppressed by the helicity factor, $(m_\mu/m_B)^2$. The SM expectation for the branching fraction is $\mathcal{B}(B^0_s \to \mu^+\mu^-) = (3.42 \pm 0.54) \times 10^{-9}$ [5]. As many new physics models can enhance the $\mathcal{B}$ significantly, these decays are among the most sensitive probes for NP. D0 selects two high-quality muon candidates with opposite-charge and a dimuon mass range of $4.0 < m_{\mu^+\mu^-} < 7.0$ GeV/c^2. Muon candidates are required to have $p_T > 1.5$ GeV/c, pseudorapidity $|\eta| < 2$ and to form a good three-dimensional vertex well separated from the primary $p\bar{p}$ interaction. These loose criteria maintain high signal efficiency, with further discrimination provided by Boosted Decision Tree, BDT. The event selection is checked with control samples of $B^\pm \to J/\psi K^\pm$ decays. This analysis is performed with the relevant dimuon mass region (4.9 and 5.8 GeV/c^2) blinded until all analysis procedures were final (see Fig. 1). D0 expects a SM signal of 1.23 ± 0.13 events and a background of 4.0 ± 1.5 events. After unblinding D0 observes 3 events, compatible with the background, and an upper limit on the branching fraction is set to $\mathcal{B}(B^0_s \to \mu^+\mu^-) < 1.5 \times 10^{-8}$ at the 95% C.L. [6] These results along with final CDF results [7], are the final Tevatron measurements on the search for $B^0_s \to \mu^+\mu^-$ decays.

3 CP violation in charmless decays

Non-leptonic two-body charmless decays of neutral B mesons ($B \to hh'$, where h is a charged pion or kaon) allow measurements and constraints on the parameters of the CKM matrix, providing also sensitivity to NP. Asymmetries up to about 10% are predicted for $\Lambda^0_b \to pK^-$ and $\Lambda^0_b \to p\pi^-$ decays in the SM [8,9], and are accessible with the current CDF data set, corresponding to an integrated luminosity of 9.3 fb^{-1}. CDF selects pairs of oppositely-charged particles with $p_T > 2$ GeV/c and $p_T(1)+p_T(2) > 5.5$ GeV/c, that form B candidates. The trigger requires also a transverse opening angle $20° < \Delta\phi < 135°$ between the two tracks for background rejection. In addition, both charged particles are required to originate from a displaced vertex with a

large impact parameter ($0.1 < d_0(1,2) < 1$ mm), while the b-hadron candidate is required to be produced in the primary $\bar{p}p$ interaction ($d_0 < 140$ μm) and to have travelled a transverse distance $L_T > 200$ μm. A maximum likelihood fit, including kinematic and PID information, is performed to disentangle the different compontents of the resulting mass peak (Fig. 2, left). Signal yields are calculated from the fractions returned by the fit. To determine the physical asymmetries these yields are corrected for detector-induced charge asymmetries extracted from control samples in data. The result $\mathcal{A}_{CP}(B^0 \to K^+\pi^-) = -0.083 \pm 0.013 \pm 0.003$, is consistent with current results from asymmetric e^+e^- colliders [10] and LHCb [11]. The result $\mathcal{A}_{CP}(B_s^0 \to K^-\pi^+) = 0.22 \pm 0.07 \pm 0.02$ confirms the LHCb observation [11]. The observed asymmetries in $\Lambda_b^0 \to pK^-$ decays, $\mathcal{A}_{CP}(\Lambda_b^0 \to p\pi^-) = 0.07 \pm 0.07 \pm 0.03$, and in $\Lambda_b^0 \to p\pi^-$ decays, $\mathcal{A}_{CP}(\Lambda_b^0 \to pK^-) = -0.09 \pm 0.08 \pm 0.04$, are consistent with zero. The limited experimental precision does not allow a conclusive discrimination between the standard model prediction (8%) and much-suppressed values (0.3%) expected in R-parity violating supersymmetric scenarios.

4 CPV B_s^0 mixing

The study of neutral B meson oscillations, which are mediated by the box-diagram weak interaction, can provide a sensitive probe for CP violation processes. An observation of anomalously large CP violation in B_s^0 oscillations can indicate the existence of physics beyond the standard model.[12]. Measurements of the like-sign dimuon asymmetry by the D0 Collaboration [13] show evidence of large CP-violating effects using data corresponding to $\approx$9 fb^{-1} of integrated luminosity. Assuming that this asymmetry originates from mixing of neutral B mesons, the measured value is $A_{sl}^b = C_d a_{sl}^d + C_s a_{sl}^s = [-0.787 \pm 0.172(stat) \pm 0.021(syst)]\%$ where $a_{sl}^{s(d)}$ is the time-integrated flavor-specic semileptonic charge asymmetry in $B_s^0(B_d^0)$ decays that have undergone flavor mixing and $C_s(C_d)$ is the fraction of $B_s^0(B_d^0)$ events. The SM predicts a tiny value of $a_{sl}^s = (1.9 \pm 0.3) \times 10^{-5}$ [12], which is negligible compared with current experimental precision. However the value extracted from the A_{sl}^b measurement is found to be $a_{sl}^s = (-1.81 \pm 1.06)\%$ [13]. D0 performs also an independent measurement of a_{sl}^s using the decay $B_s^0 \to D_s^- \mu^+ X$ where $D_s^- \to \phi\pi^-$ and $\phi \to K^+K^-$. The flavor of the B_s^0 meson at the time of decay is identified using the charge of the associated muon, and no use of initial-state tagging is made. The fraction of mixed events integrated over time is extracted using simulations. D0 assumes that any CP violation only occurs in mixing. The analysis strategy is to extract a_{sl}^s by counting the number of reconstructed $B_s^0 \to \mu^+ D_s^- X$ decays, corrected for detector-related asymmetries and by the fraction of reconstructed $D_s^- \to \phi\pi^-$ decays (F^{osc}) that originate from the decay of a B_s^0 meson after oscillation in its antiparticle, $a_{sl}^s = (A - A_{det})/F^{osc}$. The data are collected with a suite of single and dimuon triggers. The selection and reconstruction of $\mu^+ D_s^- X$ decays requires tracks and muons with standard good quality requirements. In addition, muons are required to match tracks reconstructed in the central tracking system, with momentum $p > 3$ GeV/c and $2 < p_T < 25$ GeV/c. The $\phi(\to K^+K^-)$ meson, coming form the $D_s^- \to \phi\pi^-$ decay is reconstructed if two tracks with $p_T > 0.7$ GeV/c, opposite charge, and a mass $M(KK) < 1.07$ GeV/c^2 are reconstructed in the kaon hypothesis. D0 than requires a third track with $0.5 < p_T < 25$ GeV/c to be consistent with a charged pion and to have opposite charge to the muon's one. The three tracks are combined to create a common D_s^- decay vertex[14]. D0 requires this vertex to be displaced in the transverse plane from the $p\bar{p}$ interaction vertex, with a significance (L_T/σ_{L_T}) of at least 4 standard deviations. Kinematic requirements assure that the trajectories of the muon and D_s^- candidates originate from a common vertex (assumed to be the B_s^0 decay vertex). D0 requires an effective mass consistent with B_s^0 semileptonic decays, $2.6 < M(\mu^+ D_s^-) < 5.4$ GeV/c^2. A $L_T/\sigma_{L_T} > 4\sigma$ requirement on the B_s^0 decay vertex is also imposed. A likelihood ratio combining several discriminating variables, improves the significance of the B_s^0 selection. The number of events is extracted by fitting the $M(KK\pi)$ data distribution to an appropriate model using a χ^2 fit. The resulting time-integrated flavor-specific semileptonic charge asym-

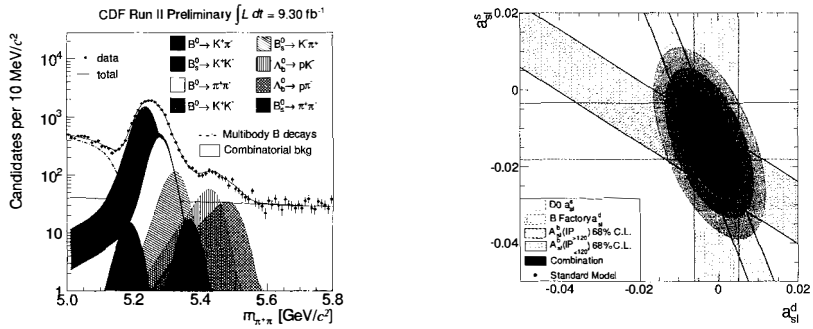

Figure 2: Left: Mass distribution of reconstructed $B \to hh'$ candidates. The charged pion mass is assigned to both tracks. The total fit projection is overlaid on the data distribution. Right: Combination of $a_{sl}^{s(d)}$ measurements. The error bands represent the ± 1 standard-deviation uncertainties on each individual measurement. The ellipses represent the 1, 2, 3, and 4 standard deviation two-dimensional C.L. regions, respectively, in the a_{sl}^s and a_{sl}^d plane.

metry is found to be $a_{sl}^s = [-1.12 \pm 0.74(stat) \pm 0.17(syst)]\%$, superseding the previous D0 measurement[13], and in agreement with the SM prediction. A combination with measurements of a_{sl}^d from B factories and di-muon asymmetries from D0[13] is shown in Fig. 2(right). The results are $a_{sl}^s = (-1.42 \pm 0.57)\%$ and $a_{sl}^d = (-0.21 \pm 0.32)\%$ with a correlation of -0.53, which is a significant improvement on the previous measurement precision[13]. These results have a probability of agreement with the SM of 0.28×10^{-2} , which corresponds to a 3.0 standard deviations discrepancy. Up to date, this discrepancy is not confirmed by measurement of mixing-induced CP violation in $B_s^0 \to J/\psi\phi$ decays as preformed by the CDF, D0 and LHCb collaborations[15].

References

1. N. Cabibbo, *Phys. Rev. Lett.* **10**, 531 (2013).
2. M. Kobayashi and T. Maskawa, *Prog. Theor. Phys.* **49**, 652 (1973).
3. T. Aaltonen *et al.*, *Phys. Rev.* D **79**, 092003 (2009).
4. CDF Collaboration, Public Note 10894.
5. A. J. Buras, *Phys. Lett.* B **566**, 115 (2003).
6. V. Abazov *et al.*, *Phys. Rev.* D **87**, 072006 (2013).
7. T. Aaltonen *et al. Phys. Rev.* D **87**, 072003 (2013)
8. C.-D. Lu *et al.*, *Phys. Rev.* D **80**, 034011 (2009).
9. R. Mohanta, *Phys. Rev.* D **63**, 056006 (2001).
10. S.-W. Lin *et al.*, *Nature* **452**, 332 (2008); B. Aubert *et al.*, *Phys. Rev. Lett.* **99**, 021603 (2007); B. Aubert *et al.*, *Phys. Rev.* D **76**, 091102 (2007).
11. R. Aaij *et al.*, *arXiv:1304.6173*, *Phys. Rev. Lett.* **108**, 201601 (2012).
12. A. Lenz and U. Nierste, *arXiv:1102.4274*; *J. High Energy Phys.* **06**, 072 (2007).
13. V. M. Abazov *et al.*, *Phys. Rev.* D **82**, 032001 (2010); *Phys. Rev. Lett.* **105**, 081801 (2010); *Phys. Rev.* D **84**, 052007 (2011); *Phys. Rev.* D **82**, 012003 (2010).
14. J. Abdallah *et al.*, *Eur. Phys. J.* **C32**, 185 (2004).
15. T. Aaltonen *et al.*, *Phys. Rev. Lett.* **109**, 171802 (2012); V. Abazov *et al. Phys. Rev.* D **85**, 032006 (2012); R. Aaij *et al.*, *arXiv:1304.2600.*

MEASUREMENTS OF DIRECT CP VIOLATION IN CHARM DECAYS AT LHCb

Sascha Stahl
Physikalisches Institut Heidelberg, Heidelberg University, Germany

Two searches for direct CP violation in $D^0 \to h^-h^+$ (where $h = K$ or π) are presented using data corresponding to an integrated luminosity of 1.0 fb^{-1} collected in 2011 by LHCb in pp collisions at a centre-of-mass energy of 7 TeV. One analysis uses D^0 mesons produced via a D^* resonance and the other analysis uses D^0 mesons originating from semileptonic b-decays. In the first case the flavour is tagged by the charge of the accompanying pion and in the latter by the muon charge. The difference of the CP-violating asymmetries ($\Delta A_{CP} = A_{CP}(K^-K^+) - A_{CP}(\pi^-\pi^+)$) in the two decay channels is measured to be

$$\Delta A_{CP}\,(\text{muon tagged}) = (0.49 \pm 0.30\,(\text{stat}) \pm 0.14\,(\text{syst}))\% \,,$$
$$\Delta A_{CP}\,(\text{pion tagged}) = (-0.35 \pm 0.15\,(\text{stat}) \pm 0.10\,(\text{syst}))\% \,,$$
$$\Delta A_{CP}\,(\text{LHCb}) = (-0.15 \pm 0.16)\% \,.$$

These results do not confirm evidence for CP violation in the charm sector.

1 Introduction

CP violation has been well established in the decays of K and B mesons. However, CP violation in the decays of D mesons has not yet been discovered. It is generally expected to be well below the 1% level in the Standard model [1,2]. The results of measurements of direct CP violation in the decays $D^0 \to K^-K^+$ and $D^0 \to \pi^-\pi^+$ reported by LHCb, CDF and Belle in 2011 and 2012 showed an evidence for CP violation (reference). The world average for direct CP violation quoted by the Heavy Flavor Averaging Group (HFAG) was $\Delta a_{CP}^{\text{dir}} = (-0.678 \pm 0.147)\%$ [4]. This generated discussion in the theory community if the size of the reported asymmetry can be accomodated within the Standard Model or if it is a sign of physics beyond the Standard Model[3]. Here, two measurements performed by the LHCb experiment using data corresponding to an integrated luminosity of 1.0 fb^{-1} collected in 2011 in pp collisions at a centre-of-mass energy of 7 TeV are presented. The measurement in promptly produced charm is a preliminary update of the previous result based on 0.6 fb^{-1} [5]. The measurement using semileptonic b decays to tag the D flavour is a new and independent measurement to be published in Physics Letter B [6]. These two measurements have a sensitivity of the same order but complementary systematical uncertainties.

2 Method

In both analyses the raw asymmetry is defined as

$$A_{\text{raw}} = \frac{N(D^0 \to f) - N(\bar{D}^0 \to f)}{N(D^0 \to f) + N(\bar{D}^0 \to f)} \,, \tag{1}$$

where N denotes the observed yield. The initial flavour of the D^0 is determined by the accompanying particle.

In the prompt analysis the decay $D^{*\pm} \to D^0\pi^\pm$ is reconstructed. Thus a D^0 meson is tagged by a π^+ and a $\overline{D}^0$ meson by a π^-. In the semileptonic analysis the charge of the muon from the decay $B \to D^0\mu X$ is used to tag the flavour of the D^0 meson. The X denotes all particles in the decay which are not reconstructed. The measured raw asymmetry $A_{\rm raw}$ can be expressed to first order in terms of the production asymmetry, A_P, the detection asymmetry, A_D, and the CP asymmetry A_{CP} as

$$A_{\rm raw} \approx A_{CP} + A_D + A_P \ . \tag{2}$$

The detection asymmetry arises from the tagging particle, either a pion or a muon and the production asymmetry, either that of the D or of the the B, is given by the production mode of the D^0 meson. Thus both differ between the two analyses. The production and the detection asymmetry are independent of the reconstructed D final state. Taking the difference of $A_{\rm raw}$ measured in $D^0 \to K^-K^+$ and $A_{\rm raw}$ measured in $D^0 \to \pi^-\pi^+$ gives a measurement of the difference in CP asymmetries between the two final states

$$\Delta A_{CP} = A_{\rm raw}(K^-K^+) - A_{\rm raw}(\pi^-\pi^+) \approx A_{CP}(K^-K^+) - A_{CP}(\pi^-\pi^+) \ . \tag{3}$$

Both production and detection asymmetries depend on the kinematics of the decay. Therfore in both analyses a weighting of $D^0 \to K^-K^+$ relative to $D^0 \to \pi^-\pi^+$ decays is applied such that they both cover the same kinematical phase space.

3 Determination of the asymmetries

3.1 Pion-tagged analysis

In the pion-tagged analysis the asymmetries in the $D^0 \to K^-K^+$ and $D^0 \to \pi^-\pi^+$ decays are determined by a chi-square fit to the binned $\delta m \equiv m(h^+h^-\pi^+) - m(h^+h^-) - m(\pi^+)$ distributions. The data set is further divided by magnet polarity and hardware trigger category. The hardware trigger distinguishes whether the D^{*+} candidate was used in the calorimeter trigger decision (TOS = Trigger On Signal) or if the event was triggered by something else (TIS = Triggered Independently of Signal). Both categories are disjoint. Two example distributions are shown in Fig. 1. The total number of signal candidates used in the pion-tagged analysis determined from the fit is 2.24×10^6 for $D^0 \to K^-K^+$ decays and 0.69×10^6 for $D^0 \to \pi^-\pi^+$ decays. The results of the individual asymmetry fits and the final ΔA_{CP} result are given in Table 1. The systematic uncertainty of this ΔA_{CP} measurement is determined to be 0.10%. The dominating systematic uncertainty is coming from selection cuts on the tagging pion.

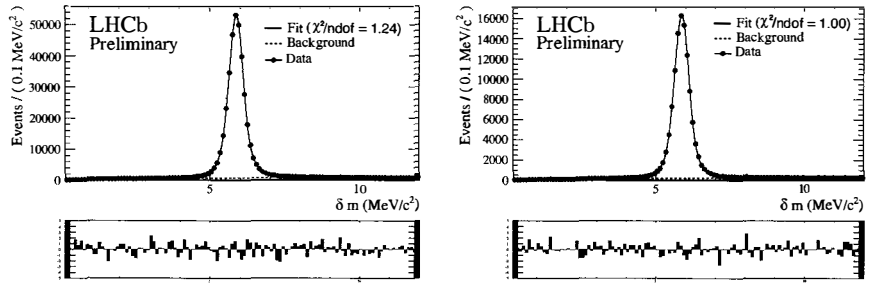

Figure 1: The δm distribution is shown for magnet up TOS (left) $D^0 \to K^-K^+$ and (right) $D^0 \to \pi^-\pi^+$

Table 1: Observed asymmetries with statistical uncertainties only. The data are divided into disjoint samples according to the $D^{*\pm}$ tag, the magnet polarity, and the hardware trigger category. The final result of ΔA_{CP} is given by the weighted average.

Quantity	Magnet polarity	Hardware trigger decision	Observed value [%]
ΔA_{CP}	Up	TOS	-0.62 ± 0.36
ΔA_{CP}	Down	TOS	-0.36 ± 0.30
ΔA_{CP}	Up	TIS	-0.30 ± 0.30
ΔA_{CP}	Down	TIS	-0.22 ± 0.25
ΔA_{CP}	combined		-0.35 ± 0.15

3.2 Muon-tagged analysis

In the muon-tagged analysis the asymmetries are determined by a binned maximum-likelihood fit to the D^0 mass distribution in the $D^0 \to K^-K^+$ and $D^0 \to \pi^-\pi^+$ decays. The sample is only divided into magnet polarity as 97% of the events are triggered by the hardware muon trigger. The events in $D^0 \to K^-K^+$ and $D^0 \to \pi^-\pi^+$ are weighted to match their kinematics. Two example distributions are shown in Fig. 2. The results of the individual asymmetry fits and

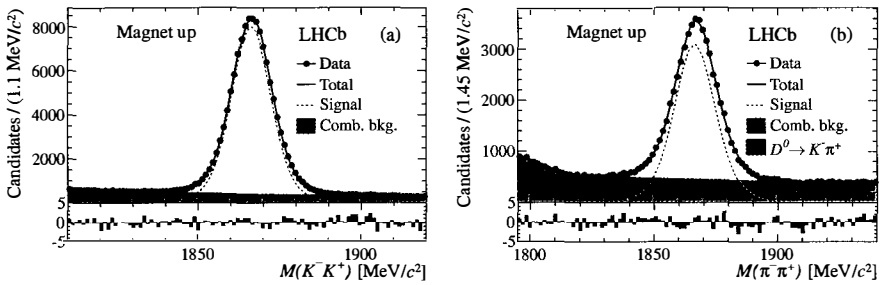

Figure 2: The D^0 mass distribution of the muon-tagged sample is shown for magnet up (left) $D^0 \to K^-K^+$ and (right) $D^0 \to \pi^-\pi^+$

ΔA_{CP} are given in Table 2. The total number of signal candidates determined from the fit is $(558.9 \pm 0.9) \times 10^3$ for $D^0 \to K^-K^+$ decays and $(221.6 \pm 0.8) \times 10^3$ for $D^0 \to \pi^-\pi^+$ decays. The systematic uncertainty of ΔA_{CP} is determined to be 0.14%. The main systematic uncertainty is coming from low lifetime backgrounds in the $D^0 \to \pi^-\pi^+$ decays below the $D^0 \to \pi^-\pi^+$ signal.

Table 2: Observed asymmetries with statistical uncertainties only. The data are divided into disjoint samples according to the D^0 decay mode, the magnet polarity. The final result of ΔA_{CP} is given by the arithmetic mean of the two magnet polarities.

	Magnet up	Magnet down	Mean
$A_{\rm raw}(K^-K^+)$	-0.39 ± 0.23	-0.20 ± 0.19	-0.29 ± 0.15
$A_{\rm raw}(\pi^-\pi^+)$	-1.25 ± 0.40	-0.29 ± 0.34	-0.77 ± 0.26
ΔA_{CP}	0.86 ± 0.46	0.09 ± 0.39	0.48 ± 0.30

4 HFAG combination

The Heavy Flavour Averaging Group (HFAG) has included the two previous reported results in their average of direct and indirect *CP* violation in charm decays [7]. The value obtained for the difference in direct *CP* violation is $\Delta a_{CP}^{\rm dir} = (-0.329 \pm 0.121)\%$ and the value for indirect *CP*

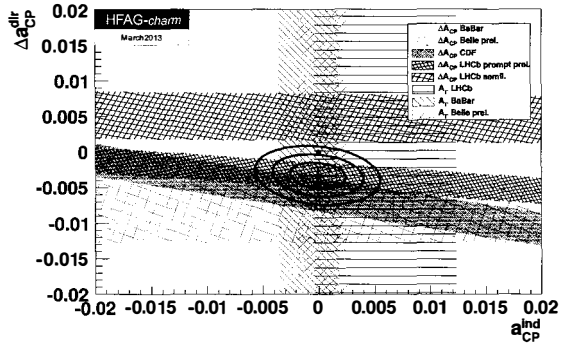

Figure 3: The D^0 mass distribution is shown for magnet up (left) $D^0 \to K^-K^+$ and (right) $D^0 \to \pi^-\pi^+$

violation is $a_{CP}^{\rm ind} = (-0.010 \pm 0.162)\%$. The combined values together with all inputs is shown in Fig. 3.

5 Conclusion

The LHCb experiment has measured the size of direct CP violation with data taken in 2011 with two independent methods. The LHCb average quoted here, assumes that indirect CP violation is negligible. The CP-violating asymmetries are found to be

$$\begin{aligned} \Delta A_{CP}\,(\text{muon tagged}) &= (0.49 \pm 0.30\,(\text{stat}) \pm 0.14\,(\text{syst}))\% \,, \\ \Delta A_{CP}\,(\text{pion tagged}) &= (-0.35 \pm 0.15\,(\text{stat}) \pm 0.10\,(\text{syst}))\% \,, \\ \Delta A_{CP}\,(\text{LHCb}) &= (-0.15 \pm 0.16)\% \,. \end{aligned}$$

These results do not confirm evidence for CP violation in the charm sector. The measurements have been used in the latest average by HFAG giving $\Delta a_{CP}^{\rm dir} = (-0.329 \pm 0.121)\%$ and $a_{CP}^{\rm ind} = (-0.010 \pm 0.162)\%$.

References

1. Bianco, S. and Fabbri, F.L. and Benson, D. and Bigi, I., *A Cicerone for the physics of charm*, Riv. Nuovo Cim. **26N7**, (2003)
2. Grossman, Yuval and Kagan, Alexander L. and Nir, Yosef, *New physics and CP violation in singly Cabibbo suppressed D decays*, Phys.Rev. **D75**, 036008 (2007)
3. LHCb Collaboration, Aaij, R. and others, *Implications of LHCb measurements and future prospects*, arXiv **hep-ex**, 1208.3355 (2012)
4. Heavy Flavor Averaging Group, Y. Amhis et al, *Combination of Direct and Indirect CP Violation*, `www.slac.stanford.edu/xorg/hfag/charm/ICHEP12/DCPV/direct_indirect_cpv.html`
5. LHCb Collaboration, Aaij, R. and others, *A search for time-integrated CP violation in $D^0 \to K^-K^+$ and $D^0 \to \pi^-\pi^+$ decays*, LHCb-CONF-2013-003 (2013)
6. R Aaij *et al.* [LHCb Collaboration], *Search for direct CP violation in $D^0 \to h^-h^+$ modes using semileptonic B decays*, arXiv:1303.2614 [hep-ex]. (2013)
7. Heavy Flavor Averaging Group, Y. Amhis et al, *Combination of Direct and Indirect CP Violation*, `www.slac.stanford.edu/xorg/hfag/charm/March13/DCPV/direct_indirect_cpv.html`

CONSTRAINTS ON NEW PHYSICS FROM RARE (SEMI-)LEPTONIC B DECAYS

David M. Straub

PRISMA Cluster of Excellence & Mainz Institute for Theoretical Physics, Johannes Gutenberg University, 55099 Mainz, Germany

The measurements of rare leptonic and semi-leptonic B decays performed at the LHC, not showing any significant deviations from the Standard Model expectations, put strong constraints on new physics. A brief account of the impact of recent measurements is given. As a concrete example, models with partial compositeness are discussed, where tree-level flavour-changing Z couplings lead to potentially visibile effects in rare B (and K) decays that will be scrutinized experimentally in the near future.

1 Introduction

The first LHC run has brought strong new constraints on physics beyond the Standard Model (SM). In the flavour sector, this is particularly true for new physics (NP) in $b \dashrightarrow s$ transitions, due to a first measurement of $B_s \dashrightarrow \mu^+\mu^-$ and improved measurements of $B \dashrightarrow K\mu^+\mu^-$ and $B \dashrightarrow K^*\mu^+\mu^-$ [1,2,3], including angular observables. While no significant deviations from the SM expectations have been found, the combined experimental and theoretical uncertainties still allow for NP effects of the order of 50% of the SM contribution in many observables. It is therefore important not only to assess the impact of the improved constraints on NP models, but also to study in which observables visible deviations from the SM are still possible. After giving a brief, model-independent account of the impact on the most important classes of NP contributions in sec. 2, a concrete model will be discussed in sec. 3, identifying the most promising observables to test it in the future.

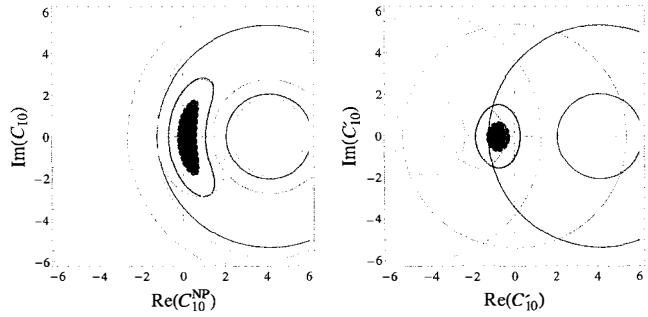

Figure 1: Individual 2σ constraints on the NP contribution to C_{10} and C'_{10} from $B \to X_s \ell^+ \ell^-$ (brown), $B \to K^* \mu^+ \mu^-$ (green), $B \to K \mu^+ \mu^-$ (blue) and $B_s \to \mu^+ \mu^-$ (gray) as well as combined 1 and 2σ constraints (red).

2 Model-independent considerations

In many concrete NP models (such as the MSSM at low $\tan\beta$ or models with partial compositeness), NP effects in the above-mentioned decays arise mainly through the operators[a]

$$O_7^{(\prime)} = \frac{m_b}{e}(\bar{s}\sigma_{\mu\nu}P_{R(L)}b)F^{\mu\nu}, \qquad O_{10}^{(\prime)} = (\bar{s}\gamma_\mu P_{L(R)}b)(\bar{\ell}\gamma^\mu\gamma_5\ell)\,, \tag{1}$$

in the effective Hamiltonian

$$\mathcal{H}_{\rm eff} = -\frac{4\,G_F}{\sqrt{2}}V_{tb}V_{ts}^*\frac{e^2}{16\pi^2}\sum_i (C_i O_i + C_i' O_i') + \text{h.c.}$$

In these models, the contributions to the operators $O_9^{(\prime)}$ are typically small since Z-mediated effects are accidentally suppressed by the small vector coupling of the Z to charged leptons.

In the case of the magnetic operators $O_7^{(\prime)}$, the impact of recent LHC measurements is mild, in view of existing constraints from the exclusive and inclusive radiative decays. The main new information is a reduced allowed size of $\text{Im}(C_7)$, stemming from the measurement of the branching ratio and F_L in $B \to K^*\mu^+\mu^-$ at low q^2 [4,5].

The impact on allowed NP contributions to $O_{10}^{(\prime)}$ is much stronger. The combination of $B \to K^*\mu^+\mu^-$ and $B \to K\mu^+\mu^-$ measurements leads to a strong constraint on C_{10} and C'_{10} that is shown in fig. 1. In the case of C'_{10}, the recent measurement of the angular observables S_3 and A_9 in $B \to K^*\mu^+\mu^-$, which were found to be in agreement with the SM, had a significant impact on CP-conserving and CP-violating contributions.[b] The operators $O_{10}^{(\prime)}$ can be generated by Z penguin diagrams and are particularly large in models where flavour-changing Z couplings are present at tree-level. This is the case in models with partial compositeness, as will be discussed in the next section.

In models with an extended Higgs sector, in particular the MSSM at large $\tan\beta$, also the (pseudo-)scalar operators can be relevant,

$$O_S^{(\prime)} = \frac{m_b}{m_{B_s}}(\bar{s}P_{R(L)}b)(\bar{\ell}\ell)\,, \qquad O_P^{(\prime)} = \frac{m_b}{m_{B_s}}(\bar{s}P_{R(L)}b)(\bar{\ell}\gamma_5\ell)\,. \tag{2}$$

While the contributions of $O_{S,P}^{(\prime)}$ to $B \to K^*\mu^+\mu^-$ turn out to be numerically irrelevant [6], they can lead to large enhancements in $B_s \to \mu^+\mu^-$. Indeed, the LHCb measurement leads to a

[a] NP effects in the chromomagnetic operators $O_8^{(\prime)}$ also enter by mixing under renormalization with $O_7^{(\prime)}$.

[b] Note that the new A_9 measurement [3] at low and high q^2 was included in the updated plot prepared for these proceedings.

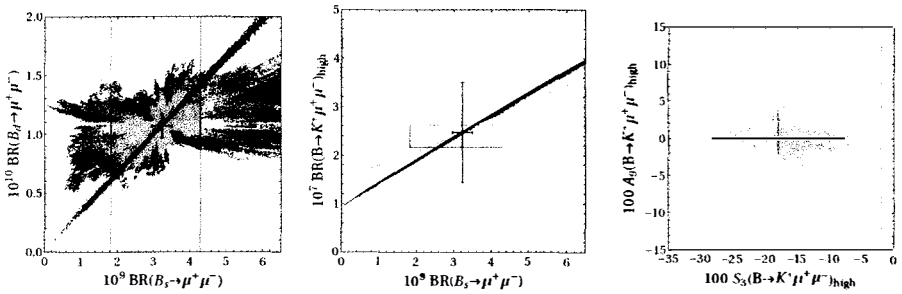

Figure 2: Correlations between rare B decay observables in three models with partial compositeness: the anarchic triplet model (yellow), the anarchic bidoublet model (red) and the bidoublet model with $U(2)^3$ left-handed compositeness (blue). For details see ref. 8.

strong bound on the MSSM with large $\tan\beta$ and a light pseudoscalar Higgs boson even for Minimal Flavour Violation (see e.g. [7]).

3 Z penguins and partial compositeness

Apart from supersymmetry, models with a composite Higgs boson (and their dual extra-dimensional theories) arguably constitute the most well-motivated solution to the gauge hierarchy problem. In these models, to avoid excessive flavour-changing neutral currents (FCNCs), one generates fermion masses by the mechanism of partial compositeness. One consequence is that the couplings of quarks to the Z boson generically receive non-universal corrections that are constrained by electroweak precision tests (EWPT) and lead to tree-level FCNCs. To avoid the EWPT constraints, discrete symmetries can be imposed that in turn lead to characteristic patterns of effects in Z-mediated FCNCs.

Recently [8], a complete numerical study of Z-mediated FCNCs in models with partial compositeness was performed for two different choices of composite fermion representations and for two choices of the flavour structure of the composite sector: anarchy and a minimally broken $U(2)^3$ flavour symmetry [9,10].

It was found that in all the scenarios, several branching ratios of rare K and B decays can exhibit visible effects at current and planned experiments. Clear-cut correlations between various observables can be used to distinguish the different models on the basis of the pattern of observed deviations from the SM expectations.

An example is shown in fig. 2: the NP contributions to $B_s \to \mu^+\mu^-$ and $B \to K^*\mu^+\mu^-$ through the operators $O_{10}^{(\prime)}$ lead to effects that are comparable to the current experimental precision. The correlation in the left-hand plot present in the $U(2)^3$ model is due to the flavour symmetry relating $b \to d$ and $b \to s$ transitions. The correlation in the centre plot is due to the fact that only C_{10} *or* $C_{10'}$ (corresponding to only left-handed or right-handed flavour-changing Z couplings) contribute in all models. In the right-hand plot, one can see that in a model with right-handed flavour-changing Z couplings, also non-zero contributions to the angular observables S_3 and A_9 can be generated, although in this concrete model they turn out to be small, such that the recent improved measurement by LHCb (not shown in the plot) does not have an impact yet.

4 Conclusions

The failure of NP to show up in rare B decays sensitive to the $b \to s$ transition has led to strong constraints on physics beyond the SM. In a large class of NP models, the most significant such

constraints are

- Less room for a CP-violating contribution to the magnetic operator O_7.
- Less room for NP in scalar and pseudoscalar operators $O_{S,P}^{(\prime)}$. This is particularly relevant for the MSSM, where it effectively sets an upper bound on the combination $\tan^3\beta/M_A^2$.
- Less room for NP in the semi-leptonic operators $O_{10}^{(\prime)}$, which can be generated for instance by Z penguin diagrams.

In the latter case, the impact of the recent first LHCb measurement of the angular CP asymmetry A_9 was shown in the right-hand plot of fig. 1.

In sec. 3, a concrete NP framework was discussed where tree-level contributions to the operators O_{10} or O'_{10} are generated. Future improved measurements, complemented with progress on the theoretical uncertainties, will allow to probe a significant part of the parameter space of these models.

Acknowledgments

I warmly thank the organizers for the invation to this conference. Thanks also to Wolfgang Altmannshofer and Christoph Bobeth for useful discussions. This work was supported by the Advanced Grant EFT4LHC of the European Research Council (ERC), and the Cluster of Excellence *Precision Physics, Fundamental Interactions and Structure of Matter* (PRISMA – EXC 1098).

References

1. R. Aaij *et al.* [LHCb Collaboration], JHEP **1302** (2013) 105 [arXiv:1209.4284 [hep-ex]].
2. R. Aaij *et al.* [LHCb Collaboration], Phys. Rev. Lett. **110** (2013) 021801 [arXiv:1211.2674 [Unknown]].
3. R. Aaij *et al.* [LHCb Collaboration], arXiv:1304.6325 [hep-ex].
4. W. Altmannshofer, P. Paradisi and D. M. Straub, JHEP **1204** (2012) 008 [arXiv:1111.1257 [hep-ph]].
5. W. Altmannshofer and D. M. Straub, JHEP **1208** (2012) 121 [arXiv:1206.0273 [hep-ph]].
6. W. Altmannshofer, P. Ball, A. Bharucha, A. J. Buras, D. M. Straub and M. Wick, JHEP **0901** (2009) 019 [arXiv:0811.1214 [hep-ph]].
7. W. Altmannshofer, M. Carena, N. R. Shah and F. Yu, JHEP **1301** (2013) 160 [arXiv:1211.1976 [hep-ph]].
8. D. M. Straub, arXiv:1302.4651 [hep-ph].
9. R. Barbieri, D. Buttazzo, F. Sala and D. M. Straub, JHEP **1207** (2012) 181 [arXiv:1203.4218 [hep-ph]].
10. R. Barbieri, D. Buttazzo, F. Sala, D. M. Straub and A. Tesi, JHEP **1305** (2013) 069 [arXiv:1211.5085 [hep-ph]].

B AND C SPECTROSCOPY AT LHCB

G. MANCA
Department of Physics, Università degli studi di Cagliari,
S.P. per Sestu, Km 0.7, 09042 Monserrato, Cagliari, Italy

We will present recent results in the field of b and c spectroscopy at LHCb, with particular attention to the latest studies on the X(3872) quantum numbers and the B_c new decay modes and mass measurement.

1 Introduction

The production of mesons and baryons containing b and c quarks is copious at the LHC. The studies on the production and spectroscopy of these particles are important inputs to other measurements and bring valuable contributions to the thorough understanding of the mechanisms of QCD production [1,2]. The LHCb detector [3] has a unique geometry optimised for these studies, as it accepts 40% of all B hadrons produced in pp interactions. The detector is a single-arm forward spectrometer [3] dedicated to flavour physics at the LHC. In the years from 2010 to 2012 LHCb has recorded an integrated luminosity of about 3 $\text{fb}^{-1}$of data at a center-of-mass energy of 7, 2.76 and 8 TeV with an efficiency of more than 90%. We discuss recent B_c and b-baryons results in Section 2 and 3, and the X(3872) results in Section 4.

2 B_c physics

The B_c is the only B meson made of two "heavy" quarks and, as such, its properties are in between the charmonium and bottomonium states. It was first observed by CDF in 1998 [4] in the $J/\psi\ell^{\pm}\nu$ decay mode, and fully reconstructed the $J/\psi\pi^{\pm}$ mode [5]. At LHCb we already measured the B_c mass and production cross section in the latter channel using 40 $\text{pb}^{-1}$of data[6]. In the larger dataset we observed two new decay modes, $B_c^{\pm} \to \psi(2S)\pi^{\pm}$ and $B_c^{\pm} \to J/\psi D_s^{(*)\pm}$.

2.1 $B_c^{\pm} \to \psi(2S)\pi^{\pm}$ observation

In 1.1 $\text{fb}^{-1}$of data we observed 595±29 $B_c \to J/\psi\pi^{\pm}$ and 20±5 $B_c \to \psi(2S)\pi^{\pm}$ candidate events (as shown in Fig. 1, left and middle), selected using the Boost Decision Tree (BDT) technique [7]

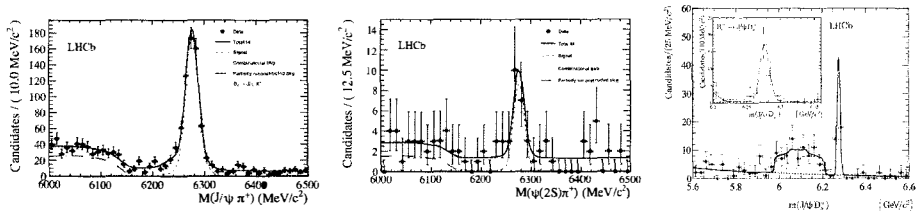

Figure 1: $J/\psi\pi^{\pm}$(left), $\psi(2S)\pi^{\pm}$(middle) and $D_s^{\pm(*)}\pi^{\pm}$(left) invariant mass distributions. The insct in the leftmost figure is the fit in the region between 6.2 and 6.35 GeV/c^2performed with different binning.

trained on the $B_c \to J/\psi\pi^{\pm}$ more abundant channel. The number of signal candidates is determined by fitting the $\psi(2S)\pi$ invariant mass distribution with a Crystal Ball function [8] for the signal and an exponential function for the background. Partially reconstructed events and combinatorial background are also accounted for. We measured the ratio of $B_c^{\pm} \to \psi(2S)\pi^{\pm}$ to $B_c^{\pm} \to J/\psi\pi^{\pm}$ branching ratios by correcting for the relative reconstruction efficiencies and found the value of

$$\frac{B_c^{\pm} \to \psi(2S)\pi^{\pm}}{B_c^{\pm} \to J/\psi\pi^{\pm}} = 0.250 \pm 0.068(stat) \pm 0.014(syst) \pm 0.006(\mathcal{B}), \quad (1)$$

where the third uncertainty is due to the uncertainties on the branching ratios of J/ψ and $\psi(2S)$ in dimuons [12]. The dominant source of systematic uncertainty is the one associated with the BDT selection, which amounts to 4.5%. The results are in good agreement with the theoretical predictions of 0.18 made by the relativistic quark model [9].

2.2 $B_c^{\pm} \to J/\psi D_s^{(*)\pm}$ observation

Using the full dataset of $\simeq 3\,\text{fb}^{-1}$ collected until 2012, we have observed the decays $B_c^{\pm} \to J/\psi D_s^{(*)\pm}$ for the first time [10]. The J/ψ is reconstructed in its dimuon decay, while the $D_s^{\pm}$ is reconstructed through its decay into $\phi\pi$, followed by $\phi \to K^{\pm}K^{\mp}$. The decay $B_c^{\pm} \to J/\psi D_s^*$ appears in the $J/\psi D_s$ invariant mass as a satellite structure at smaller mass. The number of signal events for the two decays is determined by a fit to the $D_s^{\pm(*)}\pi$ invariant mass distribution, shown in Fig. 1 (right), using a double Crystal Ball for the D_s signal and the shapes obtained from the Monte Carlo of the distributions due to the $\mathcal{A}^{\pm\pm}, A^{00}$ different amplitudes for the D_s^*. Using the $B_c^{\pm} \to J/\psi\pi^{\pm}$ as normalisation channel we can measure the ratio of branching ratios

$$\frac{B_c^{\pm} \to J/\psi D_s^{\pm}}{B_c^{\pm} \to J/\psi\pi^{\pm}} = 2.90 \pm 0.57(stat) \pm 0.24(syst), \quad (2)$$

$$\frac{B_c^{\pm} \to J/\psi D_s^{*\pm}}{B_c^{\pm} \to J/\psi D_s^{\pm}} = 2.37 \pm 0.56(stat) \pm 0.10(syst), \quad (3)$$

where the dominant systematic is the one associated with the knowledge of the branching ratio of $D_s^{\pm} \to \phi(\to K^{\pm}K^{\mp})\pi^{\pm}$ [12]. These results are in good agreement with the simple factorisation approach but generally disagree with the other models [10]. Given the small Q value associated with this decay and the precise knowledge of the D meson mass differences [11] it is possible to obtain a precise measurement of the B_c mass, which is found to be $m(B_c^{\pm}) = 6276.26 \pm 1.44(stat) \pm 0.28(syst)$ MeV/c^2, in excellent agreement with the previous LHCb result [6] and with the world average [12].

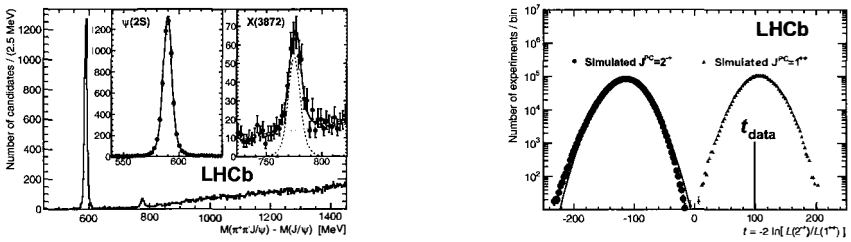

Figure 2: *Left:* Distribution of $m(J/\psi\pi^{\pm}\pi^{\mp}) - m(J/\psi)$ for $B^{\pm} \to J/\psi\pi^{\pm}\pi^{\mp}K^{\pm}$ candidates. The results of the fit around the $\psi(2S)$ and X masses are shown in the inserts. The solid blue, dashed red, and dotted green lines represent the total, signal, and background component, respectively. *Right:* Distribution of the test statistic for the simulated experiments with $J^{PC} = 2^{-+}$ (black circles) and with $J^{PC} = 1^{++}$ (red triangles). A Gaussian fit to the two distributions is overlaid (blue solid line). The value of the test statistic for the data, "t_{data}", is shown by the solid vertical line.

3 B hadron masses

At LHCb we reconstructed three of the 16 b-baryons predicted ground states, namely the Λ_b^0, Ξ_b^- and the Ω_b^- in their decays $J/\psi\Lambda^0, J/\psi\Xi^-$ and $J/\psi\Omega^-$ respectively. Using a minimal set of selections in 1 fb^{-1}of data we measured the masses [13] of the above mentioned baryons, finding the values of

$$m(\Lambda_b^0) = 5619.53 \pm 0.13(stat) \pm 0.45(syst)\text{MeV}/c^2, \quad (4)$$
$$m(\Xi_b^0) = 5795.8 \pm 0.9(stat) \pm 0.4(syst)\text{MeV}/c^2, \quad (5)$$
$$m(\Omega_b^0) = 6046.0 \pm 2.2(stat) \pm 0.4(syst)\text{MeV}/c^2, \quad (6)$$

with the dominant systematic uncertainty coming from the knowledge of the momentum scale. These results are in agreement with the previous measurements and with the world average [12].

4 X(3872) quantum numbers

The X(3872) (called X in the rest of the paper) has been the first exotic state to be discovered [14] and by far the most abundant. Its mass just above the DD^* threshold still intrigues theorists and experimentalists who wonder about its real nature. After measuring the mass and the production cross section [15], we have measured the X quantum numbers [16], resolving the ambiguity observed by Belle between 1^{++} and 2^{-+} in favour of the former. In 1.1 fb^{-1}of data we have performed a five dimensional analysis of 313±26 $B^+ \to XK^+$ decays, with $X \to J/\psi\pi^{\pm}\pi^{\mp}$ and $J/\psi \to \mu^{\pm}\mu^{\mp}$. The selection is optimised on the $B^{\pm} \to \psi(2S)K^{\pm}$ similar channel, and the signal is determined through a fit to the data using a Crystal Ball function for the signal and a linear function for the background, as shown in Fig. 2, left. A likelihood ratio test is performed to discriminate between the two quantum numbers hypotheses, which shows that the 1^{++} option is favoured and the 2^{-+} option is rejected at 8.4σ (see Fig. 2, right).

5 Conclusions

LHCb has a flourishing program in spectroscopy which is getting more and more interesting as more and more data are collected. Important results have already been achieved especially in exotic spectroscopy and more are expected in the near future.

References

1. N. Brambilla *et al.* [Quarkonium Working Group Collaboration], hep-ph/0412158.
2. N. Brambilla *et al.*, Eur. Phys. J. C **71** (2011) 1534 [arXiv:1010.5827 [hep-ph]].
3. LHCb collaboration, A. A. Alves Jr. *et al.*, 179 JINST 3 (2008) S08005.
4. F. Abe *et al.* (CDF Collaboration), *Phys. Rev. Lett.* **81**, 2432 (1998).
5. A. Abulencia *et al.* (CDF Collaboration), *Phys. Rev. Lett.* **97**, 012002 (2006).
6. R. Aaij *et al.* (LHCb Collaboration), *Phys. Rev. Lett.* **109**, 232001 (2012).
7. L. Breiman, J.H. Friedman, R.A. Olshen, and C.J. Stone, Classification and Regression Trees (Wadsworth International Group, Belmont, CA, 1984).
8. T. Skwarnicki, Ph.D. thesis, Institute of Nuclear Physics, Krakow [DESY Report No. DESY-F31-86-02, 1986 (unpublished)]
9. D. Ebert *et al. Phys. Rev.* D **68**, 094020 (2003).
10. LHCb collaboration, R. Aaij *et al.*, arXiv:1304.4530.
11. LHCb collaboration, R. Aaij *et al.*, arXiv:1304.6865.
12. J. Beringer *et al.* (Particle Data Group), *Phys. Rev.* D **86**, 010001 (2012).
13. LHCb collaboration, R. Aaij *et al.*, arXiv:1302.1072.
14. Belle collaboration, S.-K. Choi *et al.*, *Phys. Rev. Lett.* **91**, 262001 (2003).
15. LHCb collaboration, R. Aaij *et al.*,*Eur.Phys.J.* C **72**, 1972 (2012).
16. LHCb collaboration, R. Aaij *et al.*, arXiv:1302.6269.

LATTICE COMPUTATION OF $B \to D^*$, $D^{**}\ell\nu$ FORM FACTORS AT FINITE HEAVY MASSES

Mariam Atoui * †

Laboratoire de Physique Corpusculaire, Université Blaise Pascal, CNRS/IN2P3
63177 Aubière Cedex, France

We propose a strategy to compute form factors entering the semileptonic decay channel of B mesons into orbitally excited (P wave) D^{**} charmed mesons on the lattice using, for the first time, realistic charm quarks having a finite mass. We present preliminary results about the extracted transition amplitudes and form factors at different recoils and at three different b quark masses.

1 Introduction

The phenomenology of b hadrons is very rich, because owing to the large mass of the bottom quark there are many decay channels. Available semileptonic decays into any hadronic part containing a charm quark are among the decay modes of B mesons which play a critical role in the analysis of unitarity triangle and are an essential ingredient to any precise information about the CKM matrix element $|V_{cb}|$.
However, there are many puzzling features associated with the semileptonic $b \to c$ data which have existed during the last ten years as, for example, the so called "1/2 versus 3/2 puzzle" [1,2]. It corresponds to the persistent conflict between theoretical predictions and experimental measurements of semileptonic branching ratios of $\bar{B} \to D^{**}\ell\nu$:

$$\Gamma(\bar{B}_d \to D^{**}_{1/2_{\text{broad}}}\ell\nu) \ll \Gamma(\bar{B}_d \to D^{**}_{3/2_{\text{narrow}}}\ell\nu) \qquad \text{[Theory]}$$
$$\Gamma(\bar{B}_d \to D^{**}_{1/2_{\text{broad}}}\ell\nu) \gg \Gamma(\bar{B}_d \to D^{**}_{3/2_{\text{narrow}}}\ell\nu) \qquad \text{[Experimental data]}$$

where D^{**} are the first orbital excitations of D mesons having a positive parity. In the quark model picture, if we consider P wave states we see that four orbital excitations of heavy mesons should exist. In the case where the heavy quark is the charm quark c, we obtain the D^{**} represented in table 1: So, the comparison between experimental and theoretical results presents some hardships and this challenges our understanding of QCD and is of high relevance for an accurate estimate of V_{cb}.
However, in many theoretical approaches (HQET, heavy quark expansion, quark model, Lattice QCD with quenched approximation, etc...), branching ratios corresponding to the $\bar{B} \to D^{**}\ell\nu$ decay were calculated using the infinite mass limit. That is the reason why, in order to address the aforementioned questions, we propose to determine the form factors and then the branching ratios using "real" charmed quarks having a finite mass.

*email adress: matoui@in2p3.fr
†CNRS Liban scholarship

doublet	J^P values	experimental notation
$j^P = 1/2^+$	0^+	D_0^*
	1^+	D_1^*
$j^P = 3/2^+$	1^+	D_1
	2^+	D_2^*

Table 1: Classification of D^{**} states. The total angular momentum $\boldsymbol{J} = j + s_c$ is the sum of j (the angular momentum of the light component of a heavy meson) and $s_c = 1/2$ (spin of the heavy quark). The first column contains the classification in the infinite mass limit where due to the heavy quark symmetries, j is a conserved quantity and thus a good quantum number to classify the states.

In the following, I will explain the extraction of form factors corresponding to the decay of $B \to D^{**}$ in the framework of Lattice QCD and I will discuss some preliminary results we have obtained. This work is done in collaboration with B. Blossier and O. Pène (*LPT Orsay France*), V. Morénas (*LPC Clermont Ferrand France*) and K. Petrov (*LAL Orsay France*).

2 Form factors

We choose to consider in our work the decay of B into the scalar ${}^3P_0$ and the tensor ${}^3P_2$ states of D^{**}. The semileptonic decay of a pseudoscalar meson into a scalar meson is mediated by the axial part of the weak $(V-A)_\mu$ current. The operator V_μ denotes the vector current $\bar{q}\gamma_\mu b$ and the operator A_μ represents the axial current $\bar{q}\gamma_\mu\gamma_5 b$.
The matrix element for the ${}^3P_0$ state can be parametrized in terms of two form factors ($\tilde{u}_+, \tilde{u}_-$):

$$\left\langle {}^3P_0(p_{D^{**}}) \,\middle|\, A_\mu \,\middle|\, B(p_B) \right\rangle = \boxed{\tilde{u}_+}\,(p_B + p_{D^{**}})_\mu + \boxed{\tilde{u}_-}\,(p_B - p_{D^{**}})_\mu$$

and for ${}^3P_2$ state: (Here, λ is the polarization tensor corresponding to $J = 2$ states, $\lambda = \{0, \pm 1, \pm 2\}$)

$$\begin{aligned}
\left\langle {}^3P_2(p_{D^{**}}, \lambda) \,\middle|\, V_\mu \,\middle|\, B(p_B) \right\rangle &= i\boxed{\tilde{h}}\,\epsilon_{\mu\rho\sigma\tau}\,\varepsilon^{\rho\alpha *}_{(p_{D^{**}})}\,p_{B\alpha}\,(p_B + p_{D^{**}})^\sigma\,(p_B - p_{D^{**}})^\tau \\
\left\langle {}^3P_2(p_{D^{**}}, \lambda) \,\middle|\, A_\mu \,\middle|\, B(p_B) \right\rangle &= \boxed{\tilde{k}}\,\varepsilon^{(p_{D^{**}})}_{\mu\rho}\,p_B^\rho \\
&\quad + \left(\varepsilon^{(p_{D^{**}})}_{\alpha\beta}\,p_B^\alpha p_B^\beta\right)\left[\boxed{\tilde{b}_+}\,(p_B + p_{D^{**}})_\mu + \boxed{\tilde{b}_-}\,(p_B - p_{D^{**}})_\mu\right]
\end{aligned}$$

3 Going to the Lattice

The determination of many observables such as form factors, decay constants as well as numerous matrix elements, which play an important role in Flavor Physics, requires the use of non perturbative methods because when we look at the low properties of QCD, we can no longer use perturbative techniques [1]. Lattice QCD [2] is considered as the only way to systematically and rigorously solve non perturbatively the quantum theory of strong interactions starting from first principles.
Briefly, it is a means of regularizing Field Theory where the continuum and infinite space-time is replaced with a discretized grid of points in a finite volume of extent L in space and T in time, separated by a distance a (i.e. the lattice spacing). Quark fields are present on the sites of the lattice and gauge fields are the links between those sites.

3.1 LQCD action

The ***gauge action*** used in our simulation is tree-level Symanzik improved [6] with $\beta = 3.9$ corresponding to a lattice spacing $a = 0.0855$ fm and where $b_1 = -1/12$, $b_0 = 1 - 8b_1$.
The ***fermionic action*** is the Wilson Twisted-mass Lattice QCD (tmLQCD) action with two flavors of mass-degenerate quarks, tuned at *maximal twist* in the way described in full details in Ref. [5].

[1] At short distances or at high energies the quarks interact weakly, so that it is possible to study the theory of strong interactions (QCD) with perturbative techniques since the coupling constant $\alpha_{QCD} \ll 1$
[2] For further reading, I refer the reader to [3, 4]

3.2 *Simulation setup*

We have computed green functions using two ensembles of gauge configurations produced by the European Twisted Mass Collaboration (ETMC). Simulation parameters are presented in Table 2.

β	$L^3 \times T$	$\mu_{\text{sea}} = \mu_l$	μ_c	μ_h	nb. of gauge configurations
3.90	$24^3 \times 48$	0.0085	0.215	0.3498, 0.4839, 0.6694	240
4.05	$32^3 \times 64$	0.0060	0.1849	0.3008, 0.4162, 0.57757	200

Table 2: Parameters we have considered in our simulation. μ_l, μ_c, μ_h are respectively the bare twisted light, charm and heavy quark masses

4 Determination of form factors

The first step in the determination of form factors, presented in section 2, is the computation of matrix elements contributing to these form factors, and in order to access matrix elements on the lattice one computes the following three-point correlation functions.

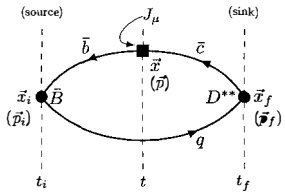

Figure 1: Sketch of the valence quark flow in the form factor of $B \to D^{**} \ell\nu$

$$\mathscr{C}^{(3)}(t, t_i, t_f, \vec{p}_i, \vec{p}_f) = \sum_{\text{positions}} \langle \mathscr{O}^\dagger_{D^{**}}(t_f, \vec{x}_f)\, J_\mu(t, \vec{x})\, \mathscr{O}_B(t_i, \vec{x}_i) \rangle \cdot e^{i(\vec{x}-\vec{x}_f)\cdot\vec{p}_f} \cdot e^{-i(\vec{x}-\vec{x}_i)\cdot\vec{p}_i}$$

where $\mathscr{O}^\dagger_{D^{**}}$, $\mathscr{O}_B$ are respectively the creation and annihilation operators of D^{**} and B mesons, J_μ is the vector or axial current. Fig. 1 represents the diagram corresponding to such correlation functions.
From the asymptotic behavior of the three-point correlation function, it is clear that the removal of the exponential factors can be achieved by considering the ratio

$$\mathscr{R}(t) = \frac{\mathscr{C}^{(3)}(t, t_i, t_f, \vec{p}_i, \vec{p}_f)}{\mathscr{C}^{(2)}_{(B)}(t - t_i, \vec{p}_f) \cdot \mathscr{C}^{(2)}_{(D)}(t_f - t, \vec{p}_i)} \cdot \sqrt{\mathscr{Z}_B} \cdot \sqrt{\mathscr{Z}_D} \tag{1}$$

where $\mathscr{Z}_M = |\langle 0|\mathscr{O}_M|M\rangle|^2$ is obtained from the fit with asymptotic behavior of the two-point correlation functions.

$$\mathscr{C}^{(2)}(t) \xrightarrow[t\to\infty]{} \frac{\mathscr{Z}_M}{2E_M}\, e^{-E_M t}$$

When the operators in the ratio (1) are sufficiently separated in time, one observes the stable signal (plateau), which is the desired hadronic matrix element:

$$\mathscr{R}(t) \xrightarrow[t-t_i\to\infty]{t_f - t\to\infty} \langle D^{**}_{(\vec{p}_f)}|(A_\mu, V_\mu)|B_{(\vec{p}_i)}\rangle$$

4.1 $\tilde{k}$ form factor

In order to obtain simpler expressions representing the interpolating fields[3] of the P wave excited states, we choose to work in the rest frame of D^{**} mesons where $p_{D^{**}} = (m_{D^{**}}, \vec{0})$ and we also choose a symmetric momentum for the B meson $p_B = (E_B, p, p, p)$. Using different values of the recoil parameter $w = \frac{E_B}{m_B} \in \{1, 1.025, 1.05, 1.1, 1.15, 1.2, 1.3\}$, we perform the extraction of $\tilde{k}$ which is the form factor contributing the most to the decay of B into D^{**}.
Combining the three point correlation functions contributing to $\tilde{k}$[4], we study the difference with respect to the infinite mass limit ones:

$$\mathscr{C}^{(3)}_{\text{infinite mass limit}} = p\,\tilde{k}_\infty \cdot \frac{\mathscr{C}^{(2)}_B\,\mathscr{C}^{(2)}_D}{\sqrt{\mathscr{Z}_B\mathscr{Z}_D}}$$

where $\tilde{k}_\infty$ is the form factor at the infinite mass limit. Using what was found in [8]:

$$\tilde{k}_\infty = \sqrt{3}\sqrt{r_{D_2^*}}\,(1+w)\,\tau_{3/2}(w) \qquad m_{D_2^*} = r_{D_2^*}\,m_B$$

$$\tau_{3/2}(w) = \tau_{3/2}(1)\left(\frac{2}{1+w}\right)^{2\sigma^2_{3/2}} \qquad \tau_{3/2}(1) \simeq 0.539 \quad \text{and} \quad \sigma^2_{3/2} \simeq 1.50$$

we find that for $w = 1.3$ (using for the moment $\beta = 3.90$):

$$\frac{\mathscr{C}^{(3)}_{\text{finite mass}}}{\mathscr{C}^{(3)}_{\text{infinite mass limit}}} = \begin{cases} a\mu = 0.34 & \rightsquigarrow\ 1.38 \pm 0.49 \\ a\mu = 0.45 & \rightsquigarrow\ 1.97 \pm 0.65 \\ a\mu = 0.67 & \rightsquigarrow\ 2.88 \pm 3.82 \end{cases}$$

The correlators corresponding to the higher b mass are characterized by large fluctuations in the effective mass plateaus and thus by large statistical uncertainties. Taking these results with a pinch of salt, and excluding data of the highest heavy quark mass from the next analysis, we estimate roughly the branching fractions $\mathscr{B}(B \to D_{(2^+)}) \cdot \mathscr{B}(D_{(2^+)} \to D^*\pi)$.

$$\mathscr{B}(B \to D_{(2^+)}) \cdot \mathscr{B}(D_{(2^+)} \to D^*\pi) = \begin{cases} m_{B_{\text{GeV}}} = 2.4 & \rightsquigarrow (3.6 \pm 2.6) \times 10^{-3} \\ m_{B_{\text{GeV}}} = 2.9 & \rightsquigarrow (7.4 \pm 4.9) \times 10^{-3} \end{cases}$$

Although we are still far from the physical B mass, we have an indication that there are many observables in B physics that can be determined using LQCD. When results are more refined we aim to do a more detailed comparison with the experimental data. Results will be published as soon as ready.

4.2 Scalar transition amplitude

The determination of matrix elements corresponding to the decay of B into ${}^3P_0(p_{D^{**}})$ state, at different recoils w, leads to the weak form factors $\bar{u}_+$ and $\bar{u}_-$. For the moment, we focus our attention on the extraction of $\langle {}^3P_0(p_{D^{**}}) \,|\, A_0 \,|\, B(p_B)\rangle$ at zero recoil. It seems that this hadronic matrix element is not equal to zero (see Fig. 2 and 3) contrary to what was already found in the infinite mass limit. Note that it is an important result that the matrix element $\langle {}^3P_0(m_{D^{**}}) \,|\, A_0 \,|\, B(m_B)\rangle$ is non vanishing. It shows us how working with a realistic charm quark could lead to much more accurate results than working with the infinite mass limit approximation.

[3] interpolating fields are the mesonic creation and annihilation operators which defines the quantum number of a state. To find the interpolating fields of 2^+ states, we followed a strategy based on group theory where non local operators are implemented [13].

[4] For example, if we consider the $\lambda = 0$ polarization of the ${}^3P_2$ state, $\tilde{k}$ could be written as:

$$-\frac{\sqrt{6}}{p}\langle {}^3P_2(0) \,|\, A_1 \,|\, B(p_B)\rangle$$

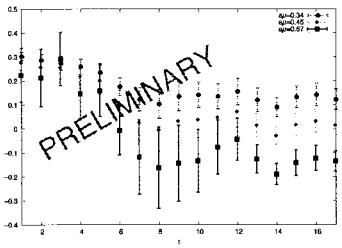

Figure 2: $\langle {}^3P_0(m_{D^{**}}) \,|\, A_0 \,|\, B(m_B) \rangle$ at $\beta = 3.9$

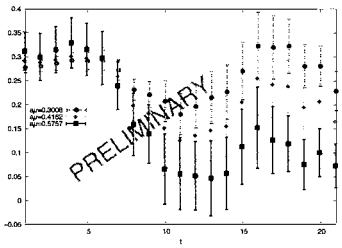

Figure 3: $\langle {}^3P_0(m_{D^{**}}) \,|\, A_0 \,|\, B(m_B) \rangle$ at $\beta = 4.05$

4.3 $\mathscr{F}_0(1)$ *at zero recoil*

As a byproduct of our analysis, we can also study the $B \to D^* \ell \nu$ decay at zero recoil. The corresponding form factor reads [11, 12]:

$$\mathscr{F}_0(1) = Z_A \, \frac{\langle D^*(p_{D^*}) \,|\, A_i \,|\, B(p_B) \rangle}{2\sqrt{m_B \, m_{D^*}}}$$

where Z_A is the axial renormalisation constant taken from [9]. The values obtained for $\mathscr{F}_0(1)$ are presented in tables 3 and 4. They do not show any contradiction with what was already found using Lattice QCD with a different fermionic action and different approximations, but the extrapolated value (Fig. 4) seems to be higher than what was already found using QCD sum rules [10].

$a\mu_b$	$\mathscr{F}_0(1)$
0.35	0.882(44)
0.48	0.874(48)
0.67	0.888(58)

Table 3: $\mathscr{F}_0(1)$ at $\beta = 3.9$ for different values of $a\mu_b$

$a\mu_b$	$\mathscr{F}_0(1)$
0.301	0.814(48)
0.416	0.821(50)
0.5757	0.827(53)

Table 4: $\mathscr{F}_0(1)$ at $\beta = 4.05$ for different values of $a\mu_b$

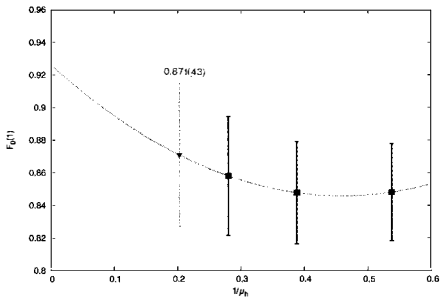

Figure 4: Extrapolation of $\mathscr{F}_0(1)$ at finite physical b quark masses

5 Discussion

During the last ten years, techniques and algorithms in LQCD have been developed and computing power has increased: this is really encouraging for the Lattice community where some important parameters in B physics are and will be calculated reaching a precision on par with the experimental one.
However, working with excited states on the lattice is not a trivial issue. On one side, analytical expressions of $B \to D^{**}$ transition amplitudes, form factors and decay rates can be calculated. On the other side, isolation of such excited states is very delicate and there is an increase in noise when going to high momentum and discretization errors become larger when the b quark mass increases. We hope that with higher statistics, results will be more clear in order to extract the sought form factors and to discuss their implications.

Acknowledgments

Mariam Atoui wants to thank the Lebanese National Center for Scientific Research CNRS Liban for the financial support and acknowledges the help from the Lebanese University during the first year of her PhD thesis.

References

1. I. I. Bigi, B. Blossier, A. Le Yaouanc, L. Oliver, O. Pene, J. -C. Raynal, A. Oyanguren and P. Roudeau, Eur. Phys. J. C **52** (2007) 975 [arXiv:0708.1621 [hep-ph]].
2. A. Le Yaouanc, L. Oliver, O. Pene, J. C. Raynal and V. Morenas, Phys. Lett. B **520** (2001) 25 [hep-ph/0105247].
3. T. DeGrand and C. DeTar, *« Lattice Methods for Quantum Chromodynamics »*, World Scientific Publishing, (2006)
4. C. Gattringer and C. B. Lang, *« Quantum Chromodynamics on the Lattice »*, Springer, (2010)
5. Ph. Boucaud *et al.* [ETM Collaboration], Phys. Lett. B **650** (2007) 304 [hep-lat/0701012].
6. P. Weisz and R. Wohlert, Nucl. Phys. B **236** (1984) 397 [Erratum-ibid. B **247** (1984) 544].
7. A. Shindler, [hep-lat/0707.4093] (2008).
8. V. Morenas, A. Le Yaouanc, L. Oliver, O. Pene and J. C. Raynal, *Phys. Rev.* D **56**, 5668 (1997) [hep-ph/9706265].
9. M. Constantinou *et al.* [hep-lat/1004.1115] (2010)
10. P. Gambino *et al.* [hep-lat/1206.2296] (2012)
11. M. Antonelli *et al.* [hep-lat/0907.5386] (2010)
12. Jon A. Bailey *et al.* [hep-lat/1011.2166] (2010)
13. P. Lacock *et al.* [UKQCD Collaboration], Phys. Rev. D **54** (1996) 6997 [hep-lat/9605025].

Charmonium study at BESIII

Changsheng.Ji [a]
University of Science and Technology of China , He Fei , An Hui

We present measurements of the charmonium state $h_c(^1P_1)$, η_c and $\eta_c(2S)$, using a sample of 1.06×10^8 $\psi(3686)$ events collected with the BESIII detector at the BEPCII storage ring. The results include the masses, widths, production and decay rates of these resonances, which shed light on the investigation of the charmonium spectroscopy.

1 Introduction

BESIII [1] is a major upgrade of the BESII experiment at the BEPCII accelerator [2] for studies of hadron spectroscopy as well as τ−charm physics [3]. The design peak luminosity of the double-ring e^+e^- collider, BEPCII, is 10^{33} cm^{-2}s^{-1} at center-of-mass energy of 3.78 GeV. The BESIII detector with a geometrical acceptance of 93% of 4π consists of a main drift chamber (MDC) with momentum resolution 0.5% at 1 GeV/c, an electromagnetic calorimeter (EMC) with energy resolution 2.5% at 1.0 GeV, a Time-Of-Flight counter (TOF), a superconductor magnet with a magnetic strength of 1 T, and a muon chamber system (MUC) made of resistive plate chambers.

Based on 106×10^6 [4] $\psi(3686)$ events taken in 2009, the charmonium spectroscopy is widely studied, and here we focused on the measurement of $h_c(^1P_1)$, η_c and $\eta_c(2S)$.

2 Measurement of $h_c(^1P_1)$ using $\psi(3686) \to \pi^0 h_c(^1P_1)$

Knowledge is sparse on the spin singlet state $h_c(^1P_1)$ although the charmonium family of mesons has been studied for many years. The CLEO Collaboration first observed the $h_c(^1P_1)$ in the cascade process $\psi(3686) \to \pi^0 h_c$, $h_c \to \gamma\eta_c$ in both inclusive and exclusive measurements [5]. The E835 experiment [6] found the evidence of $p\bar{p} \to h_c \to \gamma\eta_c$ by scanning the antiproton energy. There are also some theoretical predictions [7,8,9] about the production and decays of $h_c(^1P_1)$, which can be tested with the largest $\psi(3686)$ data sample at BESIII.

Both E1-tagged and inclusive method in $h_c \to \gamma\eta_c$ are performed at BESIII to study the process $\psi(3686) \to \pi^0 h_c(^1P_1)$. The results are shown in Fig. 2. The mass and width of $h_c(^1P_1)$ are determined to be $M_{h_c} = 3525.40 \pm 0.13 \pm 0.18$ MeV/c^2 and $\Gamma_{h_c} = 0.73 \pm 0.45 \pm 0.28$ MeV from the E1 tagged method. The mass split $\Delta M_{hf} \equiv < M(1^3P) > - M(^1P_1) = -0.10 \pm 0.13 \pm 0.18$ MeV/c^2 is consistent with no strong spin-spin interaction. The branching fractions are determined to be $\mathcal{B}(\psi(3686) \to \pi^0 h_c(^1P_1)) = (8.3 \pm 1.3 \pm 1.0) \times 10^{-4}$ and $\mathcal{B}(h_c(^1P_1) \to \gamma\eta_c) = (54.3 \pm 6.7 \pm 5.2)\%$, which are first measurement and agree with the theoretical predictions [7]. Exclusive measurements are also performed with sixteen η_c decay channels [10], and the mass and width are measured to be $M_{h_c} = 3525.31 \pm 0.11 \pm 0.14$ MeV/c^2 and $\Gamma_{h_c} = 0.70 \pm 0.28 \pm 0.22$ MeV from the simultaneous fit on the recoil-mass of π^0 as shown in Fig. 2. The measurements are consistent with the previous values at CLEO-c [11].

[a]On behalf of the BESIII Collaboration. Email: jcs@mail.ustc.edu.cn

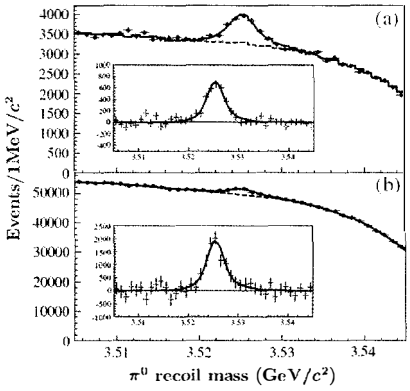

Figure 1: (a)The π^0 recoil-mass spectrum and fit for the E1-tagged analysis of $\psi(3686) \to \pi^0 h_c$, $h_c \to \gamma\eta_c$. (b)The π^0 recoil-mass spectrum and fit for the inclusive analysis of $\psi(3686) \to \pi^0 h_c$.

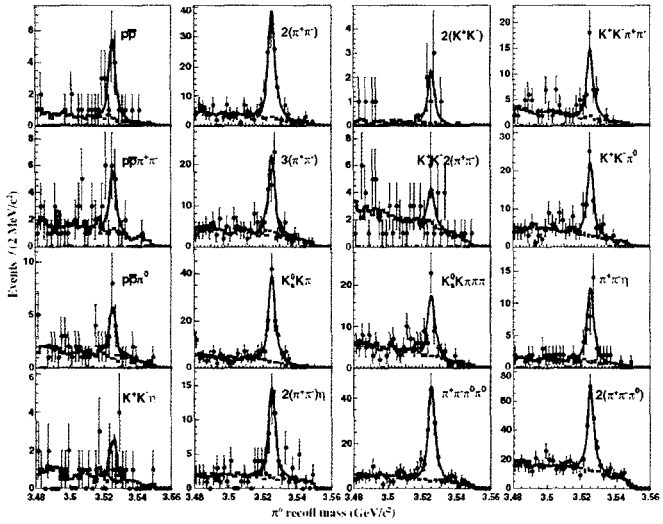

Figure 2: The simultaneously fitted π^0 recoil mass spectra in $\psi(3686) \to \pi^0 h_c$, $h_c \to \gamma\eta_c$, $\eta_c \to X_i$ for the 16 final states X_i

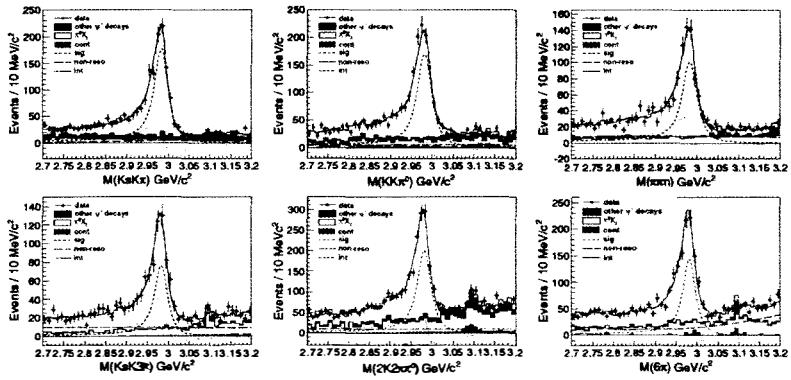

Figure 3: The fit results on the $M(X_i)$ invariant mass distributions for the decays $K_S K^+\pi^-$, $K^+K^-\pi^0$, $\eta\pi^+\pi^-$, $K_S K^+\pi^+\pi^-\pi^-$, $K^+K^-\pi^+\pi^-\pi^0$, and $3(\pi^+\pi^-)$, respectively.

3 Measurement the mass and width of η_c with $\psi(3686) \to \gamma\eta_c$

Properties of the lowest-lying S-wave spin singlet charmonium state, the η_c, are not well understood although it has been observed for many years. Early measurements of the properties of the η_c using J/ψ radiative transitions [12] found a mass and width near 2978 MeV/c^2 and 10 MeV, respectively. However, recent experiments, including photon-photon fusion and B decays, have reported a significantly higher mass and a much larger width [13]. The most recent study by the CLEO-c experiment [14], using both $\psi(3686) \to \gamma\eta_c$ and $J/\psi \to \gamma\eta_c$, pointed out a distortion of the η_c line shape in $\psi(3686)$ decays, but similar effect is not observed in $\psi(3686) \to \pi^0 h_c$, $h_c \to \gamma\eta_c$ at BESIII [10].

We measured the η_c mass and width using the radiative transition $\psi(3686) \to \gamma\eta_c$ by reconstructing η_c from six decay modes, including $K_S K^+\pi^-$, $K^+K^-\pi^0$, $\eta\pi^+\pi^-$, $K_S K^+\pi^+\pi^-\pi^-$, $K^+K^-\pi^+\pi^-\pi^0$, and $3\pi^+\pi^-$. A simultaneous fit with unique η_c mass and width is performed on the η_c mass spectra as shown in Fig. 3. The η_c line shapes were successfully described using a combination of the energy dependence of the hindered-M1 transition matrix elements and a full interference with nonresonant $\psi(3686)$ radiative decays where the quantum number of the non-η_c components are assumed to be 0^{-+}. The fit yields $M = 2983.9 \pm 0.6 \pm 0.6$ MeV/c^2, $\Gamma = 31.3 \pm 1.2 \pm 0.9$ MeV, and $\phi = 2.40 \pm 0.07 \pm 0.47$ rad (constructive) or $\phi = 4.19 \pm 0.03 \pm 0.47$ rad (destructive). Our results are consistent with those from photon-photon fusion and B decays. From this measurement, we determine the hyperfine mass splitting to be $\Delta M_{hf}(1S)_{c\bar{c}} = M(J/\psi) - M(\eta_c) = 112.6 \pm 0.8$ MeV/c^2, which agrees well with recent lattice computations [15] as well as quark-model prediction [16].

4 First observation of the M1 transition $\psi(3686) \to \gamma\eta_c(2S)$

The $\eta_c(2S)$ was first observed by the Belle collaboration in the B decays [17] and was confirmed in the two-photon production of $K^0_S K^\pm\pi^\mp$ [18] as well as in the double-charmonium production process $e^+e^- \to J/\psi c\bar{c}$ [19]. But it was absent in the M1 radiative transition of $\psi(3686) \to \gamma\eta_c(2S)$ [20,21]. The branching fractions are predicted to be $\mathcal{B}(\psi(3686) \to \gamma\eta_c(2S)) = (0.1-6.2)\times 10^{-4}$ by many authors [22].

BESIII made the first observation of $\psi\prime \to \gamma\eta_c(2S)$, with $\eta_c(2S) \to K\bar{K}\pi$. Fig. 4 shows the simultaneous fit to the $K\bar{K}\pi$ mass spectrum, where the yields of $\eta_c(2S)$ events are 81±14 for the $K^0_S K^\pm K^\mp$ channel and 46±11 for the $K^+K^-\pi^0$ channel. The combined statistical significance of

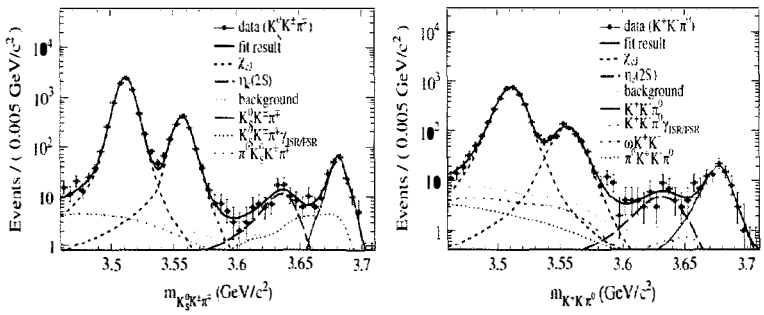

Figure 4: The simultaneous likelihood fit on the mass spectrum of $K_S K^\pm \pi^\mp$ (left panel) and $K^+K^-\pi^0$ (right panel).

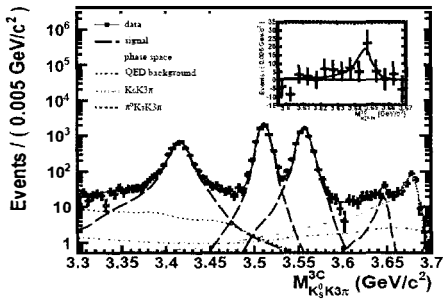

Figure 5: The fit results on the mass spectrum of $K_S K 3\pi$.

the signal in the two modes is 11.1 σ. The mass and width of $\eta_c(2S)$ are measured to be $M_{\eta_c(2S)} = 3637.6 \pm 2.9$ MeV/c^2 and $\Gamma_{\eta_c(2S)} = 16.9 \pm 6.4$ MeV, respectively. The product branching fraction is measured to be $\mathcal{B}(\psi(3686) \to \gamma\eta_c(2S)) \times (\eta_c(2S) \to K\bar{K}\pi) = (1.30 \pm 0.20) \times 10^{-5}$. Using the measurement of $\mathcal{B}(\eta_c(2S) \to K\bar{K}\pi) = (1.9 \pm 0.4 \pm 1.1)\%$ from the BARBAR experiment [23], we obtained the M1-transition branching fraction of $\mathcal{B}(\psi(3686) \to \gamma\eta_c(2S)) = (6.8 \pm 1.1 \pm 4.5) \times 10^{-4}$, which is consistent with the prediction from CLEO-c [21].

We also investigate the M1-transition $\psi(3686) \to \gamma\eta_c(2S)$ with $\eta_c(2S) \to K^0_S K^\pm \pi^\mp \pi^+ \pi^-$. Fig.5 shows the fit result to the mass spectrum of $K^0_S K^\pm \pi^\mp \pi^+ \pi^-$, from which the yield of $\eta_c(2S)$ is 57 ± 17 with a significance of 4.2σ. The mass of the $\eta_c(2S)$ is measured to be $3646.9 \pm 1.6 \pm 3.6$ MeV/c^2, and the width is $9.2 \pm 4.8 \pm 2.9$. Comparing with BESIII previous measurements [24], the width is consistent with each other within 1 standard deviation and the mass is about 2 standard deviations.

5 Summary

Based on the 1.06×10^8 $\psi(3686)$ data sample collected by BESIII detector at BEPCII, charmonium states $h_c(^1P_1)$, η_c, $\eta_c(2S)$ have been well studied: the absolute branching fractions of $\psi(3686) \to \pi^0 h_c(^1P_1)$, $h_c(^1P_1) \to \gamma\eta_c$ as well as the width of $h_c(^1P_1)$ are measured for the first time; parameters of η_c are measured with high precision, interference between η_c and the non-resonant amplitudes around the η_c mass is considered for the first time; first observation of M1-transition $\psi(3686) \to \gamma\eta_c(2S)$ with $K\bar{K}\pi$ final states and evidence for the $K_S K^\pm \pi^\mp \pi^+ \pi^-$.

Acknowledgments

The BESIII Collaboration thanks the staff of BEPCII and the computing center for their hard efforts. We think all the colleagues contributing on the physical analysis.

References

1. M. Ablikim *et al. (BESIII Collaboration),* Nucl. Instrum. Methods *A* **614**, *345 (2010).*
2. *J. Z. Bai et al. (BES Collaboration),* Nucl. Instrum. Methods *A* **344**, *319 (1994).*
3. *D. M. Asner et al.,* Int. J. Mod. Phys. *A* **24**, *No. 1, 499 (2009).*
4. *M. Ablikim et al. (BESIII Collaboration), arXiv:1209.6199 [Chin. Phys. C (to be published)].*
5. *J.L. Rosner et al. (CLEO Collaboration),* Phys. Rev. Lett. **95**, *102003 (2005); P.Rubin et al. (CLEO Collaboration),* Phys. Rev. *D* **72**, *092004 (2005).*
6. *M.Andreotti et al. (E-835 Collaboration),* Phys. Rev. *D* **72**, *051106 (2009).*
7. *Y.P.Kuang,* Phys. Rev. *D* **65**, *094024 (2002).*
8. *S.Godfrey and J.Rosner,* Phys. Rev. *D* **66**, *014012 (2002).*
9. *J.J.Dudek, R.G.Edwards, and D.G.Richards,* Phys. Rev. *D* **73**, *074507 (2006).*
10. *M. Ablikim et al. (BESIII Collaboration),* Phys. Rev. *D* **86**, *092009 (2012).*
11. *G.S.Adams et al. (CLEO Collaboration),* Phys. Rev. *D* **80**, *051106 (2009).*
12. *R.M.Baltrusaitis et al. (Mark-III Collaboration),* Phys. Rev. *D* **33**, *629 (1986); J.Z.Bai et al. (BES Collaboration),* Phys. Lett. *B* **555**, *174 (2003).*
13. *D.M.Asner et al. (CLEO-Collaboration),* Phys. Rev. Lett. **92**, *142001 (2004); B.Aubert et al. (BARBAR Collaboration),* Phys. Rev. Lett. **92**, *142002 (2004); A.Vinokurova et al. (Belle Collaboration),* Phys. Lett. *B* **706**, *139 (2011).*
14. *R.E.Mitchell et al. (CLEO Collaboration),* Phys. Rev. Lett. **102**, *011801 (2009).*
15. *T.Burch et al.,* Phys. Rev. *D* **81**, *034508 (2010); L.Levkova and C.DeTar,* Phys. Rev. *D* **83**, *074504 (2011).*
16. *K.K.Seht, arXiv:0912.2776v1.*
17. *S.K.Choi et al. (Belle Collaboration),* Phys. Rev. Lett. **89**, *102001 (2002).*
18. *B.Auber et al. (BARBAR Collaboration),* Phys. Rev. Lett. **92**, *142002 (2004); D.M.Asner et al. (CLEO Collaboration),* Phys. Rev. Lett. **92**, *142001 (2004).*
19. *B.Auber et al. (BARBAR Collaboration),* Phys. Rev. *D* **72**, *031101 (2005); K.Abe et al. (Belle Collaboration),* Phys. Rev. Lett. **89**, *142001 (2002).*
20. *C.Edwards et al. (Crystal Ball Collaboration),* Phys. Rev. Lett. **48**, *70 (1982); M.Ablikim et al. (BESIII Collaboration),* Phys. Rev. *D* **84**, *091102 (2011).*
21. *D.Cronin-Hennessy et al.(CLEO Collaboration),* Phys. Rev. *D* **81**, *052002 (2010).*
22. *See the compilation of the results in K. Gao, arXiv:0909.2812.*
23. *B.Aubert et al. (BARBAR Collaboration),* Phys. Rev. *D* **78**, *012006 (2008).*
24. *M.Ablikim et al. (BESIII Collaboration),* Phys. Rev. Lett. **109**, *042003 (2012).*

Recent results on bottomonium(-like) states at Belle

P.Krokovny, A. Bondar and A. Garmash (on behalf of the Belle Collaboration)
Budker Institute of Nuclear Physics and Novosibirsk State University

We report the first observation of the three-body $\Upsilon(5S) \to \Upsilon(1,2S)\pi^0\pi^0$ decays. Strong evidence for the $Z_b^0(10610)$ with 4.9σ significance is found in a Dalitz plot analysis of the $\Upsilon(5S) \to \Upsilon(2S)\pi^0\pi^0$ decays. First results on the analysis of the three-body $\Upsilon(10860) \to [B\bar{B}^* + \text{c.c.}]^{\pm}\pi^{\mp}$ and $\Upsilon(10860) \to [B^*\bar{B}^*]^{\pm}\pi^{\mp}$ including first observation of $Z_b^{\pm}(10610) \to [B\bar{B}^* + \text{c.c.}]^{\pm}$ and $Z_b^{\pm}(10650) \to [B^*\bar{B}^*]^{\pm}$ are also reported. The results are obtained with a 121.4fb^{-1} data sample collected with the Belle detector at the $\Upsilon(5S)$ resonance at the KEKB asymmetric-energy e^+e^- collider.

1 Introduction

Two new charged bottomonium-like resonances, $Z_b(10610)$ and $Z_b(10650)$, have recently been observed by the Belle Collaboration in decays of $\Upsilon(10860)$ to five different final states: $\Upsilon(nS)\pi^+\pi^-$, $n = 1,2,3$ and $h_b(mP)\pi^+\pi^-$, $m = 1,2$ [1,2]. The analysis of the quark composition of the initial and final states allows to assert that these hadronic objects are the first unambiguous examples of states of an exotic nature: Z_b should be comprised of (at least) four quarks. Several models have been proposed to describe the internal structure of these states. One suggests [3] that $Z_b(10610)$ and $Z_b(10650)$ states might be a loosely bound $B\bar{B}^*$ and $B^*\bar{B}^*$ systems, respectively. The proximity of the $Z_b(10610)$ and $Z_b(10650)$ masses to those of the sum of the B and B^* mesons and the sum of the two B^* mesons, respectively, supports this hypothesis. In this case, it would be natural to expect that the $Z_b(10610)$ and $Z_b(10650)$ states decay respectively to $B\bar{B}^*$ and $B^*\bar{B}^*$ final states with substantial rates. In this analysis we use 121.4 fb^{-1} of data accumulated by the Belle detector at a center-of-mass (c.m.) energy near the $\Upsilon(10860)$ to study three-body $\Upsilon(10860) \to [B^{(*)}\bar{B}^{(*)}]^{\pm}\pi^{\mp}$ decays and to search for $\Upsilon(10860) \to Z_b^{\pm}\pi^{\mp} \to [B^{(*)}\bar{B}^*]^{\pm}\pi^{\mp}$ decays. We also search for a neutral partner of Z_b states in the resonant substructure of the $\Upsilon(5S) \to \Upsilon(nS)\pi^0\pi^0$ decays.

2 $\Upsilon(5S) \to \Upsilon(nS)\pi^0\pi^0$ decays

We reconstruct $\Upsilon(nS)$ candidates from pairs of leptons (e^+e^- and $\mu^+\mu^-$). An additional decay channel is used for the $\Upsilon(2S)$: $\Upsilon(2S) \to \Upsilon(1S)[l^+l^-]\pi^+\pi^-$. Muon and electron candidates are required to be positively identified. Candidate π^0 mesons are selected from pairs of photons with an invariant mass within 15 MeV/c^2 of the nominal π^0 mass. $\Upsilon(5S) \to \Upsilon(nS)[l^+l^-]\pi^0\pi^0$ candidates are identified via the missing mass recoiling against the $\pi^0\pi^0$ system, $M_{\text{miss}}(\pi^0\pi^0)$. More details can be found in Ref. [4]. Figure 1 shows the extraction of the $\Upsilon(nS)$ signal yield. Results are summarized in Table 1. Branching fraction is calculated as $\mathcal{B} = \frac{N_{\text{sig}}}{\epsilon\mathcal{L}\sigma(e^+e^- \to \Upsilon(5S))}$, where N_{sig} is number of signal events, ϵ is reconstruction efficiency, $\mathcal{L}$ is integrated luminosity. Weighted averages are found to be $\mathcal{B}(\Upsilon(5S) \to \Upsilon(1S)\pi^0\pi^0) = (2.25 \pm 0.11 \pm 0.20) \times 10^{-3}$ and $\mathcal{B}(\Upsilon(5S) \to \Upsilon(2S)\pi^0\pi^0) = (3.66 \pm 0.22 \pm 0.48) \times 10^{-3}$.

The amplitude analysis of the three-body $\Upsilon(5S) \to \Upsilon(nS)\pi^0\pi^0$ decays utilizes an unbinned maximum likelihood fit. We parameterize the three-body decay amplitude as a sum of quasi-two-body amplitudes: $M(s_1, s_2) = A_{Z1} + A_{Z2} + A_{f_0} + A_{f_2} + A_{\text{nr}}$, where A_{Z1} and A_{Z2} are amplitudes

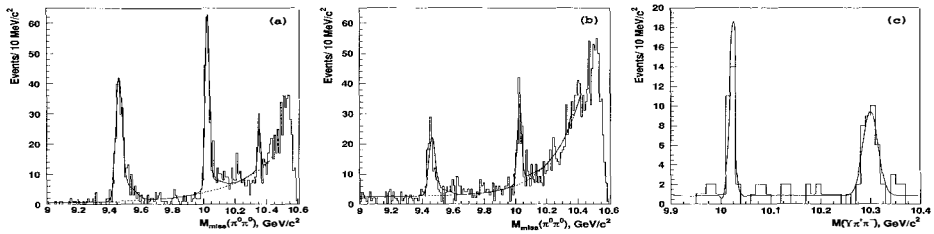

Figure 1: The $\pi^0\pi^0$ missing mass distribution for $\Upsilon(nS)\pi^0\pi^0$, (a) $\Upsilon(nS) \to \mu^+\mu^-$ and (b) $\Upsilon(nS) \to e^+e^-$ candidates. The $M(\Upsilon(1S)\pi^+\pi^-)$ distribution for $\Upsilon(2S) \to \Upsilon(1S)\pi^+\pi^-$ candidates is shown in (c). Histograms represent the data. The solid curves show the fit result while the dashed curves correspond to the background contributions.

Table 1: Signal yield, MC efficiency, measured branching fraction, number of selected events and purity.

Final state	Signal yield	ϵ, %	$\mathcal{B}$, 10^{-3}	Events	Purity
$\Upsilon(1S) \to \mu^+\mu^-$	261 ± 15	11.2	2.28 ± 0.13	247	0.95
$\Upsilon(1S) \to e^+e^-$	123 ± 13	5.61	2.15 ± 0.23	140	0.78
$\Upsilon(2S) \to \mu^+\mu^-$	241 ± 18	8.04	3.77 ± 0.28	253	0.87
$\Upsilon(2S) \to e^+e^-$	108 ± 13	3.58	3.84 ± 0.46	151	0.66
$\Upsilon(2S) \to \Upsilon(1S)\pi^+\pi^-$	24 ± 5	2.27	2.85 ± 0.60	28	0.86

for contributions from the $Z_b^0(10610)$ and $Z_b^0(10650)$, respectively; the amplitudes A_{f_0}, A_{f_2} and $A_{\rm nr}$ are the contributions from the $\pi^0\pi^0$ system in an $f_0(980)$, $f_2(1275)$ and a non-resonant state, respectively. The masses and widths of Z_b resonances are fixed at the values obtained from the $\Upsilon(nS)\pi^+\pi^-$ analysis: $M(Z_1) = 10607.2\,\mathrm{MeV/c^2}$, $\Gamma(Z_1) = 18.4\,\mathrm{MeV/c}$, $M(Z_2) = 10652.2\,\mathrm{MeV/c^2}$, $\Gamma(Z_2) = 11.5\,\mathrm{MeV/c}$ [?]. We use a Flatté function for the $f_0(980)$ and a Breit-Wigner function for the $f_2(1275)$. The non-resonant amplitude $A_{\rm nr}$ is parameterized as $A_{\rm nr} = A^1_{\rm nr}e^{i\phi^1_{\rm nr}} + A^2_{\rm nr}e^{i\phi^2_{\rm nr}}s_3$. As the fit is sensitive only to the relative amplitudes and phases between decay modes, we fix $A^1_{\rm nr} = 10.0$ and $\phi^1_{\rm nr} = 0.0$. The logarithmic likelihood function is defined as $\mathcal{L} = -2\sum\log\{\epsilon(s_1,s_2)f_{\rm sig}S(s_1,s_2) + (1-f_{\rm sig})B(s_1,s_2)\}$, where $S(s_1,s_2)$ denotes $|M(s_1,s_2)|^2$ convoluted with the detector resolution function, $\epsilon(s_1,s_2)$ describes variation of the reconstruction efficiency over the Dalitz plot and $f_{\rm sig}$ is the fraction of signal events in the data sample. The fraction $f_{\rm sig}$ is determined separately for each $\Upsilon(nS)$ decay mode (see Table 1). The function $B(s_1,s_2)$ describes the distribution of background events over the phase space. Both $\epsilon(s_1,s_2)\cdot S(s_1,s_2)$ and $B(s_1,s_2)$ are normalized to unity. Results of the fits are shown in Fig. 2 as one-dimensional projections that look similar to the corresponding distributions for the $\Upsilon(nS)\pi^+\pi^-$ decays [?]. A Z_b^0 signal is most clearly seen in $M(\Upsilon\pi^0)_{\rm max}$. The values and errors of amplitudes and phases obtained from the fit are presented in [4]. The statistical significance of the $Z_b^0(10610)$ signal in the $\Upsilon(2S)\pi^0\pi^0$ sample is 5.3σ. The signal for the $Z_b^0(10610)$ is not significant in the fit to the $\Upsilon(1S)\pi^0\pi^0$ events due to the smaller relative branching fraction. The signal of the $Z_b^0(10650)$ is not significant in either $\Upsilon(1)\pi^0\pi^0$ or $\Upsilon(2S)\pi^0\pi^0$ datasets.

We study possible uncertainties due to parameterization of the background PDF, variation of signal efficiency over the Dalitz plot and detector resolution function. The model uncertainty is estimated using various description of S-wave contribution. The significance of the $Z_b^0(10610)$ signal exceeds 4.9σ in all cases. We use this value as the final value for the $Z_b^0(10610)$ significance.

3 $\Upsilon(10860) \to B^{(*)}\bar{B}^*\pi$ Decays

B decays are reconstructed in the following channels: $B^+ \to J/\psi K^+$, $B^+ \to \bar{D}^0\pi^+$, $B^0 \to J/\psi K^{*0}$, $B^0 \to D^{(*)-}\pi^+$. We identify B candidates by their invariant mass $M(B)$ and momentum $P(B)$ in the c.m. We require $M(B)$ to be within 30 to 40 MeV/c^2 (depending on the B decay mode) of the nominal B mass. Reconstructed B^+ or B^0 candidates are then combined with a π^- candidate

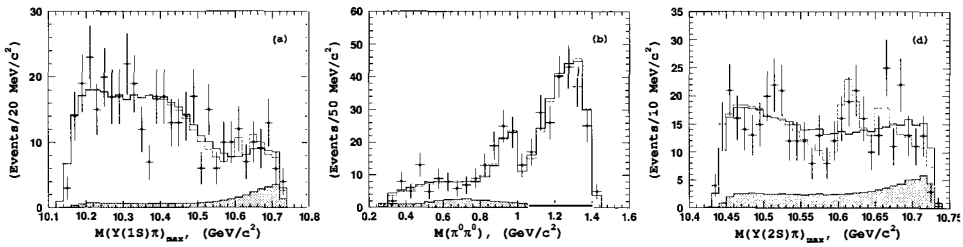

Figure 2: Comparison of the fit results (open histograms) with experimental data (points with error bars) for the (a,b) $\Upsilon(1S)\pi^0\pi^0$ and (c) $\Upsilon(2S)\pi^0\pi^0$ events in the signal region. Red and blue open histograms show the fit with and without Z_b^{0}'s, respectively. Hatched histograms show the background components.

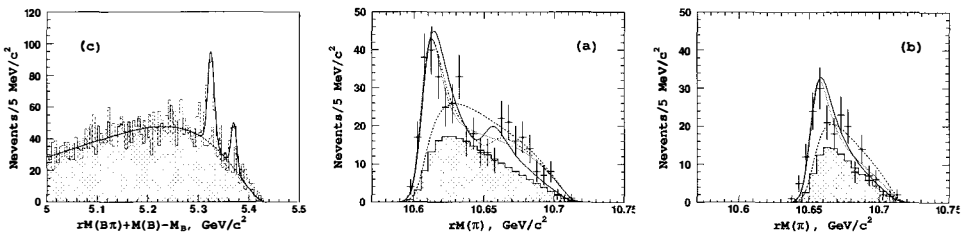

Figure 3: (a) $M_r(B\pi)$ distributions for selected B candidates in data. Hatched histogram shows distribution for events in the $M(B)$ sidebands. (b) $M_r(\pi)$ distribution for right-sign $B\pi$ combinations for $\Upsilon(10860) \to BB^*\pi$ and (c) $\Upsilon(10860) \to B^*B^*\pi$ candidate events. Points with error bars are data, the solid line is the result of the fit with the nominal model, the dashed line - fit to pure non-resonant amplitude, the dotted line - fit to a single Z_b state plus a non-resonant amplitude, and the dash-dotted - two Z_b states and a non-resonant amplitude. The hatched histogram represents background component.

and a recoil mass to the $B\pi$ combination, $M_r(B\pi)$, is calculated as $M_r(B\pi) = \sqrt{E^2_{\rm cms} - P^2_{B\pi}}$, where $E_{\rm cms}$ is the c.m. energy and $P_{B\pi}$ is the measured three-momentum of the $B\pi$ combination. More details can be found in Ref. [5]. The $M_r(B\pi) + M(B) - M_B$ distribution for the data is shown in Fig. 3(a), where clear peaks are visible in the $BB^*\pi$ and $B^*B^*\pi$ signal regions. The fit to this distribution gives $N_{BB\pi} = 1 \pm 14$, $N_{BB^*\pi} = 184 \pm 19$ and $N_{B^*B^*\pi} = 82 \pm 11$ signal events. The statistical significance of the observed $BB^*\pi$ and $B^*B^*\pi$ signal is 9.3σ and 5.7σ, respectively. For the subsequent analysis of the internal structures of the three-body decays, we require $|(M_r(B) + M(B) - M_B) - M_{B^*}| < 0.015$ GeV/c^2 to select $\Upsilon(10860) \to BB^*\pi$ events and $|(M_r(B) + M(B) - M_B) - (M_{B^*} + E_\gamma)| < 0.015$ GeV/c^2, where $E_\gamma = 0.049$ GeV, to select $\Upsilon(10860) \to B^*B^*\pi$ events. For selected $B^{(*)}B^{(*)}\pi$ candidate events, we calculate the mass recoiling against the charged pion: $M_r(\pi) = \sqrt{E^2_{\rm cms} - P^2_\pi}$, where $P_{B\pi}$ is the measured three-momentum of the charged pion.

The $M_r(\pi)$ distributions for right-sign $B\pi$ combinations in the $BB^*\pi$ and $B^*B^*\pi$ signal regions are shown in Fig. 3. Excesses of signal events over the expected background levels at lower mass edges of the $M_r(\pi)$ spectra are clearly visible for both final states. The distribution of signal $\Upsilon(10860) \to BB^*\pi$ events is parameterized with the following model $S_{BB^*\pi}(\boldsymbol{m}) = (A_{Z_b(10610)} + A_{NR}) \times E_{BB^*\pi}(\boldsymbol{m})$, where A_{NR} is the non-resonant amplitude parameterized as a complex constant and the $Z_b(10610)$ amplitude is a Breit-Wigner function. As a variation of this nominal model, we also add a second Breit-Wigner amplitude to account for possible $Z_b(10650) \to BB^*\pi$ decay. We also fit the data with only the $Z_b(10610)$ channel included in the decay amplitude. The results of these fits are shown in Fig. 3(b). Two models give about equally good description of the data: nominal model and a model with additional non-resonant amplitude. However, we select the former one as our nominal model since adding a non-resonant amplitude does not improve the fit quality that much. The worst fit

Table 2: List of branching fractions for the $Z_b^+(10610)$ and $Z_b^+(10650)$ decays.

$\mathcal{B}$, %	$\Upsilon(1S)\pi^+$	$\Upsilon(2S)\pi^+$	$\Upsilon(3S)\pi^+$	$h_b(1P)\pi^+$	$h_b(2P)\pi^+$	$B^{(*)}\bar{B}^*$
$Z_b(10610)$	0.32 ± 0.09	4.38 ± 1.21	2.15 ± 0.56	2.81 ± 1.10	4.34 ± 2.07	86.0 ± 3.6
$Z_b(10650)$	0.24 ± 0.07	2.40 ± 0.63	1.64 ± 0.40	7.43 ± 2.70	14.8 ± 6.22	73.4 ± 7.0

to the data is provided by a model with just a non-resonant amplitude. From this analysis, we find that the significance of the $Z_b(10610) \to BB^*$ signal is exceeding the 8σ level.

As the nominal model for the $\Upsilon(10860) \to B^*B^*\pi$ decay, we use the following parameterization: $S_{B^*B^*\pi}(m) = (A_{Z_b(10650)} + A_{NR})\mathrm{E}_{B^*B^*\pi}(m)$. We also fit the data without a non-resonant component and with a non-resonant amplitude alone. Results of the fits are shown in Fig. 3(c); numerical values are given in [5]. The best description of the $B^*B^*\pi$ data is achieved in a model with only the $Z_b(10650)$ amplitude included. The addition of a non-resonant amplitude does not provide any significant improvement of the fit quality. The fit with a non-resonant amplitude alone gives a much worse likelihood value. From this analysis, we determine the significance of the $Z_b(10650) \to B^*B^*$ signal to be 6.8σ. In all fits discussed above, the masses and widths of the Z_b states were fixed at the values obtained from the analysis of the $\Upsilon(nS)\pi^+\pi^-$ and $h_b(mP)\pi^+\pi^-$ final states [?].

4 Conclusion

We report the first observation of three-body $\Upsilon(5S) \to \Upsilon(1,2S)\pi^0\pi^0$ decays. The measured branching fractions are $\mathcal{B}(\Upsilon(5S) \to \Upsilon(1S)\pi^0\pi^0) = (2.25 \pm 0.11 \pm 0.20) \times 10^{-3}$ and $\mathcal{B}(\Upsilon(5S) \to \Upsilon(2S)\pi^0\pi^0) = (3.66 \pm 0.22 \pm 0.48) \times 10^{-3}$. Evidence for a $Z_b^0(10610) \to \Upsilon(2S)\pi^0$ decay has been obtained from the amplitude analysis of the $\Upsilon(5S) \to \Upsilon(2S)\pi^0\pi^0$ decay. The statistical significance of the $Z_b^0(10610)$ signal is 4.9σ including model and systematic uncertainties. Its measured mass, $M(Z_b^0(10610)) = 10609^{+8}_{-6} \pm 6\,\mathrm{MeV/c^2}$, is consistent with that measured in the analysis of $\Upsilon(5S) \to \Upsilon(nS)\pi^+\pi^-$ decays. The $Z_b^0(10650)$ signal is not significant in either $\Upsilon(1S)\pi^0\pi^0$ or $\Upsilon(2S)\pi^0\pi^0$ final decays. We also report measurement of branching fractions for three-body decays: $\mathcal{B}(\Upsilon(10860) \to [B\bar{B}^* + c.c.]^+\pi^-) = (28.3 \pm 2.9 \pm 4.6) \times 10^{-3}$ and $\mathcal{B}(\Upsilon(10860) \to [B^*\bar{B}^*]^+\pi^-) = (14.1 \pm 1.9 \pm 2.4) \times 10^{-3}$. For the $\Upsilon(10860) \to B\bar{B}\pi$ decay, we calculate a 90% confidence level upper limit of $\mathcal{B}(\Upsilon(10860) \to [B\bar{B}]^+\pi^-) < 4.0 \times 10^{-3}$ (including systematic uncertainty). In addition, we report the ratio of the branching fractions $\frac{\mathcal{B}(Z_b(10610) \to BB^*)}{\sum_n \mathcal{B}(Z_b(10610) \to \Upsilon(nS)\pi), h_b(mP)\pi} = 6.2 \pm 0.7 \pm 1.3^{+0.0}_{-1.8}$ and $\frac{\mathcal{B}(Z_b(10650) \to B^*B^*)}{\sum_n \mathcal{B}(Z_b(10650) \to \Upsilon(nS)\pi, h_b(mP)\pi)} = 2.8 \pm 0.4 \pm 0.6^{+0.0}_{-0.4}$. We calculate the relative fractions for Z_b decays assuming that are saturated by the already observed $\Upsilon(nS)$ $(n = 1, 2, 3)$, $h_b(mP)$ $(m = 1, 2)$, and $B^*B^{(*)}$ channels. Combining results reported here with results on amplitude analysis from Ref. [5] one calculate relative fractions summarized in Table 2. All presented results are preliminary.

5 Acknowledgments

This work is partially supported by grants of Russian Foundation for Basic Research 12-02-01296, 12-02-01032, 12-02-33015 and by the grant of the Russian Federation government 11.G34.31.0047.

References

1. I. Adachi *et al.*, (Belle Collaboration), [arXiv:1105.4583].
2. A. Bondar, A. Garmash, R. Mizuk *et al.* (Belle Collaboration), Phys. Rev. Lett. **108**, 122001 (2012).
3. A.E. Bondar, A. Garmash, A.I. Milstein, R. Mizuk, M.B. Voloshin, Phys. Rev. D **84**, 054010 (2011).
4. I. Adachi *et al.*, (Belle Collaboration), [arXiv:1207.4345].
5. I. Adachi *et al.*, (Belle Collaboration), [arXiv:1209.6450].

Baryon production in B decays and e^+e^- collisions

Umberto Tamponi [a]
Universita' di Torino - Department of physics, via Pietro Giuria 1, 10124 Torino - Italy
INFN - Sezione di Torino, via Pietro Giuria 1, 10124 Torino - Italy

We present a summary of the recent progresses in the study of baryonic decays of B and B_s mesons, obtained at the B-factories. In particular the first evidence of charmless, baryonic B_s decays is reported by the Belle collaboration, while a detailed study of the resonant substructures in $B^0 \to \Lambda_c^+ \bar{p}\pi^+\pi^-$ is performed by the BaBar collaboration. The Belle collaboration studied also, for the first time, the $\Upsilon(1S)$, $\Upsilon(2S)$ and $\chi_b(1P)$ exclusive annihilation modes with hyperon -anti-hyperon pairs in the final state. Finally, from the study of the inclusive $\Lambda\Lambda$ and $\Lambda p\pi^-$ mass spectrum, a first study on the H-dibaryon production from $\Upsilon(1S)$ and $\Upsilon(2S)$ is performed too.

1 Baryons from B decays

A number of exclusive decays of B mesons involving a baryon anti-baryon ($\mathcal{B}\bar{\mathcal{B}}$) pair have been reported since the early days of B-physics[1]. This is not surprising if we consider that this family represents approximatively 7% of the B decays. Among the features of such decays, one of the most studied and discussed is the invariant mass spectrum of the $\mathcal{B}\bar{\mathcal{B}}$ pair, that often (but not always) presents a large enhancement in the area close to the kinematic threshold. One possible model[2] suggests that, since the local conservation of the baryonic number requires baryon and anti-baryon to be produced simultaneously, a gluon with large virtual mass is required for a large $M(\mathcal{B}\bar{\mathcal{B}})$ value. Since it's unlikely to emit a gluon highly off mass shell, a production of $\mathcal{B}\bar{\mathcal{B}}$ near threshold is expected. The same argument can be used to explain the suppression of the two body final states, which are forced to have the highest $M(\mathcal{B}\bar{\mathcal{B}})$ possible, with respect to the multi body ones, and in general the strong dependence of the branching ratio from the number of bodies produced together with the $\mathcal{B}\bar{\mathcal{B}}$ pair. Even if this approach correctly describes the primary features of this kind of decay, it leaves som open questions: it does not describe properly the angular distribution observed in $B^+ \to p\bar{p}K^+$ and it does not predict the absence of near threshold enhancement in the process $B^0 \to \Lambda_c^+ \bar{p}\pi^+\pi^-$.
In order to describe this behavior, a more sophisticate model has been recently developed[3]. This model relies on the basic assumption that the Feynman propagators in the diagrams that contribute to the baryon decays can be collapsed in a point-like interaction, and then this collapsed diagrams can be rearranged in different categories. The category responsible for the low mass enhancement is characterized by a two-meson like rearrangement of the quarks: the decays of this intermediate, virtual mesonic state $M \to \mathcal{B}\bar{\mathcal{B}}$ is interpreted as the source of the low mass enhancement, and thus its absence can be explained with the absence of a di-mesonic contribution to the total decay amplitude.
A totally different approach is also possible, assuming the presence of a resonant, bound or quasi-bound state of the two baryons. This exotic interpretation allows to describe, in the same

[a] tamponi@to.infn.it

framework, the observed enhancement in B meson decays and in $J/\psi \to \gamma p\bar{p}$ (the so called $X(1835)$) [4]. However, despite the observed enhancement in the low mass region, it is not clear if the presence of new resonances alone could explain completely the observed phenomena in quarkonium ad B meson decays. On the other hand the model based on the Feynman diagram rearrangement cannot be directly applied in the description of the strong J/ψ decays, thus requiring a different explanation for what is observed in the B mesons and in the charmonium sector.

1.1 Charmless decays

From the experimental point of view, the Belle collaboration recently studied the decay channels $B^- \to p\bar{p}l^-\bar{\nu}$, with $l^- = e^-, \mu^-$ and $B^0 \to \bar{\Lambda}p\pi^-\gamma$. The first one allow to test two different prediction: one, obtained with the standard model calculation [5], predicts a branching fraction of $10^{-5} - 10^{-6}$ while the second one, that includes the effects due to the baryonic form factors, predicts a much larger value of $(1.04 \pm 0.38) \times 10^{-4}$ [6]. The second channel can be used as benchmark for the test of the multiplicity hierarchy, since its dynamic is very close to the one to known decay $B^0 \to \bar{\Lambda}p\gamma$. The presence of a neutrino in $B^- \to p\bar{p}l^-\bar{\nu}$ imposes the complete reconstruction of the $\Upsilon(4S) \to B^-(\to p\bar{p}l^-\bar{\nu})B^+(\to X)$ event where the B^+ is reconstructed in its most common charmed decays. Once the B^+ is reconstructed, together with the p, $\bar{p}$ and lepton from the signal B, the recoil mass is expected to peak exactly at $M_{rec} = 0$ if only a neutrino is missing. Instead of the large signal predicted by the form factor-based calculation, a weak signal with a significance of 3.05σ is observed in the e mode (Fig. 1) and the corresponding, preliminary branching ratio value is $BF[B^- \to p\bar{p}e^-\bar{\nu}] = (8.22^{+3.74}_{-3.20}\text{ (stat.) } \pm 0.55\text{ (syst.)}) \times 10^{-6}$, in agreement with the prediction from [5].

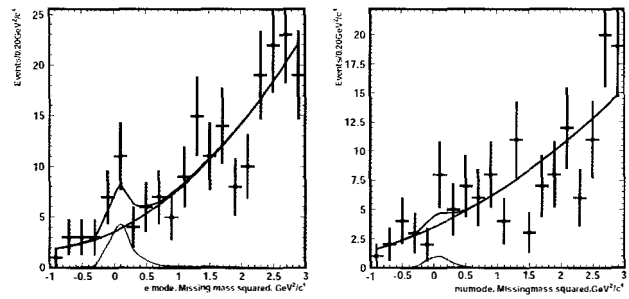

Figure 1: Missing mass in $B^- \to p\bar{p}l^-\bar{\nu}$ candidate events, for $l = e^-$ (left) and $l = \mu^-$ (right).

The analysis of $B^0 \to \bar{\Lambda}p\pi^-\gamma$ proceeds in a completely different way. Since in this case there is no expected missing energy, an inclusive reconstruction is possible. The price to be paid for an increased efficiency is a large background contribution due to the non resonant, hadronic process $e^+e^- \to q\bar{q}$. The background is rejected using a multivariate discriminant that combines different informations on the topological shape of the event, which is expected to be spheric in the case of Υ decays and jet-like in the case of non resonant $q\bar{q}$ production. The simultaneous fit of ΔM and M_{bc} do not result in a significant signal yield (Fig. 2), thus an upper limit at 90% confidence level is calculated obtaining $BF[B^0 \to \bar{\Lambda}p\pi^-\gamma] < 6.68 \times 10^{-7}$, about one order of magnitude below the measured branching fraction for $B^0 \to \bar{\Lambda}p\gamma$. This result is unexpected in a framework in which the short term interaction is the dominant effect, that predicts $BF[B^0 \to \bar{\Lambda}p\pi^-\gamma] >> BF[B^0 \to \bar{\Lambda}p\gamma]$.

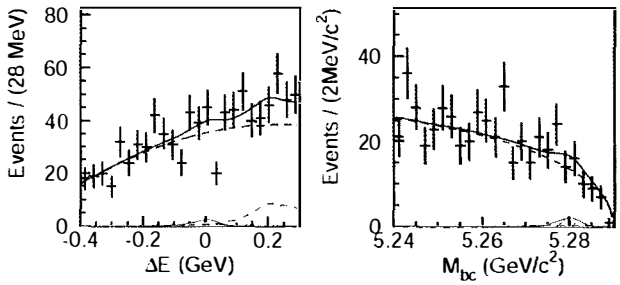

Figure 2: Distributions of ΔE (left) and M_{bc} in $B^0 \to \bar{\Lambda} p \pi^- \gamma$ candidate events.

1.2 Charmed decays

Concerning the charmed baryonic decays, two results were recently released: the evidence of baryonic decay $B_s \to \Lambda_c^+ \pi^- \bar{\Lambda}$ by Belle and a detailed study of the phase space structures in $B^0 \to \Lambda_c^+ \bar{p} \pi^+ \pi^-$ by BaBar [7]. The latter one, in particular, is the physics case that triggered the development of the quark rearrangement model. The first one represents the first evidence of a baryonic decay of the B_s, with a significance of 4.4σ (Fig. 3) and a measured branching fraction $\mathcal{B}[B_s \to \Lambda_c^+ \pi^- \bar{\Lambda}] = (3.6 \pm 1.1$ (stat.) $^{+0.3}_{-0.5}$ (syst.) ± 0.9 (Λ_c^+ decay) ± 0.7 (number of B_s)) $\times 10^{-4}$. The low statistic, unfortunately, does not allow to make any strong statement about the structures in the phase space and the invariant mass distribution of $\Lambda_c^+ \bar{\Lambda}$ pair. The study of the substructures is, on the other side, the main aim of a large study conducted by BaBar on $B^0 \to \Lambda_c^+ \bar{p} \pi^+ \pi^-$. The total branching fraction for this process is know to be large, but an analysis of the possible contribution from intermediate, 3-body states was never done before. The adopted approach relies on the analysis of the invariant mass distributions of different $\Lambda_c^+ \pi$, $p\pi$ and $\Sigma_c \pi$ pairs, where the Σ_c is reconstructed in its decay $\Sigma_c \to \Lambda_c^+ \pi$. From the invariant mass spectrum of $\Lambda_c^+ \pi^+$ (Fig. 4) and $\Lambda_c^+ \pi^-$ (Fig. 5) in reconstructed $B^0 \to \Lambda_c^+ \bar{p} \pi^+ \pi^-$ events, strong contributions from intermediate, three body decays clearly appear, with four peaks due to, respectively, $\Sigma_c(2455)^{++}$, $\Sigma_c(2455)^0$, $\Sigma_c(2520)^{++}$, and $\Sigma_c(2520)^0$. The total non Σ_c-resonant component is measured to be $(79 \pm 4(\text{stat.}) \pm 20(\text{syst.})) \times 10^{-5}$, to be compare with a total branching ratio $\mathcal{B}[B^0 \to \Lambda_c^+ p \pi^+ \pi^-] = (123 \pm 5 \pm 7 \pm 32) \times 10^{-5}$. The analysis of the baryon anti-baryon invariant mass spectrum shows, respectively, a small enhancement in $M(\bar{p}\Sigma_c(2455)^{++})$, no deviation from the expected phase-space flat trend in $M(\bar{p}\Sigma_c(2520)^{++})$ and an anti-enhancement in $M(\bar{p}\Sigma_c(2455)^0)$, while the available statistic does not allow to draw conclusions on $M(\bar{p}\Sigma_c(2520)^0)$. The contradictory behavior observed in these channels can be explained in the framework of the quark rearrangement model.

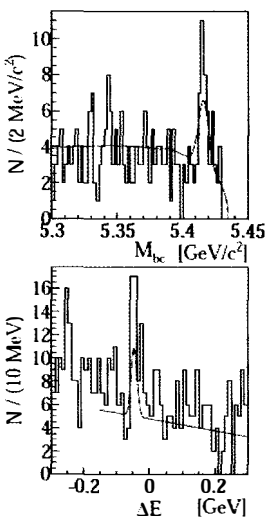

Figure 3: Distributions of ΔE (top) and M_{bc} (bottom) in $B^0 \to \Lambda_c^+ \bar{\Lambda} \pi^-$ candidate events. Λ_c is reconstructed in the $K^- p \pi^+$ mode.

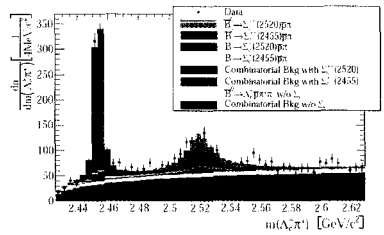

Figure 4: Invariant mass of $\Lambda_c^+\pi^+$ in reconstructed $B^0 \to \Lambda_c^+ \bar{p}\pi^+\pi^-$ candidate events. The different contributions due to intermediate 3-body decays are shown with different colors.

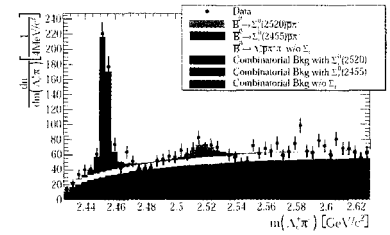

Figure 5: Invariant mass of $\Lambda_c^+\pi^-$ in reconstructed $B^0 \to \Lambda_c^+ \bar{p}\pi^+\pi^-$ candidate events. The different contributions due to intermediate 3-body decays are shown with different colors.

2 Baryons and baryonic states from bottomonium decays

One of the missing pieces of the puzzle could be the study of the baryon production in bottomonium annihilation. The main annihilation channel for $\Upsilon(nS)$ resonances is the one in three gluons, hence the partonic cnvironmcnt that evolves in the final states products is completely different from the one that describes a B mesons. Also the J/ψ decays into ggg too, but the limited phase space does not allow the decay into baryonic, many body final states, thus limiting the number of possible studies that can be carried on. Recently Dobbs et al. [8], in private study conducted using the CLEO datasets, reported the first observation of $\Upsilon(nS)$ exclusive decays with a $p\bar{p}$ pair in the final states. Even if no study of the phase space is conducted, the basic phenomenology of these decays resemble the one observed in the B meson decays: the two body final states are suppressed and the branching ration increase proportionally to the number of bodies in the final state, showing the same hierarchy dependence observed in the B meson system. No results has been presented so far concerning the exclusive annihilations of quarkonium with hyperons in the final state. Two systematic studies were conducted on the inclusive production of baryons from bottomonium decays, first by the Argus Collaboration [9] and then, more recently, by CLEO [10]. One of the features that emerge from these studies is a strong enhancement of the hyperons production from the bottomonium, with respect to the rate observe in continuum $e^+e^- \to q\bar{q}$; the nature of this enhancement, not described by the available generators, is still not understood. Two studies done at Belle aim to gain insight on the low energy QCD effects that can emerge for the three gluon state produced in bottomonium decays, focusing in particular on the inclusive and exclusive production of hyperons.

Table 1: Upper limits on branching ratios $\times 10^6$

Channel	$\mathcal{H} = \Lambda$	$\mathcal{H} = \Xi$	$\mathcal{H} = \Omega$
$\Upsilon(2S) \to \mathcal{H}\bar{\mathcal{H}}$	0.16	0.70	1.8
$\Upsilon(2S) \to \mathcal{H}\bar{\mathcal{H}}\pi^0$	0.78	2.3	6.1
$\Upsilon(2S) \to \mathcal{H}\bar{\mathcal{H}}\eta$	0.88	2.7	7.3
$\Upsilon(2S) \to \mathcal{H}\bar{\mathcal{H}}\pi^+\pi^-$	0.09	0.60	2.0
$\Upsilon(1S) \to \mathcal{H}\bar{\mathcal{H}}$	0.51	1.6	5.8
$\Upsilon(1S) \to \mathcal{H}\bar{\mathcal{H}}\pi^0$	2.3	6.9	22
$\Upsilon(1S) \to \mathcal{H}\bar{\mathcal{H}}\eta$	4.2	19	21
$\Upsilon(1S) \to \mathcal{H}\bar{\mathcal{H}}\pi^+\pi^-$	1.4	4.3	8.3
$\chi_{bJ}(1P) \to \mathcal{H}\bar{\mathcal{H}}$	0.87	3.6	11
$\chi_{bJ}(1P) \to \mathcal{H}\bar{\mathcal{H}}\pi^+\pi^-$	0.49	2.3	11

The first one consists in a large campaign for the measurement of exclusive decays with hy-

peron - antihyperon pairs involved. A total of 48 channels, consisting in $\mathcal{H}\bar{\mathcal{H}}$ plus K^+K^-, $\pi^+\pi^-$, $p\bar{p}$ pairs and π^0's are studied using the $\Upsilon(1S)$ and $\Upsilon(2S)$ samples. At the moment of this conference, only the results on the two and three body decays were available, and no signal is observed in the searched final states (Tab. 1). This results is somehow expected looking back at the know two-body suppression observed on the B decays. More detailed results are expected soon. The large amount of Hyperons and the high branching ratio for the production of deuteron[11], a bound baryon-baryon state, motivates the search for exotic hyperon-hyperon bound states in the bottomonium decays. Among these states, one of the most famous is the H dibaryon postulated by Jaffe using the MIT bag model[12]: a completely antisymmetric arrangement of 6 quark ($uuddss$, namely the same quark content of $\Lambda\Lambda$ pair) with mass close to $2M_\Lambda$. The lifetime of such object is predicted to be strongly depended on the invariant mass, ranging from 10^{-26} s if the mass largely exceed the $2M_\Lambda$ threshold, to few hours if the mass is below the $M_\Lambda + M_p + M_\pi$ threshold [13 14]. The current prediction from lattice QCD indicates a mass slightly below $2M_\Lambda$ [15 16 17]. The actual experimental measurement of the H mass are indirect, and rely on the $\Lambda\Lambda$ binding energy estimated from the decay products of doubly-Λ hypernuclei: the most stringent limit comes from the so called Nagara event, that infers $M_H > 2223.7$ MeV, 7.66 MeV below the $2M_\Lambda$ threshold[18]. Using the samples of $\Upsilon(1S)$ and $\Upsilon(2S)$, a study of the $\Lambda\Lambda$ and $\Lambda p\pi$ invariant mass is performed by Belle, in the region from the $\Lambda p\pi$ up to 50 MeV above the $\Lambda\Lambda$ threshold[19]. No significant deviation from the background-only hypothesys is found, and a mass dependent upper limit is thus determined (Fig. 6). Even if this upper limit is 20 times smaller than the value measured to the deuteron production, this is not th e final word on the existence of the H dibaryon. We know that the dominant, if not unique, production mechanism for the deuteron in quarkonium decays is the proton-nucleon recombination. If, on this basis, we postulate that the production of bound states in ggg decays is dominated by this mechanism, an unstable H dibaryon with mass above $2M_\Lambda$ can exists and a possible explanation of its absence form the bottomonium decay productions would be that its creation mechanism is not dominated by $\Lambda\Lambda$ recombination. The H dybarion could be stable or meta-stable ($c\tau > 1$ m), thus it does not decay within the acceptance of the Belle detector and escapes undetected: the main argument against this hypothesys comes form the indirect measurements of the $\Lambda\Lambda$ binding energy, but as reported by T.F. Carames and A. Valcarce[20], these measurement have given, in the past 50 years, contradictory results.

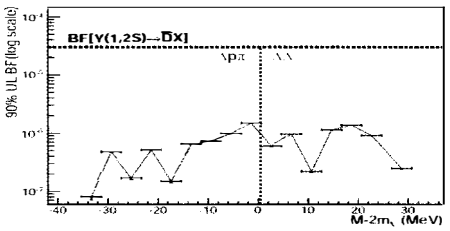

Figure 6: Upper limit for the inclusive production of H dybarion in $\Upsilon(1S)$ and $\Upsilon(2S)$ annihilations, as function of its mass. The region below $2M_\Lambda$ is studied searching for H-→ $\Lambda p\pi^-$, while for the region above $2M_\Lambda$ the reaction H-→ $\Lambda\Lambda$ is used.

References

1. M. S. Alam et al., *Phys. Rev. Lett.* **51**, 11431146 (1983).
2. M. Suzuki, J. Phys. G34 (2007).
3. Th. Hartmann, Study of the decay $B^0 \to \Lambda_c^+ \bar{p}\pi^+\pi^-$ and its intermediate states (mbv Berlin, 2011).
4. J. Z. Bai et al., (BES Collaboration), *Phys. Rev. Lett.* **51**, 022001 (2003).
5. Wei-Shu Hou and A. Soni, *Phys. Rev. Lett.* **86**, 4247-4250 (2001).
6. C.Q. Geng, Y.K. Hsiao, *Phys. Lett.* B **704**, 495 (2011).
7. J.P. Lees et al., (BaBar Collaboration) *Phys. Rev.* D **87**, 092004 (2013).

8. S. Dobbs et al., arXiv:1205.5070v2.
9. Argus Collaboration, Z.Phys. C39 (1988) 177.
10. R.A. Briere et al. (CLEO collaboration), *Phys. Rev.* D **76**, 012005 (2007).
11. D.M. Asner et al. (CLEO Collaboration) *Phys. Rev.* D **75**, 012009 (2007).
12. R. L. Jaffe,*Phys. Rev. Lett.* **195**, (1977) [Erratum-ibid. 38, 617 (1977)].
13. J. F. Donoghue, E. Golowich and B. R. Holstein, *Phys. Rev.* B **174**, 441 (1986).
14. J. F. Donoghue, E. Golowich and B. R. Holstein, *Phys. Rev.* D **34**, 3434 (1986).
15. S.R. Beane et al. (NPLQCD Collaboration), *Phys. Rev. Lett.* **106**, 162001 (2011).
16. S.R. Beane et al. (NPLQCD Collaboration), Mod. Phys. Lett. A **26**, 2587 (2011).
17. T. Inoue et al. (HALQCD Collaboration), *Phys. Rev. Lett.* **106**, 162002 (2011).
18. H. Takahashi et al., *Phys. Rev. Lett.* **87**, 212502 (2001).
19. B.H. Kim, S.L. Olsen et al. (Belle Collaboration), arXiv:1302.4028v1.
20. T.F. Carames and A. Valcarce *Phys. Rev.* C **85**, 045202 (2012).

TIME REVERSAL VIOLATION FOR ENTANGLED NEUTRAL MESONS

J. Bernabéu
Department of Theoretical Physics, University of Valencia,
and IFIC, Joint Centre Univ. Valencia-CSIC
Jose.Bernabeu@uv.es

Abstract. A direct evidence for Time Reversal Violation (TRV) means an experiment that, considered by itself, clearly shows TRV independent of, and unconnected to, the results for CP Violation. No existing result before the recent BABAR experiment with entangled neutral B mesons had demonstrated TRV in this sense. There is a unique opportunity for a search of TRV with unstable particles thanks to the Einstein-Podolsky-Rosen (EPR) Entanglement between the two neutral mesons in B, and PHI, Factories. The two quantum effects of the first decay as a filtering measurement and the transfer of information to the still living partner allow performing a genuine TRV asymmetry with the exchange of "in" and "out" states. With four independent TRV asymmetries, BABAR observes a large deviation of T-invariance with a statistical significance of 14 standard deviations, far more than needed to declare the result as a discovery. This is the first direct observation of TRV in the time evolution of any system.

INTRODUCTION

I was asked by the organizers to report about the recent discovery of Time Reversal Violation (TRV) in the Entangled Neutral B-system and the conceptual basis for such observation. This subject had an important impact in the scientific community and journals. Under the title "The arrow of time", The Economist devoted its central page on Science and Technology in the number of September 1st 2012[1)] to TRV. In particle physics one expects that not all processes run in the same way forwards in time as they do backwards.

The direct observation of this phenomenon by the BABAR Collaboration was reported[2)] in November 2012 with a high significance result, and the journals Nature[3)] and Physics Today[4)] presented it stating, that TRV has finally been clearly seen. Additionally, Physics World revealed its top breakthroughs for physics in 2012 and the first three results appear to be[5)] the Higgs-like boson discovery at CERN, a Majorana fermion excitation in solid state physics and Time-Reversal Violation.

The main point associated to a genuine test of T-invariance is that one needs an interchange between in-states and out-states for a given process, a request particularly difficult to accomplish for particles that decay. The interest in the unstable neutral meson $K^0 \to \overline{K}^0$ and $B^0 - \overline{B}^0$ systems stems from the fact that Violation of CP invariance (CPV) has been observed for them[6)]. By virtue of the CPT theorem[7)], as imposed by any local quantum field theory with Lorentz invariance and Hermiticity, one then expects that T violation should also appear in those systems. A direct evidence for TRV would mean an experiment that, considered by itself, clearly shows TRV independent of, and unconnected to, the results for CPV. No existing result before the BABAR experiment[2)] had clearly demonstrated TRV in this sense. For particles in a decaying state, T-

transformation is not defined, because the image under T is not a physical state. It looks like the decay prevents a true test of T-symmetry. What is the conceptual basis that is able to bypass this argument? Everything started with the papers[8] that used the quantum Einstein-Podolsky-Rosen (EPR)[9] Entanglement to transfer the information, lost in the irreversible decay of one particle, to its still living orthogonal partner. This correlation allows the preparation, in the quantum mechanical sense, of the state of the second neutral meson as a filtering measurement does. These ideas were scrutinized by several authors, including Wolfenstein[10], Quinn[11] and many others, with the conclusion that "it appears to be a true TRV effect". The original ideas and calculations[8] were more recently transformed into a definite experimental proposal[12] and its feasibility was demonstrated by a full simulation using the realistic statistics available in the B Factories.

DIRECT EVIDENCE FOR TRV IN UNSTABLE PARTICLES

We are interested in Microscopic T-symmetry Violation. Effects in particle physics odd under the change of sign of time $t \leftrightarrow -t$ are not necessarily T-violating. These observables can occur in theories with exact T-symmetry and are called T-odd effects, like those induced by absorptive components of the transition amplitude. On the other hand, for complex physical systems, well known time asymmetries are the Universe t-asymmetry[13] and the macroscopic t-asymmetry called the "arrow of time"[14]. But none of these t-asymmetries is a test of TRV in the fundamental Laws of Physics.

T and CPT symmetries are implemented by Antiunitary Operators in Quantum Mechanics, with the algebraic commutation rules left invariant. **A genuine TRV Observable means an Asymmetry under the interchange of in $\leftrightarrow$ out states**. The antiunitary character, rather than unitary, introduces many intriguing subtleties. Two types of experiments can demonstrate TRV:

1) A non-zero expectation value of a T-odd operator for a non-degenerate stationary state. This is the case for an electric dipole moment, which is a P-odd, C-even, T-odd quantity. It can be generated by either strong T-violation, with the non-perturbative θ-term $\varepsilon_{\mu\nu\tau\sigma} F^{\mu\nu} F^{\tau\sigma}$ of the tensor gluon field with its dual, unless it is rotated away by a Peccei-Quinn symmetry[15] leaving the axion as remnant, or by T-violation in weak interactions. In the standard model, with the CKM mechanism, a non-vanishing electric dipole moment of the neutron only appears to three loop amplitudes. The present experimental status is summarized in[16].

2) For transitions, as discussed before, the antiunitary character of the T-operator demands an asymmetry under the in $\leftrightarrow$ out exchange, i.e., the comparison between $<f|S|i>$ and $<-i|S|-f>$, where $|-i>$, $|-f>$ indicate the T-transformed of $|i>$, $|f>$ respectively. Transitions in the $K^0 \to \bar{K}^0$ and $B^0 - \bar{B}^0$ systems have demonstrated the existence of CPV. It is then natural to search for TRV in those systems.

The Kabir asymmetry $\bar{K}^0 \to K^0$ vs $K^0 \to \bar{K}^0$ was measured in 1998 by the CPLEAR experiment[17] at CERN with a non-vanishing value and a statistical significance near 4 standard deviations. But the interpretation of this observable as a direct evidence of TRV has generated some controversy. It is based[18] on several facts associated with this flavour-flavour transition with an asymmetry proportional to $\Delta\Gamma$. In the WW approach[19] the entire effect comes from the overlap of the non-orthogonal "stationary" K_L, K_S states.

Not all tests of T-symmetry are ruled out for particles that decay, as long as $\Delta\Gamma$ is not needed for the observable asymmetry. This is the situation when the interference which leads to an asymmetry is taking place for amplitudes with and without mixing. The corresponding transition is associated with flavour and CP decay products. But still we have the problem of the in$\leftrightarrow$out exchange required for a genuine test of T-symmetry. The fact that particles decay looks like it prevents performing such an exchange.

The solution arises[8] from the Quantum Mechanical Entanglement imposed by the EPR correlation between the neutral mesons produced in the B, or Φ, Factories. This idea will give us the opportunity to have separate tests of CP, T and CPT-symmetries, depending on the selection of the decay channel. At the moment of the $\Upsilon(4S) \to B^0 \bar{B}^0$ decay, the neutral meson system is in the antisymmetric state

$$|i\rangle = \frac{1}{\sqrt{2}}\left[B^0(t_1)\bar{B}^0(t_2) - \bar{B}^0(t_1)B^0(t_2)\right] \qquad (1)$$

where the states 1, 2 are defined by the time ordering of the decays, with $t_1 < t_2$. The times t_1 and t_2 in equation (1) are not time dependences, but labels to characterize the states.

But, for the entangled state of the two mesons, the individual state of each neutral meson is not defined before its collapse as a filter imposed by the observation of the decay. One can rewrite the same $|i>$ state in equation (1) in terms of any other pair of orthogonal states of the individual neutral B-mesons: a linear combination of B^0 and $\bar{B}^0$, and its orthogonal. One may considerer the states B_+ and B_- of the neutral mesons, where B_+ is the state not decaying to the decay product $J/\psi\, K_+$ and K_+ is the neutral K-meson

filtered by its decay to $\pi\pi$. The orthogonal state B_- is thus the neutral B-meson filtered by the decay to the CP = - final state. The observation of the decay to this CP-eigenstate at time t_1 generates an automatic transfer of information to the (still living) partner meson. We may call the quantum preparation of the initial state at t_1, using the filter imposed by a first observation of this decay, a "CP-tag"[20]. The same entangled state is then better to write it as

$$|i\rangle = \frac{1}{\sqrt{2}}[B_+(t_1)B_-(t_2) - B_-(t_1)B_+(t_2)] \qquad (2)$$

The main question is now: If B_- is the B-state filtered by the CP = - decay $J/\psi\ K_+$, what is the orthogonal state B_+ experimentally? For these CP-eigenstate decay products, the condition to filter a definite state is[12] that the decay amplitude has a single weak phase. The state B_+ is that filtered by the CP = + decay in the same system $J/\psi\ K_-$, where K_- is the neutral K-meson filtered by its decay to $\pi^0\pi^0\pi^0$. If, for the B-system, one neglects the small CP-violation of the K-system, one can associate B_- with $J/\psi\ K_S$ decay and B_+ with $J/\psi\ K_L$ decay.

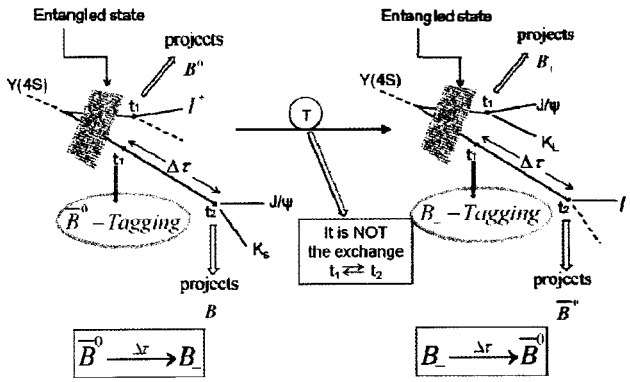

FIGURE 1. Scheme of the experimental observation of the time ordered (l^+, $J/\psi\ K_S$) and ($J/\psi\ K_L$, l^-) decays for performing the study of the time evolution of the transition $\overline{B}^0 \underline{\Delta\tau}\, B_-$ and its T-reverse $B_- \underline{\Delta\tau}\, \overline{B}^0$

This last association is the foundation of the experimental performance of the Time-Reversal Transformation for a transition of the neutral B-meson between a first flavour decay and a second decay to a CP-eigenstate. This T-transformation is illustrated in fig. 1 for the comparison between $\overline{B}^0 \underline{\Delta\tau}\, B_-$ and $B_- \underline{\Delta\tau}\, \overline{B}^0$ transitions. As seen, for the first transition one has to observe the decays (l^+, $J/\psi\ K_S$) in this time ordering, whereas the T-reversed transition corresponds to ($J/\psi\ K_L$, l^-) for the two decays. This nontrivial T-reversal is thus not given by the t-reversal exchanging the two decays. Entanglement has been essential for the quantum preparation of the initial state of the neutral B-meson in one transition and its T-reverse transition. The problem of particle unstability for a T-symmetry test has been bypassed. Experimentally, we need a very good time resolution for disentangling the ordering of the two decays.

GENUINE OBSERVABLES NOT NEEDING $\Delta\Gamma$

We may now proceed to a partition of the complete set of events into four categories, defined by the tag in the first decay at time t_1 : B_+, B_-, B^0 or $\overline{B}^0$, so we have eight different Decay-Intensities at our disposal, as function of $\Delta t = t_2 - t_1 > 0$. Each one of these eight Flavour-CP transitions has an Intensity given by

$$I_i(\Delta\tau) \sim e^{-\Gamma\Delta\tau}\{C_i\cos(\Delta m\Delta\tau) + S_i\sin(\Delta m\Delta\tau) + C'_i\cosh(\Delta\Gamma\Delta\tau) + S'_i\sinh(\Delta\Gamma\Delta\tau)\} \qquad (3)$$

where Γ is the average width. For a genuine test of a symmetry, one has to compare the $I_i(\Delta t)$ of a transition with its transformed by the symmetry operation. We proceed now to study the effects of the three symmetry operations CP, T and CPT separately:

1) Take $B^0 \rightarrow B_+$ as the Reference transition and call (X,Y) the observed decay products at times t_1 and t_2, respectively. The CP, T and CPT transformed transitions are given in Table 1, as well as the so-called Δt-operation (not a symmetry!) exchanging X↔Y

TABLE 1. Symmetry Transformations applied to $B^0 \rightarrow B_+$

Transition	$B^0 \rightarrow B_+$	$\overline{B}^0 \rightarrow B_+$	$B_+ \rightarrow B^0$	$B_+ \rightarrow \overline{B}^0$	$B_- \rightarrow \overline{B}^0$
(X,Y)	(l^-, $J/\Psi K_L$)	(l^+, $J/\Psi K_L$)	($J/\Psi K_S$, l^+)	($J/\Psi K_S$, l^-)	($J/\Psi K_L$, l^-)
Transformation	Reference	CP	T	CPT	Δt

As you may check, all transitions are experimentally independent. It is important to point out that the two sets of events, called sometimes "$\Delta t > 0$" and "$\Delta t < 0$", for the same two decay products l^- and $J/\psi K_L$, experimentally included in the same sample of events, are not connected by any symmetry.

2) Take $B^0 \to B_-$ as the Reference transition. The CP, T and CPT transformed transitions are given in Table 2

TABLE 2. Symmetry Transformation applied to $B^0 \to B_-$

Transition	$B^0 \to B_-$	$\overline{B}^0 \to B_-$	$B_- \to B^0$	$B_- \to \overline{B}^0$	$B_+ \to \overline{B}^0$
(X,Y)	(l^-, $J/\Psi K_S$)	(l^+,$J/\Psi K_S$)	($J/\Psi K_L$, l^+)	($J/\Psi K_L$, l^-)	($J/\Psi K_S$, l^-)
Transformation	Reference	CP	T	CPT	Δt

Therefore a second Asymmetry for each of the 3 symmetry transformations can be built. Again the result of the Δt-operation is a different transition from the other four transitions connected by the symmetries.

3) Select now as Reference the $B_- \to \overline{B}^0$ transition, obtained by the choice (Y, X) of decay products in the Reference 1) and proceed with the symmetry transformations.

4) Select as Reference the $B_+ \to \overline{B}^0$ transition, obtained by the choice (Y, X) of decay products in the Reference 2), and proceed with the symmetry transformations.

We thus conclude that there are 4 Model-Independent Asymmetries for each of the 3 symmetry transformations CP, T and CPT. These Asymmetries in the time dependent decay rates for any pair of symmetry-conjugated transitions would be apparent through differences between the corresponding coefficients S_i or C_i in equation (3). In the analysis for the $B^0 - \overline{B}^0$ system, we will take $\Delta\Gamma = 0$. In our notation for $S^{\pm}_{\alpha,\beta}(C^{\pm}_{\alpha,\beta})$, α will indicate the flavour decay l^+ or l^- and β the CP-eigenstate decay $J/\psi\ K_L$ or $J/\psi\ K_S$. The superindex "+" is for time ordering (Flavour, CP), whereas "-" is for the opposite time ordering of the two decays. For T-symmetry, a measure of TRV in the time evolution between the two decays is given by the asymmetry parameters

$$\Delta S_T^+ = S^-_{l^-,K_L} - S^+_{l^+,K_S} \qquad \Delta C_T^+ = C^-_{l^-,K_L} - C^+_{l^+,K_S}$$
$$\Delta S_T^- = S^+_{l^-,K_L} - S^-_{l^+,K_S} \qquad \Delta C_T^- = C^+_{l^-,K_L} - C^-_{l^+,K_S} \tag{4}$$

Similarly for the asymmetry parameters $\Delta S^{\pm}_{CP}$ ($\Delta C^{\pm}_{CP}$) and $\Delta S^{\pm}_{CPT}$ ($\Delta C^{\pm}_{CPT}$) which measure CPV and CPTV, respectively. The $\Delta S^{\pm}, \Delta C^{\pm}$ parameters for the three symmetries CP, T and CPT are represented in fig. 2 on top of the Intensities for the 8 independent transitions we are considering. These transitions are characterized by the flavour $l^{\pm}$, the CP eigenstate $J/\psi\ K_S$ (K_L) and the time ordering $\Delta t>0$ ($\Delta t<0$).

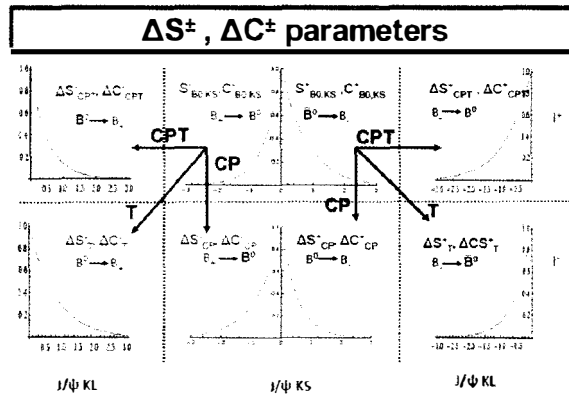

FIGURE 2. The eight Intensities, obtained for different flavours $l^{\pm}$, different CP eigenstates $J/\psi\ K_S$ (K_L) and different sign of Δt, are connected by the symmetry transformations CP, T and CPT. There are two sets of asymmetry parameters.

One should notice that a genuine test of T implies the comparison of: 1) "Opposite Δt sign", i.e., in $\leftrightarrow$ out; 2) Different CP eigenstates, $J/\psi\ K_L$ vs. $J/\psi\ K_S$; and 3) Opposite charged leptons l^+ vs. l^-.

In the SM, all 8 coefficients are related as a consequence[21] of CPT invariance and $\Delta\Gamma = 0$, and given by the value of $\sin(2\beta) = 0.67 \pm 0.02$, when using the CKM Mixing matrix[22],

$$S = S^+_{l^+,K_S} = -S^+_{l^-,K_S} = -S^-_{l^+,K_S} = S^-_{l^-,K_S} = -S^+_{l^+,K_L} = S^+_{l^-,K_L} = S^-_{l^+,K_L} = -S^-_{l^-,K_L} \approx 0.67$$

$$C = C^+_{l^+,K_S} = -C^+_{l^-,K_S} = C^-_{l^+,K_S} = -C^-_{l^-,K_S} = C^+_{l^+,K_L} = -C^+_{l^-,K_L} = C^-_{l^+,K_L} = -C^-_{l^-,K_L} \approx 0 \tag{5}$$

EXPERIMENTAL RESULTS

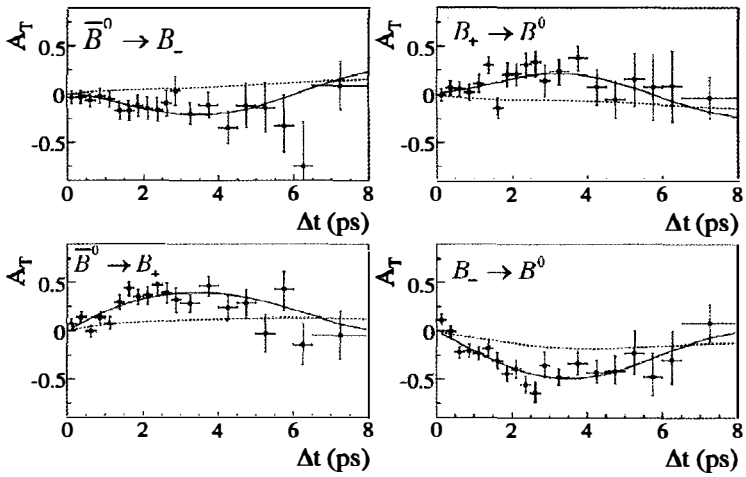

FIGURE 3. Experimental results for the four raw time dependent asymmetries associated with TRV.

TABLE 3. Measured values of the asymmetry parameters $\{ \Delta S^{\pm}, \Delta C^{\pm} \}$ for each of the three symmetries T, CP and CPT.

Parameter	Final result	SM expected val.
ΔS_T^+	$-1.37 \pm 0.14 \pm 0.06$	-1.34
ΔS_T^-	$1.17 \pm 0.18 \pm 0.11$	1.34
ΔC_T^+	$0.10 \pm 0.14 \pm 0.08$	0.
ΔC_T^-	$0.04 \pm 0.14 \pm 0.08$	0.
ΔS_{CP}^+	$-1.30 \pm 0.11 \pm 0.07$	-1.34
ΔS_{CP}^-	$1.33 \pm 0.12 \pm 0.06$	1.34
ΔC_{CP}^+	$0.07 \pm 0.09 \pm 0.03$	0.
ΔC_{CP}^-	$0.08 \pm 0.10 \pm 0.04$	0.
ΔS_{CPT}^+	$0.16 \pm 0.21 \pm 0.09$	0.
ΔS_{CPT}^-	$-0.03 \pm 0.13 \pm 0.06$	0.
ΔC_{CPT}^+	$0.14 \pm 0.15 \pm 0.07$	0.
ΔC_{CPT}^-	$0.03 \pm 0.12 \pm 0.08$	0.
$S_{\ell^+,K_S^0}^+$	$0.55 \pm 0.09 \pm 0.06$	0.67
$S_{\ell^+,K_S^0}^-$	$-0.66 \pm 0.06 \pm 0.04$	-0.67
$C_{\ell^+,K_S^0}^+$	$0.01 \pm 0.07 \pm 0.05$	0.
$C_{\ell^+,K_S^0}^-$	$-0.05 \pm 0.06 \pm 0.03$	0.

The details of the experimental analysis by the BABAR Collaboration may be consulted in reference[2].

Fig. 3 shows the four observed TRV asymmetries, overlaid with the projection of the best fit results to the Δt distribution with and without the eight T-invariance restrictions: $\Delta S_T^+ = \Delta C_T^+ = 0$, $\Delta S_{CP}^+ = \Delta S_{CPT}^+$ and $\Delta C_{CP}^+ = \Delta C_{CPT}^+$.

The measured values of the T, CP and CPT-asymmetry parameters are given in Table 3, together with the values of reference coefficients of the time dependent intensities (at the bottom).

The first uncertainty is statistical and the second systematic. In the last column, the SM expected value is also given, with such a good precision that its error from the global fit is well below the present experimental uncertainty. The significance of the T-violation signal is obtained from the CL contours assuming Gaussian errors, the result corresponds to a significance equivalent to 14 standard deviations, and thus constitutes a direct observation of T violation. The significance of CP and CPT violation is determined analogously from CL contours, obtaining a result equivalent to 17 and 0.3 standard deviations, respectively, consistent with CP violation and CPT invariance.

CONCLUSION

A unique opportunity for bypassing the problem of T-symmetry tests in unstable particles is provided by the Einstein-Podolsky-Rosen Entanglement between the two neutral mesons in B, and Φ, factories. The information transfer from the first decay, used as a filtering measurement, to the still living partner allows a quantum mechanical preparation, the flavour or CP tag, of the appropriate state for performing the T-symmetry study. Using the channels for the two decays to Flavour and CP eigenstates, we find 8 different Intensities for the time evolution of the neutral B-meson between the two decays. In appropriate combinations, the CP, T, CPT symmetries can be separately tested using 4 genuine independent

Asymmetries between the time dependent Decay Rates. These results have been expressed in terms of independent Asymmetry Parameters $\Delta S^{\pm}, \Delta C^{\pm}$ for each symmetry transformation.

BABAR has measured the time dependent Asymmetries and has extracted the Asymmetry parameters. The experimental result shows a large deviation of T-invariance with a significance of 14 standard deviations, far more than needed to declare a Discovery. In turn, the results are consistent with CPT invariance in the time evolution of the neutral B-meson between the two decays, connecting CPV and TRV in different transitions. This discovery was made possible thanks to the spectacular quantum properties of EPR entangled states: the reality of two entangled B's is much more than the sum of two separate B local realities.

ACKNOWLEDGMENTS

This work was supported by the funded Projects MINECO FPA 2011/23596 and Generalitat Valenciana PROMETEO 2008/004 and GVISIC 2012/020.

REFERENCES

1) "The arrow of time. Backward ran sentences...", *The Economist*, Sept. 1st 2012, http://www.economist.com/node/21561111
2) Lees JP et al. BABAR Collaboration *Phys. Rev. Lett.* **109**(2012)211801.
3) Nature Research Highlights: "Time's arrow in B mesons", *Nature* **491**(2012)640, Nov 2012, http://www.nature.com/nature/journal/v491/n7426/full/491640a.html
4) "Time Reversal asymmetry in particle physics has finally been clearly seen" *Physics Today* Nov 2012 pag 16 http://www.physicstoday.org/resource/1/phtoad/v65/i11/p16_s1
5) "Physics World reveals its top 10 breakthroughs for 2012" Dec 14 2012 http://physicsworld.com/cws/article/news/2012/dec/14/physics-world-reveals-its-top-10-breakthroughs-for-2012
6) Christenson JH et al. *Phys. Rev. Lett.* **13**(1964)138
Aubert B et al. BABAR Collaboration *Phys. Rev. Lett.* **87**(2001)091801
Abe K et al. (Belle Collaboration) *Phys. Rev. Lett.* **87**(2001)091802
7) Luders G *Annals Phys* **2**(1957)1
Pauli W in "Niels Bohr and the Development of Physics" Pergamon Press New York 1995 p30
8) Bañuls MC and Bernabéu J *Phys. Lett. B* **464**(1999) 117
Nucl. Phys. B **590**(2000)19
9) Einstein A, Podolsky B and Rose N *Phys. Rev.* **47**(1935)777
10) Wolfenstein L *Int. J. Mod. Phys.* **8**(1999)501
11) Quinn HR *Proc. DISCRETE'08 J. Phys. Conf. Serv.* **171**:011001(2009)
Bernabéu J *Proc. DISCRETE 2010 J. Phys. Conf. Ser.* **335**:012011(2011)
12) Bernabéu J, Martínez-Vidal F, Villanueva-Pérez P *JHEP* **1208**(2012)064
13) Ade PAR et al. Planck Collaboration *Astronomy & Astrophysics* manuscript no. PlanckMission2013, March 22, 2013
14) See Callender C "Thermodynamic Asymmetry in Time" The Stanford Encyclopedia of Philosophy E.N. Zalta ed (2008)
15) Peccei RD and Quinn HR *Phys. Rev. Lett.* **38**(1977)1440
Phys. Rev. D **16**(1977)1791
16) See Rathmann F article in DISCRETE2012 *Proc. J.Phys. Conf. Ser.* to appear(2013)
17) Angelopoulos A et al. CPLEAR Collaboration *Phys. Lett. B* **444**(1998)43
Kabir PK *Phys. Rev. D* **2**(1970)540
18) Wolfenstein L *Phys. Rev. Lett.* **83**(1999)911
19) Weisskoph VF and Wigner EP *Z. Phys.* **63**(1930)54
ibid **65**(1930)18
20) Bañuls MC and Bernabéu J, *JHEP* **9906**(1999)032
21) Bernabéu J and Bañuls MC TAUP 99 Paris *Nucl. Phys. Proc. Suppl.* **87**(2000)315
Bernabéu J and Espinoza C Venice 2009 Neutrino Telescopes p.159
22) Cabibbo N *Phys. Rev. Lett.* **10**(1963)531
Kobayashi M and Maskavo T Prog. Theor. Phys. **49**(1973)652

4.
Top

TOP QUARK MASS MEASUREMENTS AT THE TEVATRON

G. PETRILLO, on behalf of CDF and DØ collaborations
Fermi National Accelerator Laboratory, Mail Station 352
BATAVIA, IL 60510, U.S.A.

We present the most recent measurements of the mass of the top quark from Tevatron and the combination of the measurements from CDF and DØ, which yield a top mass of 173.20 ± 0.51 *(stat.)* ± 0.71 *(syst.)* GeV/c^2.

1 Introduction

The top quark (t) is the heaviest elementary particle observed so far. Its decay width of $2.0^{+0.5}_{-0.4}$GeV [1] settles the top quark in a unique position among the quarks, since it decays before "dressing" into a hadron. This feature allows a direct study of the properties of the top quark, including its mass, by the detection of its decay products, without the complication of the soft QCD interactions happening in a hadron.

The mass of the top quark is a free parameter of the Standard Model (SM). Its value affects the contributions of t loop diagrams, for example in radiative corrections to W and H masses. A precise knowledge of its mass can provide a stringent test on the SM [2].

2 Experimental Methods

Top quarks are produced in $p\bar{p}$ interactions singly by weak interaction and more abundantly in $t\bar{t}$ pairs by strong interaction. The latter, with a measured cross section [3] of about 7.65 ± 0.42 pb at $\sqrt{s} = 1.96$ TeV, is the production channel of choice for measuring the mass of the top quark.
Each of the two top quarks decays into a quark (b quark in more than 99% of the decays) and a W boson. The presence of b quarks in the events provides an important mean to discriminate the $t\bar{t}$ events, since the jets originating from b quark can have very characteristic features as the presence of a soft lepton and of a displaced decay vertex. Specific algorithms can identify these jets ("b-tagged jets"), typically achieving an efficiency within $50 - 80\%$.
The two W bosons from the $t\bar{t}$ decay define the experimental signature of the events. The final state where only one W boson decays into a charged lepton and its neutrino ("semileptonic") provides one fully reconstructed top quark and a sizeable branching fraction. The presence of the lepton allows for a sensible reduction of the background contamination.

The presence of a W boson decaying in jets is a remarkable feature for the top mass measurements. The uncertainty on the scale of the jet energy is $1 - 2\%$, and it affects directly the measured mass. The mass can be measured beyond that precision only by an alternative calibration of the jet energy. The mass of the W boson has been measured independently [4] with an uncertainty of $\approx 15\,\mathrm{MeV}/c^2$. Therefore the W boson decaying in two jets can provide a very precise scale reference for the jet energy. The top mass measurements exploit this feature by measuring also the residual jet energy scale bias, Δ_{JES}, for the selected data sample ("calibration *in situ*").

The most common techniques for the measurement of the mass of the top quark follow a shared pattern. Each event satisfying the selection criteria is assigned a likelihood, which describes its compatibility with a $t\bar{t}$ event of a given top mass m_t. This likelihood can be a function of other parameters in addition to m_t, for example Δ_{JES}. The estimator of m_t is extracted from the maximization of a sample likelihood which includes contributions from each of the events. Finally, a calibration procedure relying on the simulation removes any bias from the estimator and delivers the measurement of the top mass. The methods differ in the choice of the event likelihood.

An important consequence of the calibration procedure is the dependency of the measurement from the definition of the top mass implemented in the simulations. Conversely, a precise measurement of the top mass contributes to the full understanding of those implementations[5].

The *Matrix Element method* exploits the full topology of the event. Its likelihood is based to the leading order $q\bar{q} \to t\bar{t}$ scattering matrix element, $\mathcal{M}(y, m_t)$, including the $t\bar{t}$ decay. Since neither the initial nor the final state of the process described by $\mathcal{M}$ are observable, two layers are needed to connect $\mathcal{M}$ with the initial $p\bar{p}$ and the set of the detected objects (for example, four jets and one lepton).

The *templates method* relies on a few observables which are sensitive to the top mass. Distributions of these observables ("templates") are extracted from signal samples simulated with different top masses and from background samples. These distributions are used as probability densities to compute the likelihood for each event to be a signal event with a given mass. Correlations between the observables can be included by the use of multi-dimensional distributions. Multi-dimensional templates require large simulated samples to avoid statistical fluctuations. This limits the number of observables which can be included by this method.

The most precise measurements of the Tevatron experiments have historically been from events with semileptonic signature, using the Matrix Element method. The measurement from CDF, on 5.6 fb^{-1} of data, now superseded, had achieved a precision of 0.7% (173.0 ± 0.9 *(stat.+JES)* $\pm$ 0.9 *(syst.)* GeV/c^2 [6]). The measurement from DØ on 3.6 fb^{-1} of data achieved a precision of 0.85% (174.9 ± 1.1 *(stat.+JES)* $\pm$ 1.0 *(syst.)* GeV/c^2 [7]). The precision of both is limited by the statistical uncertainties. The combination from the two experiments from July 2012 yields to m_t=173.18 ± 0.56 *(stat.)* $\pm$ 0.75 *(syst)* GeV/c^2 [8]. By comparison, the most precise result from LHC, combination of CMS and ATLAS results, is 173.3 ± 0.5 *(stat.)* $\pm$ 1.3 *(syst)* GeV/c^2 [9]. Also in this case, it is the systematic uncertainties which limit the precision of the measurement.

3 New Measurements

3.1 From Events with One Lepton and Jets

CDF has measured the mass of the top quark from the full dataset of 8.7 fb^{-1} using a selection of events with one charged lepton (e or μ) and four or more jets [10]. This analysis uses the templates method, based on three observables and including their correlations. There are up to 12 possible assignments for each of the four reconstructed jets to the four quarks in the $t\bar{t} \to b\bar{b}qq'\ell\bar{\nu}_\ell$ (b-tagged jets will not be assigned to light quarks). For each of the assignments a χ^2 quantity is evaluated, which describes how compatible the event is with a $t\bar{t}$ configuration where the two W bosons have the nominal mass of $M_W = 80.39\mathrm{GeV}/c^2$ and the two t quarks have the same mass, a free parameter m_t^{reco}. The first two observables chosen for the templates are m_t^{reco} from the assignment with the lowest χ^2 (Fig. 1), and from the assignment with the second lowest χ^2. The third observable is chosen as the invariant mass of two jets which is closest to the known M_W value. All and only the jets which are not b-tagged are considered.

The measured top mass is

$$m_t = 172.85 \pm 0.71 \text{ (stat.+JES)} \pm 0.85 \text{ (syst.)} \text{ GeV}/c^2.$$

The energy scale shift Δ_{JES} from the calibration in situ is found to be consistent with zero. The systematic uncertainty is dominated by the residual uncertainty on jet energy scale and by the signal modelling, also including a contribution from an alternative parton shower model.

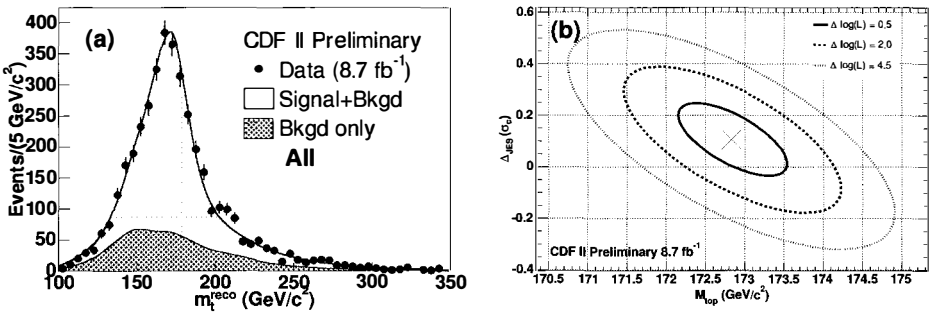

Figure 1: Measurement on 8.7 fb^{-1} of CDF data using events with lepton and jets: *(a)* template distributions of m_t^{reco} for background and signal with m_t=173.0 GeV/c^2, compared with data; *(b)* minimum of the sample likelihood, with contours corresponding to one, two and three standard deviations.

3.2 From Events with No Lepton and Jets

CDF has performed a measurement from a selection of events with no electron nor muon, and large momentum imbalance [11]. The simulation shows that such events have large contribution from $t\bar{t}$ processes where the lepton is present but not reconstructed.

The analysis is performed on the full CDF dataset of 8.7 fb^{-1}, using a template method similar to the one used in the analysis of events with one lepton (Fig. 2). The main differences are in the details of the formulation of the χ^2, modified to take into account the lack of information about one of the two W bosons, and the strategy for the reduction of background contamination. The final state without leptons is dominated by non-resonant multi-jet events. The requirement of at least one b-tagged jet is necessary to reduce the background. Further reduction is achieved by using a multivariate discriminant, which yields to a signal over background ratio of 2:1.

The result of the analysis is a top mass

$$m_t = 173.9 \pm 1.6\ (stat.+JES) \pm 0.9\ (syst.)\ \mathrm{GeV}/c^2$$

whose precision is limited by the statistical uncertainty. This measurement can't compete in precision with the previous one, but it contributes in the combination with other measurements.

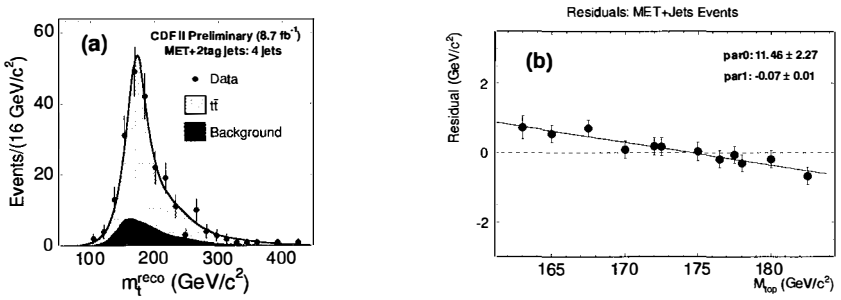

Figure 2: Measurement on 8.7 fb^{-1} of CDF data using events with large momentum imbalance and jets: *(a)* template distributions of m_t^{reco} for background and signal with m_t=173.0 GeV/c^2 compared with data for the events with four jets, two of them b-tagged; *(b)* calibration curve for the top mass estimator: bias on top mass as function of the top mass chosen in the simulated sample.

4 Tevatron Combination

A joint CDF and DØ working group performs combinations of top quark measurements, including mass, $t\bar{t}$ production cross section and other properties.

The combination technique for the top mass measurements is based on a Best Linear Unbiased Estimator [12], relying on the assumption that each source of uncertainty is assumed to be described by a normal distribution. The method requires the detailed knowledge of the correlation of the uncertainties between all the measurements to be combined. The uncertainties are split in 14 categories, defined so that the correlations within each of them are well defined. The categories include seven related to jet energy scale, two about detector modelling, two about background modelling; the remaining ones are the signal modelling, the modelling of the underlying event and the calibration method.

The choice of measurements follows two guidelines. The measurements must be as independent as possible, and the most precise available. Their independence guarantees that their statistical uncertainty is uncorrelated, and it maximises the available information. Therefore the 12 measurements chosen (Table 1) span the two Tevatron experiments, the two Tevatron runs and many final states, including the two measurements presented in this report.

Table 1: Summary of the 12 mass measurements from Tevatron in the March 2013 top mass combination, and the combination result.

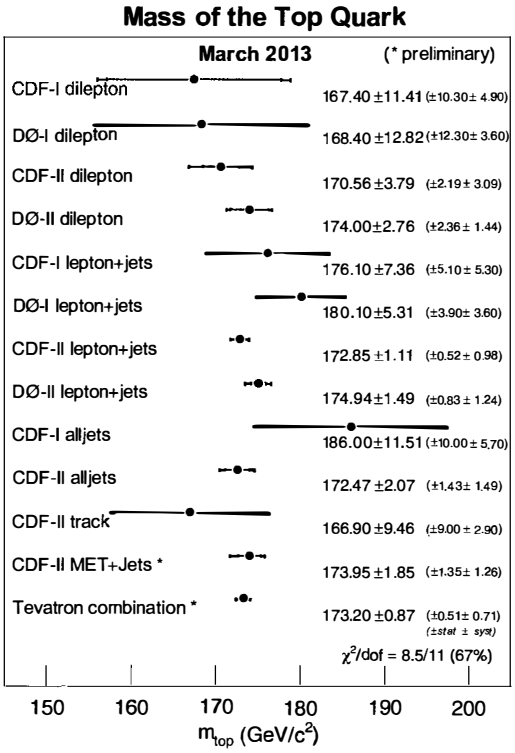

The result of the combination [13] is

$$m_t = 173.20 \pm 0.51\ (stat.) \pm 0.71\ (syst.)\ \mathrm{GeV}/c^2 = 173.20\ \pm 0.87\ \mathrm{GeV}/c^2$$

wose precision of 0.50% qualifies it as the most precise estimation of the top mass to date.

The precision of the combination is dominated, as the most precise among the contributing measurements, by the uncertainties on the energy scale of the jets and on the signal modelling.

5 Summary

The precision of the measurements of the top mass keeps being improved by the Tevatron experiments. To date, the top mass is know with an uncertainty of 870 MeV/c^2 (0.5%), with the contribution of the first measurements from the full dataset by CDF. Further improvements are expected with the inclusion of the remaining Tevatron analyses currently in preparation.
The most precise single measurements have been since long time limited by the systematic uncertainties. The leap in precision can be only achieved by the better understanding of the signal modelling, common to all measurements, and by the combination of measurements with different and independent uncertainties. The largest gain comes with the contributions from different experiments. It must be stressed that all the measurements are consistent, regardless of the detector, technique or events signature, including the measurements from the LHC pp events. This indicates the combination of all the measurements from Tevatron and LHC as the necessary mean to improve the precision of the measurement of the top mass from hadron collisions.

References

1. V. M. Abazov *et al.* [DØ Collaboration], *Phys. Rev.* D**85**, 091104 (2012)
2. The GFitter collaboration, September 2012 (`http://gfitter.desy.de/Standard_Model`)
3. The CDF and DØ Collaborations, "Combination of the $t\bar{t}$ production cross section measurements from the Tevatron Collider" DØ note 6363, CDF note 10926 (2012)
4. The CDF and DØ Collaborations, "2012 Update of the Combination of CDF and D0 Results for the Mass of the W Boson," FERMILAB-TM-2532-E
5. V. M. Abazov *et al.* [DØ Collaboration], *Phys. Lett.* B**703**, 422 (2011)
6. The CDF Collaboration, *Phys. Rev. Lett.***105**, 252001 (2010)
7. The DØ Collaboration, *Phys. Rev.* D**84**, 032004 (2011)
8. The CDF and DØ Collaborations, *Phys. Rev.* D**86**, 092003 (2012)
9. The ATLAS and CMS Collaborations, "Combination of ATLAS and CMS results on the mass of the top quark using up to 4.9 fb^{-1} of data", ATLAS-CONF-2012-095, CMS-PAS-TOP-12-001, July 2012
10. The CDF Collaboration, *Phys. Rev. Lett.***109**, 152003 (2012),
11. The CDF Collaboration, "A Measurement of Top Quark Mass Using MET + Jets Events With Full CDF Data Set 8.7 fb^{-1}", CDF note 10810, 05/16/2012
12. A. Valassi, *Nucl. Instr. Meth.* A**500**, 391 (2003)
13. The CDF Collaboration, "Combination of CDF and DØ results on the mass of the top quark using up to 8.7 fb^{-1} of $p\bar{p}$ collisions", CDF note 10976, DØ note 6381, March 2013

TOP QUARK PRODUCTION AT THE LHC

M. AOKI
on behalf of the ATLAS and CMS Collaborations
Kobayashi-Maskawa Institute for the Origin of Particles and the Universe (KMI), Nagoya University, Furo-cho, Chikusa-ku, Nagoya, Aichi 464-8602, Japan

Measurements of the production cross section for top quark pairs and the single top quark by the ATLAS and CMS collaborations at the LHC are presented. Improved measurements at $\sqrt{s}$ =7 TeV as well as new measurements at $\sqrt{s}$ =8 TeV are highlighted. All the measurements are in good agreement with the standard model predictions.

1 Introduction

The top quark is the heaviest known elementary particle, whose mass is close to the scale of the electroweak symmetry breaking. If there is physics beyond the standard model in this field, it may appear with the top quark. Events with one or two top quarks are also expected to be a large background for several new physics searches. Precise determination of the production and the kinematics of the top quark would increase the sensitivity of such searches.

2 Production cross section of the top quark pair

In the standard model, the production rate of the top quark pair is expected to be 164^{+13}_{-10} pb at $\sqrt{s}$ = 7 TeV, and 238^{+22}_{-24} pb at $\sqrt{s}$ = 8 TeV [1]. This rate has been measured by the ATLAS [2] and CMS [3] collaborations with high statistics data samples. The recent result of the LHC-combined inclusive top quark pair production cross section at $\sqrt{s}$ = 7 TeV is 173.3 ± 2.3(stat) ± 9.8(syst) pb[4]. Further improvements and understanding of $t\bar{t}$ production have been made by both collaborations, which are summarized in Table 1. The irreducible systematic uncertainty, which is coming from the signal modeling, is taking a large part in most of the measurements, therefore, it is important to measure the differential cross section in order to reduce this uncertainty.

Table 1: A summary of the recent measurements of the inclusive top quark pair production cross section [5,6,7,8,9,10,11].

Mode	Experiment	$\sqrt{s}$ [TeV]	$\int \mathcal{L}dt$ [fb^{-1}]	$\sigma_{t\bar{t}}$ [pb]	$\Delta\sigma$(stat)	$\Delta\sigma$(syst)	$\Delta\sigma(\mathcal{L})$
Dilepton [5]	CMS	7	2.3	161.9	±2.5	$^{+5.1}_{-5.0}$	±3.6
ℓ+jets with soft μ tag [6]	ATLAS	7	4.7	165	±2	±17	±3
τ_{had}+jets [7]	ATLAS	7	1.7	194	±18	±46	
τ_{had}+jets [8]	CMS	7	3.9	152	±12	±32	±3
ℓ+jets [9]	ATLAS	8	5.8	241	±2	±31	±9
ℓ+jets [10]	CMS	8	2.8	228	±9	$^{+29}_{-26}$	±10
Dilepton [11]	CMS	8	2.4	227	±3	±11	±10

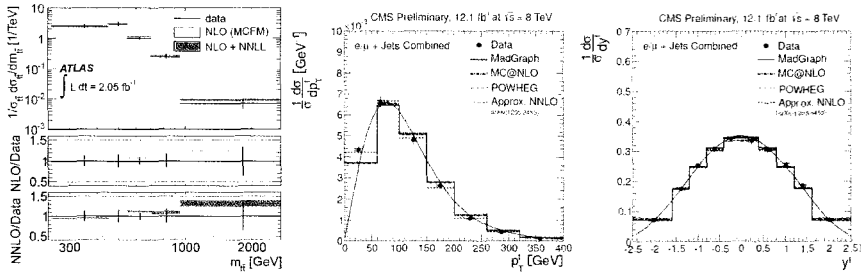

Figure 1: Differential cross section as a function of $m_{t\bar{t}}$, p_T^t and y^t [12].

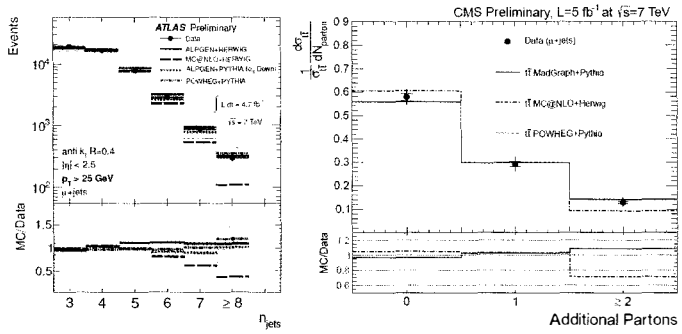

Figure 2: Distributions of the jet multiplicity in $t\bar{t}$ events. Left: inclusive jet multiplicity. Right:jet multiplicity subtracting jets from $t\bar{t}$ [13].

In Figure 1, the normalized differential cross sections as a function of $t\bar{t}$ invariant mass ($m_{t\bar{t}}$), transverse momentum of a top quark (p_T^t), and rapidity of a top quark (y^t) are shown [12]. The measured distributions agree well with the theoretical predictions within experimental uncertainties, and the approximate-NNLO provides the best description of the data.

Measurements of jets associated with the $t\bar{t}$ production could constrain models of initial and final state radiation at the scale of the top quark mass, and also provide a test of perturbative QCD in the LHC energy regime. Figure 2 shows the distributions of the inclusive jet multiplicity in $t\bar{t}$ events, and the distributions of the jet multiplicity subtracting those from the $t\bar{t}$ decay [13]. All the theoretical predictions agree well with the data, although the MC@NLO+HERWIG prediction tends to underestimate the data for events in the higher jet multiplicity bins.

An alternate method to see the jet activity is to measure the gap fraction, which is defined as the fraction of events with no additional jets with transverse momentum above a threshold. Figure 3 shows distributions of the gap fraction measured in the dilepton channel [14]. All the theoretical predications agree well with the data within experimental uncertainty for the overall rapidity region. However, the MC@NLO prediction tends to have higher gap faction in the central rapidity region, and none of the predictions agrees with data in the forward rapidity region.

Another interest is to measure the flavor of such jets. The CMS collaboration has performed the first measurement of the cross section ratio $\sigma(pp \to t\bar{t}b\bar{b})/\sigma(pp \to t\bar{t}jj)$, where the $t\bar{t}\,jj$ final state is defined by the presence of two additional jets in addition to the two b quarks from the decays of the top quark pair. The resulting measured cross section ratio is $[3.6 \pm 1.1(\text{stat}) \pm 0.9(\text{syst})]\%$ [15]. This number can be compared to the predictions using MADGRAPH [16] and POWHEG [17], which are 1.2% and 1.3%, respectively

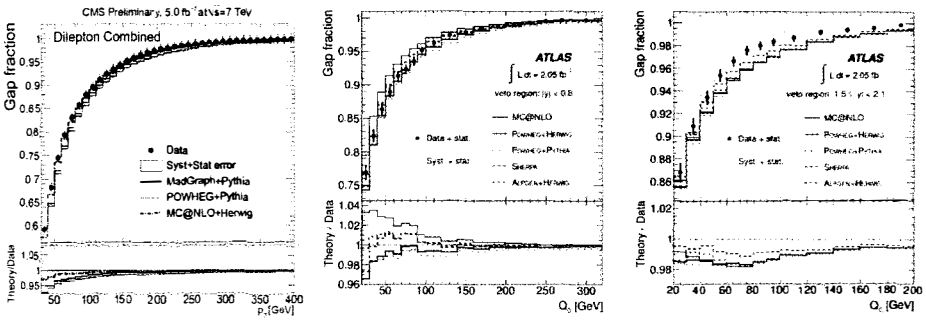

Figure 3: Distributions of the gap fraction. Left: overall detector acceptance. Center:central rapidity region. Right: forward rapidity region [14].

3 Single top production

Single top production is an alternative top quark production mechanism via the weak interaction. Measurement of this production rate allows for a measurement of $|V_{tb}|$ without assumptions about the number of quark generations. Three subprocesses contribute to single top quark production: the exchange of a virtual W boson in the t-channel, or in the s-channel, and the associated production of a top quark and an on-shell W boson.

The ATLAS collaboration has reported evidence of the associated production of a top quark and a W boson using 2.05 fb^{-1} of 7 TeV data. The signal is extracted using a multivariate analysis technique in the analysis. The measured production cross section is $16.8 \pm 2.9(\text{stat}) \pm 4.9(\text{syst})$ pb with a significance of 3.3 standard deviations, and $|V_{tb}|$ is determined as $1.03^{+0.16}_{-0.19}$ [18]. This is also confirmed by the CMS collaboration with more statistics, 4.9 fb^{-1} of 7 TeV data. The reported production cross section is 16^{+5}_{-4} pb with a significance of 4.0 standard deviations, and $|V_{tb}|$ is measured to be $1.01^{+0.16}_{-0.13}(\text{exp})^{+0.03}_{-0.04}(\text{th})$ [19]. In the standard model, this production cross section is expected to be 15.7 ± 1.1 pb [20].

With a higher beam energy of $\sqrt{s}$ =8 TeV, the single top production in the t-channel has been confirmed by both the ATLAS and the CMS collaborations. In the standard model, this production cross section is expected to be $87.8^{+3.4}_{-1.9}$ pb [21] The signal is extracted, for ATLAS, by a fit to the output distribution of a neural network discriminant in 5.8 fb^{-1} of data. The measured production cross section is $95.1 \pm 2.4(\text{stat}) \pm 18.0(\text{syst})$ pb, and $|V_{tb}|$ is measured to be $1.04^{+0.10}_{-0.11}$ [22]. The CMS collaboration measures this production using 5.0 fb^{-1} of data. The signal is extracted by a fit to the pseudo-rapidity distribution of the recoil jet, and the production cross section is measured to be $80.1 \pm 5.7(\text{stat}) \pm 11.0(\text{syst}) \pm 4.0(\text{lumi})$ pb, and resulting $|V_{tb}|$ is found to be $0.96 \pm 0.08(\text{exp}) \pm 0.02(\text{th})$ [23].

The cross-section ratio between top and anti-top quarks, $R_t = \sigma_t/\sigma_{\bar{t}}$, in single top quark production is sensitive to the momentum probability density of quarks in the proton. The up-quark density inside the proton is about twice as high as the down-quark density, and the production cross-section of single top-quarks is about twice as high as the cross section for anti-top quark production. This cross section ratio has been measured by the ATLAS collaboration using 4.7 fb^{-1} of 7 TeV data, and they report that R_t is $1.81 \pm 0.10(\text{stat})^{+0.21}_{-0.20}(\text{syst})$ [24]. This ratio has been also measured by the CMS collaboration using 12.2 fb^{-1} of 8 TeV data, and R_t has been determined as $1.76 \pm 0.15(\text{stat}) \pm 0.22(\text{syst})$ [25]. In Fig. 4, the measured R_t is compared with expectation using several different PDF sets.

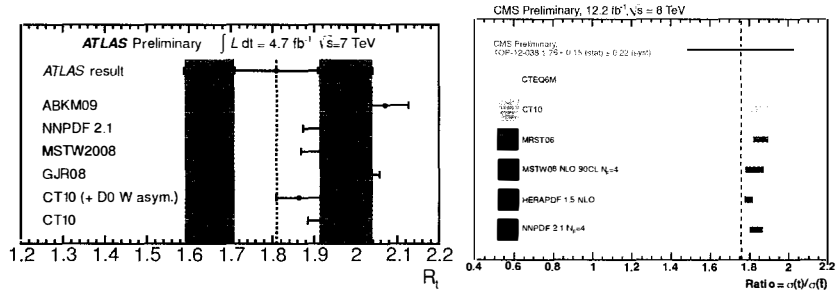

Figure 4: R_t results compared to several theoretical predictions[24,25].

4 Conclusions

Measurements of top quark production by the ATLAS and CMS collaborations have been presented. All those results are in good agreement with the standard model predictions. The high luminosity of the LHC proton-proton collider at a TeV energy allows for high precision and detailed measurements of top quark production.

References

1. M.Aliev *et al*, Comput. Phys. Commun. 182 (2011) 1034, [arXiv:1007.1327].
2. ATLAS Collaboration, 2008 JINST 3 S08003.
3. CMS Collaboration, 2008 JINST 3 S08004.
4. ATLAS Collaboration, ATLAS-CONF-2012-134, http://cds.cern.ch/record/1478422, CMS Collaboration, CMS PAS TOP-12-003, https://cds.cern.ch/record/1541952.
5. CMS Collaboration, JHEP 11 (2012) 067.
6. ATLAS Collaboration, ATLAS-CONF-2012-131, http://cds.cern.ch/record/1478370.
7. ATLAS Collaboration, Eur. Phys. J. C, 73 3 (2013) 2328.
8. CMS Collaboration, Submitted to Eur. Phys. J. C, [arXiv:1301.5755].
9. ATLAS Collaboration, ATLAS-CONF-2012-149, http://cds.cern.ch/record/1493488.
10. CMS Collaboration, CMS PAS TOP-12-006, https://cdsweb.cern.ch/record/1461939.
11. CMS Collaboration, CMS PAS TOP-12-007, http://cdsweb.cern.ch/record/1462235.
12. ATLAS Collaboration, Eur. Phys. J. C (2013) 73: 2261, CMS Collaboration, CMS PAS TOP-12-027, https://cds.cern.ch/record/1523611.
13. ATLAS Collaboration, ATLAS-CONF-2012-155, http://cds.cern.ch/record/1493494, CMS Collaboration, CMS PAS TOP-12-018, http://cdsweb.cern.ch/record/1494576.
14. ATLAS Collaboration, Eur.Phys.J. C72 (2012) 2043, CMS Collaboration, CMS PAS TOP-12-023, http://cdsweb.cern.ch/record/1478672.
15. CMS Collaboration, CMS PAS TOP-12-024, http://cdsweb.cern.ch/record/1479150.
16. F. Maltoni, T. Stelzer, JHEP 02 (2003) 027, [arXiv:0208156]
17. S. Frixione, P. Nason, C. Oleari, JHEP 11 (2007) 070, [arXiv:0709.2092]
18. ATLAS Collaboration, Phys. Lett. B 716 (2012) 142-159.
19. CMS Collaboration, Phys. Rev. Lett. 110 (2013) 022003.
20. N.Kidonakis, Phys. Rev. D 82 (2010) 054018, [arXiv:1005.4451].
21. N.Kidonakis, Phys. Rev. D 83 (2011) 091503, [arXiv:1103.2792].
22. ATLAS Collaboration, ATLAS-CONF-2012-132, http://cds.cern.ch/record/1478371.
23. CMS Collaboration, CMS PAS TOP-12-011, http://cdsweb.cern.ch/record/1478935.
24. ATLAS Collaboration, ATLAS-CONF-2012-056, http://cds.cern.ch/record/1453783.
25. CMS Collaboration, CMS PAS TOP-12-038, https://cds.cern.ch/record/1528574.

MEASUREMENTS OF TOP QUARK PROPERTIES AT THE TEVATRON

D. Orbaker on behalf of the CDF and DZero collaborations
University of Rochester, Department of Physics and Astronomy,
Bausch & Lomb Hall, Rochester, NY, USA 14627

Since the discovery of the top quark nearly twenty years ago, the CDF and DZero collaborations have been working to see if measurements of top quark properties agree with predictions from the Standard Model. We present multiple analyses of $p\bar{p}$ collisions with $\sqrt{s} = 1.96$ TeV at the Tevatron, using integrated luminosities up to 9.4 fb^{-1} for various $t\bar{t}$ decay signatures. Included in our discussion are measurements of W helicity, t quark decay branching fractions, t quark width and $t\bar{t}$ forward-backward production asymmetries.

1 Introduction

The top quark (t) was discovered in 1995 by the CDF and DZero experiments using $p\bar{p}$ collisions from the Tevatron. At the time of discovery, each experiment had tens of t quark candidate events. Now each experiment has data samples consisting of thousands of t quark candidates. The top quark is the heaviest known fermion and the only constituent of matter heavier than the Higgs Boson. Because of the extremely large mass of the top quark, mass measurements test the internal consistency of electroweak symmetry breaking in the Standard Model (SM) via the relationship between the H, W and t masses. Measurements of top quark properties are necessary to test the SM and to perhaps provide discrepancies that give insight into physics beyond the Standard Model.

In this paper, we focus on top quark pair production ($p\bar{p} \rightarrow t\bar{t}$), the main production mechanism for top quarks at the Tevatron. In the Standard Model, the top decays via the weak force to ($t \dashrightarrow Wq$), where q is a b quark nearly 100% of the time. The W boson can decay leptonically ($W \rightarrow l\nu$) or hadronically ($W \rightarrow q\bar{q}'$). The decay of the W boson decides which objects we identify the $t\bar{t}$ decay with. In this paper, we discuss measurements made in the dilepton channel ($t \rightarrow WbW\bar{b} \rightarrow ll\nu\nu b\bar{b}$) and the lepton+jets channel ($t \rightarrow WbW\bar{b} \rightarrow l\nu q\bar{q}'b\bar{b}$). In both of these channels, unless otherwise specified, l is either an electron or a muon. In the following sections we describe a group of analyses that measure properties of the production and the decay of the top quark.

2 W helicity

The W boson from top quark decay can have three possibility helicity states: right-handed (+), left-handed (-) and longitudinal (0). The Standard Model predicts that $\sim$ 70% of W bosons have longitudinal helicity (f_0), while $\sim$ 30% are left-handed (f_-) and $\sim$ 0% are right-handed (f_+). Any deviations from these fractions in a sample of top quark events could point to physics beyond the SM, either in $t\bar{t}$ production or at the $t \rightarrow Wb$ decay vertex.

The CDF collaboration recently published a measurement using the matrix element method with 8.7 fb^{-1} in the lepton+jets channel[1]. For each event, probabilities are found using the leading order matrix elements for the event to be a signal event produced with a given helicity and for the event from background production. Each jet-parton assignment is used to construct this probability. All of the probabilities are combined together to form a likelihood, and this likelihood is maximized to get

measured values for f_0, f_+ and the fraction of signal events in the data sample. By utilizing the matrix element method, this analysis uses more information from $t\bar{t}$ decay than previous CDF lepton+jets analyses and achieves better statistical power. The results are $f_0 = 0.726 \pm 0.066$ (stat) ± 0.067(syst) and $f_+ = -0.045 \pm 0.043$(stat) ± 0.058(syst), which are consistent with the Standard Model.

The CDF and DZero Collaborations published a combined result for the W helicity [2]. The result combines three measurements: a CDF matrix element analysis using 2.7 fb^{-1} of data in lepton+jets channel; a CDF template-based analysis using 5.1 fb^{-1} of data in the dilepton channel; and a DZero template-based analysis using 5.4 fb^{-1} of data in both the lepton+jets and dilepton channels. The template-based analyses use distributions in the reconstructed helicity angle, $\cos\theta^*$, to extract f_0 and f_+. The three measurements are combined using the measured values and the covariance matrices for the uncertainties. the results are $f_0 = 0.722 \pm 0.062$(stat) ± 0.052(syst) and $f_+ = -0.033 \pm 0.034$(stat) ± 0.031(syst), in good agreement with the standard model predictions.

3 Branching ratio of the t quark

The branching ratio of top quark decays is $R = \frac{t\to Wb}{t\to Wq}$. The branching ratio can also be described in terms of CKM matrix elements: $R = \frac{|V_{tb}|^2}{|V_{tb}|^2+|V_{ts}|^2+|V_{td}|^2}$. In the Standard Model, R is extremely close to 1 (0.998). Any large deviation from 1 would indicate that new physics is involved in the decay of the top quark.

The latest measurement of R from the CDF collaboration uses 8.7 fb^{-1} of data in the lepton+jets channel [3]. To differentiate between $t\bar{t}$ decays with different branching ratios, events are broken up by the number of jets and the number of b tags into six different categories: 3 jets, one b-tag; 3 jets, ≥ 2 b-tags; 4 jets, one b-tag; 4 jets, ≥ 2 b-tags; ≥ 5 jets, one b-tag and ≥ 5 jets, ≥ 2 b-tags. The analysis excludes events with 0 b-tags, which are dominated by background processes. Each category is put into a bin in a histogram. Templates are made for $t\bar{t}$ signal distributions with different R values and for the background distributions. A maximum likelihood fit is used to simultaneously measure the $t\bar{t}$ cross section ($\sigma_{t\bar{t}}$) and the branch fraction. As the background normalization has some dependence on $\sigma_{t\bar{t}}$, the fit is run iteratively until the measured value for $\sigma_{t\bar{t}}$ converges.

The results of the maximum likelihood fit are $\sigma_{t\bar{t}} = (7.5 \pm 1.0)$ pb and $R = 0.94 \pm 0.09$, with a statistical uncertainty for R of 0.04 and total systematic uncertainty for R of 0.08. As one might expect, the systematic uncertainties are dominated by uncertainties on the b-tagging, where migrations between bins would have a large effect on the measured value of R, and uncertainties on the background normalization. The measurement is good agreement with the SM, and places a lower limit on the branching ratio of $R > 0.785$ at 95% confidence level. Assuming that the CKM matrix is unitary and that there are only three generations of quarks, we measure $|V_{tb}| = 0.97 \pm 0.05$ and place a lower limit of $|V_{tb}| > 0.89$ at 95% confidence level. These results are consistent with previous measurements from the Tevatron.

4 Width of the t quark

The CDF collaboration has released result of a direct measurement of the width of the top quark, using 8.7 fb^{-1} of data in the lepton+jets channel [4]. The observed decay products are kinematically reconstructed with the constraints $m_W = 80.4$ GeV and $m_{t,1} = m_{t,2}$. The analysis essentially uses the shape of the reconstructed top mass distribution to extract the width. Probability density functions (p.d.f.) found using Kernel Density Estimation, $P(m_t^{\rm reco}, m_{jj}|\Gamma_t, \Delta_{\rm JES})$, are made for the reconstructed top mass, $m_t^{\rm reco}$ and the invariant mass of the two jets assigned to the W boson, m_{jj}, given different top widths (Γ_t) and the change in the nominal JES ($\Delta_{\rm JES}$). For signal, multiple p.d.f.s with different Γ_t and $\Delta_{\rm JES}$ are made, while for background p.d.f.s with different $\Delta_{\rm JES}$ are made. A likelihood, constructed from these probabilities for all events, is maximized to find the measured values of Γ_t and $\Delta_{\rm JES}$.

Pseudo experiments are used with the Feldman-Cousins scheme to calibrate the analysis and calculate the uncertainties. Before calibration, the width from data is $\Gamma_t = 1.63$ GeV. After calibration, the final result is

$$\Gamma_t = 2.21^{+1.46}_{-0.92}\ (\text{stat})^{+1.12}_{-0.62}\ (\text{syst})\ \text{GeV},$$

in good agreement with the standard model prediction of 1.25 GeV. As might be expected, the largest systematic uncertainties are from jet resolution and different simulated effects, such as color reconnection and the fraction of $t\bar{t}$ events arising from gg versus $q\bar{q}$. Using the Heisenberg Uncertainty Principle, the lifetime of the top quark is measured to be $\tau_t = 2.98^{+3.00}_{-1.35} \times 10^{-25}$s.

5 Forward-backward $t\bar{t}$ production asymmetry

At the Tevatron, the color charge asymmetry in production for $q\bar{q} \to t\bar{t}$ is manifested as a forward-backward asymmetry, $A_{\rm FB}$, in $p\bar{p} \to t\bar{t}$. One of the more simple quantities to reconstruct and measure is the asymmetry based on the lepton from $t\bar{t}$ decay, $A^l_{\rm FB}$, which is defined as:

$$A^l_{\rm FB} = \frac{N(q_l y_l > 0) - N(q_l y_l < 0)}{N(q_l y_l > 0) + N(q_l y_l < 0)}, \tag{1}$$

where q_l is the charge of the lepton and y_l is the rapidity of the lepton. Both the CDF and DZero Collaborations have recently released results for the lepton-based asymmetry, DZero in the dilepton channel using 5.4 fb^{-1} of data [5] and CDF in the l+jets channel using 9.4 fb^{-1} of data [7]. Both collaborations present asymmetries made from distributions of data after subtracting the predicted shapes and normalizations from background processes. As the angular resolution for leptons is extremely good, there is no need to unfold distributions from background-subtracted data for effects from reconstruction. Lepton-based distributions are corrected for effects from acceptance, which differ for the dilepton and lepton+jets channels. The CDF Collaboration applies an additional correction to extrapolate the asymmetry beyond the angular range of the CDF detector to the inclusive range for leptons from $t\bar{t}$ decay.

The results from the DZero dilepton analysis are summarized in Table 2 of the publication [5]. For the sake of brevity, they will not be shown here. All of the results are in good agreement with the predicted asymmetries from MC@NLO, with additional QCD+EW corrections. The results for $A^l_{\rm FB}$ are combined with the results from the DZero $A^l_{\rm FB}$ measurement in the lepton+jets channel [6], for value of $A^l_{\rm FB} = (11.8 \pm 3.2)\%$, which is about 2σ higher than the predicted value of $(4.7 \pm 1.1)\%$.

In the lepton+jets channel, the CDF Collaboration measures lepton-based asymmetries that are somewhat higher than the predictions. For asymmetries made from background-subtracted data, CDF measures $A^l_{\rm FB} = (7.0 \pm 1.9\ (\text{stat}) \pm 1.1\ (\text{syst}))\%$, which can be compared to the prediction from POWHEG of 2.3%. After applying an acceptance correction and extrapolating the asymmetry, CDF finds $A^l_{\rm FB} = (9.4 \pm 2.4\ (\text{stat})^{+2.2}_{-1.7}\ (\text{syst}))\%$, which is about 2σ higher than the prediction of 3.8% [8].

6 An alternative to the asymmetry

The CDF collaboration has released a new analysis that aims to measure the entire angular distribution in t production via $\cos(\theta_t)$ via Legendre moments, rather than summarize the distribution into one number, $A_{\rm FB}$ [9]. Previous $t\bar{t}$ asymmetry measurements from CDF and DZero have measured the asymmetry in multiple regions of $|\Delta y|$, which give a slightly more detailed picture about the entire distribution. The analysis uses 9.4 fb^{-1} of data in the lepton+jets channel, with almost the same selection as the CDF $A_{\rm FB}$ measurement [10]. The only change is a relaxed requirement on the E_T of one of the four jets, from 20 GeV to 12 GeV. This change reduces effects from acceptance and allows more events into the analysis. A χ^2-based kinematic fit is used to reconstruct the $t\bar{t}$ four-vectors and extract $\cos(\theta_t)$ for each event.

The following equation decomposes a given function into the Legendre moments: $a_l = \frac{2l+1}{2} \int_{-1}^{1} dx f(x) P_l(x)$, where $P_l(x)$ is the lth Legendre polynomial ($P_0 = 1$, $P_1 = x$, $P_2 = \frac{1}{2}(3x^2 - 1), \cdots$). For this analysis, the function is the sum of Dirac delta functions at the reconstructed values of $\cos(\theta_t)$, $f(\cos\theta) = \sum_i \delta(\cos\theta - \cos\theta_i)$. The combination of the equations results in $a_l = \frac{2l+1}{2} \sum_i P_l(\cos\theta_i)$. The a_i are unfolded for effects from acceptance and reconstruction by inverting the matrix in $a_l^{\rm detector} = \frac{2l+1}{2} \sum_m K_{lm} a_m^{\rm parton}$, where $a_l^{\rm detector}$ is lth reconstructed moment, $a_m^{\rm parton}$ is mth parton-level moment and K_{lm} is the migration matrix between these moments, found from simulated $t\bar{t}$ events.

Because this analysis measures the entire distribution in $\cos\theta_t$, it has more differentiating power between different new physics models than a standalone $A_{\rm FB}$ analysis. The results of this technique applied to CDF data are shown in Table 1. The moment with the largest deviation from the predicted moments[8] is a_1, which differs by 2σ. All other measured moments are in good agreement with the predictions.

Table 1: Measured Legendre moments of $\cos\theta_t$ from CDF data, with statistical and systematic uncertainties.

Legendre degree (l)	a_l for data (stat+syst)	a_l predicted from NLO (QCD+EW)
1	$0.40 \pm 0.09 \pm 0.08$	$0.15^{+0.066}_{-0.033}$
2	$0.44 \pm 0.14 \pm 0.21$	$0.28^{+0.053}_{-0.030}$
3	$0.11 \pm 0.20 \pm 0.08$	$0.030^{+0.014}_{-0.007}$
4	$0.22 \pm 0.25 \pm 0.11$	$0.035^{+0.016}_{-0.008}$

Conclusions

New results for measurements of top quark properties at the Tevatron have been presented, with many analyses using the entire Tevatron data sample. These analyses make precision measurements of various aspects of top quark production and decay, via the W helicity, branching fraction, width and asymmetry. None of the results provide a smoking gun for physics beyond the Standard Model, but some deviations from the predictions remain. These results use novel, advanced analysis techniques, and exemplify the dedication and passion of experimenters at both the CDF and DZero Collaborations.

Acknowledgments

I would like to thank my friends and collaborators at the CDF and DZero experiments for helping me and making these measurements possible. I would also like to thank the people responsible for running the Tevatron and the funding agencies. Lastly, I would like to thank the organizers of the 2013 Rencontres de Moriond for putting together such a great meeting.

References

1. T. Aaltonen *et al.* [CDF Collaboration], Phys. Rev. D **87**, 031104 (2013) [arXiv:1211.4523 [hep-ex]].
2. T. Aaltonen *et al.* [CDF and D0 Collaborations], Phys. Rev. D **85**, 071106 (2012) [arXiv:1202.5272 [hep-ex]].
3. The CDF Collaboration, CDF note 10887, `http://www-cdf.fnal.gov/physics/new/top/confNotes/cdf10887_BRratio8.7fb.pdf` (2012).
4. The CDF Collaboration, CDF note 10936, `http://www-cdf.fnal.gov/physics/new/top/2012/TMT_width_p38/publicnote.pdf` (2012).
5. V. M. Abazov *et al.* [D0 Collaboration], Phys. Rev. D **87**, 011103(R) (2013) [arXiv:1207.0364 [hep-ex]].
6. V. M. Abazov *et al.* [D0 Collaboration], Phys. Rev. D **84**, 112005 (2011).
7. The CDF Collaboration, CDF note 10975, `http://www-cdf.fnal.gov/physics/new/top/2013/AfbLep_public_page/cdf10975_afblep.pdf` (2013).
8. W. Bernreuther and Z. -G. Si, Phys. Rev. D **86**, 034026 (2012) [arXiv:1205.6580 [hep-ph]].
9. The CDF Collaboration, CDF note 10974, `http://www-cdf.fnal.gov/physics/new/top/2013/TopAngularXS/cdf10974_PubTopCosTheta.pdf` (2013).
10. T. Aaltonen *et al.* [CDF Collaboration], Phys. Rev. D **87**, 092002 (2013) [arXiv:1211.1003 [hep-ex]].

MEASUREMENTS OF TOP QUARK PROPERTIES AT THE LHC

E. Yazgan for the ATLAS and CMS Collaborations
Department of Physics and Astrophysics, University of Ghent, Proeftuinstraat 86, 9000 Gent, Belgium

Recent measurements of top quark properties at the LHC from ATLAS and CMS experiments are presented. The presented results include top quark mass, dependence of top mass measurements on event kinematics, top anti-top mass difference, bottom quark content in top quark decays, W boson polarization and anomalous couplings, search for CP violation in single top events, vector boson production associated with top-antitop pairs and top polarization.

1 Introduction

The top quark is the most massive particle known to date and has a shorter lifetime than the hadronizarion timescale, $1/\lambda_{QCD}$ which makes its bare quark properties directly accessible. The analyses presented in this note use the data collected with the ATLAS [1] and CMS [2] detectors during 2011 and 2012 data taking periods with proton-proton collisions at center-of-mass energies of 7 and 8 TeV, respectively.

2 Top Quark Mass

2.1 Combined LHC Results

Top quark mass measurements performed by the ATLAS and CMS experiments using 7 TeV data with integrated luminosities up to 4.9 fb^{-1} are combined using the measurements in lepton+jets, di-lepton and all-jets final states[3]. The combination is performed using the BLUE method [4] and yields $m_t = 173.3 \pm 0.5$ (stat) ± 1.3 (syst) GeV. For the combination, the most recent measurements have not been included yet.

2.2 Dependence of Top Quark Mass Measurement on Event Kinematics

Interpretation of the top mass measurements is not straightforward when the precision becomes smaller than the top width, $\Gamma_t \sim 1$ GeV. It is difficult to define a pole mass for an unstable and colored particle [5,6]. Based on the most precise single top quark mass measurement [7], possible kinematic biases in the measurement of top-quark mass are studied[8]. Different observables are studied which are expected to be sensitive to color reconnection effects, initial/final state radiation and b-quark kinematics (two such distributions are displayed in Figure 1). This study represents the first top quark mass measurement binned in kinematic observables. We conclude that with the current precision, there is no mis-modelling effect due to color reconnection, initial/final state radiation, or b-quark kinematics.

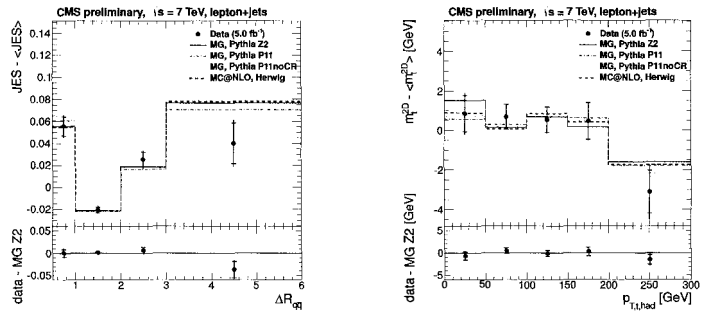

Figure 1: Jet energy scale vs the separation of the light-quark jets (left) and top-quark mass vs the transverse momentum of the hadronically decaying top quark (right). The systematic and statistical uncertainties are added in quadrature. The hatched areas represent the statistical uncertainties on the simulated quantities.

2.3 Top Antitop Mass Difference

The direct measurement of $\Delta m_t = m_t - m_{\bar{t}}$ tests CPT invariance. The measurement at $\sqrt{s} = 8$ TeV [9] has been made using the same method utilized for the most precise single LHC top-quark mass measurement in the lepton+jets final state [7]. The sample is divided into two samples with opposite lepton charge. The $m_t - m_{\bar{t}}$ difference is found to be -272 ± 196 (stat) $\pm$ 122 (syst) MeV consistent with 0. This represents the most precise measurement of Δm_t.

3 Top Quark Couplings

3.1 Measurement of the Ratio $\mathcal{R} = \mathcal{B}(t \to Wb)/\mathcal{B}(t \to Wq)$

In the standard model (SM), the top quark decays to a W boson and a b quark practically with a branching ratio of $\sim 100\%$. Decays to other down-type quarks are suppressed in the Cabibbo-Kobayashi-Maskawa (CKM) matrix with $|V_{tb}| > 0.999 >> |V_{ts}|, |V_{td}|$ under the assumptions of unitarity and exitence of three quark generations. A measurement of $|V_{tb}|$ can be made by measuring the branching fraction ratio $\mathcal{R} = \mathcal{B}(t \to Wb)/\mathcal{B}(t \to Wq)$. The measurement of $\mathcal{R}$ is perfomed in the $t\bar{t}$ di-lepton final state measured using 8 TeV data [10]. $\mathcal{R}$ is extracted from a profile likelihood fit to data-drived analytic probability models of signal purity, number of reconstructed tops in different jet categories and number of b-tags as $1.023^{+0.036}_{-0.034}$ (stat+syst) without any constraints in the fit (see Figure 2). If the physical condition of $\mathcal{R} \leq 1$ is imposed, then a lower limit for $\mathcal{R}$ is derived to be $\mathcal{R} > 0.945$ at 95% C.L. With the assumption of CKM unitarity and existence of three generations, the measurement can be converted to a measurement of $|V_{tb}|$. The CKM matrix element $|V_{tb}|$ is measured as $1.011^{+0.018}_{-0.017}$ and the lower limit is derived to be $|V_{tb}| > 0.972$ at 95% C.L. The results obtained for $\mathcal{R}$ and $|V_{tb}|$ are consistent with the SM predictions and are the most precise measurement of $\mathcal{R}$ and the most stringent direct lower limit on $|V_{tb}|$.

3.2 W Boson Polarization and Anomalous Couplings

The top quark partial with can be parametrized in terms of left-handed (F_L), right-handed (F_R), longitudinal (F_0) W boson helity fractions and the θ^* angle between the momentum of the d-type fermion in the W boson rest frame and the momentum of the W boson in the top quark rest frame. Measurements of helicity fractions probe the anomalous couplings, g_L and g_R. ATLAS and CMS made measurements of W boson helicities in $t\bar{t}$ events in dilepton and

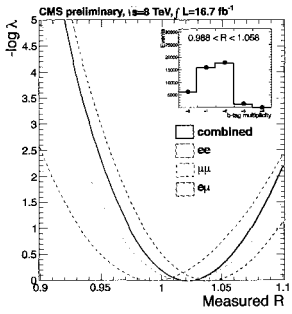

Figure 2: Variation of the profile likelihood used to extract R from the data. The inset shows the inclusive b-tag multiplicity distribution and the result of the fit.

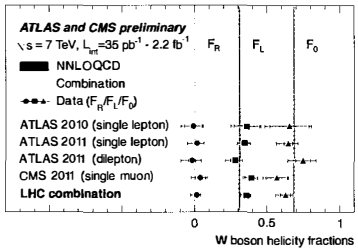

Figure 3: Input W helicity fraction measurements and the combination. The inner and outer error bars correspond to the statistical and the total uncertainty, respectively.

lepton+jets final states [11,12,13] and combined the W helicity measurements [14] at $\sqrt{s} = 7$ TeV. All measurements are found to be consistent with each other and with SM predictions at NNLO QCD (See Figure 3).

Measurement of W Helicity fractions is also performed in single-top topologies [15] studying $\mu + jets$ final state at $\sqrt{s} = 7$ and 8 TeV. The helicity fractions are obtained from likelihoods with reweighted signals including all processes involving the top quark. The measurements performed at $\sqrt{s} = 7$ and 8 TeV are combined yielding $F_0 = 0.713 \pm 0.114$ (stat)$\pm$0.023 (syst), $F_L = 0.293 \pm 0.069$ (stat)$\pm$0.030 (syst) and $F_R = -0.006 \pm 0.057$ (stat)$\pm$0.027 (syst). The results are found to be consistent with the SM and measurements in the $t\bar{t}$ channels. All the W helicity measurements discussed above are also used to set exclusion limits on the real part of the anomalous couplings.

3.3 Search for CP Violation in Single Top Events

The angle θ^* is not sensitive to the complex phases of anomalous coplings. Non-zero complex phases might indicate a CP-violating component in the top quark decay. In the t-channel single top production, the top quarks are produced with a high degree of polarization along the spectator quark direction. The vector, $\vec{N}$, normal to the top polarization and W (or b) directions in the helicity frame can be used to define forward-backward asymmetry (A_{FB}^N) which is proportional to the imaginary part of g_R. Using the unfolded distributions of $\cos\theta^N$, ATLAS collaboration measured the forward-backward asymmetry at the parton level [16] in the $lepton + jets$ channels at $\sqrt{s} = 7$ TeV as $A_{FB}^N = 0.031 \pm 0.065$ (stat)$^{+0.029}_{-0.031}$ (syst). Assuming a polarization of $P = 0.9$[17,18], the measurement is converted into limits on $\Im(g_R) = [-0.20, 0.30]$ at the 95% C.L. This represents the first limit on $\Im(g_R)$ and the results are consistent with the SM predictions.

3.4 Vector Boson Production Associated with Top-Antitop Pairs

Studying vector boson production in association with $t\bar{t}$ pairs provides a test of the SM top quark-vector boson coupling. Measurement of these couplings are important for new physics searches and also the discovery of the Higgs boson in $t\bar{t}H$ process. The first cross section measurements of the $t\bar{t}V$ processes are done at the LHC [19,20] using the same-sign dilepton for $t\bar{t}W$ and $t\bar{t}Z$ and trilepton signature for $t\bar{t}Z$ process at $\sqrt{s} = 7$ TeV. The cross section for $t\bar{t}V$ is measured by CMS to be $0.43^{+0.17}_{-0.15}(stat)^{+0.09}_{-0.07}(syst)$ pb and $t\bar{t}Z$ to be $0.28^{+0.14}_{-0.11}(stat)^{+0.06}_{-0.03}(syst)$

pb. Both ATLAS and CMS measurements are consistent with the SM NLO calculations [21,22]. The $t\bar{t}Z$ measurements represent the first direct measurements of top quark-Z boson coupling.

4 Top Polarization

Top quarks are produced unpolarized in the $t\bar{t}$ process. This is verified by ATLAS in the lepton+jets [23] and by CMS in the dilepton final state [24]. The distribution of the polar angle is proportional to $1 + \alpha_i p \cos\theta_i$ in the parent top rest frame. ATLAS used templates with different $\alpha \times p$ values to fit to the reconstructed $\cos\theta_l$ distribution and extracted the fraction of positively polarized top quarks, $f = 0.470 \pm 0.009\ (\text{stat})^{+0.023}_{-0.032}\ (\text{syst})$ compatible with the SM expectation.

5 Conclusions

Measurements of top quark properties by ATLAS and CMS at the LHC are providing thorough tests of the SM. All top quark properties measurements at the LHC show good agreement with the SM predictions.

References

1. ATLAS Collaboration, JINST **3**, S08003 (2008).
2. CMS Collaboration, JINST **3**, S08004 (2008).
3. ATLAS and CMS Collaborations, ATLAS-CONF-2012-095, CMS PAS TOP-12-001.
4. L. Lyons, D. Gibaut and P. Clifford, *Nucl. Instrum. Methods* A **270**, 110 (1988).
5. A. H. Hoang and I. W. Stewart, *Nuov. Cim.* **123** (2008).
6. M. Mangano, Talk given at TOP LHC WG meeting (2012).
7. CMS Collaboration, *J. High. Phys.* **12**, 105 (2012).
8. CMS Collaboration, CMS-PAS-TOP-12-029.
9. CMS Collaboration, CMS-PAS-TOP-12-031.
10. CMS Collaboration, CMS-PAS-TOP-12-035.
11. ATLAS Collaboration, *J. High. Phys.* **12**, 088 (2012).
12. CMS Collaboration, CMS-PAS-TOP-11-020.
13. CMS Collaboration, CMS-PAS-TOP-12-015.
14. ATLAS and CMS Collaborations, ATLAS-CONF-2013-033, CMS-PAS-TOP-12-025.
15. CMS Collaboration, CMS-PAS-TOP-12-020.
16. ATLAS Collaboration, ATLAS-CONF-2013-032.
17. G. Mahlon and S. Parke, *Phys. Lett.* B **476**, 323 (2000).
18. R. Schwienhorst, Q.-H. Cao, C.-P. Yuan and C. Mueller, *Phys. Rev.* D **83**, 034019 (2011).
19. ATLAS Collaboration, ATLAS-CONF-2012-126.
20. CMS Collaboration, CMS-PAPER-TOP-12-014, arxiv:1303.3239 [hep-ex]
21. Cambell and Ellis, *J. High. Phys.* **07**, 052 (2012)
22. Garzelli et al., *J. High. Phys.* **11**, 056 (2012)
23. ATLAS Collaboration, ATLAS-CONF-2012-133.
24. CMS Collaboration, CMS-PAS-TOP-12-016.

MEASURING TOP-QUARK POLARIZATION IN TOP-PAIR + MISSING ENERGY EVENTS

Edmond L. Berger[b], Qing-Hong Cao[a],Jiang-Hao Yu[c], Hao Zhang[b,d]
[a] *Department of Physics and State Key Laboratory of Nuclear Physics and Technology, Peking University, Beijing 100871, China*
[b] *High Energy Physics Division, Argonne National Laboratory, Argonne, IL 60439, USA*
[c] *Department of Physics and Astronomy, Michigan State University, East Lansing, MI 48824, USA*
[d] *Illinois Institute of Technology, Chicago, IL 60616-3793, USA*

The polarization of a top-quark can be sensitive to new physics beyond the standard model. We propose a novel method to measure top-quark polarization, based on the charged lepton energy fraction in top-quark decay, and illustrate the method with a detailed simulation of top-quark pairs produced in supersymmetric top squark pair production. We show that the lepton energy ratio distribution that we define is very sensitive to the top-quark polarization but insensitive to the precise measurement of the top-quark energy.

1 Introduction

Events with a top-quark pair plus missing energy ($t\bar{t}+\not{E}_T$) are promising channels in which to investigate models of new physics (NP) beyond the standard model (SM). Missing energy originates typically from non-interacting or otherwise invisible dark matter (DM) candidates in the NP models, along with neutrinos from SM weak decays. In these events the polarization of the top quark is sensitive to the chirality structure of the top quark's interaction with a postulated parent new heavy resonance and the DM. The top-quark polarization might provide a new way to gain insight into NP models. Measurements of the top-quark polarization tend to rely on the predicted angular correlation of the momentum of a charged lepton (from the top-quark decay) with the top-quark spin [1]. However, this measurement is difficult in $t\bar{t}+\not{E}_T$ events because it is generally not possible to reconstruct the top-quark kinematics, i.e., to disentangle the kinematic effects of the DM particles from neutrinos that accompany the charged leptons in the top-quark leptonic decay.

We define and examine the energy fraction of the charged lepton from the top quark as a novel measure of top-quark polarization, without the requirement of top-quark reconstruction and knowledge of the dark matter mass and spin [2]. We emphasize a few advantages of our energy ratio variable: (i) it is sensitive to the top-quark polarization; (ii) it is not sensitive to the mass splitting between a heavy resonance parent and the DM candidate, provided that this splitting is not too small; (iii) the difference between the left-handed (t_L) and the right-handed top quark (t_R) is not sensitive to the spin of a heavy parent resonance or to the collider energy.

2 The method

In the leptonic decay of a top quark, $t \to bW^+ \to b\ell^+\nu$, the correlation of the momentum of the charged lepton ℓ^+ with the polarization $\hat{s}_t$ of the top-quark, viewed in the top-quark rest frame,

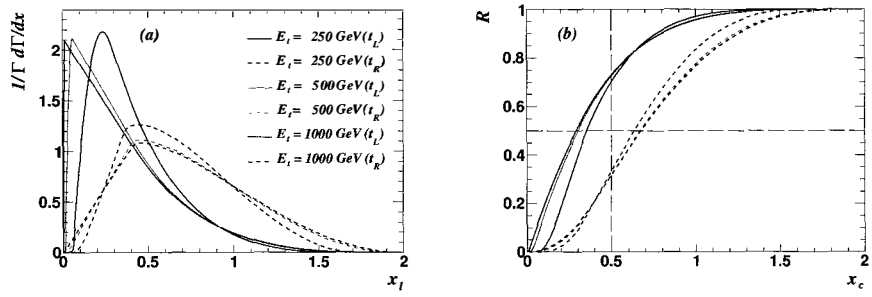

Figure 1: (a)Distributions of the energy fraction x_ℓ of a charged lepton from top-quark decay for E_t = 250, 500, 1000 GeV; (b) The ratio $\mathcal{R}$ as a function of the cut threshold x_c for E_t = 250, 500, 1000 GeV. The solid lines represent left-handed top-quark decay while the dashed lines represent right-handed top quarks.

takes the form $(1+\hat{s}_t z)/2$, where $z \equiv \cos\theta$ is the cosine of the angle between the top-quark spin axis and the lepton momentum. For a boosted top quark with energy E_t, the distribution in the energy fraction $x_\ell \equiv 2E_\ell/E_t$ of the charged lepton becomes

$$\frac{d\Gamma(\hat{s}_t)}{dx} = \frac{\alpha_W^2 m_t}{64\pi AB}\int_{z_{\min}}^{z_{\max}} x\gamma^2[1-x\gamma^2(1-z\beta)]\left(1+\hat{s}_t\frac{z-\beta}{1-z\beta}\right)\mathrm{Arctan}\left[\frac{Ax\gamma^2(1-z\beta)}{B-x\gamma^2(1-z\beta)}\right]dz. \quad (1)$$

Here, $A = \Gamma_W/m_W$ is the ratio of the W-boson width and W-boson mass, $B = m_W^2/m_t^2 \approx 0.216$ is the squared ratio of the W-boson mass and top-quark mass, and the limits of integration are $z_{\min} = \max[(1-1/\gamma^2 x)/\beta, -1]$, $z_{\max} = \min[(1-B/\gamma^2 x)/\beta, 1]$ with $\gamma = E_t/m_t$ and $\beta = \sqrt{1-1/\gamma^2}$. The function Arctan is defined as $\arctan(x)$ for $x \geq 0$ while $\pi + \arctan(x)$ for $x < 0$. We introduce a ratio $\mathcal{R}$ as a quantitative measure of the energy fractions of t_L and t_R,

$$\mathcal{R}(x_c) = \frac{1}{\Gamma}\int_0^{x_c}\frac{d\Gamma}{dx_\ell}dx_\ell \equiv \frac{\Gamma(x_\ell < x_c)}{\Gamma}. \quad (2)$$

This ratio is a function of the the cut threshold x_c of the energy fraction x_ℓ. An analytic expression can be derived for $\mathcal{R}(x_c)$ in the limit $\beta \to 1$. It takes the form

$$\mathcal{R}(x_c) = \frac{3x_c(1-\lambda_t)}{2(1+2B)} - \frac{3\lambda_t x_c^2(1-B+\ln B)}{2(1+2B)(1-B)^2}, \quad (3)$$

for $x_c \in (0,\ 2B)$, and

$$\mathcal{R}(x_c) = \frac{B^2(2B-3)}{(1+2B)(1-B)^2} + \frac{3x_c(1-\lambda_t)}{2(1-B)^2(1+2B)} - \frac{3x_c^2[1+2\lambda_t\ln(x_c/2)]}{4(1-B)^2(1+2B)} + \frac{x_c^3(1+3\lambda_t)}{8(1-B)^2(1+2B)} \quad (4)$$

for $x_c \in (2B,\ 2)$, where $\lambda_t = (-1, +1)$ for (t_L, t_R), respectively. For small x_c, these expressions show that $\mathcal{R}(x_c)$ grows linearly with x_c for t_L, whereas $\mathcal{R}(x_c)$ grows as x_c^2 for t_R ($\lambda_t = 1$).

The analytic expressions Eqs. 3 and 4 also explain why the curves for E_t = 500 GeV (β = 0.94) and E_t = 1000 GeV (β = 0.99) almost overlap. For an energetic top quark, an important consequence is that the difference between $\mathcal{R}(x_c)$ for t_L and t_R is not sensitive to E_t, i. e., the mass splitting between the parent heavy resonance and the DM candidate, as long as the mass splitting is not too small. The t_L and t_R curves are insensitive to the origin of the top quark in the collision, whether from a heavy fermion decay or from a scalar decay. In other words, $\mathcal{R}(x_c)$ quantifies the top-quark polarization but not the top-quark origin. Moreover, in order to extract NP signal events from SM backgrounds, one must normally impose a set of

hard kinematic cuts on the leptons and jets in the final state. These hard cuts force the top quark to be very energetic and thus to satisfy the limit $\beta \to 1$. Therefore, another virtue of the $\mathcal{R}(x_c)$ variable is that the difference between the t_L and t_R curves does not vary with the hard cuts. To prove this method useful, we turn to an explicit calculation of top squark ($\tilde{t}$) pair production, $pp \to \tilde{t}\bar{\tilde{t}}X \to t\bar{t}\tilde{\chi}\tilde{\chi}X$.

3 Collider simulation

We perform a parton-level Monte Carlo simulation of top squark ($\tilde{t}$) pair production $pp \to \tilde{t}\bar{\tilde{t}}X \to t\bar{t}\tilde{\chi}\tilde{\chi}X$ to demonstrate that $\mathcal{R}$ remains useful for distinguishing t_L and t_R even when E_t cannot be measured directly. We assume the colored scalar $\tilde{t}$ decays entirely into $t\tilde{\chi}$ through the effective coupling $\mathcal{L}_{\tilde{t}t\tilde{\chi}} = g_{\text{eff}}\tilde{t}\bar{\tilde{\chi}}(\cos\theta_{\text{eff}}P_L + \sin\theta_{\text{eff}}P_R)t$, where the angle θ_{eff} depends on the mass matrix mixings of the top squark and the neutralino sector, and $P_{\text{L/R}}$ is the usual left/right-handed projector. Our benchmark point has $m_{\tilde{t}} = 350$ GeV and a representative DM mass $m_{\tilde{\chi}} = 50$ GeV. We simulate $\tilde{t}$ pair production with decay to a top-quark pair plus DM candidates at the LHC with 8 TeV energy. We demand that the top-quark decays semi-leptonically, and that the antitop-quark decays hadronically. Two irreducible SM backgrounds, $t\bar{t}$ and $t\bar{t}Z$ production, are considered. The details of the simulation can be found in our paper[2]. After all cuts, we find that the numbers of signal and background events are 130 and 22 at 8 TeV and 20 fb^{-1} integrated luminosity, for a signal significance of $S/\sqrt{B} = 28$.

In $\tilde{t}$ pair production the decay chains of $\tilde{t} \to t\tilde{\chi}$ and $\bar{\tilde{t}} \to \bar{t}\tilde{\chi}$ have similar kinematics because the heavy $\tilde{t}$'s are not highly boosted. In this work we investigate the energy of the antitop quark as an estimator of the top-quark energy, with the antitop-quark required to decay into three jets[a]. We define a new energy fraction variable $x'_\ell = 2E_\ell/E_{\tilde{t}}$. After convolution with the production cross section, a ratio $\mathcal{R}'$ can be defined as

$$\mathcal{R}'(x'_c) = \frac{1}{\sigma(\text{tot})}\int_0^{x'_c}\frac{d\sigma}{dx'_\ell}dx'_\ell \equiv \frac{\sigma(x'_\ell < x'_c)}{\sigma(\text{tot})}, \tag{5}$$

where $d\sigma/dx'_\ell$ is the differential cross section, and x'_c is the cut threshold of x'_ℓ.

We use a χ^2-template method based on the W boson and top-quark masses to select the three jets from the hadronic decay of the antitop quark. For each event we pick the combination which minimizes $\chi^2 = (m_W - m_{jj})^2/\Delta m_W^2 + (m_t - m_{jjj})^2/\Delta m_t^2$, where Δm_W and Δm_t are the width of the W-boson and the top-quark, respectively. The efficiency of this method is 84%. After the antitop-quark energy is reconstructed in the lab frame, $\mathcal{R}'$ can be obtained with its cut threshold x'_c dependence.

Armed with both the Monte Carlo level momenta and the reconstructed momenta, we perform several comparisons to evaluate how faithful the $\mathcal{R}'$ distribution is to the true $\mathcal{R}$ (Fig. 2). We conclude that x'_c is a good variable when x_c cannot be obtained. Lastly, comparing $\mathcal{R}$ at the Monte Carlo level and at the reconstruction level, we see a slight downward shift for both t_L and t_R. This effect arises because the p_T cuts on the lepton reduce the number of events with $x'_\ell < x'_c$.

The results in Fig. 2 (a) establish that x'_c is a suitable variable and that $\mathcal{R}'$ serves as a good substitute for $\mathcal{R}$. After all the cuts, about 87 (101) signal events are needed to distinguish t_L (t_R) from an unpolarized top quark at 95% confidence level (C.L.) in the absence of background, with only about 23 signal events to discriminate t_R from t_L. Although the benchmark point chosen has been subsequently excluded[4], the method proposed in this work remains powerful for masses in the allowed region.

Thus far in this section, we assume the t-$\tilde{t}$-$\tilde{\chi}$ coupling is completely left-handed or right-handed, but in general the coupling is a mixture of both. Once data are obtained, we could use

[a]Another useful variable in the literature is $E_\ell/(E_\ell + E_b)$ where the b-jet and ℓ^+ originate from the same top-quark decay[3].

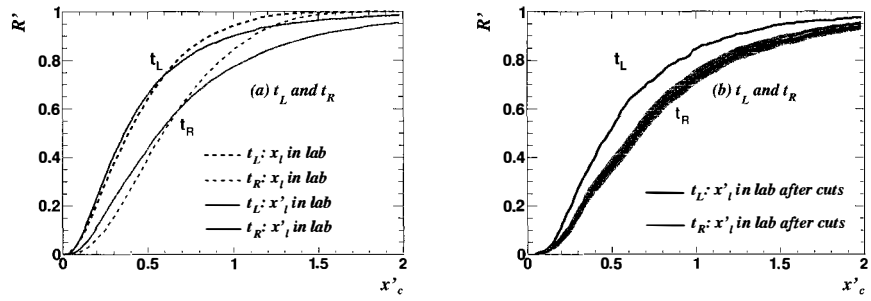

Figure 2: (a) The $\mathcal{R}$ distributions as a function of the cut threshold x_c' for a 350 GeV $\tilde{t}$ quark with pure right-handed or left-handed couplings at the LHC with 8 TeV energy. The lepton energy fraction is evaluated in the lab frame from either $\bar{t}_{\rm had}^{\rm rec}$ (x_ℓ') or the top-quark energy $t_{\rm lep}$ (x_ℓ). With $\sin\theta_{\rm eff} = 1$ $(\cos\theta_{\rm eff} = 1)$ the top quark is mainly right-handed (left-handed), and the curves are labeled by t_R (t_L). (b) The statistical uncertainty band of $\mathcal{R}$ is shown for both t_L and t_R at the 1σ confidence level for an assumed 20 fb^{-1} of integrated luminosity.

the $\mathcal{R}'$ curves shown in Fig. 2(b) as templates in fits to these data to extract $\theta_{\rm eff}$ and shed light on the nature of top squark mixing.

4 Other implications

Our method can be applied to several NP models. We performed a detailed simulation of pair production of a T-odd top-quark partner (T_-) in the Littlest Higgs Model with T-parity (LHT), $pp \to T_-\overline{T}_-X \to t\bar{t}A_HA_HX$, where A_H is the T-odd photon partner. Our numerical results are very similar to those shown for t_R in Fig. 2. Verification of mainly right-handed polarization would provide a powerful check of the model [5]. Another example is the leptophobic Z' boson, which couples only to the SM quarks. The top-quark polarization could be used to probe the handedness of the Z'-q-q coupling which is sensitive to how the SM quarks are gauged under the new gauge symmetry [6].

Acknowledgments

The work by E.L.B. and H.Z. is supported in part by the U.S. DOE under Grant No. DE-AC02-06CH11357. H.Z. is also supported by DOE under the Grant No. DE-FG02-94ER40840. Q.H.C. is supported by the National Natural Science Foundation of China under Grant No. 11245003. J.H.Y. is supported by the U.S. National Science Foundation under Grant No. PHY-0855561.

References

1. G. Mahlon and S. J. Parke, Phys. Rev. D **53**, 4886 (1996) [hep-ph/9512264]; G. L. Kane, G. A. Ladinsky and C. P. Yuan, Phys. Rev. D **45**, 124 (1992).
2. E. L. Berger, Q. -H. Cao, J. -H. Yu and H. Zhang, Phys. Rev. Lett. **109**, 152004 (2012) [arXiv:1207.1101 [hep-ph]].
3. J. Shelton, Phys. Rev. D **79**, 014032 (2009).
4. ATLAS Collaboration, ATLAS-CONF-2013-037 (2013); CMS Collaboration, SUS-12-024-PAS (2013).
5. Q. -H. Cao, C. S. Li and C. -P. Yuan, Phys. Lett. B **668**, 24 (2008); M. M. Nojiri and M. Takeuchi, JHEP **0810**, 025 (2008).
6. E. L. Berger, Q. -H. Cao, C. -R. Chen and H. Zhang, Phys. Rev. D **83**, 114026 (2011).

SINGLE TOP QUARK PHYSICS AT THE TEVATRON

C. SCHWANENBERGER
on behalf of the CDF and D0 Collaborations
Particle Physics Group, School of Physics and Astronomy,
The University of Manchester, Oxford Road, Manchester M13 9PL, United Kingdom

Recent analyses of single top quark production in proton-anti-proton scattering at a center-of-mass energy of 1.96 TeV are discussed representing up to 9.1 fb^{-1} of Tevatron data. Measurements of the inclusive single top quark production cross section in the s- and t-channels and the extraction of $|V_{tb}|$ are presented. Furthermore, top quark property measurements exploring single top quark production and searches for new physics in single top quark final states are reviewed. The extraction of the top quark width and lifetime and the search for anomalous Wtb couplings are presented in more detail.

1 Introduction

Top quarks were first observed via pair production at the Fermilab Tevatron Collider in 1995 [1]. At the Tevatron, top quarks are either produced in pairs via the strong interaction or singly via the electroweak interaction. In the framework of the standard model (SM), each top quark is expected to decay nearly 100% of the times into a W boson and a b quark W bosons can decay hadronically into $q\bar{q}'$ pairs or leptonically into $e\nu_e$, $\mu\nu_\mu$ and $\tau\nu_\tau$ with the τ in turn decaying into an electron, a muon, or hadrons, and associated neutrinos.

Single top quark production serves as a probe of the Wtb interaction [2], and its production cross section provides a direct measurement of the magnitude of the quark mixing matrix element V_{tb} without assuming three quark generations [3]. However, measuring the yield of single top quarks is difficult because of the small production rate and large backgrounds. At the Tevatron single top quarks are produced predominantly by a t-channel exchange of a virtual W boson which combines with a highly energetic b quark to produce a top quark, or by an s-channel exchange of a far off-shell W boson which decays to produce a top quark and a b antiquark.

2 Cross Section Measurements and Extraction of $|V_{tb}|$

In March 2009, the CDF and D0 Collaborations reported observation of the electroweak production of single top quarks in $p\bar{p}$ collisions at $\sqrt{s} = 1.96$ TeV based on 3.2 fb^{-1} (CDF) [4] and 2.3 fb^{-1} (D0) [5] of data. Both collaborations used events containing an isolated electron or muon and

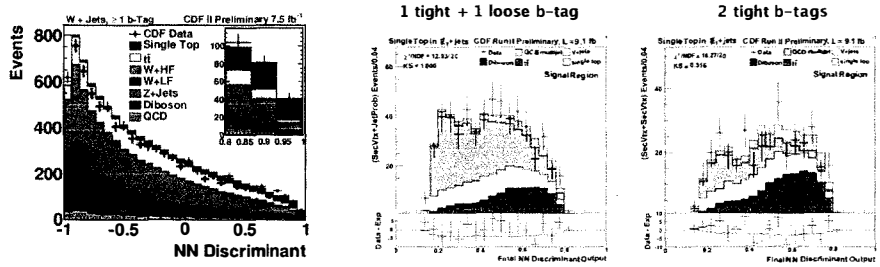

Figure 1: NN output distributions for different b-tagging requirements in the e/μ+jets analysis (left) and in the MET+jets analysis (middle, right). KS/χ^2 tests take into account statistical and systematic uncertainties on signal and background processes.

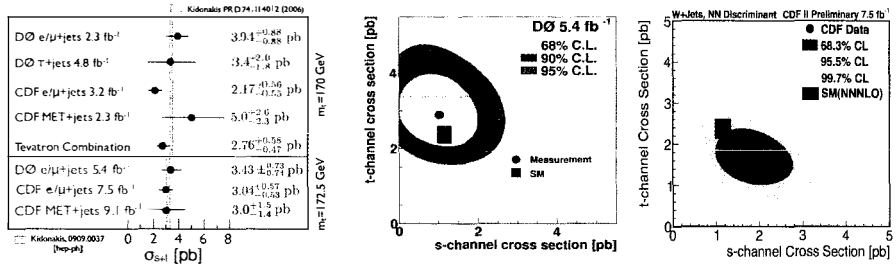

Figure 2: Summary of inclusive single top quark production cross section measurements (left), and Posterior probability density for s-channel vs. t-channel single top quark production in contours of equal probability density for D0 (middle) and CDF (right). The measured cross section and SM prediction are overlaid.

missing transverse energy ($\not\!\!E_T$), together with jets where one or two of the jets were required to originate from the fragmentation of b quarks (b-tagging). The data are divided into independent sets depending on lepton flavor, jet multiplicity, number of b-tags and in the case of D0 the run period. CDF and D0 each combine many variables using different multivariate analysis (MVA) methods such as Boosted Decision Trees (BDT), Neural Networks (NN), Bayesian Neural Networks (BNN), Matrix Elements (ME) and Likelihood functions to increase the separation power between signal and background. The discriminant outputs of each MVA are combined to one discriminant taking the correlations into account. The measurements in different final states are summarized (blue) in Fig. 2 (left).

After the observation D0 has updated the measurement of the single top quark production cross section combining BNN, BDT and neuroevolution of augmented topologies (NEAT) MVA methods in final states with an isolated electron or muon, large $\not\!\!E_T$, and two, three, or four jets, with one or two of them containing a bottom hadron (e/μ+jets) using 5.4 fb^{-1} of data [6]. Recently, CDF has updated their measurement (e/μ+jets) using the NN method analyzing final states with an isolated electron or muon, large $\not\!\!E_T$ from the W boson decay and two or three jets, at least one of them is required to be identified as originating from a bottom quark [7]. The resulting NN discriminate distribution is shown in Fig. 1 (left). To increase the acceptance in the combination, CDF has also performed a measurement of the single top quark production cross section selecting events consistent with a W+jets topology but where no electron or muon has been identified, and where the tau lepton in the $t \to Wb \to \tau\nu b$ channel is reconstructed as a jet in the calorimeters (MET+jets). A recent update with 9.1 fb^{-1} of data has been performed utilizing the NN method [8]. NN output distributions in the signal region are presented for two different b-tagging requirements in Fig. 1 (middle, right).

The three measurements since the observation are summarized (red) in Fig. 2 (left). All measurements agree with each other and the Standard Model (SM) prediction [9]. The results are translated into a direct measurement of the amplitude of the CKM matrix element V_{tb} without making assumptions on the number of quark generations and the matrix unitarity. D0 obtains $|V_{tb}| = 0.92^{+0.10}_{-0.11}$ [6], CDF derives $|V_{tb}| = 0.92 \pm 0.10$ [7], while the Tevatron combination represents the most accurate result of $|V_{tb}| = 0.88 \pm 0.07$ [10].

It is important to measure s-channel and t-channel production separately in a model-independent way, because the SM relation between the two production channels could be changed due to the existence of new physics. D0 has observed t-channel production for the first time separately considering s-channel production as background using 5.4 fb^{-1} of integrated luminosity [11]. Selecting events containing an isolated electron or muon, missing transverse energy and one or two jets originating from the fragmentation of b quarks, the cross section was measured as $\sigma(p\bar{p} \to tqb+X) = 2.90 \pm 0.59$ (stat+syst) pb for a top quark mass of 172.5 GeV, corresponding to a significance of 5.5 standard deviations.

Both collaborations have also used the measurements of the single top quark production cross section [6,7] to construct a two-dimensional (2D) posterior probability density as a function of the cross sections for the s-channel and t-channel processes. As Fig. 2 shows (middle, right) both measurements agree with the SM predictions.

3 Top Quark Properties

It is an interesting fact that the Tevatron single top quark data set allows sensitive measurements of fundamental top quark properties, such as of the top quark polarization [12] and the top quark width and lifetime [13]. The determination of the latter property has been updated using 5.4 fb^{-1} of integrated luminosity [14]. The total width Γ_t is extracted by combining the partial decay width $\Gamma(t \to Wb)$ and the branching fraction $\mathcal{B}(t \to Wb)$. Following the idea proposed in [16], $\Gamma(t \to Wb)$ is obtained from the measured t-channel single top quark production cross section [11] assuming that the coupling leading to t-channel single top quark production is identical to the coupling leading to top quark decay. $\mathcal{B}(t \to Wb)$ has been measured in top quark pair production [15]. For a top quark mass of 172.5 GeV, the resulting total width is $\Gamma_t = 2.00^{+0.47}_{-0.43}$ GeV. This translates to a lifetime of $\tau_t = (3.29^{+0.90}_{-0.63}) \times 10^{-25}$ s.

4 Searches for New Physics

Analyses of single top quark final states at the Tevatron also provide sensitive searches for new physics. So far searches for anomalous Wtb couplings [17,18], for a fourth-generation b quark coupling to the top quark [13], for single top quark production via flavor-changing neutral currents [19,20], for $W' \to tb$ resonances [21] and for charged Higgs bosons decaying to top and bottom quarks [22] have been performed.

D0 has performed a new search for physics beyond the SM in the form of anomalous Wtb right-handed vector couplings or left- or right-handed tensor couplings, described by an effective Lagrangian including operators up to dimension five [23]. It has been demonstrated that combining the anomalous Wtb couplings search in the single top quark final state [18] with the W boson helicity measurement in top quark decays [24], leads to significant improvements in sensitivity [25]. Fig. 3 shows resulting posterior density distributions for different anomalous couplings. Consistency with the SM is found and 95% C.L. limits on anomalous Wtb couplings are set.

5 Summary

The analysis of single top quark final states provides a very rich physics program at the Tevatron. The inclusive s+t-channel (separate t-channel) production cross section has been measured with

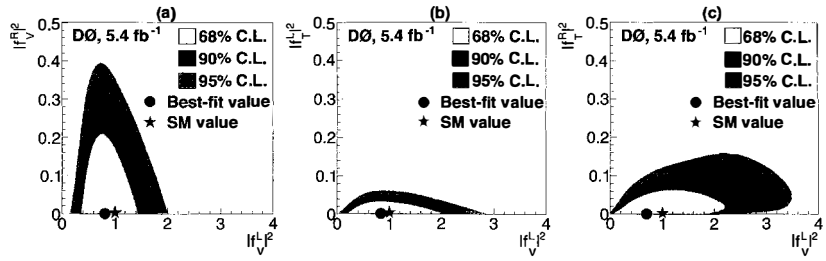

Figure 3: Posterior density distribution for the combination of W boson helicity and single top quark measurements for (a) right-vector vs. left-vector form factors, (b) left-tensor vs. left-vector form factors and (c) right-tensor vs. left-vector form factors. All systematic uncertainties are included.

an uncertainty of 18% (20%). The CKM matrix element $|V_{tb}|$ has been extracted with an uncertainty of 8%. Separate evidence of s-channel production is still one of the most important aims of the single top quark program at the Tevatron. Top quark properties such as the top quark decay width have been measured and many sensitive searches for new physics have been performed. All measurements agree with the SM predictions. Final results with the full data set of ≈ 10 fb^{-1} and a new Tevatron combination of the single top quark cross section and $|V_{tb}|$ are expected soon.

References

1. F. Abe *et al.* (CDF Collaboration), Phys. Rev. Lett. **74**, 2626 (1995); S. Abachi *et al.* (D0 Collaboration), Phys. Rev. Lett. **74**, 2632 (1995).
2. A.P. Heinson, A.S. Belyaev, and E.E. Boos, Phys. Rev. D **56**, 3114 (1997).
3. G.V. Jikia and S.R. Slabospitsky, Phys. Lett. B **295**, 136 (1992).
4. T. Aaltonen *et al.* [CDF Collaboration], Phys. Rev. Lett. **103**, 092002 (2009); T. Aaltonen *et al.* [CDF Collaboration], Phys. Rev. D **82**, 112005 (2010).
5. V. M. Abazov *et al.* [D0 Collaboration], Phys. Rev. Lett. **103**, 092001 (2009).
6. V. M. Abazov *et al.* [D0 Collaboration], Phys. Rev. D **84**, 112001 (2011).
7. CDF Collaboration, conference note 10793.
8. CDF Collaboration, conference note 10979.
9. N. Kidonakis, arXiv:0909.0037 [hep-ph]; N. Kidonakis, Phys. Rev. D **74**, 114012 (2006).
10. T. E. W. Group [CDF and D0 Collaborations], arXiv:0908.2171 [hep-ex].
11. V. M. Abazov *et al.* [D0 Collaboration], Phys. Lett. B **705** 313 (2011).
12. CDF Collaboration, conference note 9920.
13. V. M. Abazov *et al.* [D0 Collaboration], Phys. Rev. Lett. **106**, 022001 (2011).
14. V. M. Abazov *et al.* [D0 Collaboration], Phys. Rev. D **85**, 091104 (2012).
15. V. M. Abazov *et al.* [D0 Collaboration], Phys. Rev. Lett. **107**, 121802 (2011).
16. D. O. Carlson and C. P. Yuan, hep-ph/9509208.
17. T. Aaltonen *et al.* [CDF Collaboration], Phys. Rev. Lett. **103**, 041801 (2009).
18. V. M. Abazov *et al.* [D0 Collaboration], Phys. Lett. B **708**, 21 (2012).
19. T. Aaltonen *et al.* [CDF Collaboration], Phys. Rev. Lett. **102**, 151801 (2009).
20. V. M. Abazov *et al.* [D0 Collaboration], Phys. Lett. B **693**, 81 (2010).
21. V. M. Abazov *et al.* [D0 Collaboration], Phys. Lett. B **699**, 145 (2011).
22. V. M. Abazov *et al.* [D0 Collaboration], Phys. Rev. Lett. **102**, 191802 (2009).
23. G. L. Kane, G. A. Ladinsky and C. P. Yuan, Phys. Rev. D **45**, 124 (1992).
24. V. M. Abazov *et al.* [D0 Collaboration], Phys. Rev. D **83**, 032009 (2011).
25. V. M. Abazov *et al.* [D0 Collaboration], Phys. Lett. B **713**, 165 (2012).

5.
Heavy Ion

HEAVY-ION SESSION: A (QUICK) INTRODUCTION

B. HIPPOLYTE
Institut Pluridisciplinaire Hubert Curien, Département de Recherches Subatomiques, 23 rue du Loess, F-67037 Strasbourg, France

These proceedings summarise the short introduction given at the beginning of the heavy-ion session of the XLVIIIth Rencontres de Moriond – QCD. The choice is deliberately to focus on global pictures describing the collision of ultra-relativistic heavy ions and its evolution whereas highlights, recent results and latest developments are reported by the other participants of the session. Using mainly Pb–Pb data at the Large Hadron Collider, the emphasis is made on the initial state conditions as well as the observables which qualitatively illustrate how "perfect" and opaque the strongly interacting Quark-Gluon Plasma is.

The basic steps of the evolution of a heavy-ion collision could be described with a single sentence: at first Lorentz contracted ultra-relativistic heavy ions are colliding, leading to a pre-equilibrium phase dominated by initial conditions, very shortly followed by the Quark-Gluon Plasma (QGP) which expands and cools until hadronisation occurs, and eventually long lived particles reach the detectors. Such a short description would certainly not reflect the recent precision measurements presented during the heavy-ion session of this conference. These are performed both at the Large Hadron Collider (LHC) with Pb–Pb collisions at the unprecedented energy of $\sqrt{s_{\rm NN}} = 2.76$ TeV and at the Relativistic Heavy Ion Collider (RHIC) where the gold beam energy is varied (Beam Energy Scan program, BES) corresponding to $\sqrt{s_{\rm NN}} = 7.7$, 11.5, 19.6, 27, 39, 62.4 and 200 GeV with including comparisons to other colliding systems (pp and p–Pb at the LHC; pp, d–Au, Cu–Cu and U–U at RHIC). As an introduction to the session, these proceedings focus on the general picture emerging from several years of study at RHIC and the LHC. The main steps of a heavy-ion collision are presented in section 1 together with some definitions and considerations related to the initial state conditions and the fluctuations observed at that stage. Several global observables and space time properties are discussed in the next section and followed by a qualitative illustration of the QGP opacity.

1 The main steps of the system evolution

Part of the recent progress in the understanding of the evolution of the system created in heavy-ion collisions is illustrated[a] with Fig.1. The initial conditions for the two colliding nuclei are, to a large extent, driven by the geometrical overlap region. The *centrality* of the collision is defined by correlating the multiplicity of the produced particles with the geometry of the system[1]: the most central collisions are the head-on ones for which the multiplicity is the largest. Several quantities are often used to characterise the centrality of the collision: the number of participating nucleons ($N_{\rm part}$), the number of binary collisions ($N_{\rm coll}$, i.e. the number of nucleon-nuclon inelastic collisions) or the geometrical nuclear overlap function ($T_{\rm AA} = N_{\rm coll}/\sigma^{\rm inel}_{\rm NN}$). Although

[a] it is updated with respect to the one shown at the time of the conference.

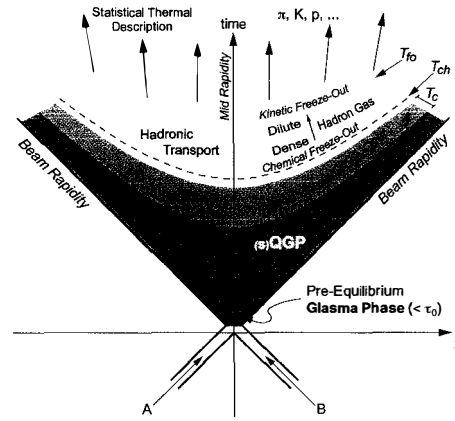

Figure 1: Light cone of the evolution of the system created in heavy-ion collisions at RHIC and the LHC. The main phases and steps are specified on the right side together with the different temperatures driving the transition from the strongly interacting QGP to the hadrons measured in the detectors (successively the critical temperature T_c for the chiral symmetry restoration, the chemical freeze-out temperature T_{ch} and the kinetic freeze-out temperature T_{fo}). Formalisms used to described successfully this evolution are shown on the left side of the schematisation.

fluctuations in the initial state and their importance were discovered quite recently, they are unambiguously needed for reproducing event-by-event measurements of the anisotropic flow coefficients $v_{n=2,3,4}$ [2] and several contributions of this session are dedicated to that topic [3]. The resulting pre-equilibrium Glasma phase, which includes fluctuations of the energy density distribution on a small scale, is now precisely modelled by combining initial nuclear wave functions and classical Yang-Mills dynamics of the produced color fields [4]. Hard parton scatterings quickly occur, leading to jet and heavy flavour production (see section 3), as well as the thermalisation of the system to the phase where deconfined partons are strongly interacting (sQGP). This fast approach to local thermodynamical equilibrium generally justifies the use of hydrodynamics which is extremely successful for modelling the expansion and the cooling of the QGP (see ref.[5] and references therein).

Lattice QCD (LQCD) calculations provide significant inputs for establishing the equation of state (EOS). The transition between the partonic matter and the hadron gas, as represented in Fig. 1, corresponds to a cross-over and, concerning the value of the (pseudo-) critical temperature for chiral symmetry restoration, there is currently a very good agreement between the Wuppertal-Budapest and HotQCD collaborations: $T_c = 155 \pm 3$ (stat.) ± 3 (sys.) MeV [6] and $T_c = 154 \pm 8$ (stat.) ± 1 (sys.) MeV [7] respectively. Some systematic uncertainties are still to be resolved for the EOS as can be seen in Fig. 2 (left) which shows the normalised trace anomaly as a function of the critical temperature: the values from both collaborations are compatible below T_c but the HotQCD ones are systematically higher by $\sim 25\%$ above T_c. Later, as it expands and cools, the system consists of a dense then a dilute hadronic gas modelled by hadronic transport codes until particles stop interacting at the kinetic freeze-out. From the statistical analysis of hadron abundances as well as the study of their transverse momentum (p_T) differential yields, both the chemical freeze-out temperature (T_{ch}) and the kinetic freeze-out temperature (T_{fo}) can be estimated.

Obviously the presented picture of Fig. 1 remains a simplified one, often used as a guideline to separate "hard" (from the first steps of the collision and involving large momentum transfer between partons) and "soft" probes (corresponding mainly to low p_T phenomena) of the QGP. it is important to remember that measures often correspond to observables which are integrated over time and that many questions which are beyond the scope of this introduction stay open,

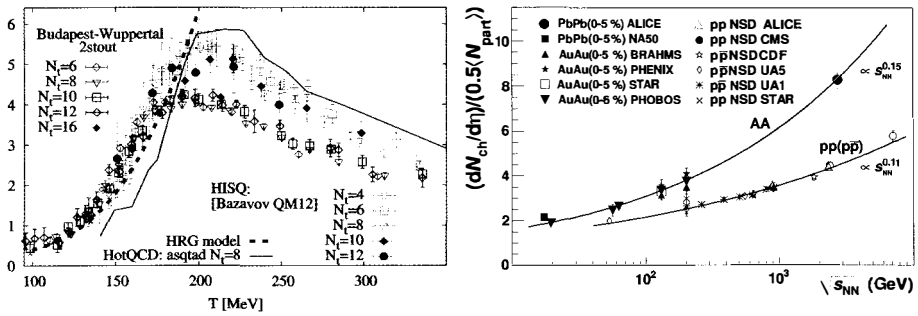

Figure 2: Normalised trace anomaly $(\varepsilon - 3p)/T^4$ as a function of the critical temperature (left): the value of the (pseudo-) critical temperature for chiral symmetry restoration T_c obtained by the Wuppertal-Budapest and HotQCD collaborations is $\simeq 155$ MeV. Number of charged particles produced per unit of pseudorapidity $\mathrm{d}N_{\mathrm{ch}}/\mathrm{d}\eta$ divided by the average number of participant nucleon pairs as a function of the centre of mass energy (right) for both central A-A and non-single diffractive pp (and $\mathrm{p\bar{p}}$) collisions. See text for references.

mainly at the interfaces (e.g. how thermalisation happens so quickly? are other hadronisation mechanisms than fragmentation at play? what are the consequences of such a fast expansion for the system?).

2 Several global observables and space-time properties

The number of charged particles produced per unit of pseudorapidity $\mathrm{d}N_{\mathrm{ch}}/\mathrm{d}\eta$ is among the first measurements performed with heavy-ion collisions at the LHC. ALICE value is shown in Fig. 2 (right) after normalisation by the average number of participant nucleon pairs [8]. Measurements obtained by ATLAS and CMS agree within uncertainties [9,10]. Comparing the value at LHC with lower energy A–A collisions at RHIC and SPS, it can be noted that the evolution of this charged particle multiplicity with $\sqrt{s_{\mathrm{NN}}}$ behaves like a power law and its scaling exponent (0.15) is slightly larger than the one (0.11) extracted from non-single diffractive pp (and $\mathrm{p\bar{p}}$) data. The energy density (ε) for heavy-ion collisions in the central rapidity region can be estimated with the following formula derived from ref. [11]:

$$\varepsilon = \frac{E}{V} = \frac{1}{\pi (r_0 A^{1/3})^2 \, \tau_0} \frac{dE_{\mathrm{T}}}{dy}, \tag{1}$$

where boost invariance is assumed for the energy E (corresponding to the transverse energy per unit of rapidity) and the volume V is defined as the cylinder which radius section is, for central collisions, the one of the colliding nuclei (i.e. $r = r_0 A^{1/3}$ with $r_0 = 1.2$ fm and $A = 208$ for ^{208}Pb) and τ_0 is the formation time. The CMS measurement of the transverse energy per unit of pseudorapidity for the 5% most central collisions gives $\mathrm{d}E_{\mathrm{T}}/\mathrm{d}\eta = 2007 \pm 100$ GeV at mid-rapidity [12]. Choosing a value for τ_0 is a sensible task. Using the conservative value of 1 fm/c, as done at RHIC, leads [b] to an initial energy density of 14 GeV/fm^3 which is almost 3 times the one obtained at RHIC [13] and about a factor 30 above the phase transition expected from LQCD [14].

Basic space-time properties can be inferred from Hanbury Brown–Twiss (HBT) analyses of selected events. The three HBT radii (R_{out}, R_{side} and R_{long}) correspond to the spatial extent along orthogonal directions at decoupling for identified particles [15]. The volume of this homogeneity region ($V \sim (2\pi)^{3/2} R_{\mathrm{out}} R_{\mathrm{side}} R_{\mathrm{long}}$) for charged pions is shown as a function of the

[b] a Jacobian of ~ 1.1 is taken into account; using the charged particle multiplicity, assuming a factor of 3/2 due to the neutral particles and a mean transverse energy per particle of ~ 1 GeV give a similar estimate.

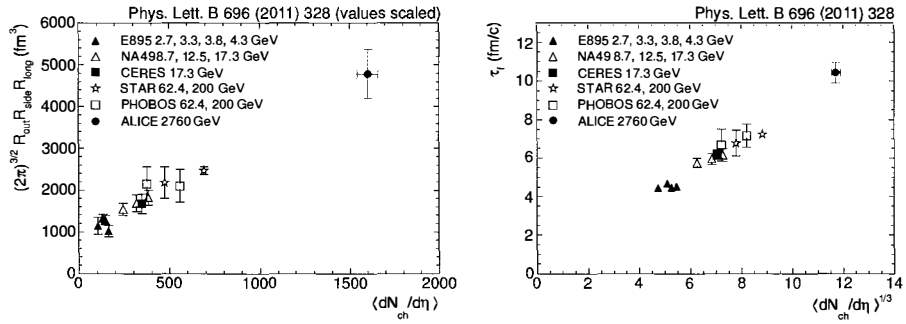

Figure 3: Volume of homogeneity region extracted from the HBT radii $R_{\rm out}$, $R_{\rm side}$ and $R_{\rm long}$ of decoupling pions at $k_\perp = 0.3$ GeV/c as a function of the charged-particle pseudorapidity density (left). Decoupling time extracted from $R_{\rm long}(k_\perp)$ (right). Error bars represent statistical and systematic uncertainties added in quadrature except for E895 where the errors are statistical only. See text for references.

charged particle density in the left panel of Fig. 3 for the most central nucleus–nucleus collisions from AGS to LHC energies [16]. An approximately linear dependence is observed and the volume obtained for Pb–Pb collisions at the LHC is twice as large as the Au–Au one at RHIC while the energy increases from $\sqrt{s_{\rm NN}} = 200$ GeV to 2.76 TeV. The duration of the longitudinal expansion of the system i.e. the decoupling time can be estimated [c] by fitting the $k_\perp$ dependence of $R_{\rm long}$ with fixing $T_{\rm fo}$. In the right panel of Fig. 3, the decoupling time is plotted vs. the cube root of the charged particle density for the most central events: the system lifetime scales linearly and reaches 10 fm/c at the LHC i.e. a value $\sim 30\%$ higher than what was measured at RHIC.

No discussion on anisotropic flow measurements nor comparison with models is given here since the latest results are presented in several other contributions of this session with great details [3]. However, as mentioned in section 1, additional insights on the transverse expansion of the system can be obtained by simply studying hadron integrated yields and low $p_{\rm T}$ spectra. At the LHC energies, the ALICE collaboration reports some tension between the measured protons yields and thermal model predictions from the extrapolation of RHIC energy results [17]: without including the possibility of sudden (non-equilibrium) freeze-out [18], thermal model calculations using $T_{\rm ch} = 164$ MeV would overestimate the proton yields despite being favoured by multi-strange baryon measurements. With respect to the latest implementations of 3D+1 hydrodynamical models followed by hadronic transport, blast-wave fits of hadron $p_{\rm T}$ spectra seem obviously simplistic and outdated. They can still be of interest for systematical studies such as the comparison of the radial flow profile and velocity between RHIC and the LHC energies. For most central events at the LHC, the average transverse flow velocity estimated with the $p_{\rm T}$ spectra of π, K and p is $\langle \beta_{\rm T} \rangle = 0.65 \pm 0.02$ i.e. a 10% increase with respect to similar measurements at RHIC. The value of $T_{\rm fo}$ extracted at the LHC is 95 MeV, similar to the one at RHIC within uncertainties, and decreases with centrality although hydrodynamics does not seem to be fully appropriate for most peripheral events [17].

3 Probing the opacity of the QGP

Characterising some of the properties of the produced matter can be done with "hard probes". The idea is here to use energetic partons produced in the early stages of the collision as a tomographic probe of the system. These partons are expected to interact with the coloured medium and the modification of their evolution can be compared with what would happen in

[c] this is actually an underestimation due to the rapid transverse expansion of the system.

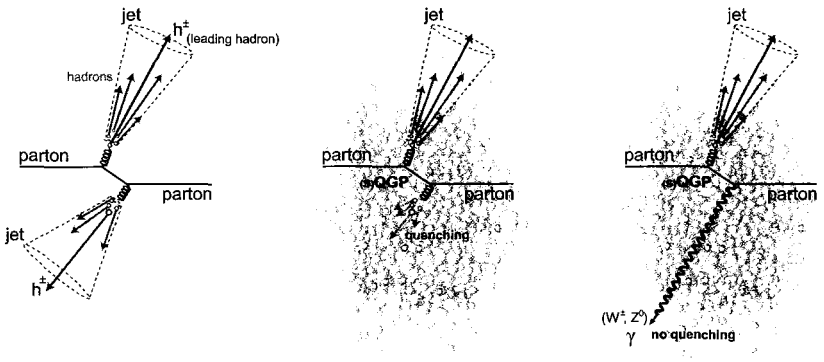

Figure 4: Illustration of jet quenching phenomenon in the presence of a coloured deconfined medium: (left) schematisation of a di-jet event originating from parton scattering in a hadronic collision (no QGP); (centre) when traversing the QGP, one of the scattered parton looses a significant fraction of its energy and the resulting jet, if ever identified and reconstructed, is quenched; (right) when traversing the QGP, photons and electroweak bosons are not affected by the coloured medium and constitute a reference for probing the opacity of the system.

vacuum (or rather for a pp or a p-A collision). For instance, quarkonia can be used to investigate the temperature of the system (for a recent review, see ref.[19]). In this paragraph, only the probes related to the characterisation of the opacity of the system will be mentioned from a qualitative point of view (for a detailed discussion on the corresponding formalism, see ref.[20]). Due to their large mass, heavy-flavoured quarks are produced primarily by gluon fusion at the beginning of the heavy-ion collision. They are supposed to lose energy in the coloured medium very early whereas light-flavoured quarks and gluons lose most of their energy at the end of their propagation. Contrarily, electroweak bosons γ, $W^{\pm}$ and Z^0 are considered as benchmark probes of the QGP because they (as well as their leptonic decays) are not supposed to interact with the hot and dense matter. Figure 4 illustrates the principles of the performed measurements. It is remarkable that a large suppression is seen in almost all hadronic processes when their production rates are compared to pp interactions after normalisation by the number of binary nucleon-nucleon collisions [21,22]. As shown in Fig. 5, for direct photons selected by isolation criteria as well as the $W^{\pm}$ and Z^0 bosons selected via their muonic decay, no deviation from the binary-scaled production is observed. More details on these CMS results can be found in refs.[23]. How these suppressions translate into quantitative measurements of the opacity of the QGP would require much more time than the one allotted for this contribution.

4 Summary

Now that measurements performed in heavy-ion collisions are entering a precision era a clear picture emerges from the main stages of the Quark-Gluon Plasma evolution. Many results are already available at the LHC but also at RHIC with the Beam Energy Scan which turns on/off key features and it is currently a question of testing thoroughly the validity of models/descriptions from 7.7 GeV to 2.76 TeV. With the upgrades of the experiments after the Long Shutdown 1 and 2, additional statistics will allow for further differential measurements.

Acknowledgments

The author wish to thank the organisers for the pleasant and inspiring atmosphere during the conference.

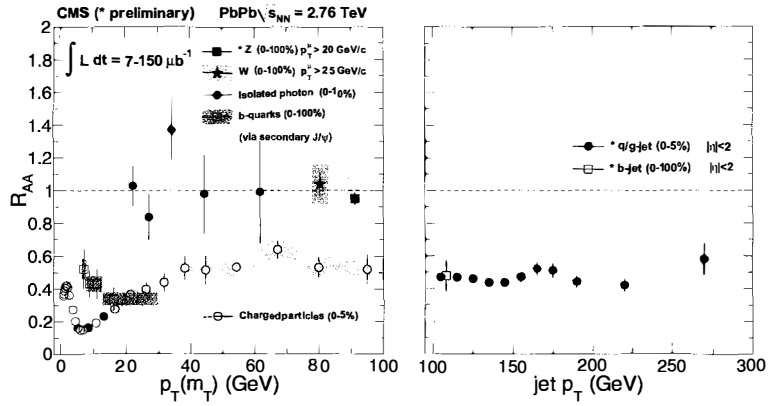

Figure 5: Nuclear modification factor as a function of transverse momentum p_T or transverse mass m_T. No suppression is observed for isolated photons, W and Z bosons contrarily to charged particles and b-quarks (identified using non-prompt J/ψ) (left). A similar suppression ($R_{AA} \sim 0.5$) is seen for quark- and gluon-jets as well as for b-jets at high p_T (right). Centrality selections vary depending on the considered particles. See text for references.

References

1. B. Abelev *et al* (ALICE Collaboration), arXiv:1301.4361.
2. B. Schenke *et al*, *Nucl. Phys.* B **904–905**, 409c (2013).
3. Y. Pandit *et al* (STAR Collaboration), these proceedings; Q. Wang *et al* (CMS Collaboration), these proceedings; A. Andreazza *et al* (ATLAS Collaboration), these proceedings.
4. B. Schenke, P. Tribedy and R. Venugopalan, *Phys. Rev. Lett.* **108**, 252301 (2012). and C. Gale *et al*, *Phys. Rev. Lett.* **110**, 012302 (2013).
5. M. Luzum, *J. Phys.* G **38**, 124026 (2011).
6. S. Borsanyi *et al* (Wuppertal-Budapest Collaboration), JHEP 1009, 073 (2010).
7. A. Bazavov *et al* (HotQCD Collaboration), *Phys. Rev.* D **85**, 054503 (2012).
8. K. Aamodt *et al* (ALICE Collaboration), *Phys. Rev. Lett.* **105**, 252301 (2010)
9. G. Aad *et al* (ATLAS Collaboration), *Phys. Lett.* B **710**, 363 (2012).
10. S. Chatrchyan *et al* (CMS Collaboration), *JHEP* **1108**, 141 (2011).
11. J.D. Bjorken *Phys. Rev.* D **27**, 140 (1983).
12. S. Chatrchyan *et al* (CMS Collaboration), *Phys. Rev. Lett.* **109**, 152303 (2012).
13. S.S Adler *et al* (PHENIX Collaboration), *Phys. Rev.* C **71**, 034908 (2005).
14. S. Borsanyi *et al* (Wuppertal-Budapest Collaboration), JHEP 1011, 073 (2010).
15. M.A. Lisa *et al Ann. Rev. Nucl. Part. Sci* **55**, 357 (2005).
16. K. Aamodt *et al* (ALICE Collaboration), *Phys. Lett.* B **696**, 328 (2011).
17. B. Abelev *et al* (ALICE Collaboration), *Phys. Rev. Lett.* **109**, 252301 (2012) and arXiv:1303.0737.
18. M. Petran, J. Letessier, V. Petracek and J. Rafelski, arXiv:1303.2098.
19. A. Mocsy, P. Petreczky and M. Strickland, *Int. J. Mod. Phys.* A **28**, 1340012 (2013).
20. N. Armesto *et al Phys. Rev.* C **86**, 064904 (2011).
21. B. Abelev *et al* (ALICE Collaboration), *Phys. Lett.* B **720**, 52 (2013).
22. S. Chatrchyan *et al* (CMS Collaboration), *Eur. Phys. J* C **72**, 1945 (2012).
23. Y. Mao *et al* (CMS Collaboration), these proceedings; G. Roland *et al* (CMS Collaboration), *Nucl. Phys.* B **904–905**, 43c (2013); C. Mironov *et al* (CMS Collaboration), *Nucl. Phys.* B **904–905**, 194c (2013).

Azimuthal Anisotropy from STAR Experiment

Yadav Pandit (for the STAR Collaboration)
Department of Physics, University of Illinois at Chicago, USA

We report the measurement of first (n = 1) and higher order(n = 2-5) harmonic coefficients (v_n) of the azimuthal anisotropy in the distribution of the particles produced in Au+Au collisions at $\sqrt{s_{NN}}$ =200 GeV and U+U collisions at $\sqrt{s_{NN}}$ =193 GeV, recorded with the STAR detector at RHIC. The differential measurement of (v_n) is presented as a function of transverse momentum (p_T) and centrality. We also present v_n measurement in the ultra-central collisions in U+U collisions. These data may provide strong constraints on the theoretical models of the initial condition in heavy ion collisions and the transport properties of the produced medium.

1 Introduction

The study of azimuthal anisotropy, based on Fourier coefficients, is widely recognized as an important tool to probe the hot, dense matter created in heavy ion collisions [1]. The distribution of particles with respect to the participant planes can be written as

$$\frac{dN}{d\Delta\phi} \propto 1 + v_1 \cos(\Delta\phi) + v_2 \cos 2(\Delta\phi) + v_3 \cos 3(\Delta\phi) + v_4 \cos 4(\Delta\phi) + .. \quad (1)$$

where v_n is the n^{th} order Fourier coefficient and $\Delta\phi$ is the difference between ϕ, the azimuthal angle of each particle, and Ψ_n, the generalized participant event planes at all orders for each event. The second harmonic also called elliptic flow v_2 has been extensively studied both experimentally and theoretically. Recently higher order harmonic also have gained considerable attention from theory [2] and experimental community [3]. These higher order harmonics can provide valuable information about the initial state of the colliding system [4] and also provide a natural explanation to the ridge phenomena in heavy ion collisions [5]. Measurement of these harmonics in different systems and collisions energy helps to further understand the heavy ion physics in general.

In uranium - uranium (U+U) collisions, there is the potential to produce more extreme conditions of excited matter at higher density and/or greater volume than is possible using spherical nuclei like lead or less deformed nuclei like gold at the same incident energy [6]. Uranium has quadrupole deformed shape. So U+U collisions may offer an opportunity to explore wider range of initial eccentricities. The collisions of special interest are the "ideal tip-tip" orientation

in which the long axes of both deformed nuclei are aligned with the beam axis at zero impact parameter, and the "ideal body-body" orientation in which the long axes are both perpendicular to the beam axis and parallel to each other at zero impact parameter. The "ideal tip-tip" and "ideal body-body" collision events allow to test the prediction of hydrodynamical models by varying the transverse particle density at spatial eccentricity similar to central Au+Au collisions.

2 The STAR experiment and Analysis Details

Data reported in this proceedings were collected in Au+Au collisions at $\sqrt{s_{NN}}$ = 200 GeV in the year 2004 with a minimum bias trigger and U+U collisions at $\sqrt{s_{NN}}$ = 193 GeV in the year 2012 with a minimum bias trigger and the ultra central events which were taken with a dedicated central trigger. The Time Projection Chamber (TPC) [7] is the primary tracking detector at STAR. Event used in this analysis are required to have the primary vertex along the beam direction to be less than 30 cm and transverse direction to be less than 2 cm from the center of the beam pipe. Centrality classes in U+U and Au+ Au collisions are defined using the number of charged particle tracks reconstructed in the TPC within pseudorapidity $|\eta| < 0.5$ and passing within 3 cm of interaction vertex. We used scalar product method as well as the

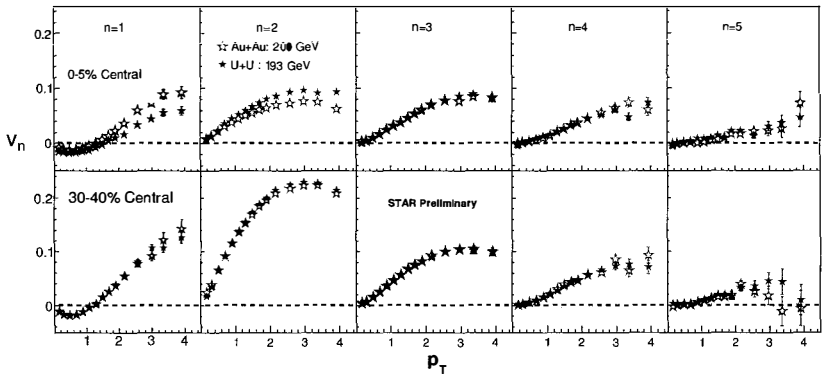

Figure 1: $v_n(p_T)$ measurement at 0-5% central in upper panels and 30-40% central collisions in the lower panels for U+U collisions at 193 GeV (solid stars) and for Au+Au collisions at 200 GeV(open stars).

event plane method to measure the signal [8]. In the scalar product method, the subevents were separated by η gap of 1.0 units between two subevents and at least 0.5 unit with the particle of interest and the subevent to which it is correlated . In the event plane method, the subevents were separated by η gap of 0.2 units. Larger pseudorapidity separation was desired but we are limited by the event plane resolution. To reduce the effects from high p_T particles in the estimation of the event plane, we used p_T weight only up to 2 GeV/c. The non-flow contribution from the jets/minijets is not known and might be a significant contributor to the systematic uncertainties especially at peripheral collisions.

3 Result and discussion

Results are presented with only statistical errors. In these studies, contribution from short range correlation such as Bose-Einstein correlations, coulomb interactions are studied using a pseudorapidity gap of at least 0.5 units in pseudorapidity between the event vector and the particle of interest using scalar product method. Results from both methods, scalar product with larger psuedorapidity gap and event plane method with smaller pseudorapidity gap are consistent

with each other, which suggests that non-flow contribution from short range correlations are small.

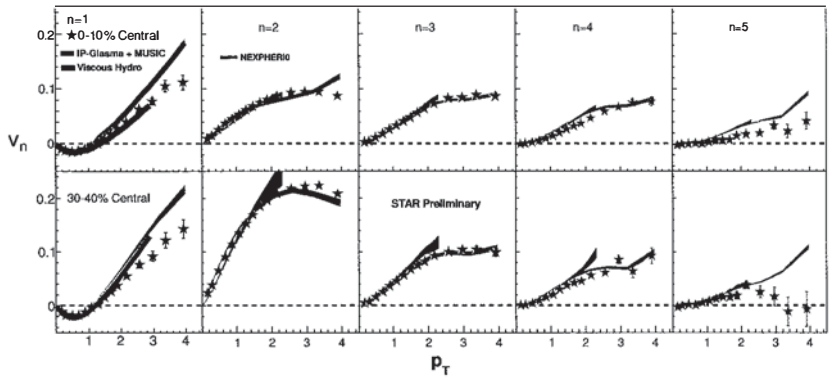

Figure 2: v_n measurement at 0-10% central in upper panels and mid central (30-40%) collisions in the lower panels as a function of p_T for Au+Au collisions at 200 GeV compared with various model calculations

The v_n of all charged hadrons, for n = 1, 2, 3, 4 and 5 as a function of p_T at various centralities, as shown in Fig. 1. The data for 0–5% centrality are shown in the upper panels, and for intermediate centrality (30–40%) in the lower panels. All v_n measurements show an increasing trend as a function of p_T. Except for v_2, we observe very weak centrality dependence. Also shown are the same measurement from Au+Au collisions at 200 GeV for the comparisons. We observe the difference in v_n for $n = 1$ and $n = 2$ at 0-5% central between U+U and Au+Au collisions. This may hint to initial overlap geometry difference in the central collisions between two systems Au+Au and U+U collisions. The difference diminishes in higher harmonics and more peripheral collisions.

Fig. 2 shows the flow harmonics v_n for $n = 1$ to $n = 5$ as a function of p_T in 200 GeV Au+Au collisions compared to the model predictions. In the ideal hydrodynamic NeXSpheRIO calculation [9](shown in black line), the fluctuating initial condition is introduced from MC event generator Nexus. The IP_Glasma + Music [10] viscous hydrodynamic calculation(shown in red line) uses IP−Glasma initial condition and low viscosity setting of η/s =0.12. For the viscous

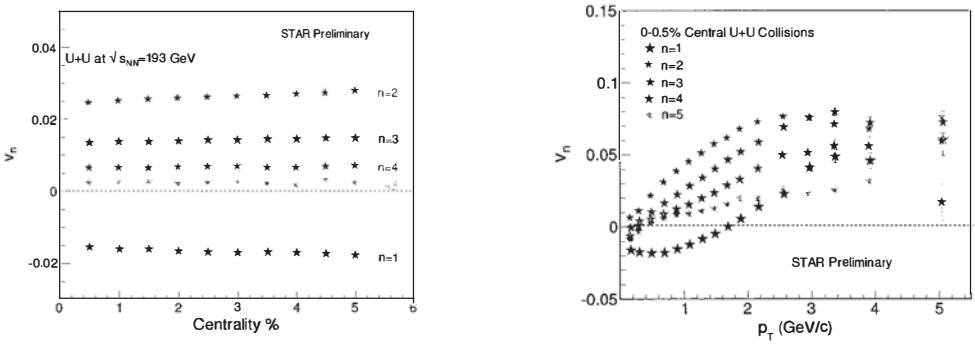

Figure 3: v_n as a function of centrality at 0-5% central collisions on left and v_n as a function of p_T at ultra central(0-0.5%) collisions on right

hydrodynamic calculation[11](shown in blue line), they use a smooth density profile with an added deformation to reproduce the data with low viscosity setting of η/s =0.16. For lower harmonics and central collisions, the models with low viscosity setting and fluctuating initial condition or added deformation to the smooth initial density profile describe the data well however the model curve overshoot in the higher harmonics and peripheral collisions at high p_T

We also report measurement of v_n for 0-5% central U+U collisions taken with a dedicated central trigger. We subdivide 0-5% central bin into 10 smaller centrality bins upto most central 0-0.5% centrality. In Fig. 3 (a), v_n as a function of centrality for ultra central collisions is shown. Other than second harmonic coefficient, the v_n do not change in this centrality range. We observe small change for v_2 since it still has some contribution from initial overlap geometry. This observation suggests that there is still a small contribution from body-body collisions. In Fig. 3 (b), the v_1 signal along with v_2, v_3, v_4 and v_5 a function of transverse momentum up to p_T $\sim$ 5 GeV/c is shown for ultra central (0-0.5%) collisions. The most central 0-0.5% collisions is expected to have dominant contribution from tip-tip collisions. In these most central events we find that higher harmonics are also significant in magnitude compared with second harmonics in the intermediate transverse momentum. Contributions from higher harmonics should not be overlooked interpreting dihadrom correlation data at intermediate transverse momentum. These higher harmonics may offer natural explanation to the novel ridge phenomena in heavy ion collisions[4]. Model comparisons with these new data may help us to better understand the medium properties.

4 Summary

We report the first measurement of azimuthal anisotropy v_n for n=1-5 as a function of transverse momentum p_T and centrality in U+U collisions at $\sqrt{s_{NN}}$ =193 GeV, recorded with the STAR detector at RHIC. Centrality dependence is weak for harmonics other than second harmonics. For higher harmonics and mid central collisions, v_n(U+U) is similar to v_n(Au+Au), the difference appears at central collisions for v_1 and v_2. At intermediate p_T range 3-5 GeV/c, v_n's are comparable to the v_2 signal in ultra central collisions. Model calculation specially at ultra central collisions may be useful to constrain the initial condition and transport coefficient of the medium produced in heavy ion collisions.

References

1. A. M. Poskanzer and S. A. Voloshin, Phys. Rev. C **58**, 1671 (1998).
2. A. P. Mishra *et al.*, Phys. Rev. C**77**, 064902 (2008)
3. Y. Pandit for the STAR Collaboration, arXiv:1211.7162 [nucl-ex]. K. Aamodt et al. (ALICE Collaboration), Phys. Rev. Lett. **107**, 032301 (2011)
4. P. Sorensen, B. Bolliet, A. Mocsy, Y. Pandit and N. Pruthi, Phys. Lett. B **705** 71 (2011). B. Alver and G. Roland, Phys. Rev. C **81**, 054905 (2010).
5. D. Teaney and L. Yan, Phys. Rev. C**83**, 064904 (2011).
6. C. Nepali *et al.*, Phys. Rev. C**73**, 2006.
7. M. Anderson *et al.*, Nucl. Instr. Meth. A **499**, 659 (2003).
8. Y. Pandit for the STAR Collaboration, arXiv:1305.0173[nucl-ex]
9. Retinskaya *et al.*, Phys. Rev. Lett. **109**, 202302(2012)
10. B. Schenke *et al.*, Phys. Rev. Lett. **110**, 012302 (2013).
11. E. Retinskaya *et al.*, Phys. Rev. Lett. **108**, 252302 (2012), M. Luzum and J. Y. Ollitrault, Phys. Rev. Lett. **106**, 102301 (2011).

SEARCH FOR CHIRAL MAGNETIC EFFECTS IN AU+AU COLLISIONS AT STAR

H. W. KE[1,2] for the STAR Collaboration
[1] *Central China Normal University, Wuhan 430079, China*
[2] *Brookhaven National Laboratory, Upton, New York 11973, USA*

We report the STAR's measurements of the electric charge separation with respect to the reaction plane in Au + Au collisions at $\sqrt{s_{NN}} = 200, 62.4, 39, 27, 19.6, 11.5$ and 7.7 GeV. It is believed to be a probe to the possible Local Parity Violation in heavy ion collisions. We also report the measurements of azimuthal anisotropy, v_2, of charged pions as a function of event-by-event charge asymmetry, $A_{\rm ch}$. We found that the v_2 of $\pi^-(\pi^+)$ linearly increases (decreases) with the increasing charge asymmetry. The slope parameter (r) of the $v_2(A_{\rm ch})$ between π^- and π^+ shows similar centrality dependency to calculations based on the Chiral Magnetic Wave and it only shows weak energy dependency at $\sqrt{s_{NN}} = 200, 62.4, 39, 27, 19.6$ GeV.

1 Introduction

In relativistic heavy ion collisions a hot and dense quark-gluon matter may be created in the collision region, where the chiral symmetry may be restored. On the other hand, the spectators in mid-central collisions can create extremely strong magnetic field in the center of the collision region. The peak intensity can reach up to $eB_y \approx m_\pi^2$ [1]. Two phenomena Chiral Magnetic Effect (CME) [1] and Chiral Separation Effect (CSE) [2,3] characterize the interplay between the quark-gluon matter and the magnetic field.

The CME is the interplay between a non-zero axial chemical potential and the magnetic filed, which separates electric charge along the magnetic field. Since the magnetic field generated in heavy ion collisions is perpendicular to the reaction plane, electric charge separation with respect to the reaction plane beyond the statistical fluctuation is expected to be observed due to CME. STAR and PHENIX experiments at RHIC and ALICE experiment at LHC have measured the charge separation in Au + Au [4,5,6,7] and Pb + Pb [8] collisions and provide possible evidences for the possible CME. The CSE refers to the chiral charge separation alone the magnetic field due to the interplay between a non-zero vector chemical potential and the magnetic field.

The CME and CSE can actually induce each other and make a collective excitation called Chiral Magnetic Wave (CMW) [9], which is a density wave of electric charge and topological charge . The CMW in heavy ion collisions induces an electric quadrupole moment in the fireball created, which acquires more negative charge near the equator of the fireball and more positive charge near the two poles. This configuration can be reflected in the azimuthal anisotropy, v_2, of final state charged

particles, in particular by charged pions as argued by theorists [10]. Based on the idea of CMW, there is another charge asymmetry dependent part of the v_2 on top of the baseline $v_2(\pi^{\pm})$.

$$v_2(\pi^{\pm}) = v_2^{\text{base}}(\pi^{\pm}) \mp \left(\frac{q_e}{\bar{\rho}_e}\right) A_{\text{ch}}, \tag{1}$$

where $A_{\text{ch}} = (N_+ - N_-)/(N_+ + N_-)$ is the event-by-event charge asymmetry, q_e reflects the electric quadrupole and $\bar{\rho}_e$ is the charge density. The v_2 difference between π^+ and π^- caused by the CMW can be written as

$$\Delta v_2^{\text{CMW}} = v_2(\pi^-) - v_2(\pi^+) \approx r A_{\text{ch}}. \tag{2}$$

The slope parameter $r = 2(q_e/\bar{\rho}_e)$ will be our interested observable, which represents the electric quadrupole momentum induced by CMW.

In these proceedings, we will present the charge separation with respect to the reaction plane measured by STAR in Sec. 2. Charge asymmetry dependency of charged pions' v_2 will be presented in Sec. 3.

2 Charge Separation with respect to the Reaction Plane

If there are small bubbles, where the parity is locally violated (LPV), created in heavy ion collisions, the Chiral Magnetic Effect will cause electric charge separation alone the magnetic field. This will lead the same charge emission tend to stay in the same side of the reaction plane. A three-particle correlator is proposed to measure such asymmetry [11],

$$\gamma = \langle \cos(\phi_\alpha + \phi_\beta - 2\psi_{\text{RP}}) \rangle \tag{3}$$

where $\alpha, \beta = +, -$ represent the charge sign of two particles involve in the correlation and ψ_{RP} is the azimuthal angle of the reaction plane. In STAR, both of the same sign correlator $\gamma_{\text{SS}}(\alpha = \beta)$ and

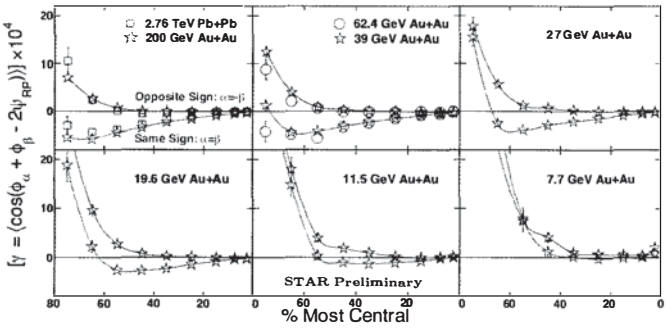

Figure 1: The centrality dependency of three-particle correlators, γ_{SS} and γ_{OS}, measured by STAR in Au + Au collisions from $\sqrt{s_{NN}} = 200$ GeV to 7.7 GeV. The ALICE measurement is showing for comparison [8].

the opposite sign correlator $\gamma_{\text{OS}}(\alpha = -\beta)$ have been measured in minimum bias triggered Au + Au collisions at all STAR energies. The data samples used include 57 M events at $\sqrt{s_{NN}} = 200$ GeV taken in year 2007, 7 M at 62.4 GeV (2005), 100 M at 39 GeV (2010), 40 M at 27 GeV (2011), 20 M at 19.6 GeV (2011), 10 M at 11.5 GeV (2010) and 4 M at 7.7 GeV (2010) [12]. The results are shown in Fig. 1. The ALICE measurement in Pb + Pb collisions at 2.76 TeV is also shown in the same figure for comparison [8].

The main background for such measurements include the radial flow, the charge conservation and the influence of the statistical fluctuations. Those sources of background are believed to be same for γ_{SS} and γ_{OS} [12]. Therefore, the difference between the two correlator $\gamma_{\text{OS}} - \gamma_{\text{SS}}$ should be a better signal, which is showing in Fig. 2. The signal does not show strong energy dependency from 2.76 TeV to 11.5 GeV and it seems to disappear at 7.7 GeV [12].

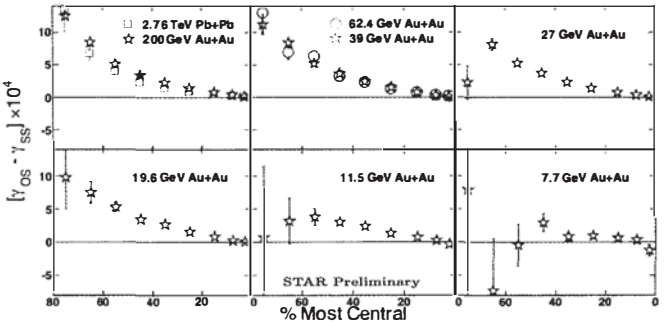

Figure 2: The centrality dependency of the difference between the two correlators $\gamma_{OS} - \gamma_{SS}$ in Au + Au collisions from $\sqrt{s_{NN}}$ = 200 GeV to 7.7 GeV. The ALICE measurement is showing for comparison [8].

3 Charge Asymmetry Dependency of Pion Azimuthal Anisotropy

To study the charge asymmetry dependency of the v_2 of charged pions, more than 200 M Au + Au minimum bias events taken in year 2010 are used. Other data samples include 60 M at 62.4 GeV (2010), 100 M at 39 M (2010), 40 M at 27 GeV (2011) and 20 M at 19.6 GeV (2011). To select charged pions, charged particles are chosen if its ionization energy loss in STAR TPC stays within 2σ from the expected value of pions. Meanwhile, the selected pions are also required to have a distance of the closest approach (DCA) to primary vertex less than 1 cm and stays in low transverse momentum range, $0.15 < p_T < 0.5$ GeV/c. To measure the event-by-event charge asymmetry $A_{\rm ch}$, all charged particles within DCA < 1 cm are used except the protons and anti-protons with $p_T < 0.4$ GeV/c. Low p_T (anti-)protons are excluded to avoid the influence of beam pipe protons. The measured $A_{\rm ch}$ are corrected subject to the limited tracking efficiency via HIJING model and GEANT simulation. The left panel of Fig. 3 shows the v_2 measurements for π^+ and

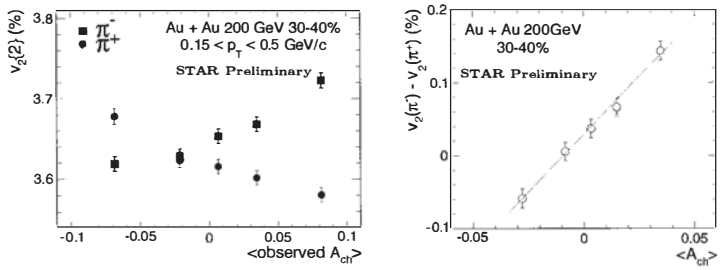

Figure 3: Left: Integrated v_2 measurement over $0.15 < p_T < 0.5$ GeV/c for π^+ and π^- as a function of measured charge asymmetry in Au + Au collisions at $\sqrt{s_{NN}}$ = 200 GeV, 30-40% centrality. Right: the v_2 difference in the same centrality as a function of corrected charge asymmetry.

π^- as a function of measured charge asymmetry in Au + Au collisions at $\sqrt{s_{NN}}$ = 200 GeV, 30-40% centrality [13]. The right panel shows the v_2 difference between π^+ and π^- as a function of corrected charge asymmetry. We observed that the v_2 of $\pi^+(\pi^-)$ linearly decreases (increases) with the increasing charge asymmetry in 30-40% centrality. The slope parameter of $\Delta v_2(A_{\rm ch})$ is extracted in all centralities and all energies under study [12]. The results are showing in Fig. 4. The behavior of $v_2^{\pi^\pm}(A_{\rm ch})$ and the rise and fall feature of the slope parameter as a function of centrality are qualitatively consistent with calculation based on CMW. However, it is not clear why the slope

parameter as a function of centrality only shows weak energy dependency from $\sqrt{s_{NN}} = 200$ GeV to 27 GeV.

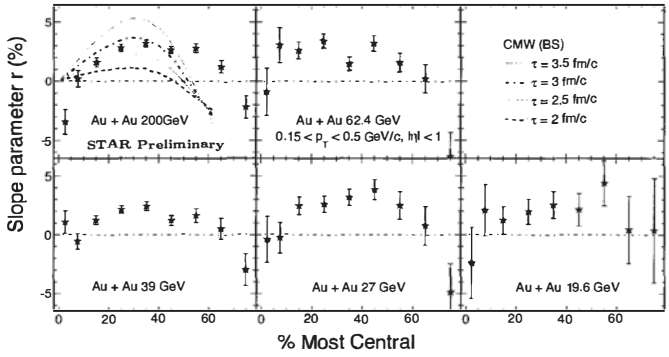

Figure 4: Centrality dependency of the slope parameter r measured in Au + Au collisions from $\sqrt{s_{NN}} = 200$ GeV to 19.6 GeV. A set of theoretical calculation based on CMW is showing for comparison.

4 Summary

The three-particle correlation have been measured in STAR, which may provide the evidence for the Local Parity Violation and Chiral Magnetic Effect. It turns out that the signal almost unchanged from 2.76 TeV to 11.5 GeV and seems to disappear in 7.7 GeV.

We also measured the charge asymmetry dependency of the charged pion v_2 from 200 GeV to 19.6 GeV. The observed $v_2^{\pi^{\pm}}(A_{\rm ch})$ and its difference between π^+ and π^- qualitatively consistent with the expectation of Chiral Magnetic Wave model. But the reason for the weak energy dependency of the slope parameter as a function of centrality is not quite clear yet.

References

1. D. E. Kharzeev, L. D. McLerran, and H. J. Warringa, *Nuclear Physics* A **803**, 227 (2008).
2. D. T. Son and A. R. Zhitnitsky, *Phys. Rev. D* **70**, 074018 (2004).
3. M. A. Metlitski and A. R. Zhitnitsky, *Phys. Rev. D* **72**, 045011 (2005).
4. STAR Collaboration, B. I. Abelev *et al.*, *Phys. Rev. Lett.* **103**, 251601 (2009).
5. STAR Collaboration, B. I. Abelev *et al.*, *Phys. Rev. C* **81**, 054908 (2010).
6. N. N. Ajitanand, S. Esumi, R. A. Lacey [PHENIX Collaboration], in Proc. of the RBRC Workshops, vol.96, 2010: "P- and CP-odd effects in hot and dense matter"
7. N. N. Ajitanand, R. A. Lacey, A. Taranenko, and J. M. Alexander, *Phys. Rev. C* **83**, 011901 (2011).
8. ALICE Collaboration, B. Abelev *et al.*, *Phys. Rev. Lett.* **110**, 012301 (2013).
9. D. Kharzeev and H.-U. Yee, *Physical Review D* **83**, 085007 (2011).
10. Y. Burnier, D. E. Kharzeev, J. Liao, and H.-U. Yee, *Phys. Rev. Lett.* **107**, 052303 (2011).
11. S. A. Voloshin, *Phys. Rev. C* **70**, 057901 (2004).
12. G. Wang for the STAR Collaboration, arXiv:1210.5498v2 [nucl-ex]
13. H. W. Ke for the STAR Collaboration, *Journal of Physics: Conference Series* **389**, 012035 (2012).

Propagation of nonlinear gauge theory and corresponding phenomenology in deconfined strong interaction matter

LI Shi-Yuan
School of Physics, Shandong University, Jinan 250100, PR China

We summarize the shock wave propagation of non-linear gauge theories, and point out that the results are the same for Abelian and Non-Abelian gauge theories. Then we argue that the deconfied strong interaction matter can be employed to study the Non-Abelian non-linear propagation. We discuss the examples for various external strong fields and investigate the way to measure the predicted polarizations

Non-linear field theory models have attracted a lot of attentions. Soliton is one example. The other interesting topic is shock wave propagation. There are yet a lot of questions to be addressed. Assuming that the classical nonlinear Lagrangian is real, i.e., Hermitian after quantizied. In the Heisenberg picture, the solution of the non-linear equation of motion of the field operators do not respect the superposition principle, and hence the Green functions. On the other hand, since the Hamiltonian is Hermitian, it still is possible to construct the linear Hilbert space of the states with the eigenstates of the Hamiltonian as bases. How to relate the field operators and the states from the Hilbert space is a complex question to address the 'wave (field) and particle (state) correspondence'. In this paper we only encounter the simple example that the field propagation select the polarization states.

A feasible framework to deal with the shock wave propagation of the non-linear theory is the Hadamard method [1]. The main point is to calculate the discontinuity in space-time to study the wave vector (dispersion relation) as well as the polarization. This method has the advantage that one need not to linearize the equation of motion, so that can be applied to the case that the propagation can not be treated as perturbation of the more strong slowly-varying background/external field. From this method, it is also very straightforward to see that the formulations of the propagation is the same for Abelian as well as non-Abelian gauge theory. The key point is that the discontinuity is only non-zero for second-order derivative of the vector gauge field.

In fact, a thorough investigation for the most general non-linear Lagrangian for the Abelian case is also needed. I.e., to write down the most generally framework to see how to set the configurations to get the specified propagation phenomenon. Here we first list the frameworks and results. We start from the general Lagrangian density $L = L(F, G)$, where F and G are the two local gauge invariants defined in terms of the tensor field $F_{\mu\nu} = \frac{i}{g}[D_\mu, D_\nu]$, and its dual

$$F*_{\alpha\beta} = \frac{1}{2}\eta_{\alpha\beta}{}^{\sigma\tau}F_{\sigma\tau}, \tag{1}$$

as

$$F = F^{\mu\nu}F_{\mu\nu} \tag{2}$$

$$G = F^{\mu\nu}F*_{\mu\nu}. \tag{3}$$

In terms of the electric $\vec{E}$ and magnetic $\vec{B}$ field strengths we have $F = -2(E^2 - B^2)$ and $G = -4\vec{E} \cdot \vec{B}$. Here the covariant derivative is $D_\mu = \partial_\mu - igA_\mu$, with g the coupling constant. In the above formulations, if applied to the non-Abelian case, the vector/tensor field such as $A_\mu, F_{\mu\nu}$, as well as the components $\vec{E}$ and $\vec{B}$ are understood as also a N-dimensional vector of the inner joint-representation space. The contraction of the field tensor are also done for the inner space. However, for the Non-Abelian case, there could be more invariants than F and G [2]. Here we will not discuss such a complexity, for our following example does not depend on all the other non-Abelian invariants. The field equation can be obtained from the least action principle. In addition, $F_{\mu\nu}$ satisfies the Bianchi identity $F\,{}^*{}^{\mu\nu}{}_{,\nu} = 0$.

The method of field discontinuities can be briefly stated as follows [1,3]. Consider a differentiable inextendible oriented borderless hyper-surface Σ, defined locally by $\phi(x^\mu) = 0$, where ϕ is a real differentiable scalar field which locally is a function of the spacetime coordinates $x^\mu = (t, \vec{x})$. Let U^+ be the spacetime points whose coordinates satisfy $\phi(x^\mu) > 0$, and similarly U^- be such that $\phi(x^\mu) < 0$. Let P be any given point of Σ. For each sufficiently small $r > 0$, let $V_r(P)$ be a neighborhood of P which consists of the spacetime points Q whose Euclidean distance from P is $[(t_Q - t_P)^2 + ||\vec{x}_Q - \vec{x}_P||^2]^{(1/2)}$ smaller than r. Let $P^+ \in U^+ \cap V_r(P)$ and $P^- \in U^- \cap V_r(P)$ be any two neighbor points from P arbitrarily chosen at opposite sides of Σ. Let f be any given tensor field defined at $V_r(P)$. The Hadamard discontinuity at P of f across Σ is defined as

$$[f]_\Sigma(P) \doteq \lim_{r \to 0^+} [f(P^+) - f(P^-)]. \tag{4}$$

Suppose f such that $[f]_\Sigma = 0$ for each $P \in \Sigma$. Following Hadamard [1], we have $[f_{,\lambda}]_\Sigma(P) = k_\lambda \bar{f}(P)$, where $k_\lambda = \phi_{,\lambda}|_P$ is the normal vector to Σ at P and $\bar{f}$ is a tensor field defined at Σ with the same rank and the same algebraic symmetries as those of f.

We assume the tensor field $F_{\mu\nu}$ to be smooth in each $U^\pm$, but merely continuous at Σ (that is to say, the $F_{\mu\nu}$ are continuous functions at Σ but their derivatives may present discontinuities at Σ). The Hadamard discontinuities at Σ of the equation of motion and the Bianchi identity lead to [3]

$$f_{\beta\lambda}k^\lambda + \frac{2}{L_F} N_\beta{}^{\mu\nu\rho} f_{\nu\rho} k_\mu = 0 \tag{5}$$

and

$$f_{\alpha\beta} = \epsilon_\alpha k_\beta - \epsilon_\beta k_\alpha, \tag{6}$$

where the quantities $f_{\alpha\beta}$ are related to the derivatives of $F_{\alpha\beta}$ on Σ by $[F_{\alpha\beta,\lambda}]_\Sigma = f_{\alpha\beta}k_\lambda$ and ϵ_μ is the polarization vector $[A_{\mu,\alpha\beta}]_\Sigma = e_\mu k_\alpha k_\beta$. Here

$$N^{\mu\nu\alpha\beta} \doteq L_{FF} F^{\mu\nu} F^{\alpha\beta} + L_{GG} F\,{}^*{}^{\mu\nu}\, F\,{}^*{}^{\alpha\beta} + L_{FG}\left(F^{\mu\nu} F\,{}^*{}^{\alpha\beta} + F\,{}^*{}^{\mu\nu}\, F^{\alpha\beta}\right). \tag{7}$$

Use is being made here of the notation $L_{X^1X^2\ldots X^n} = \partial^n L / \partial X^1 \partial X^2 \cdots \partial X^n$ previously introduced [3], where each X^i is one of the two invariants F or G upon which the Lagrangian L arbitrarily depends.

We set $k_\lambda = \omega V_\lambda + q_\lambda$ as the wave 4-vector, where $V_\lambda = \delta^0_\lambda$ is the 4-velocity of the observer which decomposes $F^{\mu\nu}$ into 'electric' and 'magnetic fields'. The components of this 4-vector k_λ are thus the frequency ω and the wave vector $\vec{q} = q\hat{q}$. Taking together Eqs. (5) and (6), we obtain the general eigenvalue equation [4,3]

$$Z^\mu{}_\nu \epsilon^\nu = 0, \tag{8}$$

where

$$Z^\mu{}_\nu \doteq k^2 \delta^\mu{}_\nu + \frac{4}{L_F} N^{\mu\alpha}{}_{\nu\beta} k_\alpha k^\beta. \tag{9}$$

Nontrivial solutions of Eq. (8) can be found only if $\det |\, Z_{\mu\nu} \,| = 0$, the well known generalized Fresnel equation, and yields

$$\alpha(k^2)^2 + \beta f^2 k^2 + \gamma (f^2)^2 = 0, \tag{10}$$

where $f^2 = F^{\alpha\mu}F_\alpha{}^\nu k_\mu k_\nu$, and

$$\alpha = L_F^2 + 2L_F(GL_{FG} - FL_{GG}) - (L_{FF}L_{GG} - L_{FG}^2)G^2, \tag{11}$$

$$\beta = 4L_F(L_{FF} + L_{GG}) - 8(L_{FF}L_{GG} - L_{FG}^2)F, \tag{12}$$

$$\gamma = 16(L_{FF}L_{GG} - L_{FG}^2). \tag{13}$$

The phase velocity $v \doteq \omega/q$ of the waves can be obtained from a fourth order equation, we could find up to four solutions for the phase velocity, in the same wave direction.

In what follows we study a particular model. Such a model appears in different contexts in the literature, for instance as the effective Lagrangian density for quantum electrodynamics.

$$L_{NL} = -\frac{1}{4}b_0 F \log\frac{F}{\lambda^2}, \tag{14}$$

where b_0 and λ are constants. Particularly λ can be chosen in order to split the above model in a Maxwellian part plus a nonlinear contribution. When the F is construted by the $SU(3)$ gauge field, this can be a good effective theory of QCD (see, e.g., [2]).

For a most interesting example, let us assume constant external electric $\vec{E} = E\hat{x}$ and magnetic $\vec{B} = B\hat{y}$ fields, much larger than their wave counterparts. The calculations [5] show there could be trirefregence. If in a gluon plasma, such external colour field configuration can be set, we can try to observe the similar novel behaviour of gluons. However, such an external field configuration is very difficult to prepare in QCD case. Since now what can be studied is only the bulk of hot matter produced in heavy ion collisions. In such an collision, as the lowest order approximation we adopt the following symmentric average

$$\overline{E_i} = 0, \qquad \overline{H_i} = 0, \qquad \overline{E_i\,H_j - H_i\,E_j} = 0, \tag{15}$$

$$\overline{E_i\,E_j} = -\frac{1}{3}E^2\eta_{ij}, \tag{16}$$

$$\overline{H_i\,H_j} = -\frac{1}{3}H^2\eta_{ij}, \tag{17}$$

We find that it behaves as a polarizer [6], since a physical propagation can only be the 'ordinary ray', with the specified polarization determined by the colour fields.

In the hadronization process, the polarization can be tranferred into hadrons. Λ is a good example. From the SU(6) quark model, one finds that in Λ the (ud) quark must be a scalar, hence the spin of the s quark is just the spin of the Λ. When the gluon splits into quark pair, because of helicity conservation, the specified helicity state of the gluon determines the helicity states of the quark and antiquark, e.g., $|1,1>\rightarrow |\frac{1}{2}\frac{1}{2}>$. As mentioned above, only the ordinary ray of the gluon field can propagate, and the polarization vector can be calculated via Eq. (8) when the direction and the colour field are definite so that $Z^{\mu\nu}$ in Eq. (8) is determined. Since any polarization vector can be expanded by the two helicity state of the gluon, then we easily deduce that the spin state of the quark pair produced from the gluon can be determined. This means that a quark which comes from the gluon moves in a specific direction must be in a definite spin state. If the quark is an s quark and combine a diquark to hadronize as a Λ, its polarization is definite.

However, in each collision, for different direction, the spin state is different. Further more, for different collision, the colour fields are different. For an average among all events and all particles the results vanishing. To construct SO(3) scalar, one experimental observable for the polarization correlation has been suggested [6]. This can be extracted from the ideal case of two Λ particles with the same polarization $\vec{P}$, with $P = |\vec{P}|$ representing the polarization rate. The conventional way to measure $\vec{P}$ of a single Λ is by measuring the direction vector (denoted as $\hat{p}$) of the momenta of the daughter particles, e.g., proton or pion from the Λ decay, at the rest

frame of Λ. Then the angular distribution,

$$\frac{dN}{dcos\theta} \sim 1 + \alpha\hat{p} \cdot \vec{P} = 1 + \alpha P cos\theta, \tag{18}$$

can give the information on the polarization. Here α is the hyperon decay parameter. From this equation we see that if the direction of $\vec{P}$ is random, the average of all $\Lambda's$ gives zero, then P is not able to be measured. However, for the two $\Lambda's$ with the same polarization, in the rest frame of *each* Λ, *respectively*, the direction vectors $\hat{p}_1$ and $\hat{p}_2$ can be measured. Then we calculate the expectation value $< \hat{p}_1 \cdot \hat{p}_2 >$, which results in

$$P = 3\sqrt{< \hat{p}_1 \cdot \hat{p}_2 >}/\alpha. \tag{19}$$

In reality, we can not expect in an event, there could be easily find two Λ move exactly parallel. So that we can only try to find two particle with the nearest moving directions. In such a case, employing the formulation right hand side of Eq. (19), we can not get the exact polarization value but an approximation P'. However, imagining the case of a heavy ion collision with the center of mass energy infinite, the multiplicity is also infinite, so that we can have $P' \to P$.

At RHIC and LHC, the center of mass energy is not infinite but very high, we will find the P' is not a bad approximation. Fig. 1 demonstrates this fact. This shows the results of RHIC energy. To mimic the true data, we employ a generator developed by the Shandong University group. Here we did not show the comparing of the kinematic details of the model and real data, but only requiring the averaged multiplicity and multiplicity distribution of this model consistent with the data.

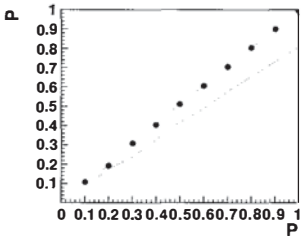

In the concrete calculations, we only employ the pairs of $\Lambda's$ with the smallest relative angles which are all smaller than $\frac{\pi}{4}$. We find that such a restriction will keep enough statistics. To have enough large multiplicity, We only investigate the most central 5% collision. This also guarantees that the asymmetries are largely reduced.

Acknowledgments

The author thanks the collaborations of V.A. De Lorenci, R. Klippert, J. P. Pereira and LI Shu-Qing. This work is partially supported by NSFC and SF of Shandong Province.

1. J. Hadamard, in *Leçons sur la propagation des ondes et les équations de l'hydrodynamique* (Ed. Hermann, Paris, 1903); G. Boillat, J. Math. Phys. **11**, 941 (1970); A. Papapetrou, in *Lectures on General Relativity* (Dordrecht, Holland,1974).
2. H. Pagels and E. Tomboulis, Nucl. Phys. B **143**, 485 (1978).
3. V. A. De Lorenci, R. Klippert, M. Novello and J. M. Salim, Phys. Lett. B **482**, 134 (2000).
4. Z. Bialynicka-Birula and I. Bialynicki-Birula, Phys. Rev. D **2**, 2341 (1970).
5. V.A. De Lorenci et al., to be published.
6. V. A. De Lorenci and S. Y. Li, Phys. Rev. D **78**, 034004 (2008).

FLOW PHENOMENA IN CMS

Quan Wang for the CMS Collaboration
Department of Physics & Astronomy,
Lawrence, KS 66045-7582, USA

Measurements by the CMS experiment of azimuthal angle correlations of charged hadrons in $\sqrt{s_{NN}}$ = 2.76 TeV Pb+Pb collisions are presented. The second-order elliptic flow harmonic v_2 is shown as a function of transverse momentum (p_T) and centrality in a broad kinematic range. Various techniques are employed to extract the signal strength of the harmonics: the event-plane method, cumulant, Lee-Yang Zeros and di-hadron correlation methods. Higher-order harmonic results, v_3 from the event-plane method and v_3, v_4, v_5 and v_6 from di-hadron correlation methods are also shown. The results indicate that higher-order, odd harmonics are mainly dominated by initial-state fluctuations. Neutral particle π^0 v_2 results and high-p_T particle (up to 60 GeV/c) v_2 results are also shown. The di-hadron correlation results of v_2 and v_3 in $\sqrt{s_{NN}}$ = 5.02 TeV p+Pb collisions are presented and compared to p+p results.

1 Introduction

In non-central, heavy-ion collisions, the initial nuclear overlap region is spatially anisotropic and is usually characterized with an "almond-like" shape. The initial spatial anisotropy leads to a final-state momentum azimuthal anisotropy resulting from the pressure gradients developed in collision. The azimuthal anisotropy, characterized by Fourier expansion coefficients, is an important feature of the hot, dense medium produced in heavy-ion collisions. The distribution of charged particles with respect to the participant plane can be written as,

$$\frac{\mathrm{d}N}{\mathrm{d}\Delta\phi} \sim 1 + 2v_2 \cos 2(\phi - \psi_2) + 2v_3 \cos 3(\phi - \psi_3) + \cdots \quad (1)$$

where v_n is the n-th order Fourier coefficient, and ϕ is the azimuthal angle of each particle. ψ_n is the n-th harmonic participant plane of each event. The second harmonic v_2 is often called elliptic flow, which is one of the most important measurements providing information of the strongly couple quark-gluon plasma (sQGP) [1]. The third harmonic coefficient v_3 is referred to as triangular flow, which is the largest coefficient next to v_2. Higher order terms, v_n where $n > 2$, can provide information of the initial-state fluctuations, whose magnitude can be sizable compare to v_2. [2]

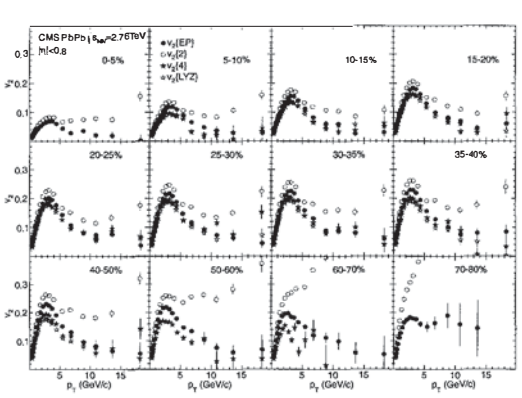

Figure 1: Elliptic flow of Pb+Pb at 2.76 TeV based on four methods.

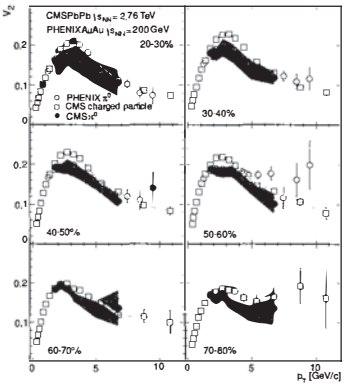

Figure 2: π^0 elliptic flow compared to lower energy PHENIX [8] and CMS charged particle results [3].

2 Data Analysis and Results

Figure 1 shows the v_2 differential results, obtained from Pb+Pb collision at a center-of-mass energy of $\sqrt{s_{NN}} = 2.76$ TeV, for the event-plane [4], two- and four-particle cumulant [5] and Lee-Yang Zeros [6] methods with $0.3 < p_T < 20$ GeV/c and for twelve centrality classes [3]. The differences between methods are understood by their different sensitivities to non-flow and fluctuation effects. Two-particle cumulant method is very sensitive to non-flow, especially at high p_T. The four-particle cumulant method and Lee-Yang Zeros method are less sensitive to non-flow due to the nature of multi-particle correlations. There is no pseudo-rapidity gap required in two- and four-particle cumulant methods, while a gap of three units of pseudo-rapidity is applied in the event-plane method between the particles used for the flow analysis and particles used for the event-plane reconstruction. Hence the event-plane method can largely suppress non-flow.

The CMS π^0 elliptic anisotropy for Pb+Pb 2.76 TeV results [7] are shown in Fig. 2, and compared to CMS charged particle event-plane v_2 [3] and PHENIX π^0 results for Au+Au at 200 GeV [8]. The CMS π^0 results are comparable to the lower energy PHENIX results, while lower than the CMS charged particle results. This is consistent with the higher elliptic anisotropy seen for baryons as previously found at RHIC.

For higher p_T particles, the lenticular-shape of the overlap region in heavy-on collisions can lead to azimuthal asymmetry as a result of the path length dependence of parton energy loss. Figure 3 shows the v_2 coefficients for six centrality classes [9] with an extended p_T range up to 60 GeV/c obtained from data selected by a dedicated high-p_T trigger in the 2011 Pb+Pb run, along with previous ATLAS [10] and CMS results from 2010 data [3]. The v_2 coefficient results remain finite up to at least $p_T = 40$ GeV/c, and become consistent with zero above that for mid-central collisions (above 30%). These results shed light on the path length dependent energy loss of high p_T partons in the medium.

In Fig. 4 the integrated v_2 values [9] for different p_T ranges are shown as a function of the number of participant nucleons (N_{part}) for two different pseudo rapidity ranges. These results demonstrate that the higher p_T asymmetries are influenced by the initial-state geometry. Below 4 GeV/c, the v_2 values are consistent with the hydrodynamic flow behavior of a hot dense medium. Above 14 GeV/c, the flow component is expected to be negligible. For these higher p_T ranges, the increase in v_2 as the collisions become more peripheral (decreasing N_{part}) reflects the corresponding increase in the eccentricity of the lenticular overlap region as N_{part} decreases.

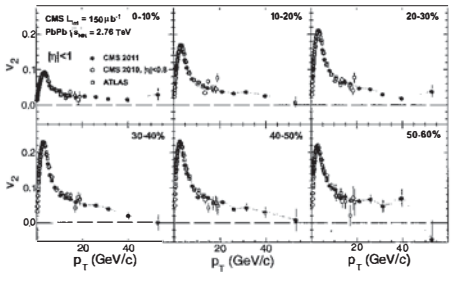

Figure 3: Extended $v_2(p_T)$ distribution up to 60 GeV/c for six centrality bins. Lower p_T results from both CMS [3] and ATLAS [10] are shown.

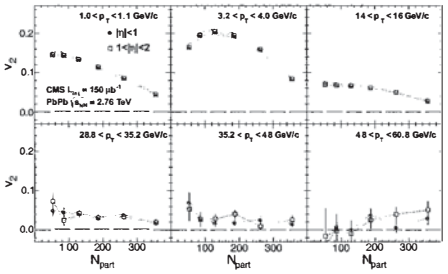

Figure 4: v_2 values as a function of the number of participant nucleons for given p_T ranges.

Higher-order harmonics have been measured at CMS for Pb+Pb at 2.76 GeV using various methods, including the event-plane method and di-hadron correlation methods [11]. Significant contributions are found up to at least the 5-th order harmonics (v_5), with little centrality dependence seen for the odd harmonics n=3 and n=5. These results suggest that these higher odd harmonic anisotropies are dominated by initial-state fluctuation of the collisions.

The initial-state geometry of the produced medium in relativistic heavy-ion collisions results in a large uncertainty for the deduced value of the shear viscosity to entropy ratio (η/s) of the medium. It has been suggested that the initial condition has less an influence on very central events where the geometry is determined only by the extent of the colliding nuclei [12 13]. Using a dedicated ultra-central collision trigger, CMS selects the most central 0-0.2% events in Pb+Pb collisions at 2.76 GeV [14]. The flow coefficients v_2 through v_6 are measured using the di-hadron correlation method. The p_T dependence of v_n is shown in Fig. 5, where higher order harmonics ($n > 2$) are strongly excited. v_3, v_4 and v_5 even rise above v_2 at higher p_T values, suggesting the strong influence of the initial-state fluctuations in these ultra-central collisions.

The recent p+Pb di-hadron correlation results of high-multiplicity triggered events at 5.03 TeV reveal a long-range, near-side ridge like structure, suggesting a flow-like behavior [15]. In Fig. 6 di-hadron correlation yield, after applying ZYAM procedure are shown for various selections of p_T and multiplicity, along with corresponding results obtained from p+p collision at 7 TeV using the same procedure. The data were recorded using a high multiplicity trigger implemented to select ultra-central events. The HIJING simulation results [16], shown as dashed curves, qualitatively reproduce the shape of the correlation yield at low multiplicity, but fail at high multiplicity. Long-range, near-side particle correlations in p+Pb collisions have been predicted using models that assume collective hydrodynamic expansion with fluctuating initial-conditions. The correlation results [17] from the predicted elliptic and triangular flow components for p+Pb collision at 4.4 TeV are shown as solid curves for $1.0 < p_T < 2.0$ GeV/c. The correlation yields in high multiplicity events are strongly enhanced compared to p+p collisions. Further analysis is needed to investigate the origin of the ridge like correlations and the collective behavior.

3 Summary

The LHC Pb+Pb runs at 2.76 TeV in 2010 and 2011 have provided abundant new results that can be informative for the understanding of the properties of the medium produced in heavy-ion collisions. The CMS program has investigated the azimuthal asymmetries in a wide kinematic range, from the hydrodynamic flow behavior at low p_T, the π^0 azimuthal anisotropies at intermediate p_T, and the asymmetric anisotropy from parton energy loss in the medium at high p_T. At low p_T, p_T differential v_n results are sensitive to the initial-state fluctuations and

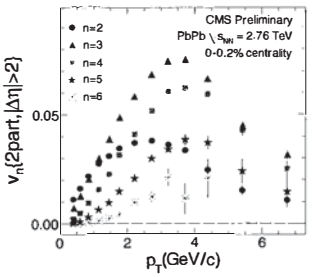

Figure 5: v_n as a function of p_T for ultra-central events.

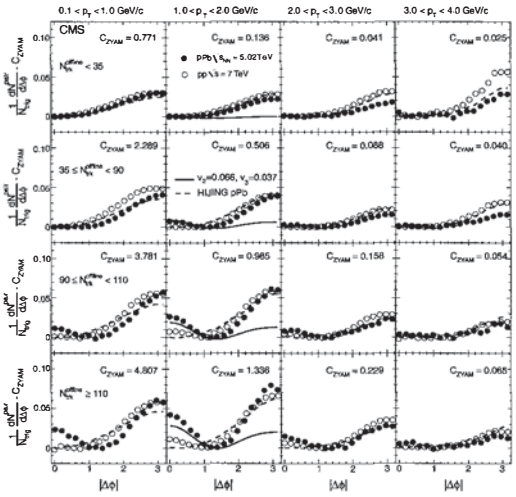

Figure 6: Di-hadron correlated yield for 5.02 TeV p+Pb and 7 TeV p+p, compared to p+Pb predictions for HIJING [16] (dashed curve) and a hydrodynamics model [17] (solid curve)

the property of the hot dense medium created in heavy-ion collisions. A single-track, high-p_T trigger enables us to extend the v_2 measurements up to 60 GeV/c, making it possible to explore the path length dependence of parton energy loss in the medium. An ultra-central collision trigger has allowed a measurement of v_n coefficients with n=2 through 6 for the top 0.2% most central events. The recent p+Pb run at 5.03 TeV in 2012 has revealed a near-side long-range ridge like structure in di-hadron correlation analysis, which could suggest hydro-like correlations arising in a small system. Further work is needed to study the origin and behavior of the ridge structure.

References

1. Poskanzer, A. M. and Voloshin, S. A. *Phys. Rev.* C **58**, 1671 (1998).
2. A. P. Mishra, R. K. Mohapatra *et al. Phys. Rev.* C **77**, 064902 (2008).
3. S. Chatrchyan *et al.* (CMS Collaboration) *Phys. Rev.* C **87**, 014902 (2013)
4. A. M. Poskanzer and S. A. Voloshin *Phys. Rev.* C **58**, 1671 (1998)
5. N. Borghini, P. M. Dinh and J. -Y. Ollitrault *Phys. Rev.* C **64**, 054901 (2001)
6. R. S. Bhalerao, N. Borghini and J. Y. Ollitrault *Nucl. Phys.* A **727**, 373 (2003)
7. S. Chatrchyan *et al.* (CMS Collaboration) *Phys. Rev.* Lett. **110**, 042301 (2013)
8. A. Adare *et al.* (PHENIX Collaboration) *Phys. Rev.* Lett. **105**, 142301 (2010)
9. S. Chatrchyan *et al.* (CMS Collaboration) *Phys. Rev.* Lett. **109**, 022301 (2012)
10. ATLAS Collaboration *Phys. Lett.* B **707**, 330 (2012)
11. S. Chatrchyan *et al.* (CMS Collaboration) *Eur. Phys. J.* C **72**, 2012 (2012)
12. R. Snellings *New J. Phys.* **13**, 055008 (2011)
13. T. Hirano, U. W. Heinz, D. Kharzeev, R. Lacey and Y. Nara *J. Phys.* G **34**, S879 (2007)
14. CMS Collaboration *CMS-PAS-HIN-12-011*, 2012
15. S. Chatrchyan *et al.* (CMS Collaboration) *Phys. Lett.* B **718**, 795 (2013)
16. M. Gyulassy and X. -N. Wang *Comput. Phys. Commun.* **83**, 307 (1994)
17. P. Bozek *Phys. Rev.* C **85**, 014911 (2012)

FLOW PHENOMENA IN ATLAS

A. ANDREAZZA, on behalf of the ATLAS Collaboration
INFN Sezione di Milano and Dipartimento di Fisica, Università di Milano
Via Celoria 16, I-20133, Milano, Italy

Measurements of flow anisotropy coefficients have been performed with the ATLAS detector at the LHC, on a sample of 8 μb^{-1} minimum bias Pb+Pb collisions at centre-of-mass energy $\sqrt{s_{\rm NN}} = 2.76$ TeV and a sample of 1 μb^{-1} p+Pb collisions at $\sqrt{s_{\rm NN}} = 5.02$ TeV. The large statistics Pb+Pb sample is used to derive event-by-event distribution of v_2, v_3 and v_4. Within uncertainties, the distributions of v_3 and v_4 agree with a pure Gaussian function over a wide centrality range, while significant deviations from this function are observed for v_2 in mid-central and peripheral collisions. In the p+Pb sample, a long-range near-side and away-side correlation is observed for events with high transverse energy in the detector. This structure can be described by v_2 anisotropy coefficients of magnitude similar to what is observed in Pb+Pb collisions.

1 Introduction

Heavy ion collisions at the Relativistic Heavy Ion Collider (RHIC) and the Large Hadron Collider (LHC) create hot, dense matter that is thought to be composed of strongly interacting quarks and gluons. A useful tool to study the properties of this matter is the azimuthal anisotropy of particle emission in the transverse plane.[1] This anisotropy is believed to result from pressure-driven anisotropic expansion (referred to as "flow") of the created matter, and is described by a Fourier expansion of the particle distribution in azimuthal angle, around the beam direction:

$$\frac{dN}{d\phi} \propto 1 + 2\sum_{n=1}^{\infty} v_n \cos n(\phi - \Phi_n) \stackrel{\text{def.}}{=} 1 + 2\sum_{n=1}^{\infty} v_{n,x}\cos n\phi + v_{n,y}\sin n\phi, \qquad (1)$$

where v_n and Φ_n represent the magnitude and phase of the n^{th}-order harmonics, respectively.

In this paper some recent measurements of the v_n in Pb+Pb and p+Pb collisions are presented.[2,3,4] They are performed by the ATLAS detector[5] at the LHC, using the charged particles reconstructed in the inner detector, within its acceptance in pseudorapidity $|\eta| < 2.5$[a]. The event centrality is derived from the transverse energy deposition in the forward calorimeter (FCal) covering $3.2 < |\eta| < 4.9$.[6]

The data samples were collected with a minimum bias trigger. They consist of 8 μb^{-1} integrated luminosity of Pb+Pb collisions at $\sqrt{s_{\rm NN}} = 2.76$ TeV from the 2010 LHC run, and of 1 μb^{-1} integrated luminosity of p+Pb collisions at $\sqrt{s_{\rm NN}} = 5.02$ TeV from a short pilot run in September 2012.

[a] ATLAS uses a right-handed coordinate system with its origin at the nominal interaction point (IP) in the centre of the detector and the z-axis along the beam pipe. The x-axis points from the IP to the centre of the LHC ring, and the y-axis points upward. Cylindrical coordinates (r, ϕ) are used in the transverse plane, ϕ being the azimuthal angle around the beam pipe. The pseudorapidity is defined in terms of the polar angle θ as $\eta = -\ln\tan(\theta/2)$.

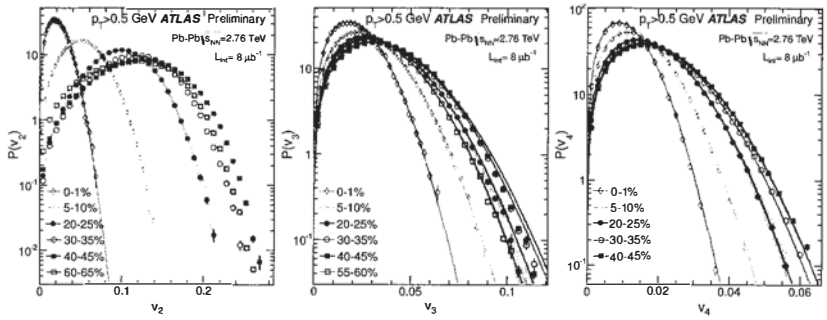

Figure 1: The probability distribution of the EbE v_n in several centrality intervals for n=2 (left panel), n=3 (middle panel) and n=4 (right panel). The errors bars are statistical uncertainties, and the shaded bands are uncertainties on the v_n-shape. The solid curves are distributions calculated from the measured $\langle v_n \rangle$ according to Eq. 2; they are shown for the 0-1% centrality interval for v_2, but for all centrality intervals for v_3 and v_4.[2]

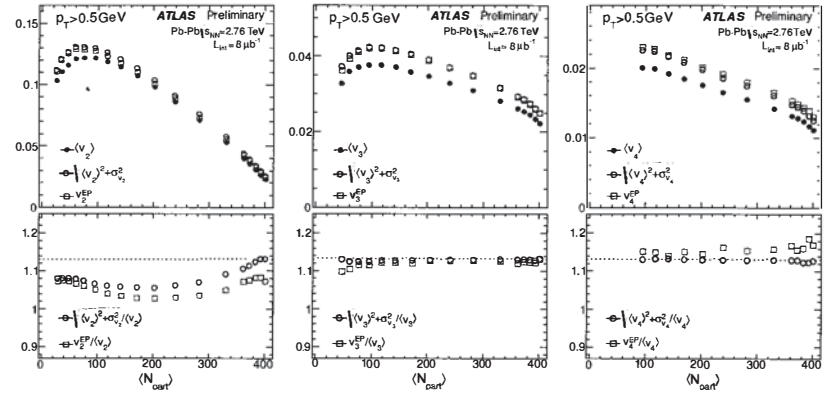

Figure 2: Top panels: Comparison of $\langle v_n \rangle$ and $\sqrt{\langle v_n^2 \rangle} = \sqrt{\langle v_n \rangle^2 + \sigma_n^2}$ derived from the EbE v_n distributions with the $v_n^{\rm EP}$, for charged particles with $p_{\rm T} > 0.5$ GeV. Bottom panels: the ratios of $\sqrt{\langle v_n^2 \rangle}$ and $v_n^{\rm EP}$ to $\langle v_n \rangle$. The shaded bands represent the systematic uncertainties. The dotted lines in bottom panels indicate $\sqrt{\langle v_n^2 \rangle}/\langle v_n \rangle = 1.13$, expected for the radial projection of a 2D Gaussian distribution.[2]

2 Event-by-Event distributions

The average values of v_n and their dependence on centrality, $p_{\rm T}$ and η, have been measured at the LHC [7,8,9] with different techniques. In particular the "elliptic flow", v_2, has large values reflecting the shape of the overlapping nuclei.[10,11,12] The Fourier coefficients in Eq. 1 can also be computed on an event-by-event (EbE) basis from the particle azimuthal distribution.[2]

The measured distributions for $v_n = \sqrt{v_{n,x}^2 + v_{n,y}^2}$ ($n = 2$–4), after unfolding for the smearing due to finite charged particle multiplicity, are shown in Figure 1. The remaining width is expected to reflect fluctuations in the initial state geometry. In case of pure Gaussian fluctuations, the distributions would be described by the radial projection of a 2D Gaussian distribution:

$$P(v_n) = \frac{v_n}{\delta_n^2} e^{-\frac{v_n^2}{2\delta_n^2}}, \quad \langle v_n \rangle = \sqrt{\frac{\pi}{2}}\delta_n, \quad \sigma_n^2 = \langle v_n^2 \rangle - \langle v_n \rangle^2 = \left(2 - \frac{\pi}{2}\right)\delta_n^2. \tag{2}$$

The data show this is the case for v_3 and v_4 on a wide centrality range, and for v_2 in the most central events. For less central events, v_2 has a significant contribution from the shape

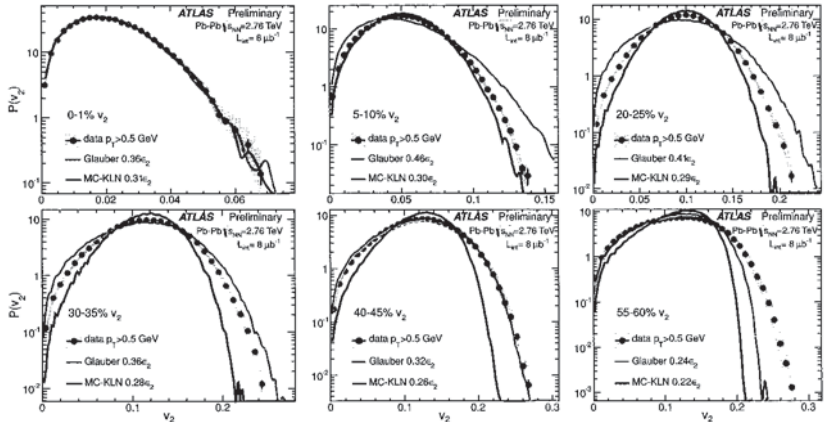

Figure 3: The EbE v_2 distributions compared with the eccentricity distributions from two initial geometry models: a Glauber model [13] (red lines) and the MC-KLN model [16] (blue lines).[2]

of the overlapping region between the interacting nuclei. This is quantitatively illustrated in Fig. 2 where the values of $\sqrt{\langle v_n^2 \rangle}/\langle v_n \rangle$ obtained by the v_n distributions are compared with the expectation from Eq. 2, as a function of the average number of participants in each centrality interval, $\langle N_{\rm part} \rangle$, as estimated from a Glauber model Monte Carlo.[13] In this Figure, $\sqrt{\langle v_n^2 \rangle}$ is also compared with the $v_n^{\rm EP}$ obtained by the event plane method.[9] This method is expected to give $\langle v_n \rangle < v_n^{\rm EP} < \sqrt{\langle v_n^2 \rangle}$, the actual value being experiment-dependent.[14] The published ATLAS values of $v_n^{\rm EP}$ are very near to the upper bound.

If anisotropy is due to the hydrodynamic expansion of the strongly interacting system, the v_n is expected to scale with the eccentricity ε_n obtained by averaging the positions of the participanting nucleons with respect to their centre-of-mass, in the transverse $r - \phi$ plane:[15]

$$\varepsilon_n = \frac{\sqrt{\langle r^n \cos n\phi \rangle^2 + \langle r^n \sin n\phi \rangle^2}}{\langle r^n \rangle}. \tag{3}$$

In Fig. 3 the eccentricity distribution ε_2 is computed using a Glauber model [13] and the MC-KLN model [16], and rescaled to the average v_2 distribution. The rescaled ε_2 of both models describe the data well in the 1% most central collisions, but start to fail towards less central events. Neither model describes the more peripheral data well.

3 The ridge in p+Pb collisions

Proton-nucleus collisions at the LHC are crucial for the interpretation of results from the Pb+Pb program.[17] In particular, the relationship between fluctuations in the initial geometry and final-state particle correlations can be further investigated by studying correlations in p+Pb collisions with observables such as the two particle correlation function[3] and the two- and four-particle cumulants.[4] These observables are studied as a function of the transverse energy deposited on the FCal in the side of the outgoing Pb beam, $\sum E_{\rm T}^{\rm Pb}$, and of the particle $p_{\rm T}$.

Figures 4a and 4b show two-particle correlation function, $C(\Delta\eta, \Delta\phi)$, at low and high $\sum E_{\rm T}^{\rm Pb}$, respectively. At high $\sum E_{\rm T}^{\rm Pb}$ a "ridge", a long-range correlation in $\Delta\eta$ at $\Delta\phi \sim 0$, is evident. The recoil component at $\Delta\phi \sim \pi$ is also enhanced. The amount of correlated pairs is evaluated using the per-trigger yield[18] after subtracting the pedestal of uncorrelated pairs (zero-yield at minimum, ZYAM, method), as shown in Figure 4c. At low $\sum E_{\rm T}^{\rm Pb}$ only a recoil contribution is

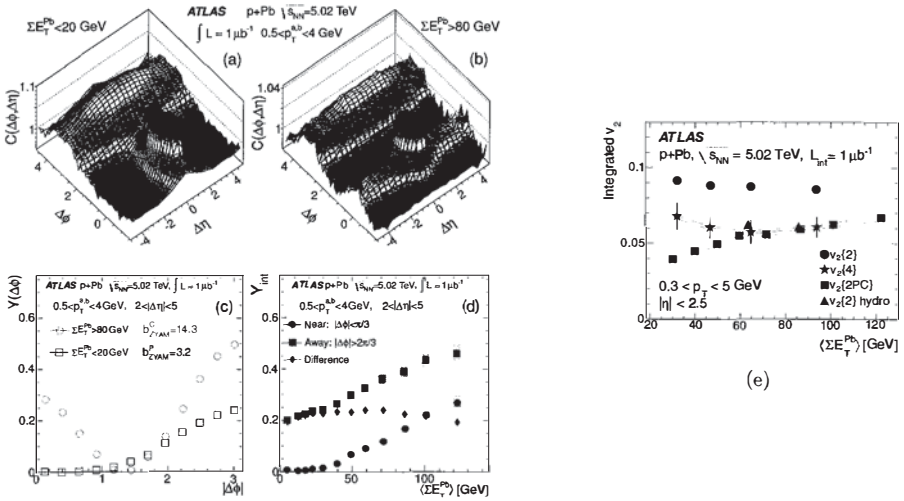

Figure 4: Two-dimensional correlation functions for (a) peripheral events and (b) central events, both with a truncated maximum to suppress the large correlation at $(\Delta\eta, \Delta\phi) = (0, 0)$; (c) the per-trigger yield $\Delta\phi$ distribution together with pedestal levels for peripheral ($b^{\rm P}_{\rm ZYAM}$) and central ($b^{\rm C}_{\rm CZYAM}$) events, and (d) integrated per-trigger yield as function of $\sum E_{\rm T}^{\rm Pb}$ for pairs in $2 < |\Delta\eta| < 5$. The shaded boxes represent the systematic uncertainties, and the statistical uncertainties are smaller than the symbols.[3] (e) The second-order harmonic, v_2, calculated with two- and four-particle cumulants (circles and stars, respectively), as a function of $\sum E_{\rm T}^{\rm Pb}$. Systematic uncertainties are shown as shaded bands. Also shown is $v_2\{2PC\}$ from two-particle correlations (squares) and predictions from a hydrodynamic model[22] (triangles) for the same selection of charged particles as in the data.[4]

visible at $|\Delta\phi| \sim \pi$. At high $\sum E_{\rm T}^{\rm Pb}$ a correlated component appears at $|\Delta\phi| \sim 0, \pi$. Figure 4d displays the per-trigger yields integrated on the "near" ($|\Delta\phi| < \pi/3$) and the "away" ($|\Delta\phi| > 2\pi/3$) sides as a function of $\sum E_{\rm T}^{\rm Pb}$. Both regions show a correlated rise with transverse energy, with same magnitude in the near- and away-side.

In order to quantify this rise, the yield of low $\sum E_{\rm T}^{\rm Pb}$ events is subtracted from high $\sum E_{\rm T}^{\rm Pb}$ events. This difference as a function of $\Delta\phi$ can be described mostly by a $\cos(2\Delta\phi)$ modulation. Such a feature in the two-particle correlation function can be converted into a v_2 Fourier coefficient of the single-particle distribution of Eq. 1.[9] These coefficients, $v_2\{2PC\}$, are compared in Figure 4e with $v_2\{2\}$ and $v_2\{4\}$ obtained by the two- and four-particle cumulants.[19] The large magnitude of $v_2\{2\}$ compared to $v_2\{4\}$ suggests a substantial contamination from non-flow correlations. The four-particle cumulant shows a value of approximately 0.06, which agrees with $v_2\{2PC\}$ at high $\sum E_{\rm T}^{\rm Pb}$. The disagreement at low $\sum E_{\rm T}^{\rm Pb}$ could be due either to the subtraction procedure in the $v_2\{2PC\}$ determination or to residual non-flow effects in $v_2\{4\}$.

The $p_{\rm T}$-dependence of v_2 has also been studied and the trend in p+Pb collisions is similar to what observed in Pb+Pb collision, with a magnitude between that measured in the most central and peripheral Pb+Pb collisions.[9,10] Comparable magnitude of v_2 has also been reported by ALICE.[20] and can be possibly explained within the colour glass condensate and hydrodynamic models.[21,22]

4 Conclusions

The high statistics Pb+Pb samples collected by the ATLAS experiment at the LHC allow for studies of flow phenomena with a wide range of analysis techniques.[9,10,11,12,23] In particular the Fourier coefficients of the anisotropy flow can be measured on an event-by-event basis, accessing their fluctuations.[2] The resulting v_3 and v_4 distributions are compatible with Gaussian

fluctuations on a wide rapidity range, while for v_2 there is a significant contribution from the initial shape of the overlapping nuclei. The observed distributions cannot be described by basic Glauber models.

Already the initial pilot run of p+Pb collision at the LHC has provided interesting observations. In high transverse energy events, the ridge in the two particle correlation function shows a flow-like anisotropy, dominated by a term $v_2 \approx 0.06$,[3,4] comparable to the value observed in Pb+Pb collisions.

References

1. J.-Y. Ollitrault, *Phys. Rev.* D **46**, 229 (1992).
2. ATLAS Collaboration, ATLAS-CONF-2012-114, [http://cdsweb.cern.ch/record/1472935].
3. ATLAS Collaboration, *Phys. Rev. Lett.* **110**, 182302 (2013), [arXiv:1212.5198].
4. ATLAS Collaboration, submitted to *Phys. Lett.* B, [arXiv:1303.2048].
5. ATLAS Collaboration, JINST **3**, S08003 (2008).
6. ATLAS Collaboration, *Phys. Lett.* B **710**, 363 (2012) [arXiv:1108.6027].
7. ALICE Collaboration, *Phys. Lett.* B **708**, 249 (2012), [arXiv:1109.2501].
8. CMS Collaboration, *Eur. Phys. J.* C **72**, 2012 (2012), [arXiv:1201.3158].
9. ATLAS Collaboration, *Phys. Rev.* C **86**, 014907 (2012), [arXiv:1203.3007].
10. ATLAS Collaboration, *Phys. Lett.* B **707**, 330 (2012), [arXiv:1108.6018].
11. ATLAS Collaboration, ATLAS-CONF-2012-117, [http://cdsweb.cern.ch/record/1472939].
12. ATLAS Collaboration, ATLAS-CONF-2012-118, [http://cdsweb.cern.ch/record/1472940].
13. M. L. Miller, K. Reygers, S. J. Sanders and P. Steinberg, *Ann. Rev. Nucl. Part. Sci.* **57**, 205 (2007).
14. M. Luzum and J.-Y. Ollitrault, *Phys. Rev.* C **87**, 044907 (2013), [arXiv:1209.2323].
15. G.-Y. Qin, H. Petersen, S. A. Bass, and B. Muller, *Phys. Rev.* C **82**, 064903 (2010), [arXiv:1009.1847].
16. A. Adil, H. J. Drescher, A. Dumitru, A. Hayashigaki and Y. Nara, *Phys. Rev.* C **74**, 044905 (2006), [arXiv:nucl-th/0605012]; H. J. Drescher and Y. Nara, *Phys. Rev.* C **75**, 034905 (2007) [arXiv:nucl-th/0611017].
17. C. Salgado *et al.*, *J. Phys.* G **39**, 015010 (2012), [arXiv:1105.3919].
18. CMS Collaboration, *Phys. Lett.* B **718**, 795 (2012), [arXiv:1210.5842].
19. N. Borghini, P. M. Dinh and J. -Y. Ollitrault, *Phys. Rev.* C **63**, 054906 (2001).
20. ALICE Collaboration, *Phys. Lett.* B **719**, 29 (2012), [arXiV:1212:2001].
21. K. Dusling and R. Venugopalan, *Phys. Rev.* D **87**, 054014 (2013), [arXiv:1211.3701].
22. P. Bożek and W. Broniowski, *Phys. Lett.* B **718**, 1557 (2013), [arXiv:1211.0845].
23. ATLAS Collaboration, ATLAS-CONF-2012-049, [http://cdsweb.cern.ch/record/1451882].

The Double Ridge Phenomenon in p–Pb Collisions Measured with ALICE

Jan Fiete Grosse-Oetringhaus for the ALICE collaboration
CERN, 1211 Geneva 23, Switzerland

The ALICE collaboration has measured two-particle angular correlations in p–Pb collisions at $\sqrt{s_{\mathrm{NN}}} = 5.02\,\mathrm{TeV}$ using data from the p–Pb pilot run in September 2012 at the LHC [1]. In these correlations, the number of associated particles (N_{assoc}) per number of trigger particles (N_{trig}) is studied as a function of the azimuthal difference ($\Delta\varphi$) and the difference in pseudorapidity ($\Delta\eta$) and expressed as associated yield per trigger particle:

$$\frac{1}{N_{\mathrm{trig}}} \frac{\mathrm{d}^2 N_{\mathrm{assoc}}}{\mathrm{d}\Delta\eta \mathrm{d}\Delta\varphi}. \tag{1}$$

This correlation is determined at mid-rapidity ($|\eta| < 1.2$) in different bins of trigger particle momentum $p_{\mathrm{T,trig}}$ and associated particle momentum $p_{\mathrm{T,assoc}}$. The event sample is divided into four multiplicity classes depending on the measured multiplicity in two forward detectors ($2.8 < \eta < 5.1$ and $-3.7 < \eta < -1.7$).

The two-particle correlation of low-multiplicity (lowest 40%) events is subtracted from the one in high-multiplicity (highest 20%) events which removes the jet contribution to the correlation to a large extent. The resulting correlation is shown in Fig. 1 for one bin in momentum and multiplicity. A double-ridge structure is observed with a near-side ridge centered at $\Delta\varphi = 0$ and an away-side ridge centered at $\Delta\varphi = \pi$. Both are independent of $\Delta\eta$.

This intriguing phenomenon has been characterized by calculating the ridge yields as well as the Fourier decomposition of the excess structure. The details can be found in Ref. 1. Theoretical explanations which aim at describing this feature involve a hydrodynamic phase [2] or the color-glass condensate [3]. While these models succeed in describing the results qualitatively, this phenomenon is a long way from being well understood.

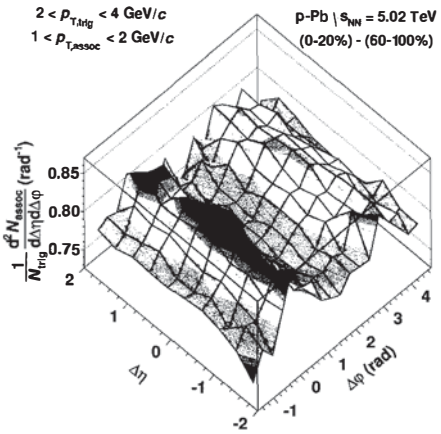

Figure 1: The associated yield per trigger particle in $\Delta\varphi$ and $\Delta\eta$ for pairs of charged particles with $2 < p_{\mathrm{T,trig}} < 4\,\mathrm{GeV}/c$ and $1 < p_{\mathrm{T,assoc}} < 2\,\mathrm{GeV}/c$ in high-multiplicity (0–20%) p–Pb collisions from which the correlation in low-multiplicity (60–100%) p–Pb collisions has been subtracted. Figure from Ref. 1.

References

[1] ALICE Collaboration, *Phys.Lett.* **B719** 29 (2013).
[2] P. Bozek, Phys. Rev. C **85** (2012) 014911.
[3] K. Dusling and R. Venugopalan, arXiv:1302.7018 [hep-ph].

Long-range angular correlations by strong color fields in hadronic collisions

Kevin Dusling
Physics Department, North Carolina State University, Raleigh, NC 27695, USA

I present an overview of the *ridge* phenomenon in proton-proton and proton-lead collisions. This novel collimation between rapidity separated hadron pairs is a consequence of non-linear gluon dynamics within the small–x wave-function of the colliding hadrons.

Multi-particle correlations in high-energy hadronic collisions can serve as sensitive tests of QCD dynanmics. In the fall of 2010 the CMS collaboration made a striking discovery [1]. In high-multiplicity proton-proton collisions a correlation was uncovered between charged-particle pairs having a large pseudo-rapidity separation ($\Delta\eta \gg 1$) and a narrow angular separation ($\Delta\phi \lesssim 1$) in azimuth. Figure 1 displays the original CMS result. As the structure of the two-particle correlation resembles a mountain range the new discovery was dubbed "The Ridge" when it was first observed in heavy-ion collisions. It should be stressed that the heavy-ion ridge has a unique physical interpretation from the ridge in p+p and p+Pb collisions. While the former is attributed primarily to final-state rescattering and hydrodynamic flow the latter, which will be the focus of this proceeding, is a consequence of gluon saturation [2].

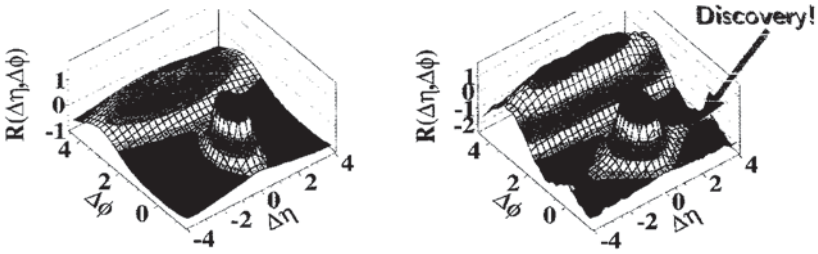

Figure 1: Two particle correlation function from minimum-bias (left) and high-multiplicity (right) events in proton-proton collisions at $\sqrt{s} = 2.76$ TeV. Data from the CMS collaboration [1].

The ridge in proton-proton and proton-lead collisions is a natural consequence of gluon-saturation and non-linear parton dynamics in the nuclear wave-function *before* the collision

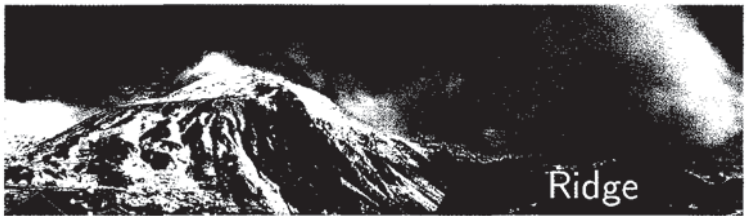

Figure 2: The ridge in La Thuile on March 14$^{\text{th}}$ 2013.

occurs. The full structure of the two-particle correlation is explained by two competing QCD diagrams; as long as they are both computed within the CGC-EFT [3]. The first diagram corresponds to the production of two gluons from a single *ladder* as shown in the right-most Feynman diagram appearing in Fig. 3. This production mechanism creates particles primarily back-to-back (*i.e.* on the away-side for $\Delta\eta \gtrsim 1$) and does not generate any near-side collimation. A second class of diagrams, herein called "Glasma Graphs", where two gluons are produced from different ladders, is responsible for the near-side collimation identified with the ridge. The two-particle correlation generated by the Glasma graphs is symmetric with respect to $\Delta\phi = \pi/2$ and therefore produces an equal away-side collimation as well; however, this is hidden underneath the away-side jet and was only recently observed after a careful subtraction of peripheral events.

Saturation dynamics comes into play when determining the relative contribution of these two diagrams towards the two-particle correlation. A power counting exercise demonstrates that the Glamsa graph is enhanced by a factor of α_S^{-8} in the presence of saturation, which we associate with central / high-multiplicity collisions. This should be compared to the α_S^{-4} enhancement of the jet-graph in going from min-bias to central collisions.

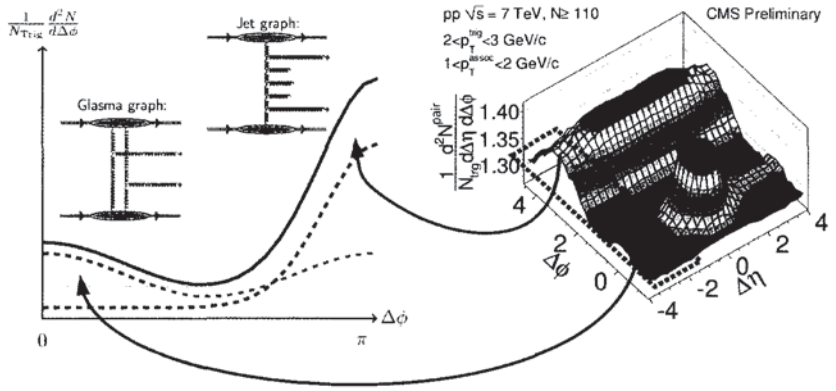

Figure 3: Anatomy of a proton-proton collision. The away-side peak, associated with mini-jet production arises from the jet-graph (two gluons produced from a single ladder) as shown in the right diagram along with its schematic contribution to the per-trigger-yield plotted in blue. The Glasma graph contribution (left diagram) is shown schematically by the orange curve. The shaded gray region (extracted experimentally by the ZYAM procedure) is referred to as the associated yield.

The near-side collimation produced by the Glasma graph can be understood by looking at the schematic form of the double-inclusive cross section

$$d^2\sigma \propto \int_{\mathbf{k}_T} \Phi_A^2(x_1, \mathbf{k}_T)\Phi_B(x_1, \mathbf{p}_T - \mathbf{k}_T)\Phi_B(x_2, \mathbf{q}_T - \mathbf{k}_T) + \cdots \tag{1}$$

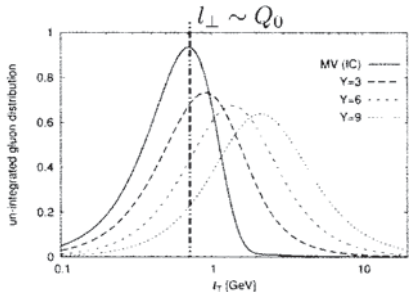

Figure 4: Unintegrated gluon distribution function evolved from the M.V. model initial condition to larger rapidities via the rcBK evolution equation.

The full expression used in computations along with all relevant details is presented in [4]. The function $\Phi(x, \mathbf{k}_T)$ appearing in these expressions is the unintegrated gluon distribution and is obtained by solving the rcBK equation with MV model initial conditions at large x. The Cauchy-Schwarz inequality dictates that the correlation strength at $\Delta\phi = 0$ must be greater than or equal to that at $\Delta\phi = \pi/2$;

$$\int d^2k_\perp \Phi_A^2(\mathbf{k}_T)\, \Phi_B^2(|\mathbf{p}_T - \mathbf{k}_T|) \geq \int d^2k_\perp \Phi_A^2(\mathbf{k}_T)\, \Phi_B(|\mathbf{p}_T - \mathbf{k}_T|)\, \Phi_B(|\mathbf{q}_T - \mathbf{k}_T|)\,. \tag{2}$$

Furthermore the equality holds if and only if

$$\Phi(|\mathbf{p}_T - \mathbf{k}_T|) \propto \Phi(|\mathbf{q}_T - \mathbf{k}_T|)\,, \tag{3}$$

and therefore, as long as the gluon distribution is a non-trivial function of momentum, there must be a collimation. The strength depends on the detailed structure of the gluon distribution function shown in fig. 4.

The rapid rise of the associated yield (see Fig. 3 for the definition) with centrality for asymmetric collisions can also be understood from equation 1 as well. If we take the unintegrated gluon distribution function as narrowly peaked around the saturation scale Q_A and Q_B of the projectile and target respectively, the associated yield increases quadratically with the larger of the two saturation scales [5],

$$\mathrm{CY} \propto \frac{\Phi_B(Q_B)}{\Phi_B\left(\sqrt{2p_T^2 + 2Q_A^2 - Q_B^2}\right)} \xrightarrow[Q_B \gg Q_A]{} 1 + \frac{Q_B^2}{Q_A^2}\,. \tag{4}$$

A recent work [6] has compared predictions made within the CGC-EFT to the CMS [7], ALICE [8] and ATLAS [9] experimental data. Two examples of the quality of the theory to data comparison is shown in figure 5. While the CGC-EFT provides a unified description of both p+p and p+Pb collisions at a quantitative level one may still question the role played by final state effects. While this can only be addressed by detailed modeling there is strong evidence that final state interactions are small and not responsible for the ridge.

A crucial piece of evidence stems from the away-side jet, which remains unmodified from peripheral to central collisions; a fact confirmed a posteriori by the successful subtraction of the peripheral jet from central data by the LHC experimentalists. If final-state rescattering was strong enough to collimate the medium's particles to create the ridge, rescattering should similarly modify the jet. This is indeed observed in heavy-ion collisions but it is not the case in p+p and p+Pb collisions.

A natural question is whether there is a unique final state interpretation of *both* the proton-proton and proton-lead ridge? The differences in systematics between these two systems is

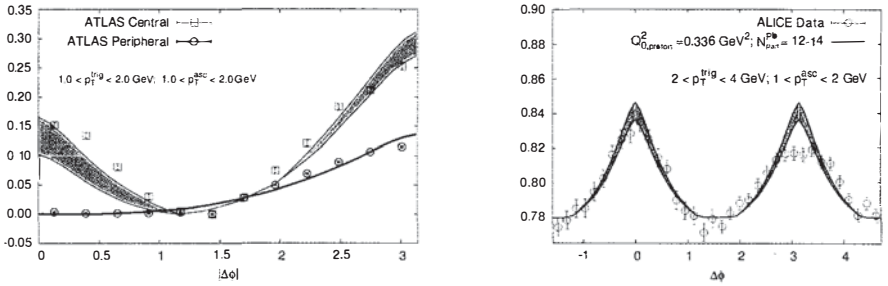

Figure 5: Comparison of calculations within the CGC-EFT framework with recent experiments. The left figure shows the ATLAS [9] per-trigger-yield as a function of azimuthal separation ($\Delta\phi$) for peripheral events as blue circles and central events as red squares. The solid curves show the theory calculation for these two event classes. For peripheral events only the jet diagram is visible in both the data and theory calculation. The right figure shows data from the ALICE collaboration [8] where the difference between central and peripheral events allowed for the discovery of the away-side ridge. The gray band shows shows the contribution from the Glasma graphs.

naturally understood within the CGC framework. Whether there is a consistent final-state model is far from clear. It seems extremely difficult for a final-state interpretation to account for an associated yield four times larger in p+Pb than in p+p at the *same* multiplicity, considering our expectation that the overlap areas in the two systems are approximately the same.

There is compelling evidence that the ridge in proton-proton and proton-lead collisions is a consequence of gluon saturation and non-linear gluon dynamics. This remarkable discovery of a novel collimation between two particles flying in opposite directions in ultra-rare high multiplicity events is probing rare quantum fluctuations within the proton and nucleus at the smallest length scales experimentally possible.

Acknowledgments

Supported by the US Department of Energy under Contract No. DE-FG02-03ER41260.

References

1. V. Khachatryan *et al.* [CMS Collaboration], JHEP **1009**, 091 (2010) [arXiv:1009.4122 [hep-ex]].
2. K. Dusling and R. Venugopalan, Phys. Rev. Lett. **108**, 262001 (2012) [arXiv:1201.2658 [hep-ph]].
3. F. Gelis, E. Iancu, J. Jalilian-Marian and R. Venugopalan, Ann. Rev. Nucl. Part. Sci. **60**, 463 (2010) [arXiv:1002.0333 [hep-ph]].
4. K. Dusling and R. Venugopalan, Phys. Rev. D **87**, 051502 (2012) [arXiv:1210.3890 [hep-ph]].
5. K. Dusling and R. Venugopalan, Phys. Rev. D **87**, 054014 (2012) [arXiv:1211.3701 [hep-ph]].
6. K. Dusling and R. Venugopalan, Phys. Rev. D to appear [arXiv:1302.7018 [hep-ph]].
7. S. Chatrchyan *et al.* [CMS Collaboration], Phys. Lett. B **718**, 795 (2013) [arXiv:1210.5482 [nucl-ex]].
8. B. Abelev *et al.* [ALICE Collaboration], arXiv:1212.2001 [nucl-ex].
9. G. Aad *et al.* [ATLAS Collaboration], arXiv:1212.5198 [hep-ex].

Jet Results in pp and Pb-Pb Collisions at ALICE

Oliver Busch for the ALICE collaboration
Universität Heidelberg, Physikalisches Institut, Heidelberg, Germany

We report results on jet production in pp and Pb-Pb collisions at the LHC from the ALICE collaboration. The jet cross section in pp collisions at $\sqrt{s}$=2.76 TeV is presented, as well as the charged particle jet production cross section and measurements of the jet fragmentation and jet shape in pp collisions at $\sqrt{s}$=7 TeV. NLO pQCD calculations and simulations from MC event generators agree well with the data. Measurements of jets with a resolution parameter R=0.2 in Pb-Pb collisions at $\sqrt{s_{NN}}$=2.76 TeV show a strong, momentum dependent suppression in central events with respect to pp collisions. The centrality dependence of the suppression of charged particle jets relative to peripheral events is presented. The ratio of jet spectra with R=0.2 and R=0.3 is found to be similar in pp and Pb-Pb events. The analysis of the semi-inclusive distribution of charged particle jets recoiling from a high-p_{T} trigger hadron allows an unbiased measurement of the jet structure for larger cone radii.

1 Introduction

Jets are collimated sprays of particles associated with hard scattered partons. The study of jet production and fragmentation allows us to test our understanding of perturbative and non-perturbative aspects of QCD. In heavy-ion collisions, jets produced in the initial stage probe the hot and dense nuclear matter created during the quark gluon plasma phase of the fireball evolution. Interactions with the medium give rise to additional induced radiation. Jet reconstruction aims to capture the full dynamics of jet quenching and to quantify the in-medium jet energy loss.

2 Data analysis

Charged jets are reconstructed in the ALICE central barrel from primary charged particle tracks measured in the Inner Tracking System (ITS) and the Time Projection Chamber (TPC). Tracks with transverse momentum $p_{\mathrm{T}} > 150$ MeV/c in the pseudo-rapidity interval $|\eta| < 0.9$ are clustered with the FastJet [1] anti-k_{T} algorithm using a boost invariant p_{T} recombination scheme. We use different values of the jet resolution parameter from R=0.2 to R=0.4. Jets are selected so that they are fully contained within the detector acceptance. For full jet reconstruction, we include neutral particles (mostly neutral pions) reconstructed with the ALICE Electromagnetic Calorimeter (EMCal). Clusters in the EMCal acceptance $|\eta| < 0.7$ and $1.4 < \varphi < \pi$ with a transverse energy $E_{\mathrm{T}} > 300$ MeV are used. The energy of charged particles pointing to EMCal clusters is subtracted to avoid double-counting. The jet shape and jet constituents' transverse momentum spectra (jet fragmentation) are measured with charged particles in the leading (highest p_{T}) jet in each event. The jet spectra, shape, and fragmentation distributions are corrected for detector effects (including the missing energy from e.g. neutrons and K^0_L in the measurements that include the EMCal) via unfolding or bin-by-bin corrections based on detector simulations.

Jet reconstruction in heavy-ion collisions proceeds against a large background from the underlying event uncorrelated to hard parton scattering. The average charged background energy density is evaluated event by event from the median p_{T} density of FastJet [1] k_{T} clusters and subtracted jet by jet. For charged+EMCal jet reconstruction, the charged background density is scaled to the level of charged+neutral particles. The spectra are corrected for detector effects and background flucutations via unfolding.

3 Results from pp collisions

In the top-left panel of Fig. 1, we present the inclusive differential jet cross sections [2] in pp collisions at $\sqrt{s}$=2.76 TeV, measured using charged+neutral particles. The data are compared to NLO pQCD results [3,4]: good agreement is found when hadronization effects are applied to the perturbative calculations.

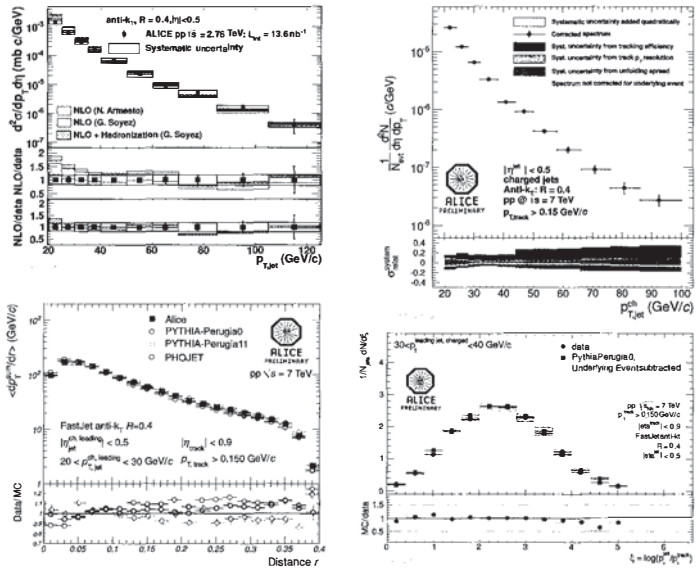

Figure 1: Results from pp collisions at $\sqrt{s}$=2.76 TeV and 7 TeV. Top left: inclusive differential jet cross section for R=0.4 at $\sqrt{s}$=2.76 TeV. Boxes show the systematic uncertainty. The data are compared to NLO pQCD calculations indicated by the bands, ratio of calculations to data are shown in the lower panel. Top right: charged jet cross section for R=0.4 at $\sqrt{s}$=7 TeV. Systematic uncertainties are indicated by the boxes, the lower panel shows the contributions from detector effects and unfolding superimposed linearly. Bottom left: radial distribution of transverse momentum density measured in leading charged jets with $20 < p^{\mathrm{ch}}_{\mathrm{T,jet}} < 30$ GeV/c. Bottom right: scaled transverse momentum distribution of jet fragments for $30 < p^{\mathrm{ch}}_{\mathrm{T,jet}} < 40$ GeV/c. Jet shape and fragmentation distributions are compared to from calculations from PYTHIA (tunes Perugia0 and Perugia2011) and Phojet MC event generators.

In the top-right panel of Fig. 1, the charged jet cross section [5] at $\sqrt{s}$=7 TeV is shown. The bottom-left panel of Fig. 1 presents the leading charged jet shape [7] distribution of particle p_{T} sum in radial slices relative to the jet axis. The slope of the distribution measures the jet collimation. The fragmentation spectrum of scaled transverse momentum $\xi = \ln(p_{\mathrm{T}}^{jet,ch}/p_{\mathrm{T}}^{particle})$ for the charged jet constituents [8] shown in the bottom-right panel exhibits the characteristic hump-backed plateau structure indicating QCD coherence. The area of the distribution is equal to the charged particle multiplicity of the fragments. The measured jet shape and fragmentation are compared to MC simulations from the PYTHIA [9] (tunes Perugia0 and Perugia2011) and Phojet [10]

event generators. The pp underlying event contribution was measured inside perpendicular cones transverse to the jet axis and subtracted from the jet cross section, fragmentation and shape measurements, consistently in data and simulations. The data are reasonably well described by the simulations.

4 Jets in Pb-Pb Collisions

Figure 2 shows the single inclusive jet cross section results [11,12] in Pb-Pb collisions at $\sqrt{s_{NN}} = 2.76$ TeV. In the top-left panel we present the charged+EMCal jet spectrum for R=0.2 for the 10% most central events. Minimum transverse momentum, $p_{\mathrm{T}} > 5$ GeV, is required for the leading charged constituent. In the top-right panel the jet nuclear modification factor R_{AA} is shown, defined as the ratio of the measured jet spectra in Pb-Pb collisions to the pp reference scaled by the number of binary collisions [15]: $R_{\mathrm{AA}}(p_{\mathrm{T}}) = \frac{1}{\langle N_{\mathrm{coll}} \rangle} \frac{\mathrm{d}^2 N_{\mathrm{jet}}/\mathrm{d}p_{\mathrm{T,jet}}\,\mathrm{d}\eta}{\mathrm{d}^2 N_{\mathrm{jet}}^{\mathrm{pp}}/\mathrm{d}p_{\mathrm{T,jet}}\,\mathrm{d}\eta}$. The measured R_{AA} is significantly smaller than unity, indicating a strong suppression of jets in Pb-Pb collisions. The suppression is strongest at low jet momentum, at high momentum R_{AA} rises to values of the order of 0.5. The centrality dependence of the quenching is investigated via the charged jet R_{CP}, a quantity conceptually similar to R_{AA}, but using peripheral Pb-Pb events as a reference. R_{CP} [13,14] is presented in Fig. 2 in the bottom-left panel for 3 different centrality intervals. The suppression is seen to increase with centrality (lower R_{CP} values), and a more pronounced momentum dependence can be observed. In the bottom-right panel, we show, for two centrality classes, the ratio of the charged jet spectra obtained for R=0.2 to R=0.3. The ratio is sensitive to the jet structure. The measured ratio is consistent with the PYTHIA values for peripheral and central events: no broadening of the hard core of the reconstructed jets is observed within the present systematic uncertainties.

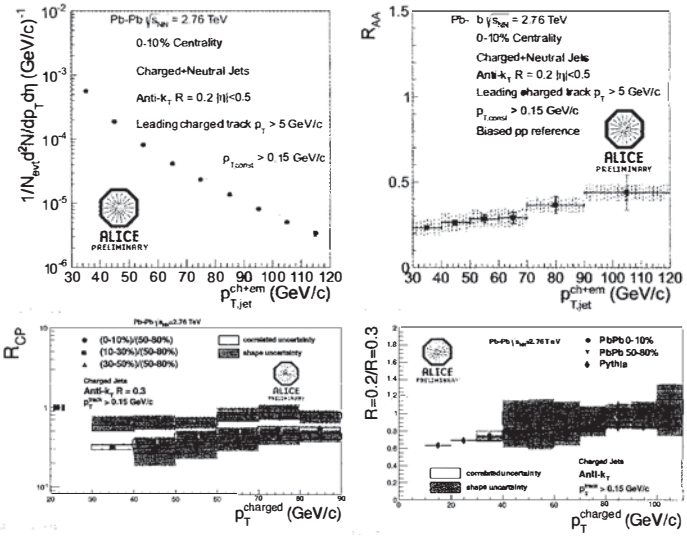

Figure 2: Single inclusive jet measurements in Pb-Pb collisions at $\sqrt{s_{NN}} = 2.76$ TeV. Top left: inclusive jet spectrum for R=0.2 in the 10% most central events, with a 5 GeV/c fragmentation bias on the leading jet constituent. Systematic uncertainties are indicated by the shaded band. Top right: nuclear modification factor for R=0.2 biased jets in 0-10% central events. Bottom left: nuclear modification factor R_{CP} for charged jets with R=0.3 for different centrality selections. Bottom right: ratio of charged jet spectra with radius parameter R=0.2 and R=0.3 in central and peripheral Pb-Pb events, compared to PYTHIA calculations.

5 Hadron triggered recoil jets in Pb-Pb

The analysis of hadron triggered recoil jets allows us to extend the study of jet quenching to larger values of R. The semi-inclusive distribution of charged jets recoiling back-to-back from a high-pt charged hadron in Pb-Pb collisions [16] is measured. Constructing the difference spectra for different intervals of trigger hadron p_{T}, we subtract the contribution of combinatorial jets uncorrelated to the hadron trigger:

$$\Delta_{recoil}((p_{\mathrm{T}}^{\mathrm{trig},1}-p_{\mathrm{T}}^{\mathrm{trig},2})-(p_{\mathrm{T}}^{\mathrm{trig},3}-p_{\mathrm{T}}^{\mathrm{trig},4}))=\frac{1}{N_{\mathrm{trig}}}\frac{\mathrm{d}N}{\mathrm{d}p_{\mathrm{T,jet}}^{\mathrm{ch}}}(p_{\mathrm{T}}^{\mathrm{trig},1}<p_{\mathrm{T}}^{\mathrm{trig}}<p_{\mathrm{T}}^{\mathrm{trig},2})-c\frac{1}{N_{\mathrm{trig}}}\frac{\mathrm{d}N}{\mathrm{d}p_{\mathrm{T,jet}}^{\mathrm{ch}}}(p_{\mathrm{T}}^{\mathrm{trig},3}<p_{\mathrm{T}}^{\mathrm{trig}}<p_{\mathrm{T}}^{\mathrm{trig},4})$$

The Δ_{recoil} spectrum for R=0.4 is shown in the left panel of Fig. 3 for hadron trigger intervals from 20-50 GeV/c and 15-20 GeV/c, using a scale factor $c = 0.956$. This novel variable allows us to study an unbiased sample of jets reconstructed with a large radius, maintaining a jet constituent cutoff as low as $p_{\mathrm{T}}^{\mathrm{const}} > 0.15$ GeV/c.

To explore the energy redistribution within recoil jets, we consider the ratio for the measured Δ_{recoil} distribution over PYTHIA (tune Perugia 2010) simulations ΔI_{AA}^{PYTHIA}, presented in the right panel of Fig. 3. We find consistent ΔI_{AA}^{PYTHIA} for different values of R and constituent p_{T} threshold [16] (not shown). Within present experimental uncertainties, we do not observe significant redistribution of the jet energy.

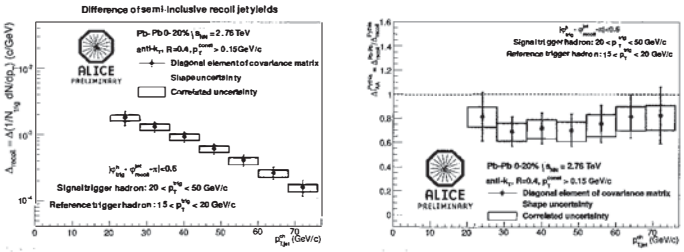

Figure 3: Semi-inclusive recoil jet spectrum difference Δ_{recoil} for 0-20% central collisions, $p_{\mathrm{T}}^{const} > 0.15$ GeV/c, jets reconstructed with anti-k_{T} for R=0.4 (left). Δ_{IAA} for recoil jets using PYTHIA as a reference (right).

References

1. M. Cacciari, G. P. Salam and G. Soyez, *Eur. Phys. J.* C **72**, 1896 (2012).
2. B. Abelev *et al.* [ALICE Collaboration], *arXiv:1301.3475 [nucl-ex].*
3. N. Armesto, private communication.
4. G. Soyez, *Phys. Lett.* B **698**, 59 (2011).
5. M. Vajzer [ALICE Collaboration] *arXiv:1212.6890 [nucl-ex].*
6. G. Aad *et al.* [ATLAS collaboration], Phys. Rev. D 84, 054001 (2011).
7. S. K. Prasad [ALICE Collaboration] *J. Phys. Conf. Ser.* **389**, 012005 (2012).
8. R. Ma [ALICE collaboration] *arXiv:1208.4537 [nucl-ex].*
9. T. Sjostrand, S. Mrenna and P.Z. Skands, *JHEP* **05**, 026 (2006).
10. S. Roesler, R. Engel and J. Ranft, Lisbon 2000 - Advanced Monte Carlo (2000), 1033-1038 *arXiv:0012252 [hep-ph].*
11. R. Reed [ALICE collaboration] *arXiv:1304.5945 [nucl-ex].*
12. S. Aiola [ALICE collaboration] *arXiv:1304.6668 [nucl-ex].*
13. M. Verweij [ALICE Collaboration] *arXiv:1208.8264 [nucl-ex].*
14. M. Verweij [ALICE Collaboration] *arXiv:1208.6169 [nucl-ex].*
15. B. Abelev *et al.* [ALICE Collaboration], *arXiv:1301.4361 [nucl-ex].*
16. L. Cunqueiro [ALICE Collaboration] *arXiv:1210.7610 [nucl-ex].*

HARD PROBES WITH ATLAS

I. GRABOWSKA-BOLD
for the ATLAS Collaboration

AGH University of Science and Technology, Al. Mickiewicza 30, Kraków, Poland

An overview of the latest results on high-transverse momentum particle production in lead-lead collisions at a center-of-mass energy $\sqrt{s_{NN}} = 2.76$ TeV obtained with the ATLAS detector is presented. Updated jet quenching measurements are discussed including inclusive jet suppression as a function of jet radius and a modification of jet fragmentation functions. Results on Z boson and isolated direct photon production are shown, also in conjunction with jets, which reveal a transverse momentum imbalance of the system. These results bring some further insight into parton shower modifications due to interactions with the medium. A majority of measurements use the entire statistics of the 2011 lead-lead run.

1 Introduction

Collisions between lead (Pb) ions at the Large Hadron Collider (LHC) are thought to create strongly interacting matter at temperatures well above the QCD critical temperature. The Relativistic Heavy Ion Collider (RHIC) has established [1] that at such temperatures, strongly interacting matter is expected to take the form of quark-gluon plasma (QGP). The energetic color charge carriers generated in hard-scattering processes during the initial stages of nuclear collisions are expected to lose energy in the QGP. Both RHIC and LHC experiments have reported a suppression of charged hadron yields by a factor of two at high transverse momenta in heavy-ion (HI) collisions [2,3,4]. On the other hand particles which are created in hard scatterings and whose products do not interact via the strong force, provide an alternative means to investigate the phenomenon of energy loss in the QGP. The PHENIX experiment at RHIC measured the properties of highly energetic photons [5] while the ATLAS and CMS experiments at the LHC provided in addition the first measurements of Z and W bosons decaying leptonically at the LHC energy [6,7,8,9]. In this context measurements of hard probes at the LHC are important as they are a valuable source of information on the matter produced in the ultra-relativistic Pb-Pb collisions.

The LHC commenced a HI program in two Pb-Pb runs which took place in 2010 and 2011 at $\sqrt{s_{NN}} = 2.76$ TeV per colliding nucleon pair. In this document a report on inclusive jet and electroweak boson measurements based on the entire data sample of 2011 from the ATLAS experiment will be given. These results give additional insight into behavior of jets in the QGP and confirm that electroweak boson production rates follow the scaling with a number of binary collisions.

2 Inclusive jets

Jets are considered to be one of the most direct probes to study hot matter through the process of *jet quenching*, which generally refers to the phenomenon by which a quark or a gluon can lose energy and/or have its parton shower modified in a medium of high color-charge density [10,11]. The ATLAS experiment has established a direct evidence of jet quenching, reporting on the modification of the dijet asymmetry distribution as a function of centrality in the early Pb-Pb data [12]. More recently the inclusive jet measurements have been released [13]. Jets were reconstructed in the calorimeter over the pseudorapidity interval $|\eta| < 2.1$ and over the transverse momentum range $38 < p_T < 210$ GeV using the anti-k_t algorithm with values for the distance parameter that determines the nominal jet radius of $R = 0.2$, 0.3, 0.4 and 0.5. The centrality dependence of the jet yield is characterized by the jet *central-to-peripheral ratio*, $R_{\rm cp}$, which is defined as a ratio of the central to peripheral events scaled by the number of binary nucleon-nucleon collisions, $N_{\rm coll}$. Jet production is found to be suppressed by approximately a factor of two in the 10% most central collisions relative to peripheral collisions as shown in the left panel of Fig. 1. The observed suppression is only weakly dependent on jet radius that is nonetheless significant when taking into account the correlations in the uncertainties between the different R values.

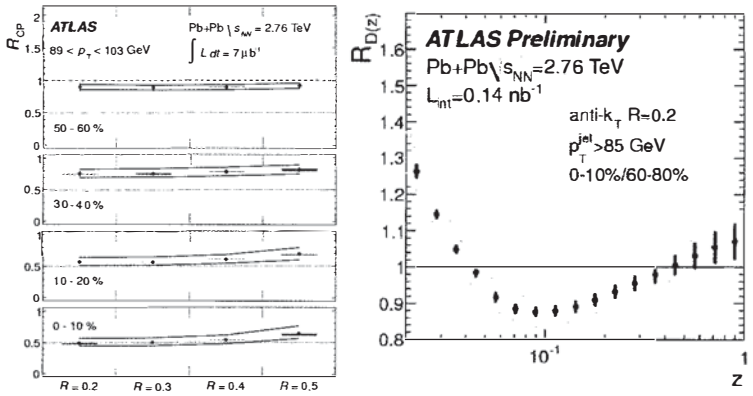

Figure 1: (left) $R_{\rm cp}$ as a function of jet radius for four centrality bins for jets with $89 < p_T < 103$ GeV [13]. (right) Ratios of the longitudinal fragmentation function, $D(z)$ for central (0-10%) collisions to those in peripheral (60-80%) collisions for $R = 0.2$ jets [14].

Different models of jet quenching predict different levels of modification of the jet internal structure. Both transverse and longitudinal structure of the jet are expected to be modified due to the medium-induced radiation. To quantify the effect of the jet modification the jet fragmentation functions have been measured as a function of z - the longitudinal fraction of the jet momentum carried by the charged particles [14]. The right panel of Fig. 1 shows a ratio of the longitudinal fragmentation functions, $D(z)$ for jets in the 0-10% centrality class to jets from the 60-80% centrality class. One can see an enhanced yield of low-z fragments and a suppressed yield of fragments at intermediate z values in more central collisions relative to the peripheral ones. The size of these observed modications was also found to decrease gradually with centrality between central and peripheral collisions.

3 Photon-jet Momentum Imbalance

Photons are hard probes which do not carry a color charge and as such they are expected not to interact with the QGP. Therefore, studying photon-jet pairs produced in hard scattering

processes offers the possibility of calibrating the energy of the initial jet. Recently ATLAS has reported on a measurement of production rates of isolated direct photons with transverse momenta $45 < p_T^{\gamma} < 200$ GeV and $|\eta^{\gamma}| < 1.3$ in Pb-Pb collisions [15]. It was found that photon production yields exhibit a linear scaling with the number of binary collisions.

More recently, a measurement of the correlation of back-to-back isolated prompt photons with jets as a function of transverse momentum and centrality has been done [16]. The left panel of Fig. 2 shows the energy fraction $x_{J\gamma} = p_T^{\rm jet}/p_T^{\gamma}$ for data and PYTHIA+Data [a] MC as a function of centrality represented by a number of participants, $N_{\rm part}$. In the peripheral centrality interval, $\langle x_{J\gamma} \rangle$ is just below what is obtained using the truth jet and true photon energies in the MC. As the centrality increases, the $\langle x_{J\gamma} \rangle$ systematically decreases, although quite slowly. However, the most central value is significantly different than the PYTHIA+Data prediction. The right panel of Fig. 2 shows an integrated yield of jets per photon, $R_{J\gamma}$ as a function of $N_{\rm part}$ in comparison to the PYTHIA+Data MC. As the centrality increases $R_{J\gamma}$ decreases significantly deviating from the MC.

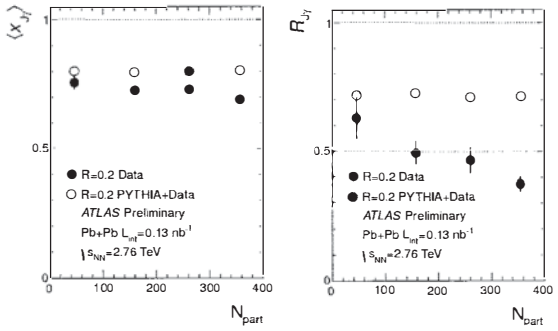

Figure 2: (left) The mean energy fraction $\langle x_{J\gamma} \rangle$ from fully corrected and unfolded distributions for $R = 0.2$ jets calculated as a function of $N_{\rm part}$ [16]. (right) The integrated yield of $R = 0.2$ jets per photon $R_{J\gamma}$ calculated as a function of $N_{\rm part}$ [16].

4 Z Boson Production

Like photons, weak bosons do not interact via strong forces, therefore they are supposed not to lose energy in the QGP. As such they are a perfect tool to calibrate energies of jets. The ATLAS experiment has performed a measurement of Z boson production decaying to di-muon and di-electron final states [18]. A left panel of Fig. 3 shows the invariant mass of selected electron and muon opposite signed signal pairs together with estimated combinatorial backgrounds from same sign pairs compared with the simulation normalized to the number of pairs in the region $66 < m_{ll} < 102$ GeV ($l = e, \mu$). The background contamination is less than 3% which makes this measurement very clean in particular in the context of Z+jet correlation studies [19]. The per-event yields of Z bosons have been extracted from the mass peak. These yields where scaled by the number of binary collisions, $N_{\rm coll}$, and are shown as a function of centrality represented by $N_{\rm part}$ for several Z boson transverse momentum intervals. Within the statistical significance of the data sample, the Z boson per-event yield obeys the binary collision scaling with centrality.

5 Summary

The updated results on high-transverse momenta particles from the ATLAS experiment based on Pb-Pb collisions from the 2010-11 LHC heavy-ion runs have been presented. Inclusive jets are found to be suppressed in central events by a factor of two relative to peripheral events,

[a] A hard process is generated by PYTHIA and embedded into a minimum-bias event from real data. The in-medium energy loss is not modelled.

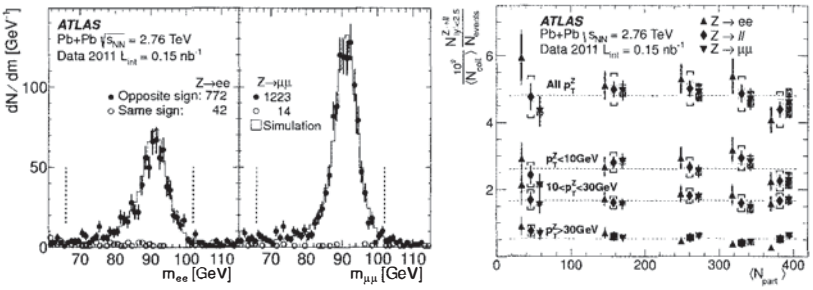

Figure 3: (left) The invariant mass distributions of $Z \to ee$ and $Z \to \mu\mu$ candidates, integrated over momentum, rapidity, and centrality [18]. (right) Centrality dependence of Z boson yields for di-electron, di-muon and combined data divided by $\langle N_{\rm coll} \rangle$ and a total number of minimum bias events $N_{\rm events}$ [18].

with no significant dependence on the jet size. At the same time jet fragmentation functions are found to be enhanced for fragments at low-z values followed by a suppression of intermediate-z fragments in the most central collisions relative to 60-80% centralities. Di-electron and di-muon pairs have been used to measure Z boson production yields which are found to scale linearly with a number of binary collisions. Events with photon-jet pairs have been analyzed to measure a transverse momentum imbalance. Both the mean energy fraction and the yield of jets per photon are found to be significantly reduced in the most central collisions. All these results may provide more insight into our understanding of the jet quenching phenomenon.

Acknowledgments

The author would like to thank the Heavy Ion session organizers for the invitation to speak at Moriond QCD 2013, and the ATLAS collaboration for their continued strong support of the ATLAS heavy-ion physics program. This work was supported in part by the National Science Center grant No. DEC-2011/03/B/ST2/02631. This research was supported in part by PL-Grid Infrastructure.

1. PHENIX Collaboration, *Nucl. Phys.* **A757**, 184-283 (2005).
2. PHENIX Collaboration, *Phys. Rev. Lett.* **93**, 152302 (2004).
3. ATLAS Collaboration, ATLAS-CONF-2012-120.
4. CMS Collaboration, *Eur. Phys. J.* **C72**, 1945 (2012).
5. PHENIX Collaboration, *Nucl. and Part. Phys.* **34**, no. 8, S1015 (2007).
6. ATLAS Collaboration, *Phys. Lett.* **B697**, 294-312 (2011).
7. CMS Collaboration, *J. Phys.* **G38**, 124132 (2011).
8. CMS Collaboration, *Phys. Lett.* **B715**, 66-87 (2012).
9. CMS Collaboration, *Phys. Lett.* **B710**, 256-277 (2012).
10. X.-N. Wang, M. Gyulassy, M. Plumer, *Phys. Rev.* **D51**, 3436-3446 (1995).
11. R. Baier, Y. L. Dokshitzer, A. H. Mueller, D. Schiff, *Phys. Rev.* **C58**, 1706-1713 (1998).
12. ATLAS Collaboration, *Phys. Rev. Lett.* **105**, 252303 (2010).
13. ATLAS Collaboration, *Phys. Lett.* **B719**, 220-241 (2013).
14. ATLAS Collaboration, ATLAS-CONF-2012-115.
15. ATLAS Collaboration, ATLAS-CONF-2012-051.
16. ATLAS Collaboration, ATLAS-CONF-2012-121.
17. ATLAS Collaboration, ATLAS-CONF-2011-074.
18. ATLAS Collaboration, *Phys. Rev. Lett.* **110**, 022301 (2013).
19. ATLAS Collaboration, ATLAS-CONF-2012-119.

Hard Probes in CMS

Yaxian Mao for the CMS Collaboration
Department of Physics and Astronomy, Vanderbilt University, Nashville, TN 37235, USA

This paper reviews recent experimental results on hard probes in heavy-ion collisions from the CMS Collaboration. These studies include various energy loss phenomena (jet nuclear modification factors, tagged b-quark jets, di-jet and photon-jet energy imbalance); observables characterizing jet properties like jet fragmentation function and jet shapes; and measurements of high-p_T charged hadrons from jet fragmentation (nuclear modification factors up to 100 GeV/c. All of the presented results utilize the high statistics PbPb data, about 150 μb^{-1}, collected in late 2011 at the LHC.

1 Introduction

Hard probes - processes involving scatterings with large momentum transfer - and their modification in Pb-Pb collisions with respect to pp collisions, can be used to study the transport properties of the hot quark-gluon plasma (QGP) medium created in heavy ion collisions at ultra-relativistic energies [1]. The objective is to understand how a color charge (carried by quarks and gluons) is transported in the colored medium. Among the observables, often chosen to be high p_T particles or jets, there are two categories: those that interact strongly and are thus expected to be modified, such as (charged) hadrons, inclusive jets and heavy-quark jets; and those that remain largely unmodified such as high-energy photons, Z^0 and $W^{\pm}$ bosons. The production of electroweak bosons can be used to calibrate the associated jet energy from $2 \rightarrow 2$ hard processes. The energy lost by energetic partons which traverse the hot and dense matter (in a phenomenon known as "jet quenching") measures the "stopping power" of the QGP, as well as its characteristic dependence on parton type (quark vs gluon), parton mass m (light vs. heavy quark), path length inside the medium, and parton energy. It is well established that the parton energy loss is a consequence of the modification of the hard-scattering processes in the final state of the heavy ion collisions at RHIC and LHC [2,3,4,5]. It is evident in the suppression of high p_T charged hadrons and jets, as well as in the associated yield in two-particle correlations measurements [6], which is accompanied by an enhancement of low p_T hadrons, suggesting a softening of jet fragmentations. The CMS experiment at the LHC is ideally suited to measure these hard probes, due to its large acceptance, good efficiency and low fake rate for track reconstructions, and high level trigger capable of full event reconstruction even in a high multiplicity environment [7]. Taking advantage of the high statistics data collected in 2011, the present analysis enables us to study the parton energy loss in more detail than previously possible.

In the following, we discuss the inclusive and b-tagged jet nuclear modification factor R_{AA}, the di-jets and $\gamma-$jets imbalance distribution, and the measurements of the jet fragmentation and the jet shapes.

2 Energy loss studies by inclusive jet properties

Jets are reconstructed using the anti-k_T jet algorithm, with a radius parameter R = 0.3, combining tracking and calorimetric information from CMS particle-flow (PF) objects [8,9]. The contribution of the underlying heavy-ion event is removed using an iterative pileup subtraction

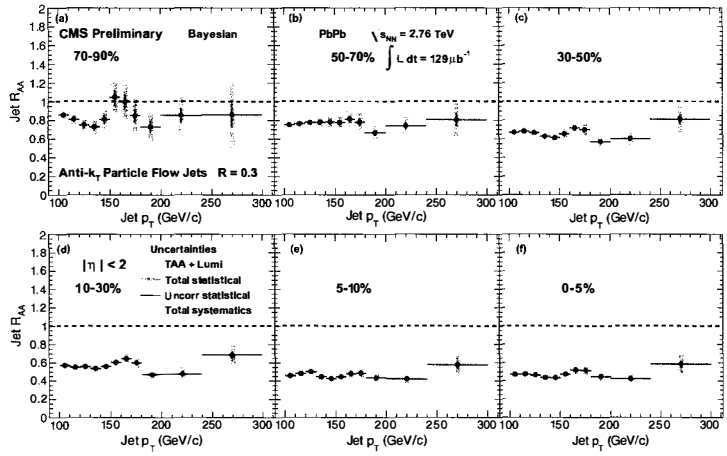

Figure 1: Nuclear modification factors, R_{AA}, for jets reconstructed with the anti-k_T algorithm using R = 0.3, after bayesion unfolding for jet p_T between 100 and 300 GeV/c in different centrality bins.

method [10]. In order to measure the inclusive jet p_T spectra in PbPb and compare them to the production in pp collisions, and form their ratios (nuclear modification factors, R_{AA}), scaled by the appropriate number of equivalent pp collisions, for each centrality bin, careful treatment of the jet energy resolutions, as well as the application of smearing or unfolding methods are necessary. The preliminiary results of the jet nuclear modification factors between 100 and 300 GeV/c of jet p_T are presented in Fig. 1, in six centrality bins, 0-5% representing the 5% most central PbPb collisions. A suppression of the jet yield reconstructed from PbPb data is observed, which is independent of the jet p_T, and increases reaching a value of about 0.5 in the most central events [11]. The jet nuclear modification factors can be compared to those of charged particles [3], and the similarity of R_{AA} obtained for charged particles in the 50 – 100 GeV/c, and for jets in the 100 – 200 GeV/c range, which implies that the hard part of the jet fragmentation in pp and PbPb collisions are very similar, taking into account that high p_T leading charged particles typically originate from the fragmentation of jets with about two times larger transverse momentum.

The inclusive jets are dominated by gluon- and light quark-jets. The parton energy loss is expected to be different for light and heavy flavor quarks due to their mass difference, arousing interest in the seperation of b-quark jets. The b-quark jets can be experimentally recognized by the presence of a B-hadron, creating a high-mass secondary vertex at its decay point. The purity of b-jet tagging is determined from template fits to the secondary vertex invariant mass distribution, and the efficiency of the secondary vertex tagging can be estimated in a data-driven way. Thus, the fraction of b-jet among inclusive jets can be measured as a function of transverse momentum after purity and efficiency corrections. The fraction of b-jets in pp and PbPb collisions are comparable, with no p_T dependence observed, indicating that b-quark jets are quenched similarly as light quark jets, i.e. the R_{AA} value is ~ 0.5 [12].

High energy photons are not modified by the strongly interacting medium, therefore serve as an energy tag for the jet parter in $\gamma-$jet events. These collisions produce a jet and a photon approximately back-to-back in azimuth, with similar transverse momenta. The ratio between momenta is denoted as $x_{J\gamma} = p_T^{jet}/p_T^{\gamma}$. The measured distribution of $x_{J\gamma}$ in central PbPb collisions is shifted to lower values with respect to the distribution in pp collisions [13]. The mean value of this ratio, $< x_{J\gamma} >$, is presented on the left panel of Fig. 2 as a function of

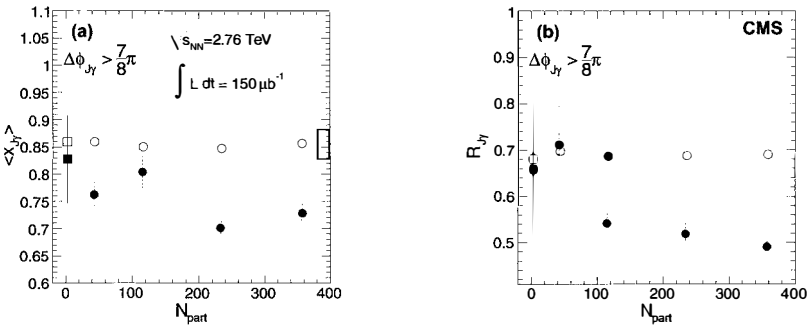

Figure 2: The average ratio of jet transverse momentum to photon transverse momentum, $< x_{J\gamma} >$ (left), and the average fraction of isolated photons are associated to a partner jet above 30 GeV/c, $R_{J\gamma}$ (right), as a function of N_{part} from PbPb (red) and pp (black rectangle) collisions and MC simulation (open circle).

the number of nucleons participating in the PbPb collision, N_{part}, used for characterizing the collision centrality. The filled rectangle indicates the results obtained from pp data taken at 2.76 TeV, limited by statistic uncertainties, but in agreement with pp events simulated by PYTHIA Monte Carlo generator, embedded in PbPb events simulated by HYDJET where no medium effect is included. While the pp reference shows almost no dependence of $< x_{J\gamma} >$ on centrality, the γ–jet PbPb events exhibit a significantly lower ratio in most central events. The right panel on Fig. 2 shows the average fraction of isolated photons that are associated to a partner jet with p_T above 30 GeV/c, $R_{J\gamma}$, as a function of N_{part}. In central PbPb events, a significant fraction of isolated photons lost their jet partner compared to pp reference. Therefore, a sizeable jet (parton) energy loss is observed in the γ–jet channel, similarly to the di-jet studies [14].

3 Anatomy of the jets

A significant amount of jet quenching was observed in inclusive jet, di-jet and γ–jet events. Those observations raise questions related to the parton energy loss mechanism: how do partons lose their energy in the nuclear medium? Does the energy loss changes the fragmentation pattern of the jets and modify the jet shape? Measurements of jet fragmentation properties provide an experimental constraint which is complementary to the measurement of the global jet properties, and can also be used to connect the jet observables to the measurements of high p_T particle production.

For the present analysis, the events with jets above $p_T > 100$ GeV/c within $0.3 < |\eta| < 2$ region are selected, where the jet trigger is fully efficient. The central pseudorapidity region $|\eta| < 0.3$ is excluded to avoid jet cones overlapping with the η-reflected cone used for the background estimation. The minimum transverse momentum for tracks entering the analysis is set to 1 GeV/c.

The jet shapes, $\rho(r)$, describing how the transverse momentum of the particles comprising the jet is distributed radially with respect to the jet axis $r = \sqrt{(\eta_{jet} - \eta_{trk})^2 + (\phi_{jet} - \phi_{trk})^2}$, are studied. The measured jet shapes in PbPb collisions are compared with the shapes obtained in pp collisions (Fig. 3 of top panels), with their ratios shown in the bottom panels. The ratios are close to unity for non-central collisions (50-100%), and show a rising trend towards large radii r for the mid-central and most central collisions (10–30% and 0–10%). This observed enhancement is consistent with the excess in the low p_T part of jet fragmentation functions, defined as the distribution of $\xi = ln(p^{jet}/p_{||}^{track})$, where $p_{||}^{track}$ is the projection of the track momentum onto the jet axis [15]. The jet shape and fragmentation function results indicate that suppression of

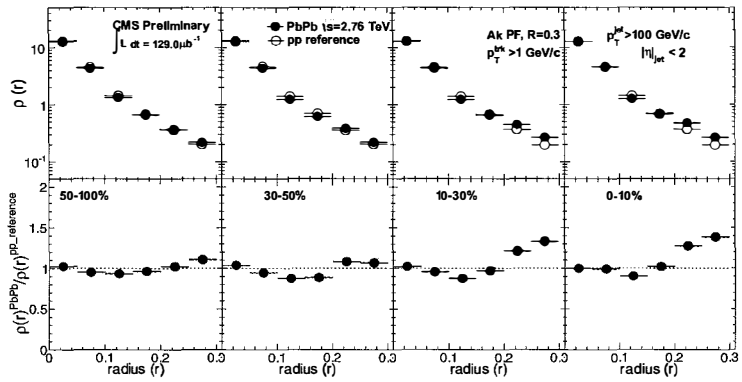

Figure 3: Differential jet shapes in PbPb and pp collisions for $p_T^{jet} > 100$ GeV/c with track $p_T > 1$ GeV/c (top panels) and the ratio of the PbPb and pp jet shapes (bottom panels).

intermediate p_T particles is transported to larger radii with low p_T particles enhancements by energy redistribution.

4 Summary

The CMS experiment has shown that the heavy quark jets quench the similar way as light quark jets, with no strong dependence on jet p_T. The photon-jet correlations support the di-jet quenching picture. Jet shapes and fragmentation functions indicate an energy transport to large distance from the jet axis (low p_T enhancement) from smaller jet radii (intermediate p_T suppression), consistent with results from two-particle correlation measurements[6]. In summary, the jet quenching picture painted by CMS hard probe results has become more precise, detailed and quantitative, providing a new insight into the behavior of the high energy density medium formed in heavy-ion collisions.

References

1. Bjorken, J. D., *FERMILAB-PUB-82-059-THY* 1982.
2. Shimomura M., *arXiv: nucl-ex/0510023* 2005.
3. CMS Collaboration, *Eur. Phys. J. C* **72** 1945 2012.
4. ATLAS Collaboration, *Phys. Rev. Lett.* **105**, 252303 (2010).
5. ALICE Collaboration, *Phys. Lett.* B **696**, 30 (2011).
6. CMS Collaboration, *CMS-PAS-HIN-12-010* 2012.
7. CMS Collaboration, *JINST* **3** S08004 2008.
8. CMS Collaboration, *CMS-PAS-PFT-09-00* 2009.
9. CMS Collaboration, *CMS-PAS-PFT-10-002* 2010.
10. Kodolova, O. *et. al.*, *Eur. Phys. J.* C **50**, 117 (2007) .
11. CMS Collaboration, *CMS-PAS-HIN-12-004* 2012.
12. CMS Collaboration, *CMS-PAS-HIN-12-003* 2012.
13. CMS Collaboration, *Phys. Lett.* B **718**, 773 (2013).
14. CMS Collaboration, *Phys. Lett.* B **712**, 176 (2012).
15. CMS Collaboration, *CMS-PAS-HIN-12-013* 2012.

Jet tomography of AA-collisions at RHIC and LHC energies

B.G. ZAKHAROV
L.D. Landau Institute for Theoretical Physics, GSP-1, 117940, Kosygina Str. 2, 117334 Moscow, Russia

We present our recent results on jet tomography of AA-collisions at RHIC and LHC. We focus on fiavor dependence of the nuclear modification factor. The computations are performed accounting for radiative and collisional parton energy loss with running coupling constant.

1. In this talk I present results of jet tomographic analysis of the RHIC and LHC data on the nuclear modification factor R_{AA} for light hadrons, single electrons, and D-mesons. A major purpose of this study is to examine whether it is possible in the pQCD picture of parton energy loss in the quark-gluon plasma (QGP) to describe simultaneously quenching of light and heavy flavors. One can expect that predictions for variation of R_{AA} from light to heavy flavors should be more robust than that for R_{AA} itself, which have significant theoretical uncertainties. The analysis is based on the light-cone path integral approach [1,2]. We evaluate R_{AA} using the scheme developed in [3].

2. We define the nuclear modification factor for a given impact parameter b as

$$R_{AA}(b) = \frac{dN(A+A \to h+X)/d\mathbf{p}_T dy}{T_{AA}(b) d\sigma(N+N \to h+X)/d\mathbf{p}_T dy}\,, \tag{1}$$

where $\mathbf{p}_T$ is the particle transverse momentum, y is rapidity (we consider the central region near $y=0$), $T_{AA}(b) = \int d\boldsymbol{\rho} T_A(\boldsymbol{\rho}) T_A(\boldsymbol{\rho}-\mathbf{b})$, T_A is the nucleus profile function. We write the differential yield for $A+A \to h+X$ process in the numerator in the form

$$\frac{dN(A+A \to h+X)}{d\mathbf{p}_T dy} = \int d\boldsymbol{\rho} T_A(\boldsymbol{\rho}) T_A(\boldsymbol{\rho}-\mathbf{b}) \frac{d\sigma_m(N+N \to h+X)}{d\mathbf{p}_T dy}\,, \tag{2}$$

where $d\sigma_m(N+N \to h+X)/d\mathbf{p}_T dy$ is the medium-modified cross section for the $N+N \to h+X$ process. As in the ordinary pQCD formula, we write it as

$$\frac{d\sigma_m(N+N \to h+X)}{d\mathbf{p}_T dy} = \sum_i \int_0^1 \frac{dz}{z^2} D^m_{h/i}(z,Q) \frac{d\sigma(N+N \to i+X)}{d\mathbf{p}_T^i dy}\,, \tag{3}$$

where $\mathbf{p}_T^i = \mathbf{p}_T/z$ is the parton transverse momentum, $d\sigma(N+N \to i+X)/d\mathbf{p}_T^i dy$ is the hard cross section, $D^m_{h/i}$ is the medium-modified fragmentation function (FF) for transition of a parton i into the observed particle h. For the parton virtuality scale Q we take the parton transverse momentum p_T^i.

In first approximation, overlap between the DGLAP and induced stages of the parton showering can be neglected at $p_T \lesssim 100$ GeV [3]. Then, assuming that the final particle h is formed outside the medium, the medium-modified FF can be written as

$$D^m_{h/i}(Q) \approx D_{h/j}(Q_0) \otimes D^{in}_{j/k} \otimes D_{k/i}(Q)\,. \tag{4}$$

Here $\otimes$ denotes z-convolution, $D_{k/i}$ is the ordinary DGLAP FF for $i \to k$ parton transition, $D^{in}_{j/k}$ is the FF for $j \to k$ parton transition in the QGP due to induced gluon emission, and $D_{h/j}$ describes fragmentation of the parton j into the detected particle h outside of the QGP.

We computed the DGLAP FFs with the help of the PYTHIA event generator [4]. For the stage outside the QGP for light partons we use for $D_{h/j}(Q_0)$ the KKP [5] FFs with $Q_0 = 2$ GeV. We treat the formation of single electrons from heavy quarks as the two-step fragmentations $c \to D \to e$ and $b \to B \to e$. For the $c \to D$ and $b \to B$ transitions we use the Peterson FF with parameters $\epsilon_c = 0.06$ and $\epsilon_b = 0.006$. The z-distributions for the $B/D \to e$ transitions have been calculated using the CLEO data [6,7] on the electron spectra in the B/D-meson decays. We did not include the $B \to D \to e$ process, which gives a negligible contribution.

The one gluon induced spectrum has been computed using the method elaborated in [8]. We take $m_q = 300$ and $m_g = 400$ MeV for the quark and gluon quasiparticle masses, for heavy quarks we take $m_c = 1.2$ GeV, and $m_b = 4.75$ GeV. We use the Debye mass obtained in the lattice calculations [9] that give $\mu_D/T \sim 2.5 \div 3$. We use the running α_s frozen at some value α_s^{fr} at low momenta. For vacuum a reasonable choice is $\alpha_s^{fr} \approx 0.7$ [10]. In plasma α_s can be reduced due to thermal effects, and we regard α_s^{fr} as a free parameter of the model. The multiple gluon emission has been accounted for employing Landau's method (for details see [3]).

We incorporate the collisional energy loss, which is relatively small [11], by renormalizing the initial temperature of the QGP, T_0, for the radiative FFs according to the following condition: $\Delta E_{rad}(T_0') = \Delta E_{rad}(T_0) + \Delta E_{col}(T_0)$, where $\Delta E_{rad/col}$ is the radiative/collisional energy loss, T_0 is the real initial temperature of the QGP, and T_0' is the renormalized temperature. We calculate the collisional energy loss within Bjorken's method with an accurate treatment of kinematics of the $2 \to 2$ processes (for details see [11]) with the same parametrization of $\alpha_s(Q)$ as for the radiative one.

We calculate the hard cross sections using the LO pQCD formula with the CTEQ6 [12] PDFs. To simulate the higher order K-factor we take for the virtuality scale in α_s the value cQ with $c = 0.265$ as in the PYTHIA event generator [4]. The nuclear modification of the parton densities (which leads to some small deviation of R_{AA} from unity even without parton energy loss) has been incorporated with the help of the EKS98 correction [13].

We describe the QGP in the Bjorken model with 1+1D expansion, which gives $T_0^3 \tau_0 = T^3 \tau$. We take $\tau_0 = 0.5$ fm. For simplicity we ignore variation of the initial temperature T_0 in the transverse directions in the overlapping of two nuclei. We fix T_0 using the entropy/multiplicity ratio $dS/dy \Big/ dN_{ch}/d\eta \approx 7.67$ obtained in [14]. It gives for central Au+Au collisions at $\sqrt{s} = 200$ GeV $T_0 \approx 320$ MeV and for Pb+Pb collisions at $\sqrt{s} = 2.76$ TeV $T_0 \approx 420$ MeV. The fast parton path length in the QGP, L, has been calculated according to the geometry of the hard process and AA-collision. To account for the fact that at times about $1 \div 2$ units of the nucleus radius the transverse expansion should lead to a fast cooling of the hot QCD matter we impose the condition $L < L_{max}$. We take $L_{max} = 8$ ($L_{max} = 10$ fm gives almost the same).

3. Fig. 1 shows comparison of our predictions for R_{AA} for $\alpha_s^{fr} = 0.4$ and 0.5 in 0–5% centrality bin for (a) π^0-mesons in Au+Au collisions at $\sqrt{s} = 200$ GeV to PHENIX data [15], and for (b,c) charged hadrons in Pb+Pb collisions at $\sqrt{s} = 2.76$ TeV to (b) ALICE [16] and (c) CMS [17] data. We show the total R_{AA} with radiative and collisional energy loss and for purely radiative energy loss. One can see that the effect of the collisional mechanism is relatively small (especially for LHC). We present the results for $p_T \gtrsim 5$ GeV since for smaller momenta our calculations of the induced gluon emission (based on the relativistic approximation) are hardly robust. Fig. 1 shows that for light hadrons the window $\alpha_s^{fr} \sim 0.4 \div 0.5$ leads to a reasonable magnitude of R_{AA}. For RHIC the agreement of the theoretical R_{AA} (radiative plus collisional energy loss) with the data is better for $\alpha_s^{fr} = 0.5$. And for LHC the value $\alpha_s^{fr} = 0.4$ seems to be preferred by the data (if one considers the complete p_T range).

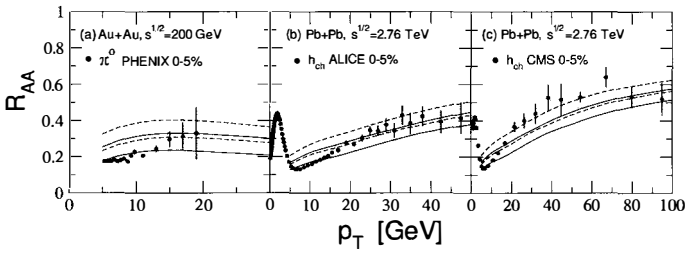

Figure 1: (a) R_{AA} for π^0 for 0–5% central Au+Au collisions at $\sqrt{s} = 200$ GeV from our calculations compared to data from PHENIX [15]. (b,c) R_{AA} for charged hadrons for 0–5% central Pb+Pb collisions at $\sqrt{s} = 2.76$ TeV from our calculations compared to data from (b) ALICE [16] and (c) CMS [17]. Systematic experimental errors are shown as shaded areas. The curves show our calculations for radiative and collisional energy loss (solid), and for purely radiative energy loss (dashed) for $\alpha_s^{fr} = 0.4$ (upper curves) and 0.5 (lower curves).

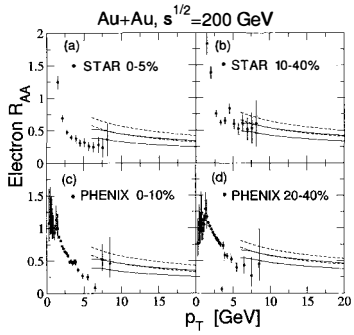

Figure 2: The electron R_{AA} in Au+Au collisions at $\sqrt{s} = 200$ GeV for (a) 0–5%, (b) 10–40%, (c) 0–10%, (d) 20–40% centrality classes. The curves show calculations for radiative and collisional energy loss (solid), and for purely radiative energy loss (dashed) including charm and bottom contributions for $\alpha_s^{fr} = 0.4$ (upper curves) and 0.5 (lower curves). Data points are from STAR [19] and PHENIX [20]. Systematic errors are shown as shaded areas.

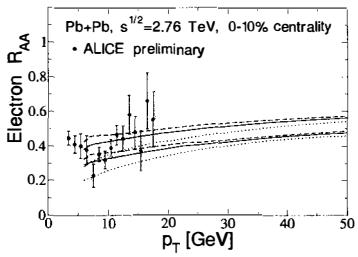

Figure 3: The electron R_{AA} for 0–10% central Pb+Pb collisions at $\sqrt{s} = 2.76$ TeV for $\alpha_s^{fr} = 0.4$ (upper curves) and 0.5 (lower curves). The total $c+b \to e$ R_{AA} (solid), $c \to e$ (dashed), $b \to e$ (dotted) with collisional energy loss. Data points are the preliminary ALICE data [21]. Systematic errors are shown as shaded areas.

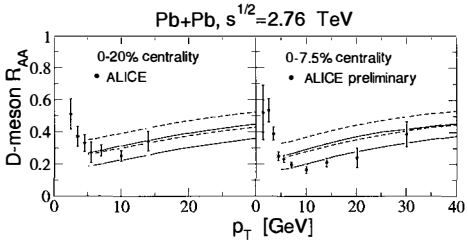

Figure 4: R_{AA} of D-mesons for 0–20% (left) and 0–7.5% (right) central Pb+Pb collisions at $\sqrt{s} = 2.76$ TeV for $\alpha_s^{fr} = 0.4$ (upper curves) and 0.5 (lower curves). The solid line: radiative and collisional energy loss. The dashed line: purely radiative mechanism. Data points are from ALICE [22] (left), [23] (right). Systematic errors are shown as shaded areas.

The tendency of the decrease of α_s^{fr} from RHIC to LHC, observed first in [18], is natural, since the thermal reduction of α_s should be stronger at the LHC energies. Thus, the values $\alpha_s^{fr} = 0.5$ and 0.4 seem to be reasonable benchmarks for calculations of nuclear suppression for heavy flavors at RHIC and LHC energies.

In Fig. 2 we compare results of our model with STAR [19] and PHENIX [20] data on the electron R_{AA}. In Fig. 2 we show the total (charm plus bottom) R_{AA} with and without collisional energy loss. Comparison to the data from ALICE [21] is shown in Fig. 3. There we show the total (charm plus bottom) and separately charm and bottom R_{AA} with collisional energy loss. Figs. 2, 3 demonstrate that the same window of α_s^{fr} as for light hadrons leads to a quite satisfactory agreement with data on the

electron R_{AA}. Similarly to data for light hadrons the electron data support $\alpha_s^{fr} \approx 0.5$ for RHIC, and $\alpha_s^{fr} \approx 0.4$ for LHC. Thus, the simultaneous description of the nuclear suppression of light hadrons and single electrons in the pQCD picture seems quite possible.

In Fig. 4 we compare our results with the ALICE data [22,23] on the R_{AA} for D-mesons in Pb+Pb collisions at $\sqrt{s} = 2.76$ TeV for 0–20% and 0–7.5% centrality bins. Fig. 4 shows the results for the $c \to D$ fragmentation. We have found that the process $b \to B \to D$ increases R_{AA} only by about 2%. From Fig. 4 we can conclude that the same window in α_s^{fr} as for light hadrons allows to obtain a fairly reasonable description of the D-meson data as well.

4. In summary, we have analyzed the RHIC and LHC data on R_{AA} for light hadrons, single electrons, and D-mesons. We have found that once α_s is fixed from data on R_{AA} for light hadrons it gives a satisfactory agreement with data on the electron and D-meson R_{AA} as well. Our results give support for the pQCD picture of parton energy loss both for light and heavy flavors.

Acknowledgments

I am grateful to the organizers for such an enjoyable and stimulating meeting and for financial support of my participation.

References

1. B.G. Zakharov, JETP Lett. **63**, 952 (1996); *ibid* **65**, 615 (1997); **70**, 176 (1999); Phys. Atom. Nucl. **61**, 838 (1998).
2. R. Baier, D. Schiff, and B.G. Zakharov, Ann. Rev. Nucl. Part. **50**, 37 (2000).
3. B.G. Zakharov, JETP Lett. **88**, 781 (2008) [arXiv:0811.0445].
4. T. Sjostrand, L. Lonnblad, S. Mrenna, and P. Skands, arXiv:hep-ph/0308153.
5. B.A. Kniehl, G. Kramer, and B. Potter, Nucl. Phys. B**582**, 514 (2000).
6. A.H. Mahmood *et al.* [CLEO Collaboration], Phys. Rev. D**70**, 032003 (2004).
7. R. Poling, invited talk at 4th Flavor Physics and CP Violation Conference, Vancouver, British Columbia, Canada, 9-12 Apr 2006, arXiv:hep-ex/0606016.
8. B.G. Zakharov, JETP Lett. **80**, 617 (2004) [arXiv:hep-ph/0410321].
9. O. Kaczmarek and F. Zantow, Phys. Rev. D**71**, 114510 (2005).
10. N.N. Nikolaev and B.G. Zakharov, Phys. Lett. B**327**, 149 (1994).
11. B.G. Zakharov, JETP Lett. **86**, 444 (2007) [arXiv:0708.0816].
12. S. Kretzer, H.L. Lai, F. Olness, and W.K. Tung, Phys. Rev. D**69**, 114005 (2004).
13. K.J. Eskola, V.J. Kolhinen, and C.A. Salgado, Eur. Phys. J. C**9**, 61 (1999).
14. B. Müller and K. Rajagopal, Eur. Phys. J. C**43**, 15 (2005).
15. A. Adare *et al.* [PHENIX Collaboration], arXiv:1208.2254.
16. B. Abelev *et al.* [ALICE Collaboration], Phys. Lett. B**720**, 52 (2013).
17. S. Chatrchyan *et al.* [CMS Collaboration], Eur. Phys. J. C**72**, 1945 (2012).
18. B.G. Zakharov, JETP Lett. **93**, 683 (2011) [arXiv:1105.2028].
19. B.I. Abelev *et al.* [STAR Collaboration], Phys. Rev. Lett. **98**, 192301 (2007) [arXiv:nucl-ex/0607012], Erratum-ibid. 106 (2011) 159902.
20. A. Adare *et al.* [PHENIX Collaboration], Phys. Rev. C**84**, 044905 (2011).
21. S. Sakai, for the ALICE Collaboration, contribution to the Quark Matter 2012 Conf., http://qm2012.bnl.gov/default.asp.
22. B. Abelev *et al.* [ALICE Collaboration], JHEP **1209**, 112 (2012) [arXiv:1203.2160].
23. A. Grelli, for the ALICE Collaboration, contribution to the Quark Matter 2012 Conf., http://qm2012.bnl.gov/default.asp

FROM JET QUENCHING TO WAVE TURBULENCE

E. IANCU
Institut de Physique Théorique de Saclay
F-91191 Gif-sur-Yvette, FRANCE

We discuss average properties of the gluon cascade generated by an energetic parton propagating through a dense QCD medium. The cascade is mostly made with relatively soft gluons, whose production is not suppressed by the LPM effect. Unlike for usual QCD cascades in the vacuum, where the typical splittings are very asymmetric (soft and collinear), the medium–induced branchings are quasi–democratic and lead to wave turbulence. This results in a very efficient mechanism for the transport of energy at large angles with respect to the jet axis, which might explain the di–jet asymmetry observed in Pb–Pb collisions at the LHC.

One remarkable phenomenon discovered in the lead–lead collisions at the LHC is the *di–jet asymmetry*, a strong imbalance between the energies of two back–to–back jets. This asymmetry is commonly attributed to the effect of the interactions of one of the two jets with the dense QCD matter that it traverses, while the other leaves the system unaffected. Originally identified[1,2] as missing energy, this phenomenon has been subsequently shown[3] to consist in the transport of a sizable part (about 10%) of the total jet energy by *soft particles* towards *large angles*. The total amount of energy which is thus lost by the jet, ~ 20 GeV, is considerably larger than the typical transverse momentum, ~ 1 GeV, of a parton in the medium. In that sense, the effect is large and potentially non–perturbative. Yet, there exists a mechanism within perturbative QCD which can naturally explain the energy loss at large angles: the BDMPSZ mechanism for medium–induced gluon radiation (from Baier, Dokshitzer, Mueller, Peigné, Schiff[4] and Zakharov[5]). Most previous studies within this approach have focused on the energy lost by the leading particle, which is controlled by rare and relatively hard emissions at small angles. More recently, in the wake of the LHC data, the attention has been shifted towards softer emissions, for which the effects of *multiple branching* become important. The generalization of the BDMPSZ formalism to multiple branchings has only recently been given[6,7], and this turns out to have interesting physical consequences[8]. These recent developments will be briefly reviewed in what follows.

The BDMPSZ mechanism relates the radiative energy loss by an energetic parton propagating through a dense QCD medium ('quark–gluon plasma') to the transverse momentum broadening via scattering off the medium constituents. A central concept is the *formation time* $\tau_f(\omega)$ — the typical times it takes a gluon with energy $\omega \ll E$ to be emitted. (E is the energy of the original parton, a.k.a. the 'leading particle'.) The gluon starts as a virtual fluctuation which moves away from its parent parton via quantum diffusion: the transverse[a] separation $b_\perp$ grows with time as $b_\perp^2 \sim \Delta t/\omega$. The gluon can be considered as 'formed' when it loses coherence w.r.t to its source, meaning that $b_\perp$ is at least as large as the gluon transverse wavelength $\lambda_\perp = 1/k_\perp$. But the gluon transverse momentum $k_\perp$ is itself increasing with time, via collisions

[a]The 'transverse directions' refer to the 2–dimensional plane orthogonal to the 3–momentum of the leading particle, which defines the 'longitudinal axis'.

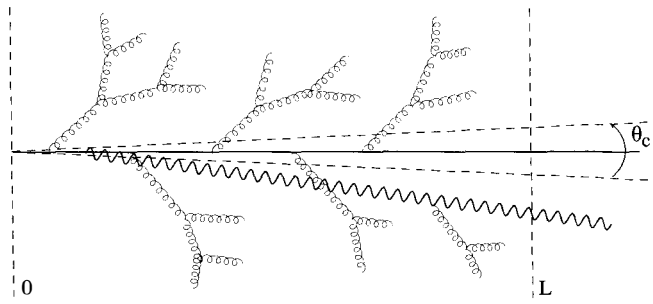

Figure 1: The jet produced in a 'rare event' which, besides the leading particle and the (quasi–deterministic) soft gluon cascades at large angles, also contains a hard gluon with $\omega \sim \omega_c$, which propagates at a small angle $\theta \sim \theta_c$.

which add random kicks $\Delta k_\perp$ at a rate given by the *jet quenching parameter* $\hat{q}$: $\Delta k_\perp^2 \sim \hat{q}\Delta t$. The 'formation' condition, $b_\perp \gtrsim 1/\Delta k_\perp$ for $\Delta t \gtrsim \tau_f$, implies (below, k_f and θ_f are the typical values of the gluon transverse momentum and emission angle at the time of formation)

$$\tau_f(\omega) \simeq \sqrt{\frac{2\omega}{\hat{q}}}, \qquad k_f^2 = \hat{q}\tau_f(\omega) \simeq (2\omega\hat{q})^{1/2}, \qquad \theta_f \simeq \frac{k_f}{\omega} \simeq \left(\frac{2\hat{q}}{\omega^3}\right)^{1/4}. \tag{1}$$

Eq. (1) applies as long as $\ell \ll \tau_f(\omega) < L$, where L is the length of the medium and ℓ is the mean free path between successive collisions. The second inequality implies an upper limit on the energy of a gluon that can be emitted via this mechanism, and hence a lower limit on the emission angle: $\omega \lesssim \omega_c \equiv \hat{q}L^2/2$ and $\theta_f \gtrsim \theta_c \equiv 2/(\hat{q}L^3)^{1/2}$. The BDMPSZ regime corresponds to[b] $\hat{q}L^3 \gg 1$ and hence $\theta_c \ll 1$. Choosing $\hat{q} = 1\,\mathrm{GeV}^2/\mathrm{fm}$ (the weak coupling estimate [4] for a QGP with temperature $T = 250$ MeV) and $L = 4$ fm, one finds $\omega_c \simeq 40$ GeV and $\theta_c \simeq 0.05$.

Eq. (1) shows that the relatively soft gluons with $\omega \ll \omega_c$ have (i) short formation times $\tau_f(\omega) \ll L$ and (ii) large formation angles $\theta_f \gg \theta_c$. Both properties are important for us here. Property (i) implies that such gluons are produced *abundantly* : their emission can be initiated at any place inside the medium, hence the associated spectrum (below, $\bar{\alpha} \equiv \alpha_s N_c/\pi$)

$$\omega\frac{\mathrm{d}N}{\mathrm{d}\omega} \simeq \frac{\alpha_s N_c}{\pi}\frac{L}{\tau_f(\omega)} = \bar{\alpha}\sqrt{\frac{\omega_c}{\omega}}, \tag{2}$$

is enhanced by a factor $L/\tau_f(\omega) \gg 1$, which expresses the relative longitudinal phase–space available for their emission. Property (ii) shows that the soft gluons have the potential to transport a part of the jet energy towards large angles. This looks like a small effect, since soft gluons carry only little energy, but this is enhanced by multiple emissions, as we shall see.

Eq. (2) is the BDMPSZ spectrum for a soft, medium–induced, gluon emission [4,5]. Note that the emission probability is small, of $\mathcal{O}(\bar{\alpha})$, for a relatively hard gluon with $\omega \sim \omega_c$. This is a consequence of the *LPM effect* (from Landau, Pomeranchuk, Migdal) — the fact that one needs a large number $\tau_f(\omega)/\ell \gg 1$ of successive scatterings in order to produce a single gluon. Such a rare but hard emission dominates the average energy loss by the leading particle, $\Delta E \equiv \int^{\omega_c} \mathrm{d}\omega\,\omega(\mathrm{d}N/\mathrm{d}\omega) \sim \bar{\alpha}\omega_c$, but it cannot contribute to the observed di–jet asymmetry, because a hard gluon propagates at a very small angle $\sim \theta_c$ w.r.t. the jet axis.

To understand di–jet asymmetry, one rather needs to focus on soft gluon emissions at large angles. For such emissions, the effects of *multiple branching* become important, as we now explain. The probability for a single emission, as measured by the spectrum (2), exceeds unity when $\omega \lesssim \bar{\alpha}^2\omega_c$. In this non–perturbative regime at small ω, Eq. (2) must be corrected to

[b] One can estimate $\hat{q} \simeq m_D^2/\ell$, where m_D is the Debye screening mass in the medium. Eq. (1) applies to a medium whose size L is much larger than both the screening length $1/m_D$ and the mean free path ℓ.

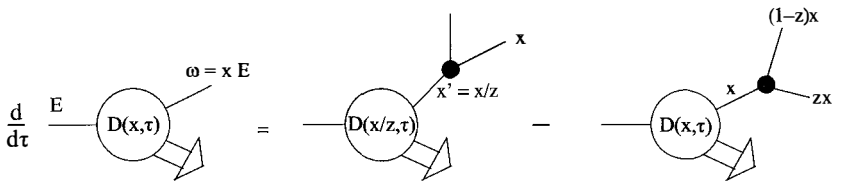

Figure 2: The change in the gluon spectrum $D(x,\tau) \equiv x(\mathrm{d}N/\mathrm{d}x)$ due to one additional branching $g \to gg$.

account for multiple emissions by the leading particle, and also for the subsequent branching of the soft primary gluons into even softer ones (thus leading to gluon cascades; see Fig. 1). The soft branchings are quasi–deterministic and can be observed in an event–by–event basis.

The treatment of multiple branching is *a priori* complicated by interference effects between emissions from different partonic sources. For the case of a jet evolving into the vacuum, such effects are known to lead to *angular ordering* between the successive emissions. Interference effects for medium–induced gluon radiation started to be investigated only recently[6,9,10,7]. The respective analysis is quite involved, but its main conclusion is very simple[7]: the interference effects for soft emissions of the BDMPSZ type are *negligible*, since suppressed by a factor $\tau_f(\omega)/L \ll 1$. To understand this result, recall that, in order to interfere with each other, two emitters must be *coherent* which each other, a situation which can occur if they have a common ancestor. However, the partons produced by a medium–induced branching lose their mutual *colour coherence* already during the formation process, because they randomly scatter in the medium. Accordingly, they can interfere with each other only during a short time $\tau_f(\omega)$, which gives a small phase–space whenever $\omega \ll \omega_c$. This implies that successive medium–induced emissions can be considered as *independent* of each other and taken into account via a *probabilistic branching process*, in which the BDMPSZ spectrum plays the role of the elementary branching rate[c].

The general branching process is a Markovian process in 3+1 dimensions which describes the gluon distribution in energy (ω) and transverse momentum ($k_\perp$), and its evolution when increasing the medium size L. This process is well suited for numerical studies via Monte–Carlo simulations. But analytic results have also been obtained [8], for a simplified process in 1+1 dimensions, which describes the energy distribution alone. These results lead to an interesting physical picture that we shall now describe.

To that aim, it is convenient to focus on the *gluon spectrum* $D(x,\tau) \equiv x(\mathrm{d}N/\mathrm{d}x)$, where $x \equiv \omega/E$ is the energy fraction carried by a gluon from the jet and the 'evolution time' τ is the medium size in dimensionless units, as defined in Eq. (3) below. The quantity $D(x,\tau)$ obeys an evolution equation [8,11,13], which is formally similar to the DGLAP equation describing the fragmentation of a jet in the vacuum: a rate equation, which involves a 'gain' term and a 'loss' term and is illustrated in Fig. 2. The 'gain' term describes the increase in the number of gluons with a given x via radiation from gluons with a larger $x' = x/z$, with any $x < z < 1$. The 'loss' term expresses the decrease in the number of gluons at x via their decay $x \to zx, (1-z)x$, with any $0 < z < 1$. What is specific to the problem at hand, is the particular form of the in–medium branching rate — the BDMPSZ spectrum in Eq. (2) —, which is very different from the DGLAP splitting function. This difference has important physical consequences, that can be best appreciated by comparing the respective solution $D(x,\tau)$ to the BDMPSZ spectrum for a single emission and to the DGLAP spectrum for gluon evolution in the vacuum.

By construction, the BDMPSZ spectrum coincides with the first iteration to the evolution

[c]Such a classical branching process, obtained by iterating the single BDMPSZ emission, has already been used in applications to phenomenology, albeit on a heuristic basis [11,12,13].

equation. For soft gluons ($x \ll 1$), it is given by Eq. (2), which in our new notations reads

$$D^{(1)}(x \ll 1, \tau) \simeq \frac{\tau}{\sqrt{x}}, \qquad \text{with} \quad \tau \equiv \bar{\alpha}\sqrt{\frac{\hat{q}}{E}}L\,. \tag{3}$$

This spectrum increases quite fast with $1/x$ and thus predicts that a non–negligible fraction of the total radiated energy is emitted directly at large angles: the energy fraction transported via a single gluon emission at angles larger than a given value θ_0 is estimated as

$$\mathcal{E}^{(1)}(\theta > \theta_0, \tau) = \int_0^{x_0} \mathrm{d}x D^{(1)}(x,\tau) \simeq 2\tau\sqrt{x_0} \quad \text{with} \quad \theta_0 \simeq \left(\frac{2\hat{q}}{x_0^3 E^3}\right)^{1/4}. \tag{4}$$

This quantity rapidly decreases with increasing θ_0 (i.e. with decreasing x_0), showing that direct radiation by the leading particle cannot explain the large energy loss at large angles observed in relation with the di–jet asymmetry at the LHC[3]. As we shall shortly argue, multiple branching provides a much more efficient mechanism in that sense.

The approximation in Eqs. (3)–(4) breaks down when $D^{(1)}(x,\tau) \sim \mathcal{O}(1)$, meaning for $x \lesssim \tau^2$. In this non–perturbative regime at small x, one needs an exact result which resums multiple branching to all orders. Before we present this result, it is instructive to summarize the picture one would expect on the basis of our experience with other parton cascades in QCD, like DGLAP. (These expectations turn out to be naive, but their failure will be instructive.)

Via successive branchings, the partons at large x get replaced via partons with smaller values of x, which must be numerous enough to carry the energy of their parents. This seems to imply that the rise in the gluon distribution $D(x,\tau)$ at small x must become steeper and steeper with increasing τ, in such a way to accommodate the energy which disappears at larger values of x. However, this last conclusion is based on the tacit assumption that 'the energy remains in the spectrum', meaning that the energy sum–rule $\int_0^1 \mathrm{d}x D(x,\tau) = 1$ is satisfied at any τ. If that was the case, this would also impose a strong limitation on the energy that can be carried by the small–x gluons for a given value of τ : in order for the function $D(x,\tau)$ to be integrable as $x \to 0$, the integral $\mathcal{E}(x_0,\tau) \equiv \int_0^{x_0} \mathrm{d}x D(x,\tau)$ must vanish as a power of x_0 when $x_0 \to 0$, meaning that the energy fraction radiated at large angles could not be too large. Such a scenario would have little chance to explain the LHC data for di–jet asymmetry. However, this is *not* the picture that emerges from the in–medium evolution equation and that we now describe.

As mentioned, an exact analytic solution is known, modulo some harmless simplifications in the branching rate[8]. This is shown here only for $x \ll 1$, where it reads

$$D(x \ll 1, \tau) \simeq \frac{\tau}{\sqrt{x}}\, \mathrm{e}^{-\pi\tau^2}. \tag{5}$$

(The global spectrum for any x is illustrated in Fig. 3 for various values of τ.) The spectrum (5) is remarkable in several aspects: (i) The 'scaling' behaviour at small x, $D(x) \propto 1/\sqrt{x}$, is the same as for the BDMPSZ spectrum, Eq. (3). Formally, one can read Eq. (5) as 'direct radiation by the leading particle $\times$ survival probability for the latter'. However, unlike Eq. (3), the spectrum (5) includes the effects of multiple branching to all orders. This demonstrates that the scaling spectrum is a *fixed point* of the evolution, for which the 'gain' term and the 'loss' term precisely cancel each other. (ii) The fact that the shape of the spectrum at $x \ll 1$ does not change with τ means that its small–x region cannot accommodate the energy which disappears via splittings at large x. This is also visible in Fig. 3: at small $\tau \ll 1/\sqrt{\pi}$, the small–x spectrum increases linearly with τ, as the BDMPSZ spectrum (3). At the same time, the leading–particle peak, which originally was at $x = 1$, moves towards $x < 1$ and gets broader. For larger times $\tau \gtrsim 1/\sqrt{\pi}$, the spectrum is globally suppressed by the Gaussian factor in (5). Clearly, the energy disappears from the spectrum with increasing τ, as confirmed by an explicit calculation of the energy sum–rule[8]: $\int_0^1 \mathrm{d}x D(x,\tau) = \mathrm{e}^{-\pi\tau^2}$. Where does the energy go ?

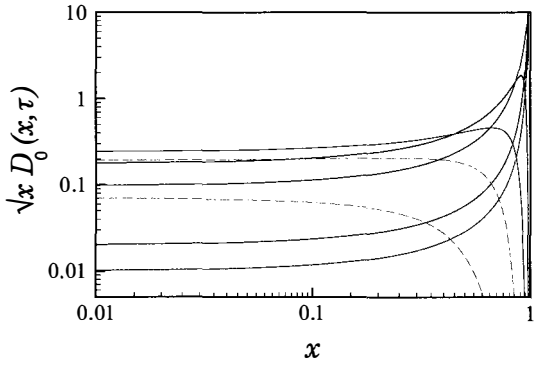

Figure 3: Plot (in Log-Log scale) of $\sqrt{x}D(x,\tau)$ as a function of x for various values of τ (full lines from bottom to top: $\tau = 0.01, 0.02, 0.1, 0.2, 0.4$; dashed lines from top down: $\tau = 0.6, 0.9$).

To answer this question, recall the 'fixed–point' property of the scaling spectrum: if one focuses on a given bin x with $x \ll 1$, then the amount of energy which enters this bin per unit time due to splittings at larger $x' > x$ is exactly equal to the amount of energy which leaves that bin via decays towards smaller $x' < x$. This shows that, via successive branchings, the energy *flows throughout the entire spectrum without accumulating at any value of* x. It therefore accumulates into a 'condensate' ($D_{\rm cond}(x) \propto \delta(x)$) at $x = 0$, according to

$$\mathcal{E}_{\rm flow}(\tau) \,=\, 1 - \int_0^1 \mathrm{d}x D(x,\tau) \,=\, 1 - \mathrm{e}^{-\pi\tau^2}\,. \tag{6}$$

So far, we have assumed that the evolution remains unchanged down to $x = 0$, but physically this is not the case: when the gluon energies become as low as the typical energy scale in the medium — say, the temperature $T \sim 1$ GeV for a QGP —, then the gluons 'thermalize' and disappear from the jet. Thus, our above conclusion about the 'condensate' should be more properly formulated as follows: *via successive branchings, the energy flows towards small–*x *at a rate which is independent of* x*, and eventually reaches the borderline at* $x_{th} \equiv T/E$ *between the 'jet' and the 'medium' at a rate which is independent of the detailed mechanism for thermalization and of the precise value of the medium scale* T. This energy will be recovered in the medium at large angles $\theta \gtrsim \theta_{th}$ w.r.t. the jet axis, with θ_{th} obtained by replacing $x_0 \sim x_{th}$ within the expression for θ_0 shown in Eq. (4).

An energy flow at a rate which is independent of the energy (i.e. uniform in x) is the distinguished signature of *wave turbulence* [14]. This phenomenon is well known in the context of scalar field theories, but it was not expected in the context of QCD, for the following reason: as above discussed, the existence of a turbulent flow requires fine cancellations between 'gain' and 'loss' terms, which in turn requires the branching process to be *quasi–local in* x. Or, the QCD radiation (bremsstrahlung) is reputed for being highly non–local: all the familiar parton cascades, like DGLAP or BFKL, are dominated by very asymmetric splittings, in which the splitting fraction z is close to zero, or to one. The medium–induced cascade is new in that respect: the splitting of a *soft* gluon, i.e. the process $x \to zx, (1-z)x$ with $x \ll 1$, is controlled by *quasi–democratic branchings* with $z \sim 1/2$: the offspring gluons carry commensurable fractions of the energy of their parent gluon [8]. This is ultimately related to the peculiar energy dependence of the BDMPSZ spectrum (2), which in turn reflects the LPM effect.

The above picture has interesting consequences for the phenomenology. To see this, let us repeat the exercise in Eq. (4), that is, compute the energy radiated at large angles $\theta > \theta_0$ or, equivalently, small $x < x_0$ (with $x_0 \gg x_{th}$ though), but including the effects of multiple

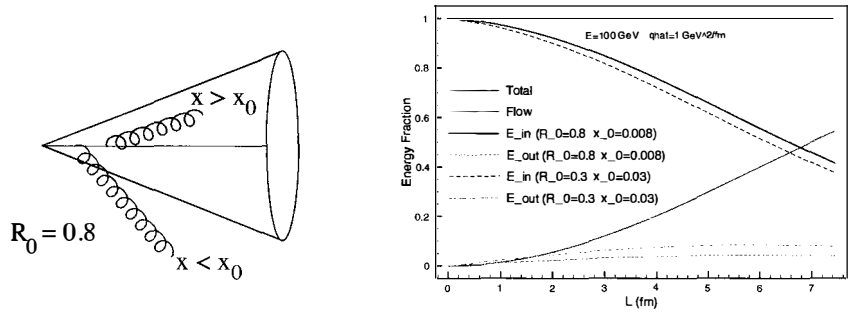

Figure 4: The energy balance between the inner part of a conventionaly defined 'jet' with angular opening R_0 and the region outside the 'jet', plotted as a function of the medium size L, for two values $R_0 = 0.3$ and $R_0 = 0.8$.

branchings. This includes two contributions: the integral over the low–x part of the spectrum (5) at $x \leq x_0$ and the energy (6) carried by the turbulent flow. One finds

$$\mathcal{E}(\theta > \theta_0, \tau) \simeq 2\tau\sqrt{x_0}\,\mathrm{e}^{-\pi\tau^2} + (1 - \mathrm{e}^{-\pi\tau^2}) \simeq 2\tau\sqrt{x_0} + \pi\tau^2\,, \tag{7}$$

where the second approximation holds for $\pi\tau^2 \ll 1$. (Notice that for a jet with $E = 100$ GeV $\approx 2\omega_c$, Eq. (3) implies $\tau \simeq \bar{\alpha} \approx 0.3$.) The flow piece in Eq. (7), which is independent of x_0, dominates over the non–flow piece for any $x_0 < \tau^2$: *the energy lost by the jet at large angles $\theta > \theta_0$ is predominantly carried by the turbulent flow and hence is independent of θ_0.*

This is illustrated in Fig. 4 which shows the energy fraction $E_{\rm in}$ *inside* a jet with angular opening R_0 ($E_{\rm in}$ is the complement of Eq. (7), i.e. the energy contained in the large–x part of the spectrum at $x > x_0$), together with the two components, "Flow" and "Non–flow" (denoted as "$E_{\rm out}$"), of the energy fraction *outside* the jet, Eq. (7), as functions of the medium size L. As visible there, when increasing the jet angle from $R_0 = 0.3$ and $R_0 = 0.8$, i.e. by almost a factor of 3, the energy captured inside the jet increases only slightly, and in any case it represents less than 80% of the total energy for $L \geq 4$ fm. The difference (more than 20%) is essentially associated with the flow component, which is independent of R_0. This picture is in a remarkable agreement with the detailed analysis of the for di–jet asymmetry by the CMS collaboration [3].

References

1. **Atlas** Collaboration, G. Aad *et al.*, Phys. Rev. Lett. **105** (2010) 252303.
2. **CMS** Collaboration, S. Chatrchyan *et al.*, Phys. Rev. **C84** (2011) 024906.
3. **CMS** Collaboration, S. Chatrchyan *et al.*, Phys.Lett. **B712** (2012) 176.
4. R. Baier, Y. L. Dokshitzer, A. H. Mueller, S. Peigne, and D. Schiff, Nucl. Phys. **B483** (1997) 291; Nucl. Phys. **B484** (1997) 265.
5. B. G. Zakharov, JETP Lett. **63** (1996) 952.
6. J. Casalderrey-Solana and E. Iancu, JHEP **1108** (2011) 015.
7. J.-P. Blaizot, F. Dominguez, E. Iancu, and Y. Mehtar-Tani, JHEP **01** (2013) 143.
8. J. -P. Blaizot, E. Iancu, and Y. Mehtar-Tani, arXiv:1301.6102 [hep-ph].
9. Y. Mehtar-Tani, C. A. Salgado and K. Tywoniuk, Phys. Lett. B **707** (2012) 156
10. Y. Mehtar-Tani, C. A. Salgado and K. Tywoniuk, JHEP **1210** (2012) 197
11. R. Baier, A. H. Mueller, D. Schiff, and D. Son, Phys.Lett. **B502** (2001) 51.
12. R. Baier, Y. L. Dokshitzer, A. H. Mueller, and D. Schiff, JHEP **09** (2001) 033.
13. S. Jeon, G. D. Moore, Phys.Rev. **C71** (2005) 034901.
14. V.E. Zakharov, V.S. L'vov, and G. Falkovich, *Kolmogorov spectra of turbulence, Vol. 1* (Springer-Verlag, 1992, 264 p.)

PHENIX RESULTS ON J/ψ AND ψ' FROM d+Au COLLISIONS AND IMPLICATIONS FOR COLD NUCLEAR MATTER

X. HE FOR THE PHENIX COLLABORATION
Department of Physics and Astronomy, Georgia State University, Atlanta, GA 30303, USA

Heavy quarkonia suppression is one of the highly cited signatures of quark gluon plasma (QGP) formed in relativistic heavy ion collisions. However, theoretical predictions remain diverse due to lack of precise knowledge of heavy flavor meson production, suppression, regeneration in hot and dense medium and other cold nuclear effects. PHENIX has carried out a comprehensive study of heavy flavors which includes baseline measurements of heavy flavor, J/ψ and Upsilon in p+p collisions, and the measurements from d+Au, Cu+Cu and Au+Au collisions over the past decade. This talk is focusing on the most recent and exciting results of J/ψ and ψ' from PHENIX in d+Au collisions at $\sqrt{s_{NN}} = 200$ GeV. An implication of these results on cold nuclear matter effects on heavy quarkonium production in heavy ion collisions is also discussed.

1 Introduction

The experimental study of matter properties at extremely high temperature and high density at the Relativistic Heavy Ion Collider (RHIC) at Brookhaven National Laboratory (BNL) is about to complete its 13th year of physics data taking since the first RHIC physics run in 2000. Data from these runs clearly demonstrate that a high temperature and density state of matter has been achieved at RHIC. This state of matter, called quark-gluon plasma (QGP), provides exciting possibilities of experimentally exploring the phase transition from hadronic to partonic degrees of freedom. This state of matter, contrary to early suggestions of a quasi-ideal state of free quarks and gluons, behaves like a dense fluid with very low kinematic viscosity, exhibiting strong hydrodynamic flow, and nearly complete absorption of high momentum hadronic particles initially created from the colliding nuclear matter [1,2].

Heavy quarkonia suppression is one of the highly cited signatures of QGP formed in relativistic heavy ion collisions [3]. The modification in the quark pair potential by the hot dense medium will lead to quarkonium suppression in comparison with quarkonium production in p+p collisions. Because of different binding energies of the quarkonium states one could gain access to the temperature of the medium [4]. However, theoretical predictions remain diverse due to lack of precise knowledge of heavy flavor meson production, suppression, regeneration in hot and dense medium and other cold nuclear effects. The understanding of the modification of the properties of the quarkonium states is very crucial for exploring the onset of a deconfined state in the hot and dense nuclear medium. In the PHENIX experiment heavy quarkonia have been measured from p+p, d+Au, Cu+Cu and Cu+Au collisions at $\sqrt{s_{NN}} = 200$ GeV and several energy scans of Au+Au collisions [5]. In this paper, we highlight the most recent J/ψ and ψ' results in d+Au collisions following a brief description of the PHENIX detector systems.

2 PHENIX Experiment

The PHENIX experiment was designed and optimized for the measurement of rare probes in heavy ion collisions [6]. Figure 1 shows the PHENIX detector setup in beam and side views. The beam view (on left) shows the West and the East arm detectors in the central rapidity region, which covers $|\eta| < 0.35$ and 90° in azimuth for both arms. The side view (on right) shows the South and the North muon arms in the forward and backward rapidity region, which covers $1.2 < |\eta| < 2.4$ and 360° in azimuth for both arms. The J/ψ results reported in this proceeding were measured in both the central arms and the muon arms, while the ψ' results were measured in the central arms only.

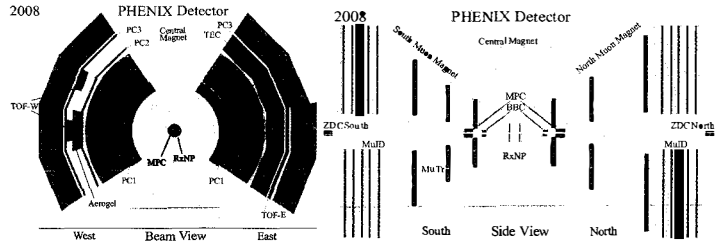

Figure 1: PHENIX detector setup: (left) Central Arms in beam view; (right) Muon Arms in side view.

3 Most Recent Results

The study of particle production in heavy ion collisions is typically characterized by the so-called nuclear modification factor, R_{AB}, with A and B representing the colliding ions. The R_{AB} is defined as the ratio of the particle yield in the heavy ion collisions to the yield in p+p collisions scaled by the number of binary nucleon-nucleon collisions. The PHENIX experiment has reported J/ψ measurements in d+Au collisions at $\sqrt{s_{NN}} = 200$ GeV using data collected in 2008 [7].

3.1 J/ψ Nuclear Modification Factor in d+Au Collisions

In Figure 2, a detailed study of the J/ψ R_{dAu} is plotted as a function of p_T in forward, central and backward rapidity, respectively. Also shown in Figure 2 are two model calculations which include a combination of physical effects such as shadowing, nuclear breakup, and the Cronin effect [8]. The shadowing effect is calculated using parameterizations of the nuclear modified parton distribution function (nPDF's). Two nPDF sets are tested against our data points, including deFlorian-Sassot (nDSg) and Eskola-Kolhinen-Salgado (EKS98) parameterizations [9,10]. For J/ψ production in d+Au collisions the relevant distributions are those providing the modification of the gluon distribution within a Au nucleus, as J/ψ's are produced primarily through gluon fusion at RHIC energies (200 GeV). Nuclear breakup is the dissociation of $c\bar{c}$ pairs that would have formed J/ψ's through collisions with nucleons. An effective value of this breakup cross section (also called as nuclear absorption cross section) is chosen as 4.2 mb. The Cronin effect (i.e., the broadening of the p_T distribution) is attributed to multiple elastic scattering of the incoming parton before the hard collision that produces the J/ψ. This effect generally causes a decrease in J/ψ production at low p_T and a compensating increase at higher p_T.

Our data indicate that, for peripheral collisions, the R_{dAu} is consistent with 1.0 in all rapidity regions while a significant deviation from 1.0 is seen in the forward rapidity (d-going direction) in more central collisions for $p_T < 4.0$ GeV/c. The data also shows a slight greater than 1.0 of the R_{dAu} value in the most central collisions in the backward rapidity (Au-going direction). The

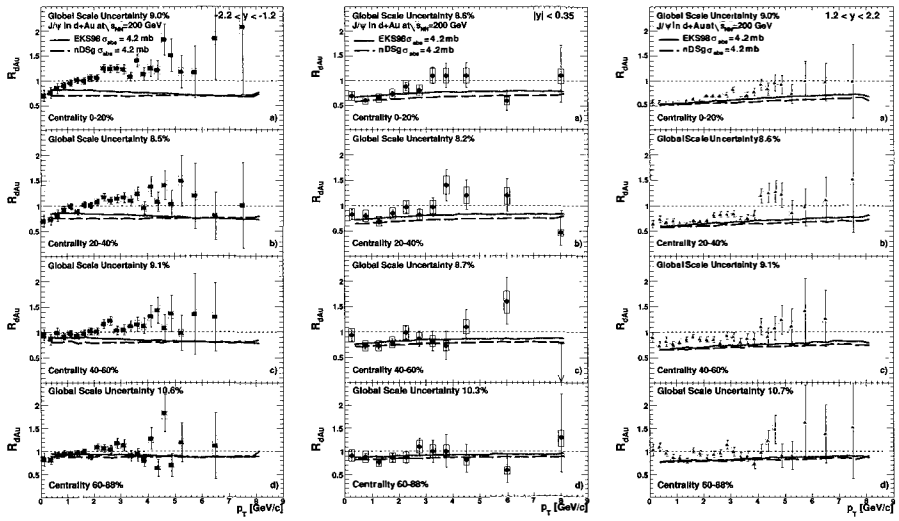

Figure 2: (left panel)) R_{dAu} as a function of p_T for (a) central, (b) midcentral, (c) midperipheral, and (d) peripheral events in the interval $-2.2 < y < -1.2$ (Au-going direction); (middle panel) for the interval $|y| < 0.35$; (right panel) for the interval $1.2 < y < 2.2$ (d-going direction). See text for details.

model calculations of R_{dAu} show a reasonable agreement with the overall level of modification seen at low p_T in the data at central- and forward rapidities, while predicting a flatter distribution with increasing p_T than is seen in the data.

3.2 ψ' Nuclear Modification Factor in d+Au Collisions

The PHENIX experiment has also measured ψ' nuclear modification factor in the central rapidity region. At the present time, there is no ψ' measurements in the forward and the backward rapidity regions. Figure 3 shows the PHENIX preliminary ψ' nuclear modification factor, R_{dAu}, as a function of the number of binary collisions, N_{coll}, which is calculated using a Glauber Monte Carlo model coupled with a simulation of the PHENIX Beam-Beam Counter response [7]. Note that the J/ψ R_{dAu} plotted in Figure 3 is not corrected for ψ' and χ_c feed-down contributions. We observe a stronger suppression of ψ' production than for J/ψ with increasing N_{coll}. The difference of R_{dAu} between J/ψ and ψ' can be intuitively understood because of a smaller binding energy of the ψ' (~ 0.05 GeV) in comparison with the binding energy of J/ψ (~ 0.64 GeV) [11]. However, a quantitative description of this difference is still lacking.

4 Summary

The PHENIX experiment has produced extensive data on J/ψ production in p+p, d+Au, Cu+Cu, Cu+Au, and Au+Au collisions at $\sqrt{s_{NN}} = 200$ GeV and in Au+Au collisions at $\sqrt{s_{NN}} = 39$ and 62.4 GeV. These rich data sets provide essential constraints on theoretical interpretations of heavy quarkonium production and its interaction with hot and dense medium created in heavy ion collisions. Experimentally, it is still imperative to make exclusive measurements of J/ψ in order to systematically test the theory of color-screening[3] assuming that one has a better knowledge of cold nuclear matter effects. Our d+Au data provide the valuable insights on disentangling the multiple effects on quarkonium production and evolution of heavy quark pairs in a nuclear environment. These effects include nuclear breakup, modification of parton-

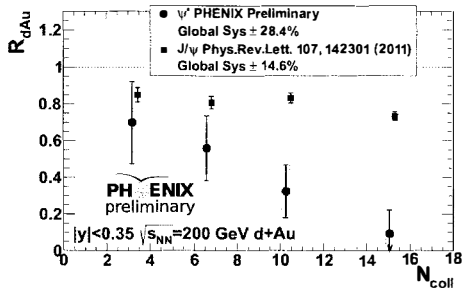

Figure 3: The ψ' nuclear modification factor, R_{dAu}, as a function of N_{coll}, in the central rapidity region. Also included are the J/ψ data points as a function of N_{coll}.

distribution functions, initial-state parton-energy loss, and comoving hadronic interactions, etc. The recent experimental results of p+Pb collisions at the LHC have extended the study of cold nuclear matter effects on quarkonium production to a much broader kinematic regions. The planned future p+A runs at RHIC will further enrich the knowledge of these effects mentioned above.

The PHENIX experiment has the capability of measuring multiple quarkonium states simultaneously with a broad kinematic coverage. Our result of ψ' and J/ψ ratio should provide more stringent test of theoretical models on heavy-quark pair evolution in nuclear medium since the production process is the same for both particles.

References

1. "RHIC Scientists Serve Up 'Perfect' Liquid", http://www.bnl.gov/bnlweb/pubaf/pr/PR_display.asp?prID=05-38.
2. K. Adcox *et. al.* PHENIX Collaboration, Nucl. Phys. A **757**, 184 (2005) [arXiv:nucl-ex/0410003]; I. Arsne *et. al.* BRAHMS Collaboration, Nucl. Phys. A **757**, 1 (2005) [arXiv:nucl-ex/0410020]; B.B. Back *et. al.* PHOBOS Collaboration, Nucl. Phys. A **757**, 28 (2005) [arXiv:nucl-ex/0410022]; J. Adms *et. al.* STAR Collaboration, Nucl. Phys. A **757**, 102 (2005) [arXiv:nucl-ex/0501009].
3. T. Matsui and H. Satz, Phy. Lett. B **178**, 416 (1986).
4. A. Mocsy and P. Petreczky, Phys. Rev. Lett. **99**, 211602 (2007).
5. A. Adare *et. al.* PHENIX Collaboration, Phys. Rev. Lett. 98, 232002 (2007); Phys. Rev. Lett. **98**, 232301 (2007); Phys. Rev. C **77**, 024912 (2008); Phys. Rev. Lett. **101**, 122301 (2008); and Phys. Rev. C **79**, 059901(E) (2009).
6. K. Adcox *et. al.*, Nucl. Instrum. Methods Phys. Res., Sect. A **499**, 469 (2003).
7. A. Adare *et. al.*, Phys. Rev. Lett., **107**, 142301 (2011); Phys. Rev. C **87**, 034904 (2013).
8. J. Cronin, H. J. Frisch, M. Shochet, J. Boymond, R. Mermod *et. al.*, Phys. Rev. D **11**, 3105 (1975).
9. D. de Florian and R. Sassot, Phys. Rev. D **69**, 074028 (2004).
10. K. J. Eskola, V. J. Kolhinen, and C. A. Salgado, Eur. Phys. J. C **9**, 61 (1999).
11. H. Satz, J. Phys. G. **G32**, R25 (2006).

HEAVY FLAVOR AND DILEPTON PRODUCTION IN STAR EXPERIMENT

JAROSLAV BIELCIK
(FOR THE STAR COLLABORATION)
Department of Physics, Faculty of Nuclear Sciences and Physical Engineering, Czech Technical University in Prague, Brehova 7, Prague, 11519, Czech Republic

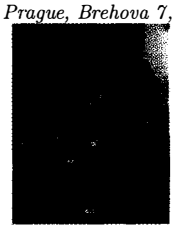

Heavy quarks are produced in early stage of the nucleus-nucleus collision and they are good probes of hot and dense nuclear matter created in such collisions. However, the mechanisms of their interaction with a nuclear medium is not yet well understood. The nuclear modification factor of non-photonic electrons from charm and beauty decays as well as open charm mesons measured in central Au+Au collisions at $\sqrt{s_{NN}}$ = 200 GeV in STAR is comparable to that of light hadrons. The heavy quarkonia production is expected to be sequentially suppressed, due to Debye screening of the quark-antiquark potential, depending on the temperature of the produced nuclear matter. The measurement of Υ meson at RHIC is a clean probe of this effect due to negligible levels of background effect such as contribution from $b\bar{b}$ recombination and non-thermal suppression from co-mover absorption. Dileptons are bulk penetrating probes of all stages of collision dynamics in heavy ion collisions. Their spectra in the low and intermediate mass regions are sensitive to vector meson in-medium modifications and the Quark Gluon Plasma (QGP) thermal radiation. These regions are as well sensitive to charm modification since the dominant physical background in intermediate mass region is from correlated charm pairs. In this paper we discuss the recent STAR results in heavy flavor and dilepton production.

1 Open heavy flavour

The study of heavy quark production in heavy ion collisions is an important probe of the properties of hot and dense nuclear matter that is produced in these collisions. The calculations of the Quantum Chromodynamics on lattice showed that at energy densities of about 1 GeV/fm^3 and at temperature of about 170 MeV, that are exceeded in energetic collisions at Relativistic Heavy Ion Collider in Brookhaven National Laboratory, the phase transition from quark-gluon-confined matter to quark-gluon-deconfined matter, Quark Gluon Plasma should take place[1]. This form of matter has several interesting properties [2]. The production of heavy quarks happens during the initial part of the collision and therefore this is a sensitive probe of properties of QGP. It is however very important to understand the heavy flavor production in elementary reference system such as p+p collisions. The STAR experiment can measure charm production both directly via hadronic decays and also indirectly by non-photonic electrons. The Figure 1(left)

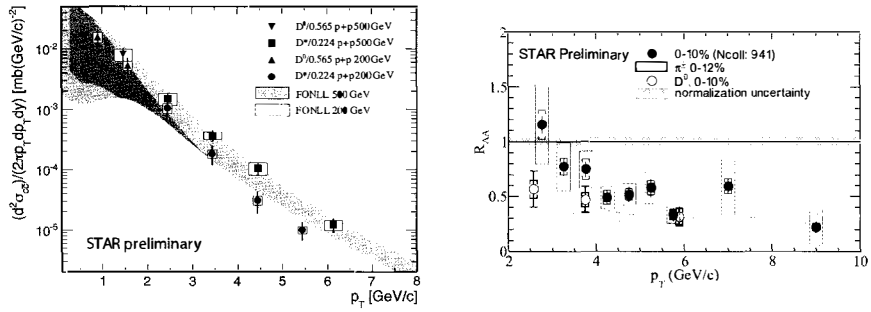

Figure 1: Right: Transverse momentum dependence of $c\bar{c}$ production cross section extracted from D^0 and D^* measurement in p + p collisions at $\sqrt{s} = 200$ GeV and $\sqrt{s} = 500$ GeV is shown. The data are compared to FONLL calculations. Left: Nuclear modification factor as function of transverse momentum of non-photonic electrons (red full circles) and D^0 mesons (blue open circles) for 0-10% most central Au+Au collisions. For reference also the pions for 0-12% centrality are also shown (grey band).

shows the measurement of $c\bar{c}$ production cross section from hadronic decays of D^0 and D^* mesons (using branching fractions) in p+p collisions at 200 GeV [3] and 500 GeV [4]. The measurement is compared to the FONLL calculations [5]. These calculations can describe the charm spectra well within the uncertainty bands of data and calculations.

It is expected that energy loss of heavy quarks could be different as compared to light quarks and gluons.The mechanism of energy loss of heavy quarks in hot and dense medium is not yet fully understood and the discussions about the importance of radiative and collisional energy loss are ongoing. The previous nuclear modification factor (R_{AA}) measurements of non-photonic electrons at RHIC, dominantly originating from c and b decays, showed no significant difference when compared with light hadrons. The new STAR measurement of R_{AA} of non-photonic electrons as well as D^0 meson in 0-10% most central 200 GeV Au+Au collisions are presented in Figure 1(right). There is no significant difference between the suppression of charm mesons and pions. The R_{AA} of non-photonic electrons and charm mesons are also consistent with each other within uncertainties and also when taking into account the momentum smearing due to kinematics of the decays.

2 Quarkonium

The quarkonium suppression is considered to be an excellent probe of color deconfinement in the QGP. This is due to a color Debye screening of di-quark potential in hot and dense nuclear matter that could play important role in production of quarkonium. It is predicted that due to different binding potential of various quarkonium states their production is suppressed above some temperature, that is different for each particular state [6]. However, the effects of color deconfinement have to be disentangled from other competing effects that could influence the quarkonium production. These include cold nuclear matter effects (nuclear interaction break-up, shadowing) and recombination. Previous measurements at RHIC energies showed that the suppression of J/ψ as a function of collision centrality is similar to that observed at the CERN SPS energy. This is puzzling since the temperature and energy density reached in these collisions is significantly lower than at RHIC.

In Figure 2(left) the nuclear modification factor of J/ψ production as a function of number of participating nucleons, measured by STAR experiment, is presented. The suppression of J/ψ production is observed with R_{AA} ~0.4 for most central collisions. No significant dependence on centrality is observed above N_{part} =150. The suppression of J/ψ with large transverse momentum $p_T > 5$ GeV/c is significantly smaller as compared to J/ψ p_T integrated values.

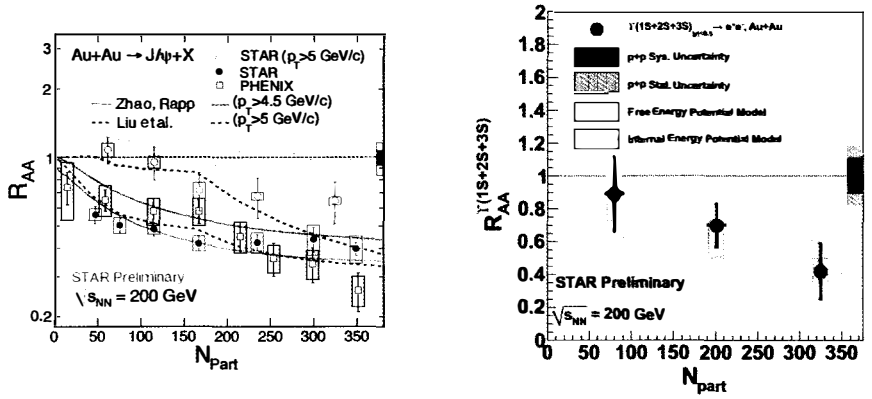

Figure 2: The nuclear modification factors as function of number of participating nucleons in Au+Au collisions with $\sqrt{s_{NN}}$=200GeV measured by STAR experiment. Left: J/ψ (red full circles), J/ψ with p_T >5 GeV/c [7](red open circles), J/ψ measurement by PHENIX (black open rectangles). Theoretical models of Liu[8] and Zhao[10] are also shown. Right: Υ(1S,2S,3S) measurement. Theoretical model of Strickland[9] is also shown

Another quarkonium that is of a great interest is the Υ. It is expected that Υ(1S) state does not dissociate at RHIC energies[6], but Υ(2S) and Υ(3S) do. This could provide the information about the temperature reached in heavy-ion collisions. STAR has reported measurements in p+p[11], d+Au[12] and Au+Au[13] collisions. However, so far it was not possible to address each Υ state separately. Recently STAR reported Υ results from large statistics data sample collected year 2010 for Au+Au 200 GeV collisions[14], see Figure2(right). The increase of suppression as a function of the number of participants was observed. The Υ(1S,2S,3S) suppression is consistent with the scenario that 2S, 3S and excited states completely melt. Future measurements with recently installed Muon Telescope Detector in STAR will make possible to separate Υ states in di-muon channel at midrapidity.

3 Dilepton production

Dileptons are sentitive to various phases of the evolution of nuclear matter in heavy ion collision. They have very low interaction cross section with created QCD matter. Different invariant mass ranges of dilepton spectrum are sensitive to different physics. In the low invariant mass $M_{ll} < 1.1$ GeV/c^2 the in-medium modifications of vector meson properties $\rho(770)$, $\omega(782)$ and $\phi(1020)$ can be studied. The modifications of mass and width of the spectral functions are expected, related to possible chiral symmetry restoration. The intermediate mass range, $1.1 < M_{ll} < 3.0$ GeV/c^2 is sensitive to the thermal radiation of the Quark-Gluon Plasma. The important source of background in this region comes from the semileptonic decays of a correlated pairs of open charm or bottom hadrons. The production of these hadrons can be modified in heavy ion collisions. In the high mass region above 3.0 GeV/c^2 the production of quarkonia and color screening effects, as it was discussed in previous section, plays a role. Additional important source here is Drell-Yan process.

The STAR experiment has measured the dielectron production in p+p collisions at 200 GeV and the spectrum is consistent with the cocktail simulation of individual sources[15]. In Figure 3 the dielectron production is shown, as it was measured at $\sqrt{s_{NN}}$ =19.6, 62.4 and 200 GeV. The enhancement above the expected cocktail of sources is observed in low mass region. This enhancement can be described, for all energies, with a hadronic cocktail of expected sources (without $\rho(770)$) and in-medium modified $\rho(770)$ spectral function[16].

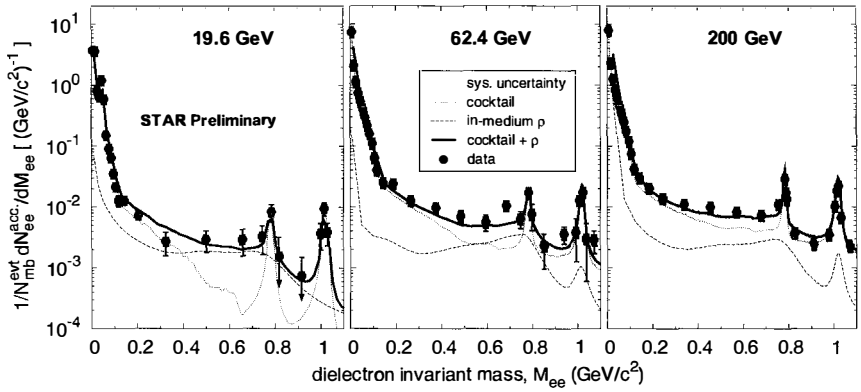

Figure 3: Dielectron invariant mass spectrum measured in Au+Au collisions $\sqrt{s_{NN}}$ =19.6, 62.4 and 200 GeV. The line correspond to the hadronic cocktail (dotted, not including the rho meson), the in-medium calculation of the rho meson[16] (dashed, including QGP contributions), and the sum of the two (solid).

4 Summary

In summary, the measurements of heavy flavor and dilepton production provide important information about the properties of hot and dense nuclear matter. The open heavy flavor production in p+p collisions is well described by FONLL calculations. The strong suppression of open heavy flavor production is observed in central 200 GeV Au+Au collision, similar to light hadrons. The suppression of J/ψ is observed and it is decreasing with larger p_T. The Υ suppression was observed in central Au+Au collisions and it is consistent with only 1S state survival. The enhancement of dielectron production in low mass region is observed in energy range down to SPS energies and it is consistent with in-medium ρ modifications. New upgrades of STAR detectors with Heavy Flavour Tracker and Muon Telescope Detector will allow to perform more precise lepton measurements in near future at RHIC.

This work was supported by the grant of Grant Agency of Czech Republic n.13-20841S.

References

1. M. Gyulassy and L. McLerran, Nucl. Phys. A **750**, 30 (2005).
2. J. Adams *et al.* [STAR Collaboration], Nucl. Phys. A **757** 102 (2005).
3. L. Adamczyk *et al.* [STAR Collaboration], Phys. Rev. D **86**, 072013 (2012).
4. D. Tlusty [STAR Collaboration], Nucl. Phys. A904-905 **2013**, 639c (2013).
5. M. Cacciari, P. Nason and R. Vogt, Phys. Rev. Lett. **95**, 122001 (2005).
6. T. Matsui, H. Satz, Phys. Lett. **B178**, 416 (1986).
7. L. Adamczyk *et al.* [STAR Collaboration], Phys. Lett. B **722**, 55 (2013).
8. Y.Liu, Z. Qu, N. Xu and P. Zhuang, Phys. Lett. B **678**, 72 (2009).
9. M. Strickland, Phys. Rev. Lett. **107**, 132301 (2011).
10. X. Zhao and R. Rapp, Phys. Rev. C **82**, 064905 (2010).
11. B. I. Abelev *et al.* [STAR Collaboration], Phys. Rev. **D82**, 012004 (2010).
12. H. Liu [STAR Collaboration], Nucl. Phys. A **830**, 235C (2009).
13. R. Reed [STAR Collaboration], Nucl. Phys. **A855**, 440 (2011).
14. B. Trzeciak *et al.* [STAR Collaboration], Nucl. Phys. A904-905 **2013**, 607c (2013).
15. L. Adamczyk *et al.* [STAR Collaboration], Phys. Rev. **C86**, 024906 (2012).
16. R. Rapp and J. Wambach, Adv. Nucl. Phys. **25**, 1 (2000) + private communication.

OPEN HEAVY–FLAVOUR AND QUARKONIUM MEASUREMENTS WITH ALICE AT THE LHC

F. FIONDA[a] on behalf of the ALICE Collaboration
[a] *Dipartimento Interateneo di Fisica "M. Merlin" and Sezione INFN, Bari, Italy*

The ALICE detector provides excellent capabilities to study heavy quark (i.e. charm and beauty) production in proton–proton (pp) and heavy–ion collisions (AA) at the Large Hadron Collider (LHC). In ALICE, open heavy–flavour hadron production is studied through the hadronic decays of D mesons at central rapidity ($|y| < 0.9$), and in the semi–leptonic decays of charm and beauty hadrons both at mid–rapidity and at forward rapidity ($2.5 < y < 4$). Quarkonia are measured in their di–electron and di–muon decay channels in the central barrel and in the muon spectrometer respectively, reaching in both cases zero transverse momentum. The latest results on open heavy–fiavour and quarkonium production in pp ($\sqrt{s} = 2.76$ TeV and $\sqrt{s} = 7$ TeV) and PbPb ($\sqrt{s_{NN}} = 2.76$ TeV) collisions are presented.

1 Introduction

In ultra–relativistic nuclear collisions the nuclear matter is predicted to undergo a phase transition into a plasma of deconfined quarks and gluons (QGP). Heavy–flavour particles are unique probes to investigate the properties of such a medium, since they are predominantly produced via hard scatterings in the initial phase of the collision and therefore could experience the full evolution of the collision. Partons are expected to lose energy while traversing the strongly interacting medium via gluon radiation and elastic collisions with the partonic constituents [1]. One observable used to study the energy loss is the nuclear modification factor ($R_{\rm AA}$), which is the ratio of particle yields in heavy–ion collisions compared to pp, scaled by the number of binary nucleon–nucleon collisions $\langle N_{\rm coll}\rangle$: $R_{\rm AA}(p_{\rm T}) = \left(\frac{1}{\langle N_{\rm coll}\rangle}\right) \cdot \left(\frac{dN_{\rm AA}}{dp_{\rm T}}\right) / \left(\frac{dN_{\rm pp}}{dp_{\rm T}}\right)$. A value of $R_{\rm AA}$ lower than unity indicates suppression. According to QCD, quarks should lose less energy than gluons, which have a larger colour charge. In addition the gluon radiation induced by the medium causes a mass dependence due to the so–called "dead–cone" effect, which predicts that small angle radiation is suppressed for heavy quarks [2]. Therefore, the following hierarchy should be observed in the measured $R_{\rm AA}$: $R^{\pi}_{\rm AA} < R^{\rm D}_{\rm AA} < R^{\rm B}_{\rm AA}$.

Quarkonium states are expected to be suppressed in the QGP due to the color–screening [3]. However, at LHC energies it is predicted that due to their abundant production in the initial state, the charm quarks would (re)combine into charmonium states along the collision history [4,5] and/or at phase boundary by statistical hadronization [6,7]. This would result in an enhancement in the observed J/ψ yield.

Further insight into the interaction mechanisms of heavy quarks with the medium and the charmonium (re)generation can be obtained by studying the azimuthal anisotropy of heavy–flavour and quarkonium production in non–central heavy–ion collisions. In particular, the second order coefficient in the Fourier expansion of the azimuthal distribution of produced particles, commonly referred to as elliptic flow v_2, was measured for D mesons, heavy–flavour decay electrons and J/ψ's. If heavy quarks thermalize in the medium or if they interact strongly with

it, the heavy–flavour hadrons and the J/ψ formed by (re)combination should inherit the medium azimuthal anisotropy.

2 Heavy–flavour measurements in ALICE

ALICE (A Large Ion Collider Experiment) is specifically optimized for the study of heavy–ion collisions at the LHC. Open and hidden heavy–flavour particles are studied in proton–proton (pp), lead–lead (Pb–Pb) and proton–lead (p–Pb) and their detection is performed at both central rapidity ($|\eta| < 0.9$) in the central barrel detectors and at forward rapidity ($2.5 < \eta < 4$) in the muon spectrometer.

A detailed description of ALICE set–up can be found in [8]. The central barrel includes the Inner Tracking System (ITS) surrounded by the Time Projection Chamber (TPC). Both are embedded in a magnetic field of 0.5 T and provide high precision in terms of vertex reconstruction and tracking of charged particles. The ITS is composed of six layers of high resolution silicon detectors with the two innermost layers consisting of Silicon Pixel Detectors (SPD). Hadron identification is provided by the ionization energy loss dE/dx in the TPC gas and information from the Time Of Flight (TOF) detector. Electrons are identified with TPC and TOF and at higher momenta using the ElectroMagnetic Calorimeter (EMCal) and the Transition Radiation Detector (TRD). In the forward region muon tracking and identification is provided by the muon spectrometer. This is equipped with a dipole magnet with a total field integral $\mathrm{B} \cdot \mathrm{l} = 3$ Tm. The spectrometer is composed of a passive absorber, a beam shield, five stations of cathode pad chambers (tracking stations), an iron wall, and two stations of resistive plate chambers (trigger stations).

Open heavy–flavour hadrons are reconstructed from their hadronic decays at mid–rapidity through the following decay channels $D^0 \to K^-\pi^+$, $D^+ \to K^-\pi^+\pi^+$, $D^{*+} \to D^0\pi^+$, $D_s^+ \to K^+K^-\pi^+$ (and their charge conjugates) and from semi–leptonic decays both at mid–rapidity ($D, B \to e + X$) and forward–rapidity ($D, B \to \mu + X$).

Quarkonia measurements are performed in the central region via the dielectron channel ($J/\psi \to e^+e^-$) and in the forward rapidity region via the dimuon channel ($J/\psi \to \mu^+\mu$), reaching in both cases $p_{\mathrm{T}} = 0$.

3 Results

In the upper left–hand panel of Fig. 1 the nuclear modification factor for (prompt) D mesons (average of D^0, D^+ and D^{*+}) measured in Pb–Pb collisions at $\sqrt{s_{NN}} = 2.76$ TeV is shown as a function of centrality for $6 < p_{\mathrm{T}} < 12$ GeV/c. Due to the limited statistics of the pp sample at the same energy the reference for Pb–Pb is obtained by applying a $\sqrt{s}$ scaling to the cross section measured at $\sqrt{s} = 7$ TeV. The scaling factor is obtained from FONLL pQCD calculations [9]. In the figure, the nuclear modification of non–prompt J/ψ from B decays, measured by the CMS Collaboration [10], is also shown. The comparison with D mesons indicates a different suppression for charm and beauty hadrons in central collisions, consistent with the expectation $R_{AA}^D < R_{AA}^B$. However, due to the different p_{T} and rapidity ranges, no firm conclusion can be drawn on this point.

A large suppression is also observed for heavy–flavour decay muons and electrons, at forward and central rapidity as shown for the centrality class 0–10% in the upper right–hand side of Fig. 1. Both lepton species exhibit a suppression by a factor of about 3 for $p_{\mathrm{T}} < 10$ GeV/c which decreases to ~2 for electrons around $p_{\mathrm{T}} = 18$ GeV/c, which is a momentum range where beauty decays should be dominant. The cross section measured in pp collisions at $\sqrt{s} = 2.76$ TeV is used as the reference for the R_{AA} of heavy–flavour decay muons. For electrons, the reference was obtained with a pQCD–driven $\sqrt{s}$–scaling of the cross sections measured at $\sqrt{s} = 7$ TeV, as done in the case of the D mesons. For $p_{\mathrm{T}} > 8$ GeV/c, where the pp measurement is not

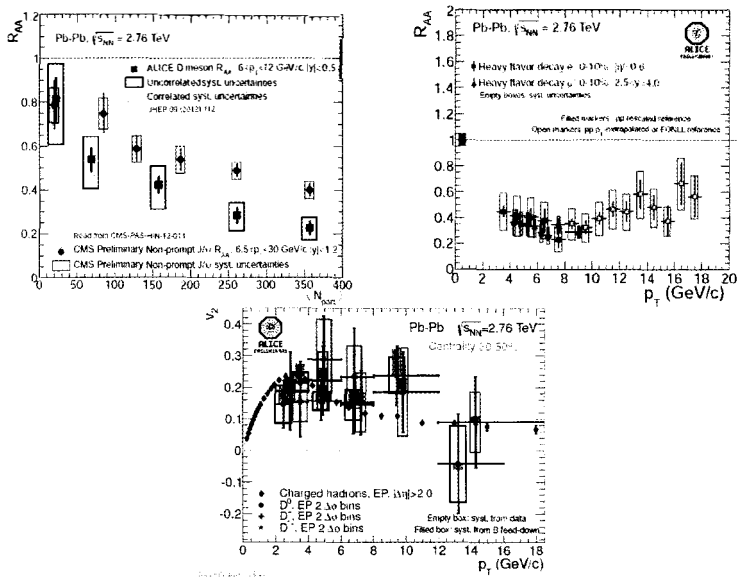

Figure 1: Upper left–hand side: average $R_{\rm AA}$ of D mesons as a function of centrality compared to that of non–prompt J/ψ from B decays. Upper right–hand side: Nuclear modification factors as a function of $p_{\rm T}$ for heavy–flavour decay muons at forward rapidity and electrons at central rapidity in central (0–10%) Pb–Pb collisions. Lower panel: D^0, D^+, D^{*+} v_2 in the 30–50% centrality. Black points show the v_2 for charged hadrons.

available, the cross section from FONLL was used as the reference.

The elliptic flow was measured for D mesons and for heavy–flavour decay electrons. The lower panel of Fig. 1 shows the D meson elliptic flow as a function of $p_{\rm T}$ for D^0, D^+ and D^{*+} mesons, measured in the centrality class 30–50%. All three D mesons agree within statistical uncertainties and show a non–zero v_2 resulting comparable in magnitude to that of charged hadrons [11] (also shown in the figure).

In Fig. 2, the nuclear modification factor of inclusive J/ψ in Pb–Pb collisions at the LHC is shown as a function of the collision centrality at central and forward rapidity in the upper left– and upper right–hand side, respectively. The pp data at $\sqrt{s}$ = 2.76 TeV were used as the reference at both central and forward rapidity. The large uncertainty on the (midrapidity) pp reference prevents a final conclusion on the question whether there is a significantly different behaviour at mid–rapidity with respect to forward rapidity. The comparison with the J/ψ $R_{\rm AA}$ measured at $\sqrt{s_{NN}}$ = 200 GeV by the PHENIX Collaboration suggests a stronger centrality dependence at lower energy, resulting in a sistematically lower $R_{\rm AA}$ for central events compared to ALICE data. Such a behaviour is indeed qualitatively expected by theoretical models that include J/ψ (re)generation. However, for a final interpretation a precise understanding of CNM effects, which will be addressed with the recent p–Pb data, is mandatory.

The elliptic flow of inclusive J/ψ was measured in the forward rapidity region. The elliptic flow v_2 as a function of $p_{\rm T}$ in the centrality interval 20–60% is shown in the lower panel of Fig. 2 and is compared to predictions from parton transport models [12,13]. A hint for a v_2 larger than zero is observed at intermediate $p_{\rm T}$ (2–4 GeV/c), whereas a similar measurement performed by the STAR collaboration at RHIC showed a value of v_2 compatible with zero in the $p_{\rm T}$ range between 2 and 10 GeV/c [14]. The magnitude of the effect is in agreement with transport model calculations that include regeneration effects. This result nicely complements the indications for

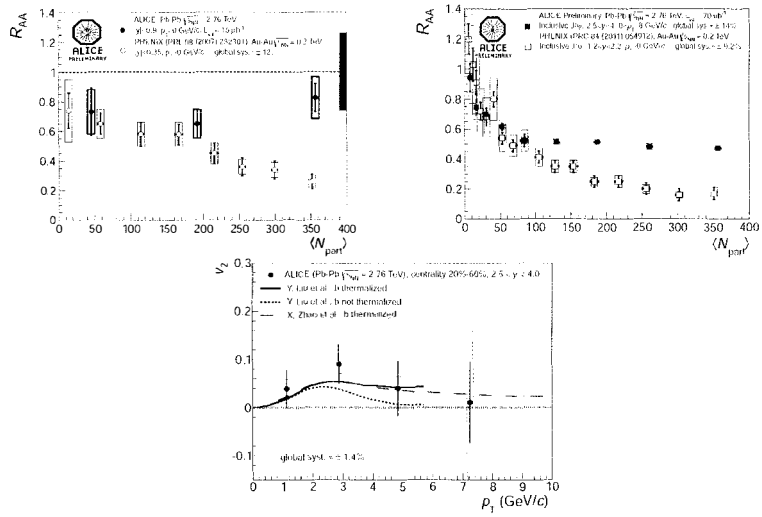

Figure 2: Upper panel: inclusive J/ψ $R_{\rm AA}$ as a function of centrality, expressed in terms of the number of participant nucleons, at central rapidity (left–hand panel) and forward rapidity (right–hand panel) respectively, compared with results from PHENIX. Lower panel: inclusive J/ψ v_2 measured in the 20–60% centrality class of Pb–Pb collisions at $\sqrt{s_{NN}} = 2.76$ TeV, compared to predictions from parton transport models.

a coalescence contribution to the J/ψ production as obtained from the $R_{\rm AA}$ studies.

4 Conclusions

The ALICE Collaboration has measured the nuclear modification factor and elliptic flow for open heavy-flavour hadrons and quarkonia. Results obtained for D mesons and heavy–flavour decay leptons give an important insight on in–medium energy loss of heavy quarks and on their partecipation in the collective flow. The measured J/ψ $R_{\rm AA}$ and v_2 are found to be consistent with a scenario where (re)combination processes play a sizable role.

Data in proton–nucleus (p–Pb) collisions will help to understand cold nuclear matter effects, allowing a correct interpretation of the Pb–Pb results.

1. A. Majumder, M. Van Leeuwen, Prog.Part.Nucl.Phys. 66 (2011) 41.
2. N. Armesto, C. A. Salgado, U. A. Wiedemann, Phys. Rev. D69 (2004) 114003.
3. T. Matsui, H. Satz, Phys. Lett. B178 (1986) 416.
4. X. Zhao and R. Rapp, Phys. Lett. B664 253–257 (2008).
5. Y. Liu, Q. Zhen, N. Xu and P. Zhuang, Phys. Lett. B678 72 (2009).
6. P. Braun–Munzinger and J. Stachel, Phys. Lett. B490 196 (2000).
7. A. Andronic et al, Phys. Lett. B652 259–261 (2007).
8. K. Aamodt et al. [ALICE Coll.], JINST 3 (2008) S08002.
9. M. Cacciari et al., JHEP 1210 (2012) 137.
10. CMS Collaboration, arXiv:1201.5069 [nucl–ex] (2012).
11. B. Abelev et al. [ALICE Coll.], arXiv:1205.5761 [nucl–ex]
12. Y. Liu, N. Xu, and P. Zhuang, Nucl. Phys. A 834, 317C (2010).
13. X. Zhao, A. Emerick, and R. Rapp, arXiv:1210.6583.
14. L. Adamczyk et al. [STAR Coll.], arXiv:1212.3304[nucl–ex].

DIFFRACTION AND ULTRAPERIPHERAL COLLISIONS AT ALICE

E. L. Kryshen for the ALICE Collaboration
Petersburg Nuclear Physics Institute, National Research Center "Kurchatov Institute"
1 Orlova Roscha, 188300 Gatchina, Russia

The ALICE experiment measured J/ψ photoproduction in Pb+Pb ultraperipheral collisions at $\sqrt{s_{NN}} = 2.76$ TeV at forward and central rapidity. The coherent J/ψ cross section is found to be in good agreement with those models which include nuclear gluon shadowing consistent with EPS09 parametrization. Results on ρ^0 photoproduction in ultra-peripheral Pb+Pb collisions are also briefly discussed. Studies on exclusive J/ψ in p+Pb and on diffraction in pp collisions are mentioned.

1 Introduction

Ultraperipheral collisions (UPC) are characterised by impact parameters larger than two nuclear radii. In this case hadronic interactions are strongly suppressed resulting in a dominance of electromagnetic processes caused by large flux of quasi-real photons from heavy nuclei.

Vector meson photoproduction on nuclear target ($\gamma A \to VA$) is one of the most interesting processes which can be studied in heavy ion UPC [1]. One has to distinguish between coherent and incoherent photoproduction. In the first case, photon couples coherently to the whole nucleus causing a narrow transverse momentum distribution of the produced meson (mean $p_{\mathrm{T}} \sim 60$ MeV/c). The target nucleus stays intact in about 80% of coherent events. In the incoherent case, the photon couples to a single nucleon in the target, thus vector meson p_{T} distribution is dictated by the nucleon form factor and becomes much broader (mean $p_{\mathrm{T}} \sim 400$ MeV/c). The incoherent process is usually accompanied by neutron emission from the target.

The coherent heavy quarkonium photoproduction is of particular interest since, in the leading order pertubative QCD, its cross section is proportional to the squared gluon density in the target. Thus the measurement of the coherent J/ψ photoproduction in Pb+Pb UPC provides a direct tool to study poorly known nuclear gluon shadowing effects which play crucial role in the calculation of initial state parton distributions in heavy ion collisions.

The ALICE experiment perfectly matches all requirements for such a measurement. On the one hand, the UPC analysis strategy relies on the selection of events with only two leptons from J/ψ decay and otherwise empty detector, therefore large continuous angular coverage in ALICE is essential to ensure event emptiness. On the other hand, ALICE can trigger on J/ψ down to zero transverse momentum which is important for the measurement of the low-p_{T} coherent J/ψ photoproduction. Further details on the ALICE experimental setup can be found in [2].

2 J/ψ photoproduction

ALICE measured J/ψ photoproduction in Pb+Pb UPC both at forward and central rapidity.

The forward J/ψ measurement was performed with the muon spectrometer and is based on 2011 Pb+Pb data at $\sqrt{s_{NN}} = 2.76$ TeV. The analysis was recently published in Ref. [3]. The

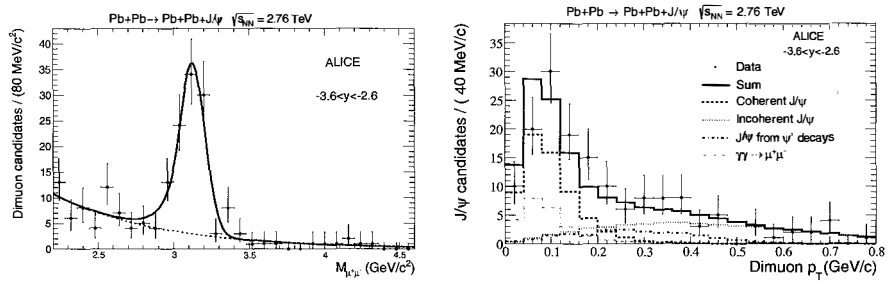

Figure 1: Dimuon invariant mass spectrum with $p_{\mathrm{T}} < 300$ MeV/c (left) and transverse momentum distribution for dimuons in the invariant mass range 2.8 GeV/c^2 $< M_{\mu^+\mu^-} <$ 3.4 GeV/c^2 (right). From Ref. [3]

trigger required a single muon with $p_{\mathrm{T}}>$ 1 GeV/c in the muon arm acceptance, at least one cell fired in VZERO-C scintillator array overlapping with the muon arm and veto on VZERO-A activity on the opposite side. Event emptiness was ensured by vetoing large activity in the neutron zero-degree-calorimeters and the silicon pixel detector at central rapidity.

The resulting invariant mass spectrum for opposite-sign dimuons with $p_{\mathrm{T}} < 300$ MeV/c in the rapidity range $-3.6 < y < -2.6$ is shown in fig. 1 (left). The signal was fitted with the Crystal Ball function on top of irreducible background fitted with an exponential shape. The background shape appeared to be in good agreement with expectations from the continuum $\gamma\gamma \to \mu^+\mu^-$ production.

The transverse momentum distribution for opposite-sign dimuons in the invariant mass range 2.8 GeV/c^2 $< M_{\mu^+\mu^-} <$ 3.4 GeV/c^2 is shown in fig. 1 (right). This spectrum was fitted with a sum of Monte-Carlo templates corresponding to four contributions: coherent and incoherent J/ψ, feed-down J/ψ from ψ' decays and $\gamma\gamma \to \mu^+\mu^-$ contribution at low p_{T}. The coherent J/ψ yield was extracted from the fit keeping relative contributions of coherent and incoherent J/ψ unconstrained.

Normalization of the coherent J/ψ cross section at forward rapidity was performed with respect to the continuum dimuon pair production cross section which is known from QED but with large uncertainties of about 20%. The cross section $d\sigma^{\mathrm{coh}}_{J/\psi}/dy = 1.00 \pm 0.18\,(\mathrm{stat})^{+0.24}_{-0.26}\,(\mathrm{syst})$ mb in the rapidity interval $-3.6 < y < -2.6$ has been recently published by ALICE [3].

The measurement of J/ψ production in UPC at midrapidity was obtained using data collected in 2011. The trigger required back-to-back topology of the fired cells in the time-of-flight detector (TOF), at least two hits in the silicon pixel detector (SPD) and vetoes on VZERO counters at forward and backward rapidity. Track reconstruction was performed with the time projection chamber (TPC) and the silicon tracking system in about two pseudorapidity units. Events with only two opposite sign good-quality tracks coming from a recontructed primary vertex have been selected. J/ψ signal was extracted both in dielectron and dimuon channels which were separated by the energy deposition in TPC. Coherent and incoherent contributions in the J/ψ peak were extracted from fits to dilepton p_{T} spectra similar to the forward case. Cross section normalization was performed with respect to the integrated luminosity which was measured using a trigger for the most central hadronic Pb+Pb collisions and corrected for the UPC trigger live time. Results have been recently published in [4].

ALICE results on coherent J/ψ photoproduction cross section at forward ($-3.6 < y < -2.6$) and central ($|y| < 0.9$) rapidity are compared with various model calculations in fig. 2. There are at least 5 predictions which have been recently published. The STARLIGHT generator is based on the Vector Dominance Model coupled with the classical probabilistic formula to account for J/ψ absorption effects [5]. A set of predictions by Adeluyi–Bertulani (AB) is based on LO pQCD calculations: the upper curve AB-MSTW08 assumes no modification of the gluon distribution

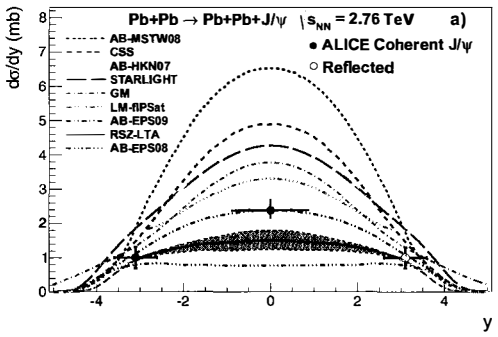

Figure 2: ALICE results on the coherent J/ψ photoproduction cross section at forward and central rapidity compared with model predictions. See Ref. [3,4] for details.

while other three incorporate gluon shadowing from various parameterizations (HKN07, EPS08, EPS09) [6]. The difference of the measured cross section with respect to the upper curve reflects the strength of the gluon shadowing effect. Goncalves-Mochado (GM) prediction is based on the color dipole model and saturation effects from the Color-Glass-Condensate framework [7]. CSS model accounts for shadowing effects by propagating $c\bar{c}$ and $c\bar{c}g$ intermediate states in the Glauber approach [8]. Finally, RSZ-LTA model incorporates gluon shadowing effects in the leading twist approximation [9].

The obtained experimental data favour the models which take into account gluon shadowing effects in the LO pQCD framework. The best agreement is found for the model [6] which incorporates gluon shadowing according to EPS09LO global fits [10].

3 ρ^0 photoproduction

In contrast to J/ψ, ρ^0 photoproduction is hardly sensitive to partonic degrees of freedom and gluon shadowing effects in nuclei. However, measurement of the coherent ρ^0 photoproduction cross section in UPC at LHC, supplemented by STAR results at RHIC energies [11], should help to verify ρ^0 photoproduction models which differ by factor 2 in the predicted cross sections [5,7,12].

ALICE measured ρ^0 photoproduction in the $\pi^+\pi^-$ channel based on 2010 Pb+Pb data with the trigger requiring at least two hits in SPD and TOF and vetoes in VZERO counters at forward and backward directions. The unfolded $\pi^+\pi^-$ invariant mass distribution, shown in fig. 3, was fitted with the function which includes variable width Breit-Wigner and non-resonant $\pi^+\pi^-$ contributions. The obtained mass $M_{\rho^0} = 767.8 \pm 3.5$ MeV/c^2 and the width $\Gamma_{\rho^0} = 154.1 \pm 8.7$ MeV/c^2 are compatible with PDG values. In order to extract the coherent ρ^0 yield, p_T distribution for the selected $\pi^+\pi^-$ pairs was fitted with Monte-Carlo templates for coherent and incoherent samples from STARLIGHT. The fraction of incoherent events was found to be $\sim 7\%$ for $p_T < 150$ MeV/c. The coherent ρ^0 peak appears to be slightly narrower in data than in the STARLIGHT simulation.

4 Conclusions and outlook

ALICE made the first measurement on the exclusive J/ψ photoproduction in Pb-Pb collisions at LHC both at forward and central rapidity. The coherent J/ψ cross section was found to be in good agreement with those models which include nuclear gluon shadowing consistent with EPS09 parametrization [10].

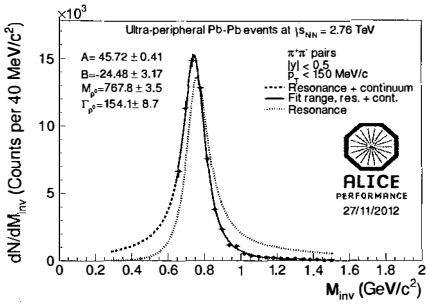

Figure 3: Unfolded invariant mass distribution for $\pi^+\pi^-$ pairs in ultraperipheral Pb+Pb collisions.

In the beginning of 2013, ALICE took p+Pb data with dedicated UPC triggers offering a unique opportunity to measure exclusive quarkonium photoproduction on protons. The exclusive J/ψ photoproduction, previously studied in ep collisions at HERA, provides a direct tool to constrain the gluon density in proton down to $x \sim 10^{-4}$ [13]. ALICE p+Pb UPC data allow to extend HERA results from $W_{\gamma p} \sim 300$ GeV up to TeV scale ($W_{\gamma p}$ is the γp center-of-mass energy) and to study gluon distributions in the wide range of Bjorken x from 10^{-2} to 10^{-5}.

Diffractive particle production in pp collisions at LHC is another interesting subject studied by ALICE and closely related to UPC. Results on inelastic, single and double diffractive cross sections at 0.9, 2.76 and 7 TeV have been recently published by ALICE [14]. Special effort is also devoted to the studies of central diffraction corresponding to the double-pomeron exchange mechanism and experimentally identified by gaps in the forward and backward directions.

References

1. A. J. Baltz *et al*, *Phys. Rept.* **458**, 1 (2008).
2. K. Aamodt *et al* [ALICE Collaboration], *J. Instrum.* **3**, S08002 (2008).
3. B. Abelev *et al* [ALICE Collaboration], *Phys. Lett.* B **718**, 1273 (2013).
4. E. Abbas *et al* [ALICE Collaboration], arXiv:1305.1467 [nucl-ex].
5. S. R. Klein and J. Nystrand, *Phys. Rev.* C **60**, 014903 (1999).
6. A. Adeluyi and C. A. Bertulani, *Phys. Rev.* C **85**, 044904 (2012).
7. V. P. Goncalves and M. V. T. Machado, *Phys. Rev.* C **84**, 011902 (2011).
8. A. Cisek, W. Schäfer and A. Szczurek, *Phys. Rev.* C **86**, 014905 (2012).
9. V. Rebyakova, M. Strikman and M. Zhalov, *Phys. Lett.* B **710**, 647 (2012).
10. K. J. Eskola, H. Paukkunen and C. A. Salgado, *JHEP* **0904**, 065 (2009).
11. G. Agakishiev *et al* [STAR Collaboration], *Phys. Rev.* C **85**, 014910 (2012).
12. L. Frankfurt, M. Strikman, M. Zhalov, *Phys. Lett.* B **537**, 51 (2002); *Phys. Rev.* C **67**, 034901 (2003).
13. A. D. Martin, C. Nockles, M. Ryskin and T. Teubner. *Phys. Lett.* B **662**, 252 (2008).
14. B. Abelev *et al* [ALICE Collaboration], arXiv:1208.4968 [hep-ex].

6.
Low Energy

RECENT RESULTS ON HADRON PHYSICS AT KLOE

P. Moskal on behalf of the KLOE and KLOE–2 Collaborations[a]
Department of Physics, Jagiellonian University, Reymonta 4, Poland

One of the basic motivations of the KLOE and KLOE-2 collaborations is the test of fundamental symmetries and the search for phenomena beyond the Standard Model via the hadronic and leptonic decays of ground-state mesons and via their production in the fusion of virtual gamma quanta exchanged between colliding electrons and positrons. This contribution includes brief description of results of recent analysis of the KLOE data aimed at (i) the search for the dark matter boson, (ii) determination of the hadronic and light-by-light contributions to the g-2 muon anomaly and (iii) tests of QCD anomalies.

1 Introduction

The KLOE detector consists of a $\sim$ 3.5 m long cylindrical drift chamber with a diameter of about 4 m surrounded by the sampling electromagnetic calorimeter [1,2,3]. Both these detectors are immersed in the axial magnetic field ($\sim$ 0.5 T) provided by the superconducting solenoid. The detector surrounds the crossing region of the positron and electron beams circulating in the rings of the DAΦNE collider [4].

Results presented in this contribution have been obtained using the data sample collected by the KLOE collaboration. Search for the U boson, and studies of the box anomaly and $e^+e^- \to \pi^+\pi^-$ process were based on the data taken at the center-of-mass energy of $\sqrt{s} = 1.02$ GeV corresponding to the mass of the ϕ meson, whereas the studies of the $\gamma^*\gamma^* \to \eta$ process were based on the data sample taken at the center-of-mass energy of $\sqrt{s} = 1$ GeV, where background from ϕ meson decay is suppressed.

[a]The KLOE–2 Collaboration: D. Babusci, D. Badoni, I. Balwierz-Pytko, G. Bencivenni, C. Bini, C. Bloise, F. Bossi, P. Branchini, A. Budano, L. Caldeira Balkeståhl, G. Capon, F. Ceradini, P. Ciambrone, F. Curciarello, E. Czerwiński, E. Danè, V. De Leo, E. De Lucia, G. De Robertis, A. De Santis, A. Di Domenico, C. Di Donato, R. Di Salvo, D. Domenici, O. Erriquez, G. Fanizzi, A. Fantini, G. Felici, S. Fiore, P. Franzini, A. Gajos, P. Gauzzi, G. Giardina, S. Giovannella, E. Graziani, F. Happacher, L. Heijkenskjöld, B. Höistad, L. Iafolla, M. Jacewicz, T. Johansson, K. Kacprzak, A. Kupsc, J. Lee-Franzini, B. Leverington, F. Loddo, S. Loffredo, G. Mandaglio, M. Martemianov, M. Martini, M. Mascolo, R. Messi, S. Miscetti, G. Morello, D. Moricciani, P. Moskal, F. Nguyen, A. Palladino, A. Passeri, V. Patera, I. Prado Longhi, A. Ranieri, C. F. Redmer, P. Santangelo, I. Sarra, M. Schioppa, B. Sciascia, M. Silarski, C. Taccini, L. Tortora, G. Venanzoni, W. Wiślicki, M. Wolke, J. Zdebik

2 Search for the dark matter boson

There are many astrophysical obsrevations indicating existence of dark matter. For example: an excess of the e^+e^- annihilation γ quanta from the galactic center observed by the INTEGRAL satellite [5], the excess in the cosmic ray positrons reported by PAMELA [6], the total electron and positron flux measured by ATIC [7], Fermi [8], and HESS [9], and the annual modulation of the DAMA/LIBRA signal [10]. The origin of this kind of enhanced stream of radiation may be explained assuming [11] that positrons are created in an annihilation of the dark matter particles into e^+e^- pairs, and that this process is mediated by the U boson with mass in the GeV scale. The existence of such U boson can manifest itself as a maximum in the invariant mass distribution of e^+e^- pairs originating from the radiative decays as e.g. $\phi \to \eta e^+e^-$. In this case a light dark-force mediator (U boson) may contribute to this process via following decay chain: $\phi \to \eta\gamma^* \to \eta U \to \eta\gamma^* \to \eta e^+e^-$. In Figure 1 we present results of the analysis of data sample of 1.7 fb^{-1} where no structures are observed in the e^+e^- invariant mass distribution over the background. Therefore, we set only an upper limit at 90% C.L. on the ratio between the U boson coupling constant and the fine structure constant of $\alpha'/\alpha < 1.7 \times 10^{-5}$ for $30 < M_U < 400$ MeV and $\alpha'/\alpha \leq 8 \times 10^{-6}$ for the sub-region $50 < M_U < 210$ MeV [14].

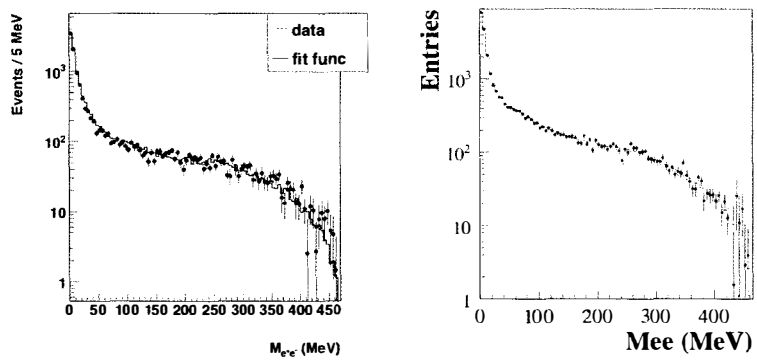

Figure 1: e^+e^- invariant mass spectrum for $\phi \to \eta e^+e^-$ decay with $\eta \to \pi^+\pi^-\pi^0$ (left) and with $\eta \to 3\pi^0$ (right). Solid lines indicate result of the fit performed assuming the Vector Meson Dominance expectations for the $\phi\eta\gamma^*$ transition form factor.

3 KLOE contribution to the determination of the g-2 anomaly

Comparison of measured and calculated value of the muon magnetic moment anomaly $a_\mu = (g_\mu - 2)/2$ constitutes one of the most precise test of the Standard Model, since a_μ was measured with the precision of 0.5 ppm [12], and FNAL experiment [13] plans to improve this accuaracy to 0.14 ppm in the near future. The predictions of the value of a_μ based on the SM are however limited by the accuracy of the determination of the hadronic contributions which in 70% originates from the two pion contribution due to the $\gamma^* \to \pi^+\pi^-$ process. Therefore, we have conducted the independent measurement of the $e^+e^- \to \pi^+\pi^-(\gamma)$ cross section below 1 GeV, which is particularly important to test the Standard Model calculation for the (g-2) of the muon, where a long standing 3 sigma discrepancy is observed.

We have determined the ratio of $\sigma(e^+e^- \to \pi^+\pi^-\gamma)/\sigma(e^+e^- \to \mu^+\mu^-\gamma)$, using a total integrated luminosity of about 240 pb^{-1}. From this ratio we obtain the cross section $\sigma(e^+e^- \to \pi^+\pi^-)$ shown in Figure 2. From the cross section we determine the pion form factor $|F_\pi|^2$ and

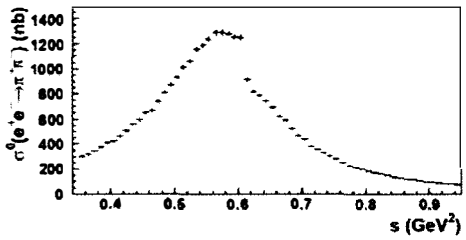

Figure 2: The bare cross section from the $\pi^+\pi^-\gamma/\mu^+\mu^-\gamma$ ratio [15].

the two-pion contribution to the muon anomaly a_μ for $0.592 < M_{\pi\pi} < 0.975$ GeV, $\Delta^{\pi\pi}a_\mu = (385.1 \pm 1.1_{\text{stat}} \pm 2.7_{\text{sys+the}}) \times 10^{-10}$. This result confirms the current discrepancy between the Standard Model calculation and the experimental measurement of the muon anomaly.

It is worth mentioning that the previous KLOE measurements were normalized to the luminosity using large angle Bhabha scattering, whereas the dereviation of $\sigma(e^+e^- \to \pi^+\pi^-)$ from the ratio of cross sections caused cancelation of many potential sources of uncertainty as e.g.: the radiator function, luminosity derivation, vacuum polarization corections, and to large extent also acceptance corrections [15]. In addition the influence of FSR was minimized by taking into account only small angular range for γ quanta.

Another large contribution to the uncertainty of the a_μ calculations originates from the uncertainty in determination of pseudoscalar transition form factors which dominates the precision in determination of hadronic light-by-light contributions. Therefore the precise studies of transition form factors is of importance for the SM predictions of the anomalous magnetic moment of the muon.

Studies of the conversion decays give information about the time-like region of the form-factor with positive q^2 equal to the square of the invariant mass of the l^+l^- pair [16,17]. Information about the space-like region with the negative values of q^2 is accessible via cross section of mesons production in $\gamma^*\gamma^*$ fusion realized in e.g. $e^+e^- \to e^+e^-\gamma^*\gamma^* \to e^+e^-\eta$ reaction [18]. From the measurement of the cross section of this process we derived the partial width $\Gamma(\eta \to \gamma\gamma) = (520 \pm 20_{stat} \pm 13_{syst})eV$ [18], which is the most precise measurement to date.

4 Tests of QCD anomalies

The η meson is particularly suited for studies of QCD anomalies because all its strong and electromagnetic decays are forbidden in the first order [19]. The most energetically favourable strong decay of η into 2π is forbidden due to P and CP invariance. Its decay into 3π is suppressed by G-parity and isospin invariance [20], and it occurs due to the difference between the mass of u and d quarks. The first order electromagnetic decays as $\eta \to \pi^0\gamma$ or $\eta \to 2\pi^0\gamma$ break charge conjugation invariance and $\eta \to \pi^+\pi^-\gamma$ is also suppressed because charge conjugation conservation requires odd (and hence nonzero) angular momentum in the $\pi^+\pi^-$ system. Therefore, this radiative decay at a massless quark limit is driven by the QCD box anomaly.

The ratio $R_\eta = \Gamma(\eta \to \pi^+\pi^-\gamma)/\Gamma(\eta \to \pi^+\pi^-\pi^0)$ has been measured by analysing 22 million $\phi \to \eta\gamma$ decays collected by the KLOE experiment, corresponding to an integrated luminosity of 558 pb^{-1}. The $\eta \to \pi^+\pi^-\gamma$ proceeds both via the ρ resonant contribution, and possibly a non-resonant direct term connected to the box anomaly. Our result, $R_\eta = 0.1856 \pm 0.0005_{stat} \pm 0.0028_{syst}$, points out a sizable contribution of the direct term to the total width [22]. The di-pion invariant mass for the $\eta \to \pi^+\pi^-\gamma$ decay could be described in a model-independent approach in terms of a single free parameter, α. The determined value of the parameter α is equal to $(1.32 \pm 0.08_{stat}{}^{+0.10}_{-0.09syst} \pm 0.02_{theo})$ GeV^{-2} [22], and it is in agreement with the result of the WASA

collaboration [23].

5 Perspectives

Taking atvantage of a successfuly commissioned [24] new electron-positron interaction region of DAΦNE, in the near future the data sample will be significantly increased by means of the KLOE-2 detector setup [11,21], which is a successor of KLOE upgraded with new components in order to improve its tracking and clustering capabilities as well as in order to tag $\gamma\gamma$ fusion processes [25,26,27,28,29].

Acknowledgments

This work was supported in part by the EU Hadron Physics Project under contract number RII3-CT-2004-506078; by the European Commission: FP7-INFRASTRUCTURES-2008-1, Grant Agreement No. 283286; by the Polish National Science Centre through the Grants No. 0469/B/H03/2009/37, 2011/01/D/ST2/00748, 2011/03/N/ST2/02652, 2011/03/N/ST2/02641 and by the Foundation for Polish Science through the MPD programme and the project HOMING PLUS BIS/2011-4/3.

References

1. M. Adinolfi et al., Nucl. Phys. A 663, 1103(2000).
2. M. Adinolfi et al. Nucl. Inst. and Meth. A 482, 364 (2002).
3. M. Adinolfi et al. Nucl. Inst. and Meth. A 488, 51 (2002).
4. J. Lee-Franzini, P. Franzini, Acta Phys. Polon. B 38, 2703 (2007).
5. P. Jean et al., Astron. Astrophys. 407, L55 (2003).
6. O. Adriani et al., Nature 458, 607 (2009).
7. J. Chang et al., Nature 456, 362 (2008).
8. A.A. Abdo et al., Phys. Rev. Lett. 102, 181101 (2009).
9. F. Aharonian et al., Astron. Astrophys. 508, 561 (2009).
10. R. Bernabei et al., Eur. Phys. J. C 56, 333 (2008).
11. G. Amelino-Camelia et al., Eur. Phys. J. C 68, 619 (2010).
12. G.W. Bennett et al., Phys. Rev. D 73, 072003 (2006).
13. R.M. Carey et al. (2009), *FERMILAB-PROPOSAL-0989*
14. D. Babusci et al., Phys. Lett. B 720, 111 (2013).
15. D. Babusci et al., Phys. Lett. B 720, 336 (2013).
16. F. Archilli et al., Phys. Lett. B 706, 251 (2012).
17. F. Ambrosino et al., Phys. Lett. B 702, 324 (2011).
18. D. Babusci et al., JHEP 01, 119, (2013).
19. B. M. K. Nefkens, J. W. Price, Phys. Scripta T99, 114 (2002).
20. M. J. Zielinski, arXiv:0807.0576, diploma thesis, JU (2008).
21. F. Bossi, J. Phys. Conf. Ser. 171, 012099 (2009).
22. D. Babusci et al., Phys. Lett. B 718, 910 (2013).
23. P. Adlarson et al., Phys. Lett. B 707, 243 (2012).
24. M. Zobov et al., Phys. Rev. Lett. 104, 174801 (2010).
25. D. Babusci et al. Nucl. Instr. Meth. A 617, 81 (2010).
26. F. Archilli et al. Nucl. Instr. Meth. A 617, 266 (2010).
27. A. Balla et al. Nucl. Instr. Meth. A 628, 194 (2011).
28. M. Codelli et al. Nucl. Instr. Meth. A 617, 105 (2010).
29. F. Happacher et al. Nucl. Phys. B 197, 215 (2009).

Study of the rare decay $K^{\pm} \to \pi^{\pm}\gamma\gamma$ in the NA48/2 and NA62 experiments at CERN

Mauro Piccini*
INFN - Sezione di Perugia, Via A. Pascoli, 06123 Perugia, Italy
E-mail: Mauro.Piccini@pg.infn.it

A sample of about 300 $K^{\pm} \to \pi^{\pm}\gamma\gamma$ rare decays with a background contamination below 10% has been collected by the NA48/2 and NA62 experiments at CERN during low intensity runs with minimum bias trigger configuration. The measurements of the decay spectrum and rate provide a crucial test of the Chiral Perturbation Theory (ChPT) describing weak processes at low energy.

1 Introduction

Radiative non-leptonic kaon decays can provide fundamental tests for the predictivity of the Chiral Perturbation Theory (ChPT) in order to describe weak processes at low energy. In this respect, an early prediction from ChPT for the rate of the $K^{\pm} \to \pi^{\pm}\gamma\gamma$ decay is reported in [1]. In the ChPT framework, the $K^{\pm} \to \pi^{\pm}\gamma\gamma$ process is described by two non-interfering contributions: one for the pion and kaon loop amplitudes depending on an unknown $\hat{c}$ parameter ($\hat{c} \sim O(1)$) which represents the total contribution of the counter-terms, the other taking into account for the pole amplitude [2]. Once the two contributions are considered, the di-photon invariant mass $m_{\gamma\gamma}$ spectrum exhibits a characteristic cusp at twice the charged pion mass due to the dominance of the pion loop amplitude. Higher order unitarity corrections ($O(p^6)$ and above) modify the lowest order $O(p^4)$ decay spectrum significantly: in particular, they lead to a non-zero value of

*for the NA48/2 and NA62 Collaborations: F. Ambrosino, A. Antonelli, G. Anzivino, R. Arcidiacono, W. Baldini, S. Balev, J.R. Batley, M. Behler, S. Bifani, C. Biino, A. Bizzeti, B. Bloch-Devaux, G. Bocquet, V. Bolotov, F. Bucci, N. Cabibbo, M. Calvetti, N. Cartiglia, A. Ceccucci, P. Cenci, C. Cerri, C. Cheshkov, J.B. Chèze, M. Clemencic, G. Collazuol, F. Costantini, A. Cotta Ramusino, D. Coward, D. Cundy, A. Dabrowski, G. D'Agostini, P. Dalpiaz, C. Damiani, H. Danielsson, M. De Beer, G. Dellacasa, J. Derré, H. Dibon, D. Di Filippo, L. DiLella, N. Doble, V. Duk, J. Engelfried, K. Eppard, V. Falaleev, R. Fantechi, M. Fidecaro, L. Fiorini, M. Fiorini, T. Fonseca Martin, P.L. Frabetti, A. Fucci, S. Gallorini, L. Gatignon, E. Gersabeck, A. Gianoli, S. Giudici, A. Gonidec, E. Goudzovski, S. Goy Lopez, E. Gushchin, B. Hallgren, M. Hita-Hochgesand, M. Holder, P. Hristov, E. Iacopini, E. Imbergamo, M. Jeitler, G. Kalmus, V. Kekelidze, K. Kleinknecht, V. Kozhuharov, W. Kubischta, V. Kurshetsov, G. Lamanna, C. Lazzeroni, M. Lenti, E. Leonardi, L. Litov, D. Madigozhin, A. Maier, I. Mannelli, F. Marchetto, G. Marel, M. Markytan, P. Marouelli, M. Martini, L. Masetti, P. Massarotti, E. Mazzucato, A. Michetti, I. Mikulec, M. Misheva, N. Molokanova, E. Monnier, U. Moosbrugger, C. Morales Morales, M. Moulson, S. Movchan, D.J. Munday, M. Napolitano, A. Nappi, G. Neuhofer, A. Norton, T. Numao, V. Obraztsov, V. Palladino, M. Patel, M. Pepe, A. Peters, F. Petrucci, M.C. Petrucci, B. Peyaud, R. Piandani, M. Piccini, G. Pierazzini, I. Polenkevich, I. Popov, Yu. Potrebenikov, M. Raggi, B. Renk, F. Retière, P. Riedler, A. Romano, P. Rubin, G. Ruggiero, A. Salamon, G. Saracino, M. Savrié, M. Scarpa, V. Semenov, A. Sergi, M. Serra, M. Shieh, S. Shkarovskiy, M.W. Slater, M. Sozzi, T. Spadaro, S. Stoynev, E. Swallow, M. Szleper, M. Valdata-Nappi, P. Valente, B. Vallage, M. Velasco, M. Veltri, S. Venditti, M. Wache, H. Wahl, A. Walker, R. Wanke, L. Widhalm, A. Winhart, R. Winston, M.D. Wood, S.A. Wotton, O. Yushchenko, A. Zinchenko, M. Ziolkowski.

the differential decay rate at $m_{\gamma\gamma} = 0$ [3]. The total decay rate, extracted in a model dependent approach, is predicted to be around 10^{-6}, with the pole amplitude contributing at the level of 5% or less [3,4].

From the experimental point of view, the only published result by the E787 experiment at BNL [5] is based on 31 K^+ decay candidates in the kinematic region 100 MeV/c < p^*_π < 180 MeV/c, where p^*_π is the π^+ momentum in the K^+ rest frame. This contribution describes the $K^\pm \to \pi^\pm\gamma\gamma$ analyses based on the minimum bias samples collected with high trigger efficiency by the NA48/2 and NA62 experiments in the years 2004 and 2007. The resulting $K^\pm \to \pi^\pm\gamma\gamma$ sample is 10 times larger than the BNL E787 one and allows the measurement of $\hat{c}$ and the extraction of the Branching Ratio of the decay.

2 Description of $K^\pm \to \pi^\pm\gamma\gamma$ decay

In the ChPT framework the kinematic variables used to describe the $K^\pm \to \pi^\pm\gamma\gamma$ decay are:

$$y = \frac{p(q_1 - q_2)}{m_K^2}, \quad z = \frac{(q_1 + q_2)^2}{m_K^2} = \left(\frac{m_{\gamma\gamma}}{m_K}\right)^2, \tag{1}$$

where p is the 4-momentum of the kaon, $q_{1,2}$ are the 4-momenta of the two photons, $m_{\gamma\gamma}$ is the di-photon invariant mass and m_π is the charged pion mass. The differential decay rate up to next-to-leading order in the ChPT framework is parameterized in the following way [3]:

$$\frac{\partial\Gamma}{\partial y \partial z}(\hat{c}, y, z) = \frac{m_K}{2^9\pi^3}\left[z^2(|A(\hat{c}, z, y^2) + B(z)|^2 + |C(z)|^2) + \left(y^2 - \frac{1}{4}\lambda(1, r_\pi^2, z)\right)^2 |B(z)|^2\right], \tag{2}$$

where $r_\pi = m_\pi/m_K$, m_π is the charged pion mass, $\lambda(1, r_\pi^2, z) = 1 + r_\pi^4 + z^2 - 2(r_\pi^2 + z + r_\pi^2 z)$ and $A(\hat{c}, z, y^2)$ and $B(z)$ are the loop amplitudes; the latter appears only at next-to-leading $O(p^6)$ order and is dominant at low z. $C(z)$ is the pole amplitude. The ChPT predictions for the decay spectrum and rate are:

- a cusp in the differential decay width (dΓ/dz) distribution at the di-pion threshold ($z_{th} = 4r_\pi^2 = 0.320$)
- a non-zero differential rate at z = 0 and a y^2-dependence of the differential rate arising both at next-to-leading order $O(p^6)$.

3 The NA48/II and NA62 experiments: beam and detector

In the 2003-2004 (2007) years the NA48/2 (NA62) experiments have collected data on charged kaon decays. The beam and the detectors were the same for both the experiments with only minor changes. Two simultaneous K^+ and K^- beams were produced by a 400 GeV/c proton beam delivered by the CERN SPS and impinging on a berillium target. The beamline was designed to select kaons with a momentum range of (60 $\pm$ 3) GeV/c in NA48/2 and (74 $\pm$ 1) GeV/c in NA62. In NA48/2 the data used for the present analysis were collected in 2004 during a dedicated run with a special trigger setup which only requires one or more tracks in the magnetic spectrometer and at least a energy deposit of 10 GeV/c in the electromagnetic calorimeter . Also the intensity of the beam was lowered and the momentum spread was reduced to obtain an acceptable rate of events to be recorded. Almost the same trigger was used during the entire 2007 run ($\sim$ 100 days) of NA62, with an average downscale factor of $\sim$ 20 applied to the number of triggers at software level.

The main components of the NA48/2 detector were a magnetic spectrometer, composed by four drift chambers with a dipole magnet in the middle deflecting charged particles in the horizontal plane, and a liquid krypton electromagnetic calorimeter (LKr) with an energy resolution

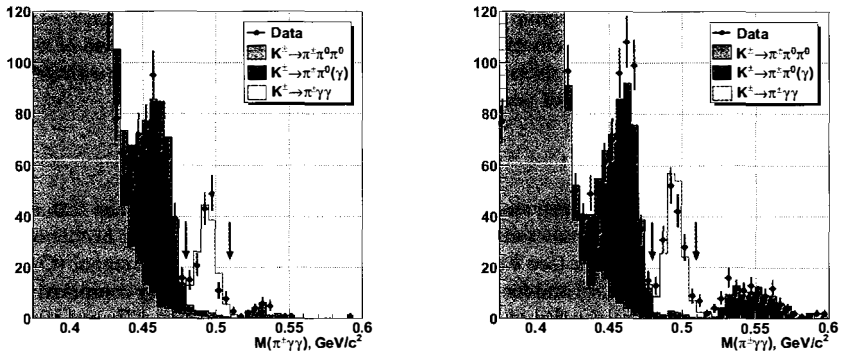

Figure 1: The $\pi^\pm\gamma\gamma$ invariant mass for the 2004 (left) and 2007 (right) samples; vertical arrows show the limits of the signal region.

of about 1% for 20 GeV photons and electrons. Giving the different kaon momenta between 2004 and 2007 the p_t kick of the dipole magnet was 120 MeV/c for NA48/2 and 265 MeV/c for NA62. A fast signal for the trigger was produced by a charged hodoscope (CHOD) consisting of two planes of horizontal and vertical scintillator strips. The NA48/2 detector is described in detail elsewhere[6].

4 Event selection and reconstruction

The decay vertex was defined searching for the Closest Distant of Approach (CDA) between the pion track and the nominal $K^\pm$ beam directions. The longitudinal coordinate of the such vertex was selected to be inside the fiducial decay volume (62 m region) of the experiment. In order to identify the pion, one and only one track was required to be reconstructed from the information collected by the spectrometer, the track had to match the acceptances of the main detectors (LKr, CHOD) and the measured momentum was required to be within 10 (8) and 40 (50) GeV/c for the NA48/2 (NA62) data. The ratio E/p between the energy E deposited by the track in the LKr and the momentum p measured by the spectrometer was required to be lower than 0.85.

To identify the two photons two independent clusters were required in the LKr with energy greater than 3 GeV. Both clusters had to be in time with the reconstructed pion track. The invariant mass of the pion and of the two photons was then computed taking into account the position of the decay vertex. Such reconstructed $\pi^\pm\gamma\gamma$ invariant mass was required to be in the range (0.48-0.51) GeV/c^2 ($\pm$15 MeV/c^2 from $K^\pm$ mass). A cut requiring $0.2 < z < 0.54$ was applied, the lower limit allowing to reject the $K^\pm \to \pi^\pm\pi^0$ background. After such selection criteria were applied to the two data samples collected in 2004 by NA48/2 and in 2007 by NA62, the number of observed events in the signal region was 147 and 175 respectively (see figure 1).

Table 1: Signal statistics and main background contributions for the two samples.

	2004	2007
$K^\pm \to \pi^\pm\gamma\gamma$ candidates	147	175
$K^\pm \to \pi^\pm\pi^0(\gamma)$ background	11.0 $\pm$ 0.8	11.1 $\pm$ 1.0
$K^\pm \to \pi^\pm\pi^0\pi^0$ background	5.9 $\pm$ 0.7	1.3 $\pm$ 0.3
$K^\pm \to \pi^\pm\gamma\gamma$ signal	130 $\pm$ 12	163 $\pm$ 13

As shown in Table 1, the main background comes from the decay $K^\pm \to \pi^\pm\pi^0(\gamma)$, with a

photon eventually lost. Non negligible background is also produced by the decay $K^{\pm} \to \pi^{\pm}\pi^0\pi^0$ with two photons lost, such contribution is higher in the NA48/2 sample because of the worse resolution on the $\pi^{\pm}\gamma\gamma$ invariant mass. The two background contributions were estimated from MonteCarlo simulation, the overall background is at the level of 9%.

5 Results

After all the selection criteria were applied, the values of the $\hat{c}$ parameter in the framework of the ChPT $O(p^4)$ and $O(p^6)$ parameterizations have been measured performing likelihood fits to the z spectra coming from data (see Figure 2). The MonteCarlo outputs for signal ($O(p^4)$ and $O(p^6)$ generators according to[3]) and for background components were directly compared to data. In Table 2 the results from the fits of the 2004 and 2007 data in the two different theoretical

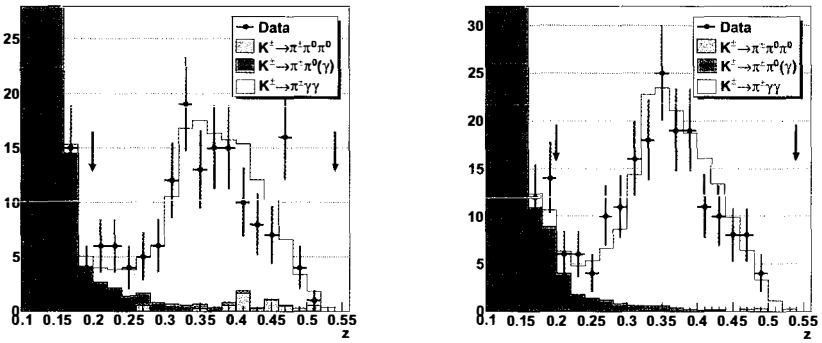

Figure 2: Distribution of the z variable for the 2004 (left) and 2007 (right) samples; vertical arrows show the limits of the signal region.

frameworks are listed. The results are then combined taking into account the correlations between the systematic errors. The main contribution to the systematic errors comes from the

Table 2: Extracted values of $\hat{c}$ for the 2004 and 2007 samples in the ChPT $O(p^4)$ and $O(p^6)$ frameworks. Combined results are also listed.

	2004	2007	Combined
$\hat{c}$ at $O(p^4)$	$1.36 \pm 0.33_{stat} \pm 0.07_{syst}$	$1.71 \pm 0.29_{stat} \pm 0.06_{syst}$	$1.56 \pm 0.22_{stat} \pm 0.07_{syst}$
$\hat{c}$ at $O(p^6)$	$1.67 \pm 0.39_{stat} \pm 0.09_{syst}$	$2.21 \pm 0.31_{stat} \pm 0.08_{syst}$	$2.00 \pm 0.24_{stat} \pm 0.09_{syst}$

background evaluation. Other effects (for example trigger efficiency and pion mis-identification) were also studied and give small contributions. Once $\hat{c}$ is measured, a Branching Ratio value (model dependent) of the decay can also be analytically derived. In the $O(p^6)$ framework, the preliminary measurement of $\hat{c}$ gives the value $BR(K^{\pm} \to \pi^{\pm}\gamma\gamma) = (1.01 \pm 0.06) \times 10^{-6}$.

References

1. L. M. Sehgal, *Phys. Rev.* D **6**, 367 (1972).
2. G. Ecker, A. Pich and E. de Rafael, *Nucl. Phys.* B **303**, 665 (1988).
3. G. D'Ambrosio and J. Portolés, *Phys. Lett.* B **386**, 403 (1996).
4. J.-M. Gérard, C. Smith and S. Trine, *Nucl. Phys.* B **730**, 1 (2005).
5. P. Kitching *et al*, *Phys. Rev. Lett.* **79**, 4079 (1997).
6. V. Fanti *et al*, *Nucl. Instrum. Methods* A **574**, 433 (2007).

$\tau^- \to \pi^- \eta^{(\prime)} \nu_\tau$ decays

PABLO ROIG
Grup de Física Teòrica, Institut de Física d'Altes Energies, Universitat Autònoma de Barcelona, E-08193 Bellaterra, Barcelona, Spain

1 Introduction

$\tau^- \to \pi^- \eta^{(\prime)} \nu_\tau$ decays belong to the so-called second-class current processes [1]: parity conservation implies that these decays must proceed through the vector current, which has opposed G-parity to the $\pi^- \eta^{(\prime)}$ system. In the limit of exact isospin symmetry G-parity is exact and these processes are forbidden. Isospin is an approximate symmetry, slightly broken both by $m_u \neq m_d$ (in QCD) and $q_u \neq q_d$ (in QED), which results in a sizable suppression of the considered decays, which have not been measured so far. The corresponding branching ratios upper limits are $9.9 \cdot 10^{-5}$ [2] and $7.2 \cdot 10^{-6}$ [3] and no second-class current process has been reported yet. This suppression motivates the study of beyond the standard model (SM) contributions to these decays [4,5].

Here we focus on the SM prediction of these processes, focusing on the scalar and vector form factors contributions.

2 Hadronic matrix element and decay width

Our conventions [6] are fixed from Ref. [7]. Therefore, we have ($P = \pi/\eta/\eta'$)

$$\left\langle \pi^- P^0 \middle| \bar{d}\gamma^\mu u \middle| 0 \right\rangle = c^V_{\pi^- P} \left[(p_P - p_\pi)^\mu f_+^{\pi^- P}(s) - q^\mu f_-^{\pi^- P}(s) \right] , \tag{1}$$

with $q^\mu = (p_P + p_\pi)^\mu$, $s = q^2$, and $c^V_{\pi^-\pi^0} = -\sqrt{2} = -c^V_{\pi^-\eta^{(\prime)}}$. $f_0^{\pi^- P}(s)$, which can be used instead of $f_-^{\pi^- P}(s)$, is defined through

$$\left\langle 0 \middle| \partial_\mu (\bar{d}\gamma^\mu u) \middle| \pi^+ P \right\rangle = i(m_d - m_u) \left\langle 0 \middle| \bar{d}u \middle| \pi^+ P \right\rangle \equiv i \Delta^{QCD}_{K^0 K^+} c^S_{\pi^- P} f_0^{\pi^- P}(s) , \tag{2}$$

with

$$c^S_{\pi^-\eta} = \sqrt{\frac{2}{3}} = c^S_{\pi^-\pi^0}\,, \quad c^S_{\pi^-\eta'} = \frac{2}{\sqrt{3}}\,, \quad \Delta_{PQ} = m_P^2 - m_Q^2. \tag{3}$$

The mass renormalization

$$m_d - m_u = \frac{\Delta^{QCD}_{K^0K^+}}{B_0}\left[1 + \frac{16c_m}{F^2M_S^2}(c_d - c_m)m_K^2\right], \tag{4}$$

needs to be taken into account to define $f_0^{\pi^-P}(s)$.

From eqs.(1) and (2) one gets

$$\left\langle \pi^- P^0 \middle| \bar{d}\gamma^\mu u \middle| 0 \right\rangle = \left[(p_P - p_\pi)^\mu + \frac{\Delta_{\pi^-P}}{s}q^\mu\right] c^V_{\pi^-P} f_+^{\pi^-P}(s) + \frac{\Delta^{QCD}_{K^0K^+}}{s} q^\mu c^S_{\pi^-P} f_0^{\pi^-P}(s)\,. \tag{5}$$

The finiteness of the matrix element at the origin imposes

$$f_+^{\pi^-P}(0) = -\frac{c^S_{\pi^-P}}{c^V_{\pi^-P}}\frac{\Delta^{QCD}_{K^0K^+}}{\Delta_{\pi^-P}} f_0^{\pi^-P}(0)\,, \tag{6}$$

which is obtained from

$$f_-^{\pi^-P}(s) = -\frac{\Delta_{\pi^-P}}{s}\left[\frac{c^S_{\pi^-P}}{c^V_{\pi^-P}}\frac{\Delta^{QCD}_{K^0K^+}}{\Delta_{\pi^-P}} f_0^{\pi^-P}(s) + f_+^{\pi^-P}(s)\right]. \tag{7}$$

In terms of these form factors, the differential decay width reads

$$\frac{d\Gamma\left(\tau^- \to \pi^- P^0 \nu_\tau\right)}{d\sqrt{s}} = \frac{G_F^2 M_\tau^3}{24\pi^3 s} S_{EW} \left|V_{ud}\right|^2 \left|f_+^{\pi^-P}(0)\right|^2 \left(1 - \frac{s}{M_\tau^2}\right)^2 \tag{8}$$

$$\left\{\left(1 + \frac{2s}{M_\tau^2}\right) q^3_{\pi^-P^0}(s)\left|\tilde{f}_+^{\pi^-P}(s)\right|^2 + \frac{3\Delta^2_{\pi^-P^0}}{4s} q_{\pi^-P}(s)\left|\tilde{f}_0^{\pi^-P}(s)\right|^2\right\}, \tag{9}$$

where

$$\tilde{f}_{+,0}^{\pi^-P}(s) = \frac{f_{+,0}^{\pi^-P}(s)}{f_{+,0}^{\pi^-P}(0)}\,, \quad q_{PQ}(s) = \frac{\lambda^{1/2}(s, m_P^2, m_Q^2)}{2\sqrt{s}}\,. \tag{10}$$

Since the $\pi^-\eta^{(\prime)}$ vector form factors are proportional to the $\pi^-\pi^0$ vector form factor we may fix the first one at the origin from the latter, see eq.(14), using that $f_+^{\pi^-\pi^0}(0) = 1$. The proportionality constants will bring an overall suppression factor which explains the smallness of the corresponding branching fractions, in agreement with the expected vanishing in the quite accurate G-parity symmetry limit.

3 Hadronic Form factors

We have worked out the involved form factors using Chiral Perturbation Theory [8] including resonances within the convenient antisymmetric tensor field formalism[9], a framework which has been shown capable of providing a good description of hadronic tau decay data [10 11 12]. The $\pi^0 - \eta - \eta'$ mixing has been parametrized by means of three Euler angles ($\epsilon^{\eta\pi}$, $\epsilon^{\eta'\pi}$ and $\theta_{\eta\eta'}$), including the small isospin breaking given by $z := \frac{f_u - f_d}{f_u + f_d}$ [13]. We have neglected terms of $\mathcal{O}(\epsilon^2)$ in the corresponding expansions.

When the vanishing of the $f_0^{\pi^-P}(s)$ form factors at large s is required, one obtains the restriction $c_d = c_m = F/2$ [15], which yields

$$f_0^{\pi^-\pi^0}(s) = c_0^{\pi^-\pi^0}\frac{M_S^2}{M_S^2 - s}\,, \quad f_0^{\pi^-\eta^{(\prime)}}(s) = c_0^{\pi^-\eta^{(\prime)}}\frac{M_S^2 + \Delta_{\pi\eta^{(\prime)}}}{M_S^2 - s}\,. \tag{11}$$

with $c_0^{\pi^-\pi^0} = \epsilon^{\eta\pi} + \sqrt{2}\epsilon^{\eta'\pi}$, $c_0^{\pi^-\eta} = \cos\theta_{\eta\eta'} - \sqrt{2}\sin\theta_{\eta\eta'}$, $c_0^{\pi^-\eta'} = \cos\theta_{\eta\eta'} + \frac{\sin\theta_{\eta\eta'}}{\sqrt{2}}$.

We will replace $1/(M_S^2 - s)$ by $1/(M_S^2 - s - iM_S\Gamma_S(s))$, with the energy-dependent $a_0(980)$ width given by

$$\Gamma_{a_0}(s) = \Gamma_{a_0}\left(M_{a_0}^2\right)\left(\frac{s}{M_{a_0}^2}\right)^{3/2}\frac{h(s)}{h\left(M_{a_0}^2\right)}, \tag{12}$$

with

$$h(s) = \sigma_{KK}(s) + \frac{2}{3}\sigma_{\pi\eta}(s)\left(c_0^{\pi^-\eta}\right)^2\left(1 + \frac{\Delta_{\pi\eta}}{s}\right)^2 + \frac{4}{3}\sigma_{\pi\eta'}(s)\left(c_0^{\pi^-\eta'}\right)^2\left(1 + \frac{\Delta_{\pi\eta'}}{s}\right)^2. \tag{13}$$

In this way we are neglecting the real part of the corresponding loop functions, which will induce a small violation of analiticity (see, however, Ref. [16]).

Finally, the $\pi^-\eta^{(\prime)}$ vector form factors are obtained in terms of the well-known $\pi^-\pi^0$ vector form factor

$$f_+^{\pi^-\eta}(s) = \left[\epsilon^{\eta\pi}\cos\theta_{\eta\eta'} - \epsilon^{\eta'\pi}\sin\theta_{\eta\eta'}\right] f_+^{\pi^-\pi^0}(s), \quad f_+^{\pi^-\eta'}(s) = \left[\epsilon^{\eta'\pi}\cos\theta_{\eta\eta'} + \epsilon^{\eta\pi}\sin\theta_{\eta\eta'}\right] f_+^{\pi^-\pi^0}(s). \tag{14}$$

Thus, we will have

$$f_+^{\pi^-\eta}(0) = \epsilon^{\eta\pi}\cos\theta_{\eta\eta'} - \epsilon^{\eta'\pi}\sin\theta_{\eta\eta'}, \quad f_+^{\pi^-\eta'}(0) = \epsilon^{\eta'\pi}\cos\theta_{\eta\eta'} + \epsilon^{\eta\pi}\sin\theta_{\eta\eta'}, \tag{15}$$

and the normalized form factors are all the same:

$$\tilde{f}_+^{\pi^-\eta^{(\prime)}}(s) = \tilde{f}_+^{\pi^-\pi^0}(s), \quad \tilde{f}_0^{\pi^-\pi^0}(s) = \tilde{f}_0^{\pi^-\pi^0}(s). \tag{16}$$

While $f_+^{\pi^-\eta}(0) \sim \mathcal{O}(\epsilon^{\eta\pi})$, an accidental cancellation makes $f_+^{\pi^-\eta'}(0) < \mathcal{O}\left[(\epsilon^{\eta\pi})^2\right]$: the $\tau^- \to \eta\pi^-\nu_\tau$ decays are suppressed, as it corresponds to a second class current process, but the $\tau^- \to \eta'\pi^-\nu_\tau$ decays are heavily suppressed.

4 Phenomenological analysis

For the vector form factor, we have taken $\tilde{f}_+^{\pi^-\pi^0}(s)$ using the dispersive representation of Ref. [11] devised in Ref. [12] for $\tilde{f}_+^{K\pi}(s)$. We have estimated the model dependent error by considering Belle's data [17] (whose extraction requires the knowledge of isospin-breaking corrections [18,19]) and the phenomenological fit made this Collaboration. This error is negligible versus the one coming from $\epsilon^{\eta\pi}$ and $\epsilon^{\eta'\pi}$. We have fixed $\Delta_{K^0K^+}^{QCD}$ [20,21] and determined the value of z that fulfils eqs.(6) within errors [6]. In this way we find $z \sim -1 \cdot 10^{-3}$, $\epsilon^{\eta\pi} \sim 0.018(2)$ and $\epsilon^{\eta'\pi} = 5(1) \cdot 10^{-3}$.

In the case of the scalar form factor the error receives important contributions both from the uncertainty on the $\epsilon^{\eta^{(\prime)}\pi}$ coefficients and on $M_{a_0} = (980 \pm 20)$ MeV and $\Gamma_{a_0} = (75 \pm 25)$ MeV. We have, however, neglected the contribution of a possible a_0' resonance, which may change sizably the result, especially for the $\tau^- \to \pi^-\eta'\nu_\tau$ decays.

Under these assumptions we find $BR_+(\tau^- \to \pi^-\eta\nu_\tau) = (0.9 \pm 0.2) \cdot 10^{-5}$, $BR_0(\tau^- \to \pi^-\eta\nu_\tau) = (2.7 \pm 1.1) \cdot 10^{-5}$, which yield to $BR(\tau^- \to \pi^-\eta\nu_\tau) = (3.6 \pm 1.3) \cdot 10^{-5}$ and $BR_+(\tau^- \to \pi^-\eta'\nu_\tau) \in [10^{-11}, 10^{-9}]$, $BR_0(\tau^- \to \pi^-\eta'\nu_\tau) \in [10^{-10}, 2 \cdot 10^{-8}]$, giving $BR(\tau^- \to \pi^-\eta'\nu_\tau) \in [10^{-10}, 2 \cdot 10^{-8}]$ [a]. While our predictions for the $\pi^-\eta$ mode are larger than previous results [5,22,23,24,25,26,27], our values for the $\pi^-\eta'$ mode tend to be smaller [26,28,29]. This is a result of our improved treatment of the $\pi^0 - \eta - \eta'$ mixing. We note in particular that, according to our findings, the $\tau^- \to \pi^-\eta\nu_\tau$ should be within discovery reach at future super-B factories.

[a] Errors coming from our theoretical approach are not included. While they have been checked to be negligible for the vector form factor contribution this does not need to be the case for the scalar form factor one.

Acknowledgments

This work has been partly funded by the Spanish grant FPA2011-25948. Financial support of the organization covering my living expenses during the conference is acknowledged.

References

1. S. Weinberg, Phys. Rev. **112** (1958) 1375.
2. P. del Amo Sanchez *et al.* [BaBar Collaboration], Phys. Rev. D **83** (2011) 032002.
3. B. Aubert *et al.* [BaBar Collaboration], Phys. Rev. D **77** (2008) 112002.
4. A. Bramon, S. Narison and A. Pich, Phys. Lett. B **196** (1987) 543.
5. S. Nussinov and A. Soffer, Phys. Rev. D **78** (2008) 033006.
6. R. Escribano, S. González-Solís and P. Roig, work in progress.
7. J. Gasser and H. Leutwyler, Nucl. Phys. B **250** (1985) 517.
8. S. Weinberg, Physica A **96** (1979) 327. J. Gasser and H. Leutwyler, Nucl. Phys. B **250** (1985) 465, Annals Phys. **158** (1984) 142.
9. G. Ecker, J. Gasser, A. Pich and E. de Rafael, Nucl. Phys. B **321** (1989) 311. G. Ecker, J. Gasser, H. Leutwyler, A. Pich and E. de Rafael, Phys. Lett. B **223** (1989) 425.
10. M. Jamin, A. Pich and J. Portolés, Phys. Lett. B **640**, 176 (2006), B **640**, 176 (2006). D. G. Dumm, P. Roig, A. Pich and J. Portolés, Phys. Rev. D **81** (2010) 034031, Phys. Lett. B **685**, 158 (2010). D. R. Boito, R. Escribano and M. Jamin, JHEP **1009**, 031 (2010). Z. -H. Guo and P. Roig, Phys. Rev. D **82**, 113016 (2010). O. Shekhovtsova, T. Przedzinski, P. Roig and Z. Was, Phys. Rev. D **86**, 113008 (2012), O. Shekhovtsova, I. M. Nugent, T. Przedzinski, P. Roig and Z. Was, arXiv:1301.1964 [hep-ph] and work in progress. D. G. Dumm and P. Roig, Phys. Rev. D **86**, 076009 (2012).
11. D. G. Dumm and P. Roig, arXiv:1301.6973 [hep-ph].
12. D. R. Boito, R. Escribano and M. Jamin, Eur. Phys. J. C **59** (2009) 821.
13. P. Kroll, Mod. Phys. Lett. A **20** (2005) 2667.
14. F. Ambrosino, A. Antonelli, M. Antonelli, F. Archilli, P. Beltrame, G. Bencivenni, S. Bertolucci and C. Bini *et al.*, JHEP **0907** (2009) 105.
15. M. Jamin, J. A. Oller and A. Pich, Nucl. Phys. B **587** (2000) 331, **622** (2002) 279, Phys. Rev. D **74** (2006) 074009.
16. R. Escribano, P. Masjuan and J. J. Sanz-Cillero, JHEP **1105** (2011) 094.
17. M. Fujikawa *et al.* [Belle Collaboration], Phys. Rev. D **78** (2008) 072006.
18. V. Cirigliano, G. Ecker and H. Neufeld, Phys. Lett. B **513** (2001) 361, JHEP **0208** (2002) 002.
19. F. Flores-Báez, A. Flores-Tlalpa, G. López Castro and G. Toledo Sánchez, Phys. Rev. D **74** (2006) 071301.
20. J. Bijnens, Phys. Lett. B **306** (1993) 343.
21. B. Moussallam, Nucl. Phys. B **504** (1997) 381.
22. S. Tisserant, and T. N. Truong, Phys. Lett. B **115** (1982) 264.
23. A. Pich, Phys. Lett. B **196** (1987) 561.
24. H. Neufeld and H. Rupertsberger, Z. Phys. C **68** (1995) 91.
25. N. Paver and Riazuddin, Phys. Rev. D **82** (2010) 057301.
26. M. K. Volkov and D. G. Kostunin, Phys. Rev. D **86** (2012) 013005.
27. S. Descotes-Genon, E. Kou, and B. Moussallam, arXiv:1303.2879 [hep-ph].
28. S. Nussinov and A. Soffer, Phys. Rev. D **80** (2009) 033010.
29. N. Paver and Riazuddin, Phys. Rev. D **84** (2011) 017302.

Hadronic Cross Section Measurements with ISR and the Implications on $g_\mu - 2$

K. Griessinger representing the *BABAR* Collaboration
Mainz University, Institute for Nuclear Physics, J.-J.-Becherweg 45, 55099 Mainz, Germany

The B-Factories have produced data of unprecedented precision for the measurement of hadronic cross sections. This data, extracted via Initial State Radiation (ISR), can be used to predict the anomaly of the muon gyromagnetic factor, $g_\mu - 2$. In this note, the recent *BABAR* -measurements of the channels $e^+e^- \to \pi^+\pi^-\pi^+\pi^-$ and $e^+e^- \to K^+K^-$ are summarized, which improve the accuracy of the Standard Model prediction of $g_\mu - 2$ significantly.

1 Introduction

The muon gyromagnetic factor g_μ can be determined directly from spin precession measurements and theoretically in the Standard Model. For the latter, the QED and weak contributions to $a_\mu \equiv (g_\mu - 2)/2$ can be calculated perturbatively to great precision ($a_\mu^{\text{QED}} = (116\,584\,718.951 \pm 0.080) \cdot 10^{-11}$ [1] and $a_\mu^{\text{weak}} = (154 \pm 2) \cdot 10^{-11}$ [2], respectively). In contrast, the contribution from strong interaction at low energies cannot be calculated perturbatively due to the magnitude of the running strong coupling constant $\alpha_s(s)$. Therefore a dispersion integral (obtained via the optical theorem) is employed to calculate the hadronic low energy part of a_μ from the experimentally determined hadronic cross section $\sigma_{\text{had}}(s)$:

$$a_\mu^{\text{had}}(s \le E_{\text{cut}}^2) = \frac{1}{4\pi^3} \int_{m_\pi^2}^{E_{\text{cut}}^2} K(s)\sigma_{\text{had}}(s)\mathrm{d}s \ .$$

$K(s)$ denotes the analytically known [3] Kernel function, which exhibits an asymptotic $1/s$ decrease. The value of E_{cut} is chosen such that $\alpha_s(s)$ is sufficiently small for $s > E_{\text{cut}}^2$ and thus the remaining part $a_\mu^{\text{had}}(s > E_{\text{cut}}^2)$ can be calculated in a perturbative expansion. This combination leads to a value of approximately $a_\mu^{\text{had}} = (6930 \pm 49) \cdot 10^{-11}$ [2].

On the purely experimental side, a_μ is determined by measuring the difference of the Larmor and Cyclotron frequency of precessing muons. This led to a very precise measurement in the E821 experiment at Brookhaven National Laboratory with the result $a_\mu = (116\,592\,089 \pm 54_{\text{stat}} \pm 33_{\text{syst}}) \cdot 10^{-11}$ [2].

The direct and theoretical results deviate by approximately 3.5σ. Since this discrepancy merely provides a hint at yet no evidence for a deficiency in the Standard Model, more precise data from both sides is of utmost importance.

2 Experimental Setup

The B-Factories *BABAR* and Belle are located at SLAC National Accelerator Center in Stanford, USA and at KEK in Tsukuba, Japan, respectively. *BABAR* achieved an integrated luminosity of $\sim 530\,\text{fb}^{-1}$, whereas Belle even exceeded $1\,\text{ab}^{-1}$. While running (mostly) at the $\Upsilon(4S)$ resonance, this produced a large data set for the study of hadronic cross sections via the process of Initial State Radiation (ISR). This process takes place when one of the particles in the initial state (e^+e^-) radiates a photon. Since the photon carries a certain amount of CMS-energy E_γ^*, the squared center-of-mass energy s ist lowered to $s' = s - 2\sqrt{s}E_\gamma^*$. Owed to the continuous spectrum of possible photon energies, this gives access to a broad range of invariant masses over which hadronic cross sections may be measured.

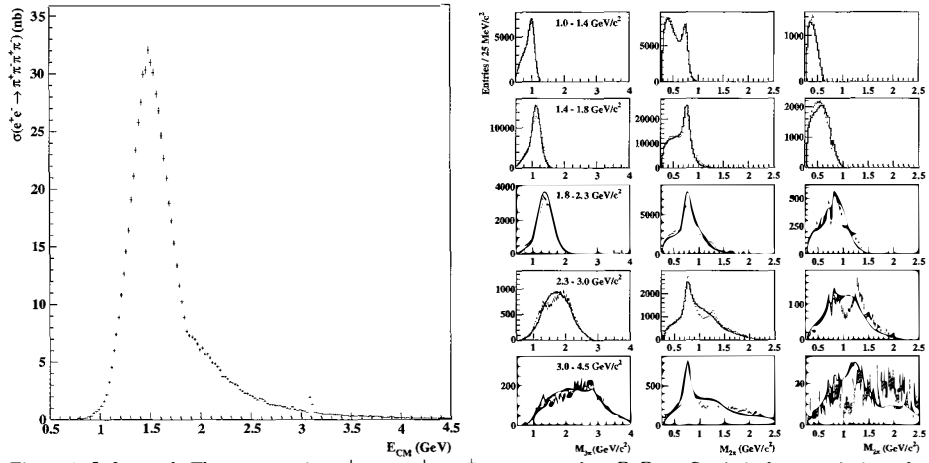

Figure 1: Left panel: The cross section $e^+e^- \to \pi^+\pi^-\pi^+\pi^-$ measured at *BABAR* . Statistical uncertainties only, systematics are listed in Tab. 1. Right panel: Internal structures, data in red, simulation in black. From top to bottom: slices in the 4π invariant mass. Left to right: 3π mass, 2π mass and 2π not originating from ρ^0.

3 Measurement of the channel $e^+e^- \to \pi^+\pi^-\pi^+\pi^-$ [4]

The channel $e^+e^- \to \pi^+\pi^-\pi^+\pi^-$ is not only interesting for its cross section, but also due to its rich internal structures. These are explored by investigating the invariant masses of different particle combinations from the final state as a function of the total invariant mass of the hadronic system, see Fig. 1 (right). In the three-pion mass (left column, 4 entries per event for all combinations), the $a_1(1260)$ is observed clearly, especially in the high-mass slices. The charge neutral two-pion mass, which also contains 4 combinations per event, exhibits a very pronounced ρ^0 signature. This peak contains approximately one fourth of all entries in each histogram. Since $e^+e^- \to \rho^0\rho^0$ is forbidden at tree level, this means that there must be one ρ^0 in each event. When excluding the $\pi^+\pi^-$ combination from the ρ^0, the third column of Fig. 1 (right) is produced. Here, the additional resonances apart from the ρ^0 show up much more clearly. In the spectrum, especially the $f_0(980)$ and $f_2(1270)$ can be observed quite nicely at intermediate and large total hadronic energies.

The cross section itself is shown in Fig. 1 (left) with its statistical uncertainties. The systematics are listed in Tab. 1. This very precise measurement improves the low-energy ($0.6\,\text{GeV} < \sqrt{s} < 1.8\,\text{GeV}$) prediction of $a_\mu^{\text{had}}(\pi^+\pi^-\pi^+\pi^-)$ from $a_\mu^{\text{had}}(\pi^+\pi^-\pi^+\pi^-) = (133.5 \pm 1.0_{\text{stat}} \pm 5.2_{\text{syst}}) \cdot 10^{-11}$, calculated using the previous world data set (including the smaller *BABAR* data set from 2006), to $a_\mu^{\text{had}}(\pi^+\pi^-\pi^+\pi^-) = (136.4 \pm 0.3_{\text{stat}} \pm 3.6_{\text{syst}}) \cdot 10^{-11}$, only with the *BABAR* measurement.

Table 1: Systematic uncertainties of the $e^+e^- \to \pi^+\pi^-\pi^+\pi^-$ cross section measured at *BABAR* .

M_{had}	$< 1.1\,\text{GeV}$	$1.1\,\text{GeV} \leq M_{\text{had}} \leq 2.8\,\text{GeV}$	$> 2.8\,\text{GeV}$
σ_{syst}	11 %	2.4 %	4 %

4 Measurement of the channel $e^+e^- \to K^+K^-$ [5]

Another channel that had yet to be measured with high precision was the production of two charged Kaons. At *BABAR* it has now been analyzed using $\sim 232\,\text{fb}^{-1}$, yielding the cross section with a very large ϕ peak shown in Fig. 2. Remarkably small uncertainties down to 0.7 % in

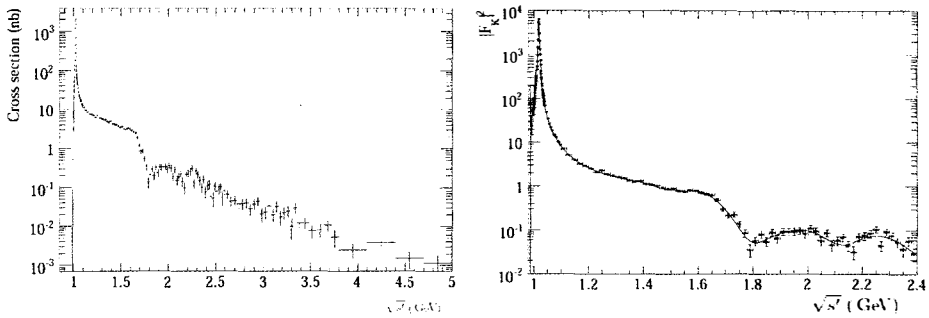

Figure 2: Cross section $e^+e^- \to K^+K^-$ measured at *BABAR* (left, J/ψ and $\psi(2S)$ removed) and the corresponding squared Kaon form factor (right) including a BW-fit (blue). Statistical and systematic uncertainties shown.

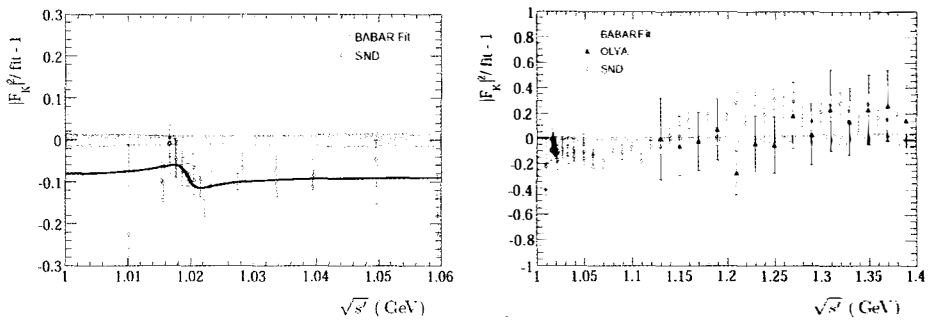

Figure 3: Deviation between the fit to the squared Kaon form factor measured at *BABAR* and SND data in the ϕ region (left) and in a wider energy range (right), also including OLYA.

the ϕ peak region were achieved especially by very diligently studying Kaon particle (mis-)identification and the ISR-luminosity, which is calculated from $e^+e^- \to \mu^+\mu^-\gamma$ event rates.

From this cross section, the corresponding form factor is extracted, see Fig. 2. It is parametrized by a sum of Breit-Wigner distributions:

$$\begin{aligned} F_K(s) &= (a_\phi \cdot BW_\phi(s) + a_{\phi'} \cdot BW_{\phi'}(s) + a_{\phi''} \cdot BW_{\phi''}(s))/3 \\ &+ (a_\rho \cdot BW_\rho(s) + a_{\rho'} \cdot BW_{\rho'}(s) + a_{\rho''} \cdot BW_{\rho''}(s) + a_{\rho'''} \cdot BW_{\rho'''}(s))/2 \\ &+ (a_\omega \cdot BW_\omega(s) + a_{\omega'} \cdot BW_{\omega'}(s) + a_{\omega''} \cdot BW_{\omega''}(s) + a_{\omega'''} \cdot BW_{\omega'''}(s))/6 \\ \text{with} \quad & a_\phi + a_{\phi'} + a_{\phi''} = 1 \ , \ a_\rho + a_{\rho'} + a_{\rho''} + a_{\rho'''} = 1 \ , \ a_\omega + a_{\omega'} + a_{\omega''} + a_{\omega'''} = 1 \ . \end{aligned}$$

Using the fit to the *BABAR* data, the results from other experiments can be compared to *BABAR* . This is shown in Fig. 3 and some interesting deviations are found. There is a small wiggle around the ϕ mass, which is due to calibration differences of the experiments and is covered by the experimental uncertainties. More importantly for the determination of $g_\mu - 2$, there seems to be a normalization difference between data from *BABAR* and the experiments from Novosibirsk (SND and CMD2). While in the low-mass region around the ϕ SND and CMD2 show a smaller form factor, above $\sqrt{s'} \approx 1.15\,\text{GeV}$ the form factor from SND is considerably larger (CMD2 has not yet published their result in the full energy range).

Furthermore the measurement of the form factor can be compared to theoretical predictions [6,7] in the high-energy regime. For large values of $\sqrt{s'}$,

$$\|F_K(s')\|^2 = 64\pi^2 f_K^4 \cdot \frac{\alpha_s^2(s')}{s'^n}$$

with $n = 2$ is predicted in a perturbative approach. While the measurement confirms the exponent with a fitted (in the regime $\sqrt{s'} > 2.5\,\text{GeV}$) value of $n = 2.10 \pm 0.23$ and agrees with the point from CLEO at $\sqrt{s'} \approx 3.8\,\text{GeV}$, the overall scaling is off by roughly a factor of 20, as seen in Fig. 4. This effect has yet to be understood.

For the SM prediction of $g_\mu - 2$, this new cross section measurement dramatically improves the precision in the energy range $0.98\,\text{GeV} < \sqrt{s} < 1.8\,\text{GeV}$ from $a_\mu^{\text{had}}(K^+K^-) = (216.3 \pm 2.7 \pm 6.8) \cdot 10^{-11}$ with the previous world data set to $a_\mu^{\text{had}}(K^+K^-) = (229.5 \pm 1.4 \pm 2.2) \cdot 10^{-11}$ only on *BABAR* data.

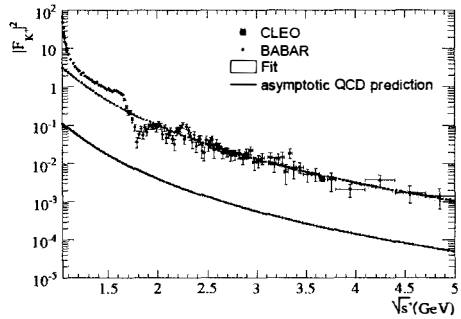

Figure 4: Comparison of the squared Kaon form factors between data and theory the from asymptotic QCD.

5 Conclusions

The recent *BABAR* results on the $e^+e^- \to \pi^+\pi^-\pi^+\pi^-$ and $e^+e^- \to K^+K^-$ cross sections reach unprecedented accuracy. Consequently, they have significantly improved the precision of the SM prediction for $g_\mu - 2$. Furthermore interesting intermediate structures were found in the 4π channel and the Kaon form factor stands in stark contrast to the high-energy QCD prediction.

Acknowledgments

We would like to thank the organizers for a great conference. We are grateful for the excellent luminosity and machine conditions provided by our PEP-II colleagues, and for the substantial dedicated effort from the computing organizations that support *BABAR* . The collaborating institutions wish to thank SLAC for its support and kind hospitality. This work is supported by DOE and NSF (USA), NSERC (Canada), CEA and CNRS-IN2P3 (France), BMBF and DFG (Germany), INFN (Italy), FOM (The Netherlands), NFR (Norway), MES (Russia), MICIIN (Spain), STFC (United Kingdom). Individuals have received support from the DFG (Germany).

References

1. Tatsumi Aoyama, Masashi Hayakawa, Toichiro Kinoshita, and Makiko Nio. Complete Tenth-Order QED Contribution to the Muon $g - 2$. *Phys.Rev.Lett.*, 109:111808, 2012.
2. Michel Davier, Andreas Hoecker, Bogdan Malaescu, and Zhiqing Zhang. Reevaluation of the Hadronic Contributions to the Muon $g - 2$ and to $\alpha(M_Z)$. *Eur.Phys.J.*, C71:1515, 2011.
3. N.N. Achasov and A.V. Kiselev. Contribution to muon $g - 2$ from the $\pi^0\gamma$ and $\eta\gamma$ intermediate states in the vacuum polarization. *Phys.Rev.*, D65:097302, 2002.
4. J.P. Lees et al. Initial-State Radiation Measurement of the $e^+e^- \to \pi^+\pi^-\pi^+\pi^-$ Cross Section. *Phys.Rev.*, D85:112009, 2012.
5. Michel Davier. e^+e^- results from BABAR and implications for $g - 2$. 2013. arXiv:1302.1907.
6. V.L. Chernyak, A.R. Zhitnitsky, and V.G. Serbo. Asymptotic hadronic form-factors in quantum chromodynamics. *JETP Lett.*, 26:594–597, 1977.
7. G. Peter Lepage and Stanley J. Brodsky. Exclusive Processes in Quantum Chromodynamics: Evolution Equations for Hadronic Wave Functions and the Form-Factors of Mesons. *Phys.Lett.*, B87:359–365, 1979.

7.
QCD

LATEST JETS RESULTS FROM THE LHC

K. RABBERTZ
(on behalf of the ATLAS and CMS Collaborations)
Karlsruher Institut für Technologie, Institut für Experimentelle Kernphysik, Campus Süd, Postfach 6980, D-76128 Karlsruhe, Germany

A fundamental characteristic of hadron colliders is the abundant production of jets, which then are studied to learn about hard QCD, the proton structure, or nonperturbative effects. In the following the latest results and developments from the LHC experiments on jet cross sections, event shapes, flavour and rapidity dependence, and cross section ratios are presented. The ratio of the inclusive 3-jet to the inclusive 2-jet event cross section is used for a first determination of the strong coupling constant at the TeV scale.

1 Jet Cross Sections

Yields of collimated streams of particles, i.e. jets, are among the most fundamental observables at hadron colliders. Through their high production rates at low jet transverse momenta, p_{T}, they serve to benchmark detector performance and to perform first cross section measurements that are compared to theory predictions. As more data are accumulated, ever higher jet p_{T}'s become accessible providing significant constraints on the parton distribution functions (PDFs) of the proton and important input to searches for new physics.

ATLAS and CMS,[1,2] both employ the anti-k_{T} jet algorithm[3] to define their jets, but with different jet size parameters R of 0.4 or 0.6 for ATLAS and 0.5 or 0.7 for CMS respectively. The dominant source of experimental uncertainty for jet measurements is the jet energy calibration, because the steeply falling jet p_{T} spectrum induces an approximately 5–6 times larger uncertainty on the jet cross sections than on the jet energies. Profiting from the excellent performance of both detectors, jet energy calibration uncertainties could be limited to about 1–3% already during the initial three-years running period, a feat that could be achieved previously only after many years. Apart from jets with less than $\approx$ 50 GeV of transverse momentum this good performance could be kept up despite the deteriorating influence of more pile-up collisions, i.e. additional proton-proton collisions in the same or neighbouring bunch crossings. At the next LHC start-up with even higher instantaneous luminosities pile-up will again pose a challenge.

The common normalization uncertainty caused by the luminosity determination could be reduced from initially more than 10% down to 2–4%. Including other systematic effects the

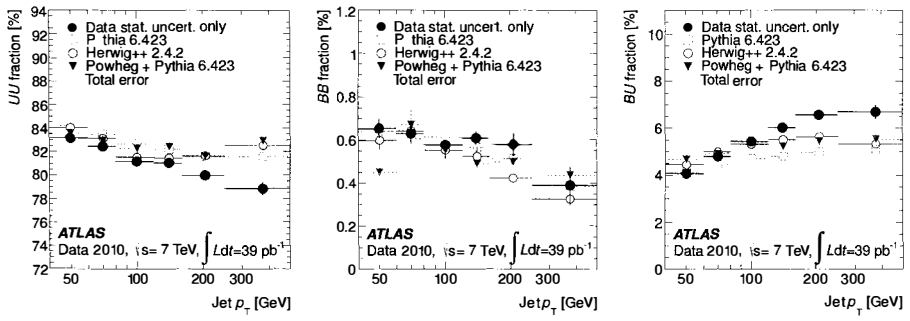

Figure 1: Relative frequency of jet flavours B, C, and light (U) in dijet events for the combinations BB (left), UU (middle), and BU (right plot).

inclusive jet p_{T} or the dijet mass cross sections could be measured by ATLAS and CMS to roughly 10 to 20% accuracy with less precision at the low end and also less data at the high end of the jet p_{T} and dijet mass ranges.[4,5,6]

It is a great achievement that these data are in general agreement with predictions of QCD over many orders of magnitude in cross section. With theoretical uncertainties of a similar order or larger these jet measurements help constrain PDFs. Recent progress in theory towards next-to-next-to-leading order (NNLO) predictions are reported elsewhere in these proceedings.[7]

2 Event Shapes

Alternatively to jet counting continuous dimensionless quantities that are not sensitive to the details of soft nonperturbative effects of QCD can be defined to characterize events. They are called *event shapes* and have been in use since the early days of QCD in the 70s. Several collinear and infrared-safe event shapes, e.g. *transverse thrust*, have been investigated by ATLAS and CMS, where the emphasis was on hard proton-proton scatterings and the phase space is subdivided into bins of p_{T} of the leading jet or the sum of all jet p_{T}'s.[8,9] In a new study ATLAS uses charged particles measured in their tracking system to investigate event shapes down to very small transverse momenta of 0.5 GeV.[10] In accordance with previous results it is found that better tunings of the MC event generators are needed in order to describe all available data.

3 Flavour and Rapidity Results

In Ref. [11] ATLAS compares the relative frequency of jet flavours in dijet events. Using template fits to kinematic properties of secondary vertices inside jets, ATLAS differentiates between the heavy, b and c quark initiated jets and *light* jets, which are labelled as B, C, and U respectively. Figure 1 shows exemplarily the measurements for the UU, BB, and BU dijet combinations, which demonstrate that light dijets compose about 80% of the total cross section while the heavy BB combination appears only in half a percent of the events. The results are described well within uncertainties by MC predictions except for the BU case, where some discrepancies can be observed.

Other analyses by ATLAS and CMS look into the dependence of the most forward and backward dijets or the ratio of all possible dijet pair distances over the leading dijet pair distance versus their separation in absolute rapidity, $|\Delta y|$.[12,13] It is expected that deviations from the usual evolution of the PDFs could show up in these quantities, where small parton momentum fractions are accessed. The comparisons of different models to the data are, however, inconclusive so far.

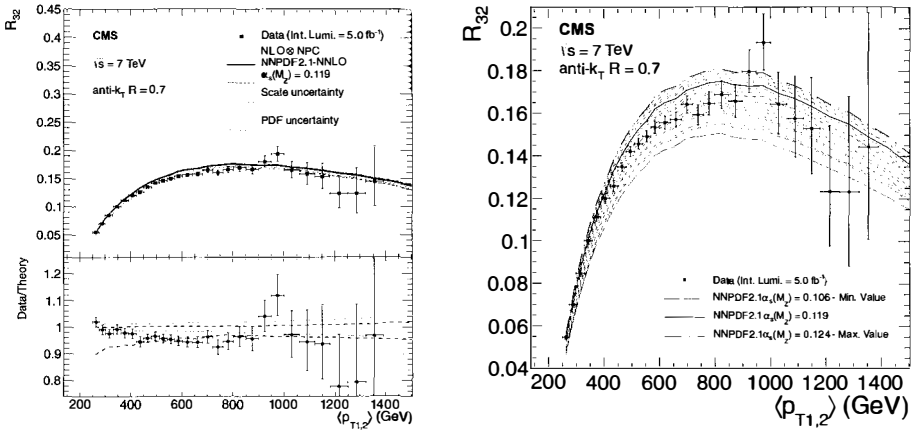

Figure 2: Left: Measured ratio R_{32} versus $\langle p_{\mathrm{T}1,2} \rangle$ (solid circles) together with the NLO prediction (solid line) corrected for nonperturbative effects (NPC), the scale uncertainty, and the PDF uncertainty. The bottom panel shows the ratio of data to the theoretical predictions, together with bands representing the scale (dotted lines) and PDF (solid lines) uncertainties while the error bars correspond to the total uncertainty. Right: The same comparison with theory but for a series of values of $\alpha_S(M_Z)$. The $\alpha_S(M_Z)$ value is varied in the range of 0.106-0.124 in steps of 0.001. In both cases the NNPDF2.1 PDF set at NNLO evolution order has been employed.

4 Ratios of Jet Cross Sections and Determination of the Strong Coupling Constant

In order to reduce experimental as well as theoretical uncertainties, jet cross section ratios are considered. Disposing of data at 2.76 TeV, the baseline proton-proton centre-of-mass energy for heavy ion collisions, in addition to the 7 TeV data, ATLAS analyzed the ratio of the inclusive jet cross section at these two energy points.[14] This provides more significant constraints on PDFs in the accessible phase space than considering each jet cross section separately.

The ALICE Collaboration followed a suggestion in Ref. [15] and examined the cross section ratio for jets defined with different jet size parameters, which in their case are $R = 0.2$ and 0.4 because of their primary focus on heavy ion physics.[16] Using this method, details of the parton showering and the nonperturbative hadronization phase are emphasized in this ratio such that even NLO calculations are not able to describe the data as shown by ALICE.[17]

In contrast, the ratio of the inclusive 3-jet to the inclusive 2-jet event cross section, R_{32}, has been demonstrated by CMS to be reliably comparable to perturbative QCD, if sufficiently high thresholds, CMS requires $p_{\mathrm{T,jet}} > 150$ GeV, are imposed on all jets including the third leading one.[18] Figure 2 presents a comparison of the data, differential in the average transverse momentum of the two leading jets, $\langle p_{\mathrm{T}1,2} \rangle$, to the theory predictions at NLO on the left and the sensitivity to a variation of the strong coupling constant $\alpha_S(M_Z)$ on the right for the NNPDF2.1 PDF set at NNLO evolution order.[19] Fits of R_{32} in the range of $420 < \langle p_{\mathrm{T}1,2} \rangle < 1390$ GeV have been used to determine the strong coupling constant α_S at the scale of the Z boson mass to be:

$$\alpha_S(M_Z) = 0.1148 \pm 0.0014\,(\mathrm{exp.}) \pm 0.0018\,(\mathrm{PDF})^{+0.0050}_{-0.0000}\,(\mathrm{scale}) = 0.1148\,^{+0.0055}_{-0.0023}, \qquad (1)$$

compatible with the world average value of $\alpha_S(M_Z) = 0.1184 \pm 0.0007$.[20] Here, the total uncertainty is derived from the experimental, PDF, and scale uncertainties by quadratic addition. This is the first determination of the strong coupling constant from measurements at scales Q of the order of 1 TeV. A comparison to other determinations at hadron colliders accessing different scales Q is shown in Fig. 3. No deviation from the expected running behaviour of the strong coupling constant is observed.

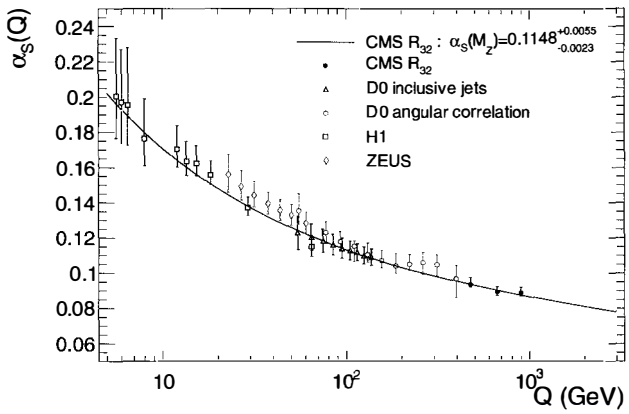

Figure 3: The strong coupling $\alpha_S(Q)$ (solid line) and its total uncertainty (band) evolved from the CMS determination $\alpha_S(M_Z) = 0.1148^{+0.0055}_{-0.0023}$ as a function of the momentum transfer $Q = \langle p_{T1,2} \rangle$. The extractions of $\alpha_S(Q)$ in three separate ranges of Q are shown together with results from other hadron collider experiments.

5 Summary

In summary, hadron colliders, which are usually conceived of as *discovery machines*, are also great *jet laboratories*, which provide many opportunities for precise measurements as demonstrated. Further results from the Tevatron are discussed elsewhere.[21] Through these measurements more insight can be gained into the workings of QCD, our theory of the strong interaction, with significant impact on e.g. other cross section predictions and searches for new physics.

References

1. ATLAS Collaboration. *JINST*, 3:S08003, 2008.
2. CMS Collaboration. *JINST*, 3:S08004, 2008.
3. M. Cacciari, G.P. Salam, and G. Soyez. *JHEP*, 04:063, 2008.
4. ATLAS Collaboration. *Phys. Rev. D*, 86:014022, 2012.
5. ATLAS Collaboration. Technical report, CERN, 2012. ATLAS-CONF-2012-021.
6. CMS Collaboration. *accepted by Phys. Rev. D*, 2012. arXiv:hep-ex/1212.6660.
7. Joao Pires. 2013. In these proceedings.
8. ATLAS Collaboration. *Eur. Phys. J. C*, 72:2211, 2012.
9. CMS Collaboration. *Phys. Lett. B*, 699:48, 2011.
10. ATLAS Collaboration. *submitted to Phys. Rev. D*, 2012. arXiv:hep-ex/1207.6915.
11. ATLAS Collaboration. *Eur. Phys. J. C*, 73:2301, 2013.
12. ATLAS Collaboration. *JHEP*, 1109:053, 2011.
13. CMS Collaboration. *Eur. Phys. J. C*, 72:2216, 2012.
14. ATLAS Collaboration. *submitted to Eur. Phys. J. C*, 2013. arXiv:hep-ex/1304.4739.
15. Gregory Soyez. *Phys. Lett. B*, 698:59, 2011.
16. ALICE Collaboration. *submitted to Phys. Lett. B*, 2013. arXiv:nucl-ex/1301.3475.
17. ALICE Collaboration. *JINST*, 3:S08002, 2008.
18. CMS Collaboration. *submitted to Eur. Phys. J. C*, 2013. arXiv:hep-ex/1304.7498.
19. R.D. Ball, V. Bertone, F. Cerutti, L. Del Debbio, et al. *Nucl. Phys. B*, 849:296, 2011.
20. J. Beringer et al. *Phys. Rev. D*, 86:010001, 2012.
21. Markus Wobisch. 2013. In these proceedings.

Theoretical developments in jet physics at hadron colliders

A. Gehrmann-De Ridder[a], T. Gehrmann[b], E.W.N. Glover[c], J. Pires[a]
[a] *Institute for Theoretical Physics, ETH, CH-8093 Zürich, Switzerland*
[b] *Institute for Theoretical Physics, University of Zürich, CH-8057 Zürich, Switzerland*
[c] *Institute for Particle Physics Phenomenology, University of Durham, Durham DH1 3LE, England*

We review the calculation of next-to-next-to-leading order (NNLO) QCD corrections to dijet production and related observables at hadron colliders in the purely gluonic channel. Our results show that the NNLO correction significantly reduces the scale uncertainties and we present the NNLO double-differential single jet inclusive and dijet cross sections. Jets are reconstructed using the anti-k_T jet algorithm and the jet resolution parameter R dependence of the inclusive cross section is given to NNLO.

1 Introduction

Single jet inclusive jet and dijet observables are the most fundamental QCD processes measured at hadron colliders. They probe the basic parton-parton scattering in $2 \to 2$ kinematics, and thus allow for a determination of the parton distribution functions in the proton and for a direct probe of the strong coupling constant α_s up to the highest energy scales that can be attained in collider experiments.

In the single jet inclusive cross section, each identified jet in an event contributes individually. The exclusive dijet cross section consists of all events with exactly two identified jets. These cross sections have been studied as functions of different kinematical variables: the transverse momentum and rapidity of the jets (of any jet for the single jet inclusive distribution, or of the two largest transverse momentum jets for the dijet distributions). Precision measurements of single jet and dijet cross sections have been performed by CDF [1] and D0 [2] at the Tevatron and by ATLAS [3] and CMS [4] at the LHC. The latest experimental results with jets as well as extractions of α_s using hadron collider jet data are reported in [5,6].

The state of the art of the theoretical predictions for these observables are accurate to next-to-leading order (NLO) in QCD[7] (with the inclusion of shower effects in[8]) and in the electroweak theory[9]. Reference[10] computed higher order logarithmic corrections in the threshold region. In this talk we present our results for the jet cross sections at NNLO accuracy in QCD in double differential form[11]

$$\frac{\mathrm{d}^2\sigma}{\mathrm{d}p_T \mathrm{d}|y|} \quad ; \quad \frac{\mathrm{d}^2\sigma}{\mathrm{d}m_{jj}\mathrm{d}y^*}$$

in the gluons-only channel at leading colour.

2 Results at NNLO

To perform our calculation we have employed the antenna subtraction scheme[12] for the analytic cancellation of infra-red (IR) singularities at NNLO extended to the case of processes with coloured particles in the initial state[13]. As demonstrated in[14], using the antenna subtraction

scheme the explicit ϵ-poles in the dimension regularization parameter of one- and two-loop matrix elements entering this calculation are cancelled in analytic and local form against the ϵ-poles of the integrated antenna subtraction terms thereby enabling the computation of jet cross sections at hadrons colliders at NNLO accuracy. This allows the combination of the two-loop virtual corrections to the basic $2 \to 2$ process [15] together with the one-loop virtual corrections to the single real radiation $2 \to 3$ process [16] and the double real radiation $2 \to 4$ process at tree-level [17] in a parton-level event generator NNLOJET.

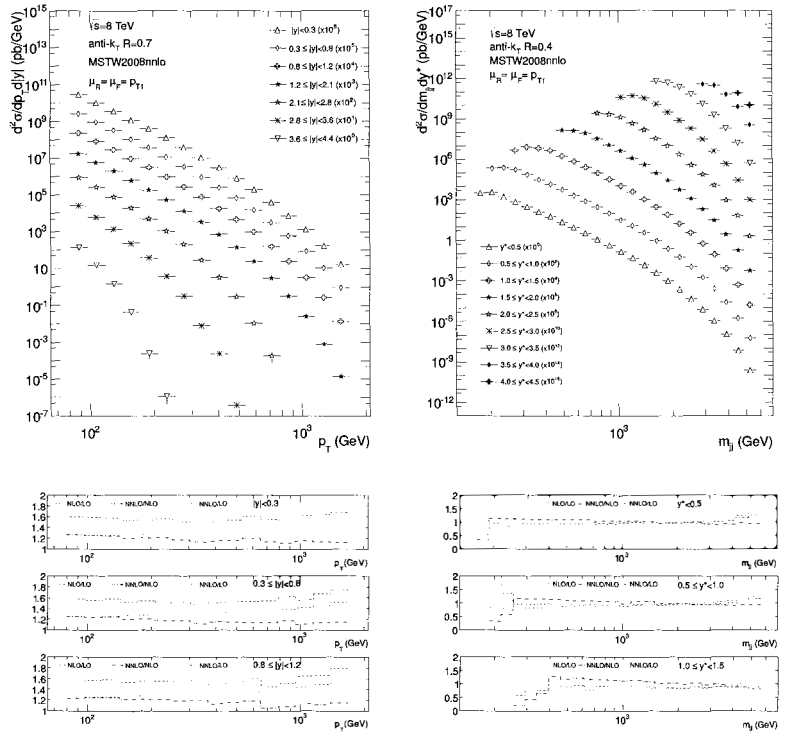

Figure 1: (Left plot) The NNLO doubly differential single jet inclusive transverse momentum distribution, $d^2\sigma/dp_T d|y|$, at $\sqrt{s} = 8$ TeV for the anti-k_T algorithm with $R = 0.7$ and for $p_T > 80$ GeV and various $|y|$ slices. (Right plot) The NNLO doubly differential dijet mass distribution, $d^2\sigma/dm_{jj}dy^*$, at $\sqrt{s} = 8$ TeV for the anti-k_T algorithm with $R = 0.4$ and for $p_{T1} > 80$ GeV, $p_{T2} > 60$ GeV and various $y^* = 1/2|y_1 - y_2|$ slices. The double differential k-factors are presented in the lower panels.

Our numerical studies for proton-proton collisions at centre-of-mass energy $\sqrt{s} = 8$ TeV concern the single jet inclusive cross section and the two-jet exclusive cross section. Jets are identified using the anti-k_T algorithm. Jets are accepted at central rapidity $|y| < 4.4$, and ordered in transverse momentum. An event is retained if the leading jet has $p_{T1} > 80$ GeV. For the dijet invariant mass distribution, a second jet must be observed with $p_{T2} > 60$ GeV. All calculations are carried out with the MSTW08NNLO gluon distribution function [18], including the evaluation of the LO and NLO contributions[a]. This choice of parameters allows us to quantify the size of the

[a]Note that the evolution of the gluon distribution within the PDF set together with the value of α_s intrinsically includes contributions from the light quarks. The NNLO calculation presented here is "gluons-only" in the sense

genuine NNLO contributions to the parton-level subprocess. Factorization and renormalization scales (μ_F and μ_R) are chosen dynamically on an event-by-event basis. As default value, we set $\mu_F = \mu_R \equiv \mu$ and set μ equal to the transverse momentum of the leading jet so that $\mu = p_{T1}$.

In Fig. 1 we present the double-differential jet cross sections at NNLO for the central scale choice. The NNLO/NLO k-factor shows the size of the higher order NNLO effect in each bin of the distribution with respect to the NLO cross section. For the single jet inclusive cross section we see that the NNLO/NLO k-factor increases the cross section between 25% at low p_T to 12% at high p_T and this behaviour is similar for the three rapidity slices $|y| < 0.3$, $0.3 < |y| < 0.8$ and $0.8 < |y| < 1.2$. For the exclusive dijet mass distribution the NNLO corrections are up to 20% with respect to the NLO cross section and increase slightly for large y^*.

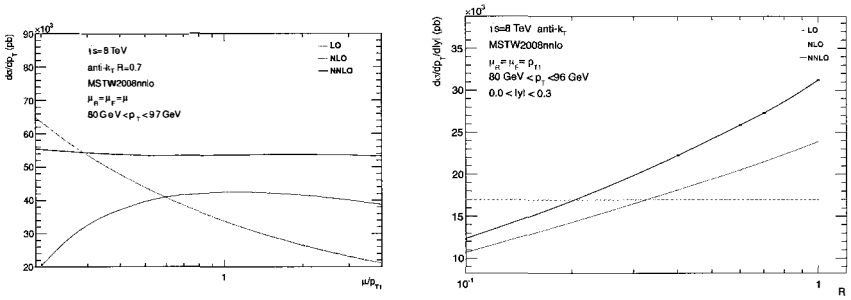

Figure 2: (Left plot) Scale dependence of the single jet inclusive cross section for pp collisions at $\sqrt{s} = 8$ TeV for the anti-k_T algorithm with R=0.7 and with $|y| < 4.4$ and 80 GeV $< p_T <$ 97 GeV at NNLO (blue), NLO (red) and LO (green). (Right plot) Single jet inclusive cross section versus resolution parameter R of the anti-k_T jet algorithm at $\sqrt{s} = 8$ TeV, 80 GeV $< p_T <$ 96 GeV and $|y| < 0.3$ at NNLO (blue), NLO (red) and LO (green).

In Fig. 2 we plot the dependence of the single jet inclusive cross section as a function of the scale choice and of the resolution parameter R of the anti-k_T jet algorithm, at each order in perturbation theory. We observe that the computation of higher order corrections to the cross section has the effect of reducing the scale uncertainties on the theory prediction. In particular for this observable we obtain a scale variation at the percent level at NNLO.

The R dependence shows that the cross section increases as the value of R increases. This is observed first at NLO where for the first time additional parton radiation can be inside or outside the jet. At NNLO up to three partons can form a jet and this should lead to a better matching of the jet algorithm between theory and experiment. We observe that the size of the NNLO correction decreases for small R.

3 Conclusions and outlook

We presented the NNLO QCD calculation in the purely gluonic channel at leading colour to the fully differential inclusive jet and dijet cross section at hadron colliders opening the path towards precision QCD phenomenology with the LHC. For all of the observables considered here, we observed a dramatic reduction of the respective uncertainties in the theory prediction due to variations of the factorization and renormalization scales. We expect similar conclusions when including the processes involving quarks.

Acknowledgments

This research was supported in part by the UK Science and Technology Facilities Council, in part by the Swiss National Science Foundation (SNF) under contracts PP00P2-139192 and 200020-

that only gluonic matrix elements are involved.

138206 and in part by the European Commission through the "LHCPhenoNet" Initial Training Network PITN-GA-2010-264564. EWNG gratefully acknowledges the support of the Wolfson Foundation, the Royal Society and the Pauli Center for Theoretical Studies.

References

1. T. Aaltonen *et al.* [CDF Collaboration], Phys. Rev. D **78** (2008) 052006 [Erratum-ibid. D **79** (2009) 119902] [arXiv:0807.2204 [hep-ex]].
2. V. M. Abazov *et al.* [D0 Collaboration], Phys. Rev. Lett. **101** (2008) 062001 [arXiv:0802.2400 [hep-ex]].
3. G. Aad *et al.* [Atlas Collaboration], Eur. Phys. J. C **71** (2011) 1512 [arXiv:1009.5908 [hep-ex]]. G. Aad *et al.* [ATLAS Collaboration], Phys. Rev. D **86** (2012) 014022 [arXiv:1112.6297 [hep-ex]].
4. S. Chatrchyan *et al.* [CMS Collaboration], Phys. Lett. B **700** (2011) 187 [arXiv:1104.1693 [hep-ex]]. S. Chatrchyan *et al.* [CMS Collaboration], Phys. Rev. Lett. **107** (2011) 132001 [arXiv:1106.0208 [hep-ex]]. S. Chatrchyan *et al.* [CMS Collaboration], JHEP **1206** (2012) 036 [arXiv:1202.0704 [hep-ex]]. S. Chatrchyan *et al.* [CMS Collaboration], arXiv:1212.6660 [hep-ex].
5. K. Rabbertz 48th Recontres de Moriond conference proceedings
6. M. Wobbisch 48th Recontres de Moriond conference proceedings
7. S. D. Ellis, Z. Kunszt and D. E. Soper, Phys. Rev. Lett. **69** (1992) 1496. W. T. Giele, E. W. N. Glover and D. A. Kosower, Phys. Rev. Lett. **73** (1994) 2019 [hep-ph/9403347]. Z. Nagy, Phys. Rev. Lett. **88** (2002) 122003 [hep-ph/0110315]; Phys. Rev. **D68** (2003) 094002 [hep-ph/0307268]. J. Gao *et. al.*, 1207.0513.
8. S. Alioli, K. Hamilton, P. Nason, C. Oleari and E. Re, JHEP **1104** (2011) 081 [1012.3380].
9. S. Dittmaier, A. Huss and C. Speckner, JHEP **1211** (2012) 095 [1210.0438].
10. N. Kidonakis and J. F. Owens, Phys. Rev. D **63** (2001) 054019 [hep-ph/0007268].
11. A. Gehrmann-De Ridder, T. Gehrmann, E. W. N. Glover and J. Pires, Phys. Rev. Lett. **110** (2013) 162013 arXiv:1301.7310 [hep-ph].
12. A. Gehrmann-De Ridder, T. Gehrmann and E. W. N. Glover, JHEP **09** (2005) 056 [hep-ph/0505111].
13. A. Daleo, T. Gehrmann and D. Maitre, JHEP **0704** (2007) 016 [hep-ph/0612257]. A. Daleo, A. Gehrmann-De Ridder, T. Gehrmann and G. Luisoni, JHEP **1001** (2010) 118 [0912.0374]. R. Boughezal, A. Gehrmann-De Ridder and M. Ritzmann, JHEP **1102** (2011) 098 [1011.6631]; A. Gehrmann-De Ridder, T. Gehrmann and M. Ritzmann, JHEP **1210** (2012) 047 [1207.5779]. T. Gehrmann and P. F. Monni, JHEP **1112** (2011) 049 [1107.4037]. E. W. N. Glover and J. Pires, JHEP **1006** (2010) 096 [1003.2824]. J. Currie, E. W. N. Glover and S. Wells, JHEP **1304** (2013) 066 [arXiv:1301.4693 [hep-ph]].
14. A. Gehrmann-De Ridder, E. W. N. Glover and J. Pires, JHEP **1202** (2012) 141 [1112.3613]. A. Gehrmann-De Ridder, T. Gehrmann, E. W. N. Glover and J. Pires, JHEP **1302** (2013) 026 [arXiv:1211.2710 [hep-ph]].
15. E. W. N. Glover, C. Oleari and M. E. Tejeda-Yeomans, Nucl. Phys. **B605** (2001) 467 [hep-ph/0102201]; E. W. N. Glover and M. Tejeda-Yeomans, JHEP **0105** (2001) 010 [hep-ph/0104178]; Z. Bern, A. De Freitas and L. J. Dixon, JHEP **0203** (2002) 018 [hep-ph/0201161].
16. Z. Bern, L. J. Dixon, D. C. Dunbar and D. A. Kosower, Nucl. Phys. **B425** (1994) 217 [hep-ph/9403226].
17. M. L. Mangano and S. J. Parke, Phys. Rept. **200** (1991) 301 [hep-th/0509223].
18. A. D. Martin, W. J. Stirling, R. S. Thorne and G. Watt, Eur. Phys. J. **C63** (2009) 189 [0901.0002].

Pileup Subtraction for Jet Shapes

Ji-Hun Kim
IPhT, CEA-Saclay, France

Many QCD studies and BSM studies involve hadron jets. For those studies, we need to precisely measure jet shapes such as jet mass, jet transverse momentum and angularity. Pileup events, however, significantly degrade jet shape measurements at the hadron collider experiments. In this talk, we introduce a general method to correct for pileup effects in jet shapes, which acts event-by-event and jet-by-jet, and accounts also for hadron masses.

1 Introduction

Colored partons radiate to produce soft and collinear quarks and gluons which evolve to a numerous hadrons collimated along some directions, so called hadron jets. Jet algorithms are for grouping them. Among them, inclusive kT, Cambridge/Aachen, Anti-kT, and SISCone jet algorithm are infrared and collinear safe and popular. Many QCD studies and BSM studies involve hadron jets, we need to precisely measure jets. At the LHC, however, signal events of our interest come together with lots of pileup events.

The effect of pileup events is a challenging issue for measuring hadron jets. When two protons are crossed at the LHC, nothing happened for most of times. Proton-proton collision events are extremely rare events. Furthermore, Hard events are even orders of smaller than that, *i.e.* $1 \gg p_{\text{soft}} \gg p_{\text{hard}}$. When two protons collide head-on, nothing would happen most of time. It's why LHC accelerate and collide not individual protons, but proton bunches. And each bunch contains more than 10^{11} protons. Whenever we see hard collision event, the law of rare events implies that it is likely to accompany additional events, which are likely to be soft, so called pileup events. At the 2012 run of LHC, the expected number of pileup events is about 30. They produce numerous low energy particles and affect jet clustering procedure. Due to the limitation of detector resolutions, we cannot identify and remove pileup particles; in effect, amount of pileup particle is a kernel, and measured jet shapes are convoluted by the kernel. The effects of pileup is mainly divided into two categories : it introduces biases to the jet shape measurements and also increases variance of uncertainties of the jet shape measurements.

One of method to reduce the pileup effects is defining an area of hadron jet [1] and using a simplified pileup model to correct pileup contribution to a jet transverse momentum [2]. Experiments including ATLAS and CMS have used this method and it is known to be almost remove the biases and also reduce the variances. However, this method is, by definition, only applicable to a jet transverse momentum.

Main contribution of this talk is extending the pileup subtraction method to be applicable to general jet shapes[3].

2 A Simplified Model of Pileup Events.

Although each pileup event is non-uniform, pileup events as a whole are roughly uniform since they are union of independent collisions. Pileup particles are evenly distributed over azimuth angle, ϕ, and nearly uniformly distributed over rapidity, y. With these assumptions, pileup particles can be modeled with a number density of pileup particle, ν, and a probability function for their p_T spectrum. Then, p_T-sum of pileup particles are propotional to jet area[1]:

$$\langle P_{\rm pileup}(p_T|A)\rangle = A\langle\nu\rangle\langle p_T^{\rm pileup}\rangle \equiv \rho A \tag{1}$$

$$\langle P_{\rm pileup}(p_T)\rangle = \int dA\, P(A)\, \rho A = \rho\langle A\rangle. \tag{2}$$

A p_T density, $\rho = \langle\nu\rangle\langle p_T^{\rm pileup}\rangle$, of pileup events can be measured for each event,

$$\rho = \underset{\rm patches}{\rm median}\left[\left\{\frac{p_{T\,\rm patch}}{A_{\rm patch}}\right\}\right]. \tag{3}$$

where patches are either jets with small radius or grids over the $\eta - \phi$ plane.

Four momentum can be written in terms of rapidity, azimuth angle, transverse momentum, mass. For a given jet area, rapidity and azimuth angle of four momenta sum of pileup particles in this model is fixed. And ρ gives transverse momentum. We introduce a parameter, ρ_m for accounting mass:

$$\rho_m = \underset{\rm patches}{\rm median}\left\{\frac{m_{\delta,\rm patch}}{\rm patch}\right\}, \tag{4}$$

where $m_{\delta,\rm patch} = \sum_{i\in\rm patch}(\sqrt{[b]m_i^2 + p_{t,i}^2} - p_{ti})$ and the sum runs over particles i in the patch.

Pileup events may affect jet clustering procedure; thus constituents of jets can be changed significantly. However, it is hard to take it account and we ignore this effect. In fact, it is found to be a good approximation for most cases. Since we ignore the back-reaction effect of pileup, a measured jet of constituents, $\{p^\mu\}_{\rm full}$, is a union of a hard part of the jet, $\{p^\mu\}_{\rm hard}$, and particles from pileup events, $\{p^\mu\}_{\rm pileup}$.

3 Pileup subtraction for jet shapes.

A jet shape, f, is a function of the jet's constituents, $\{p^\mu\}_{\rm jet}$, to a real number. What we can measure from experiments is a value of a jet shape, $f(\{p^\mu\}_{\rm full}) = f(\{p^\mu\}_{\rm hard} \cup \{p^\mu\}_{\rm pileup})$, while what we want to measure is $f(\{p^\mu\}_{\rm hard})$.

What can we do for them to reduce pileup effects? The infra-red and collinear safety of jet shapes has a critical role in here. Jet shapes are insensitive to how low energy jet constituents are distributed inside the jet. Given the four momenta sum of pileup particles, we can split each pileup particles into a bunch of small p_T particles by using collinear safety, and re-distribute them uniformly and continuously inside the jets by using infra-red safety. In case of the jet shape is infra-red and collinear safe, $f(\{p^\mu\}_{\rm full})$ does not much depends on the exact form of $\{p^\mu\}_{\rm pileup}$, and $f(\{p^\mu\}_{\rm full}) \approx f(\{p^\mu\}_{\rm hard} \cup \{p^\mu\}_{\rm uniform})$, where $\{p^\mu\}_{\rm uniform}$ represent background particles uniformly distributed inside the jet. For given $f(\{p^\mu\}_{\rm hard}$ and a jet area, we define a function of a single variable $f_H(x) \equiv f(\{p^\mu\}_{\rm hard} + x \times \{p^\mu\}_{\rm pileup})$; *i.e.* $f_H(0)$ corresponds to the $f(\{p^\mu\}_{\rm hard})$ and $f_H(1)$ is $f(\{p^\mu\}_{\rm full})$. Although it is unknown that which subgroup of the jet constituents are comes from pileup, it is possible to add another uniform background to the jet to increase $\{p^\mu\}_{\rm uniform}$. In this way, we can estimate $f_H(x)$ in a range of $x \in [1, \infty)$; thus we derive $f'(x)|_{x=1}, f''(x)|_{x=1}, \cdots$ and finally, we get $f_H(0)$. It is a brief summary for how the pileup subtraction for jet shapes works.

In Fig. 1(from [3]), we apply this pileup subtraction scheme with angularity, $\theta^{(1)}$, and N-subjettiness, τ_{21}. As expected, the pileup subtraction scheme reduce the effects of pileup events. In Fig. 2 (from[3]), we also apply this scheme for top quark tagging or quark/gluon discrimination.

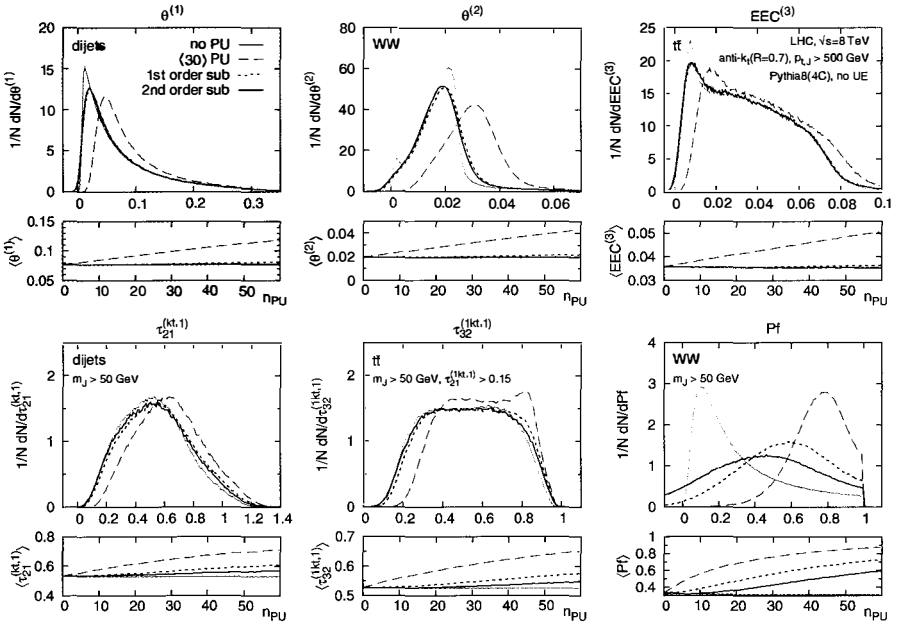

Figure 1: Impact of pileup and subtraction on various jet-shape distributions and their averages, in dijet, W W and tt production processes. The distributions are shown for Poisson distributed pileup (with an average of 30 pileup events) and the averages are shown as a function of the number of pileup events, nPU. The shapes are calculated for jets with $p_T > 500GeV$ (the cut is applied before adding pileup, as are the cuts on the jet mass mJ and subjettiness ratio τ_{21} where relevant).

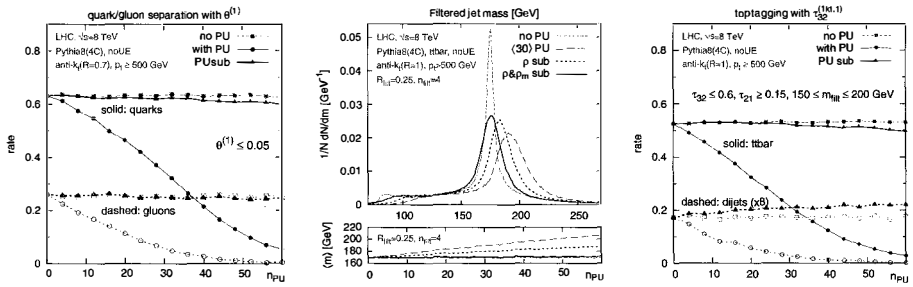

Figure 2: Left: rate for tagging quark and gluon jets using a fixed cut on the jet width, shown as a function of the number of pileup vertices. Middle: filtered jet-mass distribution for fat jets in $t\bar{t}$ events, showing the impact of the ρ and ρ_m components of the subtraction. Right: tagging rate of an N-subjettiness top tagger for $t\bar{t}$ signal and dijct background as a function of the number of pileup vertices. All cuts are applied after addition (and possible subtraction) of pileup. Subtraction acts on τ_1, τ_2 and τ_3 individually.

4 Conclusion

Using Pythia and Herwig simulation, we show that the pileup subtraction scheme works well for jet shape such as jet mass, transverse momentum, angularity, and N-subjettiness even in presence of up to 60 pileup events. On the other hands, some widely used jet shape including planar flow are not infra-red safe, and our subtraction scheme shows relatively poor performance. We hope this progress will help ensure the viability of a broad range of jet substructure tools in high-luminosity LHC running. The software for the general shape subtraction approach presented here will be made available as part of the FastJet Contrib project [4].

References

1. M. Cacciari, G. P. Salam and G. Soyez, "The Catchment Area of Jets," JHEP **0804** (2008) 005 [arXiv:0802.1188 [hep-ph]].
2. M. Cacciari and G. P. Salam, "Pileup subtraction using jet areas," Phys. Lett. B **659** (2008) 119 [arXiv:0707.1378 [hep-ph]].
3. G. Soyez, G. P. Salam, J. Kim, S. Dutta and M. Cacciari, "Pileup subtraction for jet shapes," arXiv:1211.2811 [hep-ph].
4. `http://fastjet.hepforge.org/contrib`

Nonperturbative corrections and showering in NLO-matched event generators [a]

S. Dooling[1], P. Gunnellini[1], F. Hautmann[2,3] and H. Jung[1,4]
[1] *Deutsches Elektronen Synchrotron, D-22603 Hamburg*
[2] *Theoretical Physics Department, University of Oxford, Oxford OX1 3NP*
[3] *Physics and Astronomy, University of Sussex, Brighton BN1 9QH*
[4] *Elementaire Deeltjes Fysica, Universiteit Antwerpen, B 2020 Antwerpen*

We study contributions from nonperturbative effects and parton showering in NLO event generators, and present applications to jet final states. We find p_T-dependent and rapidity-dependent corrections which can affect the shape of observed jet distributions at the LHC. We illustrate numerically the kinematic shifts in longitudinal momentum distributions from the implementation of energy-momentum conservation in collinear shower algorithms.

Monte Carlo event generators are used in analyses of complex final states at the Large Hadron Collider (LHC) [1] both to supplement finite-order perturbative calculations with all-order QCD radiative terms, encoded by parton showers, and to incorporate nonperturbative effects from hadronization, multiple parton interactions, underlying events [2,3]. In this article we report results from our study [4] of nonperturbative (NP) and parton-showering (PS) corrections in the context of matched NLO-shower Monte Carlo generators. The results we present refer to jet final states. Further results for massive states may be found in [4].

LHC experiments have measured inclusive jet production [5,6] over a kinematic range in transverse momentum and rapidity much larger than in any previous collider experiment. Baseline comparisons with Standard Model theoretical predictions are based either on next-to-leading-order (NLO) QCD calculations, supplemented with nonperturbative (NP) corrections estimated from Monte Carlo event generators [5,6], or on NLO-matched parton shower event generators [7]. The first kind of comparison shows that the NLO calculation agrees with data at central rapidities, while increasing deviations are seen with increasing rapidity at large transverse momentum p_T [5]. The question arises of whether such behavior is associated with higher-order perturbative contributions or with nonperturbative components of the cross section. The second kind of comparison, based on POWHEG calculations [8] in which NLO matrix elements are matched with parton showers [2,3], improves the description of data, indicating that higher-order radiative contributions taken into account via parton showers are numerically important. At the same time, the results show large differences between POWHEG calculations interfaced with different shower generators, PYTHIA [2] and HERWIG [3], in the forward rapidity region, pointing to enhanced sensitivity to details of the showering.

NP correction factors are obtained in [5,6] by using leading-order Monte Carlo (LO-MC) generators [2,3]. The method to determine these factors is to compare a Monte Carlo simulation including parton showers, multiparton interactions and hadronization, and a Monte Carlo simulation including only parton showers in addition to the LO hard process. While this is a natural way to estimate NP corrections from LO+PS event generators, it is noted in [4] that when these

[a] Contributed at the XLVIII Rencontres de Moriond, March 2013.

corrections are combined with NLO parton-level results a potential inconsistency arises because the radiative correction from the first gluon emission is treated at different levels of accuracy in the two parts of the calculation. To avoid this, Ref. [4] proposes a method which uses NLO Monte Carlo (NLO-MC) generators to determine the correction. In this case one can consistently assign correction factors to be applied to NLO calculations. This method allows one to study separately correction factors to the fixed-order calculation due to parton showering effects. To do this, Ref. [4] introduces the nonperturbative (NP) and showering (PS) correction factors, K^{NP} and K^{PS}, as

$$K^{NP} = N^{(ps+mpi+had)}_{NLO-MC}/N^{(ps)}_{NLO-MC} \ , \tag{1}$$

$$K^{PS} = N^{(ps)}_{NLO-MC}/N^{(0)}_{NLO-MC} \ , \tag{2}$$

where $(ps+mpi+had)$ denotes a simulation including parton showers, multiparton interactions and hadronization, while (ps) denotes a simulation including parton showers only. The denominator in Eq. (2) is defined by switching off all components beyond NLO in the Monte Carlo simulation.

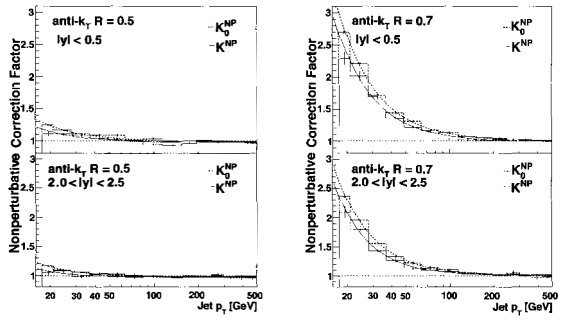

Figure 1: *The NP correction factors to jet transverse momentum distributions obtained using* PYTHIA *and* POWHEG *respectively, for* $|y| < 0.5$ *and* $2 < |y| < 2.5$. *Left:* $R = 0.5$*; Right:* $R = 0.7$.

The factor K^{NP} in Eq. (1) differs from the LO-MC NP factor [5,6] because of the different definition of the hard process. In particular the multi-parton interaction p_T cut-off scale is different in the LO and NLO cases. Numerical results are shown in Fig. 1. The factor K^{PS} in Eq. (2), on the other hand, is new. It singles out contributions due to parton showering and has not been considered in previous analyses. Unlike the NP correction, it gives in general finite effects also at large p_T. Results are plotted in Fig. 2, showing that this correction is y and p_T dependent, especially when rapidity is non-central, so that it cannot be treated as a rescaling.

The correction factor in Fig. 2 comes from initial-state and final-state showers. These are interrelated so that the combined effect is nontrivial and is not obtained by simply adding the two [4]. The effect from parton shower is largest at large $|y|$, where the initial-state parton shower is mainly contributing at low p_T, while the final-state parton shower is contributing significantly over the whole p_T range.

The main effect of initial-state showering is associated with the kinematic shifts in longitudinal momentum distributions first noted in [9]. These shifts result, quite generally, from combining the approximation of collinear, on-shell partons with the requirements of energy-momentum conservation in the Monte Carlo generator. More precisely, the Monte Carlo first generates hard subprocess events in which the momenta k_j of the partons initiating the hard scatter are on shell, and are taken to be fully collinear with the incoming state momenta. Next the showering

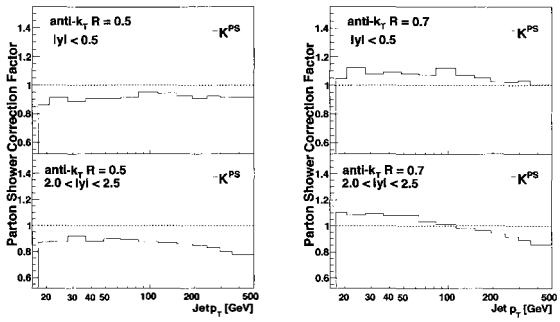

Figure 2: *The parton shower correction factor to jet transverse momentum distributions, obtained from Eq. (2) using* POWHEG *for* $|y| < 0.5$ *and* $2 < |y| < 2.5$. *Left:* $R = 0.5$*; Right:* $R = 0.7$.

algorithm is applied, and complete final states are generated including additional QCD radiation from the initial and final parton cascades. As a result of QCD showering, the momenta k_j are no longer exactly collinear. Their transverse momentum is to be compensated by a change in the kinematics of the hard scattering subprocess. By energy-momentum conservation, however, this implies a reshuffling, event by event, in the fractions x_j of longitudinal momentum carried by the partons scattering off each other in the hard subprocess.

The size of the shift is illustrated in Fig. 3[4] for the case of jets produced at different rapidities, by comparing the distribution in the parton longitudinal momentum fraction x before parton showering and after parton showering. We see that the longitudinal shift is negligible for central rapidities but becomes significant for $y > 1.5$. It characterizes the highly asymmetric parton kinematics [11] which becomes important for the first time at the LHC in significant regions of phase space. Although Fig. 3 is obtained using a particular NLO-shower matching scheme (POWHEG), the effect is common to any calculation matching NLO with collinear showers. On the other hand, this is avoided in shower algorithms using transverse momentum dependent parton distributions [12,13,14,15] from the beginning, as for instance in [16,17].

In summary, the nonperturbative correction factor K^{NP} introduced from NLO-MC in Eq. (1) gives non-negligible differences compared to the LO-MC contribution [5,6] at low to intermediate jet p_T, while the showering correction factor K^{PS} of Eq. (2) gives significant effects over the whole p_T range and is largest at large jet rapidities y. Because of this y and p_T dependence, taking properly into account NP and showering correction factors changes the shape of jet distributions, and may thus influence the comparison of theory predictions with experimental data. Besides jets, longitudinal momentum shifts as in Fig. 3 also affect massive final states [4] such as Drell-Yan Z/W production. We anticipate that the showering correction factors will be relevant in particular in fits for parton distribution functions using inclusive jet and vector boson data.

Acknowledgments

We are grateful to the Moriond organizers and staff for the invitation to an exciting conference, and to the Moriond participants for interesting discussions.

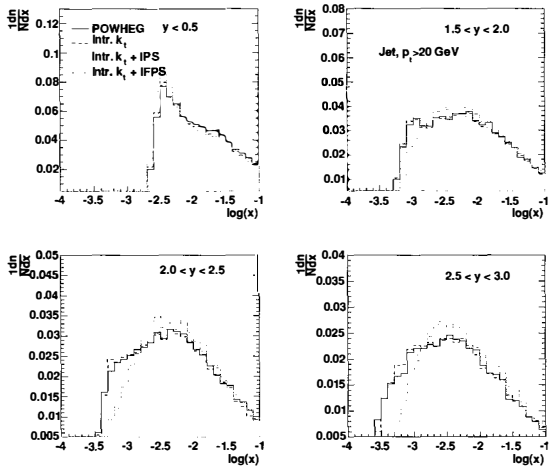

Figure 3: *Distributions in the parton longitudinal momentum fraction x before (POWHEG) and after parton showering (POWHEG+PS), for inclusive jet production at different rapidities for jets with* $p_T > 18$ *GeV obtained by the anti-kt jet algorithm with* $R = 0.5$. *Shown is the effect of intrinsic* k_t, *initial (IPS) and initial+final state (IFPS) parton shower.*

References

1. See S. Höche, SLAC preprint SLAC-PUB-14498 (2011) for a recent review.
2. T. Sjöstrand, S. Mrenna and P. Skands, JHEP **0605** (2006) 026.
3. G. Corcella *et al.*, JHEP **0101** (2001) 010 [arXiv:hep-ph/0011363]; G. Corcella *et al.*, arXiv:hep-ph/0210213.
4. S. Dooling, P. Gunnellini, F. Hautmann and H. Jung, arXiv:1212.6164 [hep-ph].
5. ATLAS Coll. (G. Aad et al.), Phys. Rev. D **86** (2012) 014022.
6. CMS Coll. (S. Chatrchyan et al.), Phys. Rev. Lett. **107** (2011) 132001; arXiv:1212.6660 [hep-ex].
7. P. Nason and B.R. Webber, arXiv:1202.1251 [hep-ph].
8. S. Alioli et al., JHEP **1104** (2011) 081.
9. F. Hautmann and H. Jung, Eur. Phys. J. C **72** (2012) 2254.
10. M. Cacciari, G. Salam and G. Soyez, JHEP **0804** (2008) 063.
11. M. Deak et al., JHEP **0909** (2009) 121; arXiv:0908.1870; arXiv:1012.6037 [hep-ph]; Eur. Phys. J. C **72** (2012) 1982; arXiv:1206.7090 [hep-ph].
12. E. Avsar, arXiv:1203.1916 [hep-ph]; arXiv:1108.1181 [hep-ph].
13. F. Hautmann, Acta Phys. Polon. B **40** (2009) 2139; Phys. Lett. B **655** (2007) 26; F. Hautmann and H. Jung, arXiv:0712.0568 [hep-ph]; arXiv:0805.1049 [hep-ph]; arXiv:0808.0873.
14. P.J. Mulders, Pramana **72** (2009) 83; P.J. Mulders and T.C. Rogers, arXiv:1102.4569 [hep-ph].
15. F. Hautmann, M. Hentschinski and H. Jung, Nucl. Phys. B**865** (2012) 54; arXiv:1205.6358 [hep-ph]; arXiv:1209.6305 [hep-ph].
16. H. Jung et al., Eur. Phys. J. C **70** (2010) 1237; arXiv:1206.1796 [hep-ph].
17. S. Jadach and M. Skrzypek, Acta Phys. Polon. B **40** (2009) 2071; S. Jadach, M. Jezabek, A. Kusina, W. Placzek and M. Skrzypek, arXiv:1209.4291 [hep-ph].

QCD RESUMMATION IN THE FRAMEWORK OF SUPERSYMMETRY

BENJAMIN FUKS[1,2 a], MICHAEL KLASEN[3], DAVID R. LAMPREA[3], MARCEL ROTHERING[3]
[1] *Theory Division, Physics Department, CERN, CH-1211 Geneva 23, Switzerland*
[2] *Institut Pluridisciplinaire Hubert Curien/Département Recherches Subatomiques, Université de Strasbourg/CNRS-IN2P3, 23 Rue du Loess, F-67037 Strasbourg, France*
[3] *Institut für Theoretische Physik, Westfälische Wilhelms-Universität Münster, Wilhelm-Klemm-Straße 9, D-48149 Münster, Germany*

Motivated by current searches for electroweak superpartners at the Large Hadron Collider, we present precision predictions for pair production of such particles in the framework of the Minimal Supersymmetric Standard Model. We make use of various QCD resummation formalisms and match the results to pure perturbative QCD computations. We study the impact of scale variations and compare our results to predictions obtained by means of traditionally used Monte Carlo event generators.

1 Introduction

After almost half a century of theoretical developments and experimental discoveries in high-energy physics, an extremely coherent picture arises as the so-called Standard Model of particle physics. Since this theory contains a fundamental scalar field, the stabilization of its mass with respect to radiative corrections is questionable. This has led to a plethora of new physics models among which weak-scale supersymmetry [1] (SUSY) is one of the most appealing option since it encompasses in addition, *e.g.*, gauge coupling unification and a candidate for dark matter.

The current non-observation of any hint for strong superpartners has shifted the experimental attention to the production of electroweak sleptons, neutralinos and charginos. Investigations at the Large Hadron Collider (LHC), at a center-of-mass energy of $\sqrt{S_h} = 7$ and 8 TeV, have already allowed to impose bounds of several hundreds of GeV on their masses [2]. These analyses however rely on leading order (LO) computations [3] supplemented by QCD next-to-leading order (NLO) corrections [4]. Since such predictions suffer from rather large theoretical uncertainties, soft-gluon resummation of the large logarithmic terms arising at small transverse momentum or close to the production threshold have to be accounted for and matched to fixed order [5, 6, 7, 8, 9, 10].

We briefly review, in Section 2, three resummation formalisms that can be employed for such precision calculations and illustrate their main effects in Section 3 for gaugino pair production.

[a] Speaker.

In addition, we also confront the resummed predictions to results obtained using LO Monte Carlo event generators including multiparton matrix element merging after parton showering. We summarize our work in Section 4.

2 Soft gluon resummation: a brief insight

We focus on the hadroproduction of pairs of electroweak superpartners with an invariant mass M and a transverse momentum p_T. After a Mellin transform with respect to M^2/S_h, the differential cross section $\mathrm{d}^2\sigma/\mathrm{d}M^2\mathrm{d}p_T^2$ can be expressed, in conjugate N-space, as a product of the partonic cross section σ_{ab} with the densities $f_{a,b}$ of the partons a, b in the colliding hadrons,

$$M^2\frac{\mathrm{d}^2\sigma}{\mathrm{d}M^2\mathrm{d}p_T^2}(N-1) = \sum_{ab} f_a(N,\mu_F^2) f_b(N,\mu_F^2) \sigma_{ab}(N, M^2, p_T^2, \mu_F^2, \mu_R^2) \ . \tag{1}$$

Under this form where factorization and renormalization scales μ_F and μ_R are explicitly indicated, we can resum to all orders in the strong coupling α_s the large logarithmic terms arising when p_T tends towards zero and/or close to the production threshold. In this case, the partonic cross section can be refactorized into a closed exponential form, respectively reading

$$\sigma_{ab}^{(\mathrm{res.})}(N, M^2, \mu_F^2, \mu_R^2) = \mathcal{H}_{ab}(M^2, \mu_F^2, \mu_R^2) \exp\left[\mathcal{G}_{ab}(N, M^2, \mu_F^2, \mu_R^2)\right] \ , \tag{2}$$

$$\sigma_{ab}^{(\mathrm{res.})}(N, M^2, p_T^2, \mu_F^2, \mu_R^2) = \int_0^\infty \mathrm{d}b \frac{b}{2} \ J_0(bp_T) \ \mathcal{H}_{ab}(M^2, \mu_F^2, \mu_R^2) \exp\left[\mathcal{G}_{ab}(N, b, M^2, \mu_F^2, \mu_R^2)\right] \ , \tag{3}$$

in the threshold (after integrating upon p_T) and small-p_T regime. The hard part of the cross section is described by the function $\mathcal{H}_{ab}$ whereas the Sudakov form factor $\mathcal{G}_{ab}$ embeds soft and collinear parton radiation and absorbs the large logarithms. Eq. (3) also contains an inverse Fourier transform, J_0 denoting the 0^{th}-order Bessel function, so that the singularities of the integrand have to be handled after deforming the integration contour into the complex plane [9].

Although the logarithmic contributions must be resummed when they are large, the full perturbative computation, only partially accounted for by resummation, is expected to be reliable otherwise. Therefore, the fixed order ($\sigma^{(\mathrm{f.o.})}$) and resummed ($\sigma^{(\mathrm{res.})}$) results have to be consistently combined by subtracting from their sum their overlap $\sigma^{(\mathrm{exp.})}$,

$$\sigma_{ab} = \sigma_{ab}^{(\mathrm{res.})} + \sigma_{ab}^{(\mathrm{f.o.})} - \sigma_{ab}^{(\mathrm{exp.})} \ . \tag{4}$$

Since both $\sigma^{(\mathrm{res.})}$ and $\sigma^{(\mathrm{exp.})}$ are computed in Mellin space, an inverse transform is in order. To handle the singularities arising at the level of the N-space cross section, the integration contour is distorted following the principal value procedure and minimal prescription [10, 11].

The form of the quantities introduced above depends on the resummation regime. Transverse-momentum resummation deals with logarithms arising at small p_T, while threshold resummation takes care of those appearing close to the production threshold. Finally, joint resummation allows for resumming both types of logarithms simultaneously. We refer to the RESUMMINO manual and references therein for the relevant analytical expressions at the next-to-leading logarithmic (NLL) accuracy [12].

3 Gaugino pair production at the next-to-leading logarithmic accuracy

In Fig. 1, we address the production of an associated $\tilde{\chi}_1^\pm\tilde{\chi}_2^0$ pair at the LHC, for $\sqrt{S_h} = 14$ TeV. We adopt the LM9 benchmark scenario [13], where both gauginos have a mass of about 150 GeV whereas gluinos and squarks lie above 1 TeV, and employ the CTEQ6 parton densities [14]. On the left panel of the figure, we present spectra in the invariant mass of the gaugino pair. The LO results (dotted) are found to be considerably smaller than NLO predictions with or without

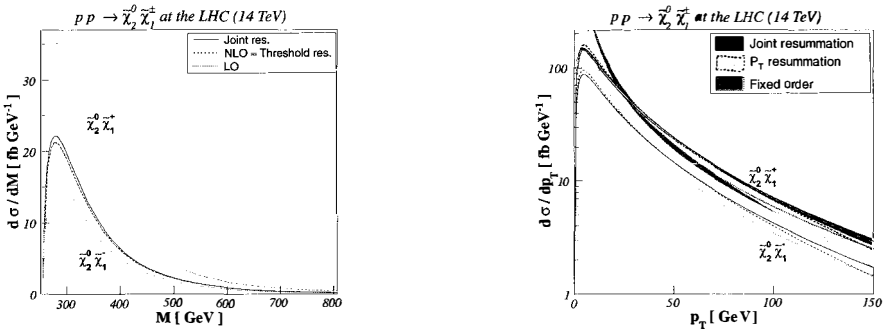

Figure 1: Invariant mass (left) and transverse-momentum (right) distributions of an associated $\tilde{\chi}_2^0\tilde{\chi}_1^\pm$ pair produced at the LHC, at fixed order and after matching to resummation. Scale uncertainties are indicated for the p_T spectra.

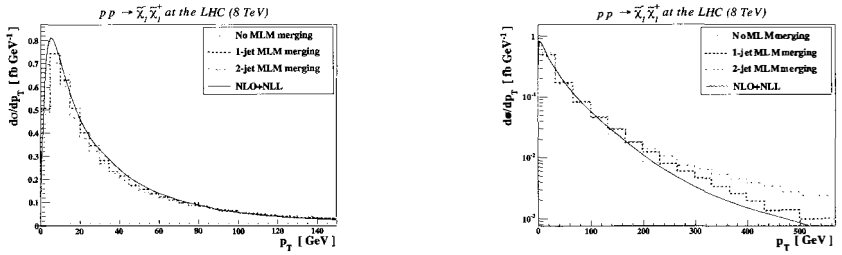

Figure 2: Distributions in the transverse momentum of a $\tilde{\chi}_1^+\tilde{\chi}_1^-$ pair produced at the LHC. We compare resummation results to several approaches by means of LO event generators including MLM merging techniques.

matching to NLL resummation. Since we restrict the distribution to the small invariant-mass region, far from the production threshold, threshold resummation does not lead to a significant effect with respect to NLO (dashed). In contrast, jointly resummed predictions (full) exceed the NLO ones due to the resummation of the large logarithms arising at small p_T.

On the right panel of Fig. 1, we show transverse-momentum spectra of the gaugino pair. While fixed-order predictions at $\mathcal{O}(\alpha_s)$ (dotted) diverge at small p_T due to uncanceled soft singularities from real gluon emission, resummed calculations exhibit a pronounced peak. For intermediate values of p_T, resummation effects are found to be still important with a K-factor greater than unity. We finally show that calculations using p_T (dashed) and joint (full) resummation agree with each other, although the scale uncertainty associated with the latter, estimated by varying both unphysical scales by a factor of two around the average mass of the two gauginos, is considerably smaller due to the resummation of threshold logarithms.

In Fig. 2, we focus on $\tilde{\chi}_1^+\tilde{\chi}_1^-$ production at $\sqrt{S_h} = 8$ TeV and on the first SUSY scenario proposed by the LPCC . It embeds sub-TeV squarks and gluinos and a lightest chargino of about 300 GeV. Using MADANALYSIS 5 , we confront joint resummation (full) to predictions of the LO event generator MADGRAPH 5 , matched to PYTHIA 6 for parton showering, the necessary UFO module being exported from FEYNRULES , , , . We allow the generated events to contain zero (dotted), up to one (dashed) or up to two (dot-dashed) additional jets and merge them following the MLM merging scheme . After normalizing the Monte Carlo results to the resummed prediction of 40.51 fb and employing the MSTW parton densities , we observe a very good agreement between all approaches in the small-p_T region. In contrast, in the large-p_T region, only Monte Carlo predictions including up to one extra parton agree with the resummed results, since both rely on the same matrix elements.

4 Summary

We have analyzed predictions for electroweak superpartner production at the LHC obtained by means of different resummation methods after a combination with NLO predictions. The results have been found to be more reliable and exhibit smaller uncertainties stemming from scale variation. A similar accuracy can be reached by means of LO Monte Carlo event generators after merging matrix elements possibly containing additional partons.

Acknowledgments

We acknowledge support from the BMBF Theorie-Verbund and the Theory-LHC-France initiative of the CNRS/IN2P3. B.F. thanks the organizers for the great conference and the invitation.

References

1. H. P. Nilles, Phys. Rept. **110** (1984) 1.
2. H. E. Haber and G. L. Kane, Phys. Rept. **117** (1985) 75.
3. [ATLAS Collaboration], ATLAS-CONF-2012-154.
4. [CMS Collaboration], CMS-PAS-SUS-12-022.
5. G. Bozzi, B. Fuks and M. Klasen, Phys. Lett. B **609** (2005) 339.
6. G. Bozzi, B. Fuks, B. Herrmann and M. Klasen, Nucl. Phys. B **787** (2007) 1.
7. J. Debove, B. Fuks and M. Klasen, Phys. Rev. D **78** (2008) 074020.
8. W. Beenakker, M. Klasen, M. Kramer, T. Plehn, M. Spira and P. M. Zerwas, Phys. Rev. Lett. **83** (1999) 3780 [Erratum-ibid. **100** (2008) 029901].
9. G. Bozzi, B. Fuks and M. Klasen, Phys. Rev. D **74** (2006) 015001.
10. G. Bozzi, B. Fuks and M. Klasen, Nucl. Phys. B **777** (2007) 157.
11. G. Bozzi, B. Fuks and M. Klasen, Nucl. Phys. B **794** (2008) 46.
12. J. Debove, B. Fuks and M. Klasen, Phys. Lett. B **688** (2010) 208.
13. J. Debove, B. Fuks and M. Klasen, Nucl. Phys. B **842** (2011) 51.
14. J. Debove, B. Fuks and M. Klasen, Nucl. Phys. B **849** (2011) 64.
15. B. Fuks, M. Klasen, D. R. Lamprea and M. Rothering, JHEP **1210** (2012) 081.
16. E. Laenen, G. F. Sterman and W. Vogelsang, Phys. Rev. Lett. **84** (2000) 4296.
17. H. Contopanagos and G. F. Sterman, Nucl. Phys. B **419** (1994) 77.
18. S. Catani, M. L. Mangano, P. Nason and L. Trentadue, Nucl. Phys. B **478** (1996) 273.
19. B. Fuks, M. Klasen, D. R. Lamprea and M. Rothering, arXiv:1304.0790 [hep-ph].
20. G. L. Bayatian *et al.* [CMS Collaboration], J. Phys. G **34** (2007) 995.
21. P. M. Nadolsky *et al.*, Phys. Rev. D **78** (2008) 013004.
22. S. S. AbdusSalam *et al.*, Eur. Phys. J. C **71** (2011) 1835.
23. E. Conte, B. Fuks and G. Serret, Comput. Phys. Commun. **184** (2013) 222.
24. J. Alwall, M. Herquet, F. Maltoni, O. Mattelaer and T. Stelzer, JHEP **1106** (2011) 128.
25. T. Sjöstrand, S. Mrenna and P. Z. Skands, JHEP **0605** (2006) 026.
26. C. Degrande, C. Duhr, B. Fuks, D. Grellscheid, O. Mattelaer and T. Reiter, Comput. Phys. Commun. **183** (2012) 1201.
27. N. D. Christensen and C. Duhr, Comput. Phys. Commun. **180** (2009) 1614.
28. N. D. Christensen, P. de Aquino, C. Degrande, C. Duhr, B. Fuks, M. Herquet, F. Maltoni and S. Schumann, Eur. Phys. J. C **71** (2011) 1541.
29. N. D. Christensen, C. Duhr, B. Fuks, J. Reuter and C. Speckner, Eur. Phys. J. C **72** (2012) 1990.
30. C. Duhr and B. Fuks, Comput. Phys. Commun. **182** (2011) 2404.
31. B. Fuks, Int. J. Mod. Phys. A **27** (2012) 1230007.
32. M. L. Mangano, M. Moretti, F. Piccinini and M. Treccani, JHEP **0701** (2007) 013.
33. A. D. Martin, W. J. Stirling, R. S. Thorne and G. Watt, Eur. Phys. J. C **63** (2009) 189.

COMBINING HIGHER-ORDER RESUMMATION WITH MULTIPLE NLO CALCULATIONS AND PARTON SHOWERS IN THE GENEVA MONTE CARLO FRAMEWORK

SIMONE ALIOLI,[1] [a] CHRISTIAN W. BAUER,[1] CALVIN BERGGREN,[1] ANDREW HORNIG,[2] FRANK J. TACKMANN,[3] CHRISTOPHER K. VERMILION,[1] JONATHAN R. WALSH,[1] SABA ZUBERI[1]

[1] *Ernest Orlando Lawrence Berkeley National Laboratory and University of California, Berkeley, CA 94720, U.S.A.*

[2] *Department of Physics, University of Washington, Seattle, WA 98195, U.S.A.*

[3] *Theory Group, Deutsches Elektronen-Synchrotron (DESY), D-22607 Hamburg, Germany*

We discuss the GENEVA Monte Carlo framework, which combines higher-order resummation (NNLL) of large Sudakov logarithms with multiple next-to-leading-order (NLO) matrix-element corrections and parton showering (using PYTHIA 8) to give a complete description at the next higher perturbative accuracy in α_s at both small and large jet resolution scales. Results for $e^+e^- \to$ jets compared to LEP data and $pp \to (Z/\gamma^\star \to \ell^+\ell^-) +$ jets are presented.

1 Introduction

Present and future colliders require accurate and reliable predictions of QCD effects, beyond the lowest perturbative accuracy in the strong coupling α_s expansion. For inclusive observables, such as total cross sections, the lowest perturbative accuracy is obtained via a fixed-order expansion in powers of α_s, truncated at the leading order. To get accurate results, one is usually forced to go at least to the next higher order, i.e., NLO, or even to NNLO. For more exclusive observables, the presence of logarithmically enhanced contributions in certain regions of phase space requires an all-orders resummation to obtain physically meaningful results. In this case, the proper lowest perturbative accuracy is the (N)LL resummation. In general, a description which aims to be valid across the entire phase space demands a combination of both types of corrections. At the lowest order, such a combination is achieved in Monte Carlo programs by the standard merging of matrix elements with parton showers (ME/PS). [1,2]

The GENEVA framework [3] extends this to higher perturbative accuracy by including the fixed NLO corrections as well as the NNLL resummation of the jet resolution parameter, which in our case is chosen to be N-jettiness [4] due to its simple factorization and resummation properties. An immediate by-product of this combination of fixed-order and resummed results for different jet multiplicities is the merging of multiple NLO calculations, which has been the subject of several recent theoretical efforts. [5,6,7,8,9] The key difference in our approach is the inclusion of higher logarithmic resummation [b] of the jet resolution scale τ^{cut}, which allows us to push it to much lower values than fixed-order perturbation theory would allow. In this way, we can avoid the restriction $\alpha_s \ln^2 \tau^{\text{cut}} \ll 1$ that limits the range of applicability of other approaches.

[a] Speaker

[b] The inclusion of higher logarithmic resummation has also been proposed in a subsequent work [10] as a possible way to remove the dependency on the jet resolution scale.

To provide further parton showering and hadronization, GENEVA is interfaced to PYTHIA 8. [11] In this way, the best possible theoretical predictions in the context of fully exclusive Monte Carlo event generators can be directly made available for experimental analyses.

2 Theoretical framework

We now give a brief description of our method, referring to the GENEVA paper [3] for a comprehensive discussion. We first separate the exclusive N-jet and inclusive $(N+1)$-jet regions,

$$\sigma_{\geq N} = \int \mathrm{d}\Phi_N \frac{\mathrm{d}\sigma}{\mathrm{d}\Phi_N}(\mathcal{T}_N^{\mathrm{cut}}) + \int \mathrm{d}\Phi_{N+1} \frac{\mathrm{d}\sigma}{\mathrm{d}\Phi_{N+1}}(\mathcal{T}_N)\,\theta(\mathcal{T}_N > \mathcal{T}_N^{\mathrm{cut}})\,, \tag{1}$$

where $\mathrm{d}\sigma/\mathrm{d}\Phi_N(\mathcal{T}_N^{\mathrm{cut}})$ is the fully differential N-jet cross section for $\mathcal{T}_N < \mathcal{T}_N^{\mathrm{cut}}$ and $\mathrm{d}\sigma/\mathrm{d}\Phi_{N+1}(\mathcal{T}_N)$ is the fully differential cross section for a given N-jettiness value $\mathcal{T}_N(\Phi_{N+1})$. The parameter $\mathcal{T}_N^{\mathrm{cut}}$ is a small infrared cutoff $\sim 1\,\mathrm{GeV}$, whose dependence in the final results cancels to the required resummation order. In the N-jet region, where $\mathcal{T}_N$ is small, we then resum the logarithms of $\mathcal{T}_N/Q$, with Q some hard scale of the process. In the $(N+1)$-jet region, at large $\mathcal{T}_N$, we instead use a fixed-order expansion in α_s. To properly combine the higher fixed-order results at large $\mathcal{T}_N$ with the higher-order resummation at small $\mathcal{T}_N$, with a smooth transition between these two regimes, we employ the following master formulas,

$$\begin{aligned}
\frac{\mathrm{d}\sigma}{\mathrm{d}\Phi_N}(\mathcal{T}_N^{\mathrm{cut}}) &= \frac{\mathrm{d}\sigma^{\mathrm{resum}}}{\mathrm{d}\Phi_N}(\mathcal{T}_N^{\mathrm{cut}}) + \left[\frac{\mathrm{d}\sigma^{\mathrm{FO}}}{\mathrm{d}\Phi_N}(\mathcal{T}_N^{\mathrm{cut}}) - \frac{\mathrm{d}\sigma^{\mathrm{resum}}}{\mathrm{d}\Phi_N}(\mathcal{T}_N^{\mathrm{cut}})\bigg|_{\mathrm{FO}}\right], \\
\frac{\mathrm{d}\sigma}{\mathrm{d}\Phi_{N+1}}(\mathcal{T}_N) &= \frac{\mathrm{d}\sigma^{\mathrm{FO}}}{\mathrm{d}\Phi_{N+1}}(\mathcal{T}_N)\left[\frac{\mathrm{d}\sigma^{\mathrm{resum}}}{\mathrm{d}\Phi_N \mathrm{d}\mathcal{T}_N} \Big/ \frac{\mathrm{d}\sigma^{\mathrm{resum}}}{\mathrm{d}\Phi_N\,\mathrm{d}\mathcal{T}_N}\bigg|_{\mathrm{FO}}\right],
\end{aligned} \tag{2}$$

where the superscript "resum" indicates an analytically resummed calculation and "FO" indicates a fixed-order calculation or expansion. This construction can be iterated in the case of several multiplicities. [3] At this stage, we have explicit control of the perturbative uncertainties and are able to estimate reliably both the fixed-order and resummation uncertainties and to combine them to provide perturbative event-by-event uncertainties.

Once the partonic GENEVA events are generated according to Eq. (2) – or its generalization in case of more jet multiplicities – they are fed through the PYTHIA 8 parton shower, whose purpose it is to fill up the jets with additional emissions. To preserve the perturbative accuracy of the higher-order resummation, the shower is constrained not to change the weight of an event and to preserve its value of $\mathcal{T}_N$. (In general, this is a nontrivial constraint and can be implemented with sufficient approximation and manageable efficiency.)

Finally, we rely on the PYTHIA 8 hadronization model to hadronize the final-state partons. No further constraints are applied in this step, since GENEVA's partonic predictions do not include any nonperturbative effects.

3 Results

We first present results for $e^+e^- \to 2/3$ jets, using 2-jettiness $\mathcal{T}_2$ as the 2-jet resolution variable,

$$\mathcal{T}_2 = E_{\mathrm{cm}}\left(1 - \max_{\hat{n}} \frac{\sum_k |\hat{n}\cdot\vec{p}_k|}{\sum_k |\vec{p}_k|}\right), \tag{3}$$

which is simply related to thrust T by $\mathcal{T}_2 = E_{\mathrm{cm}}(1-T)$. We perform the resummation in $\mathcal{T}_2$ to NNLL$'$ and include the full NLO_2, NLO_3, and LO_4 fixed-order matrix elements; i.e., we obtain NNLL$'_{\mathcal{T}}$+NLO_3 predictions.

In Fig. 1, we show our results before and after PYTHIA 8 showering, compared with analytical resummations, for 2-jettiness, heavy jet mass, and jet broadening. We focus on the

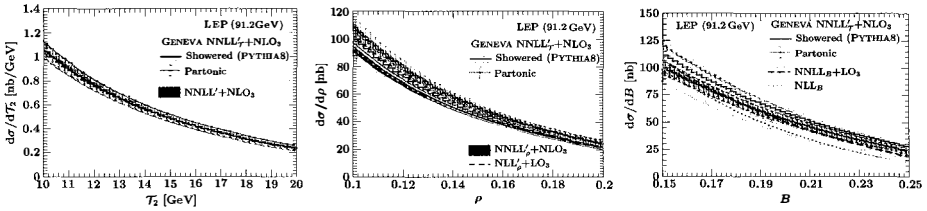

Figure 1: The 2-jettiness (left), heavy jet mass (central), and jet broadening (right) parton-level GENEVA results, compared with analytical resummation. The error bars or bands on the GENEVA histograms are built from event-by-event perturbative uncertainties. Statistical uncertainties from Monte Carlo integration are negligible.

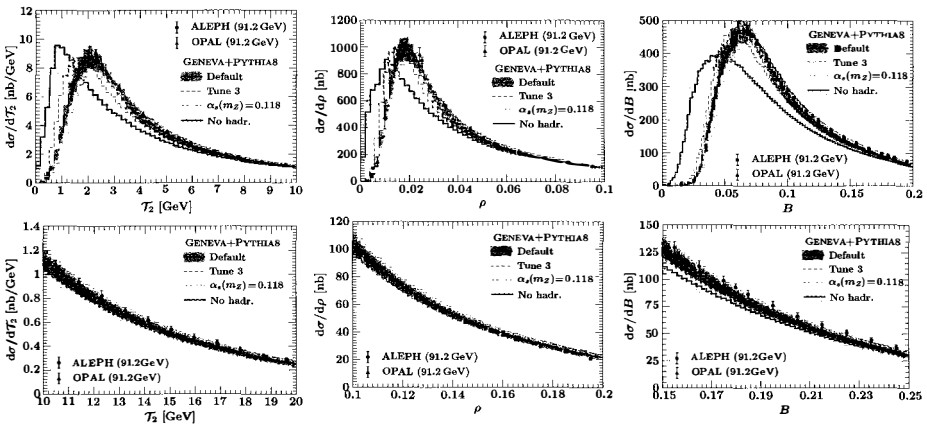

Figure 2: The 2-jettiness (left column), heavy jet mass (central column), and jet broadening (right column) distributions of GENEVA interfaced to PYTHIA 8, compared to ALEPH and OPAL data in the peak (upper line) and transition regions (lower line). Default results are obtained with PYTHIA 8 e^+e^- tune 1 and $\alpha_s(m_Z) = 0.1135$. Variations of the PYTHIA 8 tune, the $\alpha_s(m_Z)$ value, and results without hadronization are shown for comparison.

transition region, where the resummation and fixed-order calculations are both important, and their proper combination is necessary. GENEVA results are obtained with $E_{\rm cm} = 91.2\,\text{GeV}$, $\alpha_s(m_Z) = 0.1135$ (from N^{3}LL$'$ thrust fits [12]), and PYTHIA 8.170 with e^+e^- tune 1. The perfect agreement for the $\mathcal{T}_2$ distribution, in both the central value and in the theoretical uncertainties, is a nontrivial crosscheck on the correctness of our implementation. Predictions for observables other than 2-jettiness are instead important to validate the GENEVA framework, since the logarithmic structure of these observables will in general be different from that of 2-jettiness. The close agreement with the analytic resummed results we find demonstrates that GENEVA is able to capture a large set of higher-order logarithms for observables other than the jet resolution variable $\mathcal{T}_2$. In Fig. 2, we show our final results, including PYTHIA 8 hadronization, finding excellent agreement with ALEPH and OPAL data.

Next we discuss the ongoing extension to hadronic collisions. We show first results for $pp \to (Z/\gamma^* \to \ell^+\ell^-) + \text{jets}$, matching the 0- and 1-jet multiplicities, and using beam thrust, [13] as the resolution parameter. An additional complication compared to the e^+e^- case is the presence of initial-state radiation. In the resummation, the collinear radiation from the incoming partons is described by beam functions, which can be factorized into a convolution of the usual parton distribution functions and perturbatively calculable coefficients. [13] In Fig. 3, we show GENEVA results at NNLL+LO$_1$ for Drell-Yan production in pp collisions at $E_{\rm cm} = 8$ TeV, sampling the invariant mass Q of the $\ell^+\ell^-$ pair around the Z pole in the $M_Z \pm 10\,\Gamma_Z$ interval. The agreement

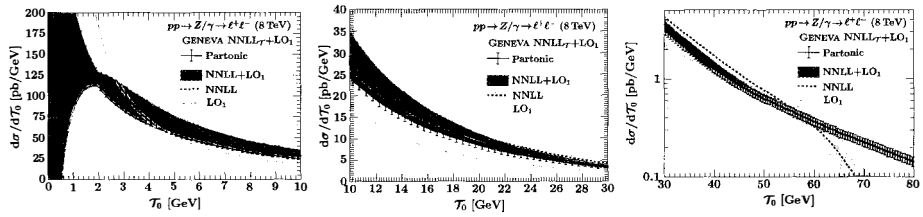

Figure 3: The GENEVA partonic results for Drell-Yan production, compared to the analytic resummation of $\mathcal{T}_0$ matched to fixed order at NNLL+LO$_1$, in the peak (left), transition (center), and tail (right) regions.

of central values and theoretical uncertainties with the fixed-order calculation at large $\mathcal{T}_0$ and with the NNLL analytic resummation at low $\mathcal{T}_0$ serves as a useful validation.

4 Conclusions

From the Monte Carlo perspective, the GENEVA framework achieves the combination of higher-order resummation with multiple NLO calculations. From the resummation perspective, it allows one to obtain fully differential results that correctly include the resummation of the jet resolution variable to higher logarithmic accuracy.

We have presented results for e^+e^- collisions, employing 2-jettiness as a resolution parameter. Using $\alpha_s(m_Z) = 0.1135$ together with tune 1 of PYTHIA 8, we obtain an excellent description of ALEPH and OPAL data, both for thrust and for observables whose resummation structure is distinct from that of 2-jettiness, namely C-parameter, heavy jet mass, and jet broadening.

The extension to pp collisions is in progress. Here, we have concentrated on the Drell-Yan process at the LHC, using beam thrust as the jet resolution variable and showing the first steps of such an implementation.

Acknowledgments

This work was supported by DOE grants DE-PS02-09ER09-26, DE-FGO2-96ER40956, NSF grants NSF-PHY-0705682, NSF-PHY-0969510, DFG EM grant No. TA 867/1-1 and used resources of NERSC, supported by the DOE grant DE-AC02-05CH11231.

References

1. S. Catani, F. Krauss, R. Kuhn, and B. R. Webber, *JHEP* **11** (2001) 063, [hep-ph/0109231].
2. L. Lönnblad, *JHEP* **05** (2002) 046, [hep-ph/0112284].
3. S. Alioli, C. W. Bauer, C. Berggren, A. Hornig, F. J. Tackmann, C. K. Vermilion, J. R. Walsh and S. Zuberi, [arXiv:1211.7049].
4. I. W. Stewart *et al.*, *Phys. Rev. Lett.* **105** (2010) 092002, [arXiv:1004.2489].
5. S. Hoeche *et al.* *JHEP* **1304** (2013) 027, [arXiv:1207.5030].
6. R. Frederix and S. Frixione, *JHEP* **1212** (2012) 061, [arXiv:1209.6215].
7. S. Alioli, K. Hamilton, and E. Re, *JHEP* **1109** (2011) 104, [arXiv:1108.0909].
8. S. Platzer, arXiv:1211.5467.
9. L. Lönnblad and S. Prestel, *JHEP* **1303** (2013) 166 [arXiv:1211.7278].
10. K. Hamilton, P. Nason, C. Oleari and G. Zanderighi, [arXiv:1212.4504].
11. T. Sjöstrand, S. Mrenna, and P. Skands, *JHEP* **05** (2006) 026, [hep-ph/0603175].
12. R. Abbate *et al.*, *Phys. Rev. D* **83** (2011) 074021, [arXiv:1006.3080].
13. I. W. Stewart, F. J. Tackmann, and W. J. Waalewijn, *Phys. Rev. D* **81** (2010) 094035, [arXiv:0910.0467].

PHOTON PRODUCTION AT THE LHC

R. LAFAYE, On behalf of the ATLAS and CMS collaborations
Laboratoire d'Annecy-le-Vieux de Physique des Particules, 9 chemin de Bellevue 74941 Annecy-le-Vieux, France

We review the lastest results on photon production at the LHC by the ATLAS and CMS experiments obtained in proton-proton collisions with a center of mass energy of 7 TeV in 2010 and 2011, corresponding to a maximum integrated luminosity of 5 fb^{-1}. We compare the prompt photon and photon-jet differential cross sections to theoretical predictions and discuss their impact on the parton distribution functions of the proton. Di-photon differential cross sections are also presented as a function of the di-photon invariant mass, transverse momentum, azimuthal separation, and $\cos\theta^*$.

1 Introduction

Photon production measurements at hadron colliders allow precise tests of perturbative QCD predictions by providing a colorless probe of the hard scattering process [1]. Since the photon originates directly from the hard interaction and does not undergo hadronization the environment tends to be cleaner than for jet production. These measurements can help to probe the gluon content of the proton [2] as the prompt photon and photon-jet production is dominated by quark-gluon fusion. In addition, isolated prompt photon production is the main background to searches for new phenomena involving photons in the final state, most notably the Higgs boson production via the $H \to \gamma\gamma$ mechanism.

At the Large Hadron Collider [3] (LHC), a significant increase of center-of-mass energy with respect to previous collider experiments allows for the exploration of new kinematic regions in the hard scattering processes in hadron-hadron collisions. The photons considered in the analyses presented in this paper include all photons produced in p-p collisions, not originating from secondary hadron decays. Isolated prompt photons are produced mainly through qg Compton scattering, $q\bar{q}$ annihilation, and in the fragmentation of partons with large transverse momentum. For di-photons the production is dominated by the $q\bar{q}$ annihilation, the gg fusion and the fragmentation of partons in association with a prompt photon.

Both the ATLAS[4] and CMS[5] Collaborations have performed measurements of the differential cross section of isolated prompt photon, photon-jet and di-photon production with data collected in 2010 and 2011. In this article we present the latest results from both experiments and compare them with theoretical predictions from fixed order calculations and parton shower simulations.

2 Photon reconstruction and signal extraction

The photon energy and position are reconstructed from the clusters in the electromagnetic calorimeter. In the case of converted photons, clusters can then be associated to one or two tracks. After cluster reconstruction, the main background comes from the decay of neutral

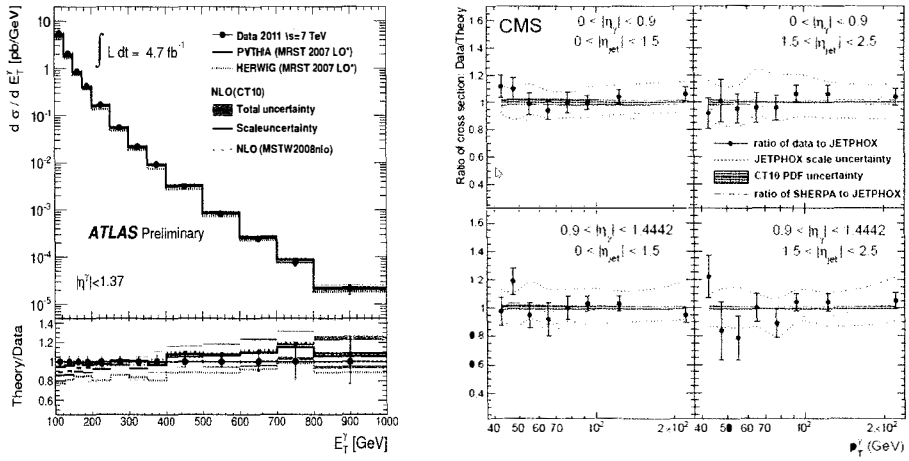

Figure 1: **Left:** Measured (dots with error bars) and expected inclusive prompt photon cross section in the ATLAS barrel η region [10]. The inner error bars on the data points show statistical uncertainties, while the full error bars show statistical and systematic uncertainties added in quadrature. The next to leading order theory prediction is shown as a shaded band which indicates theoretical uncertainties, while the leading order parton shower Monte Carlo generators are shown as lines. **Right:** The ratios of the photon-jet triple-differential cross section to the NLO QCD prediction using JETPHOX with the CT10 PDF set and scales, as measured by CMS [16] with 2.14 fb^{-1}. Errors show the statistical and systematic uncertainties added in quadrature. The two dotted lines represent the effect of varying the theoretical scales. The shaded region is the CT10 PDF uncertainty. The dash-dotted lines show the ratios of the SHERPA predictions to JETPHOX.

hadrons, such as π^0 mesons, into nearly collinear pairs of photons. This jet background contamination can be estimated using discriminating criteria, such as the profile of the electromagnetic shower (identification) and the amount of energy surrounding the photon candidate (isolation).

For photon identification, ATLAS defines shower profile variables in the different layers of its calorimeters while CMS uses a topological fit of the cluster shape. Photons are considered isolated if the extra transverse energy within a cone of radius $\Delta R = 0.4$ in $\eta \times \phi$ (η is the pseudorapidity along the z axis and ϕ is the azimuthal angle) centered around the photon, is lower than typically a few GeV.

The signal is then extracted using a sideband technique in the identification-isolation plane or with a template fit of the isolation profile. In both cases, efficiencies and profiles are taken from Monte Carlo generators for the photon signal and extracted using data-driven approaches for the jet background.

3 Isolated prompt photon production

The production cross section of isolated prompt photons is measured as a function of the transverse energy of the photon (E_T). ATLAS measurements in 2010, with 0.88 pb^{-1}, start as low as 10 GeV,[6] while ATLAS and CMS results, with 35 pb^{-1}, use 50 and 25 GeV cuts, respectively, due to the single photon trigger thresholds [8,7]. The most recent results from ATLAS cover the kinematic range $100 \leq E_T^\gamma \leq 1000$ GeV and uses the 2011 data set, corresponding to an integrated luminosity of 4.71 fb^{-1}.

ATLAS and CMS results have been compared to next-to-leading order (NLO) calculations from JETPHOX [11] and to parton shower Monte Carlo generator predictions from PYTHIA [12] and HERWIG,[13] see figure 1 left. The highest disagreements are at low E_T values, while above

100 GeV the data is systematically higher than the predictions. At very high E_T (above 700 GeV) the prediction uncertainties are dominated by the poorly determined gluon density.

4 Isolated photon plus jet production

The differential cross sections for isolated photons in association with jets are measured as functions of the photon transverse energy in different regions of rapidity of the photon (and of the leading jet for the CMS study). The chosen regions differ by the accessible x values and the amount of the fragmentation component. ATLAS performed this measurement using 35 pb^{-1} from the 2010 data set [14]. While newer CMS results use 2.14 fb^{-1} from the 2011 data set [16], see right plot of figure 1. Recently ATLAS extended the study by measuring also cross sections in terms of other kinematic properties of the photon-jet system [15]: the leading-jet transverse momentum and rapidity, the difference in azimuthal angle between the photon and the jet, the photon-jet invariant mass and the cosine of the longitudinal angle difference.

The obtained distributions have been compared to JETPHOX, PYTHIA and SHERPA [17] predictions, and using different PDFs. The worst agreement is found for high jet rapidities but still within uncertainties. The ATLAS 2010 results use a low trigger threshold allowing to scan the E_T range down to 25 GeV. In this low E_T region, as in the single photon studies, JETPHOX overestimates the data.

5 Isolated di-photon production

The differential cross section of di-photon production was measured as a function of four kinematic variables: the invariant mass and transverse momentum of the di-photon system, the azimuthal separation between the two photons, and $\cos\theta^*$. The first one is of obvious interest for resonance searches, while the second and the third provide important information in the study of higher order QCD perturbation and fragmentation. ATLAS defines $\cos\theta^*$ as the cosine of the polar angle of the highest transverse momentum photon in the Collins-Soper di-photon rest frame [18]. CMS makes use of the rapidity difference: $\cos\theta^* = \tanh|\Delta y_{\gamma\gamma}|/2$. Both definitions are useful to investigate the spin of di-photon resonances.

The analyzed data set used by CMS consists of the 7 TeV p-p collisions recorded in the year 2010,[19] for an integrated luminosity of 36 pb^{-1}. ATLAS recently updated their results [20] with the data sample collected in 2011, corresponding to 4.9 fb^{-1} of integrated luminosity. The signal extraction method is the same as for single photon analyzes, extended to two photons. The largest background comes from jets decaying into neutral hadrons and is estimated as in the single photon analyses. The second main background comes from Drell-Yan events and is subtracted using electron to photon fake rates extracted from $Z \to ee$ and $Z \to ee\gamma$ events for the 2011 analysis. For the 2010 analysis where the statistics is too low, Monte Carlo simulated events are used.

The differential distribution obtained are compared to fixed order calculations from DIPHOX[21] and 2γNNLO,[22] and parton shower Monte Carlo generators PYTHIA and SHERPA, see figure 2. The Monte Carlo generators are rescaled to correspond to the measured integrated cross section, and are in good agreement. Except for large $\cos\theta^*$ values where all predictions tend to underestimate the data. At low E_T (and $\Delta\phi \simeq \pi$) the fixed-order calculations do not reproduce the data, due to the known infrared divergences from initial-state soft gluon radiation. Everywhere else DIPHOX is missing NNLO contributions and clearly underestimates the data. Thanks to the inclusion of NNLO terms, 2γNNLO is able to match the data very closely within the uncertainties, except in limited regions where the neglected fragmentation component is still significant after photon isolation requirements.

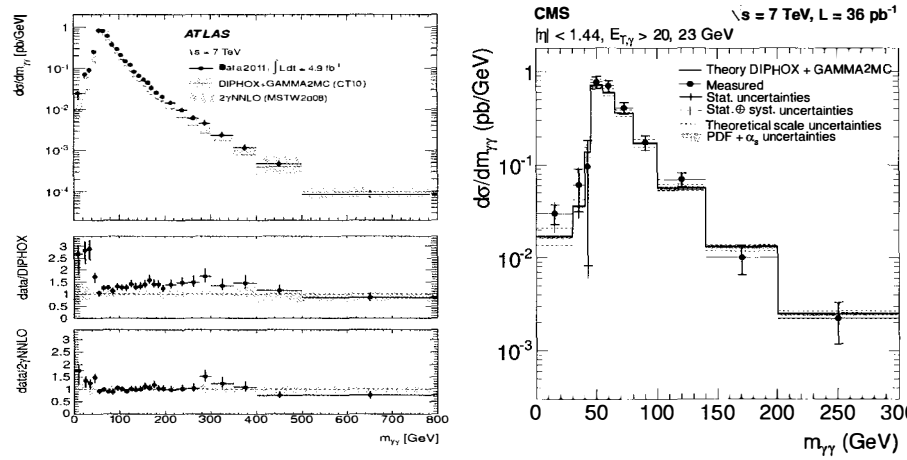

Figure 2: **Left:** Comparison between the ATLAS experimental cross sections and the predictions obtained with DIPHOX+GAMMA2MC (NLO) and 2gNNLO (NNLO) for the di-photon invariant mass [20]. The black dots correspond to data with with error bars for their total uncertainties, which are dominated by the systematic component. The theoretical uncertainties include contributions from the limited size of the simulated sample, from the renormalization and factorization scales choice and from uncertainties on the parton distribution functions and on the hadronization and underlying event corrections. **Right:** Measured cross section of di-photon production as a function of the invariant mass of the photon pair for photons within the pseudorapidity region $|\eta| < 1.44$, as seen by CMS [19]. The inner and outer error bars on each point show the statistical and total experimental uncertainties. The 4% uncertainty on the integrated luminosity is not included in the error bars. The dotted line and shaded region represent the systematic uncertainties on the theoretical prediction from the theoretical scales and the PDFs, respectively.

6 Constraining parton distribution functions with photon measurements

Precise determination of the parton distribution functions (PDFs) of the proton is an essential input for phenomenological analyzes at the LHC. These PDFs are constrained using Deep Inelastic Scattering, jet production, Drell-Yan and W, Z production data. Photon data is usually not included, as large discrepancies between data and theories at fixed-target energies, greatly reduced their impact.

However, photon data is particularly sensitive to the gluon density, which is involved in a large fraction of the scattering processes at the LHC. As a matter of fact, gluon-gluon fusion is the dominant channel for the production of the SM Higgs boson, top-quark pairs or dijets, to mention a few. Recent studies [23] have shown that in the new energy range reached by the LHC, the isolated-photon theoretical prediction uncertainties are dominated by renormalization and factorization scales, away from non-perturbative effects due to the collinear fragmentation of final-state partons.

The impact of the available ATLAS and CMS photon and photon-jet measurements on the gluon density, was quantified in recent studies [24,25] using NLO theoretical calculations from the JETPHOX program combined with the NNPDF2.1 parton densities. The central value of the gluon distribution itself is unmodified but its uncertainty could be reduced by up to 20 % around $x \simeq 0.02$. This lead to an uncertainty reduction of up to 20% for low mass Higgs production in the gluon-fusion channel.

7 Conclusion

ATLAS and CMS performed isolated-photon studies using the p-p collision data collected in 2010 and 2011. Both experiments have shown good agreement with theoretical calculations. Furthermore, the available isolated-photon data could also provide constraints on the gluon PDFs and thus on many relevant LHC processes, most importantly Higgs production in gluon-gluon fusion.

References

1. P. Aurenche, R. Baier, M. Fontannaz, and D. Schiff, *Nucl. Phys.* B **297** (1988) 661.
2. P. Aurenche et al., *Phys. Rev.* D **39** (1989) 3275.
3. L. Evans and P. Bryant (editors) 2008 *JINST* **3** S08001.
4. ATLAS Collaboration, 2008 *JINST* **3** S08003.
5. CMS Collaboration, 2008 *JINST* **3** S08004.
6. ATLAS Collaboration, *Phys. Rev.* D **83**, (2011) 052005.
7. CMS Collaboration, *Phys. Rev.* D **84** (2011) 052011.
8. ATLAS Collaboration, *Phys. Lett.* B **706** (2011) 150.
9. ATLAS Collaboration, ATL-PHYS-PUB-2011-013, http://cds.cern.ch/record/1395049.
10. ATLAS Collaboration, ATLAS-CONF-2013-022, http://cds.cern.ch/record/1525723.
11. S. Catani, M. Fontannaz, J. Ph. Guillet and E. Pilon, *JHEP* **05** (2002) 028
12. T. Sjöstrand, S. Mrenna, and P. Z. Skands, *JHEP 05* (2006) 026.
13. G. Corcella et al., *JHEP* **01** (2001) 010.
14. ATLAS Collaboration, *Phys. Rev.* D **85**, (2012) 092014.
15. ATLAS Collaboration, ATLAS-CONF-2013-023, http://cds.cern.ch/record/1525728.
16. CMS Collaboration, CMS-PAS-QCD-11-005, http://cds.cern.ch/record/1525534.
17. T. Gleisberg et al., *J. High Energy Phys.* **02** (2009) 007.
18. J. C. Collins and D. E. Soper, *Phys. Rev.* D **16**, (1977)2219 .
19. CMS Collaboration, *JHEP* **01** (2012) 133.
20. ATLAS Collaboration, *JHEP* **01** (2013) 086.
21. T. Binoth, J. Guillet, E. Pilon and M. Werlen, *Eur. Phys. J.* C **16** (2000) 311.
22. S. Catani et al., *Phys. Rev. Lett.* **108** *(2012) 072001.*
23. *R. Ichou and D. d'Enterria,* Phys. Rev. *D* **82** *(2010) 014015.*
24. *D. d'Enterria and J. Rojo,* Nucl. Phys. *B* **860** *(2012) 311-338.*
25. *L. Carminati et al.*, Europhysics Letters **101** *61002 (2012).*

QCD in 2D Flux Tube

A.V. KOSHELKIN
Moscow Institute for Physics and Engineering,
Kashirskoye shosse,31, 115409 Moscow, Russia

C.-Y.WONG
Physics Division, Oak Ridge National Laboratory,
Oak Ridge, TN 37831, USA

We show from the action integral that under the assumption of longitudinal dominance and transverse confinement, QCD_4 in (3+1) dimensional space-time can be approximately compactified into QCD_2 in (1+1) dimensional space-time. In such a process, the relation between the coupling constant g_{2D} in QCD_2 and the coupling constant g_{4D} in QCD_4 is derived. The quark and gluon masses acquired in the compactification are obtained. They depend crucially on the excitation of the partons in the transverse degrees of freedom.

1 Introduction

Previously, t'Hooft showed that in the limit of large N_c with fixed g^2N_c in single-flavor quantum chromodynamics in (3+1) dimensional space-time (QCD_4), planar diagrams with quarks at the edges dominate, whereas diagrams with the topology of a fermion loop or a wormhole are associated with suppressing factors of $1/N_c$ and $1/N_c^2$, respectively[1]. In this case a simple-minded perturbation expansion with respect to the coupling constant g cannot describe the spectrum, while the $1/N_c$ expansion may be a reasonable concept, in spite of the fact that N_c is equal to 3 and is not very big. The dominance of the planar diagrams allows one to consider QCD in one space and one time dimensions (QCD_2) and the physics resembles those of the dual string or a flux tube, with the physical spectrum of a straight Regge trajectory[2]. The properties of QCD in two-dimensional space-time have been investigated by many workers[1,2,3]. The flux tube picture of longitudinal dynamics manifests itself in various aspects of hadron spectroscopy[4].

In the high-energy arena, the flux tube picture finds phenomenological applications in hadron collisions and high-energy e^-e^+ annihilations[5,6,7,8,9]. In these high-energy processes, the (average) transverse hadron momenta of produced hadrons are observed to be limited, as appropriate for particles confined in a flux tube. The idealization of the three-dimensional flux tube as a one-dimensional string leads to the string fragmentation picture of particle production in (1+1) space-time dimensions. The particle production description of Casher, Kogut, and Susskind[5] in (1+1) dimensional Abelian gauge theory led to results that mimics the dynamics of particle production in hadron collisions and in the annihilation of e^+e^- pairs at high energies. Furthermore, the Lund model of classical string fragmentation has been quite successful in describing quantitatively the process of particle production in these high energy processes[6,7,8,9].

With the successes of lower-dimensional descriptions of high-energy collision processes in QCD, we would like to examine the circumstances in high-energy processes under which QCD_4 in (3+1) dimensions can be compactified into QCD_2 in (1+1) dimensions, if one starts with

the QCD_4 action integral. In such a process, we will be able to find out how quantities in the compactified QCD_2 can be related to quantities in QCD_4. The success of the compactification program will facilitate the examination of some problems in QCD_4 in the simpler dynamics of QCD_2.

2 $4D \to 2D$ Compactification in the Action Integral

The $4D$-action $\mathcal{A}$ resides in (3+1) dimensional space-time. There are however environments which allow the compactification of the $4D$ action to reside in two-dimensional (1+1) space-time, within which the dynamics can be greatly simplified.

We note that in hadron collisions and e^-e^+ annihilations at high energies, the string fragmentation process occurs when a valence quark pulls apart from a valence antiquark longitudinally at high energies. It is therefore reasonable to conceive that the QCD_4 compactification can take place under the dominance of longitudinal dynamics, not only of the leading valence quark and antiquark pair, but also the produced $q\bar{q}$ parton pairs. In the Lorentz gauge, as A_ν is proportional to the current j_ν, the gauge field components A_1^a and A_2^a along the transverse direction are then small in magnitude in comparison with those of A_0^a and A_3^a and can be neglected. The absence of the transverse gauge fields provides a needed simplification for compactification.

The spatially one-dimensional string being an idealization of a more realistic three-dimensional flux-tube, the description of produced $q\bar{q}$ parton pairs within the string presumes the confinement of these produced partons inside the string. Hence, it is reasonable to conceive further that the QCD_4 compactification takes place under transverse confinement. We can describe transverse confinement in terms of a confining scalar interaction $S(\mathbf{r}_\perp)$ and the quark mass function is then $m(\mathbf{r}_\perp) = m_0 + S(\mathbf{r}_\perp)$, where m_0 is the quark rest mass.

Therefore, under the assumption of longitudinal dominance and transverse confinement, the SU(N) gauge invariant action integral in (3+1) Minkowski space-time is given by [10]:

$$\mathcal{A} = \int d^4x \left\{ Tr\left[\bar{\Psi}(x)\left(\gamma^\mu_{4D}(i\partial_\mu + g_{4D}\ T_a A^a_\mu(x)) \ - \ m(\mathbf{r}_\perp)\right)\ \Psi(x)\right] - \frac{1}{4}F^a_{\mu\nu}(x)\ F^{\mu\nu}_a(x)\right\}, \quad (1)$$

$$F^a_{\mu\nu}(x) \ = \ \partial_\mu A^a_\nu(x) - \partial_\nu A^a_\mu(x) + g_{4D}\ f^a_{bc}\ A^b_\mu(x)\ A^c_\nu(x), \quad (2)$$

where $A^a_\mu(x)$ and $\Psi(x)$ are gauge and fermion fields respectively with coordinates $x \equiv x^\mu = (x^0, \mathbf{x}) = (x^0, x^1, x^2, x^3)$ and transverse coordinates $\mathbf{r}_\perp = (x^1, x^2)$, g_{4D} is the coupling constant, γ^ν_{4D} are the stanadard Dirac matrices, and T_a are the generators of the SU(N) group.

2.1 Fermion part of the action integral

We first examine $\mathcal{A}_F$, the fermion part of the $4D$ action integral in Eq. (1) that involves the fermion field. To carry out the compactification, we write the Dirac fermion field $\Psi(x)$ in terms of functions $G_\pm(\vec{r}_\perp)$ and $f_\pm(x^0, x^3)$ [7]:

$$\Psi(x) = \frac{1}{\sqrt{2}} \begin{pmatrix} G_1(\mathbf{r}_\perp)\,(f_+(x^0;x^3) + f_-(x^0;x^3)) \\ -G_2(\mathbf{r}_\perp)\,(f_+(x^0;x^3) - f_-(x^0;x^3)) \\ G_1(\mathbf{r}_\perp)\,(f_+(x^0;x^3) - f_-(x^0;x^3)) \\ G_2(\mathbf{r}_\perp)\,(f_+(x^0;x^3) + f_-(x^0;x^3)) \end{pmatrix}. \quad (3)$$

Using this explicit form of the Dirac fermion field $\Psi(x)$, we carry out the simplifications and integrations over x^1 and x^2 that eventually lead from $\mathcal{A}_F$ to $\mathcal{A}_F(2D)$,

$$\mathcal{A}_F(2D) = Tr \int d^2X \bar{\Psi}(X)\left[\left(i\gamma^\mu\partial_\mu + g_{2D}\gamma^\mu T_a A^a_\mu(X)\right) - m_{qT}\right]\Psi(X), \quad (4)$$

where $\mu = 0, 3$, and we have introduced the Dirac fermion field $\Psi(X)$, γ-matrices, and metric tensor $g_{\mu\nu}$, according to the following specifications in (1+1)-dimensional space-time in QCD_2,

$$\Psi(X) = \begin{pmatrix} f_+(X) \\ f_-(X) \end{pmatrix}, \qquad X = (x^0, x^3), \tag{5}$$

$$\gamma^0 = \begin{pmatrix} 1 & 0 \\ 0 & -1 \end{pmatrix}, \quad \gamma^3 = \begin{pmatrix} 0 & 1 \\ -1 & 0 \end{pmatrix}, \quad g_{\mu\nu} = \begin{pmatrix} 1 & 0 \\ 0 & -1 \end{pmatrix}. \tag{6}$$

The $2D$ coupling constant g_{2D} is related to $4D$ coupling constant g_{4D} by

$$g_{2D} = \int dx^1 dx^2 g_{4D}[|G_1(\mathbf{r}_\perp)|^2 + |G_2(\mathbf{r}_\perp)|^2]^{3/2}, \tag{7}$$

where the transverse wave functions $G_{1,2}(\mathbf{r}_\perp)$ are normalized according to

$$\int dx^1 dx^2 \left(|G_1(\mathbf{r}_\perp)|^2 + |G_2(\mathbf{r}_\perp)|^2\right) = 1. \tag{8}$$

The transverse quark mass m_{qT} in Eq. (4) is given by

$$m_{qT} = \int dx^1 dx^2 \left\{ m(\mathbf{r}_\perp) \left(|G_1(\mathbf{r}_\perp)|^2 - |G_2(\mathbf{r}_\perp)|^2\right) + [(G_1^*(\mathbf{r}_\perp)(p_1 - ip_2)G_2(\mathbf{r}_\perp)) - h.c.] \right\}. \tag{9}$$

In obtaining these results, we have considered $2D$ gauge fields $A^a_\mu(2D, x^0, x^3) \equiv A^a_\mu(2D) \equiv A^a_\mu(X)$ related to the $4D$-field gauge fields $A^a_\mu(x^0, x^3, \mathbf{r}_\perp)$ by

$$A^a_\mu(x^0, x^3, \mathbf{r}_\perp) = \sqrt{|G_1(\mathbf{r}_\perp)|^2 + |G_2(\mathbf{r}_\perp)|^2} A^a_\mu(X), \quad \mu = 0, 3. \tag{10}$$

The above equation means that along with the confinement of the fermions, for which the wave function $G_{1,2}(\mathbf{r}_\perp)$ is confined within a finite region of transverse coordinates $\mathbf{r}_\perp$, we also consider the confinement of the gauge field $A^a_\mu(X)$, $\mu = 0, 3$, within the same finite region of transverse coordinates, as in the case for a flux tube.

The result of Eq. (7) reveals that as a result of the compactification of QCD_4, the coupling constant $g(2D)$ in lower dimensional space in QCD_2 acquires the dimension of a mass, and is related to the confining wave functions of the fermions. Fermions in different excited states inside the tube will have different coupling constants as indicated in Eq. (7). The effective quark mass m_{qT} also depends on the transverse fermion wave functions, as indicated in Eq. (9). In the lower two-dimensional space-time, fermions in excited transverse states have a quark mass different from those in the ground transverse states.

2.2 Gauge field part of the action integral

To go from $\mathcal{A}_F$ to $\mathcal{A}_F(2D)$ we have assumed that the currents in the x^0 and x^3 directions are much larger in magnitude than the currents in the transverse directions so that A^a_1 and A^a_2 are small in comparison and can be neglected. As a consequence, $F_{12} = 0$ (we omit the superscript symbol a (color) for simplicity). The evaluation of all other components of $F_{\mu\nu}$ give for the gauge field part of the action integral

$$\begin{aligned} \int \frac{d^4x}{4} \quad F^a_{\mu\nu} F^{\mu\nu}_a &= \int \frac{dx^0 dx^3}{4} \int dx^1 dx^2 (|G_1(\mathbf{r}_\perp)|^2 + |G_2(\mathbf{r}_\perp)|^2) F^a_{03}(2D) F^{03}_a(2D) \\ &- \int \frac{dx^0 dx^3}{4} \int dx^1 dx^2 \Big(\{\partial_1 [|G_1(\mathbf{r}_\perp)|^2 + |G_2(\mathbf{r}_\perp)|^2]^{1/2}\}^2 + \{\partial_2 [|G_1(\mathbf{r}_\perp)|^2 + |G_2(\mathbf{r}_\perp)|^2]^{1/2}\}^2 \Big) \\ &\times [A_0(2D, x^0, x^3) A^0(2D, x^0, x^3) + A_3(2D, x^0, x^3) A^3(2D, x^0, x^3)]. \end{aligned} \tag{11}$$

It is useful to introduce the gluon mass m_{gT} that arises from the confinement of the gluons in the transverse direction,

$$m_{gT}^2 = \frac{1}{2}\int dx^1 dx^2 \left[\left\{\partial_1\left(\sum_{i=1}^{2}|G_i(\mathbf{r}_\perp)|^2\right)^{1/2}\right\}^2 + \left\{\partial_2\left(\sum_{i=1}^{2}|G_i(\mathbf{r}_\perp)|^2\right)^{1/2}\right\}^2\right]. \quad (12)$$

As this gluon mass m_{gT} arises from the confinement compactification of the gluon within the flux tube, we can call such a mass the compactification mass of the gluon. Equation (11) becomes

$$\int \frac{d^4x}{4} F_{\mu\nu}^a(4D)\ F_a^{\mu\nu}(4D) \quad = \quad \int \frac{dx^0 dx^3}{4}\left\{F_{03}^a(2D)F_a^{03}(2D) - 2m_{gT}^2[A_\mu^a(X)A_a^\mu(X)]\right\} \quad (13)$$

We collect all the fermion and gauge field parts of the action integral in $\mathcal{A}(4D)$ in Eq. (1). All terms in the action integral $\mathcal{A}(4D)$ (including matrices and coefficients) are in the Minkowski $(1+1)$ dimensional space-time. We can rename the action integral $\mathcal{A}(4D)$ to be $\mathcal{A}(2D)$ given explicitly by[11]

$$\mathcal{A}(2D) = \int d^2X \quad \left\{Tr\left[\bar{\Psi}(X)\left[\gamma^k\left(i\partial_\mu + g_{2D}\ T_a A_\mu^a(X)\right) - m_{qT}\right]\Psi(X)\right.\right.$$
$$\left.\left. -\frac{1}{4}F_{\mu\nu}^a(2D)\ F_a^{\mu\nu}(2D) + \frac{1}{2}m_{gT}^2[A_a^\mu(X)A_\mu^a(X)]\right\}. \quad (14)$$

Thus, in the presence of longitudinal dominance and transverse confinement, we succeed in compactifying the action integral from $\mathcal{A}(4D)$ in QCD_4 to $\mathcal{A}(2D)$ in QCD_2, by introducing g_{2D}, m_{qT}, and m_{gT} that contain information about the transverse profile. All the transverse flux tube information is subsumed under these quantities. In this way, the $2D$ gauge field appears to be massive where m_{gT} and m_{gT} arise as a consequence of the transverse confining motion of both fermion and gauge fields. The physical explanation of such effect consists in the decrease of the number of trajectories in moving from one point of the space to another point, as a direct consequence of compactification. Such constraints in movement manifest themselves as masses of field particles. The magnitudes of m_{qT} and m_{gT} depend strongly on the kind of the compactification that is dictated by the transverse functions $G_1(\mathbf{r}_\perp)$ and $G_2(\mathbf{r}_\perp)$ (see Eqs.(9) and (12)).

Acknowledgment

The research was supported in part by the Division of Nuclear Physics, U.S. Department of Energy.

References

1. G. t'Hooft, Nucl. Phys. B**72**, 461 (1974).
2. G. t'Hooft, Nucl. Phys. B**75**, 461 (1974).
3. Y. Frishman and J. Sonnenschein, Phys. Rep. **223**, 309 (1993).
4. N. Isgur and J. Paton, Phys. Rev. D**31**, 2910 (1985).
5. A. Casher, J. Kogut, and L. Susskind, Phys. Rev. **D10**, 732 (1974).
6. B. Andersson, G. Gustafson, and T. Sjöstrand, Zeit. für Phys. **C20**, 317 (1983).
7. C. Y. Wong, R. C. Wang, and C. C. Shih, Phys. Rev. **D44**, 257 (1991).
8. C. Y. Wong, *Introduction to High-Energy Heavy-Ion Collisions*, World Scientific Publisher, 1994.
9. C. Y. Wong, Phys. Rev. **C80**, 054917 (2009).
10. M. E. Peskin, D. V. Schroeder, *An introduction to Quantum Field Theory*, Addison-Wesley Publishing Company, 1995.
11. A.V.Koshelkin, C.Y.Wong, Phys. Rev. **D86**, 125026 (2012).

ASYMPTOTIC HIGH-ENERGY BEHAVIOR OF HADRONIC TOTAL CROSS SECTIONS FROM LATTICE QCD

ENRICO MEGGIOLARO[a], MATTEO GIORDANO[b], NICCOLÒ MORETTI[c]
[a] *Dipartimento di Fisica, Università di Pisa, and INFN, Sezione di Pisa, Largo Pontecorvo 3, I-56127 Pisa, Italy*
[b] *Institute of Nuclear Research of the Hungarian Academy of Sciences (ATOMKI), Bem tér 18/c, H-4026 Debrecen, Hungary*
[c] *Institut für Theoretische Physik, Universität Zürich, 8057 Zürich, Switzerland*

We will show how a *universal* and *Froissart-like* (i.e., of the kind $B \log^2 s$) hadron-hadron total cross section can emerge in QCD asymptotically at high energy, finding indications for this behavior from the lattice. The functional integral approach provides the "natural" setting for achieving this result, since it encodes the energy dependence of hadronic scattering amplitudes in a single *elementary* object, i.e., a proper correlation function of two Wilson loops.

1 Introduction

Present-day experimental observations (up to a center-of-mass total energy $\sqrt{s} = 7$ TeV, reached at the LHC pp collider [1]) seem to support the following asymptotic high-energy behavior of hadronic total cross sections: $\sigma_{\text{tot}}^{(hh)}(s) \sim B \log^2 s$, with a *universal* (i.e., *not* depending on the particular hadrons involved) coefficient $B \simeq 0.3$ mb. [2] This behavior is consistent with the well-known *Froissart-Lukaszuk-Martin* (FLM) *theorem* [3], according to which, for $s \to \infty$, $\sigma_{\text{tot}}^{(hh)}(s) \leq (\pi/m_\pi^2) \log^2(s/s_0)$, where m_π is the pion mass and s_0 is an unspecified squared mass scale. As we believe QCD to be the fundamental theory of strong interactions, we also expect that it correctly predicts from first principles the behavior of hadronic total cross sections. However, in spite of all the efforts, a satisfactory solution to this problem is still lacking. (For some theoretical supports to the universality of B, see Ref. [4] and references therein.)

This problem is part of the more general problem of high-energy elastic scattering at low transferred momentum, the so-called *soft high-energy scattering*. As *soft* high-energy processes possess two different energy scales, the total center-of-mass energy squared s and the transferred momentum squared t, smaller than the typical energy scale of strong interactions ($|t| \lesssim 1$ GeV$^2 \ll s$), we cannot fully rely on perturbation theory (PT). A nonperturbative (NP) functional-integral approach in the framework of QCD has been proposed in Ref. [5] and further developed in Ref. [6] In this approach, for example, the elastic scattering amplitude $\mathcal{M}_{(hh)}$ of two *mesons*, of the same mass m for simplicity, can be reconstructed from the scattering amplitude $\mathcal{M}_{(dd)}$ of two dipoles of fixed transverse sizes $\vec{r}_{1,2\perp}$, and fixed longitudinal-momentum fractions $f_{1,2}$ of the quarks in the two dipoles, after folding with squared wave functions $\rho_{1,2} = |\psi_{1,2}|^2$ describing the interacting hadrons, [6]

$$\mathcal{M}_{(hh)}(s,t) = \int d^2\nu \; \rho_1(\nu_1)\rho_2(\nu_2)\mathcal{M}_{(dd)}(s,t;\nu_1,\nu_2) \equiv \langle\langle \mathcal{M}_{(dd)}(s,t;1,2)\rangle\rangle, \tag{1}$$

where $\nu_i = (\vec{r}_{i\perp}, f_i)$ denotes collectively the dipole variables, $d^2\nu = d\nu_1 d\nu_2$, $\int d\nu_i = \int d^2\vec{r}_{i\perp} \int_0^1 df_i$, and $\int d\nu_i \; \rho_i(\nu_i) = 1$. In turn, the dipole-dipole (dd) scattering amplitude is obtained from the

(properly normalized) correlation function (CF) of two Wilson loops (WL) in the fundamental representation, defined in Minkowski spacetime, running along the paths made up of the quark and antiquark classical straight-line trajectories, and thus forming a hyperbolic angle $\chi \simeq \log(s/m^2)$ in the longitudinal plane. The paths are cut at proper times $\pm T$ as an infrared regularization, and closed by straight-line "links" in the transverse plane, in order to ensure gauge invariance; eventually, $T \to \infty$. It has been shown in Refs.[7,8,9] that the relevant Minkowskian CF $\mathcal{G}_M(\chi; T; \vec{z}_\perp; \nu_1, \nu_2)$ ($\vec{z}_\perp$ being the *impact parameter*, i.e., the transverse separation between the two dipoles) can be reconstructed, by means of *analytic continuation*, from the Euclidean CF of two Euclidean WL, $\mathcal{G}_E(\theta; T; \vec{z}_\perp; \nu_1, \nu_2) \equiv \langle \mathcal{W}_1^{(T)} \mathcal{W}_2^{(T)} \rangle / (\langle \mathcal{W}_1^{(T)} \rangle \langle \mathcal{W}_2^{(T)} \rangle) - 1$, where $\langle \ldots \rangle$ is the average in the sense of the Euclidean QCD functional integral. The Euclidean WL $\mathcal{W}_{1,2}^{(T)} = N_c^{-1} \mathrm{Tr}\{T \exp[-ig \oint_{\mathcal{C}_{1,2}} A_\mu(x) dx_\mu]\}$ are calculated on the following quark [q]-antiquark [$\bar{q}$] straight-line paths, $\mathcal{C}_i : X_i^{q[\bar{q}]}(\tau) = z_i + \frac{p_i}{m}\tau + f_i^{q[\bar{q}]} r_i$, with $\tau \in [-T, T]$, and closed by straight-line paths in the transverse plane at $\tau = \pm T$. Here $p_{1,2} = m(\pm \sin\frac{\theta}{2}, \vec{0}_\perp, \cos\frac{\theta}{2})$, θ being the angle formed by the two Euclidean trajectories (i.e., $p_1 \cdot p_2 = m^2 \cos\theta$), $r_i = (0, \vec{r}_{i\perp}, 0)$, $z_i = \delta_{i1}(0, \vec{z}_\perp, 0)$ and $f_i^q \equiv 1 - f_i$, $f_i^{\bar{q}} \equiv -f_i$. We define also the CFs with the infrared cutoff removed as $\mathcal{C}_{E,M} \equiv \lim_{T\to\infty} \mathcal{G}_{E,M}$. The dd scattering amplitude is then obtained from $\mathcal{C}_E(\theta; \ldots)$ [with $\theta \in (0, \pi)$] by means of analytic continuation as ($t = -|\vec{q}_\perp|^2$)

$$\begin{aligned} \mathcal{M}_{(dd)}(s, t; \nu_1, \nu_2) &\equiv -i\, 2s \int d^2\vec{z}_\perp e^{i\vec{q}_\perp \cdot \vec{z}_\perp} \mathcal{C}_M(\chi; \vec{z}_\perp; \nu_1, \nu_2) \\ &= -i\, 2s \int d^2\vec{z}_\perp e^{i\vec{q}_\perp \cdot \vec{z}_\perp} \mathcal{C}_E(\theta \to -i\chi; \vec{z}_\perp; \nu_1, \nu_2). \end{aligned} \tag{2}$$

In Refs.[10,11] the CF $\mathcal{C}_E$ were calculated in *quenched* QCD by Monte Carlo simulations in *Lattice Gauge Theory* (LGT), at lattice spacing $a(\beta = 6) \simeq 0.1\,\mathrm{fm}$, on a 16^4 hypercubic lattice, using loops of transverse size a at angles $\cot\theta = 0, \pm\frac{1}{2}, \pm 1, \pm 2$ and transverse distances $d \equiv |\vec{z}_\perp|/a = 0, 1, 2$. The longitudinal-momentum fractions were set to $f_{1,2} = \frac{1}{2}$ without loss of generality[11] and different configurations in the transverse plane were studied, including the one relevant to meson-meson scattering, that is the *average* over the transverse orientations ("*ave*").

Numerical simulations of LGT provide (within the errors) the true QCD expectation for $\mathcal{C}_E$; approximate analytical calculations of $\mathcal{C}_E$ have then to be compared with the lattice data, in order to test the goodness of the approximations involved. $\mathcal{C}_E$ has been evaluated in the *Stochastic Vacuum Model* (SVM),[12] $\mathcal{C}_E^{(\mathrm{SVM})} = \frac{2}{3} e^{-\frac{1}{3} K_S \cot\theta} + \frac{1}{3} e^{\frac{2}{3} K_S \cot\theta} - 1$, in PT,[8,12,13] $\mathcal{C}_E^{(\mathrm{PT})} = K_p \cot^2\theta$, in the *Instanton Liquid Model* (ILM),[11,14] $\mathcal{C}_E^{(\mathrm{ILM})} = \frac{K_1}{\sin\theta}$, and, using the AdS/CFT correspondence, for planar, strongly coupled $\mathcal{N} = 4$ SYM at large $|\vec{z}_\perp|$,[15] $\mathcal{C}_E^{(\mathrm{AdS/CFT})} = e^{\frac{K_1}{\sin\theta} + K_2 \cot\theta + K_3 \cos\theta \cot\theta} - 1$. The coefficients $K_i = K_i(\vec{z}_\perp; \nu_1, \nu_2)$ are functions of $\vec{z}_\perp$ and of the dipole variables $\vec{r}_{i\perp}, f_i$. The comparison of the lattice data with these analytical calculations, performed in Ref.[10] by fitting the lattice data with the corresponding functional form, is not fully satisfactory, even though largely improved best fits have been obtained by combining the ILM and PT expressions into the expression $\mathcal{C}_E^{(\mathrm{ILMp})} = \frac{K_{\mathrm{Ip}1}}{\sin\theta} + K_{\mathrm{Ip}2} \cot^2\theta$. Regarding the energy dependence of total cross sections, the above analytical models are absolutely unsatisfactory, as they do not lead to *Froissart-like* total cross sections at high energy, as experimental data seem to suggest. Infact, the SVM, PT, ILM and ILMp parameterizations lead to asymptotically constant $\sigma_{\mathrm{tot}}^{(hh)}$, while the AdS/CFT result leads to power-like $\sigma_{\mathrm{tot}}^{(hh)}$.[16]

2 How a Froissart-like total cross section can be obtained

One is thus motivated to look for new parameterizations of the CF that: i) fit well the data; ii) satisfy the unitarity condition after analytic continuation; and iii) lead to total cross sections rising as $B \log^2 s$ in the high-energy limit.[17] Regarding unitarity, from (1) and (2) one recognizes that the quantity $A(s, |\vec{z}_\perp|) \equiv \langle\langle \mathcal{C}_M(\chi; \vec{z}_\perp; 1, 2) \rangle\rangle$ is the scattering amplitude in impact-parameter space, which must satisfy the *unitarity constraint* $|A + 1| \leq 1$.[18] Since $\int d\nu_i\, \rho_i(\nu_i) = 1$, this is the case if the following *sufficient* condition is satisfied: $|\mathcal{C}_M(\chi; \vec{z}_\perp; \nu_1, \nu_2) + 1| \leq 1$, $\forall \vec{z}_\perp$, ν_1, ν_2.

The conditions above constrain rather strongly the possible parameterizations. We shall *assume* that the Euclidean CF can be written as $\mathcal{C}_E = \exp K_E - 1$, where $K_E = K_E(\theta; \vec{z}_\perp; \nu_1, \nu_2)$ is a *real* function (since $\mathcal{C}_E$ is *real*[10]). This assumption is rather well justified: in the large-N_c expansion, $\mathcal{C}_E \sim \mathcal{O}(1/N_c^2)$, so that $\mathcal{C}_E + 1 \geq 0$ is certainly satisfied for large N_c; all the known analytical models satisfy it; the lattice data of Refs.[10,11] confirm it. The Minkowskian CF is then obtained after analytic continuation: $\mathcal{C}_M = \exp K_M - 1$, with $K_M(\chi; \ldots) = K_E(\theta \to -i\chi; \ldots)$. At large χ, $\mathcal{C}_M$ is expected to obey the above-mentioned unitarity condition, which in this case reduces to $\mathrm{Re}K_M \leq 0 \;\; \forall \vec{z}_\perp, \nu_1, \nu_2$.

For a *confining* theory like QCD, $\mathcal{C}_E$ is expected to decay exponentially as $\mathcal{C}_E \sim (\sum) e^{-\mu|\vec{z}_\perp|}$ at large $|\vec{z}_\perp|$, with mass scales μ related to the masses of particles (including, possibly, also *glueballs*[19]) exchanged between the two WL. Therefore, one also expects a similar large-$|\vec{z}_\perp|$ behavior for K_E, i.e., $K_E \sim (\sum) e^{-\mu|\vec{z}_\perp|}$. (Instead, for a non-confining, let's say *conformal*, field theory, different behaviors like powers of $1/|\vec{z}_\perp|$ are typical.[15,16])

Let us now assume that the leading term of the Minkowskian CF for $\chi \to +\infty$ is of the form $\mathcal{C}_M \sim \exp\left(i\,\beta\, f(\chi)\, e^{-\mu|\vec{z}_\perp|}\right) - 1$ (i.e., $K_M \sim i\,\beta\, f(\chi)\, e^{-\mu|\vec{z}_\perp|}$) where $\beta = \beta(\nu_1, \nu_2)$ is a function of the dipole variables and $f(\chi)$ is a *real* function such that $f(\chi) \to +\infty$ for $\chi \to +\infty$. In this case, the unitarity condition is equivalent (for large χ) to $\mathrm{Im}\beta \geq 0$. By virtue of the *optical theorem*, $\sigma_{\rm tot}^{(hh)}(s) \sim s^{-1}\mathrm{Im}\mathcal{M}_{(hh)}(s, t{=}0)$, we find $\sigma_{\rm tot}^{(hh)} \sim 4\pi\mu^{-2}\langle(\frac{1}{2}\log^2 f(\chi) + \log f(\chi)(\log|\beta| + \gamma) + \ldots)\rangle$. If one takes $f(\chi) = \chi^p e^{n\chi}$, the resulting asymptotic behavior of $\sigma_{\rm tot}^{(hh)}$ is [recall $\chi \simeq \log(s/m^2)$][17]

$$\sigma_{\rm tot}^{(hh)} \sim B \log^2 s, \qquad \text{with:} \qquad B = \tfrac{2\pi n^2}{\mu^2}. \tag{3}$$

We want to emphasize that the above result is *universal*, depending only on the mass scale μ, which sets the large-$|\vec{z}_\perp|$ dependence of the leading term of the CF, since the integration over the dipole variables does *not* affect the leading term. The *universal* coefficient B is not affected by the masses of the scattering particles: for mesons of masses $m_{1,2}$, the rapidity becomes $\chi \sim \log(\frac{s}{m_1 m_2})$, which simply corresponds to a change of the energy scale implicitly contained in (3). This result can also be extended to the case in which K_M is, for large χ, the sum of different terms, each behaving like the one discussed above, but with different values of n and μ, i.e., $K_M \sim i\sum_k \beta_k \chi^{p_k} e^{n_k \chi} e^{-\mu_k|\vec{z}_\perp|}$: the resulting B comes out to be determined by the maximum value of the ratio n/μ among these terms, i.e., $B = 2\pi \max_k(\frac{n_k}{\mu_k})^2$. From a physical point of view, one expects that particles with *mass* M and *spin* J, exchanged between the two WL, contribute with $\mu = M$ and $n = J - 1$: in fact, in this case the factor $e^{n\chi}$ reduces to the well-known factor s^{J-1}, expected for the contribution of an exchanged particle of spin J.[20]

3 New analysis of the lattice data

In Ref.[17] we have found three parameterizations $\mathcal{C}_E^{(i)} = \exp K_E^{(i)} - 1$, $i = 1, 2, 3$ (among the many that we have analyzed), that satisfy the criteria i)–iii) listed above. We have focused our analysis on the *averaged* CF $\mathcal{C}^{ave}$, that is "closer" to the hadronic scattering matrix $\mathcal{M}_{(hh)}$.

The first two parameterizations, $K_E^{(1)} = \frac{K_1}{\sin\theta} + K_2\cot^2\theta + K_3\cos\theta\cot\theta$ and $K_E^{(2)} = \frac{K_1}{\sin\theta} + K_2(\frac{\pi}{2} - \theta)\cot\theta + K_3\cos\theta\cot\theta$, are essentially two proper modifications of the AdS/CFT result. The third parameterization is, instead, $K_E^{(3)} = \frac{K_1}{\sin\theta} + K_2(\frac{\pi}{2} - \theta)^3\cos\theta$: while the first term is "familiar", the second one is not present in the known analytical models, but it is a fact that the resulting best fit is extremely good. In the three cases, the unitarity condition $\mathrm{Re}K_M^{(i)} \leq 0$ is satisfied if $K_2 \geq 0$: this is actually the case for our best fits (within the errors). The leading term after analytic continuation (the third term in the first two parameterizations $K^{(1)}$ and $K^{(2)}$ and the second term in the parameterization $K^{(3)}$) is of the form $\chi^p e^\chi$ for large χ, which, according to the previous discussion, should correspond to an exchanged particle of spin $J = 2$ (being $n = 1$), and, according to (3), leads to $\sigma_{\rm tot}^{(hh)} \sim B\log^2 s$. The value of $B = 2\pi/\mu^2$, obtained through a fit of the coefficient of the leading term with an exponential function $\sim e^{-\mu|\vec{z}_\perp|}$ over the available distances, is found to be compatible with the experimental result $B_{\rm exp} \simeq 0.3$ mb

Table 1: Mass-scale μ, "decay length" $\lambda = 1/\mu$ and the coefficient $B = 2\pi/\mu^2$ obtained with our parameterizations.

	μ (GeV)	$\lambda = \frac{1}{\mu}$ (fm)	$B = \frac{2\pi}{\mu^2}$ (mb)
Corr 1	4.64(2.38)	$0.042^{+0.045}_{-0.014}$	$0.113^{+0.364}_{-0.037}$
Corr 2	3.79(1.46)	$0.052^{+0.032}_{-0.014}$	$0.170^{+0.277}_{-0.081}$
Corr 3	3.18(98)	$0.062^{+0.028}_{-0.015}$	$0.245^{+0.263}_{-0.100}$

(within the large errors) in all the three cases (see Table 1). However, this must be taken only as an estimate, as lattice data are available only for small $|\vec{z}_\perp|$. Since $\mu_{\rm exp} = \sqrt{2\pi/B_{\rm exp}} \simeq 2.85$ GeV is close to the value of the mass for the *glueball* 2^{++},[19] one could be tempted to conclude, on the basis of the results that we have found, that B is determined by the mass of this *glueball*. But this is maybe still a premature conclusion: work is in progress along this direction.[20]

References

1. G. Antchev *et al.* (TOTEM collaboration), *Eur. Phys. Lett.* **96**, 21002 (2011); *Eur. Phys. Lett.* **101**, 21002 (2013); *Eur. Phys. Lett.* **101**, 21004 (2013).
2. J.R. Cudell *et al.* (COMPETE collaboration), *Phys. Rev.* D **65**, 074024 (2002); M. Ishida and K. Igi, *Phys. Lett.* B **670**, 395 (2009); M. Ishida and K. Igi, *Phys. Rev.* D **79**, 096003 (2009); M.M. Block and F. Halzen, *Phys. Rev. Lett.* **107**, 212002 (2011).
3. M. Froissart, *Phys. Rev.* **123**, 1053 (1961); A. Martin, *Nuovo Cimento* **42A**, 930 (1966); L. Lukaszuk and A. Martin, *Nuovo Cimento* **52A**, 122 (1967).
4. H.G. Dosch, P. Gauron and B. Nicolescu, *Phys. Rev.* D **67**, 077501 (2003).
5. O. Nachtmann, *Ann. Phys.* **209**, 436 (1991).
6. H.G. Dosch, E. Ferreira and A. Krämer, *Phys. Rev.* D **50**, 1992 (1994); E.R. Berger and O. Nachtmann, *Eur. Phys. J.* C **7**, 459 (1999); A.I. Shoshi, F.D. Steffen and H.J. Pirner, *Nucl. Phys.* A **709**, 131 (2002).
7. E. Meggiolaro, *Z. Phys.* C **76**, 523 (1997); *Eur. Phys. J.* C **4**, 101 (1998); *Nucl. Phys.* B **625**, 312 (2002).
8. E. Meggiolaro, *Nucl. Phys.* B **707**, 199 (2005).
9. M. Giordano and E. Meggiolaro, *Phys. Rev.* D **74**, 016003 (2006); E. Meggiolaro, *Phys. Lett.* B **651**, 177 (2007); M. Giordano and E. Meggiolaro, *Phys. Lett.* B **675**, 123 (2009).
10. M. Giordano and E. Meggiolaro, *Phys. Rev.* D **78**, 074510 (2008).
11. M. Giordano and E. Meggiolaro, *Phys. Rev.* D **81**, 074022 (2010).
12. A.I. Shoshi, F.D. Steffen, H.G. Dosch and H.J. Pirner, *Phys. Rev.* D **68**, 074004 (2003).
13. A. Babansky and I. Balitsky, *Phys. Rev.* D **67**, 054026 (2003).
14. E. Shuryak and I. Zahed, *Phys. Rev.* D **62**, 085014 (2000).
15. R.A. Janik and R. Peschanski, *Nucl. Phys.* B **565**, 193 (2000).
16. M. Giordano and R. Peschanski, *JHEP* **05**, 037 (2010).
17. M. Giordano, E. Meggiolaro, N. Moretti, *JHEP* **09**, 031 (2012).
18. M.M. Block and R.N. Cahn, *Rev. Mod. Phys.* **57**, 563 (1985).
19. C.J. Morningstar and M. Peardon, *Phys. Rev.* D **60**, 034509 (1999); E. Gregory, A. Irving, B. Lucini, C. McNeile, A. Rago, C. Richards and E. Rinaldi, *JHEP* **10**, 170 (2012).
20. M. Giordano, E. Meggiolaro, N. Moretti, in preparation.

W/Z+Jets and W/Z+HF Production at the Tevatron

Stefano Camarda[a]
DESY - Notkestraße 85 D-22607 Hamburg Germany
On behalf of the CDF and DO Collaborations.

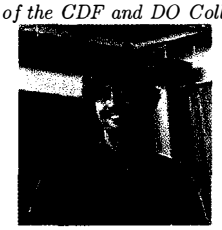

The CDF and D0 collaborations performed a comprehensive study of the production of vector bosons, W and Z, in association with energetic jets. Understanding the W/Z + jets and W/Z + c, b-jets processes is of paramount importance for the top quark physics, for the Higgs boson measurements, and for many new physics searches. In this contribution the most recent measurements of the associated production of jets and vector bosons in Run II at the Tevatron are presented. The measurements are compared to different perturbative QCD predictions and to several Monte Carlo generators.

1 Introduction

The study of the production of electroweak bosons in association with jets of hadrons constitutes a fundamental item in the high-p_T physics program at the Tevatron. Vector bosons plus jets final states are a major background to many interesting physics processes like single and pair top quarks production, Higgs, and super-symmetry. Precise measurements of W/Z + jets production provide a stringent test of perturbative QCD predictions [1–5] at high Q^2, and offer the possibility to validate Monte Carlo simulation tools [6–11]. The latest vector boson plus jets results at the Tevatron are reviewed and discussed.

2 W/Z + jets measurements

The CDF experiment recently measured Z + jets production cross sections with the full Tevatron run II dataset, corresponding to 9.64 fb^{-1} of integrated luminosity [12]. Differential cross sections as a function of several variables have been measured, including jet p_T, jet rapidity and jet multiplicity, angular variables like di-jet $\Delta\phi$ and Δy, and $H_T^{\text{jet}} = \sum p_T^{\text{jet}}$. Events are required to have two electrons or muons with a reconstructed invariant mass in the range $66 \leqslant M_Z \leqslant 116$ GeV/c^2 around the Z boson mass. Jets are clustered with the Midpoint algorithm [13] in a cone radius of 0.7, and are required to have $p_T \geqslant 30$ GeV/c and $|y| \leqslant 2.1$. The background estimation is performed both with data-driven and Monte Carlo techniques, the QCD and W+jet

[a]formerly IFAE - Barcelona

backgrounds are estimated from data, other backgrounds contributions like $t\bar{t}$, diboson and $Z/\gamma^* \dashrightarrow \tau^+\tau^-$ are estimated from Monte Carlo simulation. The cross sections are unfolded back to the particle level accounting for acceptance and smearing effects employing ALPGEN+PYTHIA Monte Carlo. The measured cross sections are compared to predictions from the Monte Carlo event generators ALPGEN+PYTHIA [6], POWHEG+PYTHIA [7], and to the fixed order perturbative QCD predictions MCFM [2], BLACKHAT+SHERPA [3], LOOPSIM+MCFM [4] and to a fixed order prediction including NLO EW corrections [5]. Fixed order predictions include parton-to-particle correction factors that account for the non-perturbative underlying event and fragmentation effects, estimated with ALPGEN+PYTHIA Monte Carlo simulation. Figure 1 shows the measured cross section as a function of H_T^{jet} in $Z/\gamma^* + \geqslant 1$ jet events.

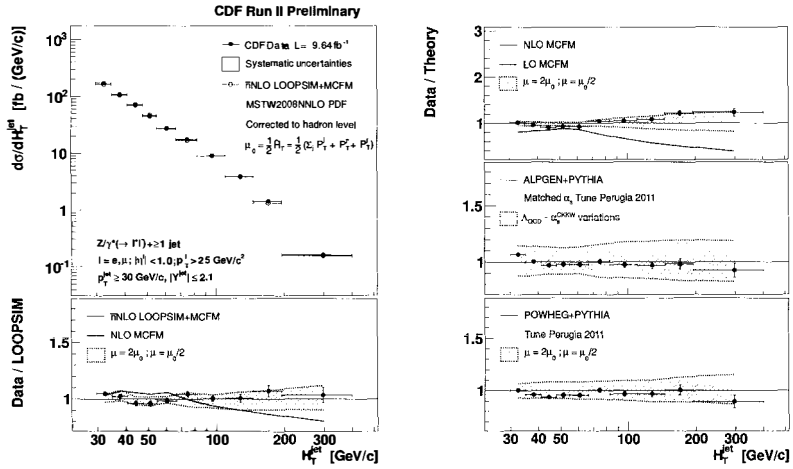

Figure 1: Measured differential cross sections as a function of H_T^{jet} in $Z/\gamma^* + \geqslant 1$ jet events. Data (black dots) are compared to LOOPSIM prediction (open circles). The shaded bands show the total systematic uncertainty, except for the 5.8% luminosity uncertainty, the blue area represents simultaneous variation of renormalization and factorization scales.

A new measurement of $W \dashrightarrow e\nu$ + jets production cross section has been performed with the D0 experiment with 3.7 fb^{-1} of integrated luminosity [14], including a comprehensive study of several kinematics variables. Events are selected with a reconstructed electron of $p_T \geqslant 15$ GeV/c and $|\eta| \leqslant 1.1$, the transverse mass of the W, reconstructed with the electron and $\not\!\!E_T$, is required to be $M_T^W \geqslant 40$ GeV/c^2, jets are reconstructed with the Midpoint algorithm in a radius $R = 0.5$ and required to have $p_T \geqslant 20$ GeV/c and $|y| \leqslant 3.2$. Data are compared to several Monte Carlo generators, ALPGEN+PYTHIA, ALPGEN+HERWIG [6], PYTHIA [8], HERWIG [9] and SHERPA [10], to perturbative NLO QCD predictions from BLACKHAT+SHERPA [3], and to the all order resummed prediction HEJ [11]. Figure 2 shows the average number of jets and the probability of third jet emission as a function of the Δy between the most rapidity-separated jets, in events with $W \rightarrow e\nu + \geqslant 2$ jets.

3 W/Z + heavy flavor jets production

The measurement of vector boson production with associated heavy flavor jets provides an important test of perturbative QCD predictions, and can be used to improve the determination

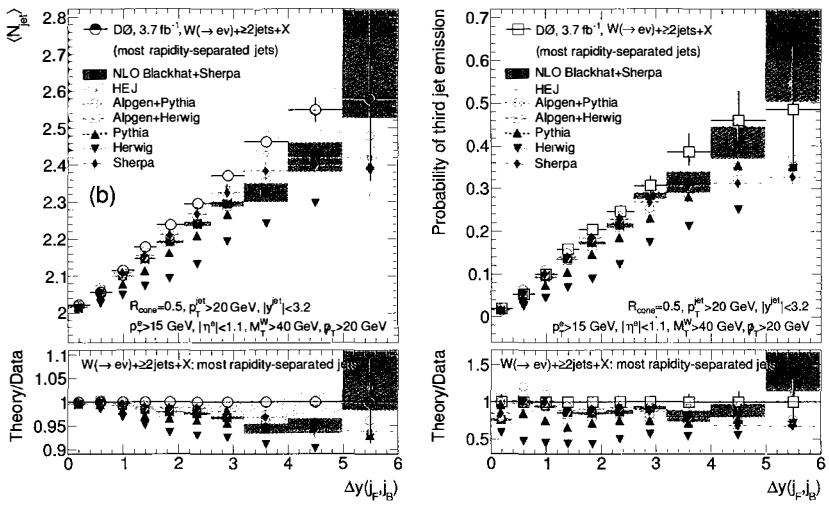

Figure 2: Measured average number of jets (left) and probability of third jet emission (right) as a function of the Δy between the most rapidity-separated jets, in events with $W \to e\nu + \geqslant 2$ jets. Data (open black dots) are compared to several Monte Carlo generators and predictions. The lower pane shows the theory/data ratio.

of PDF. Understanding these processes is also critical for the measurement of Higgs boson production in association with a W or Z and in the search for SUSY.

The W + charm production cross section has been measured by CDF with 4.3 fb^{-1} of integrated luminosity [15]. Charm jets are identified with an algorithm which identifies soft leptons coming from the semileptonic decay of the charm. The measurement exploits the charge correlation between the soft lepton and the lepton coming from the leptonic decay of the W to reduce the background contamination. The measured cross section of $13.6 \pm 2.2(\text{stat})^{+2.3}_{-1.9}(\text{syst}) \pm 1.1(\text{lum})$ pb is in good agreement with the NLO prediction of 11.4 ± 1.3 pb from MCFM.

The W + b-jet cross section has been measured by D0 with 6 fb^{-1} of integrated luminosity [16]. $W \to e\nu$ and $W \to \mu\nu$ decay channels are combined, and a multivariate technique is used to identify b-jets. The measured cross section of 1.05 ± 0.12 pb is in good agreement with the perturbative QCD NLO prediction from MCFM of $1.34^{+0.41}_{-0.34}$ pb, and consistent with predictions from the Monte Carlo generators SHERPA (1.08 pb) and MADGRAPH (1.44 pb).

The CDF and D0 collaborations recently measured differential cross sections of Z + b-jet production with the full Tevatron run II dataset [17, 18], with integrated luminosities corresponding to 9.7 fb^{-1} and 9.13 fb^{-1} respectively. Figure 3 shows the measured cross sections unfolded to particle level and compared to NLO perturbative QCD predictions from MCFM and Monte Carlo generators SHERPA and ALPGEN+PYTHIA. The measured cross sections are in reasonable agreement with theory, within large experimental and theoretical uncertainties.

Summary

W/Z + jets and W/Z + heavy flavor measurements belong to the Tevatron legacy. All the measurements are in general good agreement with the perturbative NLO QCD predictions, in the tail of some distributions like H_T^{jet} and di-jet Δy the inclusion of higher order corrections improves the agreement between data and theory. Detailed studies of differential distributions in W/Z + jets and W/Z + heavy flavour production provide an important test of the different Monte Carlo generators and theoretical predictions, and a fundamental validation of the background

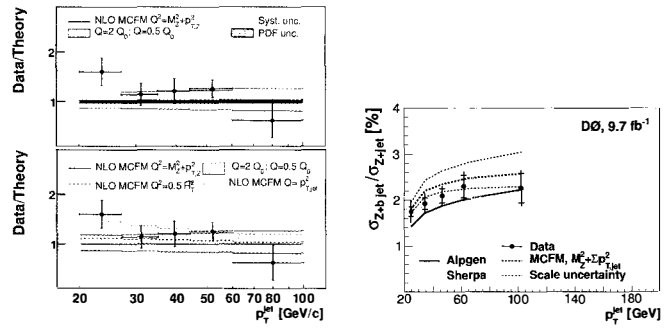

Figure 3: Measured Z + b-jet differential cross sections as a function of b-jet p_T with the CDF (left) and D0 (right) detectors. Data (black dots) are compared to MCFM NLO prediction and Monte Carlo generators.

modeling of such processes in the search for new physics.

Acknowledgments

I am grateful to the ATLAS-DESY group for supporting my participation.

References

1. D.J. Gross and F. Wilczek, *Phys. Rev.* D **8**, 3633 (1973).
2. J.Campbell and R.K. Ellis, *Phys. Rev.* D **65**, 113007 (2002).
3. C. F. Berger, Z. Bern, L. J. Dixon, F. Febres Cordero, D. Forde, H. Ita, D. A. Kosower and D. Maitre, *Phys. Rev.* D **78**, 036003 (2008).
4. M. Rubin, G. P. Salam and S. Sapeta, JHEP **1009** (2010) 084
5. A. Denner, S. Dittmaier, T. Kasprzik and A. Muck, JHEP **1106** (2011) 069
6. M. L. Mangano, M. Moretti, F. Piccinini, R. Pittau and A. D. Polosa, JHEP **0307** (2003) 001
7. S. Frixione, P. Nason and C. Oleari, JHEP **0711** (2007) 070
8. T. Sjostrand, S. Mrenna and P. Z. Skands, JHEP **0605** (2006) 026
9. M. Bahr, S. Gieseke, M. A. Gigg, D. Grellscheid, K. Hamilton, O. Latunde-Dada, S. Platzer and P. Richardson *et al.*, Eur. Phys. J. C **58** (2008) 639
10. T. Gleisberg, S. .Hoeche, F. Krauss, M. Schonherr, S. Schumann, F. Siegert and J. Winter, JHEP **0902** (2009) 007
11. J. R. Andersen and J. M. Smillie, JHEP **1106** (2011) 010
12. S. Camarda, FERMILAB-THESIS-2012-12.
13. A. Abulencia et al. (CDF Collaboration), *Phys. Rev.* D **74**, 071103(R) (2006).
14. V. M. Abazov *et al.* [D0 Collaboration], arXiv:1302.6508 [hep-ex].
15. T. Aaltonen *et al.* [CDF Collaboration], Phys. Rev. Lett. **110** (2013) 071801
16. V. M. Abazov *et al.* [D0 Collaboration], Phys. Lett. B **718** (2013) 1314
17. T. Aaltonen *et al.* [CDF Collaboration], CDF public note 10594
18. V. M. Abazov *et al.* [D0 Collaboration], arXiv:1301.2233 [hep-ex].

Vector boson production in association with jets and heavy flavor quarks at the LHC

Konstantinos Theofilatos (on behalf of the CMS and ATLAS Collaborations)
Institute for Particle Physics
ETH Zürich, Switzerland

The associated production of jets and vector bosons allows for stringent tests of perturbative QCD calculations and is sensitive to the possible presence of new physics beyond the Standard Model. The mechanism of production of heavy quarks in association with a W or a Z, in particular, is only partially understood. A measurement of jet production rates in association with W and Z bosons in proton-proton collisions at a 7 TeV center-of-mass energy is presented, using LHC data recorded by the CMS and ATLAS experiments.

Vector bosons (V = W or Z) produced in association with jets (V + jets) provide a precise way to test pertubative QCD predictions. The small theoretical uncertainty on the V + jets production together with the small experimental uncertainty on the selection of the V + jets signal, makes it possible to study higher order pertubative effects and parton distribution functions (PDFs). The V + jets signal itself is a background process in searches for new physics phenomena, therefore a good understanding of it is vital for searches at the LHC. Measurements from CMS [1] and ATLAS [2] using 5/fb data at $\sqrt{s} = 7$ TeV collected during 2011 are reported.

The experimental results are corrected for detector effects and are compared with predictions from Blackhat [3], Powheg [5], aMC@NLO [4], MCFM [6], Madgraph [7], Alpgen [8] and Sherpa [9]. The leading order (LO) matrix element (ME) Monte Carlo (MC) event generators are interfaced with Pythia [11] and HERWIG [12] for parton showering (PS) with the exception of Sherpa which uses its own built-in PS. The NLO ME calculations from Powheg and aMC@NLO are interfaced with Pythia and HERWIG and their predictions are provided at particle level (NLO+PS). The MC samples from Madgraph, Alpgen and Sherpa have been normalized, for the inclusive V production, to the next-to-next-to-leading-order (NNLO) cross section calculated with FEWZ [10]. Details on the exact MC configurations including the used PDFs and the choice of scales can be found in the cited articles.

The jet multiplicity in Z + jets data (Fig. 1 left) is well predicted by BlackHat+Sherpa parton level NLO calculation (up to four hard partons). The NLO+PS prediction from aMC@NLO is NLO for the inclusive Drell–Yan production and is only LO for the Z + 1-jet (Fig. 1 left). The complexity of an exact ME calculation increases dramatically as a function of N_{jets}. While an exact ME calculation is available here, to LO for up to five partons, jet multiplicity in data extends to $N_{\text{jets}} \geq 6$. The PS seems (within uncertainties) capable of filling the phase space in terms of event rate as a function of N_{jets}. Azimuthal correlations $\Delta\phi(Z, j_{\text{i}})$ and $\Delta\phi(j_{\text{i}}, j_{\text{j}})$ for $N_{\text{jets}} \geq 3$ are measured in an attempt to complement the picture in terms of angular properties (Fig. 2). Predictions from NLO+PS for the Z + 1−jet final state are of particular interest here, and show agreement with $N_{\text{jets}} \geq 3$ data despite the fact that, beyond the subleading jet, additional radiation comes exclusively from PS. High jet multiplicity implies a large scale and an increased phase space available for parton emission. An inclusive observable of high interest, in LHC searches, is the Z transverse momentum (Fig. 1 right) which shows a systematic trend as a function of p_{T}^{Z} for the ME+PS comparisons. ME+PS predicts a higher event yield than what is observed in data,

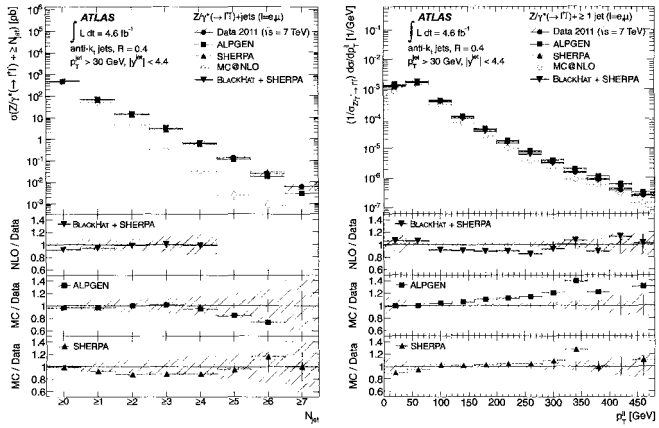

Figure 1: Cross section measured as a function of the jet multiplicity (left) and the transverse momentum of the Z boson (right).

the size of this effect is consistent with the reduction of the Z + jets cross section due to higher-order electroweak corrections [19]. In searches for new physics with jets and invisible energy that have $Z \to \nu\nu$ as irreducible background, a systematic effect of this order will decrease the discovery potential of the smallest signals of interest. The Z + jets picture is completed with the measurement of the rapidity distributions of the Z and the leading jet which are found to be in good agreement ($< 5\%$) with theory [15]. However, an interesting behavior is observed in the rapidity variables $Y_{\rm sum} = 0.5(Y_{\rm Z} + Y_{\rm jet})$ and $Y_{\rm diff} = 0.5(Y_{\rm Z} - Y_{\rm jet})$, which rely on a proper theoretical description of the correlations between $Y_{\rm Z}$ and $Y_{\rm jet}$ (Fig. 3). The $Y_{\rm sum}$ and $Y_{\rm diff}$ distributions show different level of agreement between the different implementations of ME+PS, while they agree with the NLO prediction.

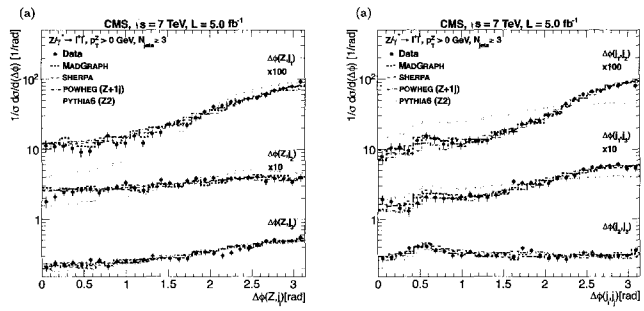

Figure 2: Cross section measured as a function of the azimuthal correlations $\Delta\phi(Z, j_{\rm i})$ (left) and $\Delta\phi(j_{\rm i}, j_{\rm j})$ (right) for $N_{\rm jets} \geq 3$.

The question of whether the strange content of the proton is suppressed with respect to the light quarks, is directly assessed here with the measurement of the W plus charm cross section and the ratio of $\sigma(\mathrm{W}^+ + \bar{c})/\sigma(\mathrm{W}^- + c)$. The measurements are consistent with the strange suppression $s/d \leq 0.5$ which is predicted by MSTW08, CT10 and NNPDF23 [16]. The production of a W in association with two b-jets is important for the studies of $\mathrm{WH} \to \mathrm{W}b\bar{b}$. This motivates the measurement of the $\mathrm{W}b\bar{b}$ cross section which is found to be 0.53 ± 0.05 (stat) ± 0.1 (sys) pb, in very good agreement with the NLO prediction 0.52 ± 0.03 pb [17]. On the other hand, a systematic

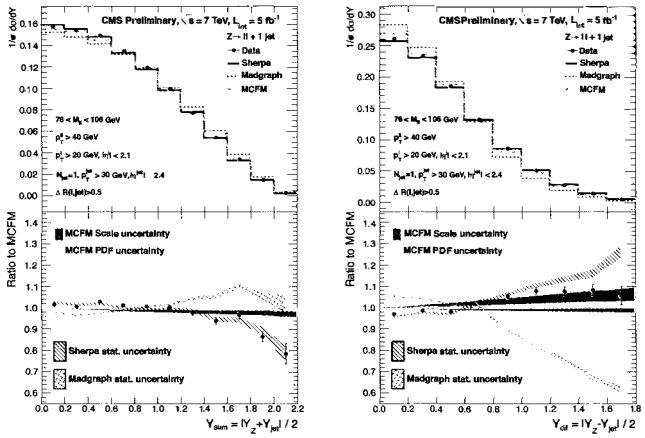

Figure 3: Cross section measured as a function of the rapidity sum $Y_{\mathrm{sum}} = 0.5(Y_{\mathrm{Z}} + Y_{\mathrm{jet}})$ (left) and the rapidity difference $Y_{\mathrm{diff}} = 0.5(Y_{\mathrm{Z}} - Y_{\mathrm{jet}})$ (right) between the Z boson and the leading jet.

bias is observed in the W plus one b-jet final state (Fig. 5 left). The disagreement becomes more significant if the single top contribution is not subtracted from the cross section measurement [18] (Fig. 5 right).

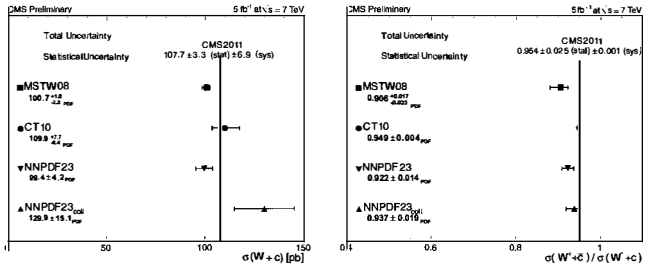

Figure 4: Cross section measured for the $\mathrm{W} + c$ process (left) and the $\sigma(\mathrm{W}^+ + \bar{c})/\sigma(\mathrm{W}^- + c)$ cross section ratio (right).

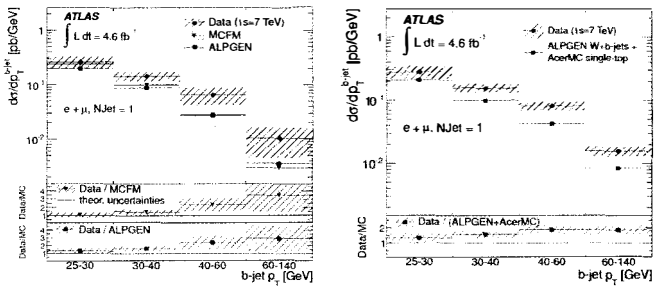

Figure 5: Cross sections measured as a function of the b-jet p_{T} for the $\mathrm{W} + b$ process (left) and for the combined $\mathrm{W} + b$ plus single top processes (right).

In summary, the LHC's substantial amount of delivered data at 7 TeV to the experiments has made it possible to probe extreme kinematics of the V + jets signal that were not previously accessible. Different levels of agreement has been observed among the various predictions and data, reflecting to some extent the current understanding of the LHC data.

References

1. CMS Collaboration, *The CMS experiment at the CERN LHC*, JINST **3**, S08004 (2008).
2. ATLAS Collaboration, *The ATLAS Experiment at the CERN Large Hadron Collider*, JINST **3**, S08003 (2008).
3. C. F. Berger et al. *An Automated Implementation of On-Shell Methods for One-Loop Amplitudes*, PRD **78**, 036003 (2008)
4. S. Frixione and B. R. Webber, *Matching NLO QCD Computations and Parton Shower Simulations*, JHEP **029**, 0206 (2002) 029, arXiv:hep-ph/0204244
5. S. Alioli et al., *Vector boson plus one jet production in POWHEG*, JHEP **01**, 0.96 (2011)
6. J. M. Campbell and R. K. Ellis, *MCFM for the Tevatron and the LHC*,Nucl. Phys. Proc. Suppl. **10**, 205 (2010), arXiv:1007.3492.
7. J. Alwall, M. Herquet, F. Maltoni et al.,*MadGraph 5: going beyond*, JHEP **06**, 128 (2011)
8. M. L. Mangano, M. Moretti, F. Piccinini et al., *ALPGEN, a generator for hard multiparton processes in hadronic collisions*, JHEP **07**, 001 (2003)
9. T.Gleisberg, S.Höche,F.Kraussetal.,*Event generation with SHERPA 1.1*,JHEP **02**, 007 (2009)
10. K. Melnikov and F. Petriello, *Electroweak gauge boson production at hadron colliders through* $O(\alpha_s^2)$, PRD **74**, 114017 (2006)
11. T. Sjöstrand, S. Mrenna and P. Z. Skands, PYTHIA 6.4 Physics and Manual, JHEP **026**, 0605 (2006)
12. G. Corcella et al.,*HERWIG 6.5: an Event Generator for Hadron Emission Reactions With Interfering Gluons (including supersymmetric processes)*, JHEP **010**, 0101 (2001), arXiv:hep-ph/0011363T.
13. CMS Collaboration, *Event shapes and azimuthal correlations in Z + jets events in pp collisions at sqrt(s) =7 TeV*, CERN-PH-EP-2013-001, arXiv:1301.1646
14. ATLAS Collaboration, *Measurement of the production cross section of jets in association with a Z boson in pp collisions at sqrt(s) = 7 TeV with the ATLAS detector*, CERN-PH-EP-2013-023, e-Print: arXiv:1304.7098
15. CMS Collaboration, *Measurement of Rapidity Distributions for a Z Boson or a Photon in Association with a Single Jet in pp Collisions at sqrt(s)= 7 TeV*, CMS-PAS-SMP-12-004
16. CMS Collaboration, *Measurement of associated charm production in W final states at sqrt(s) = 7 TeV*, CMS-PAS-SMP-12-002
17. CMS Collaboration, *Measurement of the production cross section of W bosons in association with two b jets in pp collisions at sqrt(s)=7 TeV*, CMS-PAS-SMP-12-026
18. ATLAS Collaboration, *Measurement of the cross-section for W boson production in association with b-jets in pp collisions at sqrt(s) = 7 TeV with the ATLAS detector* , CERN-PH-EP-2012-357, e-Print: arXiv:1302.2929
19. A. Denner et al. *Electroweak corrections to dilepton + jet production at hadron colliders*, JHEP **069**, 1106 (2011), arXiv:1103.0914

DIBOSON PRODUCTION CROSS SECTION AT LHC

VINCENZO P. LOMBARDO
(on behalf of the ATLAS and CMS Collaborations)
Laboratoire d'Annecy-le-Vieux de Physique des Particules
9 Chemin de Bellevue, Annecy-le-Vieux, France

This paper presents an overview of the diboson production cross-section measurements and constraints on anomalous triple-gauge boson couplings performed by the ATLAS and CMS collaborations using proton-proton collisions produced at a centre-of-mass energy of $\sqrt{s} = 7$ and 8 TeV at LHC. Results for all combinations of W, Z and γ gauge bosons (excluding $\gamma\gamma$) are presented with emphasis on the new WZ and ZZ production cross sections measured by ATLAS at $\sqrt{s} = 8$ TeV and on the new constraints on anomalous triple-gauge couplings set by CMS in the WW and $Z\gamma$ modes.

1 Introduction

In the Standard Model (SM) of particle physics, measurements of diboson final states at the TeV scale provide excellent tests of the electroweak sector. Any deviation of the diboson production cross sections or kinematic distributions from the SM predictions may be an indication of anomalous triple-gauge boson couplings (aTGC) and of the existence of new particles such as those predicted by technicolor models, little Higgs and Randall-Sundrum graviton models, to mention only a few examples. It is therefore very important to have precise diboson measurements as well as reliable and accurate theoretical predictions for these processes. In addition non-resonant diboson production processes must be understood in detail as they represent a significant background to the measurements of the Higgs boson. The diboson results presented in this note are based on the proton-proton collision data collected by the ATLAS [1] and CMS [2] detectors at the LHC [3] in 2011 and 2012.

2 Diboson production cross-section measurements

The measurements of the total production cross sections of $pp \to W\gamma + X$ and $pp \to Z\gamma + X$ have been performed in the decay channels $W\gamma \to \ell\nu\gamma$ and $Z\gamma \to \ell\ell\gamma$ [4,5] by requiring a W or a Z boson candidate in association with an isolated photon. The photon is required to be separated by the lepton to suppress QED Final State Radiation. The dominant background includes $W/Z + jets$ and $\gamma + jets$ where jet-induced photons or jet-faking leptons are selected. In addition to the total cross section both the ATLAS and CMS Collaborations have unfolded the E_T^γ spectrum observing a reasonable agreement with theoretical predictions. The $Z\gamma \to \nu\nu\gamma$ mode has also been measured by the two Collaborations [4,6] by requiring a tighter selection on the photon and on the missing transverse energy (E_T^{miss}) in order to suppress the backgrounds. A fair agreement with theoretical predictions is observed.

The $pp \to WZ + X$ production cross section has been measured in the $WZ \to \ell\nu\ell\ell$ channel by both ATLAS and CMS at a centre-of-mass energy $\sqrt{s} = 7$ TeV with 4.6 and 1.1 fb^{-1},

respectively [7,8]. The signal region is selected by requiring three isolated high-p_T leptons and E_T^{miss}. A tighter identification requirement on the lepton coming from the W decay reduces the Z+jet background where jet-faking leptons are selected. In addition to the the total cross section ATLAS has measured the inclusive WZ cross section as function of the transverse momentum of the Z boson and of the invariant mass of the WZ system. Recently, ATLAS has also released the first measurement [9] of the $pp \to WZ + X$ production cross section at 8 TeV with an integrated luminosity of 13 fb^{-1}. The measured cross section is $20.3^{+0.8}_{-0.7}(stat)^{+1.2}_{-1.1}(syst)^{+0.7}_{-0.6}(lumi)$ pb, in excellent agreement with the next-to-leading order (NLO) QCD predictions provided by MCFM + CT10 parton distribution functions [10,11].

The $pp \to WW + X$ production cross section has been measured by ATLAS and CMS at 7 TeV with 4.6 and 4.9 fb^{-1}, respectively [12,13]. The selection of the $WW \to \ell\nu\ell\nu$ channel requires two opposite charged isolated leptons. The Drell-Yan background in the ee and $\mu\mu$ channels is suppressed by means of a Z veto and a requirement on a E_T^{miss}-related variable. In addition a jet veto is applied to reduce the top-quark background. The cross section measured by ATLAS is $51.9 \pm 2.0(stat) \pm 3.9(syst) \pm 2.0(lumi)$ pb and the one measured by CMS is $52.4 \pm 2.0(stat) \pm 4.5(syst) \pm 1.2(lumi)$ pb. They agree to each other but they are higher than the NLO calculations provided by MCFM+CT10 which predicts $44.7^{+2.1}_{-1.9}$ pb. The CMS collaboration has also measured the WW cross section at 8 TeV with a dataset corresponding to an integrated luminosity of 3.5 fb^{-1} [14]. The measured cross section is $69.9 \pm 2.8(stat) \pm 5.6(syst) \pm 3.1(lumi)$ pb confirming a higher cross section with respect to the NLO predictions calculated by MCFM+CT10 which gives $57.3^{+2.4}_{-1.6}$ pb.

Both ATLAS and CMS have also measured the total cross section of $WW + WZ \to \ell\nu jj$ at 7 TeV with 4.7 and 5.0 fb^{-1}, respectively [15,16]. The request of exactly two high-p_T jets in addition to an isolated lepton and E_T^{miss} is used to select the signal region. After these selection requirements the $W/Z + jets$ background is still huge compared to signal and a binned maximum-likelihood fit to the dijet invariant mass has been used to extract the signal yield and measure the cross section. Both ATLAS and CMS report results which are in good agreement with the SM predictions.

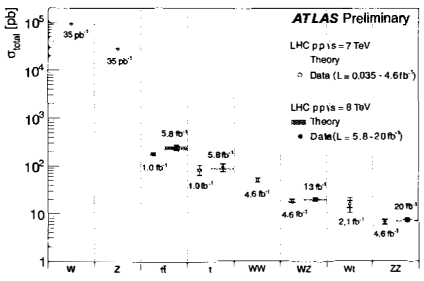

Figure 1: Summary plot of ATLAS cross-section measurements [22].

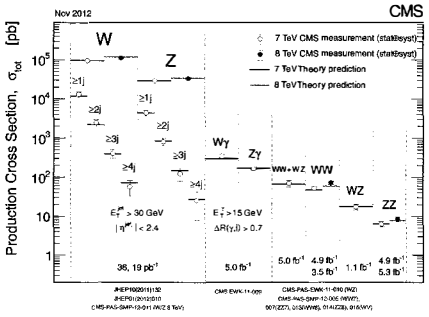

Figure 2: Summary plot of CMS cross-section measurements [23].

The $pp \to ZZ + X$ production cross section has been measured by ATLAS and CMS at the centre-of-mass energy of $\sqrt{s} = 7$ and 8 TeV [17,18,14]. The $ZZ \to 4\ell$ final state requires two pairs of isolated charged leptons (e or μ) which are compatible with two on-shell Z bosons. The ATLAS Collaboration has also measured the ZZ cross section at $\sqrt{s} = 7$ TeV in the $ZZ \to \ell\ell\nu\nu$ channel [17] by applying a tight cut on a E_T^{miss}-related variable in order to suppress the dominant $Z + jets$ background. On the other hand, the CMS measurement at 8 TeV includes the $ZZ \to 2\ell 2\tau$ mode. The ATLAS Collaboration has recently released an updated measurement of the $ZZ \to 4\ell$ cross section with 20 fb^{-1} at $\sqrt{s} = 8$ TeV [19]. The measured

cross section is $7.1^{+0.5}_{-0.4}(stat) \pm 0.3(syst) \pm 0.2(lumi)$ pb which agrees very well with the NLO calculation provided by MCFM with CT10 predicting $7.2^{+0.3}_{-0.2}$ pb.

A summary of the up-to-date diboson production cross-section measurements performed by ATLAS and CMS are shown in Figure 1 and 2. The diboson cross sections, as well as several other SM production cross sections, are compared to their theoretical predictions.

3 Anomalous triple-gauge boson couplings

In the SM, triple-gauge boson couplings (TGC) are completely fixed by the gauge structure of the electroweak theory and any deviation from the SM couplings indicates new physics beyond the SM. An effective lagrangian featuring such anomalous triple-gauge boson couplings (aTGCs) can be constructed and then compared to the experimental data. Under some general assumptions, aTGCs can be parameterized using the set of parameters shown in Table 1 [20,21]. All these parameters are equal to zero in the SM. Anomalous couplings are expected to modify the total production cross section as well as the kinematic distributions of the diboson processes, in particular in high momentum or high mass regions. The ATLAS and CMS Collaborations have searched for anomalous triple-gauge boson couplings and found no deviation from the SM values. Figure 3, 4, 5 and 6 show the limits at 95% confidence level on the aTGCs set by ATLAS and CMS as well as those set by LEP and Tevatron.

coupling	parameters	channel
$WW\gamma$	$\lambda_\gamma, \Delta k_\gamma$	$WW, W\gamma$
WWZ	$\lambda_Z, \Delta k_Z, \Delta g_1^Z$	WW, WZ
$ZZ\gamma$	h_3^Z, h_4^Z	$Z\gamma$
$Z\gamma\gamma$	h_3^γ, h_4^γ	$Z\gamma$
$Z\gamma Z$	f_{40}^Z, f_{50}^Z	ZZ
ZZZ	$f_{40}^\gamma, f_{50}^\gamma$	ZZ

Table 1: List of TGC parameters commonly used in ATLAS and CMS [20,21].

The CMS Collaboration has recently released new limits on aTGCs in the $WW \to \ell\nu\ell\nu$ channel analyzing 4.9 fb^{-1} of data collected at a centre-of-mass energy of $\sqrt{s} = 7$ TeV [13]. These limits are shown in Figure 3 and 4, together with previous results. In addition CMS has extracted limits on aTGCs in the $Z\gamma \to \nu\nu\gamma$ channel [6] setting tighter constraints on aTGCs with respect to those extracted in the $Z\gamma \to \ell\ell\gamma$ analyses [5,4].

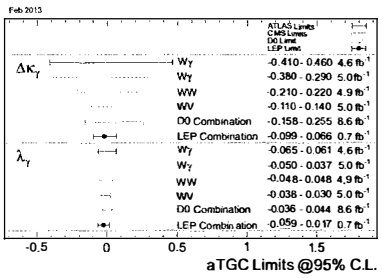

Figure 3: Limits on $WW\gamma$ anomalous triple-gauge couplings [24].

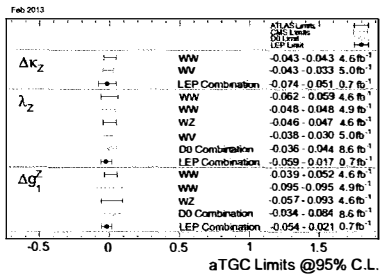

Figure 4: Limits on WWZ anomalous triple-gauge couplings [24].

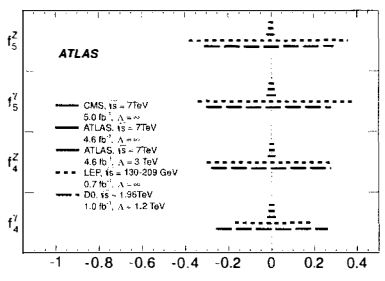

Figure 5: Limits on $Z\gamma Z$ and ZZZ anomalous triple-gauge couplings [17].

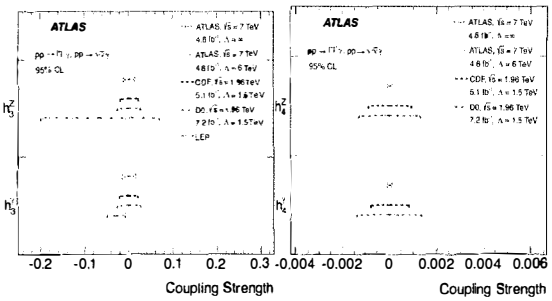

Figure 6: Limits on $ZZ\gamma$ and $Z\gamma\gamma$ anomalous triple-gauge couplings [4].

4 Summary

Measurements of the production cross sections of diboson final states performed by the ATLAS and CMS Collaborations at a centre-of-mass energy of $\sqrt{s} = 7$ and 8 TeV have been presented. The total production diboson cross sections are in reasonable agreement with the SM predictions within the uncertainties. Several distributions have also been unfolded and directly compared with the available theoretical distributions. A search for anomalous triple-gauge couplings have been performed by both ATLAS and CMS with almost 5 fb^{-1} of data collected at 7 TeV at LHC. Limits on aTGGs are set in all channels showing no deviation from the SM couplings.

References

1. ATLAS Collaboration, *JINST* **3**, (2008) S08003
2. CMS Collaboration, *JINST* **3**, (2008) S08004
3. L. Evans and P. Bryant (editors), *JINST* **3**, (2008) S08001
4. ATLAS Collaboration, arXiv:1302.1283 (accepted for publication in PRD)
5. CMS Collaboration, CMS-PAS-EWK-11-009, https://cdsweb.cern.ch/record/1537415
6. CMS Collaboration, CMS-SMP-12-020, https://cdsweb.cern.ch/record/1532433
7. ATLAS Collaboration, *EPJ* C **72**, 2012 (2173)
8. CMS Collaboration, CMS-PAS-EWK-11-010, https://cdsweb.cern.ch/record/1370067
9. ATLAS Collaboration, ATLAS-CONF-2013-021, https://cds.cern.ch/record/1525557
10. J. M. Campbell and R. K. Ellis, *Phys. Rev.* D **65**, (2002) 113007
11. H.-L. Lai *et al. Phys. Rev.* D **82**, (2010) 074024
12. ATLAS Collaboration, arXiv:1210.2979 (accepted for publication in PRD)
13. CMS Collaboration, CMS-PAS-SMP-12-005
14. CMS Collaboration, *Phys. Lett.* B **721**, (2013) 190
15. ATLAS Collaboration, ATLAS-CONF-2012-157, https://cds.cern.ch/record/1493586
16. CMS Collaboration, *EPJ* C **73**, 2013 (2283)
17. ATLAS Collaboration, *JHEP* **03**, (2013) 128
18. CMS Collaboration, *JHEP* **01**, (2013) 063
19. ATLAS Collaboration, ATLAS-CONF-2013-020
20. K. Hagiwara et al., *Nucl. Phys.* B **282**, (1987) 253
21. J. Ellison et al., Ann. Rev. Nucl. Part. Sci., 48 (1998) 33
22. ATLAS Public Results, https://twiki.cern.ch/twiki/bin/view/AtlasPublic/CombinedSummaryPlot
23. CMS Public Results, https://twiki.cern.ch/twiki/bin/view/CMSPublic/PhysicsResultsSMP
24. CMS Public Results, https://twiki.cern.ch/twiki/bin/view/CMSPublic/PhysicsResultsSMPaTGC

WZ and W+jets production at large transverse momenta beyond NLO

SEBASTIAN SAPETA
Institute for Particle Physics Phenomenology, Durham University, South Rd, Durham DH1 3LE, UK

We present a study of higher order QCD corrections beyond NLO to processes with electroweak vector bosons. We focus on the regions of high transverse momenta of commonly used differential distributions. We employ the LoopSim method, combined with NLO packages, VBFNLO and MCFM, to merge the NLO samples with different multiplicities, in order to compute the dominant part of the NNLO corrections at high p_T. We find that these corrections are indeed substantial, in the 30%-100% range, for a number of experimentally relevant observables. For other observables, they lead to significant reduction of scale uncertainties.

1 Introduction

The production of electroweak vector bosons forms one of the most important class of Standard Model (SM) processes. W boson in association with jets is a background to single and pair top production, diboson production, Higgs production as well as to searches for physics beyond the standard model (BSM). The same is true for the processes with two electroweak bosons in the final state, like WZ production, which, in addition, are sensitive to anomalous triple gauge boson coupling (TGC). The above processes are also interesting in their own right as they provide important tests of quantum chromodynamics (QCD).

In this proceedings, we present a study of WZ and W+jets processes, at the LHC energies, at approximate next-to-next-to-leading order (NNLO) in QCD. The motivation to go beyond the next-to-leading order (NLO) for those processes comes from the fact that the NLO corrections for WZ and W+jets turn out to be sizable for a number of important distributions at high transverse momentum. This corrections come about due to new production channels and new topologies absent at leading order (LO) and appearing only at NLO. An example, for the case of WZ, is shown in Fig. 1. At leading order, the production of dibosons is possible only via $q\bar{q}$ channel. At NLO, the new qg channel, with enhanced partonic luminosity, opens up and dominates the LO contribution. Similarly, at LO, only back-to-back WZ configurations are possible whereas at NLO, an electroweak boson can recoil against a parton and the other boson can be soft or collinear, which brings logarithmic enhancements for a number of distributions.

Because the NLO corrections often turn out to dominate the leading order, it is of great importance to try to assess the NNLO corrections, to check the convergence of the perturbative series, and to obtain precise and stable results. As shown in the right diagram of Fig. 1, in the case of WZ production, one can also expect genuinely new sub-processes and topologies appearing for the first time at NNLO.

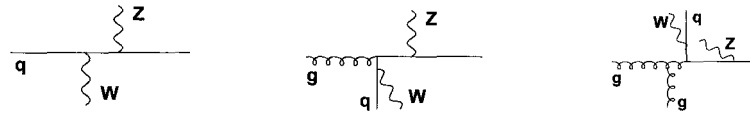

Figure 1: Example diagrams contributing to WZ production at LO, NLO and NNLO.

2 Details of the calculations

To compute the dominant part of the NNLO QCD corrections to WZ and W+jets processes, we used the LoopSim method [1] together with the NLO packages VBFNLO [2] and MCFM. [3]

LoopSim allows for a consistent merging of WZ and WZj NLO samples to obtain the result for WZ at $\bar{n}$NLO, where $\bar{n}$ denotes the approximate 2-loop contribution determined from the real and 1-loop parts of WZj at NLO. Similarly, Wj and Wjj NLO samples are used to compute the results for W+jets at $\bar{n}$NLO. The method is based on unitarity and it is supposed to work best for processes and observables with large NLO K-factors from new topologies, as $\sigma_{\bar{n}\mathrm{NLO}} - \sigma_{\mathrm{NNLO}} \sim \frac{1}{K}$. LoopSim has one parameter, R_{LS}, which affects the way the procedure assigns branching structure to the original NLO sample. By default, we set $R_{\mathrm{LS}} = 1$ and vary it by ± 0.5, to probe the related uncertainties. As we shall see, they are much smaller then the factorization and renormalization scale uncertainties at high p_T.

3 Results

The WZ production process was studied [4] with the following cuts: The charged leptons were required to be hard and central: $p_{T,\ell} \geq 15(20)$, for ℓ coming from Z(W), and $|y_\ell| \leq 2.5$. The missing transverse energy had to satisfy the cut $E_{T,\mathrm{miss}} > 30\,\mathrm{GeV}$. The same-flavor lepton pair mass had to lie in the window $60 < m_{l^+l^-} < 120\,\mathrm{GeV}$. The final state partons with $|y_p| \leq 5$ were clustered to jets with the anti-k_t algorithm with the radius $R = 0.45$. For the central value of the factorization and renormalization scales, we chose $\mu_{F,R} = \frac{1}{2}\sum p_{T,\mathrm{partons}} + \frac{1}{2}\sqrt{p_{T,W}^2 + m_W^2} + \frac{1}{2}\sqrt{p_{T,Z}^2 + m_Z^2}$. All WZ results correspond to the sum of contributions from two unlike flavor decay channels, $ee\mu\nu_\mu$ and $\mu\mu e\nu_e$, and both W^+Z and W^-Z production channels.

Fig. 2 (left) shows the differential distribution, at $\sqrt{s} = 8\,\mathrm{TeV}$, of the effective mass observable defined as

$$H_T = \sum p_{T,\mathrm{jets}} + \sum p_{T,l} + E_{T,\mathrm{miss}}\,. \tag{1}$$

As a first check, we computed the H_T distribution at $\bar{n}$LO, which can be directly compared with the exact NLO result. As we see in Fig. 2, $\bar{n}$LO matches very well the NLO at high H_T, providing the correct prediction for the large K factor, of the order of 10. The H_T observable is therefore very well suited to be studied with LoopSim. The $\bar{n}$NLO result shown in Fig. 2 yields up to 100% correction with respect to NLO. We see that the R_{LS} uncertainty is negligible at high H_T and the scale uncertainty decreases only a little at $\bar{n}$NLO. The latter is related to the fact that this observable favours new topologies that enter only at NNLO and are computed with LO accuracy (cf. the right diagram of Fig. 1).

In Fig. 2 (right), we present the distribution of the lepton with maximum p_T at $\sqrt{s} = 14\,\mathrm{TeV}$. Also here, the $\bar{n}$NLO corrections are large and beyond the NLO scale uncertainty already at 200 GeV. In addition, for this observable, we show the results with veto on the jets with $p_T > 50\,\mathrm{GeV}$. We observe that the $\bar{n}$NLO corrections with veto are negative, go beyond the NLO scale uncertainty, and exhibit larger uncertainties due to renormalization and factorization scale

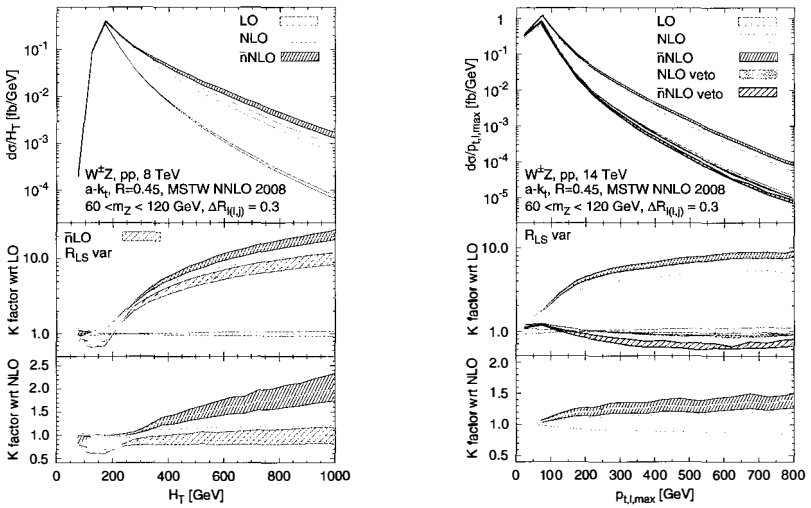

Figure 2: WZ production at the LHC. Differential cross sections and K factors for H_T, defined in Eq. (1), at $\sqrt{s} = 8\,\text{TeV}$ (left) and for the p_T of the hardest lepton at $\sqrt{s} = 14\,\text{TeV}$ (right). The bands correspond to varying $\mu_F = \mu_R$ by factors 1/2 and 2 around the central value. The cyan solid bands give the uncertainty related to R_{LS} varied between 0.5 and 1.5. The distribution is a sum of contributions from two unlike flavor decay channels.

variation than the NLO result. The latter indicates that the small scale uncertainty at NLO was partially accidental. Overall, these results clearly illustrate that the veto procedure should be used with great care as it has a non-trivial effect on the convergence of the perturbative series.

The W+jets process was studied with the cuts that match the ATLAS measurement.[5] The charged leptons were required to have $p_{T,\ell} \geq 20\,\text{GeV}$ and $|y_\ell| \leq 2.5$. The missing transverse energy had to be above $E_{T,\text{miss}} > 25\,\text{GeV}$. The transverse mass[5] of the W was required to be greater than 40 GeV. Only events with anti-k_t, R=0.4 jets with $p_{T,\text{jet}} > 30\,\text{GeV}$ and $|y_{\text{jet}}| < 4.4$ were accepted. Finally, for each jet, its distance to the lepton $\Delta R(\ell, \text{jet})$ had to be greater than 0.5, otherwise this jet was removed from the event. For the central value of the factorization and the renormalization scale, we chose $\mu_{F,R} = \frac{1}{2}\hat{H}_T = \frac{1}{2}\left(\sum p_{T,\text{partons}} + \sum p_{T,\text{leptons}}\right)$.

In Fig. 3 we show the differential distributions of the transverse momentum of the hardest jet (left) and the scalar sum of the traverse momenta of jets, leptons and missing energy, H_T (right), defined previously in Eq. (1). The results correspond $\sqrt{s} = 7\,\text{TeV}$ and are sums of contributions from W^+ and W^- for a single lepton decay channel $W \to \ell\nu$. The theoretical predictions, computed at LO, NLO and $\bar{n}$NLO, were corrected for non-perturbative effects.[5]

In the case of the p_T of the leading jet, we see a substantial reduction of scale uncertainty at $\bar{n}$NLO, while the result stays within the NLO band. Hence, that observable comes under control at $\bar{n}$NLO as no new channel or topologies appear at this order. We also note that the R_{LS} uncertainty is always smaller that the scale uncertainty and it decreases with increasing p_T. For the H_T distribution, the $\bar{n}$NLO result goes beyond the NLO uncertainty band for $H_T > 300\,\text{GeV}$ and the corrections are up to 30% with respect to NLO. The R_{LS} uncertainty is negligible above 300 GeV. The large $\bar{n}$NLO correction to H_T is a result of the third jet coming from the initial state radiation. This jet adds a small contribution to H_T but, because the spectrum is steeply falling, the enhancement in the distribution is substantial. Altogether, the $\bar{n}$NLO result, by including configurations with three partons in the final state, describes the H_T data significantly better than NLO.

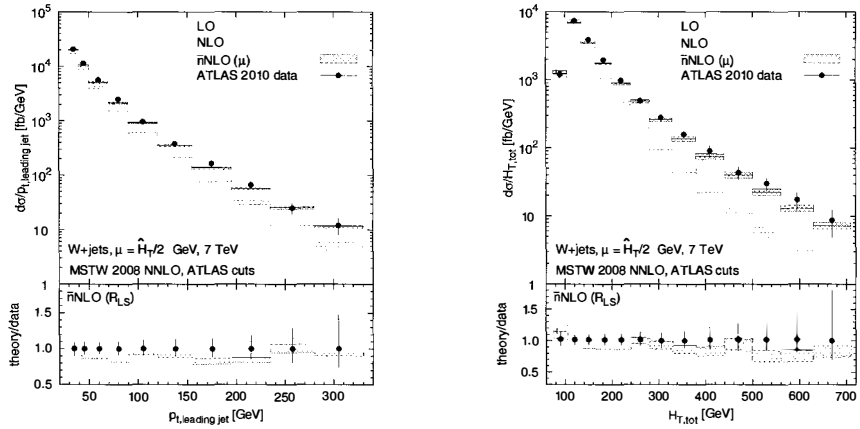

Figure 3: W+jets production at the LHC, $\sqrt{s} = 7\,\text{TeV}$. Differential cross sections as functions of the p_T of the hardest jet (left) and H_T (right) at LO, NLO and $\bar{n}$NLO. The theoretical results are corrected for non-perturbative effects and are compared to the ATLAS data. The bands correspond to varying $\mu_F = \mu_R$ by factors 1/2 and 2 around the central value. The cyan solid bands give the uncertainty related to R_{LS} varied between 0.5 and 1.5.

4 Conclusions

We used LoopSim together with VBFNLO and MCFM to compute approximate NNLO corrections to processes with vector bosons: WZ and W+jets production. Our results, referred to as $\bar{n}$NLO, are expected to account for the dominant part of the NNLO QCD corrections in some high p_T distributions.

In the case of WZ production, we found sizable effects due to $\bar{n}$NLO for a range of experimentally relevant observables: H_T, $p_{T,\ell,\text{max}}$, $E_{T,\text{miss}}$.[4] They all show non-trivial kinematic dependencies and go beyond NLO uncertainty bands. For W+jets, the H_T-type observables exhibit large $\bar{n}$NLO corrections. On the other hand, p_T of the leading jet, which gets large correction at NLO, nicely converges at $\bar{n}$NLO and shows significant reduction of scale uncertainty.

In conclusion, the QCD corrections beyond NLO to process with electroweak bosons are in many cases sizable and should be taken into account in precision studies as well as in searches for new physics.

Acknowledgments

We thank the organizers of the 48$^{\text{th}}$ Rencontres de Moriond for the opportunity to present these results and for financial support. The studies described here were performed in collaboration with Francisco Campanario, Daniel Maitre and Gavin Salam.

References

1. M. Rubin, G. P. Salam and S. Sapeta, JHEP **1009**, 084 (2010).
2. K. Arnold, J. Bellm, G. Bozzi, F. Campanario, C. Englert, B. Feigl, J. Frank and T. Figy *et al.*, *Comput. Phys. Commun.* **180**, 1661 (2009)
3. J. M. Campbell and R. K. Ellis, *Phys. Rev.* D **60**, 113006 (1999), `http://mcfm.fnal.gov`
4. F. Campanario and S. Sapeta, *Phys. Lett.* B **718**, 100 (2012)
5. G. Aad *et al.* [ATLAS Collaboration], *Phys. Rev.* D **85**, 092002 (2012).

8.
Structure, Function, Diffraction

Structure Functions and PDF determination at HERA

R. PLAČAKYTĖ
on behalf of the H1 and ZEUS Collaborations

Deutsches Elektronen-Synchrotron DESY,
Notkestr. 85, 22607 Hamburg, Germany.

Latest results on the measurements of the deep inelastic scattering (DIS) processes at HERA published by the H1 and ZEUS collaborations are presented in this report. The parton distribution functions (PDFs) of the proton extracted from the HERA data and the open source QCD framework for PDF determination, `HERAFitter`, are discussed here as well.

1 DIS ata HERA and recent measurements

The HERA (Hadron Elektron Ring Anlage) is the world's only ep collider operated in the years 1992-2007, with centre-of-mass energies $\sqrt{s} = 225 - 318$ GeV. Two different deep inelastic ep scattering processes are measured at HERA: neutral current (NC), $ep \rightarrow eX$, and charged current (CC), $ep \rightarrow \nu X$. NC reactions are mediated by the photon or a Z boson while in the CC scattering a $W^{\pm}$ boson is exchanged. The NC (and similarly CC) cross section can be expressed in terms of structure functions:

$$\frac{d^2\sigma_{NC}^{e^{\pm}p}}{dxdQ^2} = \frac{2\pi\alpha^2}{xQ^4}[Y_+\tilde{F}_2^{\pm} \mp Y_- x\tilde{F}_3^{\pm} - y^2\tilde{F}_L^{\pm}],$$

where $Y_{\pm} = 1 \pm (1-y)^2$ with y being the inelasticity. The structure function $\tilde{F}_2$ is the dominant contribution to the cross section, $x\tilde{F}_3$ is important at high Q^2 and $\tilde{F}_L$ is sizable only at high y. In the framework of perturbative quantum chromodynamics (QCD) the structure functions are directly related to the parton distribution functions, i.e. in leading order (LO) F_2 is the momentum sum of quark and anti-quark distributions, $F_2 \approx x\sum e_q^2(q + \bar{q})$, xF_3 is related to their difference, $xF_3 \approx x\sum 2e_q a_q(q - \bar{q})$. At higher orders, terms related to the gluon density distribution ($\alpha_s g$) appear.
In analogy to neutral currents, the inclusive CC ep cross section can be expressed in terms of structure functions. In LO the CC e^+p and e^-p cross sections are sensitive to different quark densities, i.e. $\tilde{\sigma}_{CC}^{e^+p} \approx x[\overline{u} + \bar{c}] + (1-y)^2 x[d + s]$ and $\tilde{\sigma}_{CC}^{e^-p} \approx x[u + c] + (1-y)^2 x[\overline{d} + \bar{s}]$.

Two collider experiments at HERA, H1 and ZEUS, have recently published their final measurements of the inclusive DIS data. Inclusive $e^{\pm}p$ single and double differential cross sections for NC and CC scattering processes are measured by the H1 experiment [1] using data with centre-of-mass energy of $\sqrt{s} = 319$ GeV and a total integrated luminosity of 333.7 pb^{-1} corresponding to the full second data taking period at HERA with longitudinal lepton polarisation (HERA II). The differential cross sections are measured in the range of negative four momentum transfer squared, Q^2, between 60 and 50 000 GeV^2, and Bjorken x between 0.0008 and 0.65. The measurements are combined with earlier published unpolarised H1 data and, among other things,

are used to determine the structure function $xF_3^{\gamma Z}$. The NC parity violating structure function $F_2^{\gamma Z}$ is measured for the first time and is show in figure 1 (left). The polarisation dependence of the charged current total cross section is also measured. The H1 measurements are well described by a next-to-leading order (NLO) QCD fit based on all published H1 inclusive cross section data which are used to extract the parton distribution functions of the proton.
The ZEUS collaboration has published the measurement of the NC cross sections for e^+p data collected in 2006-2007 years[2]. Together with the single and double differential NC cross sections, the structure functions $\tilde{F}_3$ and $F_3^{\gamma Z}$ (figure 1 right) were determined. This is the final ZEUS measurement of the inclusive cross sections from the HERA II period.

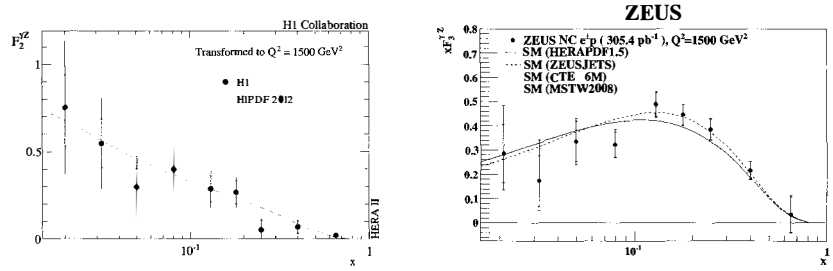

Figure 1: Left: structure function $F_2^{\gamma Z}$ transformed to $Q^2 = 1500$ GeV^2 for H1 data (solid points) and the expectation from the prediction obtained with H1PDF 2012 (solid curve). Right: structure function $xF_3^{\gamma Z}$ determined from ZEUS NC data and compared to the predictions using various PDFs.

2 HERA PDFs

A precise knowledge of the PDFs of the proton is essential in order to make predictions for basically any scattering processes at hadron colliders. This knowledge mainly comes from DIS at HERA, fixed target experiments and from TEVATRON while precise data from LHC also becomes increasingly important. The HERAPDFs are based only on HERA DIS data which allows the usage of the conventional χ^2 tolerance of $\Delta\chi^2 = 1$. Since this analysis is solely based on ep data, the PDFs do not depend on the approach for nuclear corrections needed for fixed target data.
In the HERAPDF1.0 fit [3], the combined set on NC and CC ep inclusive cross-sections for the first running period of HERA (HERA I) is used. A large fraction of the full statistics of the HERA inclusive CC and NC data are used for NLO and NNLO QCD fits resulting in HERAPDF1.5 [4]. Currently, the recently published H1 and ZEUS data presented in previous section are in the process of combination and will be used in the determination of new HERA PDF set (HERAPDF2.0).

For HERA PDFs the QCD predictions for the structure functions are obtained by solving the DGLAP evolution equations [5] at NLO (or NNLO) in the $\overline{MS}$ scheme with the renormalisation and factorisation scales chosen to be Q^2. PDFs are parametrised as a functions of x at the input scale Q_0^2 (chosen to be below the charm mass threshold) and for higher Q^2 are obtained through the DGLAP evolution equations. For the PDF parametrisation the generic form $xf(x) = Ax^B(1-x)^C(1+Ex^2)$ is used. The parametrised PDFs are the gluon distribution xg, the valence quarks xu_v, xd_v, and the u-type and d-type anti-quark distributions $x\bar{U}$, $x\bar{D}$ which at the starting scale are $x\bar{U} = x\bar{u}$ and $x\bar{D} = x\bar{d} + x\bar{s}$. The normalisation parameters A are constrained by the quark number sum-rules and momentum sum-rule, extra constrains for small-x behaviour of $d-$ and $u-$type quarks $B_{u_v} = B_{d_v}$, $B_{\bar{U}} = B_{\bar{D}}$ and $A_{\bar{U}} = A_{\bar{D}}(1-f_s)$ (f_s is the strange quark distribution) which ensures that $x\bar{u} \to x\bar{d}$ as $x \to 0$.

The break-up of the HERAPDF1.0 and HERAPDF1.5 into different flavours is illustrated in figure 2. Model uncertainties (shown as yellow bands) are evaluated by varying the input assumptions on Q^2_{min}, f_s, mass of heavy quarks m_C and m_B. Parametrisation uncertainties (green band) are formed by an envelope of the maximal deviation from the central fit varying parametrisation assumptions and therefore has an asymmetric shape. As it can be seen from the figure 2, the uncertainty bands in HERAPDF1.5 are smaller than in HERAPDF1.0 due to the inclusion of the more precise HERA II data.

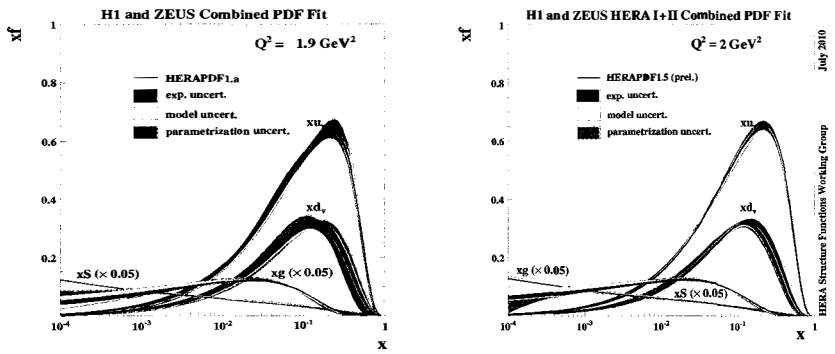

Figure 2: The parton distribution functions from HERAPDF1.0 (left) and HERAPDF1.5 (right) shown for $xu_v, xd_v, xS = 2x(\bar{U} + \bar{D}), x_g$ at $Q^2 = 1.9$ GeV^2. The gluon and sea distributions are scaled down by a factor 20. The different colour bands represent experimental, model and parametrisation uncertainties, respectively.

The effect of including the HERA charm production data in the PDF fits is studied and published in [6]. In this study, several implementations of the variable flavour number schemes (VFNS), which have different treatment of heavy quark mass terms in pQCD, are investigated. The different treatments can have different impact on the charm contribution to the sea quark and therefore affect the composition of $x\bar{U}(x)$ from the $x\bar{u}(x)$ and the $x\bar{c}(x)$ contributions. A combined NLO QCD analysis is performed using the charm production and the inclusive DIS data repeatedly for each VFN scheme with different values of the charm quark mass parameter, M_c. Figure 3 (left) shows the results of the M_c scan for all schemes considered. It is interesting to observe that first, different schemes have different optimal charm quark mass parameter M_c, and second, the χ^2 minimum values are comparable for all schemes despite of different optimal values of M_c.

The implications of this result on the NLO predictions for $W^{\pm}$ and Z production cross sections at the LHC are investigated by calculating the boson cross sections with PDF sets produced for each scheme at its optimal M_c. As an example, the W^+ cross section as a function of M_c is shown in figure 3. Good agreement between different predictions is observed at optimal M_c which results in a reduction of the uncertainties due to the heavy flavour treatment to below 2.0%.

The QCD analysis is also performed in the fixed-flavour-number-scheme at NLO and the running charm quark mass is determined: $m_c(m_c) = 1.26 \pm 0.05_{exp} \pm 0.03_{mod} \pm 0.02_{param} \pm 0.02_{\alpha_s}$ GeV.

The impact of the HERA inclusive jet data on PDFs (HERAPDF1.6 [7]) and inclusive DIS, jet, charm and low energy data together (HERAPDF1.7 [8]) were also studied but not discussed here.

HERAFitter project

`HERAFitter` project is an open source QCD fit framework designed for the extraction of PDFs and the fast assessment of the impact of the new data. The framework includes various modules and interfaces enabling a large number of theoretical and methodological options, as well as a large number of relevant data sets like inclusive cross sections from HERA DIS and fixed

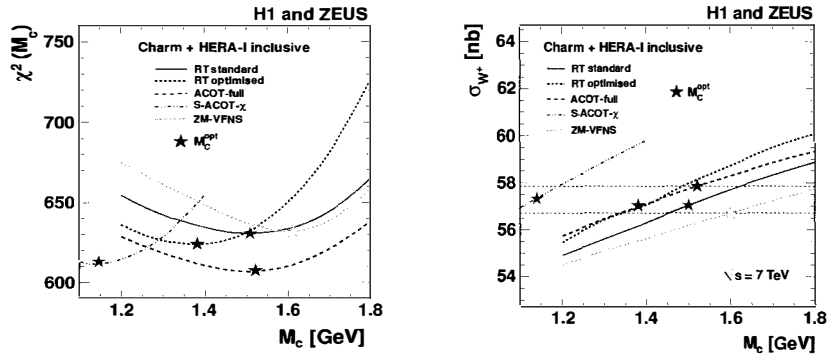

Figure 3: Left: Comparison of the χ^2 obtained by NLO fits to the inclusive HERA I and the preliminary combined charm data in different VFN schemes represented as lines of different styles. Right: W^+ production cross section σ_{W+} at the LHC for $\sqrt{s} = 7$ TeV as a function of M_c. Lines represent different schemes and the stars show the positions of the corresponding optimal M_c values obtained for each scheme.

target experiments, Drell-Yan, jet production data (ep, pp and $p\bar{p}$) and heavy quark structure functions. The structure functions may be computed in a variety of heavy quark schemes as well as the fixed flavour scheme. For the systematic uncertainty treatment of the experimental data there are several methods provided (Hessian, covariance matrix, Monte Carlo replicas).
The package is interfaced to different tools like FastNLO [9] and APPLGRID [10] for the fast input of NLO jet and Drell-Yan cross sections and HATHOR [11] for the calculation of the top cross sections. HERAFitter is under continues development and includes many useful additions. Basic plots are provided together with the fit result and the resulting PDFs are supported by the LHAPDF standards. This framework is actively used by LHC experiments.
In summary, HERAFitter contains all necessary ingredients to study the proton PDFs, it incorporates variety of different data processes and theory calculations, contains many useful tools and is an optimal platform for various benchmarking studies. More information and the package downloads can be found on the web site `http://herafitter.org`.

References

1. F. Aaron et al. [H1 Collaboration], *JHEP 1209* (2012) 061, [arXiv:1206.7007].
2. H. Abramowicz et al. [ZEUS Collaboration], *DESY 12-145*, [arXiv:1208.6138].
3. F. Aaron et al. [H1 and ZEUS Collaborations], *JHEP B* **1001** (2010) 109.
4. [H1 and ZEUS Collaborations], H1prelim-10-142, ZEUS-prel-10-018,
   [H1 and ZEUS Collaborations], H1prelim-11-042, ZEUS-prel-11-002.
5. V.N. Gribov, L.N. Lipatov, *Sov. J. Nucl. Phys.* **15**, 438, 675 (1972),
   G. Altarelli, G. Parisi, *Nucl. Phys.* B **126**, 298 (1977),
   G. Curci, W. Furmanski, and R. Petronzio, *Nucl. Phys.* B **175**, 27 (1980),
   W. Furmanski and R. Petronzio, *Nucl. Phys.* B **97**, 473 (1980),
   S. Moch, J. Vermaseren, and A. Vogt, *Nucl. Phys.* B **688**, 101 (2004)
   A. Vogt, S. Moch, and J. Vermaseren, *Nucl. Phys.* B **691**, 129 (2004).
6. H. Abramowicz et al. [H1 and ZEUS Collaborations], *Eur. Phys. J* **C73** (2013) 2311.
7. [H1 and ZEUS Collaborations], H1prelim-11-034, ZEUS-prel-11-001.
8. [H1 and ZEUS Collaborations], H1prelim-11-143, ZEUS-prel-11-010.
9. http://fastnlo.hepforge.org/
10. https://applgrid.hepforge.org/
11. M. Aliev et al., *Comput. Phys. Commun.* **182**, 1034, 2011, [arXiv:1007.1327].

PROGRESS IN THE NNPDF GLOBAL ANALYSIS

Christopher S. Deans
On behalf of the NNPDF Collaboration
Tait Institute, University of Edinburgh,
JCMB, KB, Mayfield Rd, Edinburgh EH9 3JZ, Scotland

We report on recent progress in the NNPDF framework of global PDF analysis. The NNPDF2.3 set is the first and only available PDF set with includes LHC data. A recent benchmark comparison of NNPDF2.3 and all other modern NNLO PDF sets with LHC data was performed. We have also studied theoretical uncertainties due to heavy quark renormalization schemes, higher twists and deuterium corrections in PDFs. Finally, we report on the release of positive definite PDF sets, based on the NNPDF2.3 analysis, specially suited for use in Monte Carlo event generators.

Introduction In this age of precision QCD at the LHC, the determination of the parton distribution functions which characterize the structure of the proton is becoming increasingly important. For some measurements the size of PDF uncertainties approaches that of experimental uncertainties. However, the LHC also offers a great opportunity to constrain PDFs. Some LHC observables important to PDFs have already been released using 2010 and 2011 data, and many others are now being analysed with the full 2012 data. NNPDF2.3 is the first and only publicly available PDF set which includes LHC data[1], extending the dataset from NNPDF2.1[2,3] with data on jet and electroweak boson production from the ATLAS, CMS and LHCb collaborations. The impact of the data was found to be moderate, but it will certainly increase with the release of more data with greater precision and including a wider range of different physical observables.

Here we will discuss recent work involving members of the NNPDF collaboration: a benchmarking of NNLO PDF sets, investigation of sources of theoretical uncertainties on PDF determinations, and the release of a NNPDF2.3 set for NLO Monte Carlo generators.

PDF benchmarking with LHC data An extensive benchmarking exercise comparing the modern NNLO PDFs was carried out in Ref. [4]. It benchmarked both PDFs and parton luminosities for NNPDF2.3, ABM11, HERAPDF1.5, CT10 and MSTW08, and also compared the predictions of these sets to LHC data both at the level of inclusive cross sections and of differential distributions. The comparisons to data were made quantitative using a variety of χ^2 estimators. The gluon–gluon luminosities for the PDF sets in the benchmark are shown as a ratio to NNPDF2.3 in Fig. 1 for $\alpha_S = 0.119$.

There is good agreement between the three global PDF sets (NNPDF2.3, MSTW08 and CT10), which is at least as good at NNLO as was previously found for NLO. For several LHC processes the combined PDF+α_S uncertainties determined from the envelope of MSTW, NNPDF and CT sets are found to be smaller in the 2012 PDF sets than for the 2010 sets. The HERAPDF1.5 central values also show good agreement with the global sets, with larger uncertainties due to the smaller dataset used. For ABM11, however, disagreement was found for several PDFs

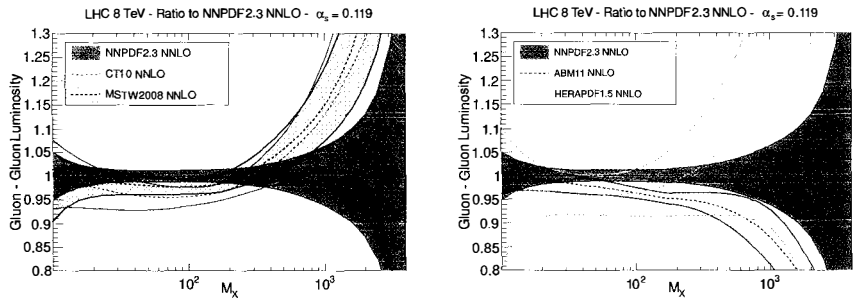

Figure 1: The gluon–gluon parton luminosity at $\sqrt{s} = 8$ TeV for $\alpha_s(M_Z) = 0.119$ as a function of the invariant mass of the final state M_X, for various NNLO PDF sets.

and LHC cross sections. Possible reasons for this disagreement are the use of an FFN scheme or the inclusion of higher twist corrections in ABM11, discussed below, but the situation will become more clear with the release of further precise LHC measurements, particularly top pair production[5].

Theoretical uncertainties in PDF analyses There has also been recent work on several theoretical issues in PDF determination and associated uncertainties which may have some impact on current PDF sets and explain some of the differences between them. In particular, Ref. [6] looked at the use of fixed-flavor number (FFN) versus variable-flavor number (VFN) renormalization schemes, higher twist corrections, and nuclear corrections. The analysis was performed in the NNPDF2.3 framework by performing fits with different theoretical assumptions and comparing the results, both in terms of PDFs and LHC cross sections.

The treatment of heavy quarks in PDF fits can potentially have a large impact on the results obtained[7]. Most modern PDF sets, including NNPDF2.3, use a variable flavor number scheme, where fixed order calculations including heavy quark masses are combined with all-orders resummation of contributions from perturbative evolution. Other sets, for instance ABM11, instead use a fixed flavor number scheme where the heavy quarks are not treated as active flavors and do not enter into QCD evolution equations. The effect of scheme dependence was studies by producing versions of the NNPDF2.3 global pdf fit using the FFN scheme, rather than the FONLL VFN which is the default[8a].

It was found that first of all the differences between FFN and VFN can be large, and in particular the use of a FFN leads to a suppressed large-x gluon distribution and increased medium and small-x quark distributions. The χ^2 fit quality for the two schemes was also studied, and it was found that FFN provides a systematically poorer description of the data, especially for the high-Q^2 and small-x HERA data, consistent with expectations given that the FFN scheme does not include the resummation of DGLAP logarithms in the PDF evolution which are potentially large in this kinematic region.

In Fig. 2 we show the $t\bar{t}$ total cross section computed at $\text{NNLO}_{\text{approx}}$ using `top++` for various PDF sets at $\sqrt{s} = 8$ TeV for a common value of $\alpha_s(M_Z) = 0.119$. Is clear that both the use of a reduced DIS-only dataset and of a FFN scheme bring NNPDF2.3 in better agreement with the ABM11 prediction.

Ref. [6] also looked at the impact of including corrections for higher twist and deuterium nuclear effects. Higher twist effects arise from power-suppressed contributions to the Wilson expansion, and whilst low-scale data most sensitive to these effects are commonly removed

[a]The NNPDF2.3 sets using the FFN scheme are available on the NNPDF hepforge webpage: `nnpdf.hepforge.org/`

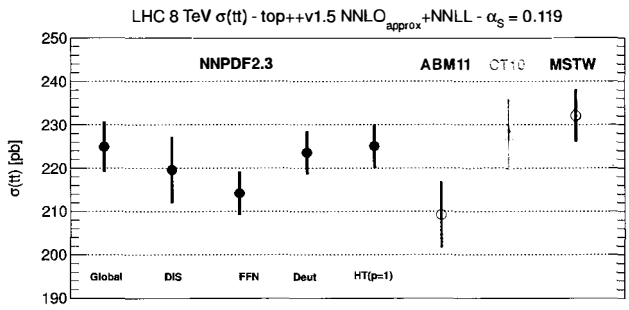

Figure 2: The $t\bar{t}$ computed at $\text{NNLO}_{\text{approx}}$ using various PDF sets at $\sqrt{s} = 8$ TeV for $\alpha_s(M_Z) = 0.119$.

by kinematic cuts, there may still be some residual effects. An NNPDF2.3 fit was performed with the leading twist DIS structure functions supplemented with a twist four correction taken from Ref. [9]. It was found that the inclusion of this correction had a negligible effect on the fit within uncertainties, and even when this size of these corrections were doubled the impact was marginal. Fits including nuclear corrections to structure function data on deuterium targets were also performed. Here the corrections do have a moderate impact, however it was limited to the large-x up-down separation. The $t\bar{t}$ total cross section for fits with higher twist and deuterium corrections are also show in Fig. 2, the differences for this particular observable are negligible.

Positive definite PDFs for Monte Carlo generators Parton distribution functions are not positive definite quantities beyond leading order, and thus some PDF groups allow for negative PDFs in their NLO and NNLO sets. This is the case in the NNPDF2.3 analysis, where instead the positivity of several physical cross sections is imposed as an additional constraint during the minimization. In practice, negative PDFs then arise only in phase space regions where experimental constraints on a given PDF combination are very scarce, such as the small-x gluon or the large-x antiquarks, and reflect the large PDF uncertainties in such extrapolation regions.

While there are no theoretical issues in dealing with negative PDFs in fixed order computations, some issues can arise in the context of Monte Carlo event generation. For instance, only positive PDFs can be used in the Sudakov form factors that determine the shower probabilities, and negative small-x PDFs may affect the description of the underlying event (UE) and of multiple interactions (MPI) in the event generator. In addition, there can also be practical issues, such as numerically inefficiencies when reweighting events starting from negative PDFs.

None of these issues are insurmountable. For instance the `Sherpa`[10] event generator includes tunes for the default NNPDF2.3 set, which correctly describe UE and MPI at hadron colliders, and NLO event generators such as `aMC@NLO` [11] provide exact PDF reweighting without the requirement of positive definite PDFs. In addition, it is a common practice to use separate PDFs for the hard matrix element and for the parton shower, since the latter includes the information from the non-perturbative tunes to the data.

Despite the absence of any conceptual issue, we believe it is useful for the community to have positive definite NLO NNPDF sets for use in event generators at the LHC. To achieve this, we have taken as a starting point the LHAPDF grids for various NNPDF2.3 NLO sets. In the interpolating grid for each PDF, any x, Q point which has a negative value is instead assigned a very small positive number. This defines the NNPDF2.3 MC PDF sets. It was also necessary to modify the LHAPDF wrapper of these sets to ensure that the output is positive definite in

any cases (to avoid negative interpolation between grid points).

Starting from LHAPDF v5.8.9, these Monte Carlo NNPDF2.3 NLO sets are publicly available. In Fig. 3 we show small-x gluon PDF (left plot) and the large-x $\bar{d}$ PDF (right plot), both at $Q^2 = 2$ GeV^2, from the `NNPDF23_nlo_as_0119_mc.LHgrid` PDF set. We have explicitly checked that the good χ^2 quality description of all datasets in the global PDF analysis is unaffected, which was expected given that the PDFs in the default sets only go negative in regions far from experimental constraints.

In summary, the NNPDF2.3 NLO MC PDF sets are positive definite PDF that are specially suited for their use in event generators, while maintaining the excellent description of all hard scattering data, and in particular of all relevant LHC data, which characterizes the default NNPDF2.3 sets.

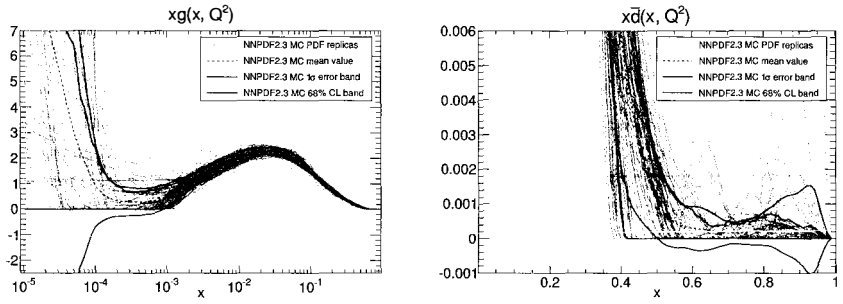

Figure 3: The small-x gluon PDF (left plot) and the large-x $\bar{d}$ PDF (right plot) at $Q^2 = 2$ GeV^2 in the `NNPDF23_nlo_as_0119_mc.LHgrid` PDF set. Each of the green lines is one PDF replica. As can be seen, in these NNPDF2.3 MC sets both the central values and the individual replicas are positive definite.

References

1. R. D. Ball, V. Bertone, S. Carrazza, C. S. Deans, L. Del Debbio, S. Forte, A. Guffanti and N. P. Hartland *et al.*, Nucl. Phys. B **867** (2013) 244 [arXiv:1207.1303 [hep-ph]].
2. R. D. Ball, V. Bertone, F. Cerutti, L. Del Debbio, S. Forte, A. Guffanti, J. I. Latorre and J. Rojo *et al.*, Nucl. Phys. B **849** (2011) 296 [arXiv:1101.1300 [hep-ph]].
3. R. D. Ball *et al.* [NNPDF Collaboration], Nucl. Phys. B **855** (2012) 153 [arXiv:1107.2652 [hep-ph]].
4. R. D. Ball, S. Carrazza, L. Del Debbio, S. Forte, J. Gao, N. Hartland, J. Huston and P. Nadolsky *et al.*, JHEP in press [arXiv:1211.5142 [hep-ph]].
5. M. Czakon, M. L. Mangano, A. Mitov, and J. Rojo, arXiv:1303.7215 [hep-ph].
6. R. D. Ball *et al.* [The NNPDF Collaboration], arXiv:1303.1189 [hep-ph].
7. R. Thorne, Phys. Rev. D **86** (2012) 074017 [arXiv:1201.6180 [hep-ph]].
8. S. Forte, E. Laenen, P. Nason and J. Rojo, Nucl. Phys. B **834** (2010) 116 [arXiv:1001.2312 [hep-ph]].
9. S. Alekhin, J. Blumlein and S. Moch, Phys. Rev. D **86** (2012) 054009 [arXiv:1202.2281 [hep-ph]].
10. T. Gleisberg, S. .Hoeche, F. Krauss, M. Schonherr, S. Schumann, F. Siegert and J. Winter, JHEP **0902**, 007 (2009) [arXiv:0811.4622 [hep-ph]].
11. R. Frederix, S. Frixione, V. Hirschi, F. Maltoni, R. Pittau and P. Torrielli, JHEP **1202**, 099 (2012) [arXiv:1110.4738 [hep-ph]].

TOWARDS AN UNBIASED DETERMINATION OF PARTON DISTRIBUTIONS WITH QED CORRECTIONS

Stefano Carrazza

On behalf of the NNPDF Collaboration
Dipartimento di Fisica, Università di Milano & INFN, Sezione di Milano
Via Celoria 16, I-20133 Milano, Italy

Electroweak corrections to hadron collider processes become relevant at the level of precision reached by present-day LHC experiments. We provide a preliminary discussion of the impact of electroweak corrections to parton distributions, concentrating on electrodynamics corrections to parton evolution equations, and showing a preliminary assessment of their impact. Furthermore, we determine the parton distribution function of the photon from deep inelastic scattering data using the NNPDF methodology.

Introduction

The inclusion of quantum elactrodynamics (QED) corrections to hadron collider processes, which in turns requires the determination of the photon parton distribution function (photon PDF) is motivated by the need for greater precision for LHC measurements, such as the W mass determination, high mass searches, WW production [1]. Moreover, a precise determination of the photon PDF is needed for a reliable computation of several new physics signals, such as the cross-section for Z' and W' production.

Here we will include QED corrections up to leading order (LO) in $\mathcal{O}(\alpha)$, to next-to-leading order (NLO, i.e. $\mathcal{O}(\alpha_s^2)$) QCD computations. This choice is motivated by the similar magnitude of $\alpha_s^2(M_Z^2)$ and $\alpha(M_Z^2)$, which suggests that LO QED corrections and NLO QCD corrections are of a similar size.

Even though our final goal is the computation of LHC processes, we start by determining the impact of QED corrections and the photon PDF from deep-inelastic scattering (DIS). In such case, the photon PDF obtained is determined indirectly by DGLAP evolution, because at LO in QED there are no photon-induced processes in DIS. Consequently, we expect the uncertainties of the photon PDF determined from DIS to be large. Further information on the photon PDF can be obtained from collider processes to which the photon contributes at LO, such as vector boson production. While we will present a first assessment of the impact of QED corrections on these processes, their inclusion in the determination of the photon PDF will be presented elsewhere.

PDFs evolution

The LO QED evolution equations[2,3] which are coupled to the standard QCD DGLAP are

$$Q^2\frac{\partial}{\partial Q^2}\gamma(x,Q^2) = \frac{\alpha(Q^2)}{2\pi}\left[P_{\gamma\gamma}(\xi)\otimes e_\Sigma^2\gamma\left(z,Q^2\right) + P_{\gamma q}(\xi)\otimes\sum_j e_j^2 q_j\left(z,Q^2\right)\right], \tag{1}$$

$$Q^2\frac{\partial}{\partial Q^2}q_i(x,Q^2) = \frac{\alpha(Q^2)}{2\pi}\left[P_{q\gamma}(\xi)\otimes e_i^2\gamma\left(z,Q^2\right) + P_{qq}(\xi)\otimes e_i^2 q_i\left(z,Q^2\right)\right], \tag{2}$$

where $\gamma(x,Q^2)$ and $q_i(x,Q^2)$ are respectively the PDF of the photon and the i-th quark flavor, $P_{ij}(\xi)$ are splitting functions, e_i the quark electric charge, and $e_\Sigma^2 = N_c\sum_i e_i^2$ the sum over all active quark flavors with $N_c = 3$. When combining QCD and QED evolution, PDFs satisfy the momentum sum rule

$$\int_0^1 dx\, x\left\{\sum_i q_i(x,Q^2) + g(x,Q^2) + \gamma(x,Q^2)\right\} = 1. \tag{3}$$

There are several methods to solve the combined QCD+QED DGLAP evolution equations, for example by finding a PDF basis which simultaneously diagonalizes the system as in Ref.[2]. We have developed a combined solution which optimizes the matching to the NNPDF implementation.

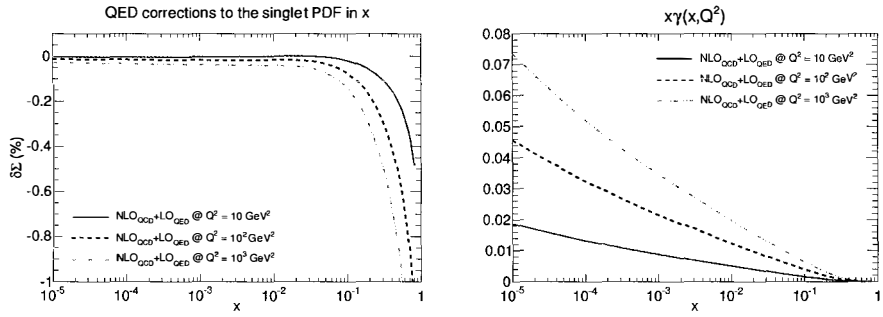

Figure 1: Impact of QED evolution on the singlet PDF, $\Sigma = \sum_i q_i$ when $\gamma(x,Q_0^2) = 0$ (left). The photon PDF generated dynamically at higher scales is shown on the right.

The effect of QED evolution on the singlet PDF is shown in the left plot of Figure 1, where the percentage correction to NLO QCD DGLAP evolution due to the inclusion of QED is shown for different scales Q^2, using as input the `Les Houches toy PDF`[4] and setting $\gamma(x,Q_0^2) = 0$ at the initial scale $Q_0^2 = 2$ GeV^2. We observe differences of the permille level at large-x, though effects are more pronounced at higher energies: LO QED corrections due to evolution are small, however the initial photon PDF has been so far assumed to vanish. The right plot of Figure 1 shows the photon PDF generated dynamically at energies above the initial scale $Q^2 > 2$ GeV^2.

Photon PDF from DIS data

With QED corrections to DIS included up to LO through QED evolution, we can now try to determine the photon PDF from a fit to DIS data. We use the DIS dataset included in the NNPDF2.3[5] determination, shown in the (x,Q^2) plane in Figure 2, which includes 2767 data points.

A consequence of the inclusion of QED corrections is isospin symmetry breaking: the neutron PDFs cannot no longer be obtained from the proton PDFs using isospin, i.e. $u^n \neq d^p$, $d^n \neq u^p$.

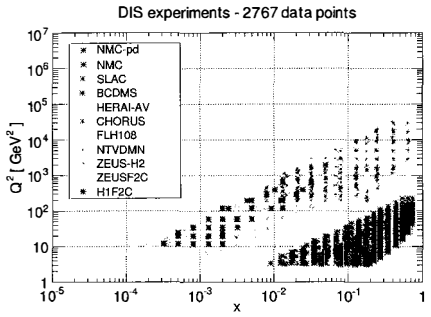

Figure 2: Kinematic coverage of the experimental DIS data used in the determination of the photon PDF.

However, we assume that isospin holds at the starting scale Q_0^2. It is then broken dynamically by DGLAP evolution.

In the NNPDF framework [5,6], we generate a set of Monte Carlo replicas of the data, then from each replica we extract a PDF set. The minimization is performed by a genetic algorithm and the best fit is determined by cross-validation. One of the most important advantages of this methodology is that it minimizes the bias related to the choice of functional form of PDFs. We parametrize the photon PDF, like all other PDFs, with a feed-forward neural network with 2-5-3-1 architecture, which corresponds to a total of 37 parameters to be determined during the minimization procedure. Positivity of the photon PDF at LO is imposed by squaring the output of the neural network. The rest of the procedure is the standard NNPDF one.

The photon PDF from DIS is showed in Figure 3, in logarithmic (left) and linear (right) scales. The plots show the central value, the 1-σ and the 68% c.l. uncertainties bands, defined around the mean value, and the 500 PDF replicas. The photon from DIS data is compatible with zero with large uncertainties. The photon PDF is less uncertain at central and large-x than at small-x, due to the lack of data points in this region (see Figure 2). The overall fit quality, as measured by the total χ^2 per data point, is $\chi^2 = 1.10$.

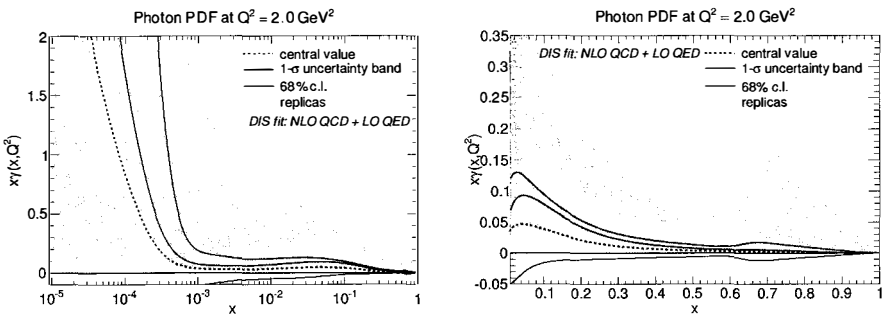

Figure 3: The photon PDF extracted from DIS data, NLO QCD + LO QED, at $Q^2 = 2$ GeV^2. The Monte Carlo PDF set includes 500 replicas.

The impact of the photon PDF from DIS

In order to understand the impact and the quality of the photon PDF just presented, we have computed $Z \to \mu^+\mu^-$ production in proton-proton collision at $\sqrt{s} = 14$ TeV with $|\eta^l| \leq 2.5$ and $p_T^l \geq 20$ GeV using `HORACE`[7], which is a Monte Carlo event generator for Drell-Yan processes including the exact 1-loop electroweak radiative corrections $\mathcal{O}(\alpha)$. `HORACE` also provides the possibility to

complement the $\mathcal{O}(\alpha)$ with photon initiated (photon-induced) processes at Born and NLO levels. The Born photon-induced contribution must be included at the order at which we are working. We have also included the NLO corrections, which however have a very small effect.

Figure 4 shows the Z invariant mass and the lepton p_T^l distributions, for 100 replicas and using the 68% c.l. uncertainty band. There is a moderate relative difference between $\mathcal{O}(\alpha)$ and $\mathcal{O}(\alpha)$ + photon-induced processes due to the photon PDF, in the region of the m_{ll} and p_T^l peaks, which rapidly increases when going away from the respective peaks. The increase of the central value is expected, in fact, for example at the Born level we are adding the $\gamma\gamma \to \mu^+\mu^-$ processes to the usual $q\bar{q} \to \mu^+\mu^-$, however also the uncertainties grow when going far from the peak region. These large uncertainties reflect the uncertainty in the photon PDF, which is insufficiently constrained by DIS data.

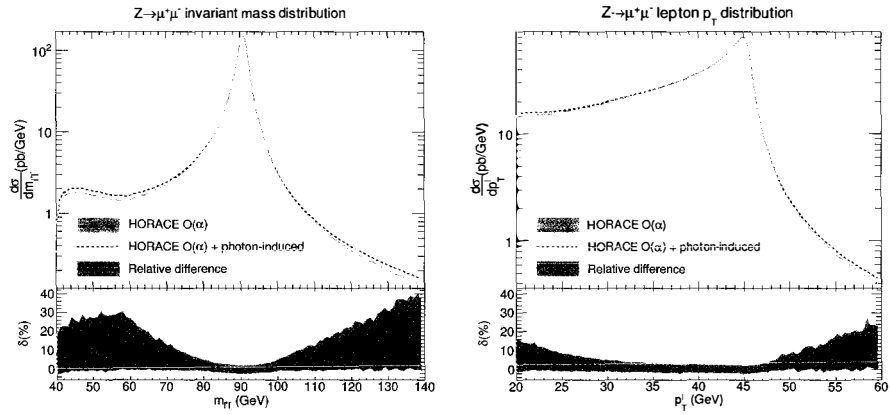

Figure 4: Z invariant mass and lepton p_T^l distribution computed using HORACE at $\sqrt{s} = 14$ TeV, with $|\eta^l| \leq 2.5$ and $p_T^l \geq 20$ GeV. Results to $\mathcal{O}(\alpha)$ with and without photon-induced contributions are compared.

Outlook

Our results show that the photon PDF is only poorly constrained by DIS data, especially at small-x. Corrections to Z production due to photon-induced processes in the presence of such a large unconstrained PDF off the peak become rapidly larger than the data allow. This suggests that these and similar data should be used to determine the photon PDF itself. This determination will be presented elsewhere.

References

1. G. Bozzi, J. Rojo and A. Vicini, Phys. Rev. D **83** (2011) 113008 [arXiv:1104.2056 [hep-ph]].
2. M. Roth and S. Weinzierl, Phys. Lett. B **590** (2004) 190 [hep-ph/0403200].
3. A. D. Martin, R. G. Roberts, W. J. Stirling and R. S. Thorne, Eur. Phys. J. C **39** (2005) 155 [hep-ph/0411040].
4. W. Giele, E. W. N. Glover, I. Hinchliffe, J. Huston, E. Laenen, E. Pilon, A. Vogt and S. Alekhin *et al.*, hep-ph/0204316.
5. R. D. Ball, V. Bertone, S. Carrazza, C. S. Deans, L. Del Debbio, S. Forte, A. Guffanti and N. P. Hartland *et al.*, Nucl. Phys. B **867** (2013) 244 [arXiv:1207.1303 [hep-ph]].
6. R. D. Ball *et al.* [NNPDF Collaboration], Nucl. Phys. B **855** (2012) 153 [arXiv:1107.2652 [hep-ph]].
7. C. M. Carloni Calame, G. Montagna, O. Nicrosini and A. Vicini, JHEP **0710** (2007) 109 [arXiv:0710.1722 [hep-ph]].

Vector Meson Production From Gauge/Gravity Duality

Miguel S. Costa
Centro de Física do Porto, Universidade do Porto, 4169-007 Porto, Portugal

Marko Djurić[a]
Centro de Física do Porto, Universidade do Porto, 4169-007 Porto, Portugal

Nick Evans
STAG Research Centre, Physics and Astronomy, University of Southampton, Highfield, Southampton, SO17,1BJ, UK

We use gauge/gravity duality to study the production of ρ, Ω, J/Ψ and ϕ mesons, in the limit of high center of mass energy at fixed momentum transfer, corresponding to the limit of low Bjorken x, where the process is dominated by the exchange of the pomeron. At strong coupling the pomeron is described as the graviton Regge trajectory, in AdS space, with a hard wall to mimic confinement effects. This is an extension of our previous work on deep inelastic scattering and deeply virtual Compton scattering. We compare our AdS/CFT calculations to experimental data collected at HERA, both for differential and exclusive cross sections.

1 Introduction

Vector meson production (VMP) is one of the diffractive processes studied in electron-proton collisions at HERA. It is conceptually similar to deeply virtual Compton scattering (DVCS), but instead of an outgoing photon a vector meson is produced. The vector mesons have the same J^{PC} values as the photon (i.e. 1^{--}), so the process is kinematically similar. The key difference comes from the vector mesons' structure functions. In the limit of high center of mass energy at fixed momentum transfer, corresponding to the limit of low Bjorken x, this process is dominated by the exchange of the pomeron Regge trajectory between the photon and the proton. Here we will study processes where the final state is a $\rho, \phi, J/\psi$ or Ω, and apply gauge/gravity duality methods. This is a continuation of our work presented at Moriond on DIS[1,2,3] and DVCS[4]. Due to the briefness of this note, very few details will be given, and we direct the interested reader to the aforementioned references, as well as the paper that this work is based on[18]. A number of authors [5,6,7,8,9,10,11] have studied vector meson production using the weak coupling analysis providing a decent fit to the data. More recently, the analysis in [12] uses AdS wave functions within a dipole approximation to fit ρ production. A new key aspect of our gauge/gravity duality description of VMP, in comparison with DIS and DVCS, will be to use a very simple holographic model for the vector mesons which gives the holographic wave function of the mesons as a function of their mass. These wave functions are normalisable modes of the AdS $U(1)$ gauge field dual to the electromagnetic current operator $j_f^\mu = \bar{\psi}_f \gamma^a \psi_f$. The meson wave functions are determined in terms of the scale z_f, but we fix this by the observed meson mass. The parameters we have in our model are the scale of the proton state, z_*, the intercept j_0 of the BPST[13] Pomeron, and g_0^2 which is determined by the coupling of the pomeron to the external states (and is therefore different

[a] speaker

for each vector final state). A fit to the data assuming the conformal propagator hence depends on three parameters and we find already a good fit. A fourth parameter can be introduced to represent confinement in the propagator, a hard-wall cut off at large $z_0 > z_f$. We also make fits including this adjustment and find a better overall χ^2 fit.

To compute the total cross section for vector meson production we need first to compute the following hadronic tensor

$$W_a{}^{\lambda}(k_j) = i \int d^4y\, e^{ik_1\cdot y} \langle k_3, \lambda; k_4 | j_a(y) | k_2 \rangle \,, \tag{1}$$

where λ is the polarization of the outgoing vector meson. Contracting with the polarization of the incoming photon, the amplitude for the transition between a photon of polarization λ and a vector meson of polarization λ' is given by

$$W^{\lambda\lambda'}(k_j) = (n^{\lambda})^a W_a{}^{\lambda'}(k_j) \,. \tag{2}$$

We will average over the incoming polarizations and sum over the final ones. The differential cross-section is then given by

$$\frac{d\sigma}{dt}(x, Q^2, t) = \frac{1}{16\pi s^2} \frac{1}{3} \sum_{\lambda,\lambda'=1}^{3} |W^{\lambda\lambda'}|^2 \,. \tag{3}$$

The different polarizations of the amplitude above can be shown to be represented by

$$W_{TT} = (n^{\lambda})^a\, W_a{}^{\lambda'}(k_j) = (\epsilon_{\lambda}\cdot\epsilon_{\lambda'})\, Qm\, W_1 \,, \qquad (\lambda, \lambda' = 1, 2) \tag{4}$$

$$W_{LL} = (n^{\lambda})^a\, W_a{}^{\lambda'}(k_j) = -Qm\, W_0 \,, \qquad (\lambda = \lambda' = 3) \tag{5}$$

where

$$W_n = 2is \int dl_{\perp}\, e^{iq_{\perp}\cdot l_{\perp}} \int \frac{dz}{z^3} \frac{d\bar{z}}{\bar{z}^3}\, \Psi_n(z)\, \Phi(\bar{z})\, \mathcal{B}(S, L) \,. \tag{6}$$

$\mathcal{B}(S, L)$ above is the propagator for Pomeron exchange in AdS, the Regge trajectory of the graviton. In this paper we are interested in the limit of large 't Hooft coupling $\lambda \gg 1$, but with sufficiently high energies such that $\sqrt{\lambda}/\ln S \ll 1$. In this limit all fields in the graviton Regge trajectory contribute to the amplitude [14], and we have

$$\mathcal{B}(S, L) = g_0^2 \left(1 + i \cot\left(\frac{\pi\rho}{2}\right)\right) (\alpha' S)^{1-\rho} \frac{e^{-\frac{L^2}{\rho \ln(\alpha' S)}}}{(\rho \ln(\alpha' S))^{3/2}} \frac{L}{\sinh L} \,, \tag{7}$$

where

$$\alpha' S = \frac{z\bar{z}s}{\sqrt{\lambda}} \,, \qquad \rho = 2 - j_0 = \frac{2}{\sqrt{\lambda}} \,, \qquad \cosh L = \frac{z^2 + \bar{z}^2 + l_{\perp}^2}{2z\bar{z}} \,. \tag{8}$$

$\Psi_n(z)$ and $\Phi(\bar{z})$ are functions of the external states, in this case

$$\Psi_n(z) = -\left(\sqrt{\frac{C\pi^2}{6}}\, z^2 K_n(Qz)\right) \left(\frac{\sqrt{2}}{\xi J_1(\xi)}\, z^2 J_n(mz)\right) , \Phi(z) = z^3 \delta(z - z_*) \,, \tag{9}$$

The first of these is a product of the incoming photon and the outgoing vector meson wave functions. They were found by solving the Maxwell equation, in the gauge $D_\mu A^\mu = 0$, given by $D^2 A_\mu = 0$. The photon corresponds to the non-normalizable mode, and the vector meson to the normalizable. To fix the asymptotic normalization of the mode we must impose a large z (IR) boundary condition on the solution. We simply include a "fermion hard-wall" at the scale $z_f \sim m_f^{-1}$ for each fermion flavour and impose Neumann boundary conditions on the field at the

wall. The value of z_f is phenomenologically fixed by the measured vector meson mass and the model contains no free parameters in the mesonic sector.

In equation (7) we use the Pomeron propagator in the conformal model. In the hardwall model, following [3], we use the approximation (with $\tau = \log(\alpha' S)$)

$$\chi_{hw}(\tau, l_\perp, z, \bar{z}) = C(\tau, z, \bar{z})\, D(\tau, l_\perp)\, \chi^{(0)}_{hw}(\tau, l_\perp, z, \bar{z})\,, \tag{10}$$

where

$$D(\tau, l_\perp) = \min\left(1, \frac{\exp[-m_1 l_\perp - (m_0 - m_1)^2 l_\perp^2/4\rho\tau]}{\exp[-m_1 z_0 - (m_0 - m_1)^2 z_0^2/4\rho\tau]}\right), \tag{11}$$

is an exponential cutoff at large $l_\perp$, known to be present asymptotically and determined by the first glueball masses m_0 and m_1, and

$$\chi^{(0)}_{hw}(\tau, l_\perp, z, \bar{z}) = \chi_c(\tau, l_\perp, z, \bar{z}) + \mathcal{F}(\tau, z, \bar{z})\, \chi_c(\tau, l_\perp, z, z_0^2/\bar{z})\,. \tag{12}$$

The function

$$\mathcal{F}(\tau, z, \bar{z}) = 1 - 4\sqrt{\pi\tau}\, e^{\eta^2} erfc(\eta)\,, \qquad \eta = \frac{-\log(z\bar{z}/z_0^2) + 4\tau}{\sqrt{4\tau}}\,, \tag{13}$$

is set by the boundary conditions at the wall and represents the relative importance of the two terms and therefore confinement.

2 Results

Using the above equations, we perform a fit to the data collected at HERA by the H1 collaboration [15,16], except for the Ω meson, where only ZEUS data is available[17]. In Table 1 we see a summary of all our fits. We show fits to the full cross-section and the differential cross-sections for each process. N labels the number of available data points.

		σ [nb]				dσ/dt [nb/GeV²]		
		ρ	φ	Ω	J/ψ	ρ	φ	J/ψ
	m [GeV]	0.77549	1.019445	0.78265	3.096916	0.77549	1.019445	3.096916
	N	48	27	6	38	35	21	84
Conformal	χ^2	0.92	0.60	0.0099	0.28	1.7	1.3	2.9
	g_0^2	4.6	1.8	0.53	0.62	1.6	0.25	0.56
	ρ	0.76	0.73	0.64	0.70	0.65	0.54	0.72
	z* [GeV^{-1}]	3.4	3.0	1.8	0.98	2.1	2.5	2.2
Hardwall	χ^2	0.88	0.61	0.015	0.30	1.7	1.4	1.8
	g_0^2	4.1	1.8	0.67	0.75	2.2	0.38	0.69
	ρ	0.76	0.73	0.66	0.71	0.69	0.59	0.75
	z* [GeV^{-1}]	3.6	3.6	1.5	0.87	2.2	2.5	2.4
	z_0 [GeV^{-1}]	4.8	4.4	7.3	5.3	7.7	8.6	4.6

Table 1: Output data for our fits.

We list the χ^2 per degree of freedom in the fit and the best fit values of the parameters. Firstly, the fits to the full cross-sections provide very good $\chi^2 < 1$ in all cases. Note the Ω

production fit is only to 6 data points. The best fit for the intercept $j_0 = 2 - \rho$ is in the range $0.64 < \rho < 0.76$ across the fits, which seems fairly stable, and consistent with the intercepts found in DIS [3] and DVCS [4]. The fits are less good than for the full cross-section data but still have $\chi^2 < 2$ in each case. To claim such a good fit for the J/Ψ meson we do need to include the hard-wall parameter z_0 and this is the only place in our fits where it makes a significant impact. For this process the momentum transfer energies t go as low as 0.05 GeV^2, which is already below the hard-wall cut off scale set by $1/z_0$. We therefore might need to improve the hard-wall model in order to obtain a better fit for this meson. We also note that these fits are not quite as good as the equivalent ones to DIS and DVCS data using the AdS methods, presumably reflecting the additional complication of fitting the mesonic wave functions holographically. In conclusion we find that the strong coupling AdS/CFT inspired model of low x vector meson production gives a very good fit to the data, providing further evidence for the strength of gauge gravity duality methods. Full details can be found in [18].

Acknowledgments

The authors are grateful to João Penedones and Chung-I Tan for helpful discussions. This work was partially funded by grants PTDC/FIS/099293/2008 and CERN/FP/116358/2010. *Centro de Física do Porto* is partially funded by FCT. The work of M.D. is supported by the FCT/Marie Curie Welcome II program. The research leading to these results has received funding from the [European Union] Seventh Framework Programme [FP7-People-2010-IRSES] under grant agreement No 269217.

References

1. L. Cornalba and M. S. Costa, *Phys.Rev.* **D78** (2008) 096010, arXiv:0804.1562 [hep-ph].
2. L. Cornalba, M. S. Costa, and J. Penedones, *Phys. Rev. Lett.* **105** (2010) 072003, arXiv:1001.1157 [hep-ph].
3. R. C. Brower, M. Djuric, I. Sarcevic, and C.-I. Tan, *JHEP* **1011** (2010) 051, arXiv:1007.2259 [hep-ph].
4. M. S. Costa and M. Djuric, *Phys.Rev.* **D86** (2012) 016009, arXiv:1201.1307 [hep-th].
5. A. Martin, C. Nockles, M. G. Ryskin, and T. Teubner, *Phys.Lett.* **B662** (2008) 252–258, arXiv:0709.4406 [hep-ph].
6. H. G. Dosch and E. Ferreira, *Eur.Phys.J.* **C51** (2007) 83–101, arXiv:hep-ph/0610311.
7. C. Marquet, R. B. Peschanski, and G. Soyez, *Phys.Rev.* **D76** (2007) 034011, arXiv:hep-ph/0702171 [HEP-PH].
8. A. Donnachie and P. Landshoff, arXiv:0803.0686 [hep-ph].
9. S. Fazio, R. Fiore, L. Jenkovszky, and A. Lavorini, *Phys.Rev.* **D85** (2012) 054009, arXiv:1109.6374 [hep-ph].
10. J. Berger and A. M. Stasto, *JHEP* **01** (2013) 001, arXiv:1205.2037 [hep-ph].
11. A. H. Rezaeian, M. Siddikov, M. Van de Klundert, and R. Venugopalan, *Phys.Rev.* **D87** (2013) 034002, arXiv:1212.2974 [hep-ph].
12. J. Forshaw and R. Sandapen, *Phys.Rev.Lett.* **109** (2012) 081601, arXiv:1203.6088.
13. R. C. Brower, J. Polchinski, M. J. Strassler, and C.-I. Tan, *JHEP* **0712** (2007) 005, arXiv:hep-th/0603115 [hep-th].
14. R. C. Brower, M. J. Strassler, and C.-I. Tan, *JHEP* **0903** (2009) 092, arXiv:0710.4378 [hep-th].
15. A. Aktas *et al.*, *Eur.Phys.J.* **C46** (2006) 585–603, arXiv:hep-ex/0510016 [hep-ex].
16. F. Aaron *et al.*, *JHEP* **1005** (2010) 032, arXiv:0910.5831 [hep-ex].
17. J. Breitweg *et al.*, *Phys.Lett.* **B487** (2000) 273–288, arXiv:hep-ex/0006013 [hep-ex].
18. M. S. Costa, M. Djurić and N. Evans, arXiv:1307.0009 [hep-ph].

Diffraction at HERA

Richard Polifka [a]
Charles University in Prague and University of Toronto
on behalf of H1 and ZEUS Collaborations

The latest results from the H1 and ZEUS experiments at HERA on the measurements of diffractive production are presented. Precision measurements of reduced diffractive cross sections are described, first measurements of longitudinal diffractive structure function and jet cross sections with a tagged leading proton are shown and the results are discussed in terms of diffractive parton densities and Regge factorisation.

1 Inclusive Diffraction

In the ep [b] high-energy collisions at HERA in the low x region of the deep-inelastic scattering (DIS), approximately 10% of all events are of type $ep \to eXY$, where the final state consists of two systems M_X and M_Y. The M_X system, which contains the products of the interaction with the photon emitted by the electron, is clearly separated from the system M_Y, which contains the outgoing proton or its low mass excitations, by a region without any energy flow (*Large Rapidity Gap*). These events are called diffractive. According to the Regge phenomenology, the event topology is explained in terms of exchange of an colourless object which carries quantum numbers of the vacuum, a *Pomeron.* Extensive measurements of inclusive DIS have been performed at HERA using two experimental methods of detecting diffraction - the *Large Rapidity Gap* (LRG) method [1] and the tagging of the outgoing proton (FPS and $VFPS$ for the H1 experiment, LPS for the ZEUS experiment) [2,3].

The diffractive kinematics is defined apart from the standard DIS variables Q^2 (the photon virtuality) and x_{bj} (the fraction of the momentum of the parton, which undergoes the interaction with the photon, to the momentum of the incoming proton) with the $x_{I\!P}$, β and t variables. The $x_{I\!P} = 1 - E'_p/E_p$ stands for the longitudinal proton momentum energy loss, $\beta (= x_{bj}/x_{I\!P})$, similarly to the X_{bj}, is defined as the momentum fraction of the interacting parton with respect to the Pomeron and t stands for the squared energy transfer at the proton vertex.

The inclusive cross section measurements are presented in form of the diffractive reduced cross section defined as

$$\sigma_r^{D(4)} = F_2^{D(4)} - \frac{y^2}{2(1-y+y^2/2)} F_L^{D(4)}. \quad (1)$$

The $F_2^{D(4)}$ is the diffractive structure function in Q^2, β, $x_{I\!P}$ and t, the $F_L^{D(4)}$ is the longitudinal diffractive structure function. The contribution of the $F_L^{D(4)}$ is assumed to be negligible in the low and medium y regions of the phase space. For the comparison between the two experimental methods the integration over t is performed, since the LRG method is incapable of the t measurement.

Fig. 1 presents the comparison of the two different experimental methods of the diffractive reduced cross section measurements within H1. The data show a good agreement and are consistent over a wide kinematical range.

[a] The work was supported by the grant SVV-2010-261 309.

[b] The lepton-proton scattering involves electrons as well as positrons, will be referred as electron-proton scattering in the following text

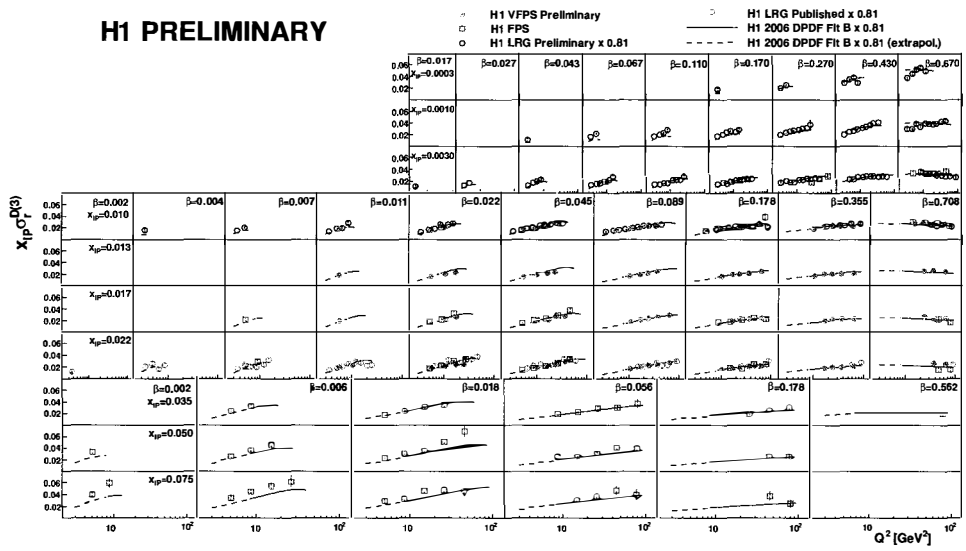

Figure 1: Compilation of diffractive reduced cross section measurements performed with the FPS, $VFPS$ and the LRG methods. The LRG data are corrected for proton dissociation by multiplication by a constant factor of 0.81.

The comparison of the H1 FPS and ZEUS LPS measurements is presented on the left side of Fig. 2 and the results are in agreement within 15% arising from the overall normalisation uncertainties. In order to gain in statistical and systematic precision of the measured data sets, a combination of H1 and ZEUS data was performed in the kinematical range of $|t|$ directly measurable by both detectors: $0.09 < |t| < 0.55$ GeV^2[21]. The Fig. 2 middle shows data sets used for the combination, on the right side of Fig. 2, the result of the combination compared with the individual measurements for bin of $x_{I\!P} = 0.05$ are presented. The improvement in the reduction of the total error is visible.

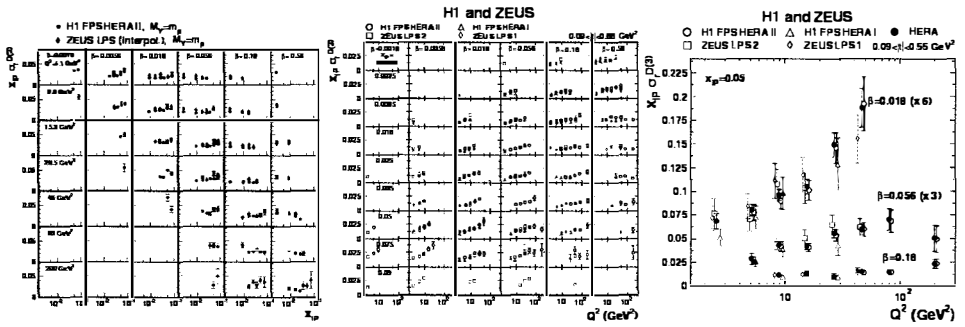

Figure 2: Comparison of the H1 FPS and the ZEUS LPS measurements of reduced diffractive cross sections measured in the kinematical range of $|t| < 1.0$ Gev^2 (left), in the restricted range of $0.09 < |t| < 0.55$ Gev^2 as used for the H1-ZEUS combination (middle) and the comparison of the combined data points with the individual measurements for bin of $x_{I\!P} = 0.05$.

The measurement of the longitudinal diffractive structure function F_L^D directly investigates the gluonic part of the exchanged object (Pomeron) and has to be perfomed in the kinematical domain of high y (see Eq. 1)[5]. Due to the relation $Q^2 = x_{I\!P}\beta ys$ in order to obtain different values of y for the fixed Q^2,$x_{I\!P}$ and β the central mass energy of the collision has to be changed. Special runs with medium ($E_p = 575\ GeV$) and low ($E_p = 460\ GeV$) proton beam energies have been dedicated to the

F_L and F_L^D measurements. Inclusive diffractive DIS reduced cross sections have been measured and the Rosenbluth plot [5] has been constructed in order to obtain the F_L^D (See Fig. 3).

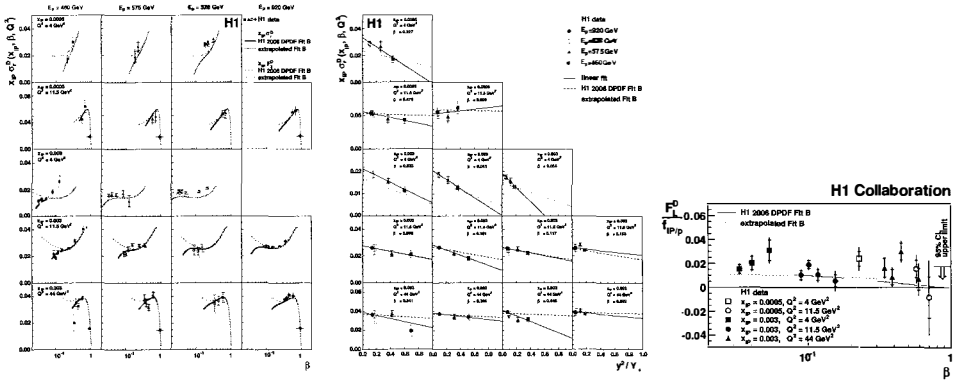

Figure 3: The σ_r for runs with different proton energies compared to the H1 2006 Fit B (grey), the Rosenbluth plots with the F_L^D as the slope of the linear fit (middle), F_L^D as a function of β. - UPDATE

2 Jets in Diffraction

It has been proved[6], that the diffractive cross section can be factorised into a hard process (due to the presence of the photon virtuality or high transverse momentum of the interacting parton, denoted as $d\hat{\sigma}^{ei}$) calculable within the pQCD framework and the diffractive parton distribution function f_i^D (DPDF) which has to be provided by the experiment:

$$d\sigma^{ep\to e'XY}(Q^2, |t|, M_Y, \beta, x_{I\!P}) = \sum_i f_i^D(Q^2, |t|, M_Y, \beta, x_{I\!P}) \otimes d\hat{\sigma}^{ei}(Q^2, \beta), \tag{2}$$

here the sum runs over all partons. Regge factorization (also called proton vertex factorization) is usually assumed in addition, where the dependence on the variables characterizing the proton vertex ($x_{I\!P}$ and t) factorizes from the hard interaction depending on β and Q^2: $f_i^D(Q^2, |t|, \beta, x_{I\!P}) = f_{I\!P/p}(x_{I\!P}, t) \cdot f_i(\beta, Q^2)$, where the $f_{I\!P/p}$ stands for the Pomeron flux and f_i is the probability of finding a parton i in the Pomeron. The quark densities within the Pomeron are well constrained by the inclusive diffractive DIS measurements ([2]), whereas a better constraint on the gluon density in the Pomeron is provided by measurement of jets in the final state. In addition, dijet measurements allow tests of perturbative QCD calculations, various models for modelling diffractive processes and serve as a tool for studying the parton evolution.

The measurements of central di-jet production with a proton measured in the *FPS*[7] and *VFPS*[8] spectrometers have been performed for the first time at HERA. The cross sections are corrected to the level of stable hadrons with a matrix (*FPS*) and bin by bin (*VFPS*) unfolding. They are compared to pNLO DGLAP QCD calculations, DPDF-based RAPGAP Monte Carlo, two-gluon Pomeron RAPGAP Monte Carlo and soft colour interaction (SCI) model as implemented in the LEPTO Monte Carlo. The left side of Figure 4 presents the comparison of the *VFPS* (data to NLO). The direct comparison of the *FPS* and *LRG* methods and the extension of the phase space for the *FPS* method is presented on the right side of Fig. 4. All methods agree well within errors, the *LRG* measurement is corrected for proton dissociation by a constant factor of 1.2.

A unique measurement of diffractive forward jets has been performed in order to search for the physics beyond DGLAP evolution equations [7]. The phase space defined by hard jet production collinear with the outgoing proton with transverse momentum squared of the same order as the photon virtuality suppress strongly the DGLAP evolution in favour to other models. The diffractive jet production with tagged elastic outgoing proton allows a clear signal of forward jets to be reconstructed. Within the

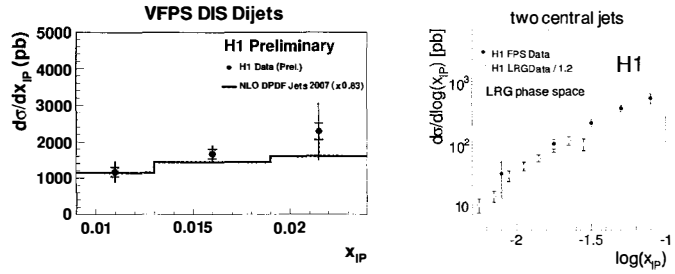

Figure 4: The single differential cross section measured in $x_{I\!P}$ with the VFPS method (left) and FPS and LRG method (right) as a fuction of $\log(x_{I\!P})$ (left). The VFPS data are compared to the hadron level corrected NLO-DGLAP predictions, the LRG dataset was corrected for proton dissociation with a constant factor of 1.2.

phase space accessible by the H1 detector the DGLAP evolution gives a good description of the production of one central and one forward jet as shown in Fig. 5.

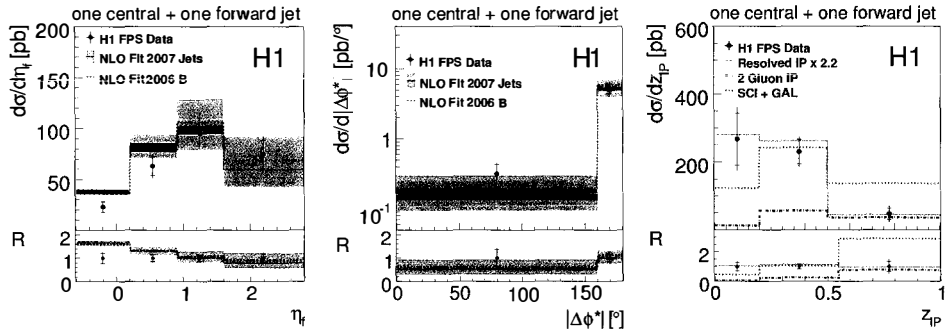

Figure 5: The sinlge differential cross section for the production of one central + one forward jet shown as a function of $z_{I\!P}$ (left) and $|\Delta\phi^*|$ (middle) compared to the NLO QCD DGLAP predictions based on DPDFs H1 2007 Jets and H1 2006 Fit B. Comparison of the cross section measured as a function of $z_{I\!P}$ with several MC models is on the right.

Further new measurements of diffraction at HERA include the production of exclusive vector mesons - J/Ψ by H1 [9] and Υ by ZEUS [10] and provide an interplay between soft and hard physics. They were not discussed due to lack of space.

References

1. C. Adloff *et al.* [H1 Collaboration], Z. Phys. C **76** (1997) 613 [hep-ex/9708016].
2. A. Aktas *et al.* [H1 Collaboration], Eur. Phys. J. **C 71** (2011) 1578 [arXiv:1010.1476].
3. ZEUS Collaboration, M. Derrick *et al*, Z. Phys. C **73**, 253 (1997).
4. F. D. Aaron *et al.* [H1 and ZEUS Collaborations], Eur. Phys. J. C **72** (2012) 2175 [arXiv:1207.4864 [hep-ex]].
5. F. D. Aaron *et al.* [H1 Collaboration], Eur. Phys. J. C **72** (2012) 1836 [arXiv:1107.3420 [hep-ex]].
6. J. Collins,Phys. Rev. **D 57** (1998) 3051; [Erratum-ibid. **D 61** (2000) 019902]; [hep-ph/9709499].
7. F. D. Aaron *et al.* [H1 Collaboration], Eur. Phys. J. **C 72** (2012) 1970 [arXiv:1111.0584].
8. H1prelim-11-013, available from http://www-h1.desy.de/h1/publications/htmlsplit/H1prelim-11-013.long.html
9. C. Alexa *et al.* [H1 Collaboration], arXiv:1304.5162 [hep-ex].
10. S. Chekanov et al [ZEUS Collaboration], *et al.* Phys. Lett. B **680** (2009) 4-12

New Model for Hadroproduction tested with DIS at HERA

A. A. Bylinkin
on behalf of the H1 Collaboration
Institute for Theoretical and Experimental Physics, ITEP, Moscow

Shapes of particle spectra observed in pp and $\gamma\gamma$ collisions are quite different as shown recently. This difference could be explained by a newly introduced phenomenological approach. Deep inelastic scattering at HERA is the unique possibility to study the change in hadroproduction dynamics predicted by this model. Therefore, charged particle production is measured in deep inelastic ep scattering at $\sqrt{s} = 225$ GeV with the H1 detector at HERA. The kinematic range of the analysis covers low photon virtualities, $5 < Q^2 < 10$ GeV^2, and medium to high values of inelasticity $y, 0.35 < y < 0.8$. The analysis is performed in the virtual γp centre-of-mass system. The charged particle production cross sections are investigated double-differentially as a function of pseudorapidity η^* and transverse momentum p_T^* in the range $0 < \eta^* < 3.5$ and $p_T^* < 10$ GeV.

1 Introduction

Inclusive charged particle distributions have been studied for a long time to understand the physics of hadron production at high energies. A large amount of experimental data on charge particle production spectra in baryon-baryon, γ-baryon and $\gamma\gamma$ collisions has been accumulated during last forty years. However, the underlying dynamics of hadron production in high energy particle interactions is still not fully understood. A detailed comparative analysis of charged particle spectra measured in different types of collisions could shed light on the hadroproduction mechanisms. Recently, a new unified phenomenological approach to describe the particle production spectra shape was proposed [1]. It was suggested to approximate the charged particle spectra as a function of the particles transverse momentum by a sum of an exponential (Boltzmann-like) and a power-law statistical distributions:

$$\frac{d\sigma}{p_T dp_T} = A_e \exp\left(-E_{Tkin}/T_e\right) + \frac{A}{(1 + \frac{p_T^2}{T^2 \cdot N})^N}, \tag{1}$$

where $E_{Tkin} = \sqrt{p_T^2 + M^2} - M$ with M equal to the produced hadron mass. The free parameters A_e, A, T_e, T, N are determined by fits to the data. The detailed arguments for this particular choice are given in [1] and are summarized in section 2. For the charged hadron spectra the mass of the hadrons is assumed to be equal to the pion mass.

The relative contribution of these terms is characterized by ratio R of the power-law term alone to the sum of both contributions integrated over p_T^2:

$$R = \frac{ANT^2}{ANT^2 + A_e(2MT_e + 2T_e^2)(N-1)} \tag{2}$$

It was found that the exponential contribution dominates the charged particle spectra in baryon-baryon collisions while it is completely absent in $\gamma\gamma$ interactions [1]. Moreover, the expo-

nential contribution is characteristic for charged pion production and is much less pronounced in kaon or proton (antiproton) production spectra[3,4].

2 Phenomenological model

The hadroproduction process in baryon-baryon high energy interactions could be decomposed into at least two distinct parts. These parts are characterized by two different sources of produced hadrons. The first one is associated with the baryon valence quarks and a quark-gluon cloud coupled to the valence quarks. Those partons preexist long time before the interaction and could be considered as being a thermalized statistical ensemble. When a coherence of these partonic systems is destroyed via strong interaction between the two colliding baryons these partons hadronize into particles released from the collision. The hadrons from this source are distributed presumably according to the Boltzmann-like exponential statistical distribution in transverse plane w.r.t. the interaction axis. The second source of hadrons is directly related to the virtual partons exchanged between two colliding partonic systems. In QCD this mechanism is described by the BFKL Pomeron exchange. The radiated partons from this Pomeron have presumably a power-law spectrum typical for perturbative QCD. Figure 1 shows schematically these two mechanisms of particle production in high energy (a) baryonic and (b) $\gamma\gamma$ collisions. Obviously, there are no thermalized partons preexisted long time before the $\gamma\gamma$ interactions. This simplified model explains the observed absence of the Boltzmann-like term in the spectra of hadrons produced in $\gamma\gamma$ collisions [1]. This explanation is qualitative, however.

Figure 1: Two different sources of hadroproduction in high energy (a) baryonic and (b) $\gamma\gamma$ collisions: red arrows - particles produced by the preexisted partons, green - particles produced via the Pomeron exchange.

This simple model is naive, though it allows for making a number of predictions which can be checked experimentally [4].

3 DIS at HERA

At HERA DIS processes are mediated by photon exchange. In the proposed hadroproduction model it is natural to expect that in γp interaction hadron production in the photon hemisphere of event produced at HERA shows similarity with that observed in $\gamma\gamma$ collisions. At the same time hadron production in the proton hemisphere of DIS events at HERA should resemble to what is measured in pp collisions. Therefore a change in the hadron production dynamics is expected at central rapidities of produced particles in γp centre-of-mass system.

Due to the strong asymmetry in the beam energies of electron (27.6 GeV) and proton (920 GeV) beams at HERA the previous inclusive hadron production measurements [5] had only limited access to the central rapidity region in the γp frame and, thus, the change in hadron production dynamics could be hardly observed [1]. However, it is likely to observe a transition in the hadron production dynamics in the rapidity region around central rapidity values where one could observe a smooth transition between two different types of the spectra shapes: one is characteristic to the photon and another to baryon regimes described above. The experimental challenge for such a measurement at HERA is the acceptance limitation for track measurements close to zero rapidity values in the γp centre-of-mass system. Figure 2 shows, that the maximal reach in the rapidity space towards the proton hemisphere at HERA could be obtained using a

set of the data collected with reduced proton beam energy. At the same time one should keep a selection of the ep events with high energy of the photon exchanged in these interactions. Thus, high values of inelasticity $0.35 < y < 0.8$ have to be chosen.

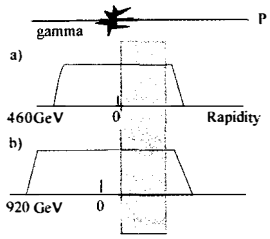

Figure 2: Charge particle rapidity distributions at HERA for (a) reduced ($E_p = 460GeV$) and (b) nominal ($E_p = 920GeV$) beam energies. Green area shows a typical coverage in rapidity space of the central tracking detectors at HERA experiments.

In 2007 the HERA ep-collider was operated at nominal electron beam energy ($E_e = 27.5$ GeV) and reduced proton beam energy ($E_p = 460$ GeV) during three months in which an integrated luminosity of 12.45 pb^{-1} has been collected. These data are used in the present analysis of the charged particle spectra shapes in the virtual γp rest frame as a function of rapidity.

4 Results and Discussions

The measured differential cross sections for central and forward fragmentation (photon direction) regions are shown in figure 3 together with the fit (1) respectively. A clear increase of the exponential contribution is observed at central rapidities.

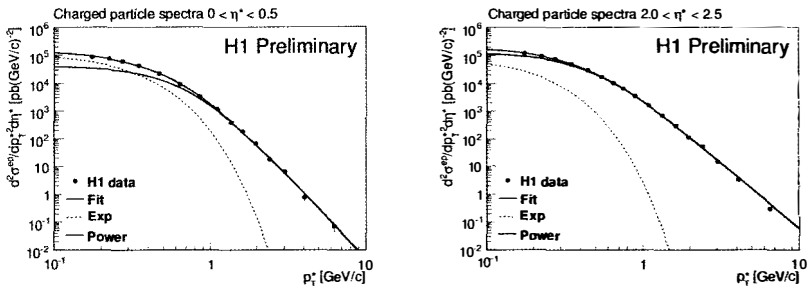

Figure 3: Charged particle double differential cross section together with the fits of the function (1) for central and forward regions respectively. The red line shows the exponential term and the blue one the power-law.

In figure 4 the relative contribution of the power-law type distribution to the charged particle production spectra is shown as function of charged particle rapidity (η^*) in the γp centre-of-mass system. This contribution is calculated according to equation (2) from fits of the function (1) to the H1 data. One could observe that the particles produced in the photon fragmentation region at high rapidity values are described by the power-law statistical distribution only. However, the data require a significant exponential (Boltzmann-like) contribution for particles produced centrally in the rapidity space. Moreover, the closer particles are produced towards the proton hemisphere the larger the exponential statistical contribution is required to be in order to describe the inclusive charged particle spectrum. Note, that in the pp interaction at about the same collision energy as here for γp at HERA the data require only about 30% of the

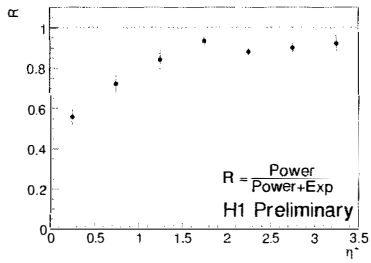

Figure 4: Power-law term contribution of (1) in charged particle spectra as function of pseudorapidity ($\eta*$).

power-law type contribution to the charged particle spectrum measured at central rapidities, while the residual 70% of the particle spectrum is described by the exponential contribution [1]. Thus, the H1 data support the hypothesis of the simple phenomenological model discussed that the particle production dynamics changes when approaching the proton hemisphere.

5 Conclusion

The first measurement of charged particle production spectra in ep collisions at reduced proton beam energy $E_p = 460$ GeV with the H1 detector in the γp centre-of-mass frame was performed. The kinematic range of the analysis covers low photon virtualities, $5 < Q^2 < 10$ GeV^2, and from medium to high values of inelasticity y, $0.35 < y < 0.8$. The differential cross sections of charged particle production are measured in the pseudorapidity region $0 < \eta^* < 3.5$ in seven bins. The shape of the measured transverse momentum distributions changes with η^*.

In order to investigate the change in hadroproduction dynamics with η^* the data are approximated by the recently introduced approach (1). This parameterization provides a much better description of the experimental data than those used traditionally [6]. Moreover, the observed change in the particle production dynamics when particle rapidity values approach the proton hemisphere in the rapidity space of DIS events, is rather well explained by this qualitative model.

Acknowledgments

We are grateful to the HERA machine group whose outstanding efforts have made this experiment possible. We thank the engineers and technicians for their work in constructing and maintaining the H1 detector, our funding agencies for financial support, the DESY technical staff for continual assistance and the DESY directorate for support and for the hospitality which they extend to the non DESY members of the collaboration. We would like to give credit to all partners contributing to the WLCG computing infrastructure for their support for the H1 Collaboration. We also thank Mikhail Ryskin for helpful phenomenological discussions.

References

1. A. A. Bylinkin and A. A. Rostovtsev, arXiv:1008.0332 [hep-ph]
2. G. Bocquet et al. (UA1 Collaboration), Phys.Lett.B366:434-440,1996
3. A. A. Bylinkin and A. A. Rostovtsev, Eur. Phys. J. C **72**, 1961 (2012) arXiv:1112.5734 [hep-ph]
4. A. A. Bylinkin and A. A. Rostovtsev, arXiv:1203.2840, 1205.4432, 1205.6382 [hep-ph]
5. C. Adloff *et al.* [H1 Collaboration], Nucl. Phys. B **485** (1997) 3 [hep-ex/9610006].
6. R. Hagedorn, Riv. Nuovo Cim. **6N10** (1984) 1.

One-loop multi-leg calculations in gauge theories: the Golem library

M. S. ZIDI

Laboratoire d'Annecy-le-Vieux de Physique Théorique (LAPTh), 9 Chemin de Bellevue, B.P 110, 74941 Annecy-le-Vieux, France

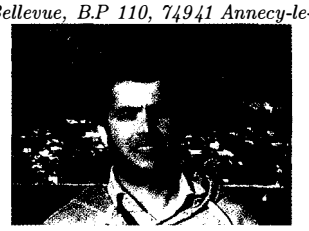

I present a program designed for the numerical evaluation of one-loop multi-leg scattering amplitudes. This program, called `Golem95`, is written in `FORTRAN-95`, and it contains all the form factors involved in one-loop calculations of amplitudes with up to six external legs, for arbitrary internal masses (complex masses are supported). This library is based on the traditional algebraic reduction (Golem reduction) of the form factors into a certain redundant set of basis integrals; this reduction formalism is able to avoid the problem of the Gram determinant spurious singularity. `Golem95` can be used to calculate one-loop amplitudes in the framework of an algebraic reduction approach, as well as in the framework of inspired-unitarity reconstruction of the amplitudes (`GoSam`) [1].

1 Introduction

Higher order corrections in gauge theories play a crucial role in studying physics within the standard model and beyond at TeV colliders, like Tevatron, LHC and ILC. Therefore, it is of extreme importance to provide a tool for next-to-leading order (NLO) computation which is fast, stable, efficient in a highly automated way.
In the last few years, an important progress in the automation of multi-leg one-loop scattering amplitude calculations have been made. Various programs and libraries have been developed for this task, many of them are publicly available.
The library of one-loop integrals is one of the main ingredient of any NLO automatic program. In this article, I present the `Golem95` library, which is a program written in `FORTRAN-95`, designed for one-loop calculations of amplitudes with up to six external legs, for arbitrary internal masses (complex masses are supported). This library is based on the traditional algebraic reduction (Golem reduction) of the form factors into a certain redundant set of basis integrals; this reduction formalism is able to avoid the problem of the Gram determinant spurious singularity ($\det(G)$). In addition, `Golem95` can be used to calculate one-loop amplitudes in the framework of inspired-unitarity reduction method, and it can be used as library of master integrals.

2 Golem algebraic reduction

The Golem reduction formalism [2, 3] is designed to express any one-loop N-point Feynman diagram, up to six external legs, as a linear combination in term of a set of redundant basic integrals and given coefficients without facing any inverse of Gram determinants. A general N-point tensor integral of rank r in dimension $n = 4 - 2\epsilon$ is defined as

$$I_N^{n;\mu_1,\ldots,\mu_r}(a_1,\ldots,a_r;S) = \int \frac{d^n q}{i\,\pi^{n/2}} \frac{q_{a_1}^{\mu_1}\cdots q_{a_r}^{\mu_r}}{\Pi_{i\in S}^N (q_i^2 - m_i^2 + i\,\delta)} \tag{1}$$

where $q_i = q + r_i$, q is the loop momentum, r_i is a combination of external momenta and m_i is the mass of the internal line "i", S is an ordered set containing the labels of the propagators.

2.1 Form factors

The tensor integral presented above can be expressed as a linear combination of such Lorentz tensors and scalar quantities "$A^{N,r}$, $B^{N,r}$, $C^{N,r}$" called form factors, i.e. it can be written in the following form

$$\begin{aligned} I_N^{n;\mu_1,\ldots,\mu_r}(a_1,\ldots,a_r;S) &= \sum_{j_1\cdots j_r\in S} [\Delta^{\bullet}_{j_1\bullet}\cdots\Delta^{\bullet}_{j_r\bullet}]^{\{\mu_1\cdots\mu_r\}}_{\{a_1\cdots,a_r\}} A^{N,r}_{j_1\cdots j_r}(S) \\ &+ \sum_{j_1\cdots j_{r-2}\in S} [g^{\bullet\bullet}\,\Delta^{\bullet}_{j_1\bullet}\cdots\Delta^{\bullet}_{j_{r-2}\bullet}]^{\{\mu_1\cdots\mu_r\}}_{\{a_1\cdots,a_r\}} B^{N,r}_{j_1\cdots j_{r-2}}(S) \\ &+ \sum_{j_1\cdots j_{r-4}\in S} [g^{\bullet\bullet}\,g^{\bullet\bullet}\,\Delta^{\bullet}_{j_1\bullet}\cdots\Delta^{\bullet}_{j_{r-4}\bullet}]^{\{\mu_1\cdots\mu_r\}}_{\{a_1\cdots a_r\}} C^{N,r}_{j_1\cdots,j_{r-4}}(S) \end{aligned} \tag{2}$$

the shift invariant vector Δ^{μ}_{ij} is defined as difference of the two propagator momenta q_i and q_j. $A^{N,r}$ is the coefficient of the Lorentz structure containing only these vectors. $B^{N,r}$ and $C^{N,r}$ are the coefficients of the Lorentz tensors containing one and two metric tensor, respectively. The square brackets $[\cdots]^{\{\mu_1\cdots\mu_r\}}_{\{a_1\cdots,a_r\}}$ are interpreted as the distribution of the r Lorentz indices μ_i, and the momentum labels a_i in all distinguishable ways to the vectors $\Delta^{\mu_i}_{ja_i}$ and the metric tensors. As an example, the scalar, the tensor of rank one and the tensorial of rank two N-point integrals can be written, respectively, in the following form

$$\begin{aligned} I_N^n(S) &= A^{N,0}(S) \qquad\qquad I_N^{n,\mu_1}(a_1;S) = \sum_{l\in S} \Delta^{\mu_1}_{l\,a_1}\, A^{N,1}_l(S) \\ I_N^{n,\mu_1\,\mu_2}(a_1,a_2;S) &= \sum_{l_1,l_2\in S} \Delta^{\mu_1}_{l_1\,a_1}\,\Delta^{\mu_2}_{l_2 a_2}\, A^{N,2}_{l_1 l_2}(S) + g^{\mu_1\,\mu_2}\, B^{N,2}(S) \end{aligned} \tag{3}$$

After Feynman parameterization, one can prove that any of these form factors can be expressed in term of integrals without Feynman parameters in the numerator called scalar integrals, and integrals with Feynman parameters in the numerator called tensorial integrals. These integrals can be reduced to some set of basic integrals using the traditional algebraic approach.

2.2 Reduction by subtraction

The scalar one-loop integral $I_N^n(S)$ is obtained from Eq. (1), by replacing the numerator by 1; this integral can be split into an IR and a finite part by making the ansatz

$$\begin{aligned} I_N^n(S) &= \sum_{i\in S} b_i(S) \int \frac{d^n q}{i\,\pi^{n/2}} \frac{(q_i^2 - m_i^2)}{\Pi_{j\in S}\,(q_j^2 - m_j^2 + i\,\delta)} + \int \frac{d^n q}{i\,\pi^{n/2}} \frac{1 - \sum_{i\in S} b_i(S)(q_i^2 - m_i^2)}{\Pi_{j\in S}\,(q_j^2 - m_j^2 + i\,\delta)} \\ &= I_{div}(S) + I_{fin}(S) \end{aligned} \tag{4}$$

the b_i are fixed in such way that this integral is reduced to an IR divergent integral in n-dimension with one less propagator I_{div}, and a finite integral in $n+2$-dimension with the same number of

propagators I_{fin}. By repeating this procedure several times, ultimately any Feynman diagram is expressed in term of integrals up to 4-point [a].

2.3 Basis integrals

Using Golem reduction formalism, the one-loop integrals and consequently the form factors are reduced to a set of redundant basic integrals. This set of integrals does not form a basis in the mathematical sense, but it contains the end point of our reduction. This reduction formalism plays a crucial rule on the numerical stability of `Golem95` in some region of phase space where the Gram determinant becomes arbitrary small; thanks to the choice of basic integrals which avoid these spurious Gram singularities.
It turns out that, the set of basic integrals that allows us to express any one-loop amplitude up to 6-external legs without producing any spurious Gram determinant singularities consists of the following scalar and tensorial integrals:

$$\{I_2^n(l_i;S), I_3^n(l_i;S), I_3^{n+2}(l_i;S), I_4^{n+2}(l_i;S), I_4^{n+4}(l_i;S)\}$$

l_i stands for Feynman parameters. This basis contains: the 4-point functions in $n+2$, which are IR and UV finite, the 4-point functions in $n+4$ dimensions which are UV divergent, the 3-point functions in $n+2$ dimensions, the 3-point functions in n dimension where all possible IR divergences are isolated, and various two point functions.

3 Avoiding spurious Gram singularities

A further reductions of the tensorial elements of Golem basis to a scalar integral leads to expressions containing inverses $\det(G)$ [b]. The philosophy of `Golem95` to avoid such spurious singularities is the following:
we provide for each basic integral, an analytical formula and a one-dimensional integral representation. The former representation is obtained by performing all the integrations analytically; and the later one is obtained by performing the first integrations analytically and keeping the last one, which will be performed numerically after modifying the integrand such that the inverse of Gram determinant is avoided.
Lets focus on the 4-point basic integrals. We notice that before modifying the integrand of the one-dimensional integral representation, we encounter terms have the following form:

$$\int dy \frac{\ln(1-F(y,x_\pm)+\sum_{i=1}^{m-1}\frac{F(y,x_\pm)^{m-i}}{m-i}}{F(y,x_\pm)^m}, \qquad m=1,2,3,4 \tag{5}$$

$x_\pm$ are the two solutions of a given quadratic equation, where the associated discriminant is proportional to the Gram determinant associated to the triangle (obtained by pinching a given propagator of the box) and $F(y,0)=0$. Since the box Gram determinant $\det(G) \propto x_+ x_-$, the function F vanishes if $\det(G)$ vanishes. This means that the term given in Eq.(5) is not any more numerically stable in this configuration. To deal with this problem, we write Eq.(5) in the following form

$$-\int dy \sum_{n=0}^{\infty} \frac{F(y,x_\pm)^n}{n+m} \tag{6}$$

This Taylor expansions provide a numerical stable results for $x_\pm \to 0$, hence for $\det(G) \to 0$.
To summarize, the strategy of Golem95 to avoid Gram determinant spurious singularities is:
- a) if $\det(G)$ is large, the basic integrals are evaluated analytically, which provide a fast and

[a] For $N=5$ and $N \geq 6$, the N-point finite parts I_{fin} are absent at one-loop order.
[b] For example, the redundant integral I_4^{n+2} can be expressed in term of the master integrals as the following:

$$I_4^{n+2}(S) = \det(S)/\det(G)\,[I_4^n(S) - \textstyle\sum_{i=1}^4 b_i\, I_3^n(S\setminus\{i\})] \propto 1/\det(G)$$

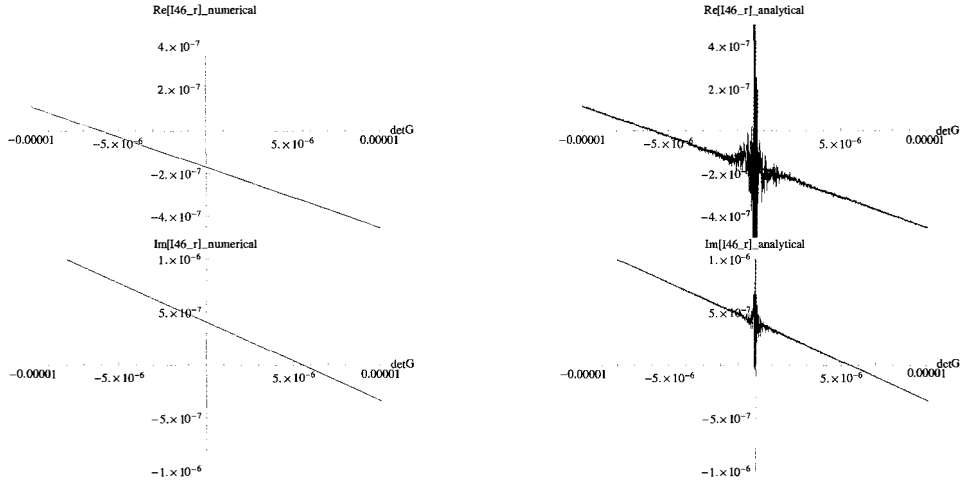

Figure 1: I_4^{n+2} versus $\det(G)$, Comparison of the numerical and the analytical modes

efficient numerical evaluation in large phase space region

- **b)** if $\det(G)$ is small, we switch to the numerical mode by integrating the one-dimensional representation of each basic integral numerically

In Figure 1, a comparison between the numerical and the analytical modes of evaluating the redundant basic integral $I_4^6(S)$. The two plots in the right hand side, represent the real (up) and the imaginary (down) parts of a normalized I_4^6 in the analytical mode, versus $\det(G)$. These plots show fluctuations of the function in the region $\det(G) \to 0$, which means that the result is not any more stable. However, in the numerical mode (plots in the left hand side represent the same function evaluation numerically) the function is smooth near and for $\det(G) = 0$, i.e. it is numerically stable.

4 Conclusion

I have presented the library `Golem95` for the numerical evaluation of tensor integrals up to 6-point functions, valid for arbitrary internal masses. The library is based on Golem reduction method to reduce the form factor to a certain set of basic integrals; this reduction formalism is able to avoid the problems occurring by spurious Gram singularities. The basic integrals are implemented in both analytical and one-dimensional integral forms; if the Gram determinant is large the program uses the former form, otherwise it switches to the numerical integration of the later form. `Golem95` can be used as a library of master integrals as the scalar integrals are related directly to form factors without Feynman parameters labels. It can be used also to calculate one-loop amplitudes in the framework of inspired-unitarity reduction (`GoSam`).

References

1. G. Cullen et al, *Automated One-Loop Calculations with GoSam*, Eur.Phys. J.C72: 1889, 2012, arXiv: 1111.2034.
2. T. Binoth et al, *An algebraic/numerical formalism for one-loop multi-leg amplitudes*, JHEP 0510 (2005) 015, arXiv:hep-ph/0504267.
3. T. Binoth et al, *Golem95: a numerical program to calculate one-loop tensor integrals with up to six external legs*, Comput.Phys.Commun. 180 (2009) 2317-2330, arXiv:0810.0992

9.
Summary Talks

MORIOND QCD 2013 EXPERIMENTAL SUMMARY

Dmitri Denisov
Fermilab, Batavia, IL 60510 USA

The article presents experimental highlights of Moriond 2013 QCD conference. This was fantastic conference and the first Moriond QCD since the discovery of the Higgs boson. Many new results about its properties have been presented at the conference with "Higgs-like" particle becoming "a Higgs" as it properties match expected for the Higgs boson pretty well. There were many new results presented in all experimental areas including QCD, electroweak, studies of the top, bottom and charm quarks, searches for physics beyond Standard Model as well as studies of the heavy ion collisions. 56 experimental talks have been presented at the conference and it is impossible to cover each result in the summary, so highlights are limited to what I was able to present in my summary talk[1] presented on March 16 2013. The proceedings of the conference cover in depth all talks presented and I urge you to get familiar with all of them. Theoretical Summary of the conference was given by Michelangelo Mangano, so theory talks are not covered in the article below.

1 Introduction

2013 Moriond QCD conference had many important experimental results presented. Many of them contribute to our understanding of the particle physics deeply from the extremely precise measurements of the fundamental constants to hints of new physics effects and phenomena. The results presented in most cases were obtained by large experimental collaborations and I would like to congratulate all of them with providing great advances for the experimental particle physics. All speakers did an excellent job with presentations in some cases presenting results which have been approved just a few hours before the talk. All of the above made 2013 Moriond QCD conference very exciting with talks eagerly awaited and many interesting and productive discussions during the conference.

The article is divided by the main topics which coincide with general themes of the conference established by the conference organizers: QCD, heavy ion physics, new physics searches, heavy flavor studies, studies of the top quark and at the end I'll summarize most recent results on a Higgs boson. As with all conferences by the time the proceedings are published many experimental results are superseded and/or improved. My summary will follow closely actual results and plots presented at the conference, so for the updates readers should go to the experimental collaborations Web sites, arXiv, and the refereed journals.

2 QCD

Parton scattering with production of jets is the most copious process at hadron colliders such as LHC and Tevatron. Fig. 1[2] presents general diagram of the scattering process highlighting parameters which could be extracted from the studies of jets. These studies include precision parton distribution functions determination critical for calculations of all cross sections at hadron colliders, measurement of the strong coupling constant as well as measurements of vast array of QCD processes to verify and improve QCD theoretical calculations and search for effects beyond those predicted by the Standard Model.

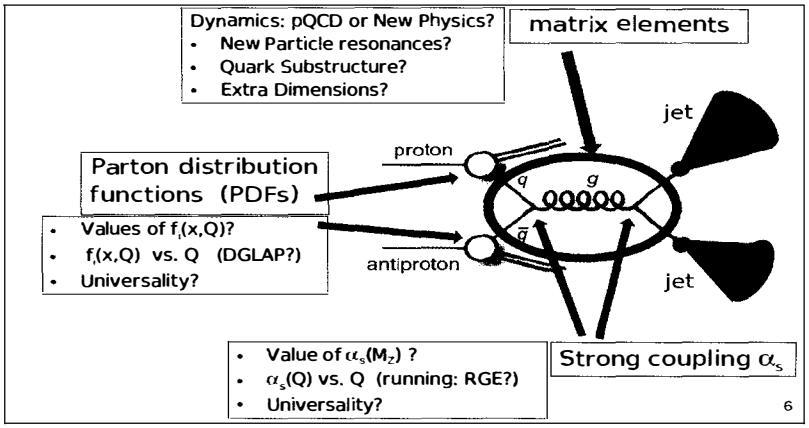

Figure 1. Diagram of a process with the production of a pair of jets and QCD parameters which could be extracted from studies of such process.

Tevatron experiments presented 100's of new measurements from di-jet production to studies of vector bosons production in association with jets. Over many orders of magnitude and up to energies of ~ 1 TeV QCD describes all measured distributions well. Jets studies at the LHC are now probing considerably larger phase space region in both Q^2 and values of x as demonstrated on Fig. 2[3]. Presented at the conference di-jet cross sections by CMS are shown on Fig. 3[3]. The span of the cross section measurements covers 10 orders of magnitude and is in

excellent agreement with modern QCD predictions in the wide range of jets rapidity and transverse momentum.

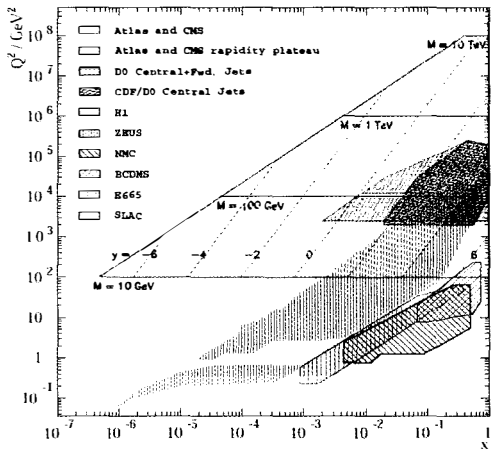

Figure 2. Range in Q^2 and x accessible for studies at different accelerators demonstrates unique capabilities of the LHC to study high Q^2 and low x processes.

These measurements is a clear indication that in the currently available for experiments kinematical range strong interactions between partons are well described by QCD. Higher energies, including 14 TeV LHC data coming in a few years, will be critical to find if any deviations from the QCD predictions exist at higher energies and accordingly smaller probed distances.

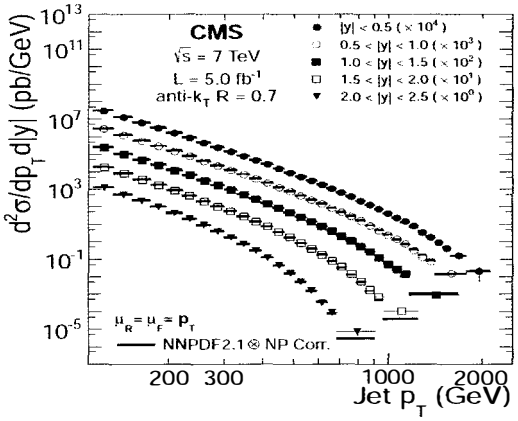

Figure 3. Inclusive di-jet cross section measurements at √s 7 TeV by the CMS experiment at the LHC.

Interesting result presented at the conference was extraction of the strong coupling constant from the ratio of 3-jets to 2-jets cross sections[2]. In such ratio many uncertainties, for example coming from the choice of PDFs, are greatly reduced in comparison with inclusive jet's studies. The results of this measurement provide value of α_s = 0.1191(+0.0048/-0.0071) where main uncertainty is due to factorization and renormalization scales. Same measurement provides first test of strong coupling constant running above ~0.2 TeV: new result from D0 indicates that α_s runs as expected all the way to 0.4 TeV as presented on Fig. 4a[2]. CMS, using higher energy LHC beams and similar method based on ratio of 3-jets to 2-jets cross sections improved Tevatron result as presented on Fig. 4b[3] demonstrating running of the strong coupling constant all the way to 1.0 TeV or ~$2 \cdot 10^{-16}$ cm. This result has fundamental importance as it provides test of QCD up to the smallest distances studied as of today.

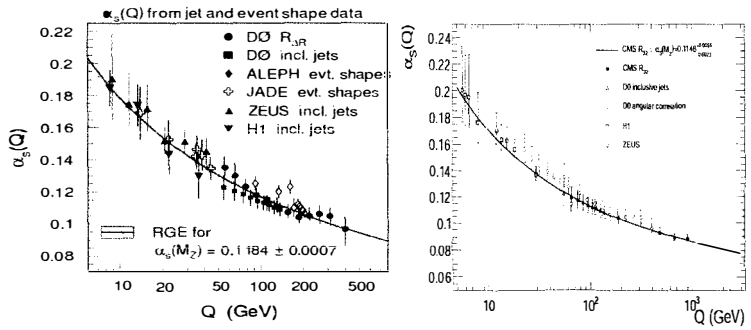

Figure 4. Results on the running of the strong coupling constant at the Tevatron (left, 4a) and at the LHC (right, 4b).

Expected increase in the LHC energy and relatively minor effect on high energy jets from multiple pp interactions will provide test of the running of the strong coupling constant at much smaller distances with LHC 14 TeV data.

Another area where many new results have been presented is studies of direct photons. In addition to testing QCD, probing gluon content of the proton, and understanding background to Higgs studies in two photons decay mode, these results provide unique information about fragmentation as well as test collinear and k_T factorization approaches and soft gluon logarithmic resummation techniques. Fig. 5[4] presents ATLAS results covering direct photon production between 0.1 and 1.0 TeV. Overall there is a good agreement with predictions. Expectation is that these direct photon results will improve gluon PDFs substantially decreasing theoretical error on the Higgs boson production and decay to a pair of photons by as much as 20%. Direct di-photon effective mass spectra are also well described by the theory, except for the masses below ~50 GeV where fragmentation process becomes important.

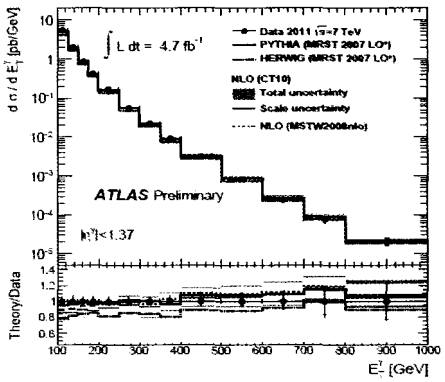

Figure 5. Direct photon production with the ATLAS experiment.

Among process under active experimental scrutiny is W/Z+jets production at the Tevatron and LHC. This process is critical not only for tests of QCD predictions, but as a background to top quark and Higgs boson studies (similar final states) as well as for improvements in PDFs. Large number of kinematic distributions have been obtained providing wealth of information for improvements in theoretical description of these processes. On Fig. 6a ATLAS experiment result[5] for studies of Z boson associated production with up to 7+ jets is presented.

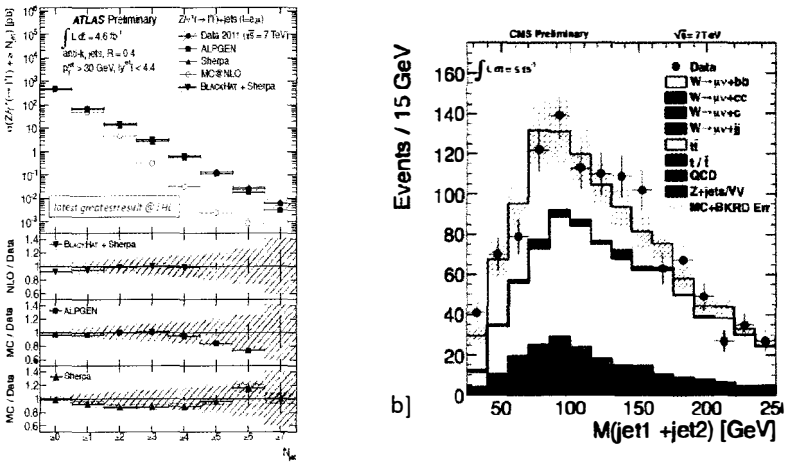

Figure 6. ATLAS studies of Z+jets production (left, 6a) and CMS studies of W+2 b-jets (right, 6b).

Results obtained demonstrate overall agreement with QCD calculations while in some kinematical regions modeling improvements are needed. CMS presented important measurement of W boson production in association with a pair of b-quark jets[5]. Both absolute value of the cross section and shape of the kinematic distributions are in a good agreement with predictions which is important for Higgs boson searches in the decay mode to a pair of b-quarks where associated production of W boson with heavy quark jets is among main backgrounds.

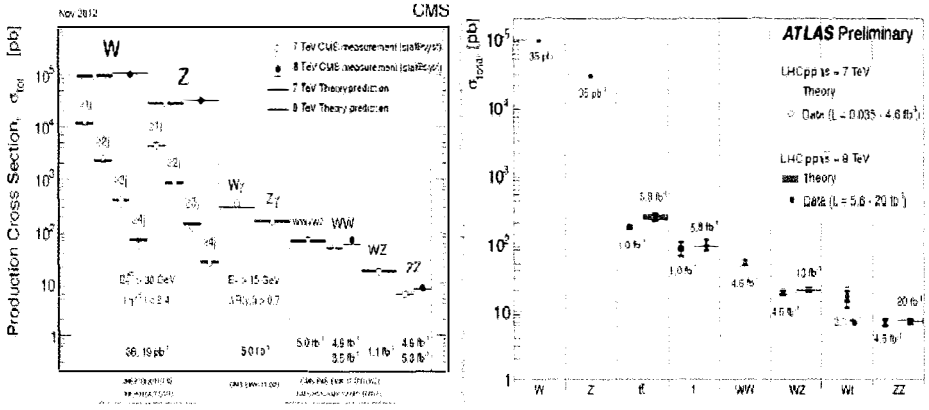

Figure 7. Cross sections of di-boson production as measured by CMS (left) and ATLAS (right).

Di-boson production (W/Zγ, WW, WZ and ZZ) is rare while clean process for tests of electroweak theory and perturbative QCD at TeV scale. These processes are also backgrounds to many channels of searches for physics beyond Standard Model as well as studies of a Higgs boson. Figure 7[6] presents studies of di-boson processes by ATLAS and CMS at the LHC. All cross section measurements as well as kinematic distributions (anomalous triple gauge boson couplings could greatly enhance high energy tails of the distributions) are in good agreement with theory predictions indicating that higher energy data are needed for detection of potential signs of new physics.

3 Heavy Ions

Studies of heavy ion collisions at the LHC and RHIC provide critical information to understand behavior of the quark-gluon plasma as well as properties of strongly interacting multiple partons. There is wealth of experimental information obtained recently. LHC provides world highest energy collisions between protons and Pb ions as well as PbPb collisions with up to $\sqrt{s}$ of 2.76 TeV per nucleon. RHIC collides different types of ions with energies in the $\sqrt{s}$ range between 7 GeV and 200 GeV per nucleon. With vast array of data not only properties of the quark-gluon plasma are studied, but the whole evolution of quark-gluon plasma is now

understood much better from the initial state conditions (including fluctuations), "perfect" fluid approach, and opaque properties of the plasma where hadronic processes are strongly quenched.

LHC heavy ion collisions provide access to new phase space due to substantially higher energy[7]. Energy density at the LHC reaches ~10 GeV/fm^3, volume ~4800 fm^3, lifetime 10 fm/c and temperature ~300 MeV. ALICE, ATLAS and CMS presented interesting new results in heavy ion collisions. Below some highlights of these studies are presented. By comparing production of different particles in pp and PbPb collisions important information about quenching of particles produced in quark-gluon plasma is obtained. On Fig. 8[8] results of CMS experiment on R_{AA}, or nuclear modification factor, vs type of the secondary particle and its transverse momentum, p_t, are presented. R_{AA} compares production of secondary particles in heavy ion collisions with similar final state in pp collisions.

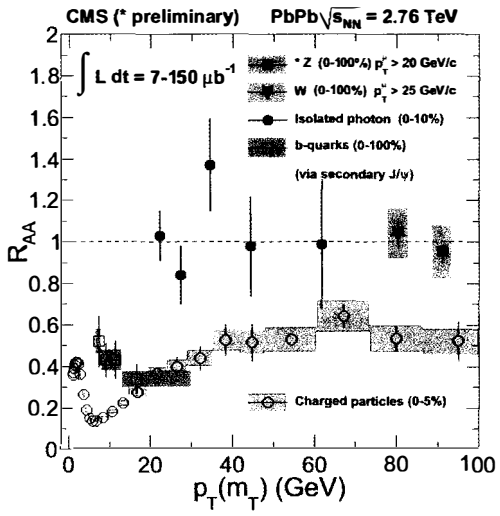

Figure 8. Nuclear modification factor measured for different types of particles by CMS collaboration at $\sqrt{s_{NN}}$ 2.76 TeV.

As clear from Fig. 8 particles which are not affected by strong interaction have R_{AA} close to 1.0 as they propagate through excited nuclear matter of quark-gluon plasma mainly without interactions. But for hadrons R_{AA} is well below 1.0 due to their interaction in the nuclear matter after production. These data are useful for the development of models of quark-gluon plasma.

Angular correlations between particles produced in heavy ion collisions are among key properties to understand quark-gluon plasma. Near side "ridge" have been observed by CMS[9] in

high multiplicity collisions in pPb collisions at $\sqrt{s_{NN}}$ of 5.02 TeV as illustrated in Fig. 9. This effect is similar to the effect observed in pp high multiplicity events and in heavy ion collisions. CMS presented many interesting properties of this effect including dependence on charged particles multiplicity and momentum selection.

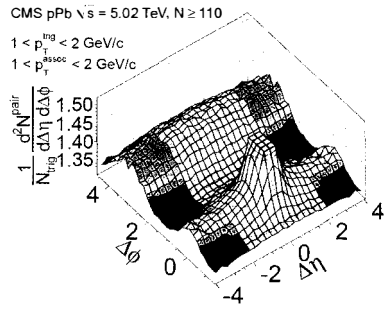

Figure 9. Ridge at $\Delta\varphi \sim 0$ observed by the CMS collaboration in pPb collisions at $\sqrt{s_{NN}}$ of 5.02 TeV.

New result[10] was presented by the ALICE experiment at the LHC on angular correlations in pPb collisions and is presented on Fig. 10. All pPb collisions were separated into classes, depending on the charged particles multiplicity with events in 0-20% range been highest multiplicity and in 60-100% range lowest multiplicity. No $\Delta\varphi \sim 0$ ridge is observed in low multiplicity events (similar to pp collisions). But if low multiplicity events distribution is subtracted from high multiplicity "double ridge" structure appears as presented on Fig. 10. Many double ridge properties are studied, while explanation of its origin is yet to come.

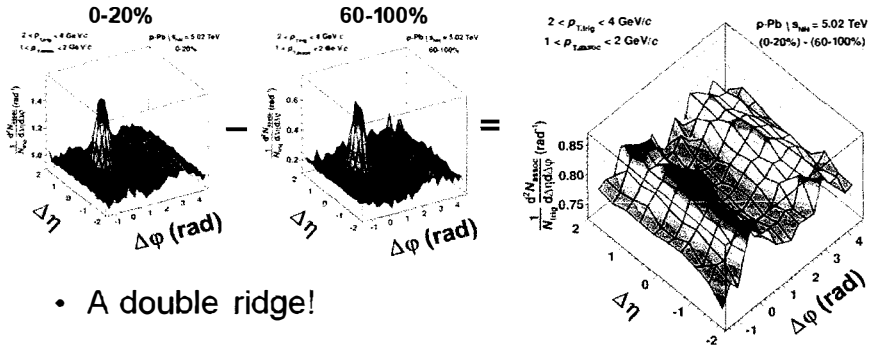

Figure 10. ALICE observation of the "double ridge" structure.

Many other exciting results from heavy ion experiments have been presented adding invaluable data to understand dense and hot quark-gluon plasma state of the nuclear matter.

4 Searches for New Physics

There are good experimental and theoretical reasons to believe that Standard Model is not complete description of the Nature, so searches for physics effects and new particles beyond those known today is among key priorities for high energy physics. Most natural place to look for new physics is at the energy frontier accelerator where particles with highest masses could be produced. Large number of new physics searches has been presented by the ATLAS and CMS experiments many using full 2012 LHC data set collected at the center of mass energy of 8 TeV.

One of the most attractive new physics models is Supersymmetry (SUSY) which predicts super-symmetric particle for each particle of the Standard Model. While some properties of these particles are predicted, mass scale is not well defined, so searches in the largest accessible phase space are required. ATLAS and CMS experiments both presented many new results at the conference on SUSY searches. Searches are usually divided into strongly produced 1st and 2nd generation scalar quarks and gluinos, 3rd generation scalar quarks (key ingredient in natural SUSY) as well as electroweak production of gauginos and sleptons.

Fig. 11a presents ATLAS result[11] in searches for inclusive squarks and gluinos produced via strong interaction. No excess events are observed in the performed searches and very stringent limits on the masses of SUSY particles have been set: up to ~1.6 TeV for gluino and ~3 TeV for squarks. On the Fig. 11b[12] experimental limits on the masses of stop quark by the ATLAS experiment are presented with exclusion now reaching masses in the 600-700 GeV range. Strict limits on SUSY were presented by the CMS collaboration as well[11,12].

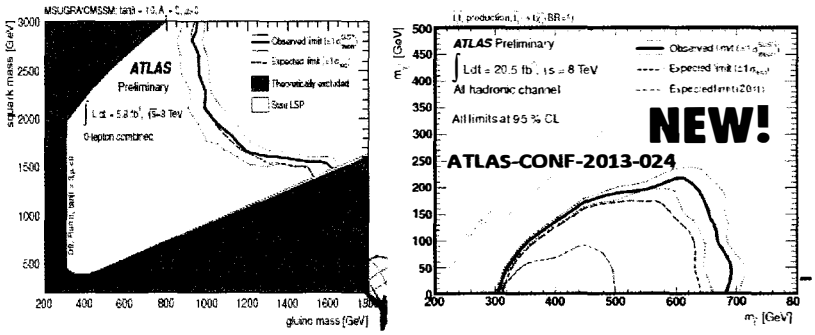

Figure 11. Squark and gluino mass exclusion plot from ATLAS experiment (left plot, 11a). Newest results on stop quarks mass exclusion (right plot, 11b).

An interesting discussion during the conference was devoted to the question "Is SUSY dead?" as searches over ~30 years with ever increasing sensitivity and mass range produced no indication of it existence. In addition to the direct searches there are many indirect searches of SUSY which for now produce "no observation" and in many cases provide strict limits including at high masses. On Fig. 12[13] constrains from direct searches and indirect searches are combined providing (blue points) remaining allowed areas of phase space for CMSSM SUSY particles. It is clearly becoming rather restricted! Conclusions of the discussion about SUSY viability could be summarized as follows:

1. Phase space for SUSY is strongly constrained by direct and indirect searches.
2. Due to ~125 GeV Higgs mass, SUSY particles masses are "multi-TeV" and not yet probed directly.
3. Input from searches, not only at accelerators, but, for example, cold dark matter searches, are important to take into account.
4. It is important to continue searches of both direct and indirect manifestations of SUSY particles, especially with LHC energy of 14 TeV.

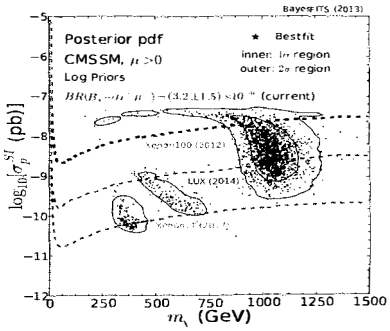

Figure 12. Combination of direct and indirect SUSY (CMSSM version) searches.
With expected by 2017 cold dark matter Xenon experiment sensitivity practically all remaining allowed phase space of CMSSM could be excluded.

In addition to "model specific" searches many generic "bump hunting" searches are progressing actively at the LHC. Among those which brought fundamental discoveries in the past (like discovery of the b-quark) are searches for peaks in effective mass spectra of a pair of objects such as leptons, photons or jets. On Fig. 13[14] results of resonance searches in di-electron mass spectra are presented. Excellent energy resolution of LHC detectors and well understood backgrounds provide an opportunity to set limits on such particles as Z' all the way to ~ 3 TeV as no excess events in comparison with Standard Model predictions are observed.

The observed di-lepton mass spectra (or similar quantities when lepton and missing transverse energy are studied) are used to set stringent limits on many different models including extra dimensions, excited leptons, heavy W' bosons and others.

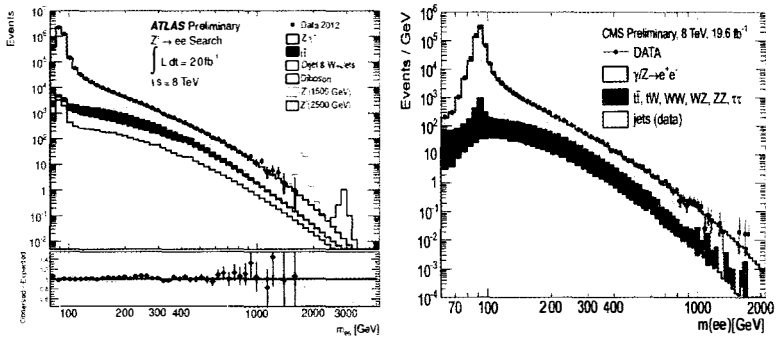

Figure 13. Search for heavy resonances in di-electron spectra by ATLAS and CMS experiments.

Searches for resonances decaying into a pair of jets provide access to the highest masses studied. With available statistics masses up to ~1/2 of the LHC center of mass energy are investigated. On Fig. 14[15] ATLAS and CMS results on searches for di-jets resonances are presented which demonstrate very good agreement with the Standard Model predictions up to the highest masses probed.

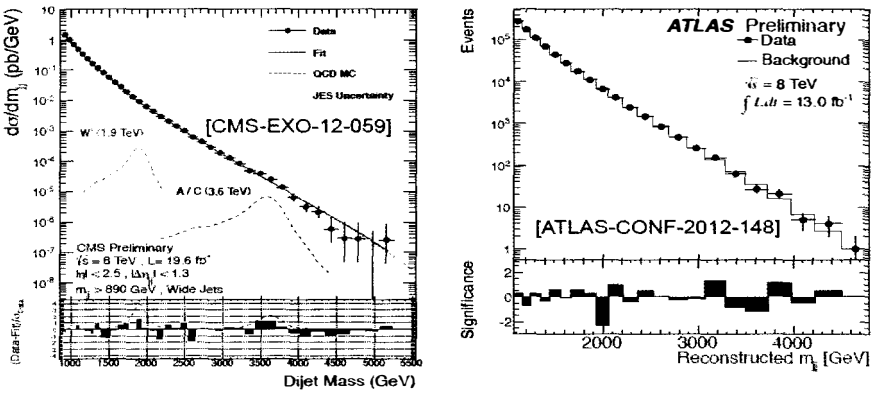

Figure 14. Search for the di-jet resonances by the CMS and ATLAS experiments.

Limits on the mass of the objects decaying to a pair of jets, such as excited quarks, are set at ~ 4 TeV. These searches demonstrate in turn excellent predictions of QCD up to the highest masses studied.

Summary[16] of the LHC experiments searches for new physics are presented on Fig. 15 (ATLAS) and 16 (CMS). With wide array of different searches and masses of objects probed reaching ~10 TeV no hints of beyond Standard Model physics have been seen with 8 TeV LHC data. As major factor in improving reach for new physics (using established methods) is increase in collision energy we will most probably have to wait for 14 TeV LHC data in about 2015 to substantially improve direct searches for new physics at the energy frontier.

There were interesting results on low energy searches for new physics presented at the conference[17,18,19]. They include such important studies as searches for low mass dark matter candidates and rare decays which are enhanced by physics beyond Standard Model. None of these searches indicate excess of events predicted beyond known backgrounds and produce stringent limitations on the theoretical models of new physics.

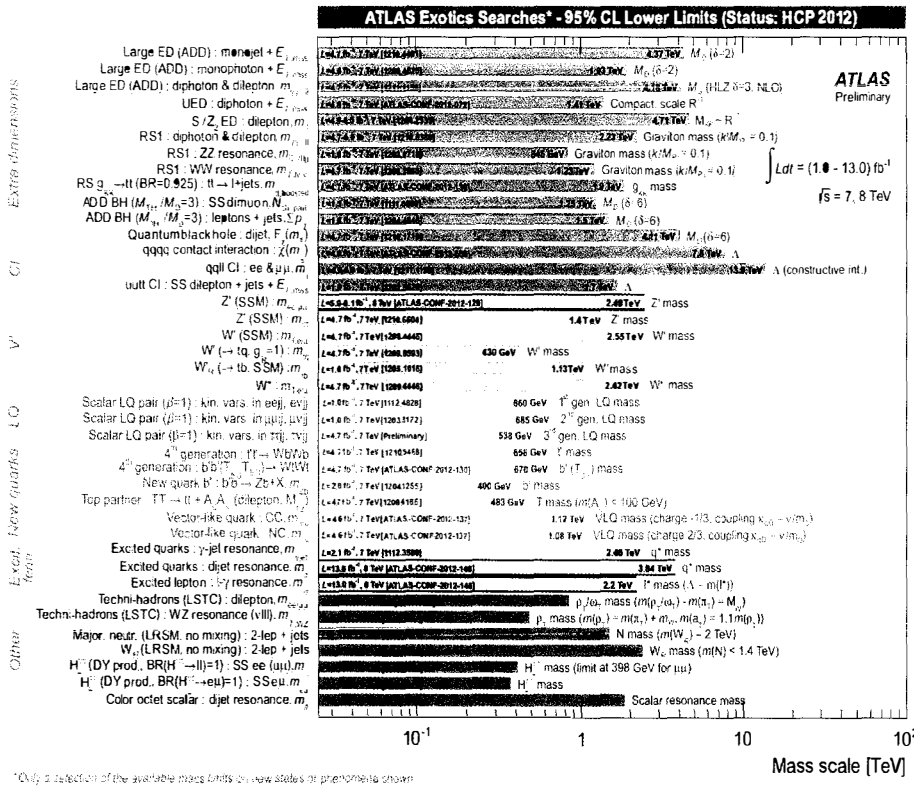

Figure 15. Summary of ATLAS searches for physics beyond Standard Model as of Hadron Collider Physics 2012 conference.

Figure 16. Summary of CMS searches for physics beyond Standard Model as of International Conference on High Energy Physics 2012 conference.

5 Heavy Flavor Physics

Studies of particles with heavy c or b-quarks attract a lot of experimental and theoretical attention. Special experiments, like LHCb at the LHC or Belle upgrade at KEK, are designed specifically to study such particles. In depth investigation of the heavy quarks with relatively long life time is important for both our understanding of the Standard Model and for searches for hints of new physics due to quantum effects in flavor loops. Long life time of the c and b-quarks

provides an experimental opportunity to identify particles with heavy quarks via secondary decay vertices in high precision silicon detectors. Triggering on events with production and decays of heavy quarks at hadron colliders is usually done via displaced vertex triggers or via soft leptons, mainly muons, which accompany production and/or decay of the particles with c and b-quarks.

Quantum effects in the flavor loops in the presence of new physics, such as SUSY, will affect rates of rare decays. One of the most searched processes is decay of B_s meson to a pair of muons. Any deviation from the Standard Model prediction of $\sim 3 \cdot 10^{-9}$ for the branching fraction will indicate presence of new particles in the quantum loops. Search for this rare decay was progressing for many years with limits decreasing by many orders of magnitude thanks to analyses at both the Tevatron and recently the LHC. LHCb reported first evidence for this rare decay as indicated on the Fig. 17a[20] where mass bump in the effective mass spectrum of pairs of oppositely charged muons is observed.

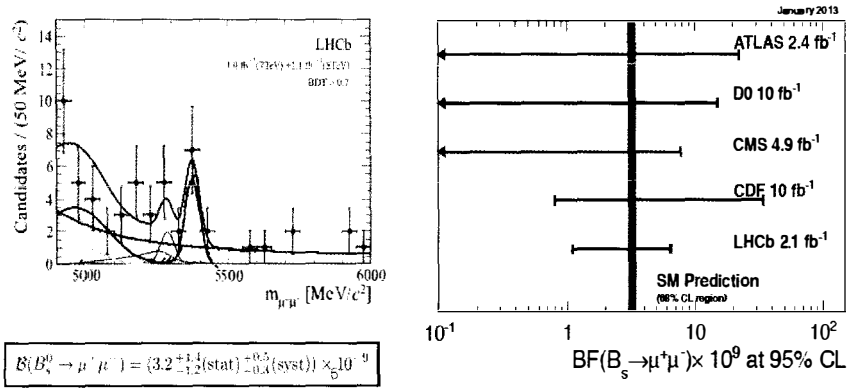

Figure 17. LHCb plot demonstrating evidence for B_s to μμ decay (left, 17a). Compilation of results from different experiments on searches for B_s to μμ decay (right, 17b).

The value of branching fraction observed of 3.2 (+1.4/-1.2) $\cdot 10^{-9}$ (statistical errors which dominate quoted here only) is in a good agreement with the Standard Model predictions further restricting models of the physics beyond Standard Model. Figure 17b[21] presents results of the B_s to μμ decay search by various experiments: all of them are in agreement between each other and with LHCb evidence for this rare process. With more data analyzed by the LHC experiments 5 sigma discovery of this rare decay is expected with full 2012 LHC data set.

Among puzzles in heavy flavor physics is origin of X(3872) particle. All collider experiments see this particle in J/ψππ decay mode, while understanding of its nature is still lacking. In this situation more experimental data are critical and such results are coming from

different experiments. CMS experiment presented interesting result studying ratio of X(3872) production (times branching fraction) to $\psi(2S)$ vs transverse momentum of the particles[22]. No significant dependence in the 10-50 GeV range has been observed. LHCb experiment[23] presented studies of spin and parity of X(3872) using angular distributions of the decay products and with high significance determined state as 1^{++} which rules out, for example, conventional charmonium state $\eta_{c2}(2^{-+})$. Remaining interpretations of X(3872) involve exotics (non-qq) states.

Belle collaboration reported discovery of new resonances, called Z_b, in the decays of Y(5S) to lower energy Y states and a pion[24]. Representative plot of effective mass spectra obtained is presented on Fig. 18a. Belle also provided in depth studies of decay fractions of the new resonances indicating that B(*)B* is the dominant mode of Z_b decays (Fig. 18b).

Fig. 18b indicates that this new state is consistent with B*B* molecule providing further information for the development of heavy quark spectroscopy models.

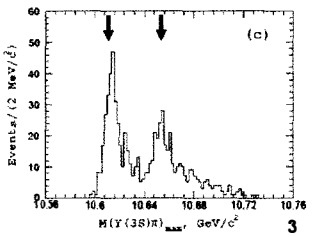

Channel	Fraction, %	
	$Z_b(10610)$	$Z_b(10650)$
$\Upsilon(1S)\pi^-$	0.32 ± 0.09	0.24 ± 0.07
$\Upsilon(2S)\pi^-$	1.38 ± 1.21	2.40 ± 0.63
$\Upsilon(3S)\pi^-$	2.15 ± 0.56	1.64 ± 0.40
$h_b(1P)\pi^-$	2.81 ± 1.10	7.43 ± 2.70
$h_b(2P)\pi^-$	1.34 ± 2.07	11.8 ± 6.22
$B^-\bar{B}^{*0} + \bar{B}^0 B^{*-}$	86.0 ± 3.6	..
$B^*\ \bar{B}^{*0}$	..	73.4 ± 7.0

Figure 18. Observation of $Z_b(10610)$ and $Z_b(10650)$ resonances (left, 18a) by the Belle experiment. Decay fractions for the Z_b resonances (right, 18b).

On studies of mesons with b-quarks LHCb collaboration presented extremely precise results on measurements of B_s mixing which is second order weak process sensitive to contributions to beyond Standard Model physics. Using ~34 thousand signal candidate events (1 fb^{-1} of luminosity) mixing frequency was measured with unprecedented precision Δm_s = 17.768+-0.023(stat)+-0.006(stat). This measurement is in agreement with theoretical predictions and has accuracy much better than theoretical calculations. Further improvements in the theoretical predictions are welcome while Standard Model stays strong in the heavy flavor sector for now.

While CP violation was observed in the decays of K and B-mesons, no such effect has been observed in the decays of charm mesons and it is expected to be very small in the Standard Model. Recently measurements of CP violation in decays of charm mesons attracted a lot of attention as combined ~4.6σ significance was reported from three experiments: LHCb, CDF and Belle. What is remarkable is the scale of CP violation, about 1%, which is well above Standard

Model expectations. Experimental status before Moriond QCD conference is presented on Fig. 19a[25]. As a measure of CP violation the relative difference between number of D^0 mesons and anti-D^0 mesons decaying to pions or kaons is used. In the directly produced charm decays pion charge is used as a flavor tag, while in the charm from semileptonic B decays muon charge tags flavor. LHCb results[25], presented on a data set of 1 fb^{-1}, demonstrate that asymmetry in semileptonic decays is actually positive (while within errors in agreement with zero expected), while in prompt production the updated result moved closer to the "no-CP" region (see Fig. 19b).

Results of all experiments are in a reasonable agreement between each other and when combined are within ~2σ compatible with no CP violation in charm decays. While excitement is diminished in this case only analysis of more data will clarify if the original deviation from the Standard Model was a fluctuation or it is a hint of physics beyond Standard Model.

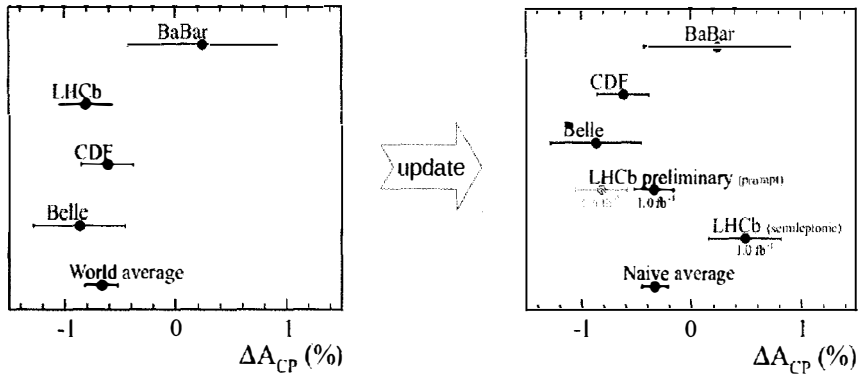

Figure 19. Results on CP violation in charm decays before Moriond QCD conference (left, 19a) and with new results presented by the LHCb experiment (right, 19b).

But puzzles are still remaining in the heavy flavor sector. LHCb experiment reported[26] observation of isospin asymmetry in decays of neutral and positive B-mesons well below zero with significance of ~4.4σ, see Fig. 20. While no such asymmetry observed in K^{*0}/K^{*+} decays, in K^0_s/K^+ decays asymmetry up to ~50% is observed. There are no natural theoretical explanations for such effect and as this result was obtained on ~30% of the data available most prudent is to wait for the update of this measurement with full 2012 data set.

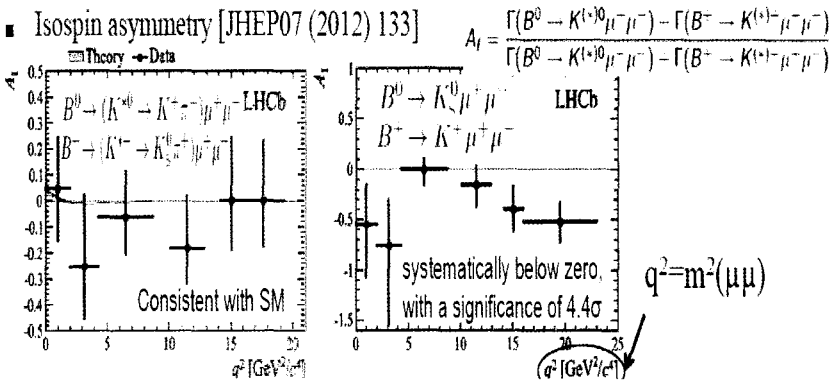

Figure 20. Isospin asymmetry as measured by the LHCb experiment using 1 fb^{-1} of data.

6 The Top Quark

There was tremendous progress in our understanding of the heaviest known elementary particle, the top quark, since it discovery which was first reported at Moriond QCD conference in 1995. Precision measurements of the top quark properties are important: to obtain fundamental constants of the Standard Model and as a way to search for physics beyond Standard Model which naturally could demonstrate itself in the properties of the heaviest known particle.

Mass of the top quark is among fundamental parameters and experiments from both LHC and Tevatron presented new measurements in different top quark decay channels. Fig. 21[27] is a summary of the Tevatron top mass measurements updated in March 2013 for Moriond QCD conference.

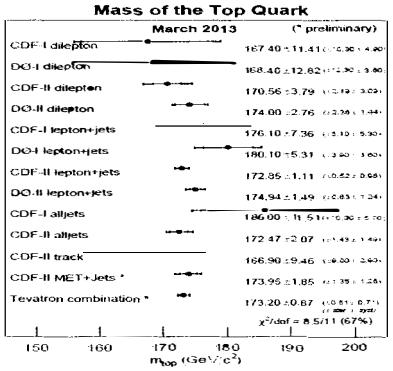

Figure 21. Top quark mass measurements at the Tevatron.

The combined value of the top quark mass is 173.20+-0.87 GeV. The uncertainty reached is 0.5% or twice better in comparison with Tevatron Run II projections. While LHC experiments did not update top mass combination for 2013 winter conferences, summer 2012 result of 173.3+-0.5(stat)+-1.3(syst) GeV is in good agreement with Tevatron measurement and getting similar precision limited now by the systematic uncertainties. It is important to mention that different channels and different methods of measurement of the top quark mass all give consistent results. Still theoretically consistent description of "what mass" is experimentally measured is required for mass measurements with accuracy below ~1 GeV.

CMS experiment at the LHC presented most accurate result on the difference between masses of top quark and top anti-quark[28]. It is -277+-196(stat)+-122(syst) MeV. Within errors the difference is consistent with zero as prescribed by CPT invariance.

Among new measurements in the top quark sector are wide array of top quark pair production cross section measurements including total cross sections and various differential distributions including with the center of mass energy of 8 TeV. On Fig. 22[29] recent 8 TeV results of differential cross sections measurements from the CMS experiment are presented. These measurements are important to test QCD predictions for the heaviest quark, to find limits of QCD applicability, as well as to search for physics beyond Standard Model as it could demonstrate itself through subtle variations in kinematic distributions. For now, as it is seen from Fig. 22 and other top quark cross sections measurements, all results are in good agreement with the Standard Model predictions.

	$L[fb^{-1}]$	t-channel cross section [pb]	$\lvert V_{tb}\rvert$
ATLAS	5.8	$95.1 \pm 2.4(\text{stat.}) \pm 18.0(\text{syst.})$	$1.04^{+0.10}_{-0.11}$
CMS	5.0	$80.1 \pm 5.7(\text{stat.}) \pm 11.0(\text{syst.}) \pm 4.0(\text{lumi.})$	$0.96 \pm 0.08(\text{exp.}) \pm 0.02(\text{th.})$

Figure 22. Top quark differential distributions at 8 TeV center of mass energy LHC.

In addition to the pair production of the top quarks via strong interaction, electroweak production of the top quarks at the LHC has sizable cross sections. Both ATLAS and CMS are now measured t-channel single top quark production with high precision (Fig. 23[29]) and extracted direct limits on the value of CKM matrix element V_{tb}. All results for the single top quark production are in agreement with the Standard Model predictions and stringent limits on model-independent value of V_{tb} matrix element are set: V_{tb} value differs from 1.0 by less than ~10%.

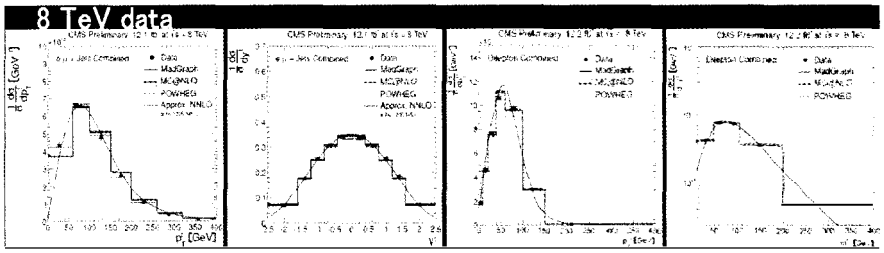

Figure 23. Single top quark production cross sections in t-channel at 8 TeV LHC. Standard Model prediction is 89 pb with ~3% uncertainty.

An interesting puzzling effect in the top quark pair production at the Tevatron continues to attract attention of both experimentalists and theorists. Anomalous forward-backward asymmetry was observed by both CDF and D0 experiments: more top quarks follow the direction of the proton, then expected in the Standard Model. Both Tevatron experiments observe ~2σ effect and both see deviation in the same direction. No similar effect has been seen at the LHC by ATLAS and CMS, while top pair production mechanisms at the LHC are quite different. CDF experiment presented updated results on the full Tevatron data set on A^{l}_{FB} (asymmetry calculated using leptons from decays of W bosons coming from the decays of top quarks) in lepton+jets decay channel as presented on Fig. 24[30].

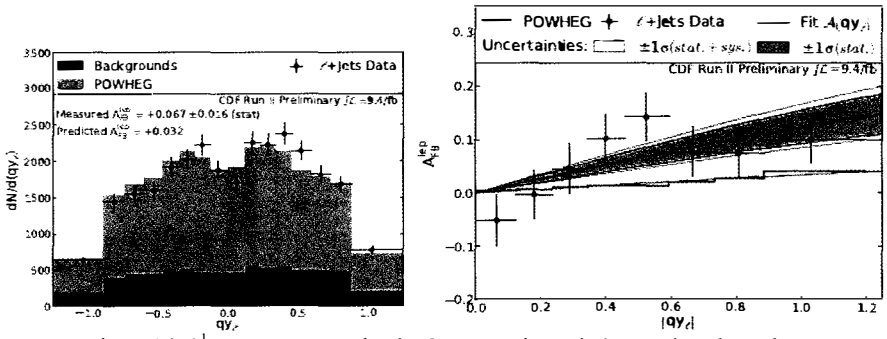

Figure 24. A^{l}_{FB} measurements by the CDF experiment in lepton+jets channel.

After corrections for acceptance A^{l}_{FB} is 9.4+-2.4(stat)+2.2/-1.7(syst)% compared to the theoretical prediction of 3.6% (including electroweak corrections) or ~2σ away. In order to address this puzzle results on the full Tevatron data set from the D0 experiment as well as higher accuracy results from the LHC are needed.

7 Higgs Boson

Discovery of a Higgs boson, particle responsible for electroweak symmetry breaking, last summer is among most important discoveries in the particle physics. Now with new particle observed main efforts are concentrated on studies of its properties, such as measurement of its mass, as well as verifying that this particle has indeed parameters predicted by the Standard Model, including spin and parity. Large number of new and updated results, from both Tevatron and LHC experiments, have been presented at the conference.

Tevatron experiments presented update of the Higgs boson searches on the full Tevatron 2 TeV data set of 10 fb^{-1}. Both Tevatron experiments, CDF and D0, see excess of events at ~2σ level. When all search channels from both experiments, including decays to bb, WW, γγ and ττ, significance of the excess at a mass of 125 GeV is 3.1σ[31]. Fig. 25a presents combined background p-value (or probability of background to fluctuate to or above number of events observed in data) demonstrating very low probability that signal observed at the Tevatron could be explained by the background fluctuation. As presented on Fig. 25b excess of events above background is observed in all studied Higgs decay channels, including decay into a pair of fermions. All Tevatron results are in agreement with the Standard Model Higgs boson production and decay adding important information to our understanding of the Higgs boson produced in conditions different than at the LHC.

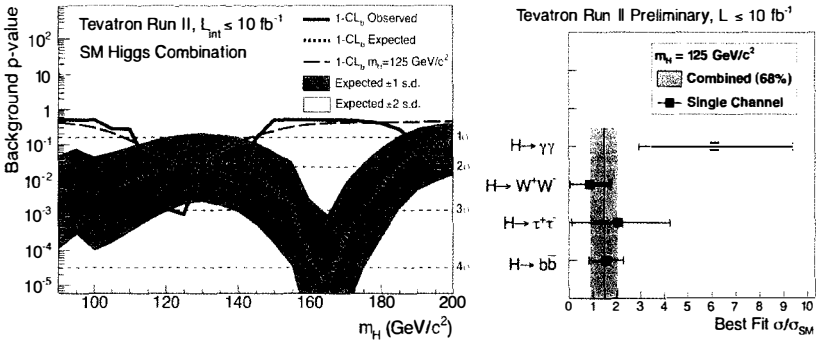

Figure 25. Background p-value for combined Tevatron Higgs boson searches result (left, 25a). Best fit Higgs boson production cross sections normalized to the Standard Model predictions for the Higgs decay channels studied at the Tevatron (right, 25b).

LHC experiments presented wealth of new experimental results about Higgs boson at the winter conferences 2013 in most cases using full 2013 8 TeV data set where studies now, with very high significance of Higgs observation already achieved, concentrate on precision measurements of its properties. We will start from discussing studies of the Higgs boson decay modes. For the decay to a pair of b-quarks[32], most probable decay mode of the Higgs boson with a mass of ~125 GeV, CMS reported 2.2σ observed excess with 2.1σ expected, providing a strong

indication of the Higgs boson decaying to a pair of quarks. ATLAS expected sensitivity in this decay channel is 1.9 times above the Standard Model with observed limit 1.8 times above predictions not yet providing significant sensitivity for studies in this channel. With full 2013 data set, improvements in the analysis methods and potentially combining LHC and Tevatron experiments increases in sensitivity are expected with currently available data sets.

Decays of the Higgs boson to the heaviest lepton, τ-lepton, are searched by both ATLAS and CMS experiments. Using close to the full available data set observed(expected) significances of excess are[32]: ATLAS 1.1σ (1.7σ), CMS 2.9σ (2.9σ). CMS reached Standard Model sensitivity and for all practical purposes established evidence for the Higgs boson decay to a pair of τ-leptons. Both ATLAS and CMS results are compatible with Standard Model Higgs boson decays to τ-leptons.

One of the most stringent tests if a Higgs boson discovered is indeed particle as predicted by the Standard Model is the ratio of production cross section times branching fraction to the Standard Model predicted values. Such ratio is called μ. Both ATLAS and CMS measured μ values for a large number of different Higgs production and decay processes as presented on Fig. 26[33,34].

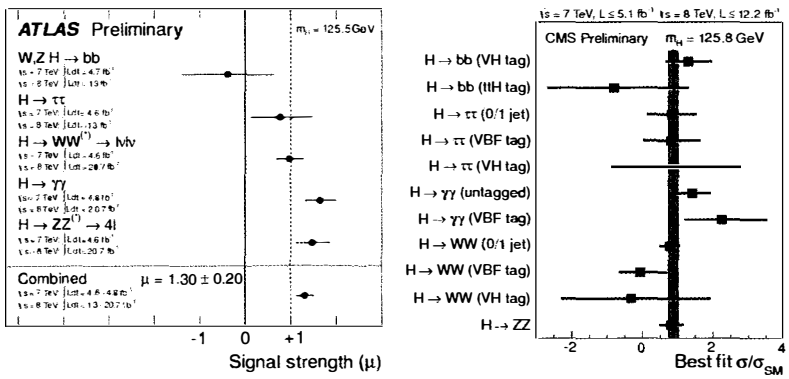

Figure 26. μ values for different Higgs boson production and decay modes by ATLAS and CMS experiments. Combined μ value for ATLAS 1.30+-0.20 and for CMS is 0.88+-0.21 (before update presented on Fig. 27).

Both ATLAS and CMS results are compatible with Standard Model, while some tension for Higgs to γγ decay existed before the conference as both experiments saw somewhat enhanced values of μ. My un-official combination of ATLAS and CMS measurements provides μ value of 1.1+-0.15 in good agreement with the Standard Model. CMS experiment updated their boson decay modes results during the conference[35] and updated CMS plot for bosonic decay channels is presented on Fig. 27. Excess originally observed in this channel has disappeared with more data and improved analyses and results are in a good agreement with the Standard Model predictions.

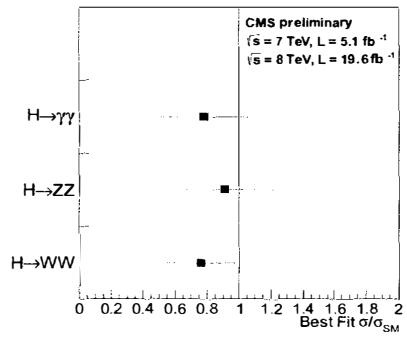

Figure 27. Updated μ values from CMS experiment on full 2013 data set.

The only parameter of the Higgs boson in the Standard Model (all other properties are predicted) is its mass. As a result precision measurements of the Higgs boson mass are very important, if not the most important measurements after a Higgs boson discovery. Both ATLAS and CMS presented full 2013 data set results on the mass of the Higgs boson. Decay channels used for the mass measurements are decays to γγ and ZZ where energy and angles of the decay products (photons and leptons) could be measured with high precision. In fact designs of both ATLAS and CMS detectors were optimized to detect Higgs boson and measure its mass with high precision and these efforts are now paying off well. Fig. 28[35] presents CMS results of measurements of the Higgs boson mass. Both channels provide consistent results with average mass of 125.8+-0.4(stat)+-0.4(syst) GeV[34].

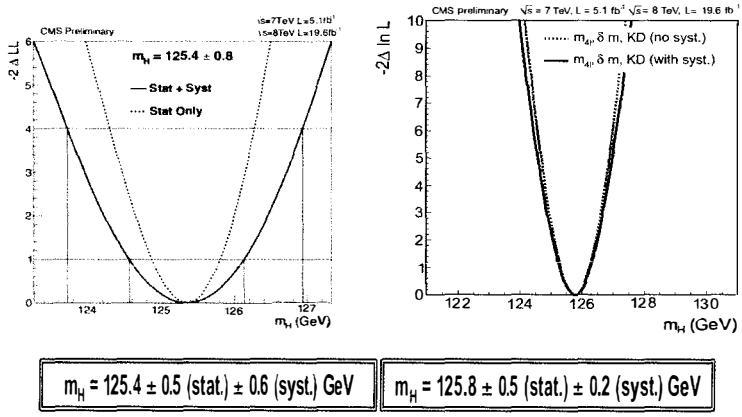

Figure 28. CMS experiment Higgs boson mass measurements in γγ (left) and ZZ (right) decay channels.

Fig. 29[33] presents ATLAS results of the Higgs boson mass measurement. Small tension between these two results exists: $\gamma\gamma$ channel best fit mass is somewhat above mass measured in ZZ channel. These two results are compatible at 2-8% level which provides an opportunity for the ATLAS experiment to combine these two results and obtain Higgs boson mass value of 125.5+-0.2(stat)+0.5-0.6(syst) GeV in a good agreement with CMS mass measurement. It is too early to say where the difference between Higgs masses measured in two different channels by the ATLAS experiment is coming from. Using existing data set with improvements in the detector calibration might reduce the tension (or enhance it?). It could be that with more data (to be collected in 2015 and beyond) this difference will go down, while there is a chance there is yet un-known physics which affects measured values in these two channels. In any scenario it is critical to continue to improve Higgs boson mass measurement by both ATLAS and CMS experiments.

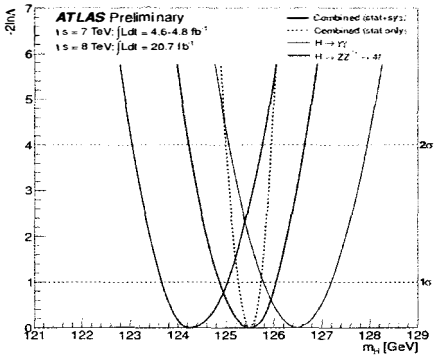

Figure 29. ATLAS experiment Higgs boson mass measurements in $\gamma\gamma$ and ZZ channels.

Back of an envelope combination of ATLAS and CMS Higgs boson mass results provides mass of 125.6+-0.3GeV. The accuracy of this result, 0.24%, is already impressive – less than a year after the Higgs boson discovery. For both experiments mass accuracy is limited by systematic uncertainties, so improvements in mass measurement methods are needed to improve precision.

Measuring spin and parity of the newly discovered particle is critical to assure that signal observed is indeed coming from the Standard Model Higgs boson (0^+). Both ATLAS and CMS presented extensive results on this topic. Separation between different states is mainly coming from low background, high angular resolution ZZ Higgs decay mode with Z's decaying to leptons. Fig. 30[34,36] presents some of the observed results. There is already very good separation between Standard Model prediction and exotic states, such as 0^-, excluding this state with over 3σ significance. There are strong exclusion limits set by ATLAS and CMS for other spin-parity states.

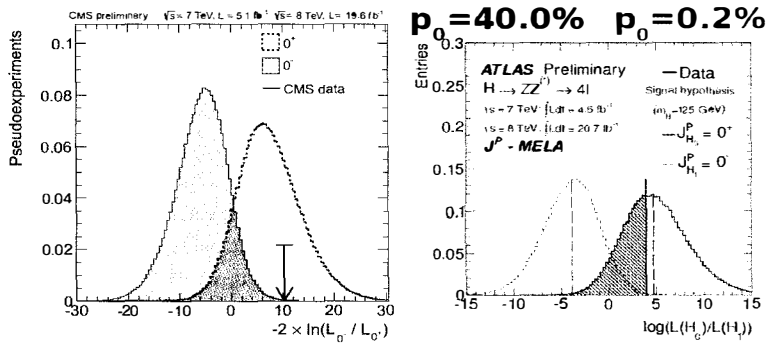

Figure 30. CMS (left) and ATLAS (right) exclusion plots for a particle with spin parity 0^- vs Standard Model Higgs boson prediction of 0^+.

Another fundamental property of the Higgs boson is couplings to other particles which are expected to be proportional to the mass of a particle. The approach here is to measure couplings, normalized to their Standard Model values, K_i, using both production and decay rates. As different couplings might be involved in the production and decays of the Higgs boson, there are correlations between limits on different couplings. Fig. 31[33,34] presents results on the couplings obtained by the ATLAS and CMS experiments. Sub-script "F" means fermion couplings and "V" means vector boson couplings.

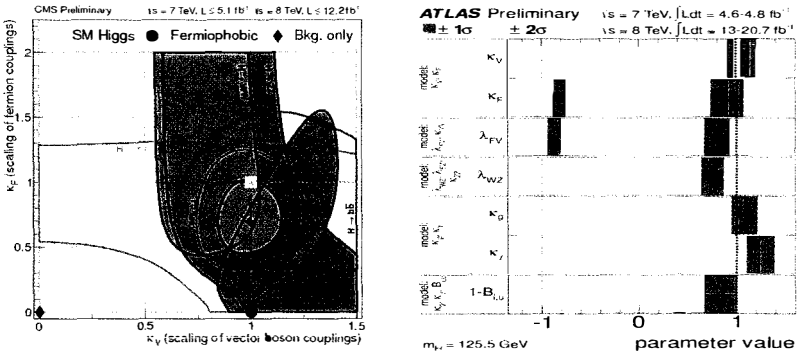

Figure 31. Higgs boson couplings measurements by CMS(left) and ATLAS(right) experiments.

All couplings results obtained so far are in good agreement with the expected in the Standard Model, while uncertainties are on a larger size: ~30% for K_F and ~20% for K_V.

Measurements of couplings will continue to improve as more data will be accumulated at the LHC and analysis methods will improve.

With all Higgs boson studied properties matching well Standard Model predictions the particle discovered in July 2012 looks more and more as the Standard Model Higgs boson. Ultimate test is the verification of the self-consistency of the Standard Model using relation between masses of the Higgs boson, the top quark and the W boson and other electroweak parameters. Gfitter collaboration[37] presented at the conference such self-consistency check with top quark and W boson masses from the Tevatron and Higgs boson mass as measured at the LHC. The plot of such a comparison is presented on Fig. 32.

The goodness of the fit is ~8% demonstrating impressive self-consistency of the Standard Model and supporting the hypothesis that the newly observed particle is indeed the Higgs boson of the Standard Model. Improvements in the measurements of the top quark, W boson and the Higgs boson masses are critical for continuing improvements of our understanding of the Standard Model applicability.

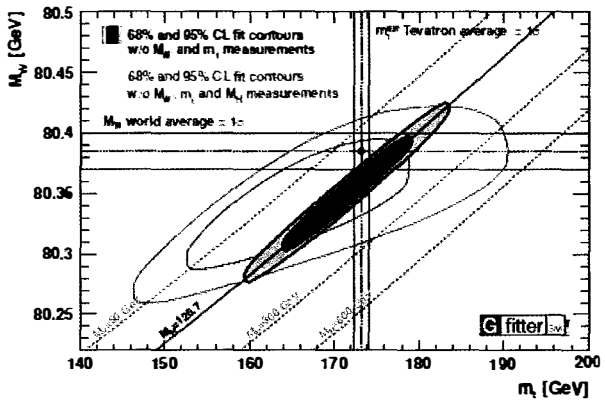

Global fit of measurements in the SM [1]

Figure 32. Standard Model self-consistency check in the top quark mass vs W boson mass plane.

8 Future LHC Running

Many of the key topics of modern particle physics depend heavily on data produced by the LHC. In the talk[38] status and plans of the LHC accelerator complex for the next run, to be started in early 2015, are summarized as presented on Fig. 33. With excellent LHC performance during Run I in 2010-2013 there is high confidence that next running period plans will be realized. The center of mass energy of the collider will be in the range 13-14 TeV with ~150

days per year of delivering pp luminosity to the experiments. With planned 25ns bunch spacing in 2015 integrated luminosity per year will be in 25-45 fb^{-1} range (for ATLAS and CMS experiments) with number of pile-up interactions of ~25-50. There are different options how to optimize delivered luminosity while keeping number of pile-up interactions reasonably low. The final strategy is expected to be developed in close cooperation between machine experts and LHC experiments.

	Number of bunches	Bunch intensity [10^{11} ppb]	β^*/ crossing angle	Emittance LHC [μm]	Peak Luminosity [$cm^{-2}s^{-1}$]	~Pile-up	Int. Lumi per year [fb^{-1}]
25 ns	2760	1.15	55/189	3.75	0.93×10^{34}	25	~24
25 ns BCMS	2520	1.15	45/149	1.9	1.7×10^{34}	52	~45
50 ns	1380	1.6	42/136	2.5	1.6×10^{34} level to 0.8×10^{34}	87 level to 44	~40*
50 ns BCMS	1260	1.6	38/115	1.6	2.3×10^{34} level to 0.8×10^{34}	138 level to 44	~40*

Figure 33. LHC parameters for the next run planned to start in early 2015.

10 Concluding Remarks

With 56 excellent experimental talks presented at the conference it is impossible to do justice to all of them in the relatively brief summary. I recommend to all readers to study all of the submitted contributions presented in these proceedings. Main experimental highlights of the conference (see talk[39] of Michelangelo Mangano for the conference Theoretical Summary) based on the new results presented at Moriond QCD 2013 include

a) New results from the LHCb experiment do not confirm anomalously large CP violation in the charm sector;
b) Unexplained double-ridge structure seen by ALICE experiment in charged particles correlations in pPb collisions;
c) No *new* hints of beyond Standard Model effects in direct or indirect searches;
d) All measured Higgs boson properties match Standard Model Higgs boson very well;
e) Mass of the Higgs boson is 125.6+-0.3 GeV.

Standard Model stands stronger than ever indicating its fundamental character and importance of even deeper studies of one of the most successful theories of Nature.

I would like to thank all speakers of the conference for presenting excellent talks and the experimental collaborations for the large number of new, exciting, and sometime puzzling results. It was great pleasure to work closely with Michelangelo Mangano on the conference summary talks. I thank the Moriond QCD 2013 organizers for the excellent organization of the conference and for the invitation to give experimental summary talk which was challenging while exciting experience.

11 References

1. D. Denisov, "Experimental Summary", Moriond QCD 2013, http://moriond.in2p3.fr/QCD/2013/Saturday/Denisov.pdf
2. M. Wobisch, "Jets Production and Properties at the Tevatron", these proceedings.
3. K. Rabbertz, "Latest Jets Results from the LHC", these proceedings.
4. R. Lafaye, "Photon Production at the LHC", these proceedings.
5. K. Theofilatos, "W/Z+Jets and W/Z+HF Production at the LHC", these proceedings.
6. V. P. Lombardo, "Di-Boson Production Cross Section at the LHC", these proceedings.
7. B. Hippolyte, "Introduction to Heavy ion session", these proceedings.
8. Y. Mao, "Hard Probes at CMS", these proceedings.
9. Q. Wang, "Flow Phenomena at CMS", these proceedings.
10. J.- F. Grosse-Oetringhaus, "The double-ridge phenomena in p-Pb collisions measured with ALICE", these proceedings.
11. A. Mann, "SUSY Searches for Inclusive Squark and Gluino Production at the LHC", these proceedings.
12. A. Favareto, "Third Generation SUSY Searches at the LHC", these proceedings.
13. L. Roszkowski, "Are current LHC data really a problem for constrained SUSY?", these proceedings.
14. S. J. Harper, "Searches for Heavy Resonances at the LHC", these proceedings.
15. J. P. Chou, "Search for Exotica at the LHC", these proceedings.
16. H. J. Stelzer, "Searches for Extra Dimensions, LeptoQuarks, and Technicolor at the LHC", these proceedings.
17. P. Moskal, "Recent results on hadron physics at KLOE", these proceedings.
18. M. Piccini, "Study of the rare decay $K^{+-} \dashrightarrow \pi^{+-}\gamma\gamma$", these proceedings.
19. K. Griessinger, "Exclusive hadronic cross sections at low energies with ISR at BaBar", these proceedings.
20. E. Ben-Haim, "Latest results in rare decays at LHCb", these proceedings.
21. S. Leo, "Searches for New Physics in Charm and Bottom Decays at the Tevatron", these proceedings.
22. E. V. Bouhova-Thacker, "Heavy Flavor Production at ATLAS and CMS", these proceedings.

23. G. Manca, "b & c hadron spectroscopy at LHCb", these proceedings.
24. P. Krokovny, "Recent results on charmonium/bottomonium(-like) states at BaBar and BELLE", these proceedings.
25. S. Stahl, "Properties of b & c hadrons at LHCb", these proceedings.
26. E. Ben-Haim, "Latest results in rare decays at LHCb", these proceedings.
27. G. Petrillo, "Top Quark Mass Measurements at the Tevatron", these proceedings.
28. E. Yazgan, "Measurements of Top Quark Properties at the LHC", these proceedings.
29. M. Aoki, "Top Quark Production at the LHC", these proceedings.
30. D. Orbaker, "Measurements of Top Quark Properties at the Tevatron", these proceedings.
31. M. Cooke, "Measurements of Higgs Boson Coupling and Properties at the Tevatron", these proceedings.
32. D. M. Puigh, "Study of Higgs Production in Fermionic Decay Channels at the LHC", these proceedings.
33. T. Adye, "Measurements of Higgs Boson Properties in ATLAS", these proceedings.
34. A. J. Whitbeck, "Measurements of Higgs Boson Properties in CMS", these proceedings.
35. C. Ochando, "Study of Higgs Production in Bosonic Decay Channels at CMS", these proceedings.
36. E. Mountricha, "Study of Higgs Production in Bosonic Decay Channels at ATLAS", these proceedings.
37. M. Baak, "The EW fit after the discovery of a new boson at the LHC", these proceedings.
38. M. Kuhn, "LHC beam operations past, present and future", these proceedings.
39. M. Mangano, "Theoretical Summary", Moriond QCD 2013, http://moriond.in2p3.fr/QCD/2013/Saturday/Mangano.pdf

QCD AND HIGH-ENERGY HADRONIC INTERACTIONS: THEORETICAL SUMMARY

M.L. MANGANO
CERN, PH Department, Theoretical Physics, 1211 Geneva 23, Switzerland

1 Introduction

The 2013 edition of Moriond QCD offered a complete and exciting overview of the latest progress in a broad variety of topics in elementary particle physics. While the highlight of the meeting was the release of the latest data from the LHC, particularly the update on Higgs studies, excellent contributions on both theoretical and experimental recent results gave a clear sense of vitality, progress, and expectation for further exciting developments to come. The experimental search for and the theoretical speculations about possible phenomena beyond the Standard Model (BSM), remain the driving theme of most studies, but great efforts are fortunately still dedicated to the pursuit of precision, and to a deeper understanding of dynamical issues.

I will loosely group the various contributions in five areas: low-Q^2 dynamics of strong interactions, heavy ion (HI) collisions, precision physics in hadronic collisions, status of BSM and flavour physics and status of electroweak (EW) symmetry breaking (EWSB). The experimental contributions have been reviewed in the excellent Summary talk by Dmitri Denisov [1]. Rather than a summary of the theory talks, I will present a theoretical perspective on the whole set of results, including reference to several experimental talks, to underline issues of theoretical relevance: there is no doubt that the multitude of results made available by the experiments, their precision and diversity, remain the key drivers of today's theoretical progress, and the interplay between theory and experiment represents the most valuable asset of our scientific community.

The following summary shows an unavoidable unbalance between different topics, reflecting the bias due to my personal expertise, understanding, and taste. For the sake of space, I shall refer to the proceedings for a complete bibliography relative to the individual contributions.

2 Low-Q^2 dynamics

After many decades since the acceptance of QCD as the fundamental theory of hadronic interactions, the study of its behaviour in the domain of strong coupling remains as vital as ever. This is confirmed by the diversity of the theoretical and experimental results shown at this meeting. The former covered approaches to the problem of confinement [2], studies of vector meson production from gauge/gravity duality [3], phenomenological models of hadroproduction in DIS [4], the use of lattice QCD to calculate the large-energy behaviour of total hadronic cross sections [5], lattice studies of semileptonic $B \to D^{(*,**)}$ decays, and predictions for the rare decays $\tau \dashrightarrow \nu_\tau \eta P$ ($P = \pi, K$) [8]. The latter reviewed data on multiparticle production at the B factories [6], diffractive phenomena at HERA [7], low-energy cross sections for $e^+e^- \dashrightarrow$hadrons [16] and a broad range of studies of production [9], spectroscopy and decay form factors of heavy hadrons [10,11,12,13,14].

The latest analyses of low energy hadronic cross sections in e^+e^- collisions in BaBar and KLOE[16] greatly improved the accuracy of the theoretical predictions for the anomalous magnetic moment of the muon, $(g-2)_\mu$, confirming a discrepancy with the experimental data at a level in excess of 3σ.

Recent measurements of open heavy quark production [9] confirm the good agreement with theory. In the case of quarkonium [9], on the other hand, the situation is still rather opaque. Non-relativistic QCD (NRQCD) gives overall a good description of production cross sections [15]. However, this is the result of combining a large number of independent production channels, mediated by different states in the NRQCD expansion over color and quark velocity in the meson CM frame. Each production channel has at least one overall parameter, namely a non-perturbative matrix element, to be fitted on data. Since various channels have different p_T shapes, one can fit almost every p_T distribution, and several equally good fits can be obtained. Thus, even though by now most relevant channels have been evaluated to NLO in QCD [15], the situation is still rather unsatisfactory. In addition, no choice of parameters compatible with the cross section measurements seems to allow a good description of the experimnetal data on charmonium polarization [15]. Having followed the development of this field for several years, I start being skeptical about the possibility to ever make solid theoretical predictions, at least for charmonium!

Hadronic spectroscopy is still a fascinating laboratory to explore the manifestations of confinement and test the theoretical models of bound-state formation, as confirmed by the continued interest by some among the deepest thinkers of our times [17,18]. The latest inputs in this field are emerging from the study of hadrons containing heavy quark-antiquark pairs. LHCb [12] determined the quantum numbers of the $X(3872)$, obtaining $J^{PC} = 1^{++}$, consistent with both the tetraquark ($qc\bar{q}\bar{c}$) and the molecular ($D^0 D^{*0}$) interpretation, but not with being a charmonium D-wave. Belle [13], on the other hand, reported the lack of evidence for charged or CP-odd partners of the $X(3872)$, states that are expected in the tetraquark case [a]. Further support of the molecular interpretation of these exotic states came from the observation of BB^* and B^*B^* decays of the $Z_b^+(10610)$ and $Z_b^+(10650)$ states. Finally, new clues on the origin of the $X(3872)$ were reported in the CMS study of its prompt and non-prompt production rates [9]: on one side, the prompt rate is almost an order of magnitude smaller than what predicted at leading order (LO) in non-relativistic QCD; on the other, the fraction of $X(3872)$ from B decays does not show a p_T dependence, contrary to the steep rise observed in typical charmonium states. The interpretation of these results is still lacking, as is an overall coherent picture of the nature of these states. I am fascinated by these puzzles, and look forward to the evolution of this challenge for QCD theory.

[a] Following the meeting, however, evidence for a charged state at $\sim$ 3900 MeV was presented by BES [19] and Belle [20].

3 Heavy ions

We have seen spectacular results: it's mind boggling that we can create such complex phenomena and explore their underlying dynamics[21]! The study of soft probes (e.g. inclusive multiplicities, flow) is complemented by the observation of a rich spectrum of hard probes (jets, photons and Z bosons, heavy quarks). These two classes of phenomena, once complementary, are now integrated in a single overall picture, which more and more relies on a common first-principle understanding of the underlying dynamics. Soft-probe observables are now used to examine in greater detail hard-probe processes (see e.g. the study of elliptic flow in heavy-quark final states). The simplicity and elegance of the phenomenology emerging from the measurements of hard probes is accompanied both by successful agreement with theoretical predictions, and by challenging puzzles. The field is thus widely open to major progress, coming from higher-precision studies and from measurements of new classes of observables, which will become available with higher luminosity.

The early dramatic evidence of jet quenching, observed in the first HI run of the LHC, is now accompanied by detailed quantitative studies of several new observables[23,24,25] and by continued theoretical scrutiny[26]. The measurement of prompt photons and Z^0 bosons up to $p_T \sim 200$ GeV shows rates that scale linearly with the number of participants, confirming a lack of interaction of these EW probes with the plasma. The unbalance in momentum of the recoiling jet, on the other hand, fully confirms the observation of quenching in inclusive jets. The fragmentation functions of these jets are being studied[24], as a function of event centrality, and show the expected softening[26]. The comparison of these observables across different samples (γ/Z+jet, jets) will allow studies of quark vs gluon quenching. In parallel, the measurement of charm and bottom production, as a function of p_T, shows the first weak evidence of the anticipated hierarchy in the nuclear modification factor, namely a reduced level of quenching for heavy quarks[27]. On the other hand, jets including a b quark appear to be quenched like light jets[25].

A new element emerging from the LHC data is the similarity between phenomena occurring in AA collisions[28] and features of large-multiplicity final states in pp and pA (e.g. the "ridge"): this is suggestive of a new picture of the underlying structure of the proton at very small x[29]. The modeling of the "soft" component of inclusive pp collisions is usually based on the picture of multiple collisions of parton pairs. Various degrees of correlations are required to fit the data (e.g. colour correlations, impact-parameter correlations of the partonic densities), and can be modeled with suitable parameters in the standard Pythia, Herwig or Sherpa MC generators. To which extent is this phenomenological modeling sufficient to capture the complexity of the highest-multiplicity final states? Is there some deeper multi-body dynamics (like the colour-glass model) that underlies these phenomena, both in pp and in pA/AA, and which would allow a more physics-driven parameterization of the event generators? A rich programme of exploration is now made possible by the variety of available data, with different beam types, from RHIC and LHC.

The behaviour of quarkonium in the QGP remains an exciting and prone-to-surprises playground. The LHC data[24,25,27] show a reduced amount of charmonium suppression, relative to RHIC[30]. This observation was anticipated as a possible manifestation of regeneration, namely the recombination of charm and anticharm quarks produced in the collision of different nucleon pairs. The recombination rate grows like the square of the average charm multiplicity, and is indeed expected to become numerically relevant at the LHC energy. Large cold-nuclear effects observed in dA at RHIC[30], however, could undermine this interpretation. Further tests of the kinematical dependence of charmonium suppression, and the study of charmonium production in pA at the LHC, will thus be needed to confirm regeneration.

Finally, we were reminded[31] of the versatility of HI collisions. For example, the high-intensity EM fields that are generated during the approach of such high-Z objects create a unique environment for the study of hard $\gamma\gamma$ and γg collisions.

4 Precision QCD in hadronic collisions

Hadron colliders have delivered precision measurements for a long time. Most notably the mass of the W and of the top, and various properties of charm and beauty hadrons (mixing, spectroscopy, decays). The interpretation and use of cross-sections, on the other hand, has typically suffered from large theoretical and experimental systematics (with notable exceptions, like the production rates and asymmetry of W bosons at the Tevatron, which have given valuable input for the extraction of the quark densities).

Great progress has taken place over the last few years, and is now delivering its fruits, with implications not only for the basic understanding of the proton structure and of QCD properties, but also for our ability to explore possible BSM phenomena.

The improved determination of PDFs is made possible by powerful and flexible global fitting tools [32], which can now account for and include LHC data. Direct use of LHC data offers many advantages: on one side they cover wide ranges of x at the large values of Q that are of interest for most applications. On the other, the statistical and systematic accuracy is often at the percent level. Furthermore, the data taken at different CM enegies provide further opportunities to control systematic errors and improve the precision [33]. The overall experimental precision achieved with measurements of gauge bosons [34,35], of jets [33,36] and of photons [37] starts challenging the theoretical accuracy. The report [38] of the first partial results (for the gg initial state channel) for the next-to-next-to-leading order (NNLO) jet cross section is therefore particularly timely! The scale variation is reduced to a few percent, in presence of a rate increase of about 20% relative to the NLO result. The completion of this calculation will strengthen the program of extraction of PDF densities from the LHC data, and improve the already remarkable precision obtained in the extraction of α_s from jet data [33,36]. At this level of precision, however, it is necessary to understand the impact of the complete shower evolution of (N)NLO, parton-level results on the resulting predictions for jet cross sections. Current indications [39,33] are that these effects are significant, and lead to differences with respect to the parton-level results that are as large as the scale or PDF systematics. A clarification of the origin of these effects will be necessary to fully benefit from the intrinsic accuracy of the jet cross section result that are becoming available.

At the LHC, large cross sections and the kinematical access to extended domains of phase space enable very sensitive tests of the theoretical modeling of complex final states. Recent progress in this area reported at this meeting includes: new tools for the automatic calculation of NLO corrections to multibody final states [40,41]; estimates of the NNLO corrections to processes with very large NLO K factors [42]; new tools aiming at an improved next-to-leading-logarithmic accuracy in the description of the shower, with application to W+jet production [43]; new tools to exploit event shapes in hadronic collisions, reducing the impact of large pile-up [44]; the inclusion of multiple jet emission and resummation of Sudakov effects in the production of BSM particles, enabling a more realistic description of their final states [45,41]. Overall, there is an excellent agreement between theoretical predictions and data for a large variety of complex final states such as multijet topologies [33,36], associated production of W/Z plus jets and heavy quarks [34], vector boson pairs [46]. Some residual issue is still left in the case of associated production of W and heavy quarks, although the early large discrepancy observed by CDF is now significantly reduced in the latest Tevatron and LHC measurements [34].

The overall success of theoretical calculations in describing the fine details of complex hadronic final states encourages their use to design new strategies and propose new observables, possibly sensitive to new physics. We saw, for example, interesting new ideas, based on the use of jet masses instead of the usual H_T, to separate the QCD background from BSM multijet final states [47].

Last but not least, the large statistics of top quarks accumulated at the Tevatron and at the LHC are finally promoting the studies of top quarks [48,49,50,51] to the level of "high-precision" physics, with increasing sensitivity to the possible presence of BSM effects [52]. The most notable

examples in the area of precision are the latest CDF/D0 combination of the top quark mass at the Tevatron[53], 173.20±0.87 GeV, and the precise cross section measurements at the LHC[50]. In the area of BSM, the foward-backward asymmetry reported by CDF and D0 remains a puzzle, which even the latest interesting measurements[48] do not seem to shed further light on.

The relevance of the new knowledge on m_{top}, in view of the new knowledge of the Higgs mass, was illustrated by the latest global fits of EW parameters[54]. If, on one side, the agreement between direct measurements of the top and W masses and the result of EW fits is remarkable, it is clear nevertheless that further improvements in precision would be extremely interesting. The knowledge of the Higgs mass, in fact, has greatly tightened the correlation between top and W masses, and a slight tension is observed, at the level of 1-2σ. An outstanding theoretical challenge is now the proper understanding of the systematics in the interpretation of the measured top mass. New studies by CMS[49] start addressing part of this issue, by monitoring the dependence of the measured top mass on the event kinematics. This probes the accuracy of the Monte Carlo event generators to model the fine details of top production and decay, including the impact of non-perturbative and hadronization effects.

5 BSM searches, and flavour physics

The search for BSM phenomena is driven by two considerations. On one side, there is clear and incontrovertible evidence for physics beyond the SM (dark matter, the baryon asymmetry of the universe, the origin of neutrino masses). On the other, the existence of a Higgs boson with features fully consistent with those anticipated by the SM gives more concreteness to the puzzle of the hierarchy, namely the naturalness of the EW scale and its stability with respect to the Planck scale. It is natural to expect that the solution to the latter problem will also include ingredients for the solution of the former ones, and most theoretical BSM theories that have been proposed do precisely this. Searches for their evidence have been ongoing for decades, and the access at the LHC to a new energy scale has offered new opportunities for discovery. At this meeting, we saw many new results, ranging from the direct searches of new particles (supersymmetric ones, new gauge interactions, new heavy quarks, Kaluza-Klein excitations, etc), to indirect evidence of new phenomena at large Q^2 (quark substructure, anomalous gauge couplings, anomalous properties of the top quark, etc), to indirect evidence at low Q^2 (rare decays or CP violation in flavour physics, anomalous magnetic moment of the muon, etc). No conclusive evidence, unfortunately, has matured as yet.

The study of the flavour sector of the SM, as an indirect probe for new phenomena, is strongly motivated theoretically[55,56,57], and accounts for a large fraction of the experimental programme at the flavour factories[58], at the Tevatron[59] and at the LHC[60,61,62]. Intriguing anomalies are present. For example recent data on e^+e^- annihilation to hadrons[16] confirm the $O(3\sigma)$ data vs theory discrepancy for $(g-2)_\mu$. The decays $B \to D^{(*)}\tau\nu$ and $B \to \tau\nu$, potentially sensitive to new physics such as charged Higgses, show some anomaly, but the overall picture is not fully consistent with a BSM interpretation either. The 4σ isospin asymmetry in $K^{(*)}\mu^+\mu^-$ decays of charged and neutral B mesons is puzzling[60,62], but no firm conclusion can be drawn, due to highly uncertain SM predictions. Earlier evidence for CP violation in D decays has weakened[11], but it still large enough to challenge the (rather uncertain) SM predictions. Several observables are nevertheless available[56] to further test the origin of this effect, should it be confirmed.

Lack of direct evidence of new particle production at the Tevatron[63] and at the LHC[64,65] is starting to question the viability of several BSM models. In particular, the parameter space of highly constrained models, such as the constrained minimal supersymmetric SM (CMSSM), is being strongly reduced. It would be a mistake, however, to draw general conclusions on these theoretical frameworks. In a theory such as supersymmetry, the existence of a large number of a-priori free parameters to describe its symmetry breaking pattern makes it impossible to make general statements. One is forced to simplify the task of the searches by selecting benchmark

classes of models, parameterized by a reduced set of parameters. As the room left to these simpler classes of models gets reduced, the experimental searches start shifting to new benchmarks, whose manifestation can be more subtle and hard to detect. There is still a large room of exploration, and even more will be opened once the LHC restarts, at the higher energy. The whole picture was best summarized at the meeting by this statement[64]: "Physics beyond the SM did not show up yet. There is no need for preliminary conclusions. Lets continue our work and look were we havent looked so far". At a time when all theoretical wisdom on what lies beyond the SM seems to be challenged by the data, this sounds like a healthy pragmatic attitude.

The status of the CMSSM was reviewed[66]. In this framework, 125 GeV is a rather large value for the Higgs, and demands a heavy stop quark (in the TeV range), with a large mixing among the scalar partners of the left- and right-handed top quark, and a large overall mass scale for the squarks of the first two generations. Furthermore, the direct constraints on the gluino mass, setting it well above the TeV, imply large neutralino masses, and a limited range allowed for it to be the dark matter particle. Global fits, including direct limits as well as low-energy phenomenology (flavour physics) and dark matter, call for multi-TeV squarks and gluons, and for neutralino dark matter in the few-hundred to TeV range, accessible nevertheless to ton-scale detectors.

While the CMSSM is therefore still alive, I think it is fair to state that is has almost exhausted its value as a reference benchmark for direct searches. Less constrained (or otherwise constrained) supersymmetric models can easily loosen the constraints from DM and from the Higgs. There is therefore a strong motivation in exploring possible supersymmetric signals from models other than the CMSSM, as is being done with great investment of efforts and ingenuity by the LHC experiments.

6 Status of EWSB

The key questions raised at the time of the meeting concerned the real nature of the $\sim$ 126 GeV resonance: is it *a* Higgs boson? is it *the* Higgs boson? A Higgs boson can be defined as a scalar field, whose expectation value breaks spontaneously the $SU(2) \times U(1)$ symmetry. In the SM, the Higgs boson is furthermore constrained to be an elementary field (i.e. not composite), to be the member of a single $SU(2)_W$ doublet, and thus to be the only responsible for the masses of gauge bosons and of quarks and leptons. The highlight of the experimental contributions on the Higgs[67] was the proof that its decay distributions largely favour its scalar nature, relative to other possibilities (e.g. pseudoscalar, or tensor). It has been remarked[41] that, when modeling the lowest-dimension effective coupling of a spin-2 state, the coupling to the quarks and gluon currents must be kept equal, to avoid a unitarity-violating and unphysical growth of the cross-section at large p_T.

While this is very valuable information, I would not consider it as a breakpoint in our assessment of the nature of the $\sim$ 126 GeV resonance. After all, the data still do not prove that this is an elementary scalar, and we do know already of many CP-even scalars, among the hadronic states, which however have nothing to do with a Higgs boson. So the "scalar-ness" of the new particle is only a piece in the whole picture. In my view the strongest evidence that this particle is a Higgs boson comes from its couplings to gauge bosons, which follow precisely the pattern dictated by EWSB. A generic gauge-invariant coupling, would not reproduce the experimental observation of the hierarchy of couplings, namely $g(H\gamma\gamma) \ll g(HWW) \sim g(HZZ)$ and $g(HZ\gamma) \ll g(HWW)$. For example, a gauge invariant coupling like the following (see e.g. [68,69] for a more exhaustive discussion):

$$\begin{aligned} L_H &= k_W\, H W^a_{\mu\nu} W^{\mu\nu}_a + k_B\, H B_{\mu\nu} B^{\mu\nu} \\ &= 2k_W\, H W^+_{\mu\nu} W^{-\mu\nu} + (k_B + k_W)\, H F_{\mu\nu} F^{\mu\nu} \end{aligned}$$

$$+ \quad \left(k_W \frac{c_W^2}{s_W^2} + k_B \frac{s_W^2}{c_W^2} \right) H Z_{\mu\nu} Z^{\mu\nu} + \left(k_W \frac{c_W}{s_W} + k_B \frac{s_W}{c_W} \right) H F_{\mu\nu} Z^{\mu\nu} \qquad (1)$$

would require $k_B \sim k_W$ at the percent level, in order to agree with the observation $B(\gamma\gamma) \sim 10^{-2} B(WW^*)$. As a result, we would have:

$$L_H = 2 k_W \, H W^+_{\mu\nu} W^{-\mu\nu} \; + \; \frac{k_W}{c_W s_W} H F_{\mu\nu} Z^{\mu\nu} \; + \; \ldots \qquad (2)$$

and $B(Z\gamma) = O[B(WW^*)]$, in clear contradiction with the existing limits [70] on $B(Z\gamma)$. In my view, this is the strongest experimental evidence we have that this particle is related to EWSB, and it is therefore legitimate to assume it is a Higgs boson. Alternative interpretations must explain the observed hierarchy of Higgs couplings to gauge boson pairs and, in those specific frameworks, explain what else if not this particle breaks EW symmetry, and how EW precision tests are satisfied. I am not aware of any compelling such alternative framework, and certainly none was shown at this meeting.

As the precision of the measurements improves, initial deviations of the measured branching ratios from their SM values become weaker. The residual differences of the results of ATLAS and CMS from the SM are no bigger than the differences between the results of the two experiments, and are thus diluted after a naive combination of the two sets of data. This is true, for example, of the combined ratios $\mu = (\sigma \times BR)_{exp}/(\sigma \times BR)_{SM}$, for which ATLAS reported a value of $\mu = 1.30 \pm 0.18$, and CMS $\mu = 0.88 \pm 0.21$. While we should all be patient and wait for an official combination by the experiments, I think it is safe to assume that the final average will be consistent with $\mu = 1$ within the overall uncertainty. And the same will likely be true of the rates into individual final states, as well as of the mass.

Given the large overall uncertainties, nevertheless, there is clearly room for deviations to be detected with the future studies and larger statistics. Theoretical work is therefore ongoing, to set up the appropriate formalism to parameterize and interpret possible anomalies. Many examples of this work were discussed during the meeting: tools for trustworthy generation of Higgs look-alikes [41]; parameterizations of non-SM couplings, used in fits of the current data [71], and in handy analytical formulae for rates induced by non-SM couplings [72]; discrimination between composite and elementary Higgs [73]; analysis of J^{PC} [74]; implications for 2-Higgs-doublet models [75]; flavour implications of extended Higgs sectors [76].

7 Concluding remarks

The observation of a Higgs boson opens a new era for particle physics. Its apparent consistency with the SM Higgs boson is, on one side, a remarkable confirmation of an apparently naive theoretical setup, formulated over 40 years ago, to explain the consistency of EW symmetry with the gauge boson and fermion masses. On the other, the complete lack of evidence for new physics makes more concrete and urgent the understanding of the naturalness of the EW scale, whose stability relies, in the context of the SM, on an incredible amount of fine tuning. Very precise measurements of the Higgs properties, and a continued search for signals of BSM physics, will drive our field for many years to come. Both directions will demand an increased precision in both the experimental analyses and in the theoretical tools used for their interpretation. The broad spectrum of progress on both fronts, illustrated by many contributions to this meeting, are an encouraging indication that the community is determined, ready and capable to tackle such a gigantic challenge!

Acknowledgments

I am grateful to the organizers for the invitation to give this summary and for setting up such an exciting agenda, and I thank and praise all participants for sharing with us very inspiring material!

References

1. D. Denisov, Experimental Summary talk.
2. A.Koshelkin
3. M.Djuric
4. A.Bylinkin
5. E.Meggiolaro
6. A.Lusiani
7. R.Polifka
8. P.Roig
9. E.Bouhova-Thacker
10. R.Covarelli
11. S.Stahl
12. G.Manca
13. P.Krokovny
14. D.Wei, C.Ji, U.Tamponi
15. J.Wang
16. P.Moskal, K.Griessinger
17. G. 't Hooft, G. Isidori, L. Maiani, A. D. Polosa and V. Riquer, Phys. Lett. B **662** (2008) 424 [arXiv:0801.2288 [hep-ph]].
18. S. Weinberg, arXiv:1303.0342 [hep-ph].
19. M. Ablikim *et al.* [BESIII Collaboration], arXiv:1303.5949 [hep-ex].
20. Z. Q. Liu *et al.* [Belle Collaboration], arXiv:1304.0121 [hep-ex].
21. B.Hippolyte
22. Y.Pandit, H.Ke, S.Y.Li.
23. O.Busch
24. I.Grabowska-Bold
25. Y.Mao
26. B.Zakharov, E.Iancu
27. F.Fionda
28. Q.Wang, A.Andreazza, J-F.Grosse-Oetringhaus
29. K.Dusling
30. X.He, J.Bielcik
31. E.Kryshen
32. C.Deans, S.Carrazza, R.Placakyte
33. K.Rabbertz
34. S.Camarda, K.Theofilatos
35. D.Kawall
36. M.Wobisch
37. L.Bellantoni, R.Lafaye
38. J.Pires
39. F.Hautmann
40. G.Luisoni, M.S.Zidi
41. M.Zaro
42. S.Sapeta
43. S.Alioli
44. J.Kim
45. B.Fuks
46. V.Lombardo
47. E.Izaguirre
48. D.Orbaker
49. E.Yazgan

50. M.Aoki
51. C. Schwanenberger
52. Y.Oksuzian, H.Zhang
53. G.Petrillo
54. M.Baak
55. D.Straub
56. D.Atwood
57. J.Bernabeu
58. M.Piccini
59. S.Leo
60. A.Golutvin
61. W.Hulsbergen
62. E.Ben Haim
63. J.Nett
64. A.Favareto
65. A.Mann, P.Everaerts, S.Harper, H.Stelzer, J.Chou
66. L. Roszkowski
67. M.Cooke, M.Boehler, E.Mountricha, C.Ochando, D.Puigh, T.Adye, A.Whitbeck
68. I. Low, J. Lykken and G. Shaughnessy, Phys. Rev. D **86** (2012) 093012 [arXiv:1207.1093].
69. M. E. Peskin, arXiv:1208.5152.
70. T.Adye
71. B.Dumont
72. L.Carpenter
73. A.Kaminska
74. M. Muehlleitner
75. R.Santos
76. M.Rebelo

List of Participants

Family name	First name	Institution	Country	Email address
Adye	Tim	Rutherford Appleton Lab. STFC	UK	T.J.Adye@rl.ac.uk
Alioli	Simone	LBNL	USA	salioli@lbl.gov
Andreazza	Attilio	Università degli Studi di Milano INFN	Italy	Attilio.Andreazza@mi.infn.it
Antos	Jaroslav	Institute of Experimental Physics SAS	Slovakia	antos@saske.sk
Aoki	Masato	Nagoya University KMI	Japan	masato.aoki@cern.ch
Artuso	Marina	Syracuse University	USA	artuso@physics.syr.edu
Atoui	Mariam	LPC Clermont	France	matoui@in2p3.fr
Atwood	David	Iowa State University	USA	atwood@iastate.edu
Augé	Étienne	Université Paris-Sud	France	etienne.auge@lal.in2p3.fr
Augustin	Jean-Eudes	LPNHE	France	augustin@in2p3.fr
Baak	Max	CERN	Switzerland	mbaak@cern.ch
Barabanov	Mikhail	JINR	Russia	barabanov@jinr.ru
Bellantoni	Leo	Fermilab	USA	bellanto@fnal.gov
Belloni	Alberto	University of Maryland	USA	alberto.belloni@cern.ch
Ben Haim	Eli	LPNHE	France	benhaim@in2p3.fr
Bernabeu	Jose	IFIC - Valencia	Spain	jose.bernabeu@uv.es
Bielcik	Jaroslav	Czech Technical University FNSPE	Czech Republic	jaroslav.bielcik@fjfi.cvut.cz
Blekman	Freya	Vrije Universiteit	Belgium	freya.blekman@cern.ch
Boehler	Michael	Albert-Ludwigs Universität	Germany	michael.boehler@cern.ch
Bouhova-Thacker	Evelina	Lancaster University	UK	e.bouhova@cern.ch
Busch	Oliver	Universitaet Heidelberg	Germany	o.busch@gsi.de
Bylinkin	Alexander	ITEP	Russia	alexander.bylinkin@gmail.com
Camarda	Stefano	DESY	Germany	stefano.camarda@desy.de
Carpenter	Linda	Ohio State University	USA	lmc@physics.osu.edu
Carrazza	Stefano	Università di Milano	Italy	stefano.carrazza@mi.infn.it
Castro	Nuno	LIP	Portugal	Nuno.Castro@cern.ch
Chou	John Paul	Rutgers University	USA	johnpaul@physics.rutgers.edu
Cooke	Michael	Fermilab	USA	mpc@fnal.gov
Covarelli	Roberto	University of Rochester	USA	roberto.covarelli@cern.ch
Deans	Christopher	University of Edinburgh	UK	c.s.deans@sms.ed.ac.uk
Dell'Acqua	Andrea	CERN	Switzerland	dellacqu@mail.cern.ch
Denisov	Dmitri	Fermilab	USA	denisovd@fnal.gov
Djuric	Marko	Universidade do Porto	Portugal	djuric@fc.up.pt
Dumont	Béranger	LPSC	France	dumont@lpsc.in2p3.fr
Dusling	Kevin	North Carolina State University	USA	kdusling@gmail.com
Everaerts	Pieter	UCLA	USA	pieter.everaerts@cern.ch
Favareto	Andrea	Università degli Studi di Milano INFN	Italy	andrea.favareto@cern.ch
Fionda	Fiorella	Università di Bari INFN	Italy	fiorella.fionda@ba.infn.it
Fuks	Benjamin	CERN	Switzerland	fuks@cern.ch
Golutvin	Andrey	Imperial College	UK	andrey.goloutvin@cern.ch
Grabowska-Bold	Iwona	AGH Univ. of Science & Technology	Poland	Iwona.Grabowskabold@gmail.com
Griessinger	Konrad	Mainz Univ. - Inst. Nuclear Physics	Germany	griess@slac.stanford.edu
Grosse-Oetringhaus	Jan Fiete	CERN	Switzerland	jgrosseo@cern.ch
Guimarães da Costa	João	Harvard University	USA	guimaraes@physics.harvard.edu
Gurrola	Alfredo	Vanderbilt University	USA	Alfredo.Gurrola@cern.ch
Harper	Sam	Rutherford Appleton Lab.	UK	sam.james.harper@cern.ch
Harz	Julia	DESY	Germany	julia.harz@desy.de
Hautmann	Francesco	Oxford University	UK	francesco.hautmann@cern.ch
He	Xiaochun	Georgia State University	USA	xhe@gsu.edu
Heintz	Ulrich	Brown University	USA	ulrich_heintz@brown.edu
Hippolyte	Boris	IPHC	France	hippolyt@in2p3.fr
Hulsbergen	Wouter	Nikhef	The Netherlands	wouter.hulsbergen@nikhef.nl
Iancu	Edmond	CEA Saclay IPhT	France	edmond.iancu@cea.fr
Igonkina	Olga	Nikhef	The Netherlands	Olga.Igonkina@nikhef.nl
Izaguirre	Eder	Perimeter Institute for Th. physics	Canada	eizaguirre@perimeterinstitute.ca
Ji	Changsheng	IHEP	China	jcs@mail.ustc.edu.cn
Kaminska	Anna	Rudolf Peierls Centre for Th. Physics	UK	anna.kaminska@fuw.edu.pl
Kawall	David	University of Massachusetts	USA	kawall@physics.umass.edu
Ke	Hongwei	Central China Normal University	China	kehw@rcf.rhic.bnl.gov
Kim	Jihun	CEA Saclay DSM /IPhT	France	jihuni@phya.snu.ac.kr
Klima	Boaz	Fermilab	USA	klima@fnal.gov
Koshelkin	Andrey	Moscow Inst. Physics & Engineering	Russia	a_kosh@internets.ru
Krawczyk	Maria	University of Warsaw	Poland	krawczyk@fuw.edu.pl
Krokovny	Pavel	Budker Institute of Nuclear Physics	Russia	krokovny@inp.nsk.su
Kryshen	Evgeny	Petersburg Nuclear Physics Institute	Russia	evgeny.kryshen@cern.ch
Kuhn	Maria	CERN	Switzerland	maria.kuhn@cern.ch

Lafaye	Remi	LAPP	France	remi.lafaye@lapp.in2p3.fr
Landsberg	Greg	Brown University	USA	landsberg@hep.brown.edu
Lenzi	Bruno	CERN	Switzerland	Bruno.Lenzi@cern.ch
Leo	Sabato	Università di Pisa	Italy	sabato.leo@gmail.com
Li	Shi-Yuan	Shandong University	China	lishy@sdu.edu.cn
Lombardo	Vincenzo	LAPP	France	vincenzo.lombardo@cern.ch
Lu	Cai-Dian	IHEP	China	lucd@ihep.ac.cn
Luisoni	Gionata	Max Planck Institute for Physics	Germany	luisonig@mpp.mpg.de
Lusiani	Alberto	Scuola Normale Superiore INFN	Italy	alberto.lusiani@pi.infn.it
Manca	Giulia	University of Cagliari	Italy	giulia.manca@cern.ch
Mangano	Michelangelo	CERN	Switzerland	michelangelo.mangano@cern.ch
Mann	Alexander	Ludwig-Maximilians-Univ. München	Germany	a.mann@lmu.de
Mao	Yaxian	Vanderbilt University	USA	yaxian.mao@vanderbilt.edu
Martinez	Homero	CEA Saclay IRFU/SPP	France	homero.martinez-bruzual@cea.fr
Meggiolaro	Enrico	Università di Pisa	Italy	enrico.meggiolaro@df.unipi.it
Moskal	Pawel	Jagiellonian University	Poland	p.moskal@uj.edu.pl
Mountricha	Eleni	Brookhaven National Lab	USA	Eleni.Mountricha@cern.ch
Muehlleitner	Margarete	KIT	Germany	margarete.muehlleitner@kit.edu
Mulhearn	Michael	University of California	USA	mulhearn@physics.ucdavis.edu
Narain	Meenakshi	Brown University	USA	Meenakshi_Narain@brown.edu
Nett	Jason	Texas A&M University	USA	jnett80@fnal.gov
Ochando	Christophe	Lab. Leprince Ringuet	France	ochando@llr.in2p3.fr
Oksuzian	Yuri	University of Virginia	USA	oksuzian@fnal.gov
Orbaker	Douglas	University of Rochester	USA	dorbaker@pas.rochester.edu
Pandit	Yadav	University of Illinois	USA	ypandit@uic.edu
Petrillo	Gianluca	University of Rochester	USA	petrillo@fnal.gov
Piccini	Mauro	INFN	Italy	Mauro.Piccini@pg.infn.it
Pietrzyk	Bolek	LAPP	France	pietrzyk@lapp.in2p3.fr
Pires	João	ETH	Switzerland	pires@itp.phys.ethz.ch
Placakyte	Ringaile	DESY	Germany	ringaile@mail.desy.de
Polifka	Richard	Charles University	Czech Republic	richard.polifka@cern.ch
Puigh	Darren	Ohio State University	USA	darren.michael.puigh@cern.ch
Qian	Wenbin	LAPP	France	WENBIN.QIAN@CERN.CH
Rabbertz	Klaus	Inst. Experimentelle Kernphysik - KIT	Germany	klaus.rabbertz@cern.ch
Rangel Smith	Camila	LPNHE	France	crangel@cern.ch
Rebelo	Margarida	Centro de Fisica Teórica de Partículas	Portugal	rebelo@ist.utl.pt
Rimoldi	Adele	Università di Pavia	Italy	adele.rimoldi@cern.ch
Roig	Pablo	Univ. Autonoma de Barcelona IFAE	Spain	proig@ifae.es
Roszkowski	Leszek	National Centre for Nuclear Research	Poland	leszek@fuw.edu.pl
Santos	Rui	ISEL	Portugal	rsantos@cii.fc.ul.pt
Sapeta	Sebastian	IPPP	UK	sebastian.sapeta@durham.ac.uk
Schwanenberger	Christian	University of Manchester	UK	schwanen@fnal.gov
Skwarnicki	Tomasz	Syracuse University	USA	tomasz@physics.syr.edu
Stahl	Sascha	Physikalisches Institüt	Germany	sstahl@physi.uni-heidelberg.de
Stelzer	Joerg	Michigan State University	USA	stelzer@cern.ch
Stone	Sheldon	Syracuse University	USA	stone@physics.syr.edu
Straub	David	Johannes Gutenberg Universität	Germany	david.straub@uni-mainz.de
Tamponi	Umberto	Università di Torino	Italy	tamponi@to.infn.it
Tan	Chung-I	Brown University	USA	Tan@het.brown.edu
Theofilatos	Konstantinos	ETH	Switzerland	konstantinos.theofilatos@cern.ch
Thomas	Marc	University of Southampton	UK	mct1g11@soton.ac.uk
Tokarev	Ilya	Moscow State University	Russia	tokarev.ilya.msu@gmail.com
Tran Thanh Van	Jean		France	jtrantv@gmail.com
Wang	Jianxiong	IHEP	China	jxwang@ihep.ac.cn
Wang	Quan	University of Kansas	USA	quan.wang@cern.ch
Wei	Daihui	Guangxi Normal University	China	weidh@ihep.ac.cn
WennersHerron	Ashley	Fermilab CERN	USA	ashley.wh@cern.ch
Whitbeck	Andrew	Johns Hopkins University	USA	whitbeck@pha.jhu.edu
Wobisch	Markus	Louisiana Tech University	USA	wobisch@fnal.gov
Yang	Yongxu	Guangxi Normal University	China	yyxu@mailbox.gxnu.edu.cn
Yazgan	Efe	University of Ghent	Belgium	efe.yazgan@cern.ch
Zakharov	Bronislav	LD Landau Institute for Th. Physics	Russia	bgz@itp.ac.ru
Zaro	Marco	Université Catholique de Louvain CP3	Belgium	marco.zaro@uclouvain.be
Zhang	Hao	Argonne National Lab.	USA	haozhang.pkuphy@gmail.com
Zidi	Mohamed Sadok	LAPTh	France	zidi@lapp.in2p3.fr

Dépôt légal : septembre 2013
COPYMÉDIA
Achevé d'imprimer
en septembre 2013 par
www.copy-media.net
CS 20023 - 33693 MÉRIGNAC CEDEX